Geology and genesis of the Lewis Ponds carbonate and volcanic-hosted massive sulfide deposits, New South Wales, Australia

Michael W. Agnew

B.Sc. Hons

UNIVERSITY OF TASMANIA

Submitted as fulfilment of the requirements
for the degree of Doctor of Philosophy

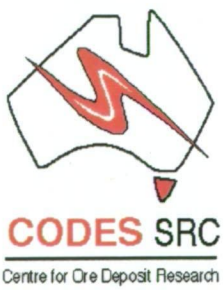

School of Earth Sciences
University of Tasmania
June, 2003

Declaration

This thesis contains no material that has been accepted for the award of a degree or diploma at any other institution. To the best of the authors' knowledge, this thesis contains no material previously written or published by another person, except where due acknowledgement is made in the text. All referenced material is listed at the back of the thesis.

M. Agnew
Michael Agnew

10/11/03
Date

Authority of access

This thesis is available for loan or limited photocopying in accordance with the *Copyright Act* of 1968.

M. Agnew
Michael Agnew

10/11/03
Date

Abstract

The Lewis Ponds carbonate and volcanic-hosted Zn-Pb-Cu-Ag-Au-rich massive sulfide deposits are located near the western margin of the Hill End Trough, in the eastern Lachlan Fold Belt of New South Wales. Two stratabound massive sulfide zones, Main and Toms occur in a tightly folded Late Silurian marine succession of volcaniclastic sandstone, polymictic breccia, limestone-clast breccia, siltstone and mudstone. They have a combined indicated resource of 5.7 Mt, grading 3.5% Zn, 2.0% Pb, 0.19% Cu, 97 g/t Ag and 1.9 g/t Au. Main zone occurs within a thick unit of poorly-sorted mixed provenance breccia, limestone-clast breccia and pebbly-granular sandstone, whereas Toms zone is hosted by siltstone. The sedimentary rocks unconformably overlie a thick succession of quartz-plagioclase phyric dacite and strongly foliated, chlorite-sericite-altered dacite.

Variably recrystallised fossiliferous limestone occurs throughout the Lewis Ponds host sequence in thick, tabular units of poorly-sorted breccia and fault-bound lenses of megabreccia. Limestone clasts vary in size from small pebbles to 90 m boulders. The mixed provenance breccia, limestone-clast breccia and sandstone were deposited in a moderately deep water, below wave-base slope environment, around the margins of a high-level intrusive dacite centre. Detrital volcanic and sedimentary components were derived from multiple source areas within the basin and in the adjacent hinterland.

The massive sulfide lenses occur along the eastern limb of a regional-scale D_1 anticline. The adjacent syncline has been partly truncated by a 200-250 m wide, NNW-trending high strain zone termed the *Lewis Ponds fault*. Syn-tectonic quartz ± sulfide veins and steeply dipping, anastomosing shear zones surround the Toms massive sulfide lens. The variably folded and boudinaged quartz veins resulted from periodic brittle shear failure and extension during and after the D_1 deformation. Pinch-and-swell structures, boudins, catalcastic breccia and kink folds occur in the massive sulfide. Main zone, located west of the fault is significantly less deformed than Toms zone. However, reversals in stratigraphic facing and vergence indicate that tight parasitic folds occur in the Main zone host sequence. Mineralisation at Lewis Ponds probably pre-dated shearing along the Lewis Ponds fault.

An asymmetric, semiconformable Mg-Fe-Ca-Ba-rich hydrothermal alteration envelope surrounds the massive sulfide lenses. Mg-chlorite occurs at the top the footwall volcanic succession south of Main zone and grades outwards into a weak pervasive sericite-quartz ± Fe-Mg-chlorite assemblage. The compositions of recrystallised phyllosilicates vary systematically with whole rock geochemistry, alteration intensity and proximity to the Toms massive sulfide lens. Hydrothermal alteration of dacite in the Toms zone footwall involved

MgO, Fe_2O_3, K_2O and Ba enrichment and Na_2O, CaO and Sr depletion. The addition or removal of SiO_2 contributed to net gains of 0-75 g/100g in dacite C and net losses of 0-50 g/100g in dacite A, except where MgO and Fe_2O_3 gains offset the loss of SiO_2. In contrast, weak sericite-chlorite-calcite alteration of coherent dacite in the Main zone footwall led to net losses of 10-40 g/100g.

Conformable, texturally destructive alteration assemblages associated with the two mineralised zones include dolomite-chlorite-talc, chlorite-pyrite, quartz-dolomite-chlorite and quartz-sericite ± hyalophane. Dolomite, Mg-chlorite, talc, phlogopite, calcite, quartz and sulfides have overprinted the clasts and matrix in the breccia and sandstone units in Main zone. Relict crinoid fossils are preserved in even the most intensely altered rocks, where dolomite, chlorite and talc have replaced the original calcite. Irregular honeycomb vuggy and botryoidal sulfide-dolomite textures in the breccia and sandstone units indicate dissolution and precipitation of dolomite during mineralisation.

Dolomite associated with the massive sulfide lenses is characterised by low $\delta^{18}O_{VSMOW}$ (6 to 16‰) and $\delta^{13}C_{VPDB}$ (-11 to 0‰) values relative to the regional fossiliferous limestone. Fluid inclusion and stable isotope data indicate that the dolomite precipitated from a low temperature (166-232°C for 1 000 m water depth), weakly saline (1.4 to 7.7 eqiv wt % NaCl) fluid, possibly depleted in O and C isotopes ($\delta^{18}O$ = -2.5 to 0.3‰, $\delta^{13}C$ = -14 to -4‰). The dolomite probably formed during diagenesis and hydrothermal alteration, by fluid-rock interactions between evolved seawater at 150-250°C and the limestone-bearing host sediment, and/or mixing between evolved seawater at 350°C and a seawater-dominant pore fluid at 100°C.

The massive sulfide lenses consist of pyrite, sphalerite and galena, with subordinate tetrahedrite, chalcopyrite, arsenopyrite, pyrrhotite, stannite, pyrargyrite and electrum. Paragenetically early framboidal, dendritic, reticulate, botryoidal and spongy Fe-sulfide aggregates and bladed pyrrhotite pseudomorphs of sulfate occur throughout the breccia and sandstone beds that host Main zone, but are rarely preserved in the coarse grained, annealed massive sulfide in Toms zone. Pre-tectonic carbonate-chalcopyrite-pyrite veins in the footwall volcanic succession, immediately south of Toms zone may represent a stringer zone displaced from the Toms massive sulfide lens. The stringer veins also contain native bismuth, sphalerite and Se-Bi-Ag-rich galena.

Sulfur isotope values in the massive sulfide ($\delta^{34}S$ = 1.7-5.0‰) and footwall stringer veins ($\delta^{34}S$ = 3.9-7.4‰), indicate that the hydrothermal fluid contained a homogenous mixture of magmatic S, derived from the host volcanics rocks and reduced seawater sulfate. The lower

average $\delta^{34}S$ values in the massive sulfide lenses may have resulted from a component of partially reduced seawater sulfate or biogenic S, leached out of the host sediment.

Textural, geochemical and isotopic data indicate that the Main zone massive sulfide lenses formed by lateral fluid flow and sub-sea floor replacement of the poorly-sorted, carbonate-bearing breccia and sandstone beds. Low temperature dolomitisation of the carbonate-bearing sediment during diagenesis created secondary pore spaces and provided a reactive host for fluid-rock interactions. Base metal sulfides, chlorite, dolomite, calcite, quartz and talc filled pore spaces throughout the carbonate-altered breccia and sandstone units. Toms zone probably formed in fine-grained sediment at or near the sea floor, above a zone of focused up-flowing hydrothermal fluids.

Pyrite, pyrrhotite, sphalerite, galena, tetrahedrite and electrum precipitated from a relatively low temperature 150-250°C, reduced hydrothermal fluid. Paragenetically early dendritic, reticulate and spongy Fe-sulfide aggregates in the Main zone host sequence formed by rapid mixing between the hydrothermal fluid and cooler pore fluids in the matrix of the breccia and sandstone. Base metal sulfide deposition in Main zone probably resulted from fluid mixing, dissolution of dolomite and increased fluid pH. Galena, sphalerite and chalcopyrite overprinted the primitive Fe-sulfide textures. As the hydrothermal system intensified, a high temperature >280°C, strongly reduced fluid carrying Sn, Cu, Se and Bi was sourced from deep within the footwall volcanic succession. Carbonate-chalcopyrite-pyrite stringer veins and dolomite-chalcopyrite-pyrite-stannite veins formed in the Footwall Copper zone and Toms zone Central lens respectively. Chalcopyrite partly replaced the Zn-Pb-rich massive sulfide in Main zone.

During the D_1 deformation, fracture-controlled fluids remobilised sulfides into syn-tectonic, quartz and carbonate veins within the Lewis Ponds fault zone and adjacent footwall volcanic succession, resulting in extensive Cu, Au and Zn anomalies. Massive sulfide remobilisation may have occurred over tens to hundreds of metres. Talc, quartz-sericite, chlorite and Fe-Mg-Mn-carbonate assemblages overprinted the dolomite, chlorite and sericite-altered rocks in the Toms zone host sequence.

Lewis Ponds is an unusual stratabound, carbonate and volcanic-hosted massive sulfide deposit. The intimate spatial association between fossiliferous limestone, hydrothermal carbonate and base metal sulfides at Lewis Ponds provides a basis for new exploration targets in Siluro-Devonian marine successions elsewhere in New South Wales.

Acknowledgements

This research was funded by Tri Origin, the Australian Research Council and the Centre for Ore Deposit Research, University of Tasmania. For their respective contributions, I am most grateful.

This project would not have been possible without the generous financial support of Tri Origin Australia NL and Tri Origin Exploration Ltd. My sincerest thanks to Mr Bernard Roe and Dr Robert Valliant, who provided the maps, drill hole information, assays, geochemical data and field support required for the project and a guided tour of the Lewis Ponds prospect. I have enjoyed working on this challenging massive sulfide deposit. Thanks also to Rob Payne and Peter Spicer for supplying field equipment and for helping me shift the heavy core trays.

I would like to sincerely thank my two supervisors; Professor Ross Large and Dr Stuart Bull for their guidance, enduring patience and enthusiasm during the past four years. I have been privileged to share their wealth of knowledge on volcanic successions and massive sulfide deposits. The following staff are also thanked for assisting me in the field, reviewing chapters and/or providing stimulating geological discussions: Wally Herrmann, Robert Scott, Mike Solomon, Gary Davidson, Tony Crawford, and Ron Berry. Thanks especially to Robert Scott for helping me with the structural model.

My close friends and fellow PhD students at the University of Tasmania are thanked for their support, guidance and words of wisdom.

I extend my gratitude to the technical support and administrative staff at the School of Earth Sciences and CODES; Simon, June, Phil, Alistair, Katie, Di, Nilar and Peter for all of your assistance. A special thank you to Dr David Steele at the Electron Microscopy Facility, Central Science Laboratory for teaching me how to use the electron microprobe and enabling me to analyse sulfides using high detection limits.

Finally, to my parents, Betty and David, thank you for providing continued loving support and encouragement throughout my career. Without both of you, I would not have achieved my goals.

Table of Contents

List of figures

CHAPTER 1

INTRODUCTION

1.1 Preamble

Submarine volcanic successions host various types of precious and base metal rich deposits. These include "classical" sea floor exhalative volcanic hosted massive sulfide (VHMS) deposits, intrusion-related replacement deposits with transitional VHMS and high sulfidation epithermal characteristics, carbonate-hosted massive sulfide deposits and shallow water, Au-rich, stratabound replacement deposits. In the submarine environment, volcanic facies architecture, water depth, syn-volcanic structures, hydrothermal fluid chemistry and fluid temperature control the overall morphology, mineralogy and metal content of VHMS deposits (Sillitoe et al., 1996; Gibson et al., 1999; Hannington et al., 1999a; Hannington et al., 1999c; Large et al., 2001a). Zinc-rich, sea floor massive sulfide lenses and discordant, pipe-like Cu-Au deposits occur in volcanic successions dominated by lavas, volcaniclastic rocks and/or shallow subvolcanic intrusions. Porous volcanic facies host polymetallic, sheet-style replacement deposits (Gibson et al., 1999; Large et al., 2001a). Massive sulfide deposits undergo varying degrees of post-depositional metamorphism and remobilisation during diagenesis, basin inversion, regional deformation and orogenic granite emplacement. These processes may obscure or even destroy the primary mineralogy, mineral textures, paragenetic relationships and geochemical trends (Huston et al., 1995; Khin Zaw et al., 1999; Hutchinson, 2000; Marshall et al., 2000; Herrmann and Hill, 2001).

Water depth influences the metal content of the deposit and volcanic facies architecture of the host sequence (Takahashi and Suga, 1974; Huston and Large, 1989; Sillitoe et al., 1996; Gibson et al., 1999). At depths of less than 1 500 m, sub-sea floor boiling of the hydrothermal fluid tends to produce epithermal-like accumulations with high precious to base metal ratios rather than sea floor massive sulfide mounds (Herzig and Hannington, 1995; Hannington and Herzig, 2000). Many ancient shallow water VHMS deposits lack chemical and physical evidence for boiling (eg. Huston and Large, 1989; Sainty, 1992; Halley and Roberts, 1997). Instead, palaeogeographic reconstructions rely on the occurrence of shallow marine sedimentary structures, marine faunal assemblages and pyroclastic textures (Table 1.1). However, limestone and pyroclastic facies are not necessarily indicative of water depth (Cas, 1992; Gibson et al., 1999; Huston and Cas, 2000). Fossiliferous limestone and shallow

marine faunal assemblages have to be in situ. Non-welded pyroclastic units may accumulate at considerable depths (>1 000 m) due to re-sedimentation of pre-existing debris or non-explosive quench fragmentation of vesiculated lava.

Deposit	Water Depth	Evidence	Comments	Reference
Mt Chalmers, Queensland	100-200 m	Shallow faunal assemblage and pumiceous peperite	In situ trace fossils located at ore equivalent horizon; exhalative deposit	Large and Both (1980); Sainty (1992); Hunns and McPhie (1999)
Henty, Tasmania	"Shallow"	Fossiliferous limestone lenses and welded ignimbrite	Hydrothermal and sedimentary carbonate; replacement deposit	Halley and Roberts (1997); Callaghan (2001)
Lyell-Comstock, Tasmania	Below wave-base	Fossiliferous limestone lenses, polymictic breccia and limestone-clast breccia	Hydrothermally altered and mineralised limestone and breccia; exhalative and replacement origin	Jago et al., (1972); Corbett (2001)
Dresser, Western Australia	50 m	Stromatolites, evaporites and sedimentary structures	Associated with silicified sinters and chert-barite veins; exhalative	Nijman et al., (1998)
Selbaie, Québec	Very shallow to subaerial	Thick sequence of welded tuffaceous rocks	Inferred submarine, intracaldera setting; replacement deposit	Larson and Hutchinson (1993)
Horne, Québec	<500 m	Cryptodomes comprising highly vesicular coherent facies and peperite and abundant volcaniclastic deposits	Authors acknowledge that evidence is equivocal; replacement origin	Kerr et al., (1993)
Boliden, Sweden	Initially above storm wave-base, then below	Erosion of exposed dacite intrusion and overlying pyroclastic deposits	Occurs close to intervals of shallow water to subaerial facies associations; epigenetic deposit	Allen et al., (1996b)
Eskay Creek, British Columbia	Shallow to subaerial	Welded ash flow tuff, terrestrial plant fossils	Bimodal volcanic succession of pillow basalt, rhyolite flows and domes, hyaloclastite and mudstone; exhalative deposit	Macdonald et al., (1996)

Table 1.1 Ancient shallow water VHMS deposits where depositional depth is constrained by the lithofacies. Modified from Huston and Cas (2000).

Massive and brecciated limestone facies occur in shallow and deep water settings adjacent to volcanic edifices and along the margins of sedimentary basins. Coral reef terraces commonly surround actively forming volcanic islands in water depths of 0-1 500 m (Moore and Clague, 1992). Collapse of the submarine terraces may produce large quantities of fossiliferous limestone debris. On Lihir Island, Indonesia, raised fringing reefs adjacent to the Ladolam Au deposit are absent from the collapsed margin of the Luise Caldera (Moyle et al., 1990), indicating that volcaniclastic mass flows have re-deposited limestone debris further down-slope. Late Silurian stratabound polymetallic massive sulfide deposits in New South Wales, Australia commonly occur in close proximity to fossiliferous limestone and felsic volcanic rocks (Stanton, 1955; Stevens, 1974; Davis, 1990).

Lewis Ponds is an unusual stratabound, Zn-Pb-Cu-Ag-Au-rich massive and disseminated base metal sulfide deposit, located 190 km northwest of Sydney in central western New South Wales (Fig. 1.1). Massive sulfide lenses are hosted in a strongly deformed, Late Silurian felsic volcanic and marine sedimentary succession. The mineralised zones are spatially associated with variably recrystallised, fossiliferous limestone, siltstone and hydrothermal carbonate. These deposits overlie a thick, massive succession of strongly foliated quartz phyric volcanics previously interpreted as lava flows, intrusions and pyroclastic or epiclastic facies (Australian Geophysical report, 1965; Shepherd, 1972; Castle, 1976; Valliant and Meares, 1998). Valliant and Meares (1998) provided the most recent published interpretation of the Lewis Ponds deposits. They suggested that the massive sulfide lenses formed on the sea floor, in shallow basins bound by limestone reefs or syn-volcanic growth faults.

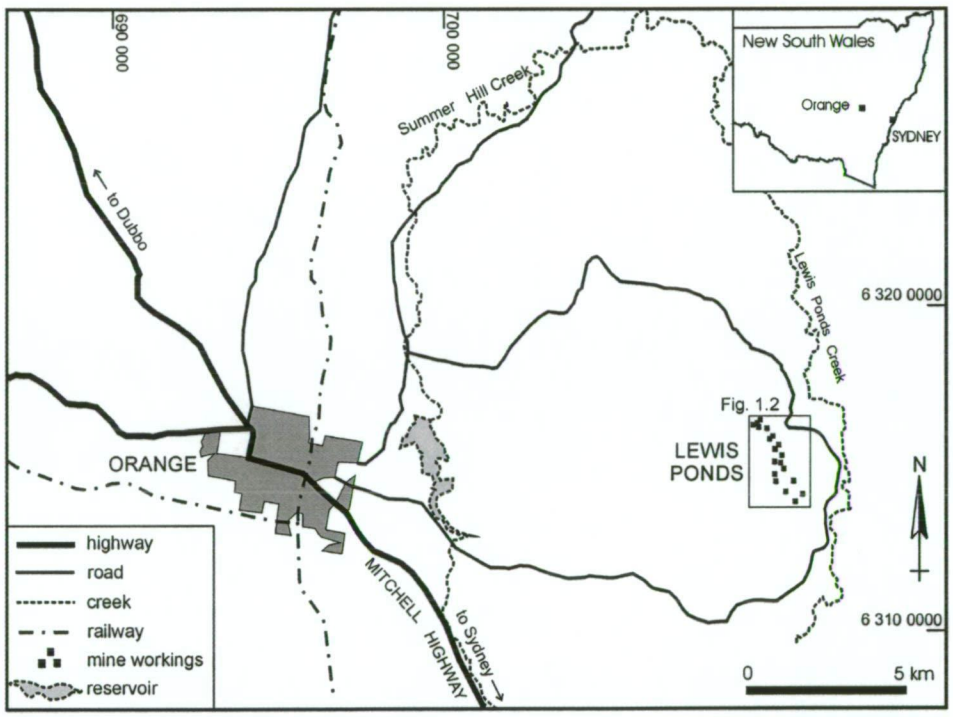

Figure 1.1 Locality map of Lewis Ponds and the Orange district. Compiled from the following base maps: Orange 1:25 000 topographic map, 8731-3-N, second edition; and Fremantle 1:25 000 topographic map, 8731-2-N, second edition, Central Mapping Authority of New South Wales. Australian Map Grid.

The Lewis Ponds prospect is at an advanced stage of exploration. Tri Origin NL, the operating company, has completed approximately 50 000 m of resource definition and exploration diamond drilling. Two stratabound massive sulfide lenses, Main and Toms zones have been delineated (Table 1.2). These have a combined indicated resource of 5.7 Mt, grading 3.5% Zn, 2% Pb, 0.19% Cu, 97 g/t Ag and 1.9 g/t Au (Tri Origin pers comm., 2002). Main zone consists of 4.9 Mt, grading 2.7% Zn, 1.3% Pb, 0.16% Cu, 78 g/t Ag and 1.93 g/t Au. Toms zone, although volumetrically smaller (0.8 Mt), has significantly higher Zn, Pb, Cu and Ag grades than Main zone: 8.0% Zn, 5.6% Pb, 0.33% Cu, 210 g/t Ag and 1.9 g/t Au.

The Lewis Ponds district has a long history of prospecting, mining and exploration activity dating back to the 1850s. Many costeans, shafts and adits occur over the prospect (Figs. 1.2 and 1.3). Core trays are stored on a slag dump at the site of the abandoned New Lewis Ponds mine and smelter (Fig. 1.4).

	Total	Zn %	Pb %	Cu %	Au g/t	Ag g/t
Main zone	4.9 Mt	2.7	1.3	0.16	1.93	78
Toms zone	0.8 Mt	8.0	5.6	0.33	1.9	210
TOTAL	**5.7 Mt**	**3.5**	**2.0**	**0.19**	**1.9**	**97**

Table 1.2 Lewis Ponds indicated resource (Tri Origin pers comm., 2002 and www.Tri Origin .com).

1.2 Rise and fall of the Lewis Ponds mining district

Lewis Ponds is one of the oldest mining districts in Australia. Copper was discovered on land owned by Richard Lane and John Glasson, near a tributary of Lewis Ponds Creek in 1849 (Carne, 1899). The discovery attracted Cornish miners from England (Rule, 1978; Weathersten, 1988). In January 1872, the Great Western Copper Mining Company commenced operations at numerous copper deposits north of the Cornish settlement, discovered between 1851 and 1865 including Britannia, Gurophian, Big Bell, Lady Belmore, Icely and Ophir (Carne, 1899; Pittman, 1901; Rule, 1978; Weathersten, 1988). Under the management of Captain W. R. Renolds, the company produced 4 000 tons of ore from eight lodes near Lewis Ponds Creek to yield 640 tons of copper (Lucas, 1875; Carne 1899). However, all of the mines had closed by 1886. At this time, it was reported that land between Orange and Lewis Ponds, "had the appearance of being highly auriferous, argentiferous and cupriferous" (p. 112, Department of Mines annual report for 1887).

William Williams, a Welshman who immigrated to Australia to manage the Cadia copper mine discovered silver on his Lewis Ponds property in about 1886 while extracting limestone from a nearby quarry (Folster, 1946). The limestone later provided flux for the smelters. His discovery coincided with a silver boom accompanying the enormous wealth generated from the Broken Hill lodes. Hundreds of prospectors and small mining companies sought money from investors keen to cash in on the over-inflated silver prices. Pittman (1901) noted that, "large fortunes were made on paper." However, falling metal prices in 1888 ended the short-lived silver boom.

By 1887, Williams' Lewis Ponds Silver Mining Company had sunk three shafts to 35 m and produced 293 tons of ore from a 1-6 m wide gossan lode (Department of Mines annual report for 1887; unpub. mine record). The ore was initially sent to Germany for treatment. In 1888, Williams sold his land at Lewis Ponds for a profitable £12 000 (Folster, 1946).

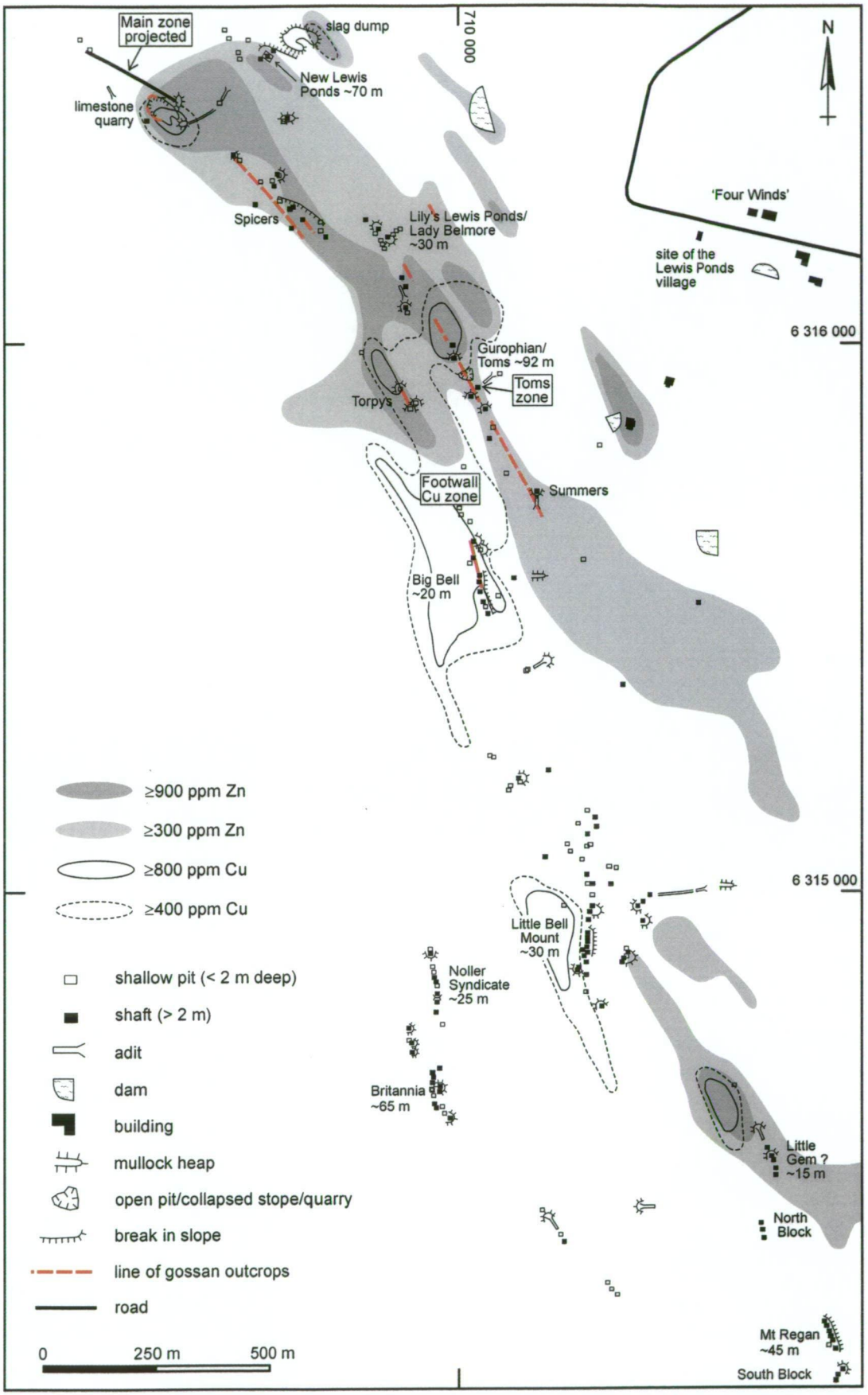

Figure 1.2 Map of Lewis Ponds prospect illustrating mine workings, gossan outcrops and soil geochemistry. The contoured Zn and Cu soil geochemistry data are from Shepherd (1972). Soil samples were collected at 30 m intervals along lines spaced 150 m apart. Approximate depths of the major mines are shown (Department of Mines annual report for 1887; Carne, 1901; Mine record for Little Bell Mount, 1906; Shepherd, 1972).

Figure 1.3 Decline at the Toms Lewis Ponds pyrite mine. The mine produced 2 400 tons of gold-silver-lead ore during 1887 and 1888. Approximately 30 000 tons of pyrite ore were extracted from Toms mine during World War I for sulfuric acid manufacture at Cockle Creek, Newcastle. Maximum depth of the workings was 90-92 m.

Figure 1.4 New Lewis Ponds slag dump and smelter ruins surrounded by eucalypt forest in the foreground and open sheep grazing land in the background. Looking east from the limestone quarry.

The New Lewis Ponds Gold and Silver Mining Company, under the management of J. E. Potter erected a headframe and expensive smelting equipment, including a water jacket furnace (Fig. 1.5). Smelting commenced on the 2nd January, 1899. The company employed 132 men. Toms Lewis Ponds Gold and Silver Mining Company sank three shafts into a 4.5 m wide lode near the old Gurophian mine to the south, initially producing 500 tons of ore at 10% Pb, 30 oz (930 g/ton) Ag and 5 dwt (7 g/ton) Au. The mine, managed by Captain James Hebbard, employed 35 men in 1888 and 75 men in 1889 (Department of Mines, annual reports). Tom's company acquired the New Lewis Ponds mine and together, 8 116 tons of ore were produced during 1890. The Spicers Gold and Silver Mining Company worked a nearby lead, silver and gold prospect between 1887 and 1892.

By the late 1880s the thriving Lewis Ponds village had a population exceeding 600 (Daily Orange, 1954; 1956). There were three hotels – the *Commercial*, *Royal* and *Clubhouse*, three general stores, four butchers, two churches, a post office, police lock-up, public school and skating rink (Folster, 1946; Daily Orange, 1954; Daily Orange, 1956; Maroney, 1982; Cook and Garvey, 1999). The miners lived in modest huts and tents. A local sawmilling company provided timber for the buildings and mine shafts. Limestone and ironstone were obtained for flux in the smelters and silver bars supplied from Broken Hill assisted fusion of the complex ore. Some 300 horses and 16 wagons, employed to transport matte bars and silver bullion to Orange would return with coke and stores (Folster, 1946). The Lewis Ponds settlement is now deserted, except for several sheep grazing families.

All mining and smelting activities ceased at Lewis Ponds during 1891 and 1892 amid claims by Warden John S. Lane of improper company practises including the release of misleading newspaper reports (Department of Mines, annual report for 1891). Demand for copper allowed several small operations to continue immediately south of Lewis Ponds. The Britannia, Mount Regan, Little Gem and Little Bell Mount mines produced small quantities of copper from quartz veins and cupriferous country rock in the early 1900s (Carne, 1908).

Brown and Party dewatered the Toms mine in 1913. They erected a new headframe and installed winches. Between 1915 and 1921, the Sulfide Corporation raised approximately 30 000 tons of pyrite ore for sulfuric acid manufacture at Cockle Creek, Newcastle (Department of Mines annual reports for 1913 to 1930). Small amounts of gold were also recovered from the massive sulfide. Paine and Riley conducted minor surface prospecting around the flooded New Lewis Ponds and Spicers workings. They strip mined the gossan lodes in 1917 and sank a new shaft in 1918.

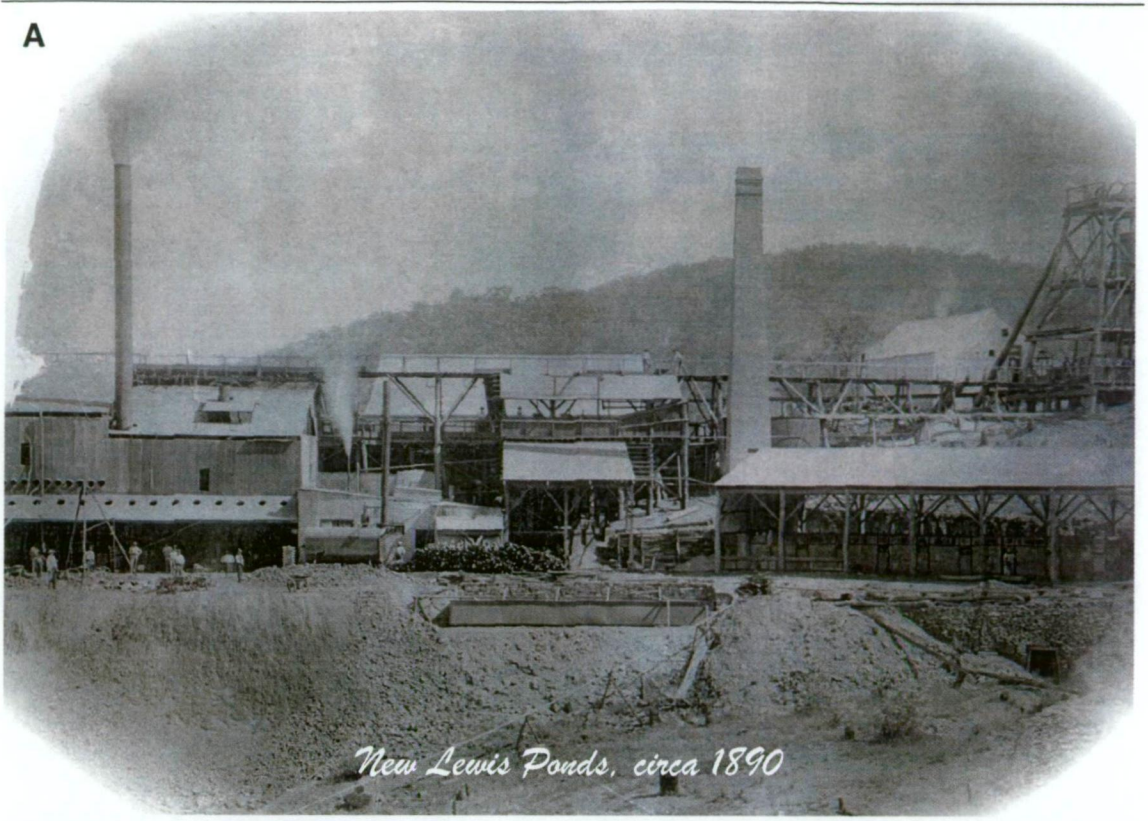

"Many will remember the immense smoke stack which stood like a beacon long after mining activity had died down...It was the loftiest of all the chimneys in western New South Wales."

William Folster, *Daily Orange*, 25th April, 1946

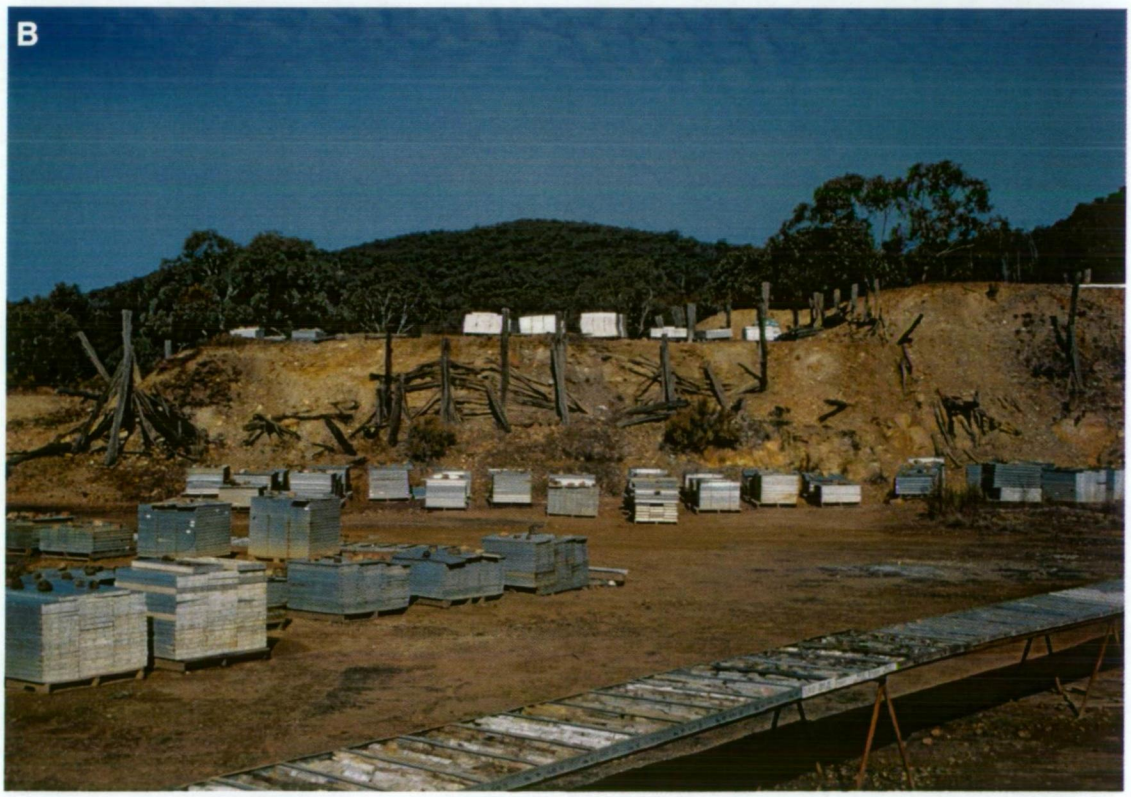

Figure 1.5 **A:** New Lewis Ponds mine and smelter in 1890. Photo courtesy of Tri Origin and enhanced by M. Agnew. Quotation from newspaper report by William Folster. **B:** Remains of the smelter looking south toward Mt Britannia and Toms mine. Drill core trays are now stored on the slag dump.

1.3 Modern exploration

Modern exploration of the Lewis Ponds prospect commenced during the early 1960s. Numerous companies and joint ventures held the ground including Cominco Exploration, Amax Exploration, Aquitaine Australia Minerals, Shell Company of Australia Limited and Homestake Australia Limited. They conducted:

- rock chip, soil and stream sediment sampling;
- airborne electromagnetic and magnetometer surveys;
- induced polarisation surveys; and
- shallow reversed circulation and diamond drilling around the old workings.

Tri Origin, a Canadian-based company, commenced exploration at Lewis Ponds in 1991 (Valliant and Meares, 1998). Further geological mapping, soil and rock chip sampling and geophysical surveys were undertaken to delineate new targets. Induced polarisation data revealed steeply-dipping conductors at depth. A deep diamond drilling program proved successful in 1992. The third and forth holes intersected a new mineralised area at depth (Main zone), located 250 m northwest of the Spicers mine (Fig. 1.2; Valliant and Meares, 1998). In 1995, further step-out exploration drilling encountered high-grade massive sulfide underneath the Toms mine workings (Toms zone). A conformable halo of anomalous Zn soil geochemistry surrounds the two mineralised zones (Fig. 1.2). Soil geochemical haloes of 400-1 500 ppm Cu extend south of Toms mine. These are discordant to both bedding and the major NNW-trending structural fabric in the rocks.

1.4 Aims and methods

The overall purpose of this study was to determine the volcanic-sedimentary setting, geological and geochemical characteristics and origin of the Lewis Ponds massive sulfide deposits. The specific aims were to:

- characterise the volcanic-sedimentary facies architecture and depositional environment of the host sequence;
- determine the origin of the footwall volcanic succession and overlying limestone-bearing units;
- identify any structures that may have controlled emplacement of the footwall volcanic succession or circulation of hydrothermal fluids;
- study the mineralogy, mineral compositions, whole rock geochemistry and stable isotope geochemistry of the hydrothermal alteration envelope;
- examine metal grades, sulfide mineral compositions and sulfide textures in the mineralised zones to determine metal distribution and paragenetic relationships;

- develop a genetic model for the formation and potential structural modification of the Lewis Ponds deposits; and
- compare the geological and geochemical features of Lewis Ponds to other eastern Australian and worldwide Zn-Pb-Ag-rich massive sulfide deposits.

These aims were achieved by undertaking a multidisciplinary study to characterise the volcano-sedimentary facies architecture, structures and regional context of the Lewis Ponds host sequence and the geochemical and mineralogical zonation in the hydrothermal alteration envelope. The following investigations were conducted:

- 1:2 500 scale prospect mapping to supplement previous mapping carried out by the exploration companies;
- detailed logging and sampling of drill core from thirty diamond drill holes to determine the spatial distribution of lithofacies and hydrothermal alteration mineral assemblages;
- measurement and calculation of structural fabric orientations, vergence relationships and stratigraphic facing directions in drill core;
- regional road and creek traverses of the volcanic-sedimentary succession;
- petrological observation of mineralogy, textures and paragenetic relationships in unaltered, altered and mineralised samples;
- whole rock, XRF analysis of selected drill core and surface samples to delineate magmatic suites in the footwall volcanic succession and to quantify geochemical gradients associated with the hydrothermal alteration envelope;
- electron microprobe analysis of silicates, carbonates and sulfides for the purpose of identifying variations in mineral chemistry between mineralised zones;
- examination of available assay data to determine any lateral or vertical metal zonation;
- fluid inclusion and C-O isotope study of limestone clasts, carbonate veins and hydrothermal carbonate surrounding the massive sulfides;
- S isotope study of the sulfides to determine the source of S; and
- fluid modelling of geochemical data to characterise the temperature, source and composition of the hydrothermal fluid(s) and the mechanisms of sulfide deposition.

CHAPTER 2

GEOLOGICAL SETTING

2.1 Introduction

Lewis Ponds is located near the western margin of the Hill End Trough, in the eastern Lachlan Fold Belt (LFB) of New South Wales, Australia. The Hill End Trough is one of numerous elongate, fault-bound stratotectonic units comprising Middle Silurian to Early Devonian sedimentary and silicic volcanic rocks (Fig. 2.1). In New South Wales, the mixed volcanic-sedimentary successions host significant polymetallic massive sulfide, barite and structurally controlled Cu-Au deposits, including Woodlawn, Mineral Hill, CSA, Elura, Kempfield, Peelwood and Wisemans Creek (Davis, 1990; Scheibner, 1998; Suppel et al., 1998). The distribution and general characteristics of these deposits reflects mineralisation in an evolving, active plate margin setting (Gray et al., 2002). This chapter focuses on the tectonic and structural evolution of the LFB in New South Wales and in particular, the development and closure of the Siluro-Devonian sedimentary basins. The local structural geology and stratigraphy of the Hill End Trough and adjacent Molong High are also introduced in this chapter.

2.2 Tectonic setting of the Lachlan Fold Belt (LFB)

The LFB is part of a 20 000 km long Palaeozoic orogenic belt extending around the margin of Gondwana, from the northern Andes, through Antarctica to eastern Australia (Foster and Gray, 2000; Gray et al., 2002). It comprises Ordovician to Devonian quartz turbidites, calcalkaline to shoshonitic volcanic and volcaniclastic rocks, granite, limestone and mudstone. In the western subprovince, the quartz turbidites overlie a Cambrian greenstone basement with oceanic affinities (Crawford and Keays, 1978).

The stratotectonic units constituting the LFB were progressively accreted onto the Australian craton during a series of eastward migrating, Late Ordovician to Early Carboniferous (~455-360 Ma) deformation and metamorphic events, resulting in the closure of a marginal oceanic basin, fragmentation of a volcanic arc and tectonic inversion of numerous rift basins. These orogenic events were accompanied by voluminous granitic magmatism across the LFB (Collins and Vernon, 1992; Foster and Gray, 2000).

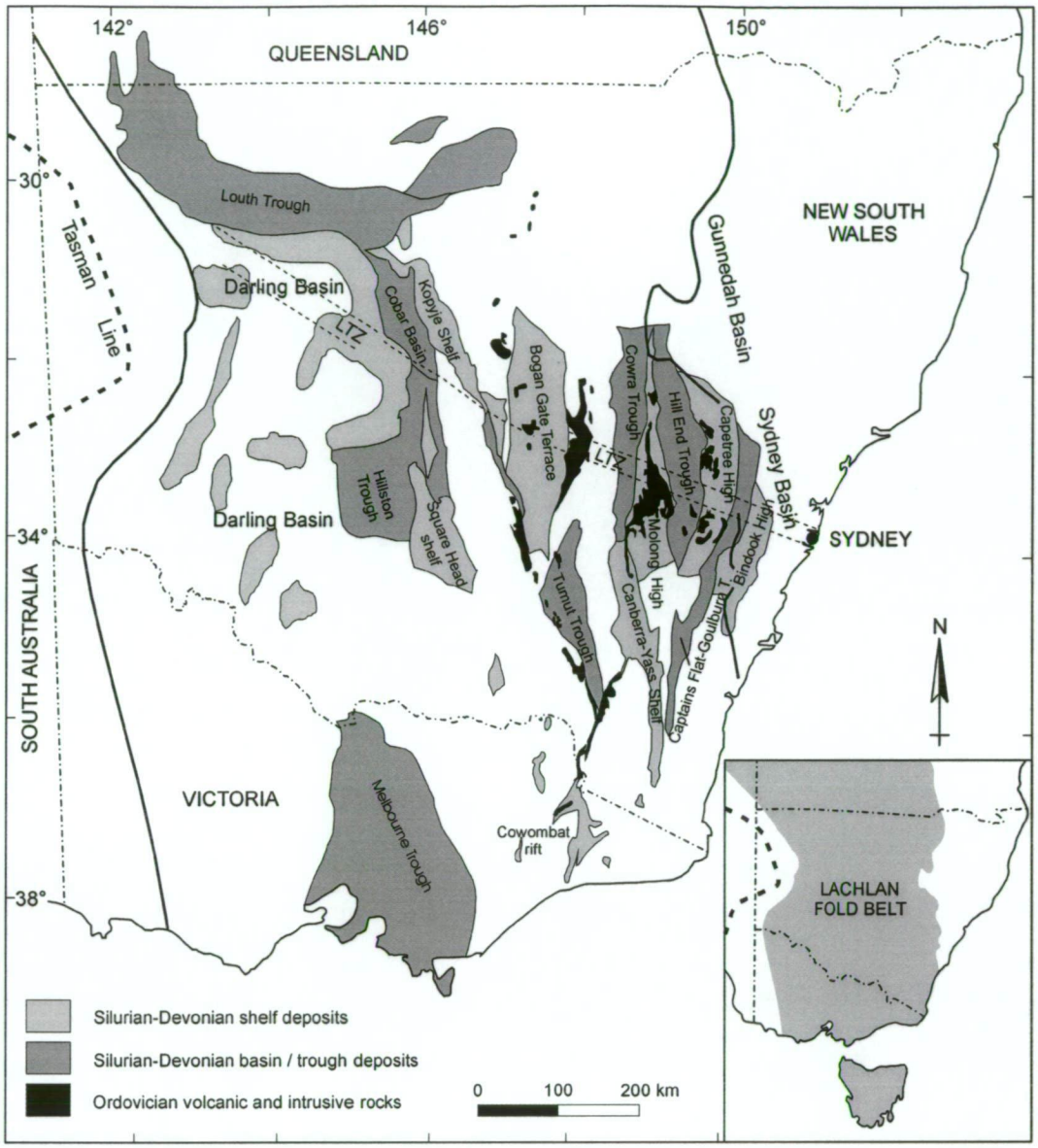

Figure 2.1 Distribution of Silurian, Devonian and Ordovician stratotectonic units in the Lachlan Fold Belt (modified from Scheibner, 1998). Outlines of the Lachlan Fold Belt and Tasman Line are from Fig. 178 (Scheibner and Veevers, 2000). Approximate position of the Lachlan Transverse Zone (LTZ) is based on figure 1 in Glen and Walshe (1999).

Pre-Cambrian to Early Silurian

The Tasman line marks the eastern margin of the Palaeo- to Meso-Proterozoic, Australian craton (Fig. 2.1; Scheibner, 1996; Scheibner and Veevers, 2000). East of this line, the oldest rocks exposed in the western subprovince of the LFB are Early to Middle Cambrian metavolcanics (tholeiitic basalt, boninite, andesite and ultramafic rocks), volcaniclastics and cherts (Crawford and Keays, 1978; Crawford et al., 1984). These were accreted onto the Australian craton to form the Kanmantoo Fold Belt in the Late Cambrian (Scheibner, 1998; Foster and Gray, 2000; Scheibner and Veevers, 2000).

During the Cambrian and Early Ordovician, an active, southwest Pacific-style convergent margin developed along the east coast of Australia. In New South Wales, this comprised an inferred west-dipping subduction zone, accretionary prism, forearc basin, volcanic arc and marginal basin (Fig. 2.2; Scheibner, 1996; Scheibner, 1998; Glen and Walshe, 1999; Scheibner and Veevers, 2000). The four Ordovician volcanic belts in the eastern LFB (Fig. 2.1) originally existed as a continuous volcanic arc system, termed the Macquarie Arc (Cas, 1983; Collins and Vernon, 1992; Glen et al., 1998; Glen and Walshe, 1999). High K, calcalkaline to shoshonitic volcanic and intrusive rocks formed in an ocean island arc, above a micro-continental fragment or Pre-Cambrian to Cambrian substrate (Scheibner, 1998; Scheibner and Veevers, 2000). These rocks host the world class Cadia and Endeavour porphyry Cu-Au deposits.

Middle Silurian to Late Devonian

A re-organisation of the active continental margin of eastern Australia in the Early to Middle Silurian caused major changes in palaeogeography and the nature of magmatism across the LFB. The volcanic arc migrated eastward or re-developed further to the east due to roll-back of the subduction zone, oblique convergence and collapse of the Ordovician crust (Collins and Vernon, 1992; Scheibner, 1998; Foster and Gray, 2000; Gray et al., 2002). A broad area of backarc extension developed inboard of the Calliope Volcanic Arc (Fig. 2.2), resulting in widespread granite emplacement, subaerial to submarine silicic and rarely basic calcalkaline volcanism and the formation of shallow to deep marine grabens, half-grabens and pull-apart basins separated by shallow marine platforms (Cas, 1983; Powell, 1983; Scheibner, 1998; Scheibner and Veevers, 2000). Major volcanic centres existed predominantly along basin margins (Fig. 2.2). Late Silurian palaeogeography in the eastern LFB has been compared to the Philippines archipelago (Cas, 1983). The Hill End, Cowra, Captains Flat-Goulburn, Melbourne and Tumut troughs, Cowombat Rift and Cobar Basin (Fig. 2.1) progressively filled with sediment derided from the adjacent shallow marine areas. The term *trough*, although not ideal, is widely used in the literature to describe these Silurian and Devonian volcanic-sedimentary successions. Backarc extension, subsidence and limited volcanism continued into the Early Devonian (Fig. 2.2).

During the Middle to Late Devonian, contraction events were diachronous with extension and deposition of shallow marine to terrestrial sediment in the basins (Cas, 1983; Scheibner, 1998). The Middle Devonian Tabberabberan orogeny (~390-370 Ma) was part of an eastward migrating 'wave' of continuous or episodic deformation (Gray, 1997; Gray et al., 2002) which led to uplift, erosion and reactivation of syn-sedimentary faults (Cas, 1983; Glen and Watkins, 1994, 1999). Deformation involved transpressional strike-slip movement and thrusting on

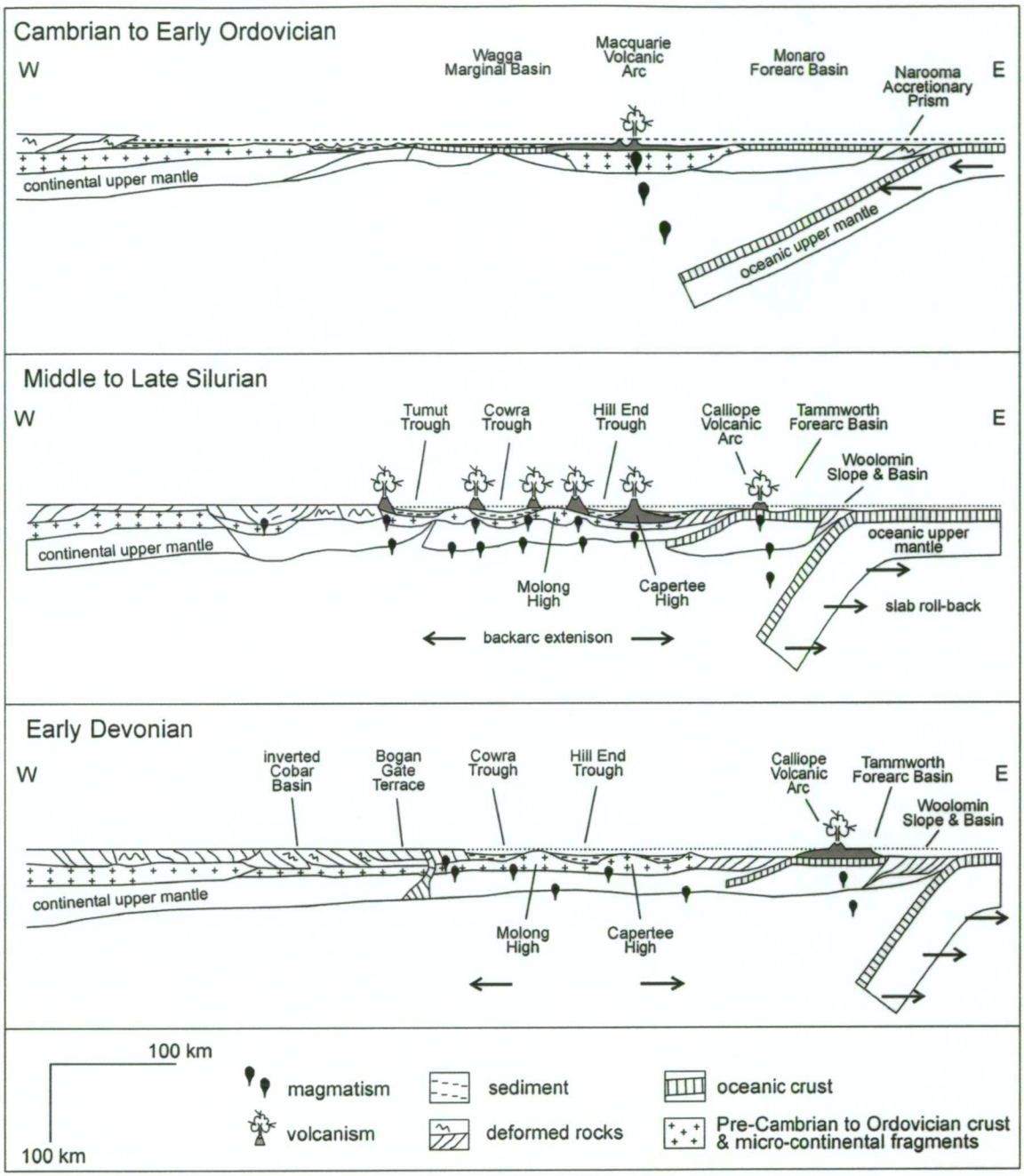

Figure 2.2 Tectonic evolution of the Lachlan Fold Belt in New South Wales from the Cambrian to the Early Devonian (modified from Figs. 15.3 and 16.1 in Scheibner, 1998).

faults linked to low-angle, mid-crustal detachments (Glen, 1992; Glen and Watkins, 1994; Glen, 1995). The contraction imparted a strong N- to NNW-trending structural grain across the eastern LFB due to the development of cleavage, upright chevron folds and steep, reverse faults.

Although most authors attribute the complex facies architecture of Silurian and Devonian units to palaeogeography and basin inversion, the overall tectonic framework and geodynamics of the LFB during this time remain speculative. In particular, the following inter-related issues occur in the literature.

Overall crustal architecture of the Lachlan Fold Belt

The Silurian and Devonian periods were characterised by high heat flow, voluminous granitoid emplacement, widespread silicic or rarely bimodal volcanism and local areas of high temperature-low pressure metamorphism (Cas, 1983; Coney et al., 1990; Gray, 1997; Gray et al., 2002). The silicic magmatism resulted from partial melting of thick continental crust (Cas, 1983; Coney et al., 1990; Collins and Hobbs, 2001). However, heat required for partial melting of the lower to middle crust has been attributed to mantle upwelling and subduction processes involving underplating (Stolz et al., 1997; Collins and Hobbs, 2001; Gray et al., 2002). The S-type granitoids are interpreted to originate from partial melting of Proterozoic crust (Chappell et al., 1988) or magma mixing of components derived from Cambrian metavolcanics and Ordovician metasediments (Collins and Vernon, 1992; Collins, 1998).

Nature of the basement to the sedimentary basins

The nature of the basement to the LFB is an unresolved issue. Previous models have included Proterozoic to Cambrian, oceanic and mixed oceanic-continental crust (references cited in Glen, 1992 and Stolz et al., 1997). Recent structural, geochemical and geophysical studies indicate that Ordovician volcanic rocks underlie at least part of the Hill End Trough. Evidence for an Ordovician basement comes from interpretation of structural cross-sections (eg. Glen, 1992), regional gravity data (Glen and Walshe, 1999; Glen et al., 2002) and the rare earth element compositions of Carboniferous, I-type granites (p. 262-264; Pogson and Watkins, 1998).

Timing and mechanisms of basin formation

The current geometry of Silurian-Devonian belts is an artefact of tectonic inversion rather than primary orientation of the basin axes (Cas, 1983; Glen and Walshe, 1999). Detailed facies analysis of the Merrions Formation, for example, indicated a northwest depositional strike despite stratigraphic units in the Hill End Trough currently trending north (Cas, 1983). Most of the sedimentary basins are interpreted to have opened obliquely by sinistral transpression during the Middle to Late Silurian and earliest Devonian, as in the Hill End Trough (Glen and Watkins, 1994; Glen and Walshe, 1999), Tumut Trough (Powell, 1983), Cobar Basin (Glen, 1990) and Cowombat Rift (Stolz et al., 1997). Recent interpretation of modelled gravity data over the Hill End Trough indicates that it may have formed in response to northwest and northeast-oriented components of extension (Glen et al., 2002).

2.3 Introduction to the Hill End Trough

Detailed structural and stratigraphic descriptions of the Molong High and western Hill End Trough are provided by Glen and Walshe (1999), Pogson and Watkins (1998), Glen and Watkins (1994) and Packham (1968). The Hill End Trough has an elliptical outline due to concave, curvilinear, fault-controlled boundaries with the adjacent Ordovician volcanic units (Fig. 2.3). Silurian and Devonian rocks in the northern part of the trough, are interpreted to narrow and terminate against Carboniferous granite (David et al., 2002). The Capertee High and Molong High define the eastern and western margins respectively (Fig. 2.3). Regional gravity data over the Hill End Trough indicate southward thickening of the volcanic-sedimentary pile above a basement of interpreted Ordovician tilt blocks, cut by NE and NW to NNW-trending normal faults (Glen and Walshe, 1999; Glen et al., 2002). This complex geometry has been attributed to oblique extension/transtension during basin formation (Glen, 1992; Glen et al., 1999).

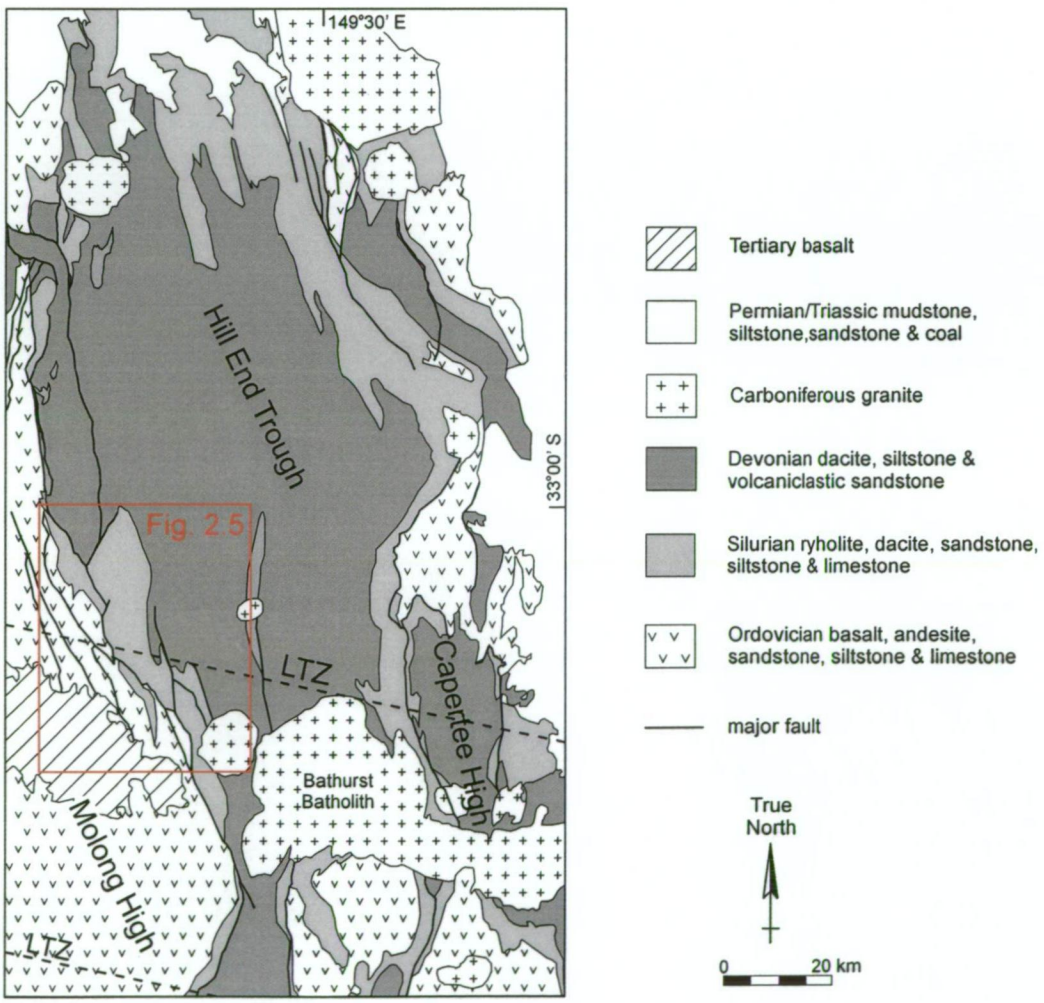

Figure 2.3 Simplified geology of the Hill End Trough, Molong High and Capertee High showing the distribution of Palaeozoic units. Modified from Colquhoun et al. (1997) and Raymond, Pogson and others (1998). Location of the Lachlan Transverse Zone (LTZ) is based on figure 1 in Glen and Walshe (1999).

The Hill End Trough comprises an 8 km sequence of Ludlowvian to Emsian, hemipelagic siltstone, mudstone and minor sandstone (Fig. 2.4; Packham, 2002). These rocks are interbedded with coarse-grained pyroclastic and epiclastic mass flow deposits sourced from the south or southeast (Pogson and Watkins, 1998; Jagodzinski and Cas, 2000; Packham, 2002). Limestone, mudstone, breccia, volcaniclastic sandstone and rhyolite occur along the Molong and Capertee highs (Pogson and Watkins, 1998). Sedimentary facies in the Hill End Trough and adjacent Molong and Capertee highs are interpreted to record progressively deepening conditions during the Late Silurian. Shallow marine deposits became restricted to the bounding platforms as the basin subsided (Pogson and Watkins, 1998). Active submarine or subaerial volcanic centres existed along the basin margins at this time.

A two stage rift model has been proposed for the Hill End Trough (Glen, 2002). Crustal heating, magmatism and fault-controlled extension during the syn-rift phase were followed by a post-rift phase involving crustal cooling, deposition of low energy, fine-grained sediments and widening of the basin margins. Glen (2002) documented syn-rift and post-rift cycles extending from the Ludlow to Emsian (Fig. 2.4). The major volcanic/volcaniclastic units including the Mullions Range Volcanics, Bells Creek Volcanics, Turondale Formation, Merrions Formation, Bay Formation and Chesleigh Formation characterise the syn-rift phase. Deposition of the Cunningham Formation occurred during the subsequent sag phase.

2.4 Local geology

According to recent mapping carried out by the Geological Survey of New South Wales, the massive sulfide lenses at Lewis Ponds occur near the contact of the Anson Formation and overlying Mullions Range Volcanics (Figs. 2.4 and 2.5). These two units, together with the Barnby Hills Shale, are collectively known as the northwestern Mumbil Group or less conventionally, *Mumbil shelf* (Glen and Watkins, 1994; Pogson and Watkins, 1998). Contemporaneous Mumbil Group rocks also occur on the eastern side of the Hill End Trough. The Mumbil Group unconformably overlies Ordovician volcanic rocks (Fairbridge Volcanics, Oakdale Formation and Byng Volcanics). Although the Ordovician units predominantly crop out west of Lewis Ponds in the Molong Belt, small fault-bound lenses of Byng Volcanics and associated unnamed Ordovician ultramafic rocks occur 3 km south of Lewis Ponds (Fig. 2.5). The Anson Formation and Mullions Range Volcanics host numerous small (less than 1 Mt), stratabound, massive to semi-massive sulfide deposits including Mt Bulga, Mt Shorter, Pride of the Hills, Calula and Daydawn (Fig. 2.5).

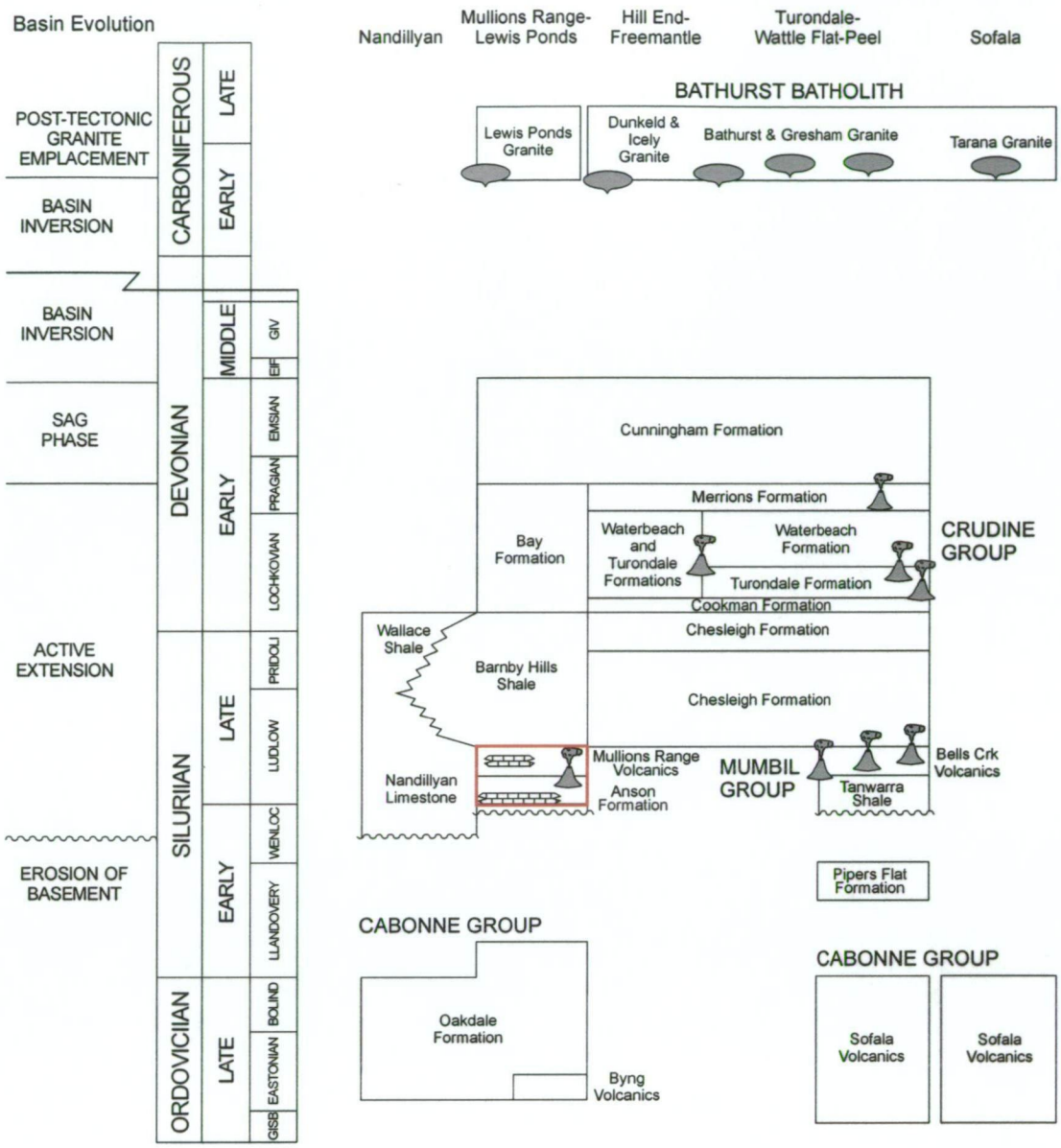

Figure 2.4 Time-space plot for the Hill End Trough, Molong High and Capertee High. The Anson Formation and Mullions Range Volcanics are highlighted in red. Modified from Raymond, Pogson and others (1998). Basin evolution section is based on the interpretations of Glen (2002) and Glen et al. (1999).

Byng Volcanics (early Late Ordovician)

The Byng Volcanics (Fig. 2.5) consist of basalt-andesite flows and volcaniclastic sandstone. Unnamed ultramafic bodies, altered to serpentinite have intruded the volcanic rocks. The total estimated thickness of the unit is 2 000 m. Quench textures in the basalt and the occurrence of mass flow deposits indicate that the Byng Volcanics formed in a predominantly submarine environment (Pogson and Watkins, 1998).

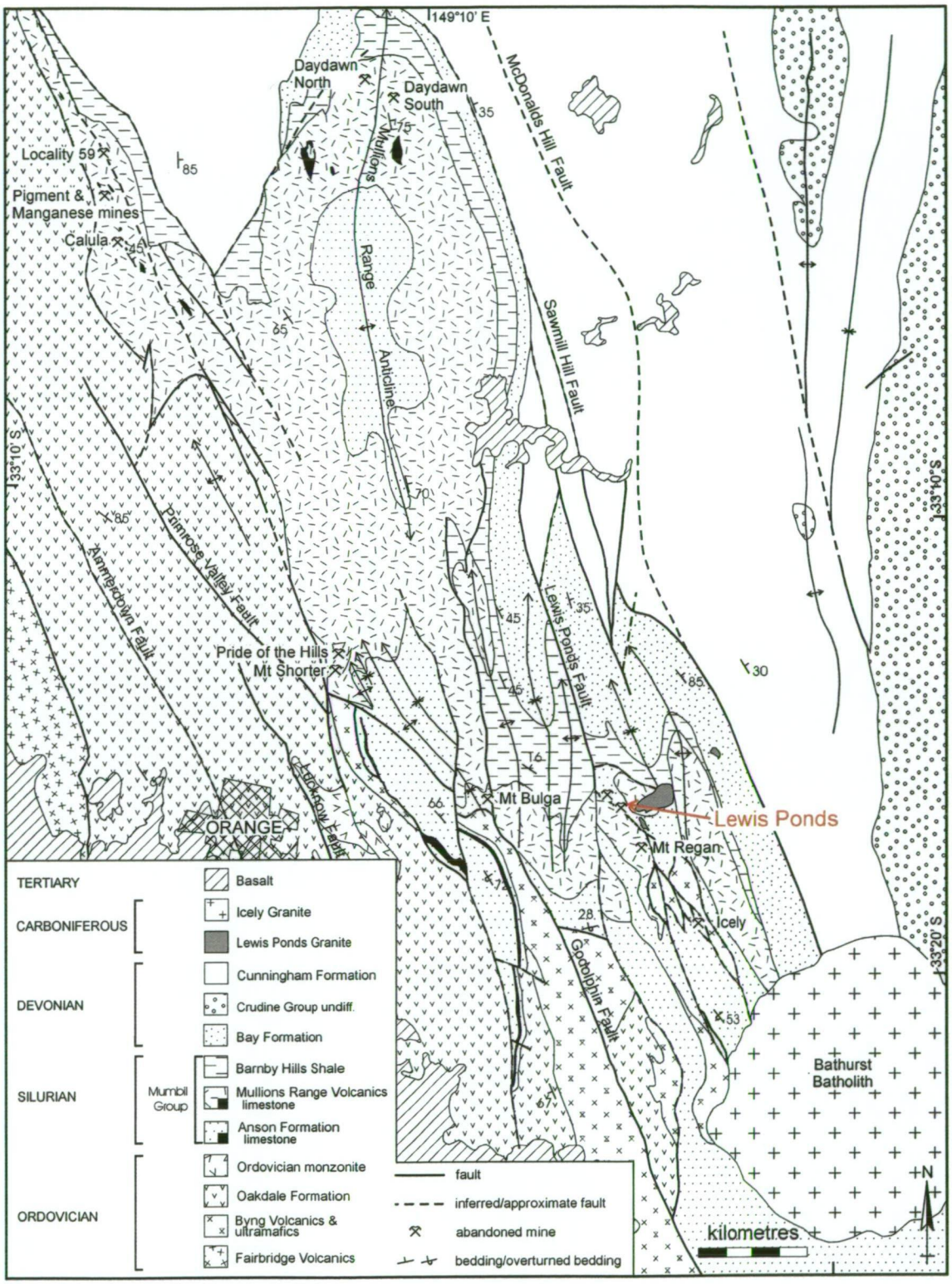

Figure 2.5 Regional geology of the Mumbil Group, Hill End Trough and Molong High. Modified from Meakin et al. (1997) and Raymond, Pogson and others (1998).

Anson Formation (early Late Silurian)

Part of the Anson Formation, as defined by Pogson and Watlkins (1998) was included in the Mumbil Formation of Packham (1968). More recently, Glen and Watkins (1994) briefly referred to it as the Clifton Grove Formation. Packham described the Mumbil Formation as a non-volcanic unit of fine-grained sedimentary rocks and limestone lenses, conformably overlying the Mullions Range Volcanics. However, the Anson Formation is now interpreted to pre-date the Mullions Range Volcanics (Fig. 2.4; Pogson and Watkins, 1998). Upper parts of the unit are exposed in the Lewis Ponds area and in the core of a large anticline to the north (Fig. 2.5). Lower parts crop out discontinuously west and southwest of Lewis Ponds, where conglomerate, limestone and siltstone unconformably overlie the Byng Volcanics. Bedding in the Anson formation is locally overturned in this area (Fig. 2.5).

The basal conglomerate member of the Anson Formation (not shown in Fig. 2.5) comprises graded beds of conglomerate, sandstone and siltstone. Conglomerates contain chert, mudstone, basalt, basaltic-andesite and ultramafic clasts (Pogson and Watkins, 1998). These lithic clasts were probably derived locally from the underlying Ordovician units. The coarse-grained deposits pass up into a 50-200 m thick limestone member containing broadly Ludlovian shallow marine fossils including algae, crinoids, brachiopods, conodonts and in situ corals (Pickett, 1993; Pogson and Watkins, 1998). The remainder of the unit consists of siltstone, mudstone and sandstone. Minor limestone lenses, rhyolitic lava and volcaniclastic sandstone occur toward the top of the unit (Pogson and Watkins, 1998).

Pogson and Watkins (1998) argued that lower parts of the Anson Formation were deposited in a fluvial to shallow marine environment. The basal conglomerate member contains oxidised clasts that were probably derived from exposed Ordovician rocks. In situ corals and algae in the limestone member formed in the photic zone (Pickett, 1993; Pogson and Watkins, 1998). They suggested that limestone lenses near the top of the unit, in the Lewis Ponds-Mt Bulga area may also indicate a shallow marine setting.

Mullions Range Volcanics (early Late Silurian)

The Mullions Range Volcanics occur in three areas; a doubly-plunging anticline (Mullions Range anticline), structurally dismembered southern section and northerly-thinning western lobe (Fig. 2.5). Packham (1968) originally described the unit and defined a 460 m thick type section occurring along Kerrs Creek (see Chapter 3, section 3.10). However, approximately 2 000 m of volcanic rocks are exposed on the eastern limb of the Mullions Range anticline (Pogson and Watkins, 1998).

The three areas are characterised by different facies associations (Hilyard, 1981). Quartz-feldspar phyric rhyolite-dacite and volcaniclastic sandstone occur in the Mullions Range anticline and southern areas. The western lobe consists of flow-banded and columnar-jointed rhyolite and dacite, pumiceous volcaniclastic deposits and minor limestone lenses containing Ludlowvian fossils (Packham, 1968; Hilyard, 1981; Pogson and Watkins, 1998).

The Mullions Range Volcanics is interpreted as a submarine to partly emergent silicic volcanic succession, for which numerous volcanic centres have been proposed (Hilyard, 1981; Pogson and Watkins, 1998). Hilyard (1981) suggested that variations in facies architecture and stratigraphic thickness in the western lobe reflect a source area to the south. Hudson et al. (1997) interpreted the Mullions Range anticline as a possible deformed rhyolite dome.

Barnby Hills Shale (Late Silurian to earliest Early Devonian)

The uppermost unit of the northwestern Mumbil Group, the Barnby Hills Shale has previously been included in the Molong Beds, Gamboola Formation, Panuara Formation and Mumbil Formation (Strusz, 1960; Packham, 1968; Pogson and Watkins, 1998). It occurs as a series of narrow folded/faulted belts, extending over 100 km. In the Orange district, shale and graptolite-bearing carbonaceous mudstone conformably overlie the Mullions Range Volcanics (Fig. 2.5). Limestone-clast breccia, siltstone and volcaniclastic sandstone occur elsewhere in the unit. Pogson and Watkins (1998) suggested that the Barnby Hills Shale was deposited in a deep, below wave-base environment.

Bathurst Batholith (Middle to Late Carboniferous)

Middle to Late Carboniferous, post-tectonic, I-type granites have intruded the Hill End Trough and Capertee High. The Bathurst Batholith is a large, discordant, multi-intrusion complex (Fig. 2.3). It is part of a 70 km long, NNW-trending belt of granite and gabbro intrusions with Rb/Sr ages of 340-312 Ma (Shaw and Flood, 1993). Small, Middle to Late Carboniferous granite bodies also occur in the Lewis Ponds district (Fig. 2.5). Volcanic equivalents of the Carboniferous granites do not occur in the LFB (Shaw and Flood, 1993; Pogson and Watkins, 1998).

Structural geology and metamorphism

The northwestern margin of the Hill End Trough is characterised by steep reverse faults and upright, open to tight folds (Fig. 2.5). North of Orange, folded Palaeozoic rocks are cut by a complex system of closely spaced, NNW-trending thrust faults. Glen (1998) interpreted this area, including Lewis Ponds as a major east-dipping thrust-imbrication zone, floored by the Lucknow fault to the west (Fig. 2.5). The Godolphin, Sawmill Hill and McDonalds Hill faults

are inferred roof thrusts on the eastern side. Faults in the Mullions Range imbricate zone show normal and reverse displacement, possibly indicating reactivation of syn-sedimentary structures (Glen and Watkins, 1994).

WNW-trending faults and folds occur within a corridor, termed the *Lachlan Transverse Zone* (LTZ). Glen and Walshe, (1999) argue that this cross-orogen structure, which extends from the western margin of the LFB to the Sydney Basin in the east (Figs. 2.1 and 2.3), may have influenced Palaeozoic tectonics in the eastern LFB since at least the Middle Ordovician. The LTZ controls the distribution of numerous Ordovician Cu-Au deposits, Carboniferous and Jurassic intrusions and Triassic volcanics in the eastern LFB. North of the LTZ and Bathurst Batholith, Upper Silurian to Lower Devonian units on both sides of the Hill End Trough are flanked by the Mumbil Group (eg. Fig. 2.5). However, Lower Devonian rocks directly overlie the Mumbil Group south of the LTZ. Therefore, Glen and Walshe (1999) argued that the LTZ separated deep marine sediments to the north from shallow marine shelf deposits (Mumbil Group) to the south during the Late Silurian, thereby controlling the margin of the Hill End Trough.

Glen et al. (1999) dated white mica and biotite growth during deformation in the Orange district using the ^{40}Ar-^{39}Ar technique and assuming relatively fast cooling rates. Samples were chosen from foliated Late Silurian volcanics adjacent to NNW-trending faults and Early Carboniferous granites (Table 2.1). Results were correlated with previous studies to define three deformations:

- 387-378 Ma previously referred to as Tabberabberan Orogeny;
- 370-371 Ma possible younger phase of the Tabberabberan Orogeny; and
- ~ 340 Ma Kanimblan deformation, pre-dating Carboniferous granites.

Unit	Locality	Mineral	Kinematics	Cooling Age
Foliated granite	Reids Flat area	Biotite	West-over-east thrusts	387 ± 2 Ma
Kangaloolah Volcanics	Kempfield area near Copperhannia Thrust	White mica		358 ± 2 Ma
Mullions Range Volcanics	Ophir Road at Summerhill Creek	White mica	Barnby Hills Shale thrust over Mullions Range Volcanics	370 ± 4 Ma
Mullions Range Volcanics	Icely Road, ~ 4 km south of Lewis Ponds	Biotite	Byng Volcanics thrust over Mullions Range Volcanics	332 ± 3 Ma
Mullions Range Volcanics	Icely Road, ~ 4 km south of Lewis Ponds	White mica	Byng Volcanics thrust over Mullions Range Volcanics	340 ± 3 Ma

Table 2.1 Selected results from ^{40}Ar-^{39}Ar dating of white mica and biotite in foliated granite and volcanic samples (Glen et al., 1999).

The oldest deformation (387-378 Ma) is interpreted to result from both north-south and east-west shortening during the initial phase of basin inversion, prior to deposition of the Upper Devonian Lambie Group on the Capertee High. Middle Devonian WNW-trending faults were recognised in the eastern part of the Hill End Trough, where Ordovician basement rocks are

thrust over Late Silurian deposits (Glen and Watkins, 1999). Many of these structures may have been reactivated during the Early to Middle Carboniferous, ~ 340 Ma Kanimblan deformation. In contrast, Powell and Edgecombe (1978) concluded that there was insufficient evidence in the northeastern LFB for a major orogenic event in the Middle Devonian and that many of the faults formed in response to local folding.

The Hill End Trough and flanking areas are characterised by greenschist facies metamorphic assemblages. Biotite and actinolite have overprinted the Silurian and Devonian rocks (Barron, 1998). Extensive areas of overlapping biotite-actinolite and prehnite-pumpellyite assemblages occur throughout the Molong High.

2.5 Massive sulfide deposits

Silurian and Devonian volcanic-sedimentary successions in New South Wales host polymetallic massive sulfide deposits, many of which were mined periodically between 1890 and 1960 (Davis, 1990). They occur predominantly in the Hill End Trough, Captains Flat-Goulburn Trough and Cobar Basin (Figs. 2.1 and 2.6). The following section outlines the overall deposit characteristics in these stratotectonic units.

Base metal deposits in the Hill End and Captains Flat-Goulburn troughs are generally small (<5 Mt), with the exception of Woodlawn, which had a resource of 17.7 Mt grading 9.9% Zn, 3.8% Pb, 1.7% Cu, 80 ppm Ag and 1.4 ppm Au (quoted in Large, 1992). Lake George, Captains Flat produced over 4 Mt at 10% Zn, 6% Pb, 0.67% Cu, 56 g/t Ag and 1.7 g/t Au, between 1937 and 1962 (Davis, 1975). The base metal occurrences include vein-controlled, skarn, iron oxide, barite and massive sulfide deposits (Gilligan, 1974; Stevens, 1974; Davis, 1990). Stratabound massive sulfide and barite lenses are hosted in siltstone, mudstone or fine-grained volcaniclastic rocks, adjacent to the contacts with rhyolitic and dacitic volcanics (Fig. 2.6). Woodlawn, however occurs in a bimodal volcanic succession characterised by pillow basalt, dolerite sills and rhyolite flows (McKay and Hazeldene, 1987). Extensive chlorite, sericite and pyrite haloes surround the stratabound massive sulfide lenses. Some of the deposits have Cu-rich footwall stockwork zones consisting of disseminated pyrite and chalcopyrite or stringer veins (Gilligan, 1974; Chisholm, 1976; Seccombe et al., 1984). The massive sulfide consists of pyrite, sphalerite, galena, chalcopyrite, arsenopyrite and tetrahedrite with rare gold, electrum, bismuthinite and stannite (Mcleod and Stanton, 1984; Seccombe et al, 1984; Davis; 1990).

The larger stratabound deposits occur in strongly folded successions adjacent to major north-trending structures including the Lake George fault (Fig. 2.6; Davis, 1990).

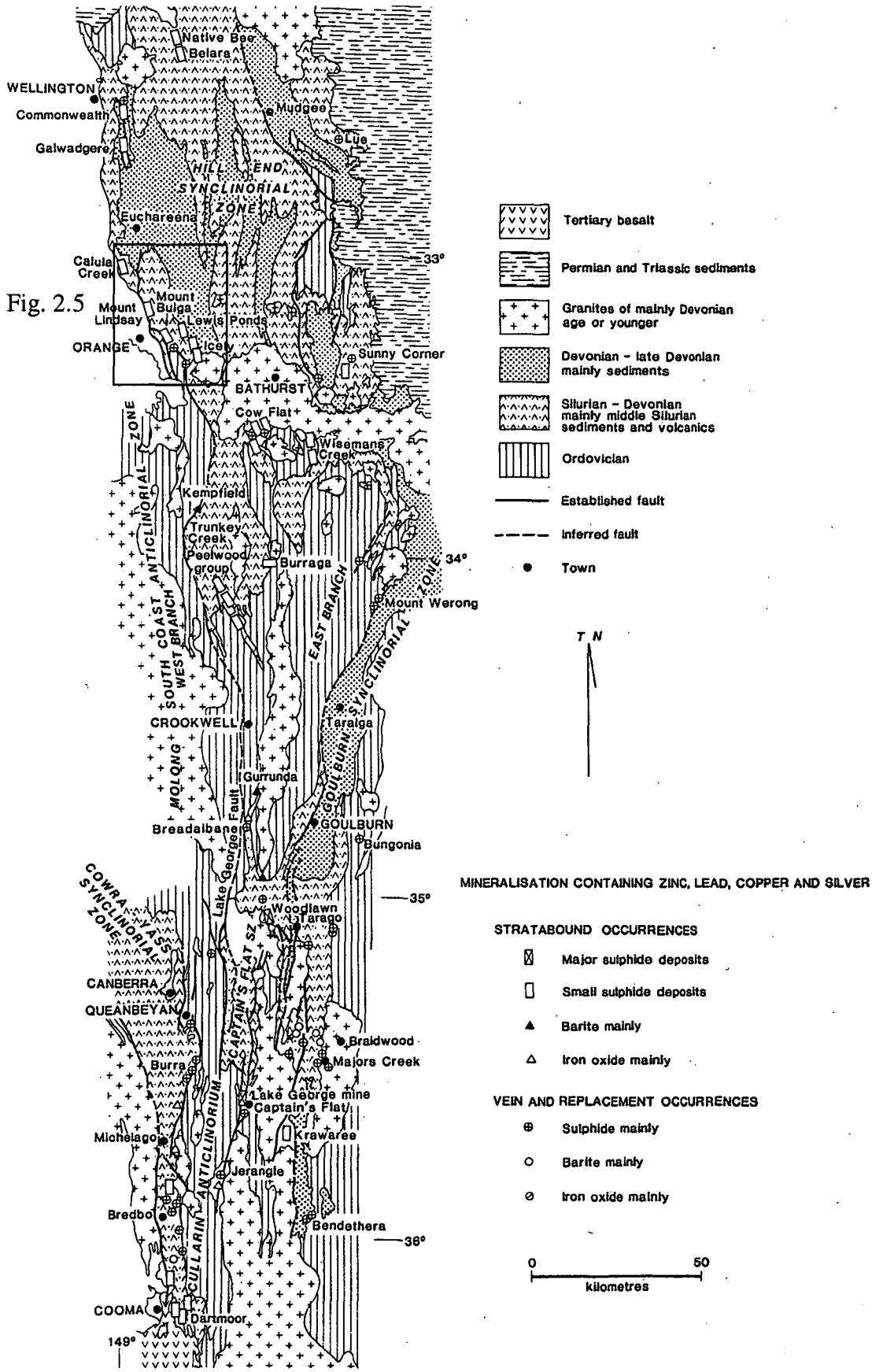

Fig. 2.5

Figure 2.6 Massive sulfide, barite and iron oxide deposits in the Hill End and Captains Flat-Goulburn troughs, after Davis (1990).

Some of the faults may have controlled magma emplacement and hydrothermal fluid flow (Davis, 1990). Glen (1995) interpreted thrust faults at Woodlawn and Captains Flat as reactivated syn-sedimentary structures associated with extension of the Captains Flat-Goulburn Trough.

In contrast, the Cobar Basin hosts small to large Cu-Au and Cu-Pb-Zn-Ag deposits, including CSA, Elura and Peak. These occur in fine-grained sedimentary successions. However, fault-bound units of flow-banded rhyolite and rhyolitic breccia have been documented in the footwall of the Peak deposit (Hinman and Scott, 1990). Cook et al. (1998) interpreted these bodies as subvolcanic rhyolite intrusions with quench-fragmented margins. The base metals occur in cleavage-parallel, quartz veins and discordant, pipe-like, semi-massive to massive sulfide bodies (Shi and Reed, 1998; Webster and Lutherborrow, 1998). Sulfides are associated with silicified rocks of varying alteration intensity. Mg-chlorite, dolomite and calcite occur locally in shears at the Peak deposit (Cook et al., 1998). The Cobar deposits occur adjacent to high strain zones or thrust faults (Cook et al., 1998; Shi and Reed, 1998). Many of these structures are interpreted to result from basin formation and inversion (Glen, 1995).

2.6 Summary

Lewis Ponds occurs in a Late Silurian succession of silicic volcanic and marine sedimentary rocks that flank the northwestern side of the Hill End Trough, north of the Bathurst Batholith and Lachlan Transverse Zone. The massive sulfide lenses are located at the contact of the Anson Formation and stratigraphically overlying Mullions Range Volcanics. These units host other small, stratabound massive sulfide deposits including Mt Bulga, Mt Shorter, Pride of the Hills, Calula and Daydawn.

The Hill End Trough is one of numerous elongate belts of Silurian and Devonian volcanic-sedimentary rocks in New South Wales. The basins opened obliquely in a backarc extensional environment, due to roll-back of the subducting slab, oblique convergence and collapse of the Ordovician crust. High heat flow resulted in partial melting of the crust, extensive granitic magmatism and widespread submarine to subaerial, silicic volcanism along the basin margins. granites (Table 2.1).

The Lewis Ponds area is characterised by a complex system of NNW- to N- trending thrust faults, linked to an inferred low angle detachment. Fold and fault repetition of the Mullions Range Volcanics and Anson Formation occurs in this area. Deformation accompanied basin inversion during the Middle Devonian to Early Carboniferous and possibly involved reactivation of syn-sedimentary, basin marginal faults.

CHAPTER 3

VOLCANIC-SEDIMENTARY SETTING OF THE HOST SEQUENCE

3.1 Introduction

The massive sulfide lenses at Lewis Ponds occur in a Late Silurian marine sedimentary succession (Figs. 3.1 and 3.2) of interbedded polymictic breccia, siltstone and quartz crystal-rich sandstone (Transitional Unit) and massive siltstone (Hangingwall Siltstone Unit). These deposits unconformably overlie altered and metamorphosed, dacitic quartz ± feldspar crystal-rich volcanics (Western Volcanic Succession). Limestone, quartz-feldspar phyric dacite, volcaniclastic sandstone and strongly foliated quartz-chlorite-sericite schist also occur in the Hangingwall Siltstone Unit. However, these lithologies are bound by steeply dipping faults. Figure 3.2 illustrates the lithological units and their interpreted stratigraphic and structural relationships. Polymictic limestone-clast breccia and mixed provenance breccia host the Main zone massive sulfide lenses. Toms zone occurs in the overlying siltstone unit. Massive granite and non-foliated quartz-feldspar porphyry dykes (Lewis Ponds Granite) have intruded Late Silurian rocks in eastern and southeastern parts of the prospect.

Previous facies interpretations of the Lewis Ponds host sequence were based on the recognition of abundant fossiliferous limestone in outcrop and drill core. Workers interpreted the sedimentary facies to record a shallow marine to emergent depositional setting during the waning stages of volcanic activity in the area (Hilyard, 1981; Parton, 1981; Pogson and Watkins, 1998; Valliant and Meares, 1998). Numerous authors documented the occurrence of limestone 'beds' intercalated with schist or altered slate (Wilkinson, 1888; Carne and Jones, 1919; Australian Geophysical report, 1965). Valliant and Meares (1998) interpreted limestone-bearing polymictic breccia units in the Main zone footwall as gravity flow deposits derived from a nearby limestone reef. They suggested that the massive sulfide lenses formed in shallow sub-basins bound by limestone reefs or sedimentary growth faults. Distinguishing between in situ and transported (allochthonous) fossiliferous limestone has important implications for determining the depositional environment of the host sequence and genesis of the Lewis Ponds deposits.

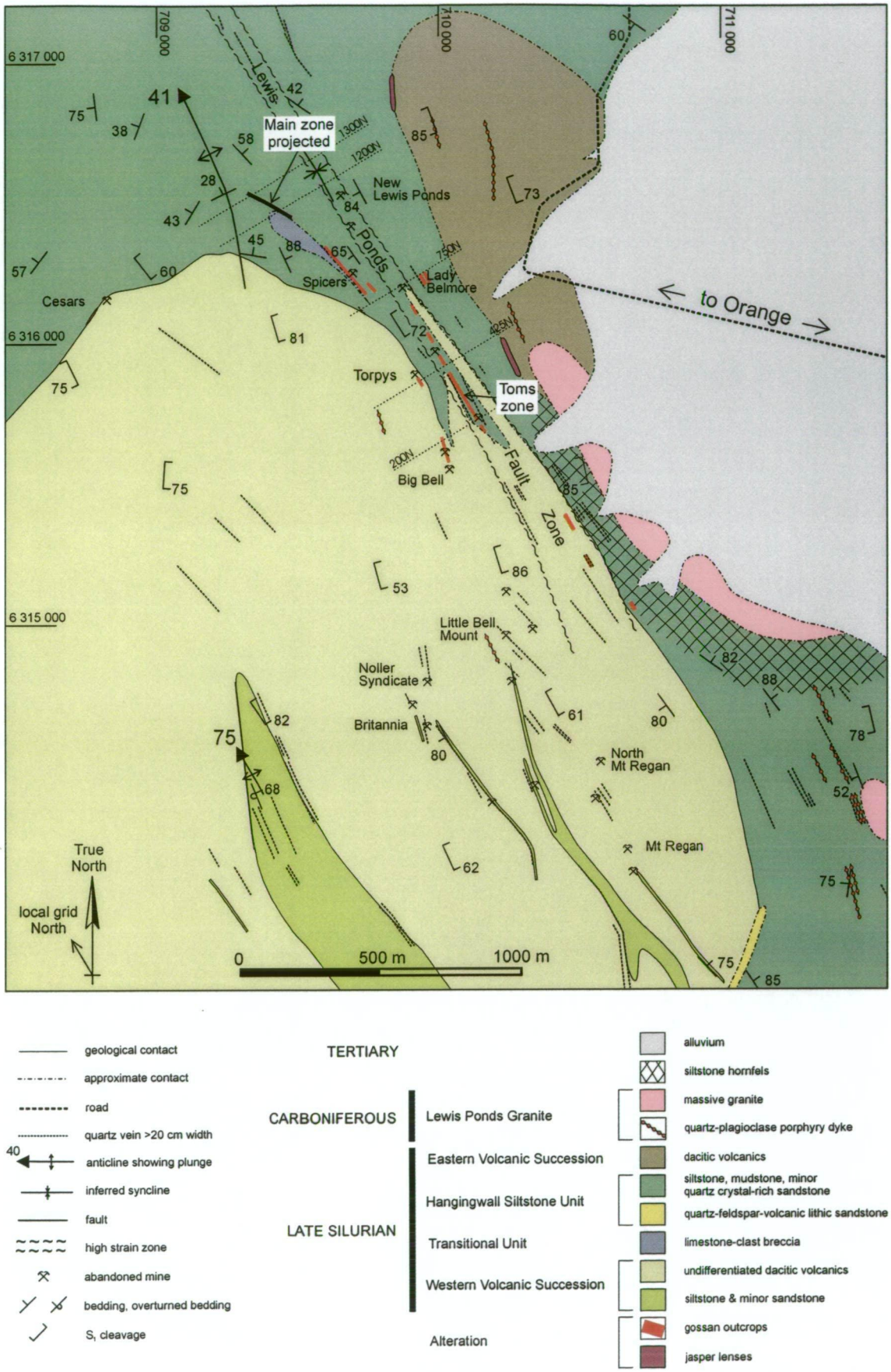

Figure 3.1 Lewis Ponds local surface geology map. Cross-sections referred to in this study are marked as dashed lines.

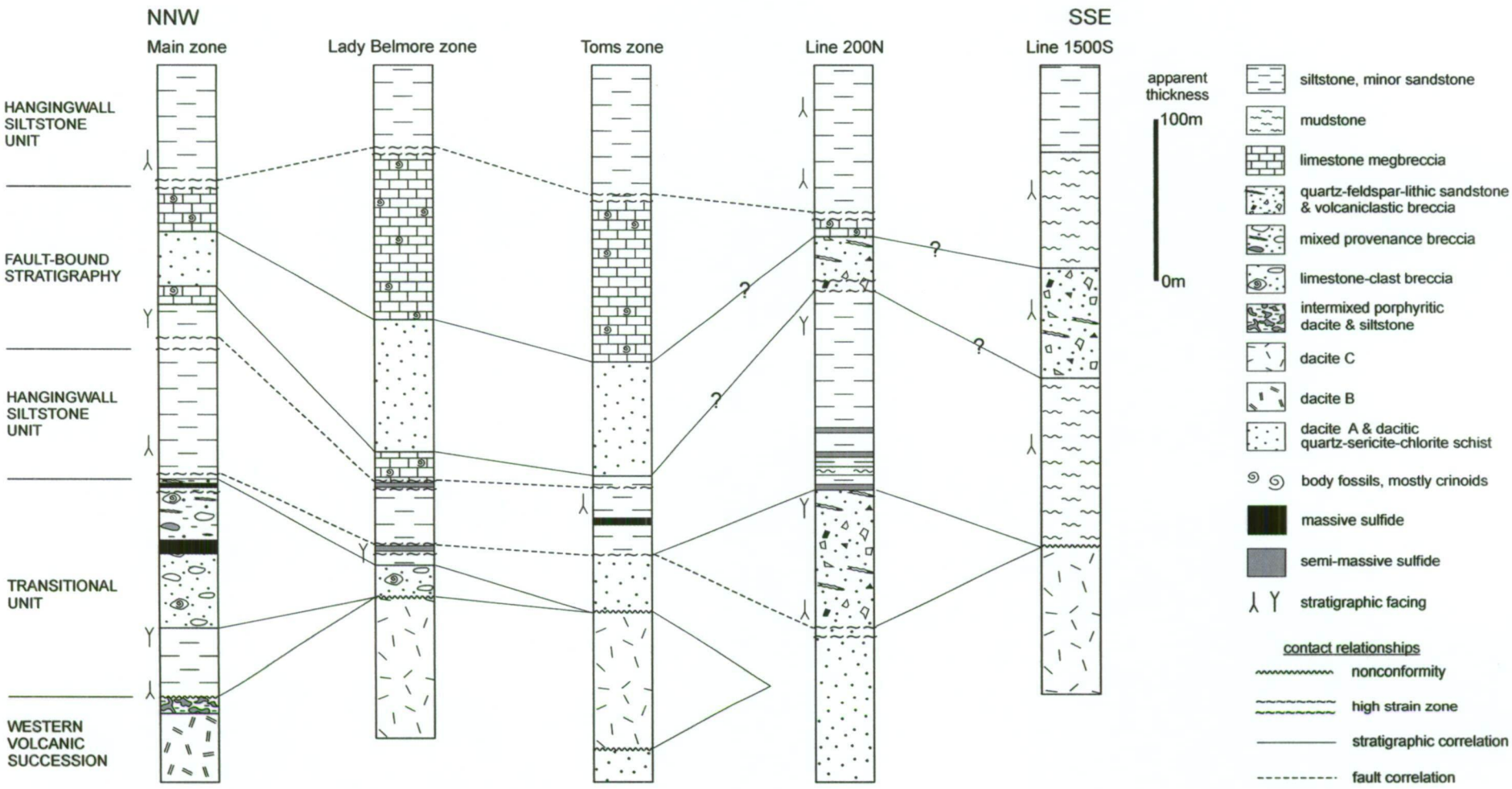

Figure 3.2 Generalised stratigraphy of the Lewis Ponds prospect showing stratigraphic and structural relationships. Apparent stratigraphic thicknesses are represented.

The Western Volcanic Succession, previously termed *Western Crystal Tuff* has been interpreted as lava flows, intrusions and pyroclastic or epiclastic deposits (Australian Geophysical report, 1965; Shepherd, 1972; Castle, 1976; Valliant and Meares, 1998). Shepherd (1972) suggested that the footwall pyroclastics were sourced from a volcanic centre occurring in the vicinity of Main zone. Valliant and Meares (1998) found evidence for a rhyolite dome and associated clastic facies in the Toms zone footwall. Hydrothermal alteration and strong cleavage development have obscured primary textures in the matrix of the volcanic rocks, complicating the interpretation of their origin. Therefore petrological descriptions, drill logs and analysis of whole rock geochemical data are required to distinguish between different clastic and coherent facies in the footwall.

This chapter outlines the volcanic and sedimentary facies observed at Lewis Ponds. Petrological descriptions, cross-sections and level plans are used to constrain the depositional environment and overall volcano-sedimentary facies architecture. The Lewis Ponds host sequence is placed in a regional context by considering the overall palaeogeography, eruption styles and volcanic provenance of the Mullions Range Volcanics.

3.2 Methods

Table 3.1 summarises the lithofacies defined in each of the local stratigraphic units at Lewis Ponds. Their definition is based on field observations, petrological descriptions and whole rock geochemistry (for the volcanic rocks). Field work involved prospect-scale mapping and logging the core from thirty diamond drill holes and wedges. The location and trend of these drill holes are presented on a level plan diagram in Appendix 1. In addition, Tri Origin logs were reinterpreted to generate cross-sections and level plans for determining the facies geometry (Fig. 3.3).

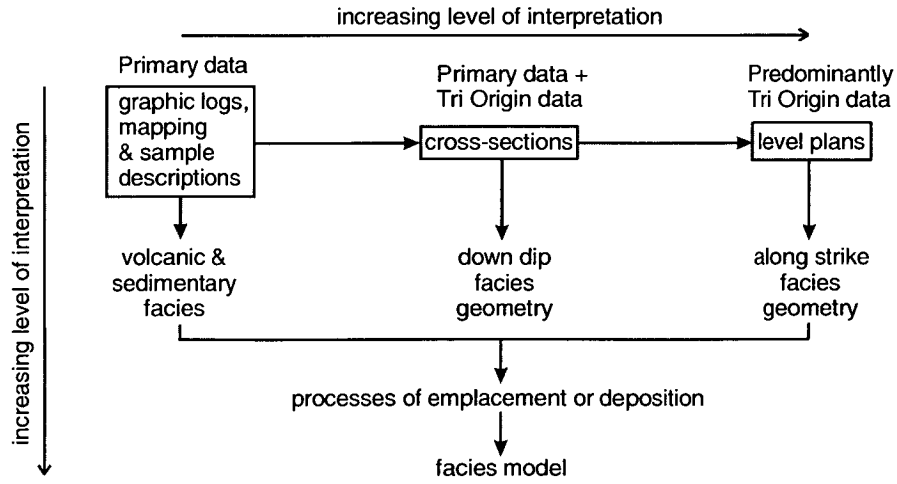

Figure 3.3 Flow diagram illustrating the use of primary data and drill log information provided by Tri Origin for the description and interpretation of volcanic and sedimentary facies at Lewis Ponds.

	Lithofacies association	Description	Interpretation
Western Volcanic Succession	Siltstone lenses	5-300 m wide, discontinuous, broadly concordant with bedding	Siltstone beds or screens of host rock separating large porphyritic dacite sills
	Lithofacies association A: dacitic quartz-sericite schist and quartz-feldspar phyric dacite	Massive, 5-10% 0.1-4 mm euhedral quartz phenocrysts ± 5-20% 0.1-2.5 mm euhedral plagioclase phenocrysts in a very fine-grained microcrystalline groundmass	Coherent dacite - lava flows or intrusions
	Lithofacies association B: quartz-plagioclase phyric dacite	10-25% 0.2-1.5 mm euhedral-subhedral embayed quartz phenocrysts, 15-30% 0.1-2.5 mm plagioclase phenocrysts and 2-5% altered biotite phenocrysts in weakly foliated, microcrystalline groundmass	Syn-sedimentary porphyritic dacite cryptodome
	Lithofacies association C: dacitic quartz-chlorite-sericite schist and quartz-plagioclase phyric dacite	5-20% 0.5-5 mm euhedral-subhedral embayed quartz phenocrysts ± 5-20% 0.5-3 mm plagioclase phenocrysts, trace K-feldspar and biotite phenocrysts in strongly foliated, microcrystalline groundmass	Syn-sedimentary porphyritic dacite sills
	Intermixed siltstone, quartz crystal-rich sandstone and quartz-plagioclase porphyry	Non-stratified monomictic, consists of angular quartz-plagioclase porphyry clasts in silicified siltstone; and siltstone stringers in coherent quartz-plagioclase porphyry	Fluidal peperite, grading into massive quartz-plagioclase phyric dacite
Transitional Unit	Lower lithofacies association: massive breccia and pebbly-granular sandstone; minor quartz crystal-rich sandstone and siltstone	Monomictic to polymictic, matrix-supported, consists of elongate pebbles-boulders of fossiliferous limestone, siltstone, mudstone, dacite and sandstone in quartz crystal-rich, granular-sandy-mudstone matrix	Thick subaqueous polymictic debris flow deposits
	Upper lithofacies association: interbedded siltstone, sandstone and breccia	Massive or thinly-laminated siltstone, minor poorly-sorted fossiliferous quartz crystal-rich sandstone and polymictic breccia	Subaqueous polymictic mass flow deposits
Hangingwall Siltstone Unit	Interbedded quartz crystal-rich sandstone and siltstone	**Sandstone:** moderately to well-sorted, consists of 25-30% angular quartz crystal fragments in clay-rich matrix. **Siltstone:** light grey, sandy in part, fissile, massive or thinly laminated	Turbidites and hemipelagic deposits
	Interbedded mudstone, siltstone and sandstone	**Sandstone:** moderately to well-sorted strongly calcareous quartz crystal-rich sandstone **Mudstone:** medium to dark grey	Turbidites and hemipelagic deposits
	Interbedded volcaniclastic breccia, sandstone and mudstone	**Breccia:** polymictic, clast or matrix-supported, comprises mudstone, siltstone and aphyric-porphyritic dacite pebbles in feldspar crystal-rich muddy-sandstone matrix **Mudstone:** medium to dark grey	Syn-eruptive to post-eruptive volcaniclastic, polymictic mass flow deposits and hemipelagic deposits

Table 3.1 Lithofacies associations at Lewis Ponds. The term 'schist' is used to denote strongly foliated coherent or clastic volcanic rocks where hydrothermal alteration and deformation have destroyed primary textures in the rock.

	Lithofacies association	Description	Interpretation
fault-bound stratigraphy	Massive and fragmented recrystallised fossiliferous limestone	Angular pebbles to 90 m thick blocks of variably recrystallised limestone in siltstone or quartz crystal-rich sandstone matrix	Fragmented bioherm, talus or mass flow deposits; possible lateral facies variation of the Transitional Unit
	Dacitic quartz-sericite schist and quartz-feldspar phyric dacite	5-10% 0.1-2 mm euhedral-subhedral quartz phenocrysts, crystal fragments ± 0.1-2 mm plagioclase and pyroxene phenocrysts in strongly foliated, microcrystalline groundmass	Porphyritic dacite, grading into volcaniclastic deposits along-strike south of Toms zone
	Interbedded volcaniclastic breccia, sandstone and siltstone	**Sandstone and breccia:** contains 5-30% siltstone and fine-grained, siliceous rhyolitic clasts in a quartz-feldspar crystal-rich muddy-sandstone matrix	
Eastern Volcanic Succession	Dacitic quartz-sericite schist and quartz-feldspar phyric dacite	3-4% 0.4-4.2 mm euhedral quartz phenocrysts and 20-25% 0.1-2.5 mm weakly albitised or sericitised plagioclase phenocrysts in chlorite altered microcrystalline groundmass	Porphyritic dacite and minor quartz crystal-rich volcaniclastic deposits

Table 3.1 continued. Lithofacies associations at Lewis Ponds. The term 'schist' is used to denote strongly foliated coherent or clastic volcanic rocks where hydrothermal alteration and deformation have destroyed primary textures in the rock.

An attempt was made to estimate the true stratigraphic thickness of beds and units from cross-sections and drill core. However, the host sequence is tightly folded, and dissected by high strain zones.

An eight kilogram fossiliferous limestone sample (LPD001), collected from near the old quarry was dissolved in dilute acetic acid for palaeontological analysis and dating. After six weeks, components of the residue were examined under a low-magnification, binocular microscope. Non-calcareous fossils were separated from the residue using a dense sodium polytungstate solution.

3.3 Western Volcanic Succession

The Western Volcanic Succession is a thick (>1 000 m), massive unit of quartz ± plagioclase phyric volcanics, quartz-chlorite-sericite ± biotite schist and minor siltstone (Figs. 3.1 and 3.2). Phyllosilicate minerals have variably overprinted primary textures throughout the volcanic unit. The upper contact is rarely exposed in outcrop. It is characterized by local faults and a downward deflection of cleavage due to the competency contrast between the volcanics and stratigraphically overlying siltstone.

Three lithofacies associations; A, B and C were distinguished in the Western Volcanic Succession using overall texture, phenocryst abundance, crystal size and immobile element geochemistry. All of the rocks contain visible quartz phenocrysts, consistent with rhyolitic compositions and least altered rocks contain 68-76 wt % SiO_2 (Appendix 4). However, immobile element and major element compositions indicate that they are dacite and andesite (see Chapter 6, section 6.4). In this thesis, the rocks are referred to as dacite.

Lithofacies association A

A thick (>100 m) non-stratified package of dacitic quartz-chlorite-sericite ± biotite schist and weakly altered quartz-plagioclase phyric dacite occurs in the Toms zone footwall (Table 3.1; Figs. 3.4 and 3.5). These lithofacies differ from the remainder of the Western Volcanic Succession in having finer grained textures, a wide variation in crystal size and fewer quartz crystals. The weakly to strongly foliated rocks consist of glomerocrysts and euhedral to subhedral phenocrysts of quartz and plagioclase in a fine-grained chlorite-sericite-altered microcrystalline groundmass (Fig. 3.6A).

Many samples have irregular pseudoclastic textures in thin section. Some consist of patchy biotite-rich and biotite-poor domains. Arcuate chlorite-biotite bands wrap around elongate fine-grained quartz lozenges in the biotite-poor domains (Fig. 3.6B). This texture may represent relict perlite or an anastomosing disjunctive cleavage. The groundmass rarely contains round, 0.2-1 mm quartz-biotite-chlorite-carbonate aggregates and wispy, cleavage-parallel biotite lenses, up to 9 mm long (Fig. 3.6C and D). Radiating internal textures suggest that the round aggregates are altered amygdales or spherulites. The wispy lenses have identical textures to the surrounding fine-grained groundmass and are interpreted as flow-banding rather than clasts. False pyroclastic textures resulting from phyllosilicate alteration of perlitic and flow-banded coherent volcanics have been documented by numerous authors (eg. Allen, 1988; Doyle, 2001).

The weakly altered quartz-plagioclase phyric volcanics are interpreted as coherent dacite. Clastic textures including angular crystal fragments, volcanic lithics and glass shards are not present. The rocks contain texturally unmodified plagioclase glomerocrysts. False clastic textures resulting from hydration and alteration of coherent glassy domains or infilling of vesicles occur in numerous samples. The dacite, lacking internal structure may be a series of overlapping lava flows or thick massive intrusions. However, hydrothermal alteration and strong cleavage development prevents further interpretation of the rocks.

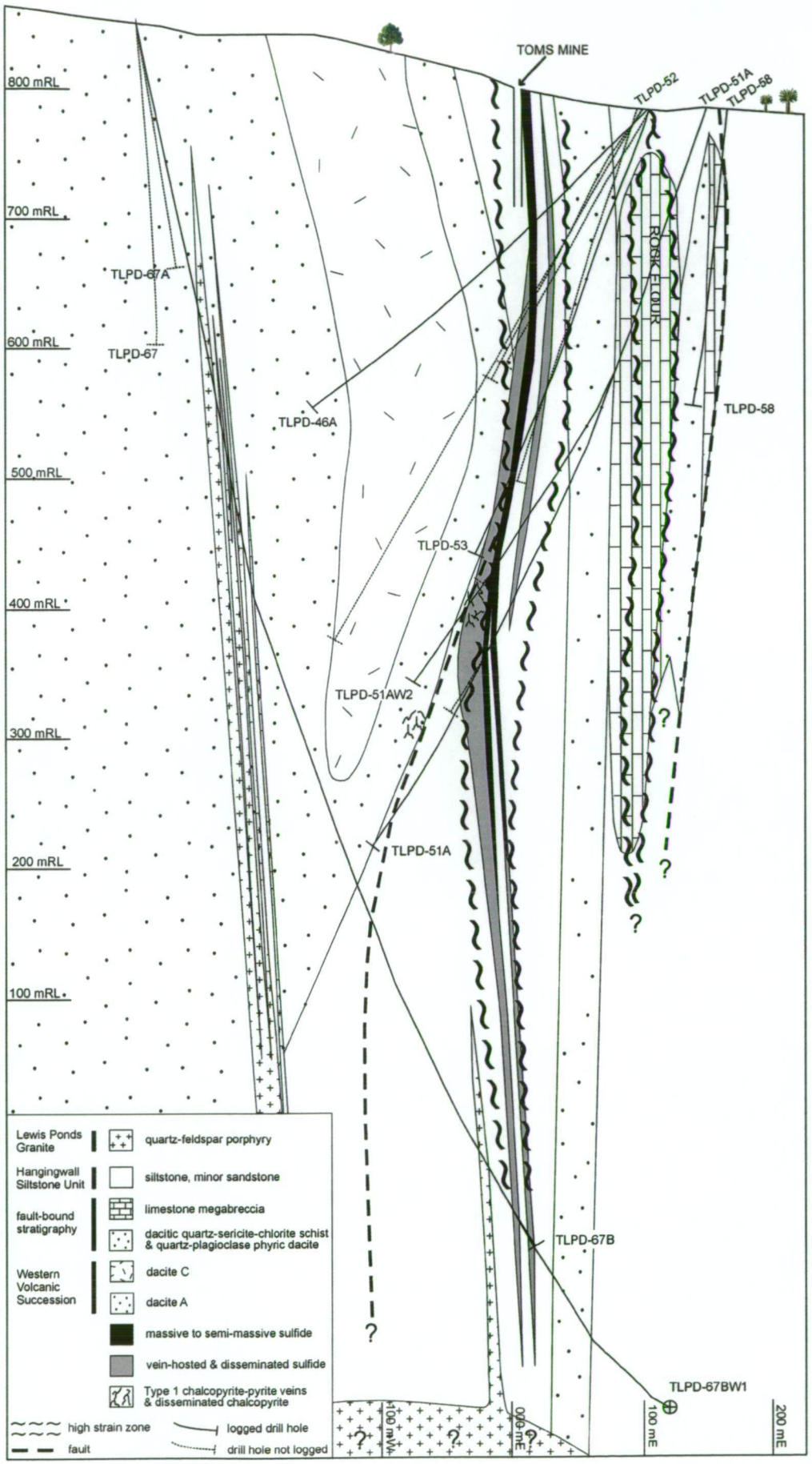

Figure 3.4 Line 425N section showing the Toms zone host sequence. Refer to Figure 3.1 for location of cross-section.

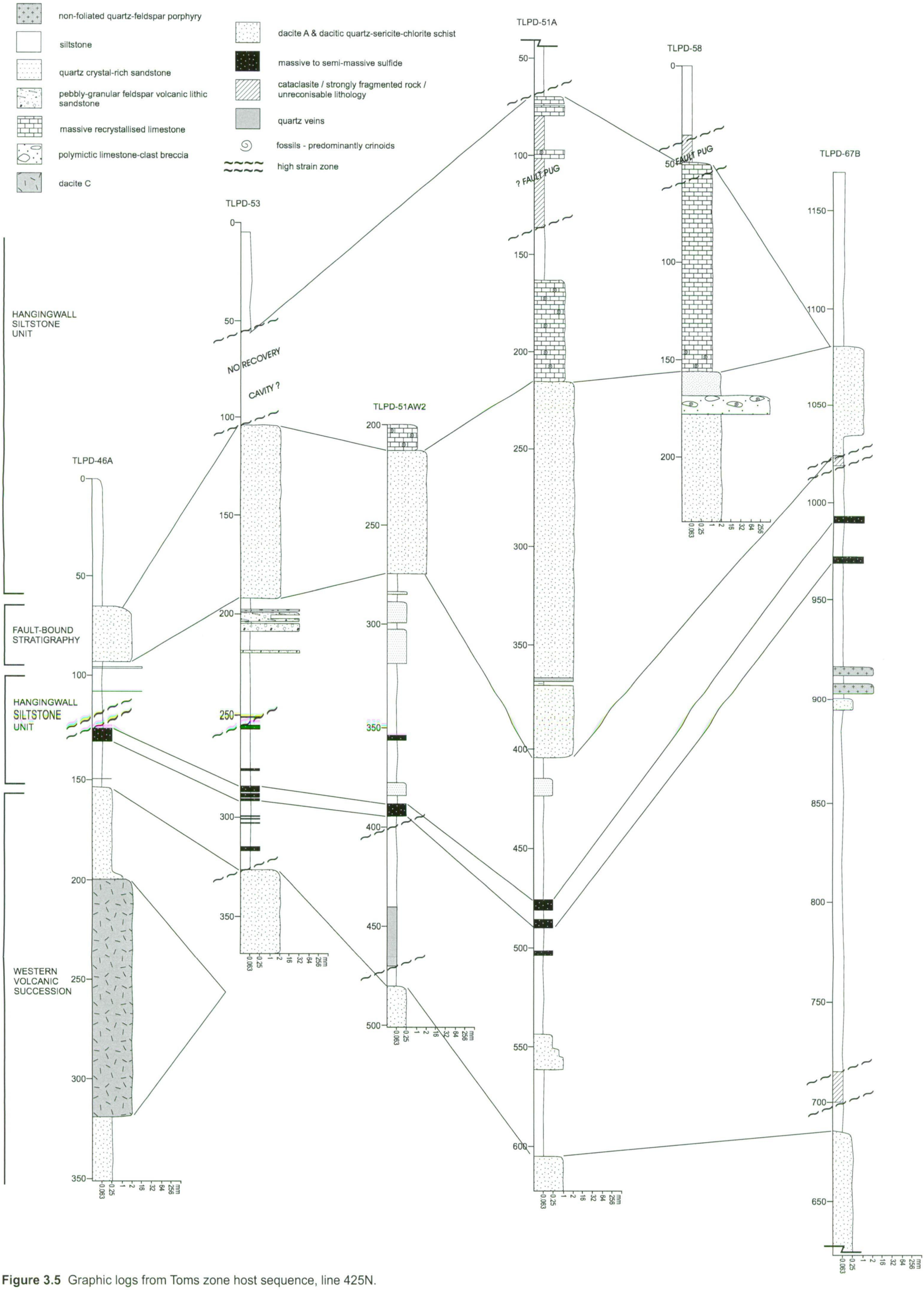

Figure 3.5 Graphic logs from Toms zone host sequence, line 425N.

Figure 3.6 Lithofacies in the Western Volcanic Succession

A Quartz-plagioclase phyric dacite A, consisting of euhedral to subhedral quartz phenocrysts, albitised plagioclase phenocrysts and plagioclase glomerocrysts in a weakly altered microcrystalline groundmass with secondary biotite and pyrite. TLPD-51A, 609 m.

B Photomicrograph of dacitic quartz-sericite-biotite schist The arcuate, anastomosing biotite-muscovite bands, resembling perlitic fractures (p) wrap around lozenges of fine-grained quartz. TLPD-46A, 346 m. Plane polarised light.

C Dacitic quartz-sericite-biotite schist with a false clastic texture. The round aggregates consist of quartz, biotite, chlorite and opaque minerals. TLPD-67B, 306 m. Plane polarised light.

D Dacitic quartz-sericite-biotite schist characterised by elongate, wispy biotite-muscovite-quartz lenses. These lenses have similar internal textures to the surrounding fine-grained groundmass. TLPD-67B, 306 m. Plane polarised light.

E Quartz-plagioclase phyric dacite B. Consists of 20% euhedral to subhedral embayed quartz phenocrysts and 30% euhedral plagioclase phenocrysts in a microcrystalline groundmass. Weakly foliated. Sample LPD-024.

F Photomicrograph of quartz-plagioclase phyric dacite B, characterised by embayed, euhedral to subhedral quartz phenocrysts, albitised plagioclase phenocrysts and chlorite-Fe oxide-altered biotite phenocrysts in a microcrystalline groundmass. Weak pervasive sericite-calcite alteration assemblage. TLPD-18, 532 m.

G Chlorite-sericite-altered quartz-plagioclase phyric dacite B. Perlitic fractures (p) are preserved in the groundmass as overlapping, arcuate white mica bands. Sample LPD-24.

H Quartz-plagioclase phyric dacite C. Consists of euhedral quartz and altered biotite phenocrysts in a non-foliated microcrystalline groundmass. Biotite phenocrysts have been replaced by chlorite and Fe-Ti oxide minerals. TLPD-46A, 297 m.

Abbreviations: qtz = quartz, fsp = plagioclase, bt = biotite, op = opaque, p = perlitic fractures.

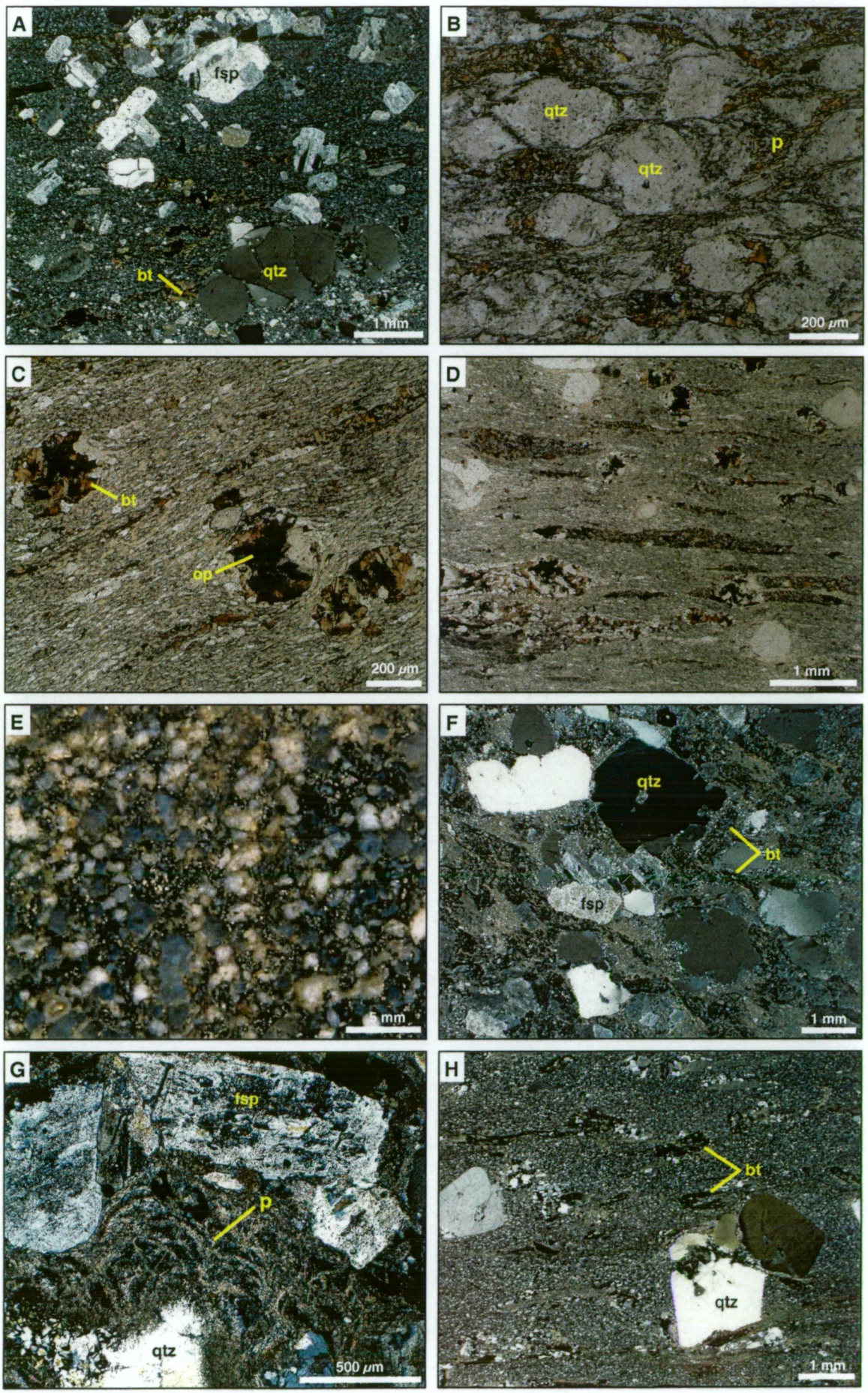
A
fsp
bt
qtz
1 mm
B
qtz
p
qtz
200 μm
C
bt
op
200 μm
D
1 mm
E
5 mm
F
qtz
bt
fsp
1 mm
G
fsp
p
qtz
500 μm
H
bt
qtz
1 mm

Lithofacies association B

Lithofacies association B occurs in the Main zone footwall (Fig. 3.2). Contacts with the adjacent volcanic rocks were not observed in drill holes or outcrop. The upper contact is characterised by a thin (<10 m) unit of intermixed quartz-plagioclase porphyry and siltstone. This unit grades down into massive, texturally homogeneous dacite. The highly porphyritic rocks consist of euhedral to subhedral, embayed phenocrysts and glomerocrysts of quartz, plagioclase and biotite in a microcrystalline groundmass (Fig. 3.6E and F). Biotite phenocrysts have been preferentially replaced by quartz, chlorite and Ti-Fe-oxides. Relict perlite textures occur in the groundmass of altered samples (Fig. 3.6G). The perlitic fractures are preserved as overlapping arcuate white mica bands. Dacite B is distinguished from the other volcanic rocks by the high phenocryst abundance and weakly-developed foliation.

Intermixed siltstone, quartz crystal-rich sandstone and quartz porphyry

The upper contact of lithofacies associations B and C is characterized by 1-10 m thick intervals of monomictic breccia (Fig. 3.7). This distinctive lithofacies also occurs within polymictic mass flow deposits in the Transitional Unit. It comprises very angular, ragged clasts of quartz-plagioclase porphyry and quartz-chlorite schist in a silicified siltstone or fine-grained sandstone matrix (Fig. 3.8A and B), or ragged siltstone stringers in a matrix of quartz-plagioclase porphyry (Fig. 3.8C and D). In one drill hole, massive porphyritic dacite grades up into siltstone with isolated quartz-plagioclase porphyry clasts (TLPD-36W in Fig. 3.7).

The irregular porphyry-siltstone lithofacies could represent peperite, deformed sedimentary breccia or tectonic breccia. However, fluidal peperite is the preferred interpretation for the following reasons:

- Siltstone adjacent to the quartz-plagioclase porphyry domains is indurated and occasionally bleached (eg. Fig. 3.8B), consistent with localised thermal metamorphism.
- The quartz-plagioclase porphyry occurs in highly irregular patches, suggesting that it behaved in a ductile fashion before solidifying. The clasts were further attenuated by deformation and possibly the compaction of vesicles.
- In places, individual quartz crystals occur within adjacent siltstone domains, implying fragmentation of the porphyry and mixing with unconsolidated, fine-grained sediment.
- Although the overlying siltstone is interbedded with sandstone, the peperite host sedimentary rock is unstratified. This homogenisation is likely to reflect re-arrangement of the grains during fluidisation and mixing with the porphyry. However, strong cleavage development could also contribute to the loss of bedding structures in the siltstone.

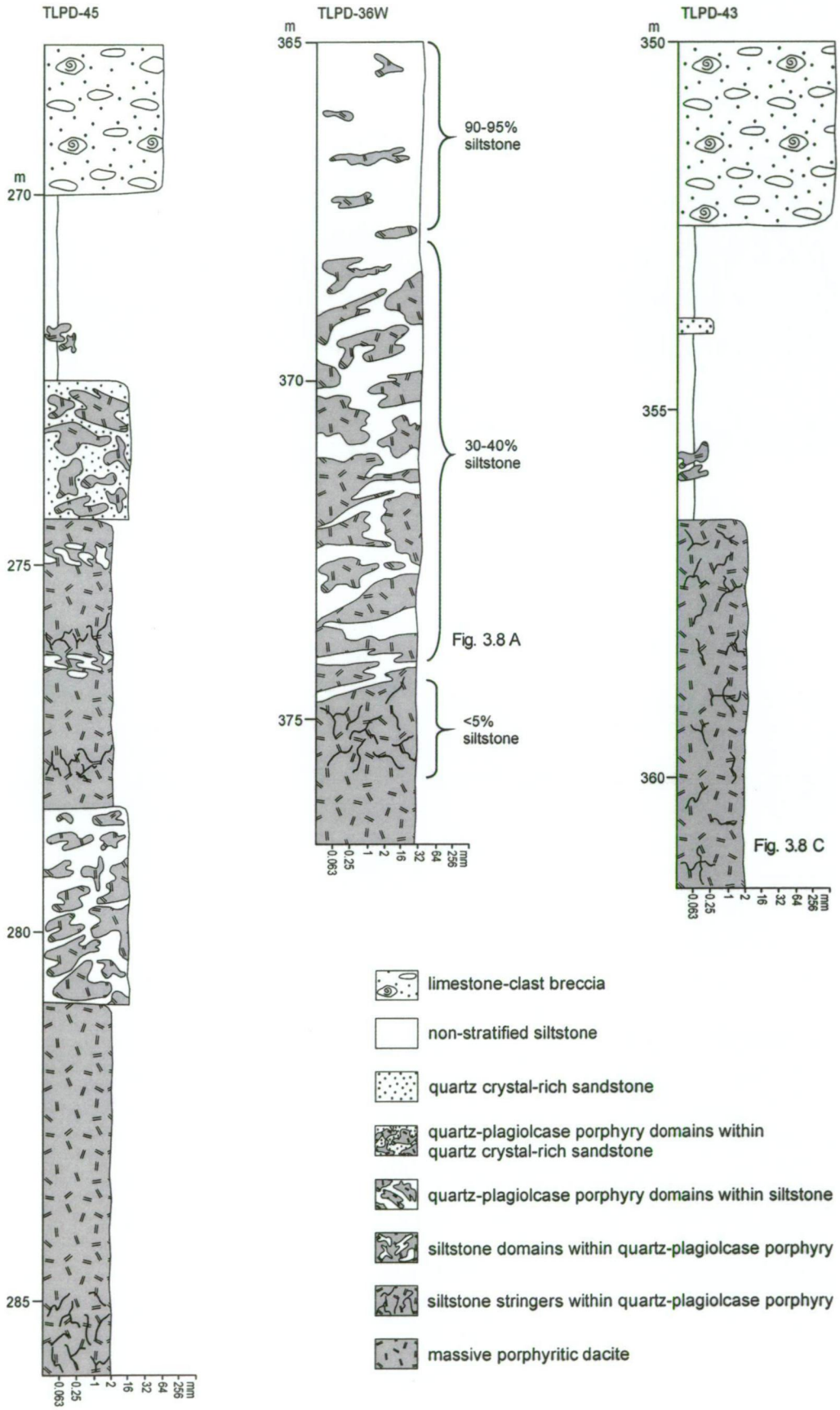

Figure 3.7 Graphic logs of intermixed quartz-plagioclase porphyry and siltstone facies. Drill holes TLPD-45, TLPD-36W and TLPD-43.

Figure 3.8 Photos of intermixed quartz-plagioclase porphyry and siltstone facies

A Very angular, ragged quartz-plagioclase porphyry clasts in a matrix of indurated siltstone. Upper contact of dacite B. TLPD-36W, 374 m.

B Coherent quartz-plagioclase porphyry domains in quartz crystal-rich sandstone. Bleached zones surround the quartz-feldspar porphyry. Upper contact of dacite B. TLPD-27, 771 m.

C Indurated siltstone stringers in quartz-plagioclase porphyry from the upper contact of dacite B. TLPD-43, 361 m.

D Wispy, indurated siltstone domains in a matrix of intensely altered quartz-chlorite schist. Transitional Unit, Main zone hangingwall. TLPD-12, 431 m.

Abbreviations: d = quartz-plagioclase porphyry, s = siltstone, sst = sandstone, b = bleached rim.

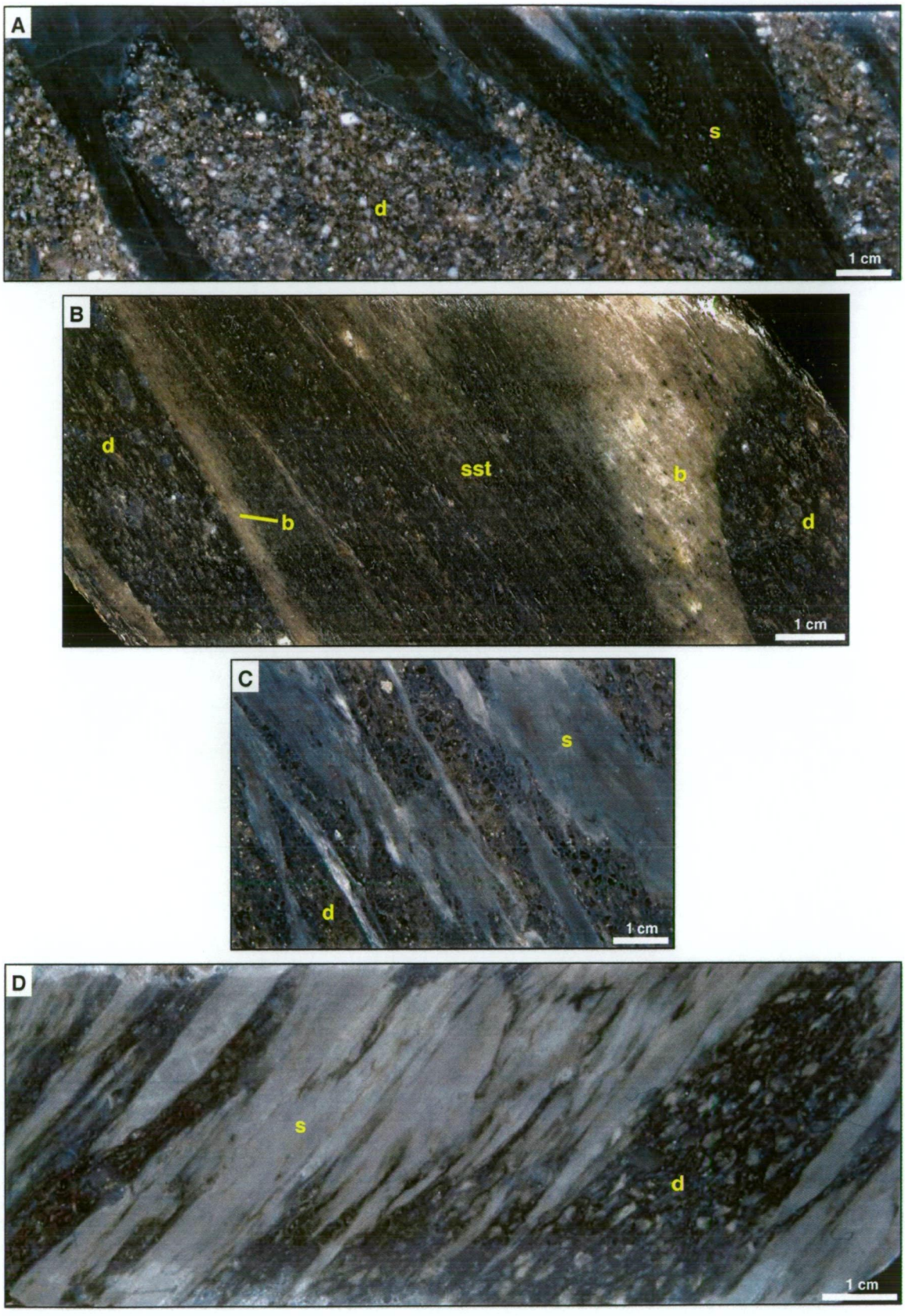
A
s
d
1 cm
B
d
sst
b
b
d
1 cm
C
s
d
1 cm
D
s
d
1 cm

- Jigsaw-fit clasts and angular blocky clasts are uncommon, indicating that in situ brittle fracturing was not the predominant mechanism of fragmentation, forming these breccias.

Fluidal peperite associated with rhyolite or dacite has been documented by numerous authors (eg. Busby-Spera and White, 1987; Messenger et al., 1997; Hunns and McPhie, 1999). It forms when fine-grained wet sediment becomes fluidised due to the shallow intrusion or extrusion of magma. Displacement of the fluidised sediment is facilitated by a continuous vapour-film existing at the magma-sediment interface, preventing rapid cooling and brittle fracturing of the rock (Busby-Spera and White, 1987). Disintegration of the magma is aided by vesiculation when emplaced in shallow water (Hunns and McPhie, 1999). At Lewis Ponds, the lack of vesicles in porphyry and siltstone domains indicates a low volatile content in the magma or suppression of volatile exsolution due to high confining pressures.

Intervals of intermixed quartz porphyry and siltstone occurring in the Transitional Unit (Fig. 3.8D) are not spatially associated with coherent dacite. These units may have developed as peperite beyond the margins of small porphyritic dacite lobes that intruded the polymictic breccia, but were not intersected by drill holes. Alternatively, they may represent altered and deformed siltstone-clast breccia deposited from subaqueous mass flows. In both cases, wispy quartz porphyry and siltstone domains may occur as the clasts.

Interpretation of lithofacies association B

Lithofacies association B is interpreted as a relatively thick, massive syn-sedimentary dacite cryptodome. In plan view, the discordant body is onlapped by tightly folded beds of polymictic breccia and siltstone to the north, suggesting that it formed a topographic high on the seafloor or was associated with local up-doming of the host sediment. The intermixed siltstone and quartz-plagioclase porphyry facies occurring along the upper margin is probably dacitic fluidal peperite, resulting from magma-wet sediment interactions and quench fragmentation of the outer carapace.

Lithofacies association C

Lithofacies association C occurs in the Toms zone footwall within finer grained dacitic quartz-chlorite-sericite schist (Figs. 3.4, 3.5 and 3.9). It defines an elongate concordant unit, 700-800 m long and up to 100 m thick. Pervasive chlorite-sericite alteration has obscured the upper and lower contacts, which are only recognisable in drill core by the increased quartz crystal size and abundance. Texturally similar dacitic volcanics also crop out extensively south of Toms mine.

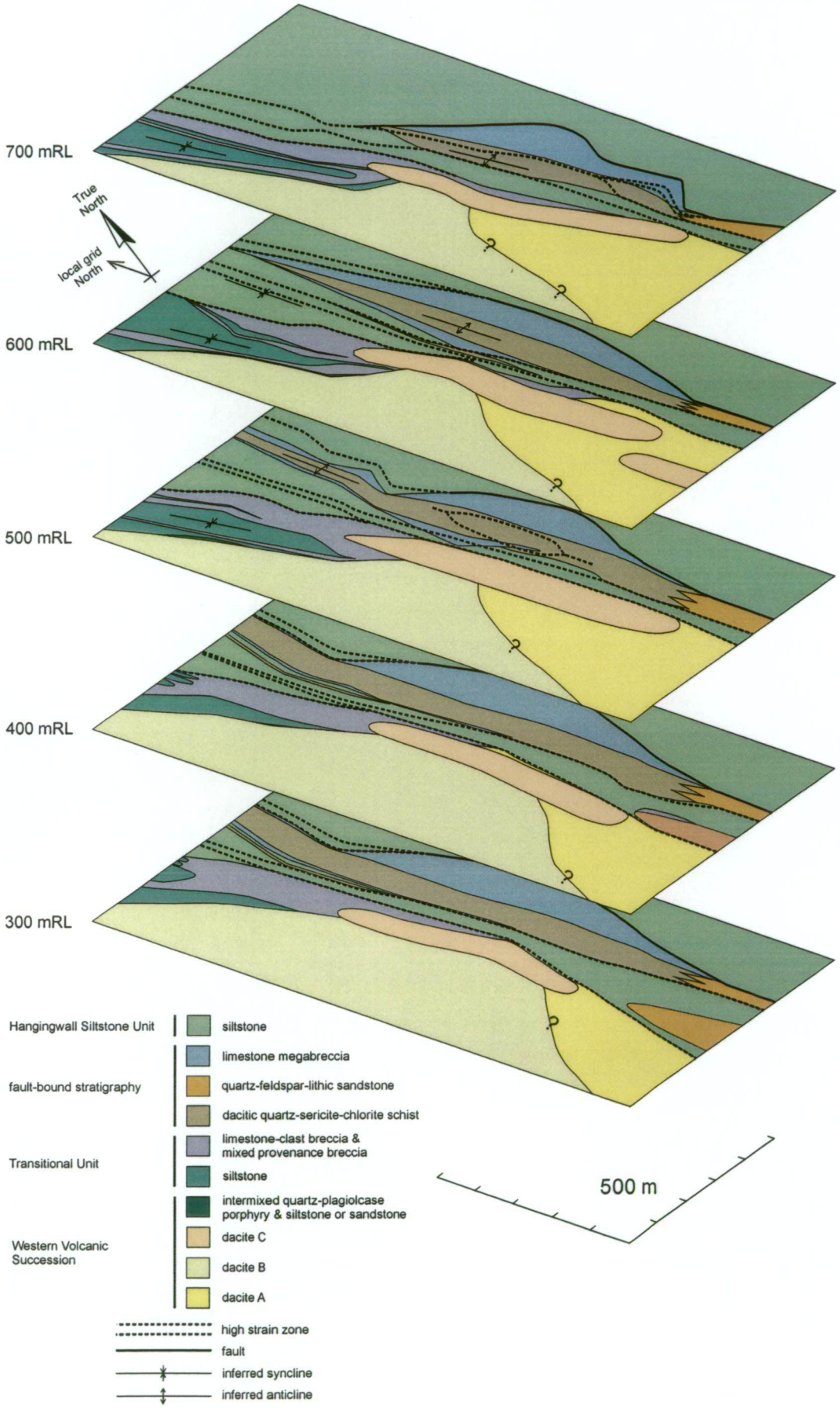

Figure 3.9 Composite level plan diagram illustrating the facies geometry and interpreted structures from drill log data. Level plans were constructed in *Mapinfo* and *Discover* using 50 m thick envelopes.

Lithofacies association C comprises dacitic quartz-chlorite-sericite schist and weakly altered quartz-plagioclase phyric dacite (Table 3.1). The volcanics consist of 5-20% euhedral to subhedral, embayed quartz phenocrysts in a strongly foliated, chlorite-sericite-altered, microcrystalline groundmass (Fig. 3.6H). Weakly altered samples contain sericitised plagioclase phenocrysts, rare K-feldspar phenocrysts, and chlorite-Fe-oxide-altered biotite. Parts of the upper contact are characterised by ragged quartz porphyry clasts in a siltstone matrix (see discussion of intermixed siltstone and quartz porphyry).

Lithofacies association C is interpreted as a coherent porphyritic dacite sill that intruded the polymictic breccia to the north and quartz-feldspar phyric volcanics to the south (Fig. 3.9). The intermixed quartz-feldspar porphyry and siltstone lithofacies (peperite) probably results from emplacement of the intrusion into unconsolidated sediment. Extensive areas of quartz-plagioclase phyric dacite C occurring south of Toms mine may occur as a large intrusive dome or series of stacked sills.

Siltstone lenses

Siltstone lenses occur in the southern part of the prospect within coherent dacite (Fig. 3.1). The 5-300 m wide, NNW-trending lenses have sharp, irregular margins characterised by small rounded clasts (<10 cm) and larger cleavage-parallel rafts (up to 1 m) of quartz-plagioclase phyric dacite in a siltstone matrix. These irregular lobate contacts may have been further attenuated by deformation. The sedimentary rock contains silt and sand grains of quartz.

These lenses are interpreted as sections of host rock separating large sill-like porphyritic dacite intrusions (screens) or discontinuous siltstone beds deposited with the volcanics. Irregular contacts occurring between the siltstone and adjacent dacite may result from intrusion of a fine-grained sediment. The lenses are sub-parallel to bedding in the overlying Hangingwall Siltstone Unit. Although bedding is rarely observed, some of the siltstone lenses may be folded. Shepherd (1972) incorrectly interpreted a chlorite-biotite-altered siltstone lens at the Britannia mine (Fig. 3.1) as a body of ultramafic tremolite schist.

3.4 Transitional Unit

The Transitional Unit has been described as a sequence of "tuff, siltstone, limestone and heterolitihc fragmental rock" (Valliant and Meares, 1998). Interbedded polymictic breccia, pebbly-granular sandstone and siltstone unconformably overlie the Western Volcanic Succession, forming a northerly-thickening wedge, north of Toms zone (Table 3.1; Figs. 3.9 and 3.10). The unit occurs over at least 1 100 m strike length. Stratigraphic facing and bedding-cleavage (vergence) relationships obtained from drill core indicate the presence of a

tight syncline in the Main zone footwall (Fig. 3.10). These stratigraphic and structural relationships are discussed in Chapter 4. The Transitional Unit is subdivided into an upper and lower lithofacies association (Table 3.1; Fig. 3.11).

Lithofacies associations

Lower lithofacies association: massive breccia and pebbly-granular sandstone with minor siltstone and quartz crystal-rich sandstone

The lower lithofacies association is characterised by very thick (10-100 m), massive, extremely poorly-sorted, monomictic to polymictic breccia and pebbly-granular sandstone units with sharp bases and tops (Figs. 3.10 and 3.11). These stratigraphically overlie a thin (<5 m) layer of siltstone at the top of the Western Volcanic Succession. A high strain zone separates the lower mixed provenance breccia from the Hangingwall Siltstone Unit in the Main zone hangingwall (Fig. 3.10). Although the lithofacies extends for 1 100 m strike length at depth, limestone-clast breccia only crops out over a small area surrounding the old quarry (Fig. 3.1 and map enclosure). The breccia deposits thin toward the north, laterally grading into interbedded limestone-clast breccia, siltstone and mixed provenance breccia (Figs. 3.9 and 3.10). High-grade massive sulfide lenses overlie thick intervals of limestone-clast breccia.

The matrix-supported breccia comprises lenticular and blocky, foliation-parallel pebbles, cobbles and boulders of recrystallised fossiliferous limestone, siltstone, dark grey mudstone, calcareous sandstone, feldspar crystal-rich sandstone and quartz porphyry, and aphyric felsic volcanic pebbles in a poorly-sorted, quartz crystal-rich, granular-sandy-mudstone matrix (Fig. 3.12A and B). Variations in average clast size and abundance suggest that internal layering or numerous depositional units occur within the breccia. The upper 1-3 m consists of either finer grained, matrix-supported breccia or poorly-sorted, pebbly-granular sandstone (Fig. 3.11).

Three types of breccia are recognised, each with a different clast population (Table 3.2). Siltstone-clast breccia and polymictic breccia with a mixed provenance overlie a 10-80 m thick monomictic to polymictic, limestone-rich unit (Figs. 3.10 and 3.11). The breccia deposits contain predominantly one clast type (limestone, siltstone, mudstone or felsic volcanic lithics) or a mixture of all clast types.

Breccia Type	**Clast Type**				
	limestone	sandstone	siltstone	mudstone	volcanic lithics
limestone-clast breccia	25-90%	trace	trace - 5%	trace - 5%	trace - 5%
siltstone-clast breccia	5-10%	trace - 5%	50-80%	trace - 5%	trace
mixed provenance breccia	5-15%	trace - 5%	5-30%	trace - 5%	trace - 5%

Table 3.2 Approximate relative clast abundance in polymictic breccia deposits occurring in the Transitional Unit. Based on drill hole logs.

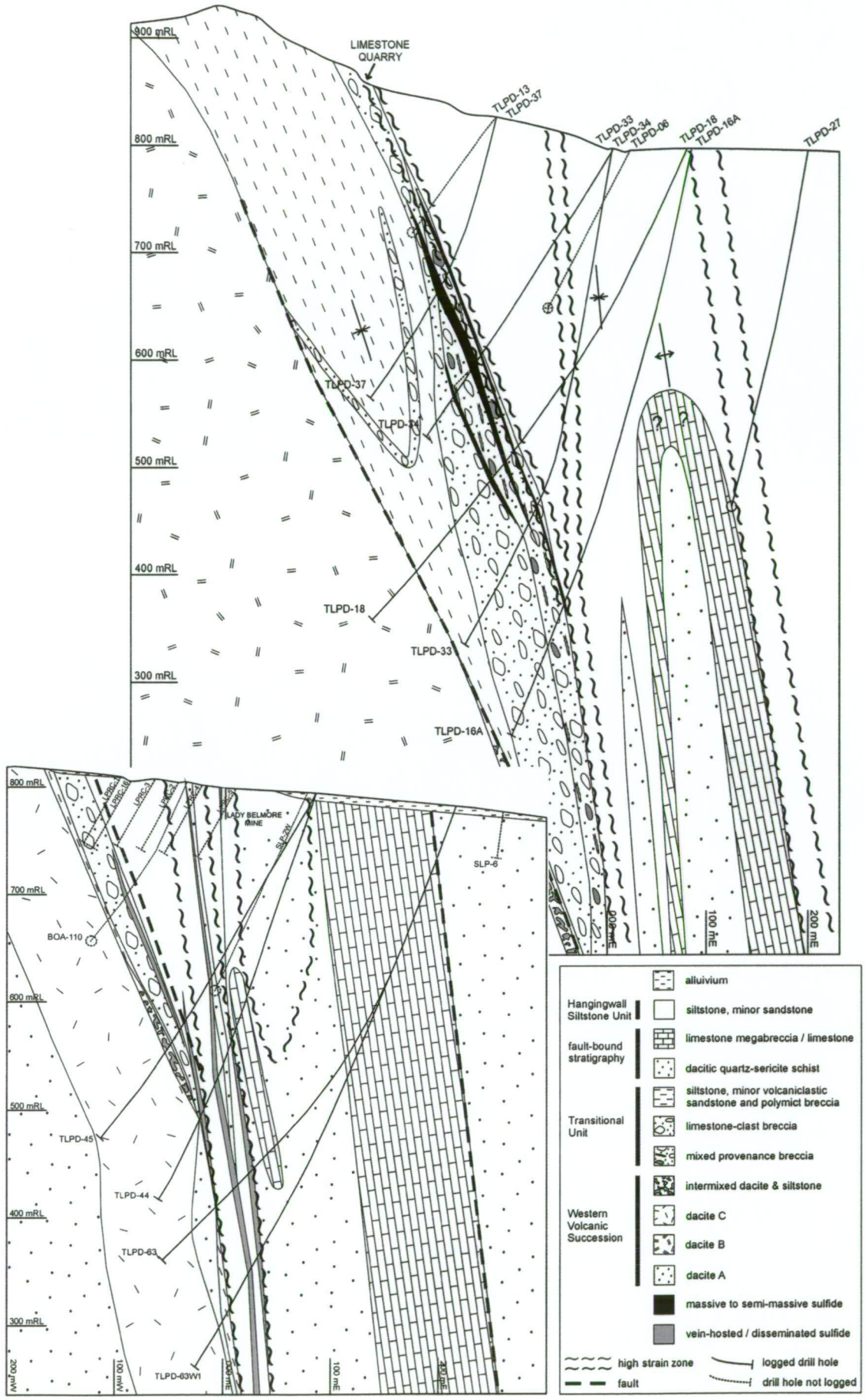

Figure 3.10 Line 1200N section (top) and Line 750N section (bottom) showing the Main zone and Lady Belmore zone host sequences. Refer to Figure 3.1 for location of cross-sections.

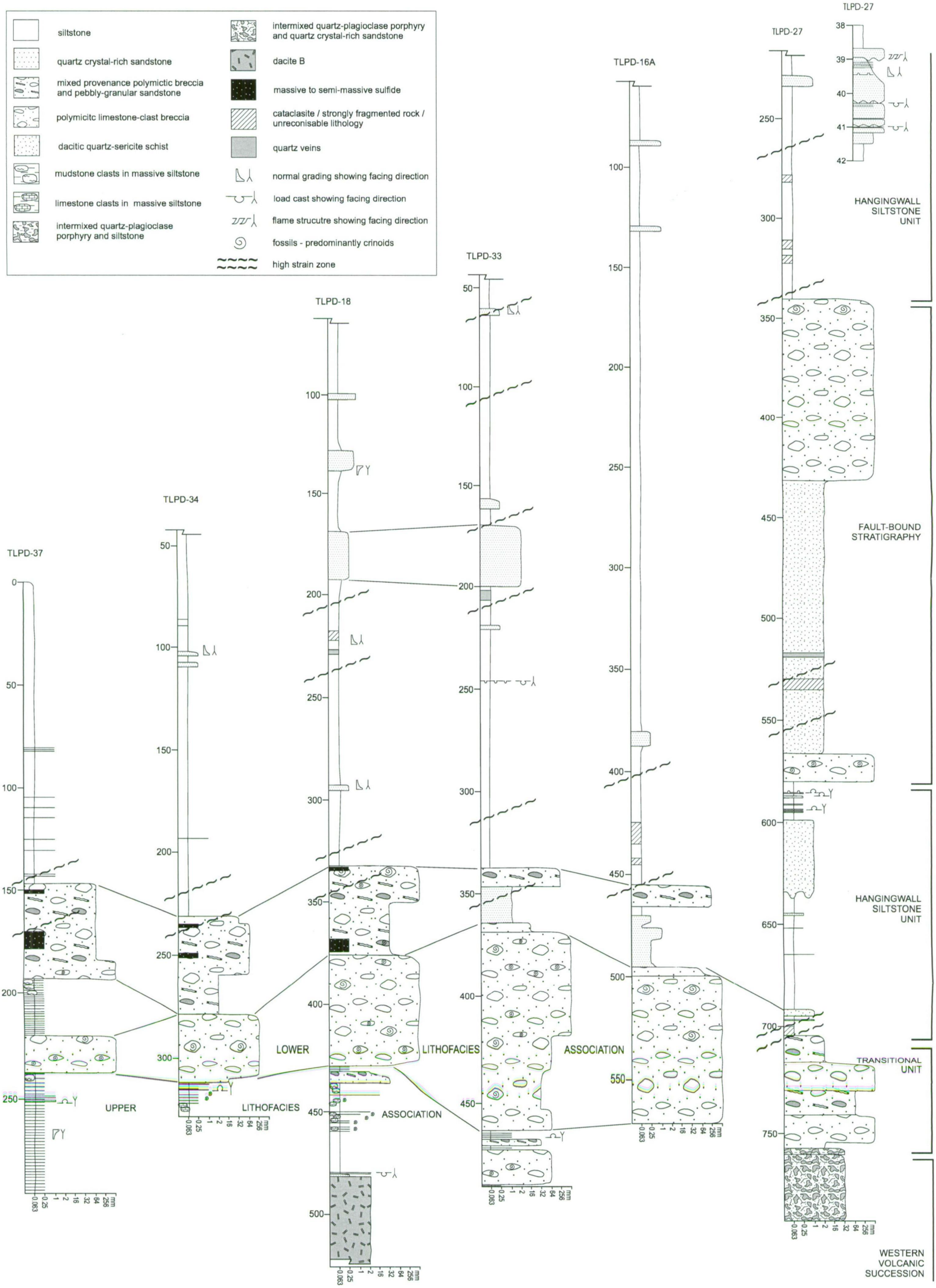

Figure 3.11 Graphic logs from Main zone host sequence, line 1200N.

Upper lithofacies association: interbedded siltstone, breccia and sandstone

Thinly-laminated siltstone, minor sandstone and breccia conformably overlie the massive polymictic breccia. These deposits occur in the core of the inferred syncline (Fig. 3.10). Isolated, elongate pebbles, cobbles and boulders of fossiliferous limestone, mudstone and quartz-feldspar phyric dacite occur sporadically in the siltstone (Fig. 3.12C and D).

The siltstone is interbedded with 1-50 cm thick beds of very poorly-sorted to well-sorted quartz crystal-rich sandstone. These beds typically have graded tops. Basal load casts indicate rapid deposition and fluidisation of the underlying sediment. The sandstone consists of euhedral quartz crystals, angular crystal fragments, crinoid fossils and shelly fragments in a calcite-chlorite-altered matrix (Fig. 3.12E and F).

Polymictic, matrix-supported breccia and pebbly-granular sandstone occurs in 5 cm to 4 m thick, massive or graded beds with sharp, planar bases and tops. Some of the beds fine upward into to pebbly-granular sandstone with siltstone laminations. The breccia and sandstone contain lenticular granules to boulders (predominantly pebbles) of recrystallised fossiliferous limestone, siltstone and mudstone and aphyric to porphyritic felsic volcanic lithics in a quartz crystal-rich sandstone matrix (eg. Fig. 3.12G).

Limestone clasts

Limestone crops out as large, recrystallised, massive or bedded rectangular boulders (up to 2x10 m), thin tabular blocks (up to 0.3x3m) with a high aspect ratio and smaller elongate pebbles and cobbles in a matrix of weathered quartz-chlorite-sericite schist or shale (Fig. 3.13A). The cleavage-parallel limestone boulders are fractured, boudinaged and weakly kink folded. Bedding is preserved in some of the clasts as crinoid-rich horizons, shelly layers or planar, calcareous mudstone laminations. Siltstone, mudstone and quartz porphyry clasts are not evident in the strongly weathered surface exposures in the limestone quarry.

In drill core, limestone clasts vary from granules to 5 m long boulders. Many clasts have irregular foliation-parallel margins characterised by delicate interpenetration of the adjacent matrix. These textures are attributed to compaction of the breccia deposits during diagenesis, partial recrystallisation of the limestone and/or structural modification during subsequent deformation. Clast margins are obscured where recrystallised calcite-altered domains occur in the surrounding matrix (eg. Fig. 3.13H).

Figure 3.12 Lithofacies in the Transitional Unit

A Matrix-supported limestone-clast breccia containing fractured and very angular, recrystallised fossiliferous limestone quartz-feldspar porphyry pebbles in a siltstone matrix with minor euhedral quartz crystals and angular crystal fragments. Crinoid ossicles (c) and shell fragments (s) are preserved in the limestone. TLPD-37, 238 m.

B Strongly sheared polymictic breccia consisting of elongate, lenticular pebbles of siltstone, mudstone, limestone and aphyric dacite in a siltstone matrix. TLPD-12, 522 m.

C Elongate mudstone pebbles in massive siltstone. TLPD-12, 576 m.

D Very angular pebbles and cobbles of recrystallised fossiliferous limestone in massive siltstone. TLPD-18, 449 m.

E Thin (1-1.5 cm) beds of poorly-sorted, coarse-grained calcareous sandstone in light gray siltstone. The sandstone contains angular quartz crystals, quartz crystal fragments, crinoid ossicles (c) and shelly fragments in a calcite-altered matrix. TLPD-20, 433 m.

F Photomicrograph of very poorly-sorted quartz crystal-rich sandstone consisting of euhedral to subhedral quartz crystals and very angular crystal fragments in a sandy-mudstone matrix. TLPD-36W, 366 m.

G Poorly-sorted, pebbly-granular sandstone characterised by elongate granules to pebbles of aphyric dacite or siltstone, angular quartz crystals and crystal fragments. Sphalerite and pyrite disseminations occur throughout the matrix. TLPD-18, 480 m.

Abbreviations: c = crinoid ossicle, s = shell fragment, r = quartz-plagioclase phyric dacite clast, qtz = quartz, ca = calcite, py = pyrite, sph = sphalerite.

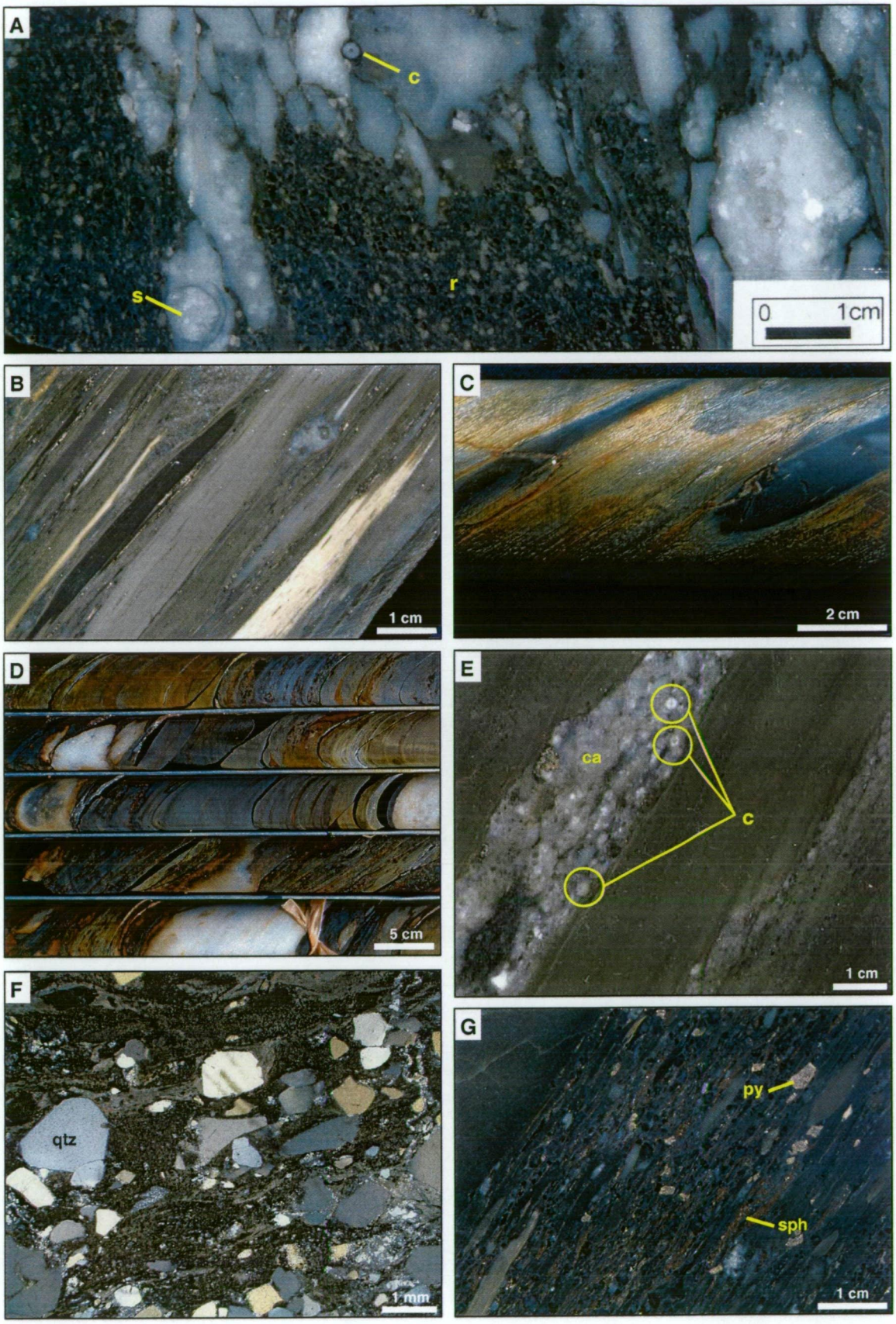
A
c
r
s
0 1cm
B
1 cm
C
2 cm
D
5 cm
E
ca
c
1 cm
F
qtz
1 mm
G
py
sph
1 cm

Figure 3.13 Limestone clasts in the Transitional Unit breccia deposits

A Exposure in the limestone quarry showing angular, blocky and lenticular boulders of variably recrystallised, massive and bedded crinoidal limestone in a strongly weathered, chalky matrix. Clasts are parallel to the regional cleavage orientation. Notebook for scale.

B Fossiliferous limestone clast containing a brachiopod shell. TLPD-43, 273 m.

C Photomicrograph of a crinoid stem segment. The central columella has been infilled by microcrystalline, sparry calcite. TLPD-37, 227 m.

D Photomicrograph of a lenticular limestone pebble containing crinoid ossicles in a fine-grained, recrystallised sparry calcite matrix. Crinoids have narrow calcite overgrowths. TLPD-12, 531 m.

E Scanning electron microscope image of a conodont similar to *Oulodus sp.* Extracted from LPD001, near limestone quarry.

F Scanning electron microscope image of euhedral feldspar crystal. Sample LPD001.

G Scanning electron microscope image of euhedral, detrital volcanic quartz crystal. Sample LPD001.

H Crinoidal limestone and quartz porphyry clasts surrounded by irregular, patchy domains of recrystallised calcite. TLPD-33, 422 m.

Abbreviations: c = crinoid ossicle, L = fossiliferous limestone clast, r = quartz porphyry clast.

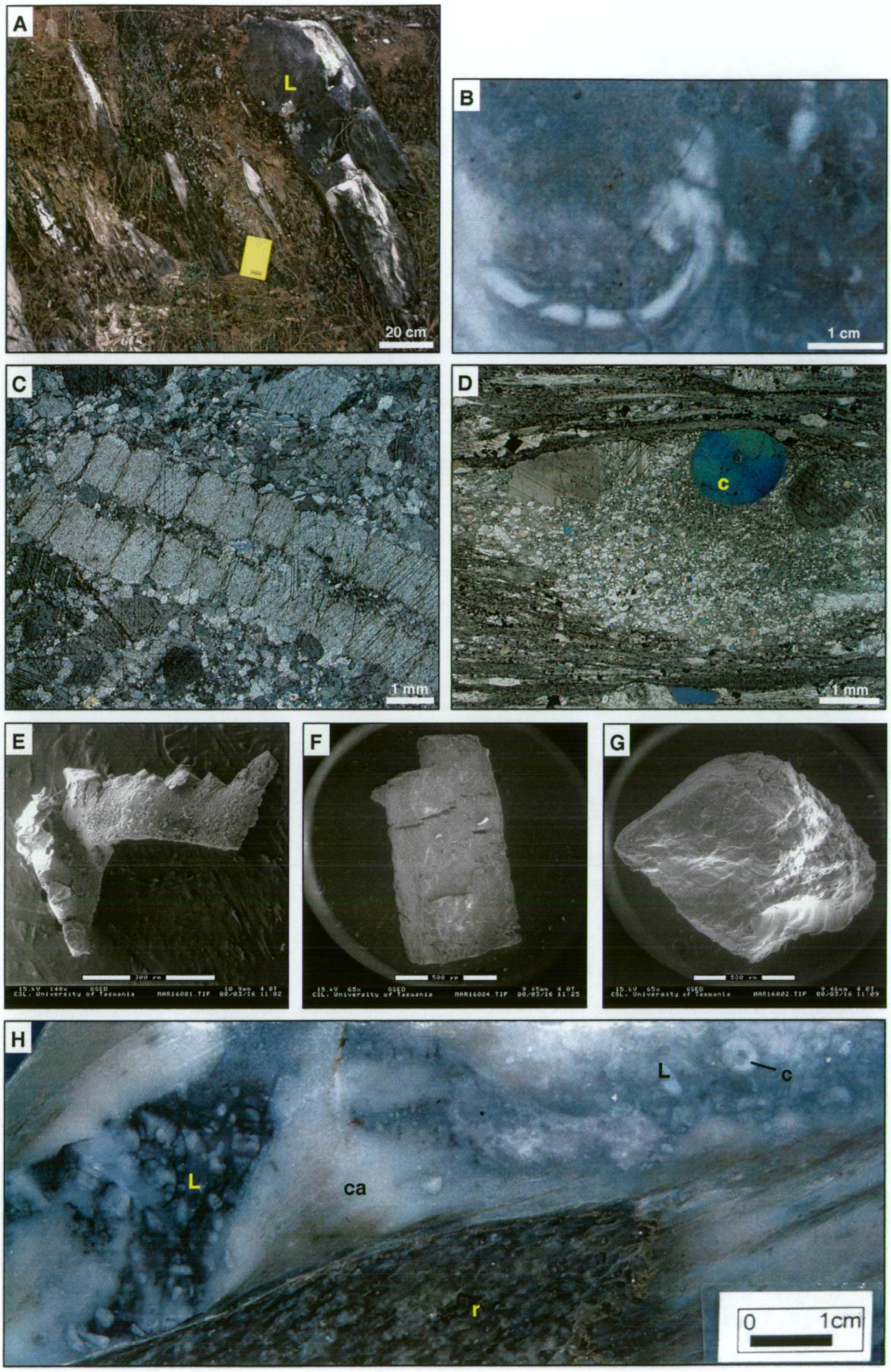
A
L
20 cm
B
1 cm
C
1 mm
D
c
1 mm
E
F
G
H
L
c
L
ca
r
0
1cm

Where primary textures are preserved, the variably recrystallised limestone consists of crinoid ossicles, crinoid stem fragments, brachiopods, bivalves, solitary corals and trace conodonts in an equigranular mosaic of polygonal calcite crystals (Fig. 3.13 B-E). Narrow calcite overgrowths and internal calcite cements have filled secondary porosity within and between the bioclasts. Euhedral detrital volcanic quartz, feldspar and zircon crystals also occur in trace amounts (eg. Fig. 3.13F and G).

Quartz porphyry clasts

Isolated, sub-rounded to very angular clasts and wispy patches of quartz ± feldspar porphyry occur throughout the limestone-clast breccia. Clasts have 'delicate' shapes characterised by irregular margins and narrow projections into the adjacent matrix or limestone clasts (Fig. 3.14A-E). Some of the patches occur in a bleached, strongly indurated, quartz crystal-rich mudstone matrix (Fig. 3.14B and C).

The highly porphyritic clasts consist of euhedral to subhedral, partly resorbed quartz and feldspar phenocrysts or glomerocrysts in a chlorite-sericite-calcite-altered microcrystalline groundmass (Fig. 3.14F). Relict perlite, occurring in several samples indicates that the groundmass was originally glassy. Perlitic fractures are preserved as overlapping, anastomosing white mica bands, whereas angular patches of fine-grained chlorite have replaced the glassy domains (Fig. 3.14G). The clasts have similar whole rock, immobile element compositions (see Chapter 6, section 6.4) and textures to lithofacies association B in the Western Volcanic Succession.

Interpretation

Thick, polymictic breccia units of the lower lithofacies association probably represent subaqueous debris flow deposits. The fine-grained, granular-sandy-mudstone matrix supports pebbles, cobbles and extremely large boulders, up to 10 m length. Normal-grading and an increase in matrix content in the upper 1-4 m of many beds is interpreted to record suspension settling. This reflects the tendency for subaqueous debris flows to evolve into high-density turbidity currents (Lowe, 1982; Nemec and Steel, 1984; Sohn, 2000). Abrupt changes in bed thickness, clast size, provenance and matrix content may indicate that channels or structural complexities (folds/faults) occur in the breccia units. Alternatively, the mass flows may have undergone rapid hydrological flow transformations (eg. Sohn, 2000).

Figure 3.14 Quartz porphyry pebbles in the Transitional Unit breccia deposits

A Recrystallised limestone cobble penetrated by a very angular quartz porphyry clast. TLPD-37, 224 m.

B & C Very angular fossiliferous limestone and chlorite-altered quartz porphyry pebbles in a bleached, poorly-sorted, sandy-siltstone matrix. TLPD-37, 223 m.

D Elongate quartz porphyry clast in matrix-supported polymictic breccia. Diagenetic compaction and/or deformation has caused deflection of the matrix around the clast. TLPD-18, 393 m.

E Matrix-supported polymictic breccia consisting of angular to sub-rounded quartz porphyry pebbles, mudstone clasts and fossiliferous limestone pebbles in a sandy-siltstone matrix. One of the clasts has perlitic fractures while the other does not. TLPD-37, 238 m.

F Photomicrograph of quartz porphyry clast consisting of embayed, euhedral to subhedral quartz phenocrysts in a chlorite-calcite-altered groundmass. Feldspar phenocrysts have been entirely replaced by chlorite and calcite. TLPD36W, 262 m.

G Photomicrograph of quartz porphyry clast with relict perlite texture. The perlitic fractures are preserved as anastomosing, curviplanar muscovite bands in a chlorite-altered groundmass that was originally glassy. TLPD-37, 238 m.

Abbreviations: d = quartz phyric dacite clast, qtz = quartz.

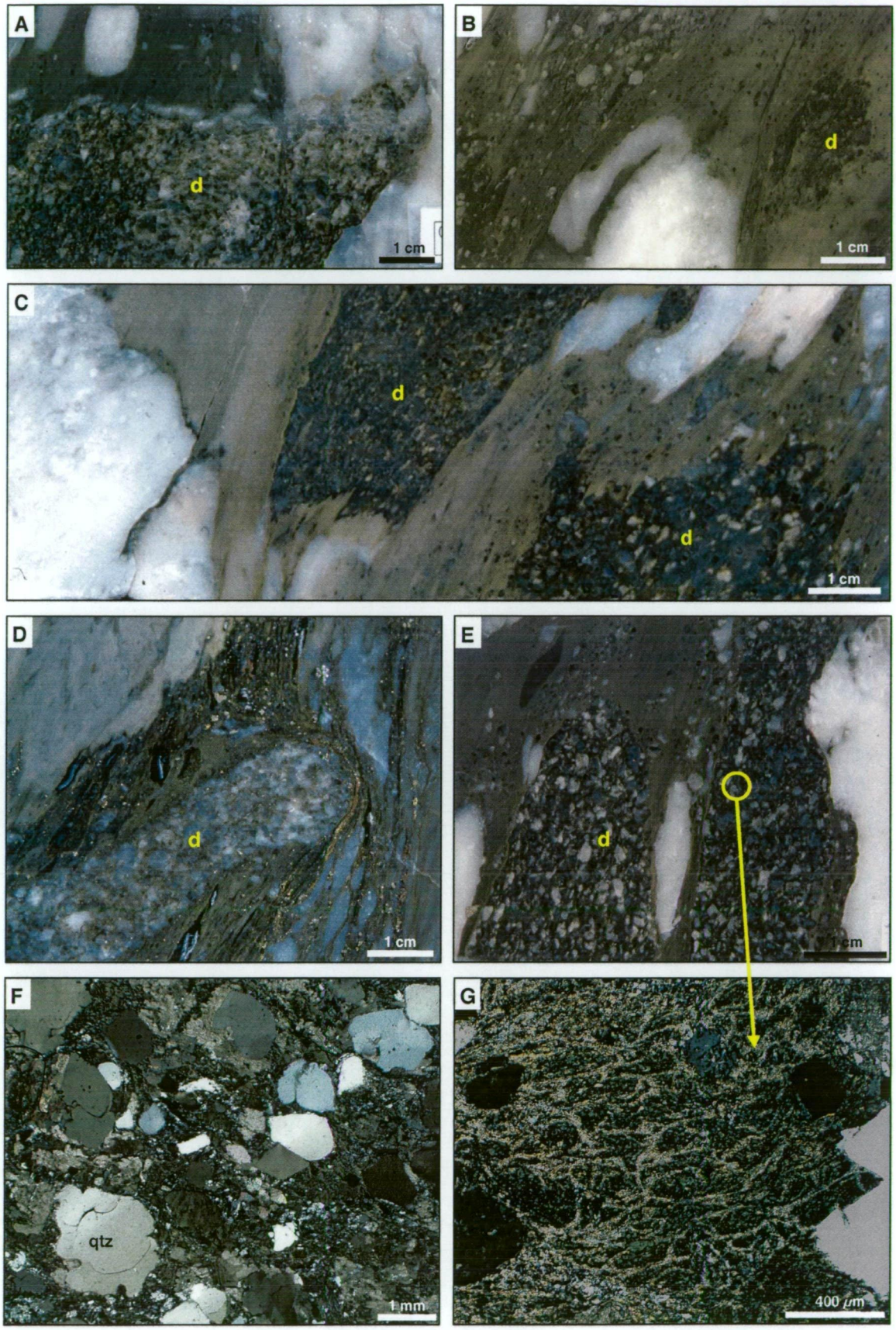
A
d
1 cm
B
d
1 cm
C
d
d
1 cm
D
d
1 cm
E
d
1 cm
F
qtz
1 mm
G
400 μm

The breccia deposits contain a mixture of volcanic and sedimentary components. A lithified bioherm or fringing reef provided fossiliferous limestone debris. Mudstone and siltstone pebbles were probably derived from the underlying substrate. The texturally immature porphyritic dacite clasts and angular quartz crystals were potentially sourced from a nearby quench-fragmented porphyritic dacite intrusion. However, the large volume of detrital quartz crystals and angular crystal fragments occurring in sandstone and breccia deposits throughout the Transitional Unit and Hangingwall Siltstone Unit suggests that a major explosive volcanic centre probably existed along the basin margin or in the adjacent hinterland.

Fragmentation of the porphyritic dacite could have occurred before and after deposition of the breccias. A mixture of very angular to sub-rounded dacite clasts, some with perlitic fractures (eg. Fig. 3.14G) indicates minor reworking of the sediment, prior to deposition. In situ magma-wet sediment interactions possibly accompanied emplacement of lithofacies association C within the breccia. Some of the dacite clasts occur in a bleached matrix, indicating local thermal induration. Coherent dacite was not identified. However, intense hydrothermal alteration and deformation have destroyed original textures in parts of the breccia unit.

The upper lithofacies association records the transition from coarse to fine-grained clastic sedimentation at Lewis Ponds. Massive and normal-graded beds of sandstone and breccia were deposited from subaqueous mass flows. These deposits become less abundant and thinner up-section. Limestone, siltstone and mudstone intraclasts were probably derived from the underling coarse-grained deposits. Unlike the lower lithofacies association, sandstone beds contain loose crinoid fossils and shell fragments, suggesting that unconsolidated bioclastic sediment existed in the source area of the mass flows at the time of deposition.

Age of the limestone clasts

The limestone clasts could not be dated accurately due to the poor representation of index fossils. A badly damaged white translucent conodont with missing denticles was recovered from a limestone quarry sample following partial dissolution in acetic acid (Fig. 3.13E). Ian Percival, Geological Survey of New South Wales (pers comm., 2000) suggested that it was similar to Sc[1] elements of *Oulodus sp.* This genus was widespread during the Early to Middle Silurian (Llandovery to Wenlock) in the Orange district. However, it ranged from Late Ordovician (though not locally) to the Early Devonian.

[1] The term, Sc refers to a specific type of skeletal element within the Conodont apparatus (Sweet, 1988).

Percival (1995) reported finding an Sb[1] and Sa[1] element belonging to the conodont *Panderodus unicostatus*, a rugose coral: *Pseudoamplexus sp.* and a Pb[1] element attributed to *Ozarkodina excavata excavata* in two samples extracted from limestone clasts in drill core from TLPD-19. These conodonts are known to range throughout most of the Silurian in southeastern Australia (Simpson and Talent, 1995). However, Cantrill (1991) proposed that *Ozarkodina excavata excavata* was a useful indicator for the commencement of the Sagitta zone (Middle Wenlock, Middle Silurian) in the Bunyarra district of New South Wales.

Apart from crinoids, the Lewis Ponds limestone contains a different faunal assemblage to limestone lenses occurring elsewhere in the Mullions Range Volcanics and Anson Formation (this study; Pickett, 1972, 1993; Percival, 1995; Pogson and Watkins, 1998). Lishmund et al. (1986), argued that the bioclastic debris probably accumulated "on small topographic highs on the flanks of the Molong Rise." The restricted occurrence of limestone-clast breccia and angular, blocky shape of the clasts may indicate a local source. However, mass flows are capable of transporting clasts long distances on low-angle slopes with minor textural modification (Cook et al., 1972; Lowe, 1976; Loucks et al., 1985).

3.5 Hangingwall Siltstone Unit

The Hangingwall Siltstone Unit unconformably overlies the Western Volcanic Succession in the Toms zone footwall and structurally overlies the Transitional Unit (Figs. 3.4 and 3.10). It is a thick (>200 m) unit of siltstone with minor mudstone, quartz crystal-rich sandstone, matrix-supported volcaniclastic breccia and quartz-feldspar-volcanic lithic sandstone (Table 3.1; Fig. 3.15). A discordant, steeply dipping, fault-bound lens of limestone, dacitic quartz-chlorite-sericite schist, quartz-plagioclase phyric dacite and pebbly-granular volcanic lithic sandstone occurs in the structural hangingwall of Main and Toms zones (Figs. 3.2 and 3.9). Over six hundred metres of siltstone are apparently exposed in the northern part of the prospect between the Transitional Unit and Eastern Volcanic Succession, where the Hangingwall Siltstone Unit occurs as a structurally controlled northerly-thickening wedge (Figs. 3.1 and 3.9).

Lithofacies associations

Massive to thinly-laminated siltstone

Light grey, massive to thinly laminated siltstone and sandy-siltstone dominate the Hangingwall Siltstone Unit. Rare, medium to dark grey mudstone pebbles occur at the base of the unit in places (eg. TLPD-36W, 185 m), suggesting minor reworking of underlying polymictic breccia or mudstone deposits. The siltstone contains 1-5% disseminated pyrrhotite and rare pyrite.

[1] The terms Sa, Sb and Pb refer to various types of skeletal elements within the Conodont apparatus (Sweet, 1988).

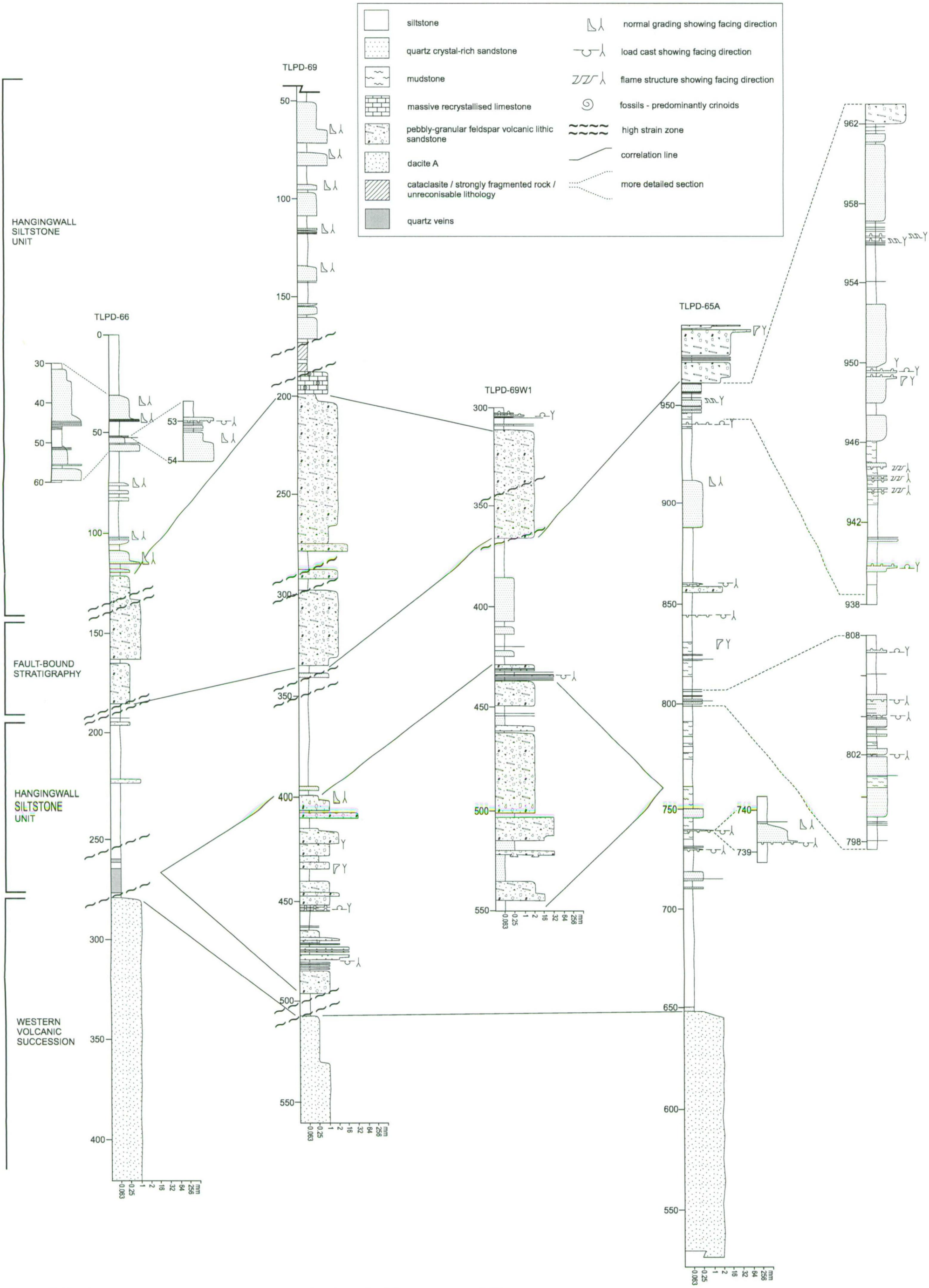

Figure 3.15 Graphic logs of the host sequence immediately south of Toms zone, line 200N.

Interbedded quartz crystal-rich sandstone and siltstone

Quartz crystal-rich sandstone constitutes up to 25% of the Hangingwall Siltstone Unit. The 1 -130 cm thick, massive or normal-graded sandstone beds have sharp, planar or irregular contacts. Basal load casts, flames and ball and pillow structures result from rapid deposition and fluidisation of the underlying sediment. Individual beds consist of massive, very fine-grained to very coarse-grained sandstone with siltstone laminations (Fig. 3.15). Upper parts are characterised by thin, planar to wavy laminations of sandstone and siltstone. The moderately-sorted to well-sorted quartz sandstone consists of angular quartz crystal fragments in a clay-rich matrix. Irregular, angular to rounded chlorite patches occurring in the sandstone may represent altered feldspar crystals.

Interbedded mudstone, siltstone and calcareous quartz crystal-rich sandstone

Dark grey mudstone occurs north and south of the two massive sulfide zones. Interbedded siltstone, sandstone and mudstone grades laterally into massive mudstone with minor volcaniclastic breccia, along strike, south of Toms zone (Figs. 3.2 and 3.15). The 0.5-12 m thick mudstone units have sharp or gradational contacts with overlying and underlying siltstone and sandstone deposits. Pyrite and pyrrhotite disseminations occur throughout the sedimentary rocks.

Very fine- to medium-grained quartz crystal-rich, calcareous sandstone beds occur in the mudstone (Fig 3.15, drill hole TLPD-65A). The 1-300 cm thick, massive or normal-graded sandstone beds have sharp, planar bases characterised by flame structures and load casts. Elongate mudstone pebbles occur in places.

Interbedded pebbly-granular feldspar-volcanic lithic sandstone, polymictic volcaniclastic breccia, quartz crystal-rich sandstone and mudstone

Pebbly-granular, feldspar-volcanic lithic sandstone and volcaniclastic breccia occur southeast of the Mt Regan mine (Fig. 3.1) and in drill holes south of Toms zone (Fig. 3.2). These lithofacies are interbedded with siltstone and mudstone. The 5-10 m thick, breccia beds have sharp, irregular contacts and basal load casts. Many grade vertically into pebbly-granular sandstone in the uppermost 1-2 m (Fig. 3.15). Sandstone occurs in 1-40 m thick massive units with sharp planar contacts.

The poorly-sorted sandstone and breccia consist of very angular to sub-angular granules, pebbles and cobbles of aphyric to feldspar phyric dacite, siltstone, sandstone and mudstone in a muddy-sandstone matrix containing euhedral albitised plagioclase crystals, angular crystal fragments and rare quartz (Fig. 3.16A). The crystals are sub-rounded, indicating either

resorption in the magma chamber prior to eruption or textural modification during surface erosion and transport. The juvenile porphyritic volcanic clasts have very angular shapes with delicate interpenetrations of the surrounding matrix. They contain euhedral plagioclase and K-feldspar phenocrysts in a microcrystalline groundmass.

Interpretation

The Hangingwall Siltstone Unit is a predominantly fine-grained succession of hemipelagic volcanic detritus. Dark grey mudstone was deposited in local areas not diluted by volcanogenic sediment. Therefore, the southerly transition from light grey siltstone to dark grey mudstone is consistent with a progressively deeper, more restricted, possibly anoxic environment away from the interpreted volcanic centre at Lewis Ponds.

The massive to normal-graded breccia and quartz-crystal-rich sandstone beds are interpreted as turbidite and debris flow deposits. Flame structures and load casts resulted from rapid deposition and liquefaction of the underlying sediment. Volcaniclastic deposits south of Toms zone are characterised by texturally immature volcanic lithics and feldspar crystals, indicating the rapid influx of juvenile pyroclasts into the basin. The massive internal structure, uniform composition and relatively narrow range of clast types is consistent with the products of syn-eruptive or post-eruptive mass flows, which re-deposit non-welded pyroclasts and intraclasts downslope (McPhie et al., 1993). These lithofacies have a discrete volcanic provenance, represented only in the southern part of the Lewis Ponds prospect.

3.6 Fault-bound stratigraphy

Two limestone lenses, separated by a 10-100 m thick unit of dacitic quartz-chlorite-sericite ± biotite schist, quartz-plagioclase phyric dacite, volcaniclastic breccia, sandstone and siltstone occur in the structural hangingwall of both mineralised zones (Table 3.1; Figs. 3.2 and 3.9). Although quartz crystal-rich volcanics are exposed near Toms mine, limestone does not crop out at the surface. The 5-100 m thick upper limestone lens extends over a strike length of 700-1 200 m and is truncated by faults (Figs. 3.2 and 3.4). The lower, thinner (2-10 m) lens occurs discontinuously over 700 m. Limestone intervals do not occur in every drill hole. Numerous faults and high strain zones cut across the limestone and volcanic rocks.

Lithofacies associations

Limestone

The lenses consist of massive recrystallised fossiliferous limestone, very large (1 to 90 m thick) angular limestone blocks and smaller, elongate pebbles and cobbles of limestone in a

siltstone matrix. Crinoid ossicles, crinoid stem fragments, brachiopods and embayed detrital volcanic quartz crystals are recognisable in areas where recrystallisation has not destroyed primary textures (Fig. 3.16B). Clast margins are irregular and parallel to the regional foliation. Irregular, elongate carbonate patches occur along the margins of larger clasts. Pseudobreccia textures are common in the lower limestone lens due to anastomosing, calcite veinlets.

Dacitic quartz-chlorite-sericite schist and quartz-plagioclase phyric dacite

Quartz-plagioclase phyric dacite underlies the upper limestone lens in the Toms zone hangingwall (Fig. 3.16C). It consists of euhedral to subhedral quartz, sericitised plagioclase, chlorite-epidote-altered biotite and pyroxene phenocrysts in a microcrystalline groundmass. The highly irregular upper contact is characterised by cleavage-parallel fragments of crinoidal limestone and calcite ribbons in a matrix of chlorite schist and may represent tectonic breccia (Fig. 3.16D).

North of Toms zone, the quartz phyric rocks consist of micro-fractured euhedral quartz crystals and very angular, lenticular crystal fragments in a strongly foliated, sericite-altered groundmass (Fig. 3.16E). These volcanic rocks are termed *schist* because pervasive hydrothermal alteration, ductile deformation and cleavage development have destroyed the primary fabric. The quartz-chlorite-sericite schist has a similar immobile element composition to lithofacies association A in the Western Volcanic Succession and quartz-plagioclase phyric dacite overlying Toms zone (see Chapter 6, section 6.4).

Interbedded volcaniclastic breccia, sandstone and siltstone

South of Toms zone, the limestone is underlain by interbedded, matrix-supported, polymictic volcaniclcastic breccia, pebbly-granular quartz-feldspar lithic sandstone and siltstone (Fig. 3.15). These deposits occur in 50-300 cm thick, massive beds with planar bases and sharp or normal-graded tops. The volcaniclastic breccia and poorly-sorted sandstone contains up to 30% elongate siltstone pebbles and angular, siliceous rhyolitic clasts in a quartz and feldspar crystal-rich, muddy-sandstone matrix. The massive beds are interpreted as subaqueous mass flow deposits.

Interpretation

The fault-bound unit is interpreted as a folded, fault repetition of the Transitional Unit and Western Volcanic Succession (see Chapter 4, sections 4.3 and 4.4). Quartz phyric volcanic rocks occurring within the unit have similar textures and immobile element compositions to lithofacies association A in the Western Volcanic Succession. The monomictic, clast-

supported limestone megabreccia may be a lateral facies variation of the polymictic breccia deposits in the Transitional Unit.

The limestone represents a fragmented bioherm, mass flow or talus deposit. It may have been the source of limestone debris in the Transitional Unit. Clast sizes vary from large pebbles to 90 m thick boulders. However, clast orientations cannot be determined from drill core because of cleavage-parallel margins, unrecognisable bedding and absence of geopetal fabrics. Therefore, although a mass flow origin is favoured for the limestone lenses, recrystallisation and deformation have overprinted the original disorganised clast fabric.

Quartz-chlorite-sericite schist separating the limestone lenses may be part of a porphyritic dacite intrusion flanked by poorly-sorted quartz and feldspar crystal-rich volcaniclastics. Weakly altered coherent dacite occurs in the Toms zone hangingwall, suggesting possible intrusion of the overlying limestone lens. The dacitic volcanics grade into matrix-supported breccia, sandstone and siltstone, along strike, south of Toms zone. The volcaniclastic facies were deposited from subaqueous, quartz and feldspar crystal-rich mass flows.

3.7 Eastern Volcanic Succession

The Eastern Volcanic Succession, previously termed *Eastern Crystal Tuff* by Valliant and Meares (1998), is a discordant body of poorly exposed quartz ± feldspar phyric volcanics surrounded by siltstone. It is located in the northeastern corner of the prospect (Fig. 3.1). Tertiary alluvium and Carboniferous granite obscure the western and southern parts of the unit. Two 15x150 m jasper lenses occur along the western margin of the Eastern Volcanic Succession (see Chapter 5, section 5.4).

Lithofacies associations

Dacitic quartz-feldspar-chlorite -sericite schist and quartz-plagioclase phyric dacite

The volcanic rocks consist of euhedral to subhedral quartz and albitised plagioclase phenocrysts and glomerocrysts in a chlorite-sericite-altered microcrystalline groundmass (Fig. 3.16F). Schistose samples are characterised by a strong foliation and micro-fractured, lenticular quartz crystal fragments.

Interpretation

Contacts around the margins of the Eastern Volcanic Succession are poorly exposed. Irregular structural contours indicate that the shallowly-dipping northern and eastern margins are non-planar and therefore unconformable.

Figure 3.16 Lithofacies in the Hangingwall Siltstone Unit, fault-bound stratigraphic unit, Eastern Volcanic Succession and Lewis Ponds Granite

A Polymictic, clast-supported volcaniclastic breccia characterised by very angular to sub-rounded aphyric to feldspar phyric dacite pebbles, elongate mudstone clasts and abundant euhedral plagioclase crystals in a granular sandstone matrix. Many volcanic lithics have curviplanar or feathery margins, indicating that they were not texturally modified prior to deposition. TOD-10, 149 m.

B Fossiliferous limestone from the upper limestone lens containing crinoid ossicles, crinoid stem segments and shelly fragments in a fine-grained, hematite-altered, sparry calcite matrix. It is overprinted by irregular, patches of chlorite and recrystallised calcite. TLPD-58, 155 m.

C Quartz-plagioclase phyric dacite from the fault-bound stratigraphic unit, containing euhedral to subhedral quartz and plagioclase phenocrysts in a weakly foliated, chlorite-sericite-altered microcrystalline groundmass. TLPD-58, 205 m.

D Lower contact of the upper limestone lens in TLPD-27. It is characterised by an interval of monomictic limestone breccia (b), occurring between a large limestone boulder (l) and quartz-chlorite-sericite schist (chl). TLPD-27, 432-435 m.

E Strongly foliated dacitic quartz-sericite-biotite schist (fault-bound stratigraphic unit). Most quartz crystals occur as very angular, lenticular fragments 'strung out' along the cleavage planes. TLPD-44, 197 m.

F Photomicrograph of weakly altered quartz-plagioclase phyric dacite from the Eastern Volcanic Succession, characterised by embayed euhedral to subhedral quartz and sericitised plagioclase phenocrysts and glomerocrysts in a microcrystalline groundmass. Sample LPD009.

G Non-foliated quartz-feldspar porphyry occurring as a post-tectonic dyke that intruded the Western Volcanic Succession. Note the very weak patchy sericite. TLPD-67B, 369 m.

Abbreviations: d = plagioclase phyric dacite and dacite, m = mudstone, c = crinoid fragments, ca = calcite, qtz = quartz, fsp = plagioclase, L = limestone megaclast, hem = hematite, b = breccia, chl = chlorite schist, ser = sericite.

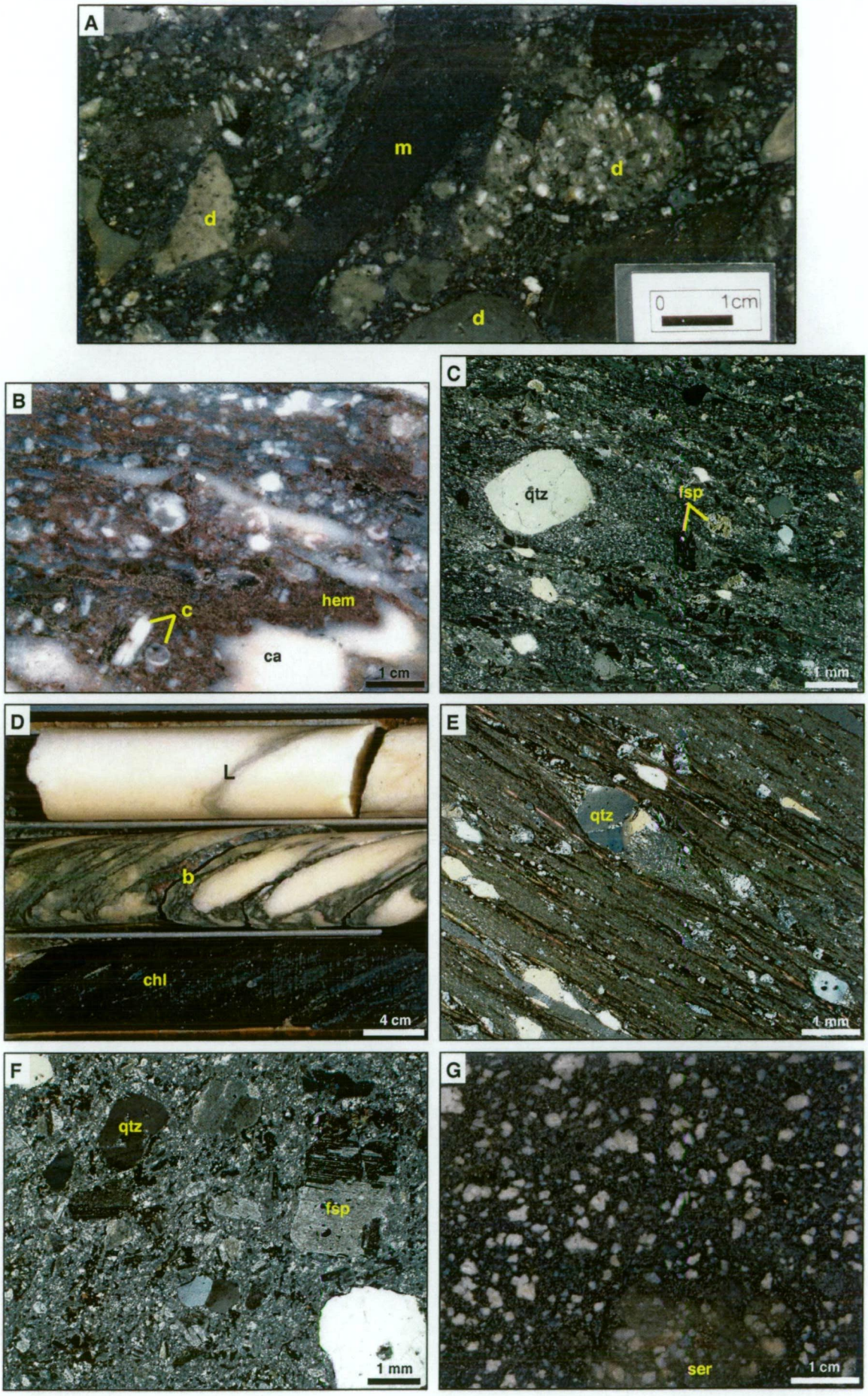
A
m
d
d
d
0 1cm
B
hem
c
ca
1 cm
C
qtz
fsp
1 mm
D
L
b
chl
4 cm
E
qtz
1 mm
F
qtz
fsp
1 mm
G
ser
1 cm

Previous studies have suggested that the western margin may be truncated by a NNW-trending strike-slip fault (Castle, 1976). The volcanic rocks have a similar texture and immobile element composition to lithofacies association A in the Western Volcanic Succession (see chapter 6, section 6.4). The Eastern Volcanic Succession is therefore interpreted as a discordant body of coherent quartz-plagioclase phyric dacite or quartz-plagioclase crystal-rich volcaniclastics.

3.8 Lewis Ponds facies model

Constraints on water depth

Fossiliferous limestone occurs abundantly at Lewis Ponds. However, the host sequence is interpreted to record a moderately deep, below wave-base (>200 m) depositional setting due to the following considerations:

- There are no wave and current-generated sedimentary structures.
- Shallow marine trace fossils are absent.
- Loose body fossils only occur in mass flow deposits and are not a major component of the sedimentary package.
- All of the limestone is allochthonous; occurring either in mass flow deposits (Transitional Unit) or fault-bound lenses (Hangingwall Siltstone Unit).
- The host sequence consists of predominantly siltstone and mudstone, consistent with deposition in a relatively quiet submarine environment.
- The intermixed quartz-plagioclase porphyry and siltstone facies is non-vesiculated, suggesting that confining pressures may have been too high for the release of volatiles.

The near-basin margin setting of Lewis Ponds precludes water depths of greater than 1 500 m. Therefore, the most likely range of possible water depths is 200 to 1 500 m.

The preservation of carbonate bioclasts and skeletal debris on the modern sea floor is constrained by the Calcite and Aragonite Compensation depths. The CCD and ACD represent the level below which calcium carbonate dissolves. In the southeast Pacific, the CCD varies from 3.5-4.5 km (Jenkyns, 1986; Stow, 1994, based on the preservation of foraminifera and coccoliths). Therefore, allochthonous limestone blocks originally sourced from a shallow water environment may be preserved in deep water settings.

Depositional environment

Submarine mass flow deposits dominate the Lewis Ponds host sequence. These deposits have a mixed volcanic-sedimentary provenance, indicative of post-eruptive reworking. The breccia, sandstone and siltstone beds were probably deposited in a moderately deep, below wave-base, submarine ramp or slope environment. The distribution of clast types reflects variations in the

source area, local topography and physical nature of the flows.

In the Main zone host sequence, polymictic breccia and pebbly-granular quartz crystal-rich sandstone facies contain:

- limestone clasts and loose crinoids derived from a bioclastic carbonate deposit (reef or bioherm), located within the basin or at the basin margin;
- sandstone, siltstone and mudstone intraclasts and rip-up clasts;
- texturally immature quartz phyric dacite fragments originating from exposed cryptodomes or intrusions within the breccia; and
- abundant detrital quartz crystals and angular crystal fragments sourced from a major explosive volcanic centre, located along the basin margin or in the adjacent hinterland.

In contrast, volcaniclastic breccia and sandstone deposits occurring south of Toms zone contain: texturally immature aphyric and feldspar phyric dacite clasts, euhedral plagioclase crystals and mudstone intraclasts, without a significant component of quartz and limestone.

The Lewis Ponds facies model is summarised in Figure 3.17. Relative timing relationships between lithofacies in the Western Volcanic Succession and Transitional Unit are based on limited surface and drill core observation of lithological contacts and interpretation of sub-surface structures and facies geometries. Dacite B is interpreted to pre-date deposition of the overlying polymictic breccia and sandstone deposits because a thin layer of indurated siltstone and peperite surrounds it. This suggests that dacite B did not directly intrude the overlying polymictic breccia deposits. Furthermore, quartz porphyry clasts with a similar magmatic affinity to dacite B occur throughout the limestone-clast breccia.

Stage 1. Dacite (lithofacies association A) was emplaced as a series of lava flows or sill-like intrusions into fine-grained sediment. Some of the textures observed in thin sections may represent flow-banding, spherulites and amygdales. However, the dacite appears to lack internal structure. Siltstone lenses occurring in the Western Volcanic Succession, south of Toms zone are interpreted as screens of host rock or discontinuous beds.

Stage 2. A porphyritic dacite cryptodome (lithofacies association B) intruded the thick sequence of dacite and fine-grained sediment. Angular rhyolite clasts and ragged peperitic fragments were liberated from the outer carapace of the cryptodome by quench fragmentation and magma-wet sediment interactions.

Stage 3. Erosion of the overlying sediment partly exposed the cryptodome as a topographic high on the seafloor, allowing mass flows to deposit local and basin margin-derived debris around its flanks. Preferential erosion of sedimentary rocks surrounding rhyolite-dacite

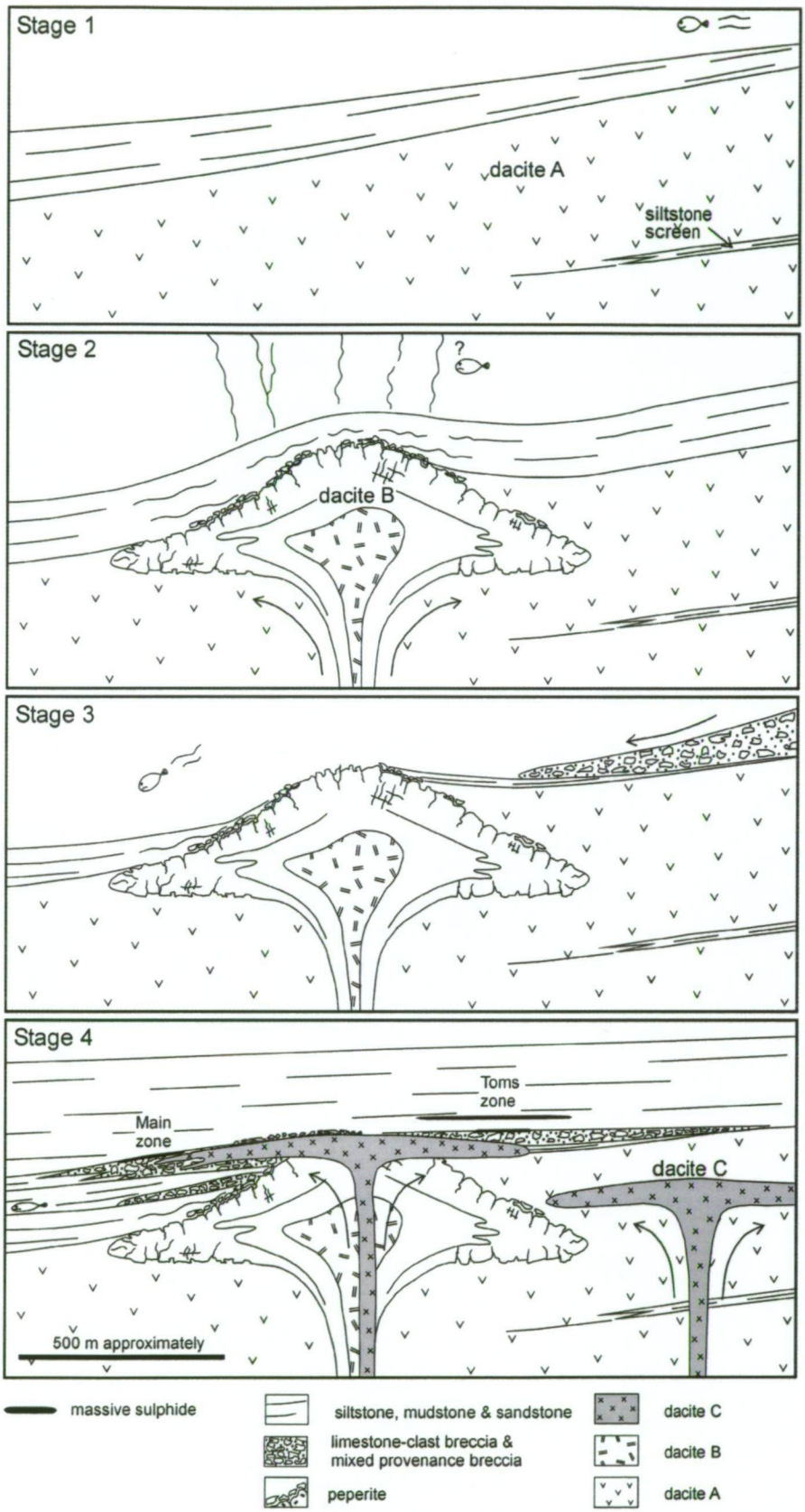

Figure 3.17 Facies model. **Stage 1** Emplacement of dacite as a series of sill-like intrusions or lava flows. **Stage 2** Passive, sub-sea floor emplacement of dacite cryptodome into unconsolidated fine-grained sediment. **Stage 3** Preferential erosion of the overlying sediment and partial exposure of the cryptodome on the seafloor. Limestone-clast breccia and mixed provenance breccia were then deposited from mass flows around the flanks of the eroded cryptodome. **Stage 4** Intrusion of porphyritic dacite sills into the breccia and volcanic sequence followed by deposition of volcanogenic, quartz crystal-rich sandstone and siltstone. The massive sulfide lenses are shown for reference only.

cryptodomes has been recorded at other localities, such as the Miocene Momo-iwa dome, Hokkaido, Japan (Goto and McPhie, 1998).

Stage 4. Porphyritic dacite sills (lithofacies association C) were emplaced into the siltstone, sandstone and breccia succession. Parts of the Transitional Unit consist of texturally immature quartz-feldspar porphyry clasts, indurated/metamorphosed siltstone (Fig. 3.14B and C) and irregular mixtures of siltstone and quartz-chlorite schist (Fig. 3.8D). However, pervasive alteration associated with Main zone has obscured most of the primary textures and contact relationships within these zones.

Following cessation of volcanic activity in the region, fine-grained quartz and feldspar crystal-rich, volcanogenic, hemipelagic sediments were deposited from subaqueous mass flows. Dark grey mudstone accumulated in restricted, possibly anoxic areas mainly south of Toms zone, where organic matter was not diluted by the volcanogenic sediment.

Lewis Ponds is analogous to eastern Australian VHMS deposits in that high-level, syn-sedimentary felsic volcanic intrusions occur in the host sequence. Other examples include Benambra (Allen, 1992), Mount Morgan (Messenger et al., 1997), Mount Chalmers (Hunns and McPhie, 1999) and Thalanga (Paulick and McPhie, 1999). The tuff cone model of Cas et al., (1990) describes the deposition of pyroclastic material down the flanks of partly emergent cryptodomes due to phreatic/phreatomagmatic eruptions. However the explosiveness of these eruptions depends on the temperature, viscosity and volatile content of the magma, eruption rate, vent geometry, water depth and thickness of the overlying sediment (Horikoshi, 1969; Allen, 1992; Gibson et al., 1999; Huston and Cas, 2000).

Little evidence exists at Lewis Ponds for explosive volcanic activity accompanying the emplacement of the dacite cryptodome underlying Main zone. The polymictic mass flow deposits overlying dacite B have a mixed volcanic-sedimentary provenance, resulting from reworking of debris derived from multiple sources rather than emplacement and erosion of an underlying intrusion.

3.9 Lewis Ponds Granite

The Lewis Ponds Granite crops out southeast of Toms zone as small pods of massive pink granite (Fig. 3.1 and map enclosure). A 100-150 m wide aureole of hornfelsed siltstone surrounds the intrusion. NNW-trending, 0.5-1.5 m wide, non-foliated quartz-feldspar porphyry dykes crop out south of Toms zone. These cut across siltstone and mudstone in the Hangingwall Siltstone Unit (Fig. 3.1). Quartz-feldspar porphyry dykes have also intruded the

Western Volcanic Succession in the Toms zone footwall (Figs. 3.4 and 3.5). The porphyritic rocks consist of quartz, plagioclase and biotite phenocrysts in a microcrystalline groundmass containing secondary biotite and sericite (Fig. 3.16G).

The quartz-plagioclase porphyry and granite plot within the volcanic arc granite field of Pearce et al. (1984). Samples contain 69-70 wt % SiO_2, 2-4 wt % K_2O, 46-127 ppm Rb, 1-8 ppm Y and 2-4 ppm Nb (Appendix 4). Aluminium Saturation Index values range from 1.0 to 1.2, indicating that it is an I-type granite suite. The dykes probably represent a late phase of the Lewis Ponds granite as they have similar compositions to the massive, phaneritic granite.

Pogson and Watkins (1998) interpreted post-tectonic granitic intrusions in the Lewis Ponds district as possible shallow apophyses of the Bathurst Batholith (Fig. 2.5). Geophysical data indicates that the batholith dips shallowly northwards at depth. Although contact metamorphism appears to be minimal, the authors suggested that granite emplacement may have been accompanied by sulfide remobilisation at Lewis Ponds.

3.10 Facies of the Mullions Range Volcanics

Previous studies of the Mullions Range Volcanics concentrated on areas north and northwest of Lewis Ponds. Packham (1968) defined a 460 m type section on Kerrs Creek (Fig. 3.18), comprising rhyolite to dacite flows, volcaniclastic breccia and sandstone. Hilyard (1981) divided the unit into a lower member of intercalated aphyric rhyolite, siltstone, volcaniclastic breccia and sandstone and an upper member of massive, coarsely porphyritic rhyolite.

Following re-mapping of the Bathurst 1:250 000 sheet by the Geological Survey of New South Wales, Pogson and Watkins (1998) provided a thorough stratigraphic and lithological description of the unit. Pogson and Watkins interpreted the Mullions Range Volcanics as a predominantly submarine succession due to non-welded volcaniclastic gravity flow deposits, the sporadic occurrence of fossiliferous limestone lenses and massive sulfide deposits. They recognised the general lack of shallow water sedimentary structures in the unit and acknowledged that some of the limestone lenses might be allochthonous. Hilyard (1981) suggested that the volcanic pile accumulated in a moderately deep water (~500 m) environment which may have later become partly emergent. Other studies concluded that the volcanic pile was progressively submerged during the Late Silurian (Byrnes, 1976; Pogson and Watkins, 1998).

The source area for the Mullions Range Volcanics remains speculative. Hilyard (1981) interpreted the southerly increase in stratigraphic thickness of the western lobe (Fig. 3.18) to

indicate proximity to a major silicic volcanic centre. The Mullions Range anticline has also been cited as a possible source area (Packham, 1968; Hudson et al., 1997).

A regional study was undertaken to compare lithofacies throughout the Mullions Range Volcanics with the Lewis Ponds host sequence and to interpret the overall palaeogeography and volcanic provenance. This involved traverses along suitable roads and creeks, as well as examining abandoned quarries and mine sites north of Orange (Fig. 3.18). The lithofacies are summarised in Table 3.3. Three areas are described in detail below.

Area	Lithofacies associations	Interpretation
Summer Hill Creek	Massive and flow-banded, quartz-feldspar phyric dacite; interbedded cherty siltstone, matrix-supported polymictic breccia and granular quartz-feldspar crystal-rich sandstone	Quartz-feldspar-lithic mass flow deposits intercalated with porphyritic dacite lava flows or sill-like intrusions
Long Point Road	Thick, massive quartz-feldspar phyric daccite bodies overlying quartz-feldspar crystal-rich sandstone and siltstone	Massive, porphyritic dacite intrusions? and quartz-feldspar crystal-rich volcaniclastics
Cullya Road quarry and surrounds	Aphyric and quartz-feldspar phyric rhyolite; interbedded massive to diffusely-stratified siltstone, sandy-siltstone, pumiceous volcanic lithic sandstone and pumice breccia	Cold, pumiceous mass flow deposits containing reworked and juvenile clasts, surrounded by lavas and porphyritic rhyolite intrusions
Belgravia Road	Massive and flow-banded aphyric to quartz-feldspar phyric rhyolite; minor siltstone	Rhyolite lava flows and domes
Coalmans Creek	Massive and columnar-jointed aphyric to sparsely porphyritic rhyolite with rare amygdales	Rhyolite lava flows and domes
Calula Creek and surrounds	Massive and flow-banded aphyric rhyolite and feldspar phyric dacite; interbedded thinly-laminated siltstone, pebbly-granular quartz-feldspar-lithic sandstone and monomictic volcaniclastic breccia; minor fossiliferous limestone lenses	Lava flows and domes intercalated with re-sedimented autobreccia, pumiceous-volcanic lithic mass flow deposits and minor allochthonous? limestone
Kerrs Creek to Calula Creek	Laterally extensive volcanic lithic, shard-rich siltstone and sandstone; massive and flow-banded spherulitic aphyric rhyolite and feldspar phyric dacite	Rhyolite lava flows and domes; minor intercalated pumiceous-volcanic lithic mass flow deposits
Kerrs Creek (type section)	Thick, massive or flow-banded aphyric rhyolite; minor volcaniclastic sandstone and breccia	Rhyolite lava flows and domes; minor intercalated volcaniclastics

Table 3.3 Lithofacies associations in the Mullions Range Volcanics. Refer to highlighted areas in Figure 3.18 for the localities.

Summer Hill Creek

Coherent and clastic, dacitic volcanics crop out discontinuously along Summer Hill Creek, northwest of Lewis Ponds (Fig. 3.18). The east-dipping sequence consists of interbedded siltstone, sandstone and breccia, intercalated with thick (>100 m) units of massive and flow-banded, coarsely porphyritic dacite and quartz-feldspar crystal-rich sandstone (Table 3.3; Fig. 3.19).

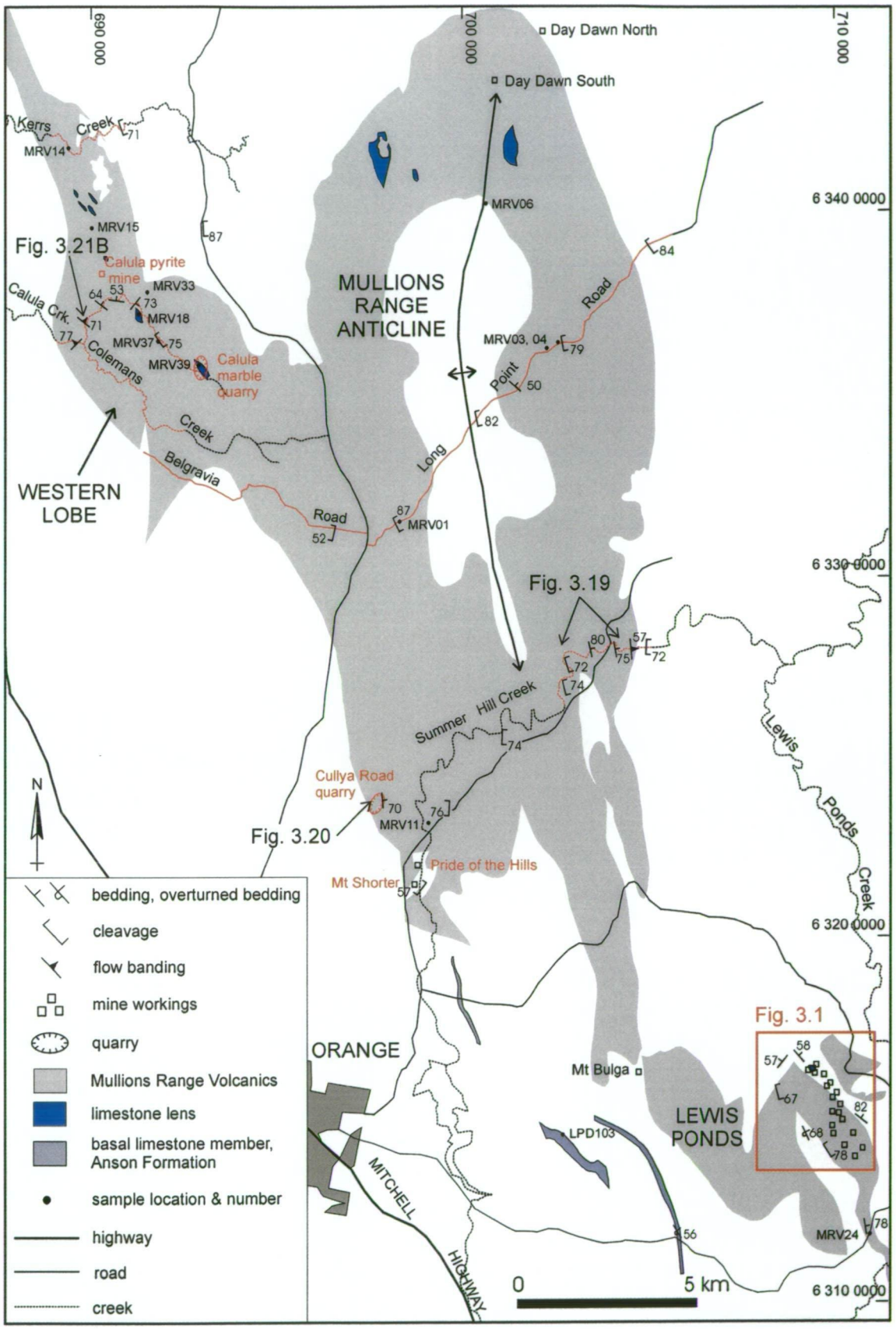

Figure 3.18 Locality map illustrating the road and creek sections, quarries and abandoned mine sites studied in the Mullions Range Volcanics (highlighted in red). All bedding, cleavage and flow banding measurements are from the current study. Compiled from Meakin et al. (1997); Kerrs Creek 1:25 000 topographic map, 8731-4-N, first edition; and Ophir 1:25 000 topographic map, 8731-4-S, first edition, Central Mapping Authority of New South Wales.

Interbedded cherty siltstone, pebbly-granular sandstone and breccia

A thick (100-150 m) sequence of interbedded cherty siltstone, sandstone and breccia occurs in Summer Hill Creek (Fig. 3.19), southwest of the Fourth Crossing. The pebbly-granular sandstone and matrix-supported polymictic breccia includes angular to well rounded pebbles and cobbles of cherty siltstone or aphyric rhyolite/dacite and thinly-laminated siltstone (Fig. 3.19A). The thickness of individual beds could not be determined from outcrops.

Granular quartz-feldspar crystal-rich sandstone

Massive, diffusely-stratified, very coarse-grained, crystal-rich sandstone occurs in a 50-100 m thick unit, overlying the breccia and cherty siltstone deposits (Fig. 3.19; 250-350 m). The poorly sorted sandstone consists of 60-75% embayed, euhedral to subhedral quartz and albitised plagioclase crystals in a siltstone matrix. Wispy lenses of siltstone occur throughout the sandstone. These may represent siltstone rip-up clasts, disrupted siltstone beds or flattened pumice rafts (Fig. 3.19B).

Quartz-feldspar phyric dacite

Thick bodies (>50m) of massive and flow-banded porphyritic dacite are intercalated with the volcaniclastic rocks (Fig. 3.19C). The medium- to coarse-grained porphyritic dacite is characterised by 5-10% euhedral quartz phenocrysts, 10-15% plagioclase phenocrysts and 1-2% biotite in a microcrystalline groundmass.

Interpretation

The Summer Hill creek sequence accumulated in a moderately deep, submarine environment in close proximity to an extrusive and/or intrusive dacitic volcanic centre. Polymictic breccia and quartz-feldspar crystal-rich sandstone occurs in thick, diffusely stratified, non-graded beds, interpreted as mass flow deposits. There are no wave or current-generated sedimentary structures preserved in the volcaniclastic deposits. Contacts between the coherent porphyritic dacite and adjacent volcaniclastics are not easily discernable in outcrop. The flow-banded dacite may represent the margins of lava flows or thick sill-like intrusions.

Cullya Road quarry and surrounds

An 80-100 m thick, east-dipping sequence of strongly weathered volcaniclastic rocks occurs at the Cullya Road quarry, northwest of Lewis Ponds (Fig. 3.18). It comprises massive siltstone, overlain by interbedded diffusely-stratified pumice breccia, siltstone, sandy-siltstone and pebbly-granular volcanic lithic sandstone (Table 3.3; Fig. 3.20). Quartz-feldspar phyric rhyolite and aphyric rhyolite crop out poorly around the quarry and along Summerhill Creek.

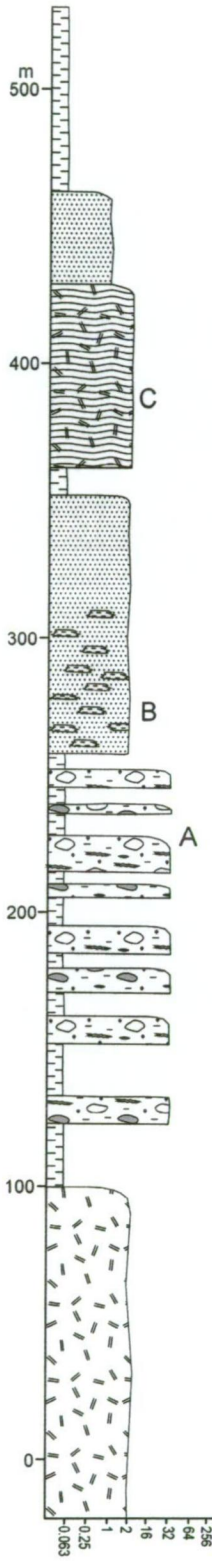

C. flow-banded, porphyritic dacite

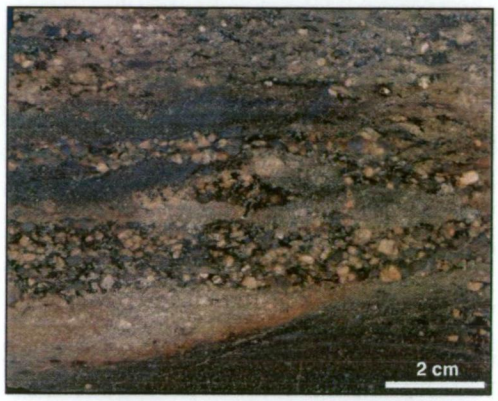

B. quartz-feldspar-lithic sandstone, sample MRV-12

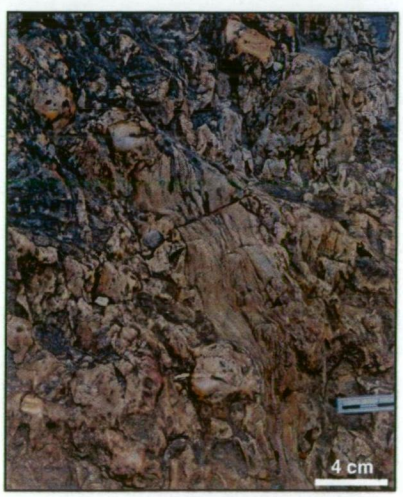

A. matrix-supported, polyictic breccia

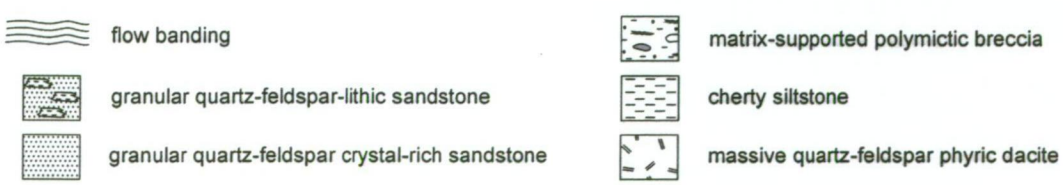

Figure 3.19 Summerhill Creek section illustrating stratigraphic relationships between coherent and clastic units observed in the creek bed. The true thickness of individual sandstone and breccia beds is poorly constrained due to limited outcrop. From GR 704875E 6328100N to 702725E 632665N.

Pumiceous siltstone

The massive to diffusely-stratified, cream to light green, clay-altered siltstone occurs in 50-500 cm thick beds. Angular quartz and feldspar crystals and pumiceous pebbles occur throughout.

Pebbly-granular pumice-lithic sandstone

Poorly sorted, diffusely-stratified, fine to very coarse-grained pebbly-granular sandstone is interbedded with the siltstone (Fig. 3.20A and C). It contains poorly preserved, round pumice clasts to 5 cm, granules and cobbles of siltstone, euhedral quartz crystals and angular crystal fragments in a fine-grained matrix. The sandstone occurs in 5-350 cm thick, massive or normal-graded beds with sharp planar lower contacts. Some of the beds are laterally discontinuous, lensing out along strike over 1-5 m. Low-angle planar cross-bedding occurs in places (eg. Fig. 3.20 B). Foresets in the cross-stratification trend toward from the north-west and south-east. Many beds grade up into thinly-laminated, fine-grained sandstone and siltstone (Fig. 3.20B).

Pumice breccia

A ten metre thick, massive, diffusely-stratified pumice breccia unit grades up into pebbly-granular pumiceous sandstone (Fig. 3.20; 30-40 m). The matrix-supported, polymictic breccia consists of elongate, wispy pebbles to one metre long boulders of siltstone, 5-40% rounded granules to pebbles of pumice - many showing tube-vesicle textures, and minor angular to very angular, small to large aphyric rhyolite pebbles in a poorly-sorted matrix of ash, quartz crystals and volcanic lithics.

Interpretation

The volcaniclastic succession exposed in Cullya Road quarry was probably deposited from dilute, subaqueous, pumiceous mass flows. These transported quartz and feldspar crystals, juvenile aphyric rhyolite clasts, pumice and ash away from an explosive submarine or subaerial volcanic centre.

Pumice clasts are not flattened, suggesting that temperatures were too low for compaction welding. Lateral discontinuity of beds implies that some of the flows may have occurred in channels. Siltstone and volcanic lithic clasts are very angular to rounded, indicating minor reworking of the sediment prior to deposition. The low-angle cross-stratification indicates that sediment was sourced from the northwest or southeast.

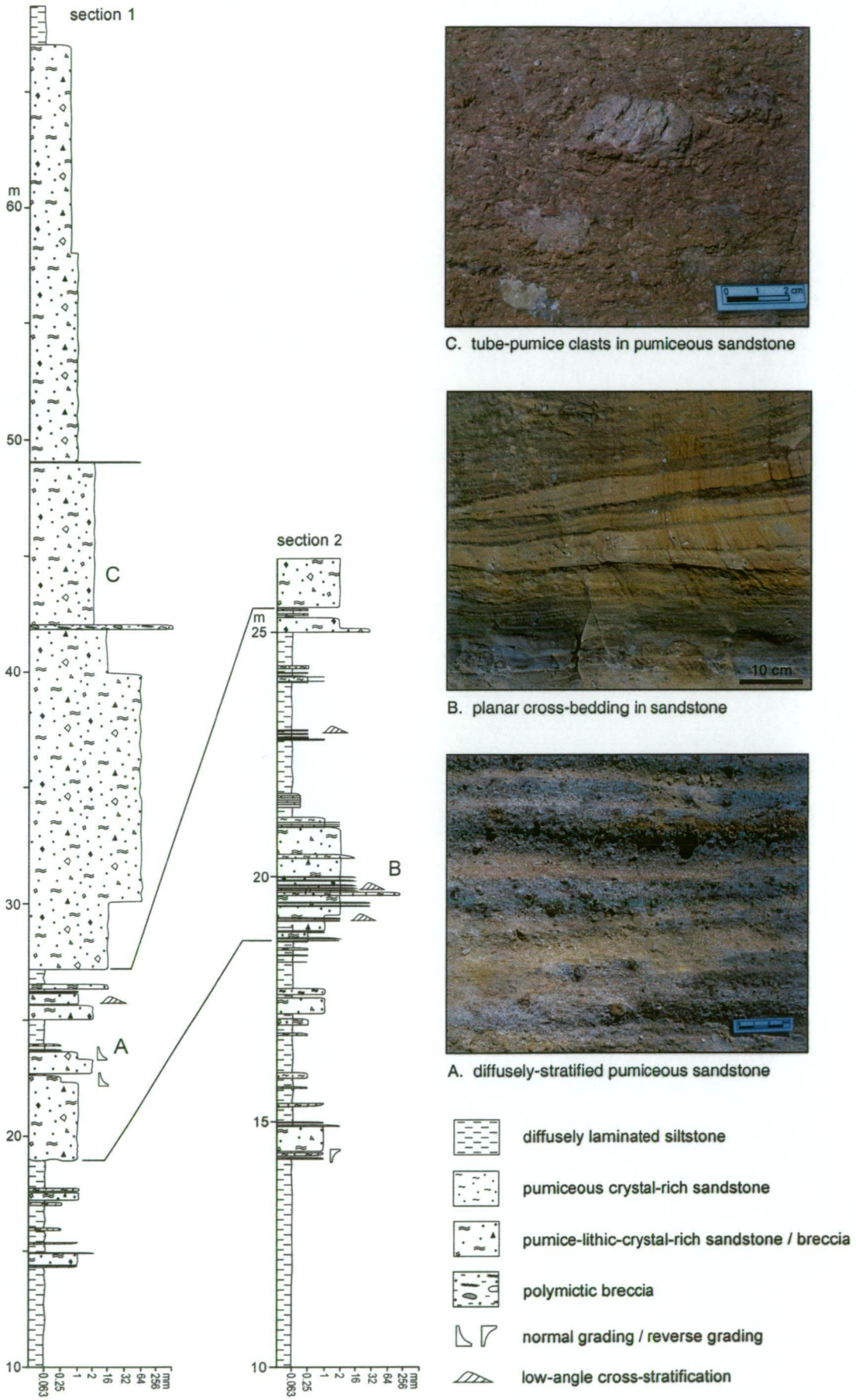

Figure 3.20 Cullya Road quarry section showing a thick unit of pumice breccia overlying interbedded, diffusely-stratified siltstone and pumiceous crystal-rich sandstone. Measured at the western side of the quarry, GR 697600E 6323650N.

Upper and lower contacts of the massive rhyolite unit are not exposed in the Cullya Road quarry. However, Hermann (1997) noted regular, conformable contacts between quartz feldspar phyric rhyolite and the adjacent siltstone units at nearby Mt Shorter (Fig. 3.18). He suggested that they may represent syn-sedimentary sills rather than coherent lava flows.

Calula-Colemans-Kerrs creek area

The Calula-Colemans-Kerrs creek area (Fig. 3.18) has a complex volcanic facies architecture characterised by coherent aphyric to porphyritic rhyolite and dacite, monomictic breccia, pumiceous volcanic lithic sandstone, siltstone and minor fossiliferous limestone (Table 3.3; Fig. 3.21). Numerous NNW-trending faults and folds have caused local repetition of the sequence. However, these were not mapped in detail during this study.

Rhyolite and dacite

Aphyric rhyolite and feldspar phyric dacite crop out extensively in the area. Planar, locally folded and brecciated flow banding occurs in Calula Creek, Kerrs Creek and Belgravia Creek (Fig. 3.22A). Columnar joints, spherulites, lithophysae and amygdales are present along sections of Colemans Creek and Calula Creek. Well-developed columns have a regular polygonal or hexagonal form and diameters of up to 30 cm (eg. Fig. 3.22B). The amygdales and lithophysae are filled with fine-grained quartz/silica. In thin section, the feldspar phyric dacite consists of euhedral, albitised plagioclase and K-feldspar phenocrysts in a microcrystalline, quartzo-feldspathic or glassy groundmass. Spherulites and perlitic fractures, resulting from devitrification and hydration are preserved throughout the groundmass of many samples (eg. Fig. 3.22C and D).

Columnar jointing, amygdales and thin (<50 cm) flow-banded intervals occur between massive aphyric rhyolite units. The massive intervals have sharp planar contacts. Columnar joints are typically perpendicular to the flow foliation. The rhyolite and dacite units are therefore interpreted to occur as flows and/or domes. Hilyard (1981) documented 1-60 m thick individual flow units, comprising flow-banded or highly vesicular rhyolite overlying columnar-jointed rhyolite with an autobrecciated base.

Massive monomictic volcaniclastic breccia

Thick (2-40 m) deposits of non-stratified, monomictic, matrix-supported to clast-supported breccia are intercalated with the rhyolite (Figs. 3.21 and 3.22E-F). These consist of sub-rounded to very angular, typically cuspate, pebbles and cobbles of massive and flow-banded, aphyric to sparsely porphyritic rhyolite in a fine-grained matrix containing crystals and

volcanic-lithics. The thick (>1 m) massive beds of breccia probably represent submarine mass flow deposits. They contain a mixture of juvenile and reworked volcanic lithics derived locally from the underlying rhyolite.

Interbedded shard-rich pumiceous sandstone, quartz-feldspar crystal-rich sandstone and thinly-laminated cherty siltstone

The coherent rhyolite and breccia facies are intercalated with a sequence of interbedded pebbly-granular quartz-feldspar-lithic sandstone, thinly-laminated, cherty siltstone and shard-rich pumiceous sandstone. Pebbly-granular pumiceous sandstone crops out near the pyrite mine and along sections of Calula Creek (Fig. 3.18). The poorly-sorted volcaniclastic rocks consist of very angular to sub-rounded, massive and flow-banded rhyolite-dacite pebbles, wispy tube pumice clasts, and quartz and feldspar crystal fragments in a shard-rich matrix (Fig. 3.22G and H). Uncompacted cuspate, glass shards and pumice clasts indicate that deposition of the sandstone occurred at low temperatures. Diagenetic quartz filled tube vesicles in the pumice fragments, preventing compaction-induced flattening and allowing primary textures to be preserved (Fig. 3.22H).

The sandstone and cherty siltstone deposits are interpreted to result from dilute, pumiceous mass flows. These transported juvenile pumice fragments, volcanic lithics, glass shards and ash away from a nearby explosive-effusive volcanic centre. Rounding of the rhyolite clasts (eg. Fig. 3.22H) indicates minor reworking prior to deposition.

Limestone lenses

Large (400-1 000 m long) fossiliferous limestone lenses occur in the Calula Creek area (Fig. 3.18). The largest of these is located at the Calula marble quarry. Poorly exposed, massive, volcaniclastic or coherent dacitic rocks surround them. The partly recrystallised, fine- to very coarse-grained, massive limestone contains crinoids, branching rugose coral fragments and solitary corallites in a granular calcite matrix.

Interpretation

The Calula-Colemans-Kerrs creek area is characterised by proximal volcanic and volcaniclastic facies. Marked variations in lithology and lithological thickness occur over relatively short distances. Extensive coherent flows or domes occurring along Colemans Creek and Belgravia Creek indicate a source area toward the south or southwest. This corresponds to an increase in stratigraphic thickness of the western lobe of the Mullions Range Volcanics. However, thick flows in the Kerrs Creek area, to the north suggest multiple eruptive volcanic centres may have existed in the area. The volcanic centres were effusive and partly explosive.

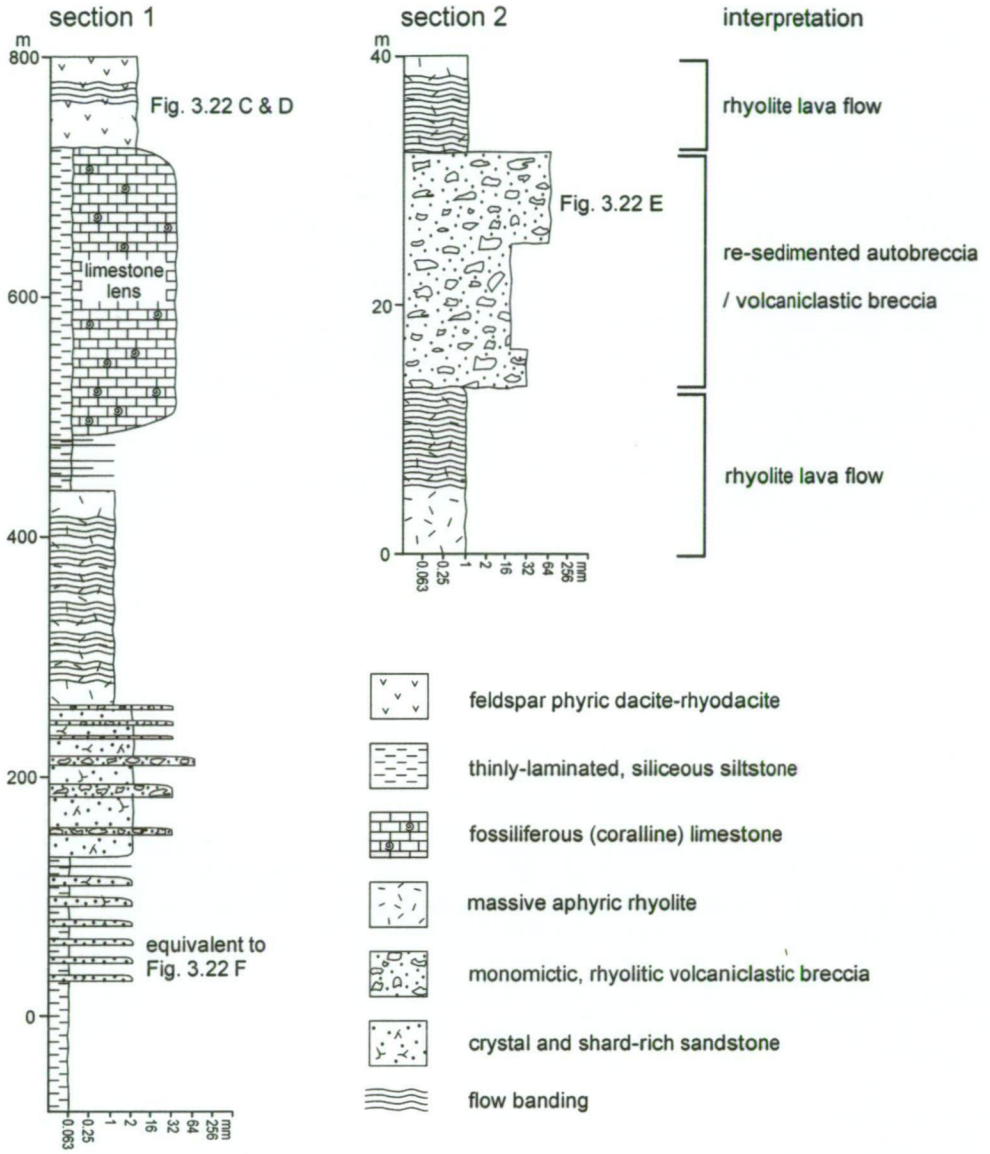

Figure 3.21 Section 1. Generalised Calula Creek section. Based on discontinuous outcrops along Calula Creek. The true thickness of individual volcaniclastic sandstone and breccia beds is poorly constrained. **Section 2.** Calula Creek waterfall section, illustrating massive, matrix-supported breccia deposits occurring between aphyric rhyolite units with flow-banded bases and tops. Contacts between coherent and clastic facies were poorly exposed in outcrops. GR 689 851E 6336919N.

The volcaniclastic breccia and sandstone deposits contain reworked, sub-rounded volcanic lithics derived from the underlying massive and flow-banded rhyolite. Therefore, some of the flows were exposed to surface erosion or submarine wave action. Uncompacted glass shards and pumice clasts suggest that the mass flows were not sufficiently hot to allow compaction welding to occur. The sandstone and breccia contains a limited range of clast types, indicating that they were deposited from syn-eruptive and/or proximal subaqueous flows.

Figure 3.22 Lithofacies in the Calula-Colemans-Kerrs Creek area

A Flow-banded aphyric rhyolite with weakly folded flow bands. Sample MRV-14 from Kerrs Creek (type section for Mullions Range Volcanics), GR 689525E 6341550N.

B Hexagonal columnar-jointed aphyric rhyolite. The horizontal polygonal columns are 5-10 cm wide. Coalmans Creek, GR 690164E 6335841N.

C Photomicrograph of flow-banded, spherulitic feldspar phyric dacite consisting of euhedral, albitized plagioclase and K-feldspar phenocrysts in a glassy groundmass. Spherulites occur throughout the groundmass. Sample MRV-33, Calula Creek area, GR 691625E 6337625N. Plane polarised light.

D Feldspar phyric dacite consisting of euhedral plagioclase and K-feldspar phenocrysts in a glassy groundmass with overlapping, arcuate perlitic fractures. Sample MRV-36, GR 691460E 6337135N. Plane polarised light.

E Matrix-supported polymictic volcaniclastic breccia characterised by sub-rounded to very-angular flow-banded aphyric rhyolite pebbles in a feldspar crystal-rich, granular sandstone matrix. The breccia occurs in non-stratified beds between tabular units of massive and flow-banded rhyolite. Calula Creek waterfalls, GR 689857E 6336919N.

F Clast-supported, polymictic volcaniclastic breccia consisting of sub-rounded to very-angular massive and flow-banded aphyric rhyolite pebbles in a granular sandstone matrix. Calula Creek, GR 690441E 6337578N.

G Photomicrograph of uncompacted cuspate bubble-wall glass shards in chlorite-sericite-altered crystal-rich siltstone. Sample MRV-15 from Calula Pyrite Mine area GR 690100E 6339375N. Plane polarised light.

H Pumiceous-volcanic lithic sandstone containing angular to subrounded feldspar phyric rhyolite-dacite pebbles, wispy tube pumice clasts and angular quartz crystal fragments in a poorly-sorted, shard-rich matrix. Sample MRV-37, GR 691900E 6336275N. Plane polarised light.

Abbreviations: s = spherulites, fsp = plagioclase and K-feldspar, p = perlitic fractures, r = flow-banded or massive rhyolite clasts, g = glass shards, p = pumice clast, qtz = quartz crystal fragment.

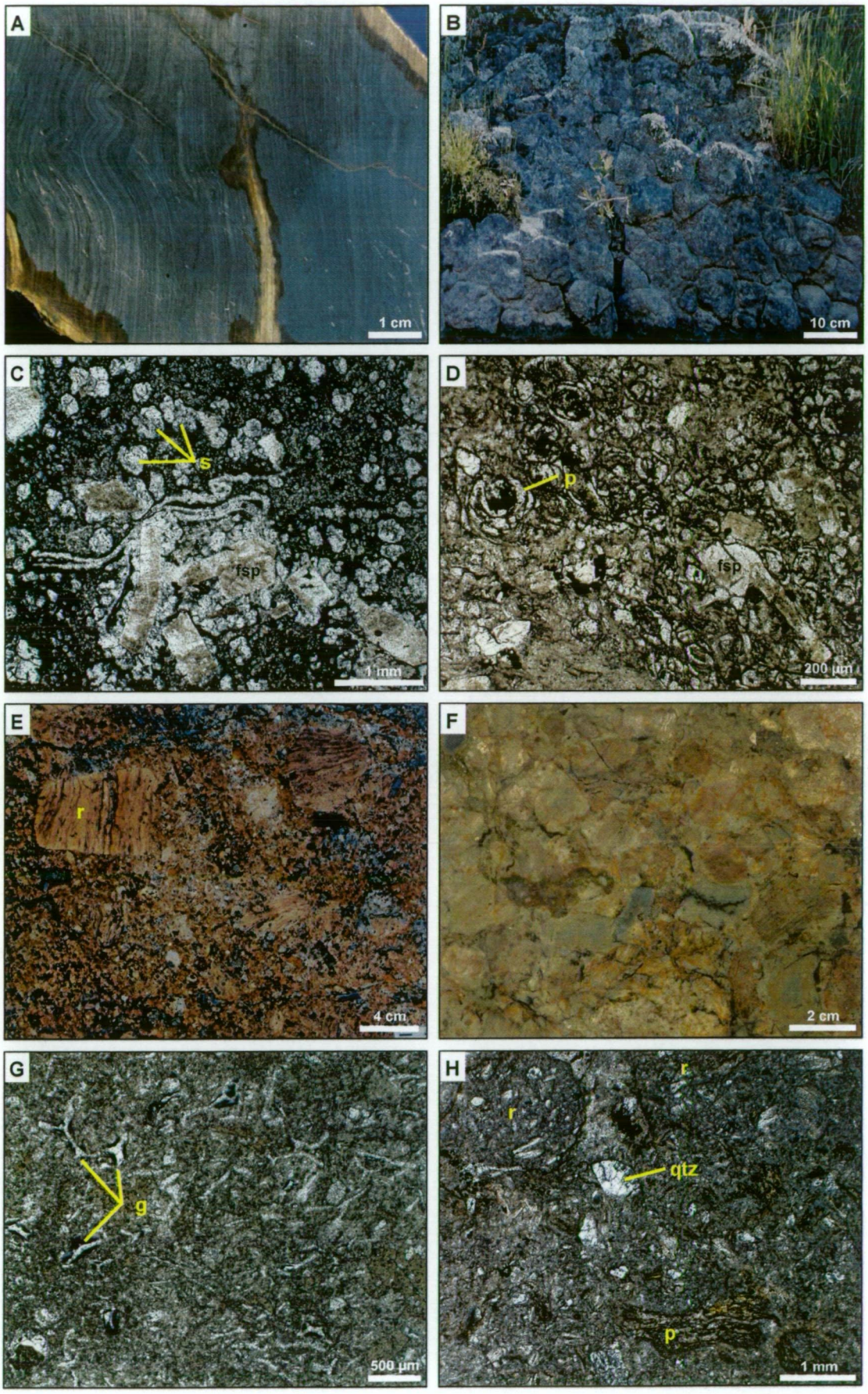
A
1 cm
B
10 cm
C
s
fsp
1 mm
D
p
fsp
200 µm
E
r
4 cm
F
2 cm
G
g
500 µm
H
r
r
qtz
p
1 mm

The limestone lenses may represent allochthonous blocks or in situ bioherms, which were engulfed by lava flows and sediments. Bedding discordance between the lenses and adjacent clastic rocks cannot be demonstrated. However, abundant rugose corals indicate that the limestone initially accumulated in a shallow marine environment prior to lithification and possible re-deposition by subaqueous mass flows.

3.11 Palaeogeography of the Mullions Range Volcanics

In summary, the products of subaerial or submarine, effusive to explosive volcanic centres dominate the western lobe of the Mullions Range Volcanics (Figs. 3.18 and 3.23). Coherent lithofacies include extensive, massive to flow-banded and columnar-jointed rhyolite-dacite lavas and/or domes. Associated volcaniclastic deposits contain reworked volcanic lithics, angular crystal fragments, uncompacted pumice clasts and glass shards. The pyroclasts probably resulted from explosive volcanic activity associated with rhyolite emplacement. The fossiliferous limestone lenses and mass flow deposits indicate broadly submarine conditions. However, facies characteristic of the submarine emplacement of lava flows and high-level intrusions were not recognised during this study. Therefore, partial emergence of the sequence cannot be discounted.

In contrast, thick units of coarsely porphyritic, massive and flow-banded dacite dominate central and northern parts of the Mullions Range anticline (Figs. 3.18 and 3.23). These are intercalated with coarse-grained submarine mass flow deposits that contain angular quartz and feldspar crystals and intraclasts of chert and siltstone. Pumiceous deposits and aphyric rhyolite lavas were only observed at Cullya Road Quarry.

The Lewis Ponds area is characterised by a mixed volcanic and sedimentary sequence of limestone-clast breccia, siltstone-clast breccia, volcaniclastic breccia, fossiliferous quartz crystal-rich sandstone and siltstone. The deposits overlie syn-sedimentary porphyritic dacite bodies and massive dacite. Facies analysis indicates deposition from submarine mass flows in a moderately deep, below-wave base slope environment (Fig. 3.23).

Late Silurian fossiliferous limestone occurs sporadically throughout the Mumbil Group, indicating predominantly submarine conditions. The extensive basal limestone member of the Anson Formation (Fig. 3.18) contains algae and corals preserved in their growth position (Pogson and Watkins, 1998). Other occurrences in the Mullions Range Volcanics and Anson Formation may represent in situ fringing reefs, bioherms, fore-reef talus deposits, deep marine carbonate deposits or allochthonous megaclasts. The origin of limestone lenses in the Calula Creek area is uncertain, as contacts with the surrounding host rocks are not exposed.

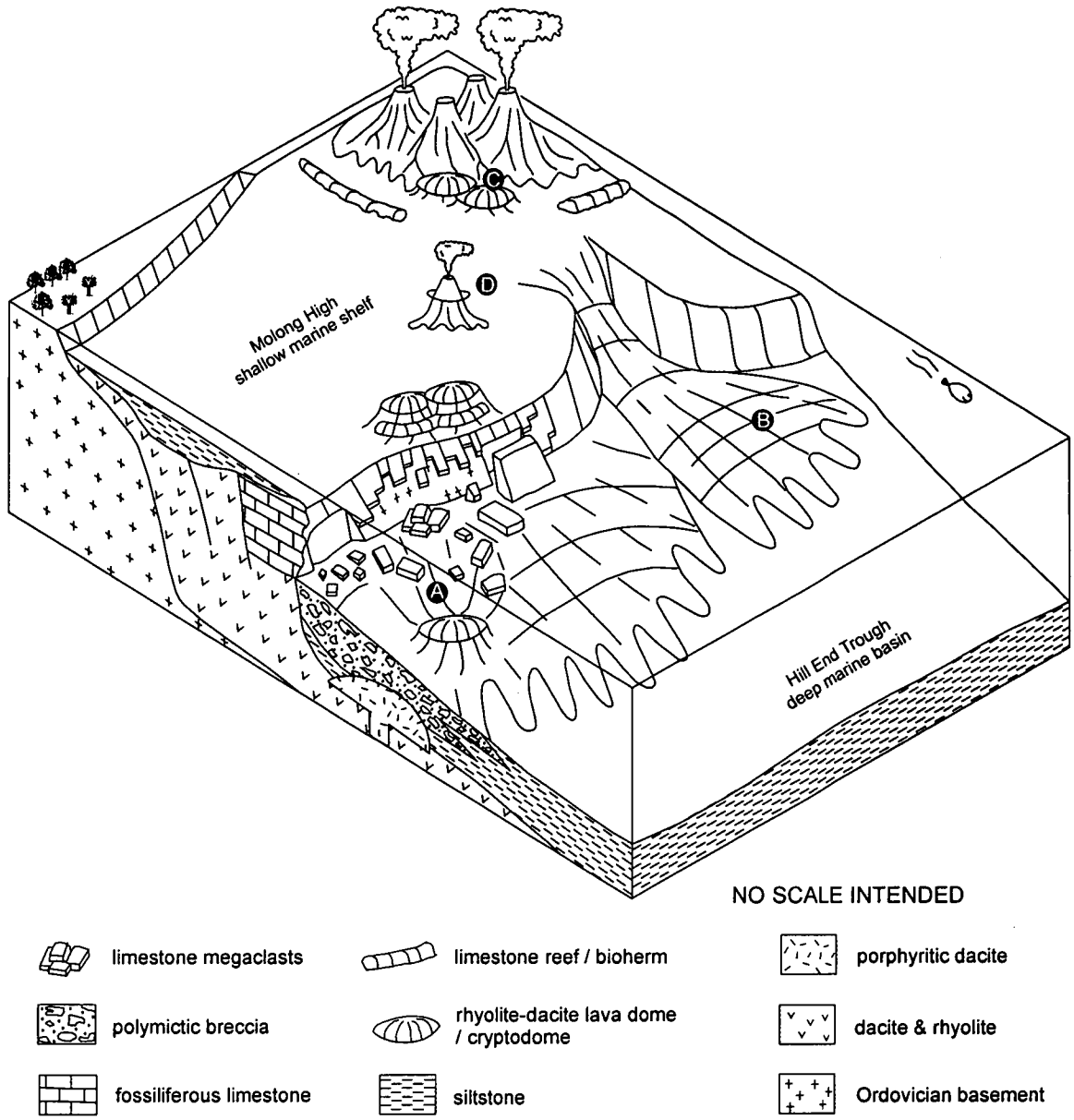

Figure 3.23 Palaeogeography model of the Mumbil Group illustrating the Late Silurian acid volcanic pile and marine sedimentary succession, overlying Ordovician basement rocks at the faulted western margin of the Hill End Trough. Sediments occurring in the Lewis Ponds (A) and Mullions Range anticline (B) areas were deposited in moderately deep water, slope environments, around the margins of high-level intrusive and/or extrusive rhyolitic centres. Volcanic and sedimentary detritus was derived locally and from the basin margin. The western lobe of the Mullions Range Volcanics (C) and Cullya Road Quarry area (D) formed in close proximity to shallow submarine to subaerial, effusive to partly explosive volcanic centres located at the basin margin. The volcanic and intrusive centres may have been surrounded by fringing reefs.

All of the limestone at Lewis Ponds is interpreted to be allochthonous. It occurs in mass flow deposits sourced from a lithified bioherm or fringing reef, possibly located on the flanks of a nearby submarine volcanic centre (Fig. 3.23). The limestone-clast breccia and megabreccia lithofacies have similarities to carbonate debris flow deposits outlined in Loucks et al. (1985) and Mountjoy et al.(1972), including an enormous range in clast size, wide variety of clast types and disorganised clast fabric (although this was not demonstrated in the fault-bound,

megabreccia). Deposits typically occur as sheets, beds or lenses in fine-grained siltstone / mudstone successions, adjacent to a reef complex or platform margin (Mountjoy et al., 1972). Debris flow deposits, talus and allochthonous reef blocks are important marginal-slope facies in many modern and ancient reef complexes (Enos and Moore, 1983; Playford, 1984; Loucks et al., 1985). They typically result from gravity-induced collapse of the platform margin or secondary debris flows initiated on the adjacent slope.

Limestone megabreccia deposits have been documented in the Nubrigyn Formation, western margin of the Hill End Trough, northwest of Lewis Ponds. Large algal limestone lenses (up to 1 km length) occurring in mudstone and volcaniclastic sandstone were referred to as bioherms and biostromes by Wolf (1965). However, Conaghan et al. (1976) re-interpreted these lenses as allochthonous megaclasts due to a wide range in clast size and composition, bedding discordance between clasts and adjacent matrix, and random truncation of internal fabrics at the clast margins. The authors suggested that large individual blocks may have slid into the basin, up to 10 km from the inferred source area, which is now preserved in the Lower Devonian Garra Formation and Cuga Burga Volcanics to the west. Allochthonous limestone megaclasts also occur in fore-reef facies in the Canning Basin, northwestern Australia (Enos and Moore, 1983; Playford, 1984; George et al., 1995) and the Delaware Basin, New Mexico (Loucks et al., 1985).

In the Late Devonian Lochenbar Beds, central Queensland, pebbles to five metre long boulders of fossiliferous limestone occur in a thick, massive unit of clast-supported volcaniclastic conglomerate. The limestone-bearing lithofacies is characterised by very angular, coralline limestone clasts and minor siltstone rip-up clasts in a matrix consisting of rounded aphyric, mafic to intermediate volcanic pebbles and rare crinoid and brachiopod fragments (Agnew, 1998). It occurs in a 12 m thick, laterally discontinuous bed with an erosive base that truncates the underlying thinly-laminated siltstone. The volcaniclastic succession is interpreted to overlie volcanic facies resulting from the submarine emplacement of lava, including hyaloclastite, re-sedimented hyaloclastite and pillow lavas (Bryan et al., 2001).

CHAPTER 4

LOCAL STRUCTURAL GEOLOGY

4.1 Introduction

The footwall volcanic succession at Lewis Ponds occurs in the core of a regional-scale, NNW-plunging anticline (Fig. 3.1). The adjacent tight parasitic syncline has been partly sheared out by a steeply dipping high strain zone, termed the *Lewis Ponds fault*. In Main zone, massive sulfide lenses occur in polymictic breccia units on the western limb of the syncline (Fig. 3.10). Toms zone (Fig. 3.4) and several smaller Au-Ag-base metal occurrences (Lady Belmore and New Lewis Ponds) lie within the Lewis Ponds fault. The host rocks are overprinted by an intense, NNW-trending cleavage and weakly developed kink folds and kink bands.

Abundant variably folded and boudinaged, NNW-trending quartz veins occur throughout the Lewis Ponds fault zone and adjacent footwall volcanic succession (Fig. 3.1). Some of these contain base metal sulfides. Cleavage-parallel quartz veins surround the Toms zone massive sulfide lens. However, the quartz-sulfide veins do not occur in Main zone.

Previous structural interpretations of the Lewis Ponds district have been limited by the lack of drill core, poor outcrop, inaccessible sub-surface exposures in abandoned mine workings and absence of marker horizons to allow correlation across faults. Some of the early studies found evidence for structural repetition of the mineralised zones on a fold limb cut by numerous northwest-trending sinistral, reverse-slip faults (Fig. 4.1). One of these faults was interpreted to pass through the New Lewis Ponds and Toms mines (Glasson, 1977). The structural complexity at New Lewis Ponds was recognised by Wright (1979), who argued that sulfide deposition was fault-controlled.

Numerous studies concentrated on the abandoned Cu mines, located in the southern part of the prospect (Fig. 3.1). At the Britannia mine, quartz-chlorite-chalcopyrite veins occurring in a deformed siltstone lens lead to the suggestion that shearing had remobilised metals from the massive sulfide lenses (Parton, 1981). However, footwall Cu stockwork zones were not discounted because Cu-Pb-Zn soil anomalies were observed at both the Britannia and Mt Regan mines (Parton, 1981; Heape, 1982).

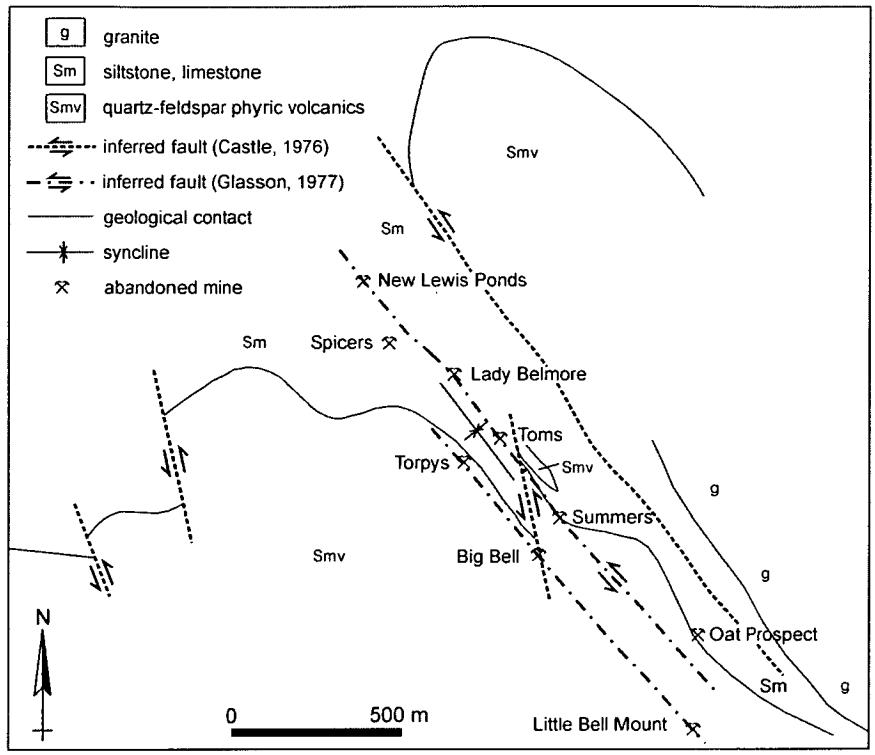

Figure 4.1 Compilation structural geology map of Lewis Ponds prospect showing the inferred sinistral strike-slip faults described in Castle (1976) and Glasson (1977). Modified from the map of Castle (1976).

In this chapter, the orientation and relative timing of major faults, folds and structural fabric elements are used to constrain the deformation history of the Lewis Ponds district. Comparisons are made with regional-scale structures occurring elsewhere in the Molong High. The chapter also assesses the potential role of deformation in focusing hydrothermal fluids into the host sequence and structurally modifying pre-existing massive sulfide.

4.2 Methods

Stratigraphic facing and structural fabric orientation data obtained from diamond drill core and surface observations were used to identify and interpret major structures occurring in the Lewis Ponds host sequence. Field mapping involved measuring bedding (S_0), cleavage (S_1), stretching lineation (L_1) kink fold (F_{12}), dyke and quartz vein orientations on outcrops. Surface structures are summarised on the enclosed 1:10 000 scale map. However, this data was limited by poor exposure in northern and eastern parts of the prospect.

Geometrical data derived from diamond drill core supplemented limited surface observations in the hangingwall and footwall of Main zone. As the core was not oriented prior to extraction, the true orientation of structural elements was lost due to core rotation in the barrel. However, useful geometric data can be obtained when the core contains a pervasive and consistently-oriented 'reference' foliation (Laing, 1977; Hinman, 1993). The method involves

measuring the orientation of an unknown fabric (eg. bedding or veins) relative to the reference foliation (Laing, 1977). The most likely orientation of the unknown fabric is estimated by minimising the angle between possible orientations of the reference fabric in core and the prescribed reference foliation. This fixes the orientation of the core and therefore the orientation of other fabrics contained within it (Scott and Berry, in press).

Robert Scott and Ron Berry (University of Tasmania) developed a *Microsoft Excel*-based program for reorienting drill core to determine the 'best-fit' orientation of down-hole structural fabrics. Measurements were made easily and quickly using a specially modified protractor, that wraps around the core. The measurement parameters are schematically illustrated in Appendix 2. Table 4.1 provides an example of field measurements for drill hole TLPD-12.

The aim of the down-hole structural analysis at Lewis Ponds was to compliment surface measurements with geometric data from diamond drill core. Bedding (S_0), cleavage (S_1), stretching lineation (L_1) and kink band (F_{12}) orientations were obtained from thirteen drill holes. The reference fabric orientation, S_1 = 78-061 was the numerical average of all surface cleavage measurements. In figures 4.2 and 4.6, the results are presented on contoured equal area stereonets for comparison with surface structural orientations. All results are listed in Appendix 2.

Drill hole	Depth (m)	S_1	S_0		L_1	F_{12}	QV	
		β	β	Ω	δ	δ	β	Ω
TLPD-12	397.15	29				25	37	185
TLPD-12	402.5	42			354		37	195
TLPD-12	417.94	58	52	343				
TLPD-12	515.7	43	39	0	18			
TLPD-12	516.0	47	37	82	10			
TLPD-12	516.3	60	40	323	18			
TLPD-12	567.4	42			321		32	185
TLPD-12	569.1	33	49	5	344			
TLPD-12	569.7	55	29	330	335			
TLPD-12	570.4	53	30	355	323	323		

Table 4.1 Example of data collected from TLPD-12 for down-hole structural calculations. Refer to drill core diagram in Appendix 2 for the measurement parameters.

where: S_0 = bedding
S_1 = cleavage (reference foliation)
F_{12} = kink bands (measured on S_1)
L_1 = mineral stretching lineation (measured on S_1)
QV = quartz veins
β = the angle between the core axis and the planar fabric (eg. S_0 or S_1)
Ω = angle between the down-hole ends of the long-axes of ellipses formed by the S_0 and S_1 fabrics, measured anticlockwise from S_1 in a plane perpendicular to the core axis, looking down hole
δ = angle between a lineation (eg. L_1 or F_{12}) and the down-hole end of the long axis of the plane in which it is contained, measured anticlockwise in the S_1 plane, looking down-hole

4.3 Folds and structural fabric elements

Two generations of structures and structural fabric elements occur in the Lewis Ponds host sequence (Tables 4.2 and 4.3). The first generation consists of a strong pervasive NNW-trending cleavage (S_1), steeply-plunging mineral stretching lineation (L_1) and open to tight cylindrical folds in bedding (F_1). Weakly developed second generation, sub-horizontal and sub-vertical kink folds post-date the S_1 cleavage. In addition, high strain zones are characterised by a strongly developed shear fabric (S_S), kink folds and a weak S-C fabric, interpreted to be late-D_1 in age. The preferred orientations of D_1 and D_2 structures are summarised in Table 4.4.

Age	Fold		Lithology	Description
D_1	F_1	First generation folds in S_0	Sandstone and siltstone	Large-scale anticline-syncline
				Small-scale isoclinal folds in drill core and reversals in stratigraphic facing and vergence
Late-D_1	F_S	Kink folds in high strain zones in S_0, S_1 and quartz veins	Siltstone and fine-grained sericite schist	Sub-vertical and sub-horizontal open to tight kink folds observed around Lewis Ponds fault
D_2	F_2	Second generation folds in S_1	Siltstone and limestone breccia	Sub-horizontal SW-verging monoclinic kink folds observed in limestone quarry

Table 4.2 Fold generations.

Age	Fabric		Lithology	Description	Intensity
D_1	S_1	First axial planar cleavage	Fine-grained schist, siltstone and limestone	Closely-spaced, rough to smooth disjunctive cleavage	Strong
			Coarse grained schist and porphyritic volcanic rocks	Anastomosing disjunctive cleavage	
	L_1	Mineral stretching lineation on S_1	Siltstone	Elongate pyrrhotite or pyrite blebs	Weakly developed
			Fine-grained schist	Alignment of phyllosilicate minerals	Strong
Late-D_1	C' or C	S-C fabric	Siltstone	Bands of aligned white mica (C'-type and C-type) cut across anastomosing, folded white mica bands (S)	Weak
	S_S	Shear fabric within high strain zones	Fine-grained schist and siltstone	Smooth disjunctive cleavage	Strong
D_2	F_{12}	Kink band intersection lineation on S_1	All lithologies	Sub-horizontal, oblique and sub-vertical kink bands in S_1	Weakly-developed

Table 4.3 Structural fabric elements. Cleavage classification is based on Powell (1979) and Passhier and Trouw (1996).

Fabric	Calculation	Surface measurements	Calculated orientations from drill core
S_0	Beta axis (F_1 fold axis)	41-331	37-334
L_{10}	Preferred mean direction (F_1 fold axes)	32-340	44-345
S_1 / S_S	Preferred mean orientation	78-061	79-061
L_1	Preferred mean direction	84-103	66-118
F_{12}	Preferred mean direction	65-358	70-007
F_2	Preferred mean orientation (F_2 fold axes)	16-325 and 69-153	
QV	Preferred mean orientations	87-230	81-060 and 11-202

Table 4.4 Calculated surface and drill hole bedding, cleavage, lineation, fold axis and quartz vein orientations.

First generation structures

F_1 folds

Surface bedding orientations in the Hangingwall Siltstone Unit and Transitional Unit define a broad, NNW-trending, open cylindrical anticline, plunging 41-331 (Figs. 3.1 and 4.2A). Apparent synclinal fold closures occur in the Transitional Unit south of Toms mine, adjacent to and within the Lewis Ponds fault. Small-scale isoclinally folded or kink folded sandstone beds occur in drill core from the Transitional Unit (Fig. 4.3A). Calculated down-hole bedding measurements from the eastern limb of the anticline have steep southwest to northeast dipping orientations (Fig 4.2A).

S_1 cleavage

S_1 is a strongly developed, generally northeast dipping cleavage, with a preferred orientation trending 78-061 (Table 4.4; Fig. 4.2B). Significant scatter occurs in surface measurements due to outcrop slumping and reorientation around F_2 kink folds. Calculated S_1 cleavage orientations from drill core dip toward the northwest and southwest. Scott and Berry (in preparation) found that 70% of calculated solutions for down-hole S_1 orientations at Lewis Ponds were within 11° of their reference foliation of 77-060.

S_1 morphology varies with the type of host rock. The closely-spaced, smooth disjunctive cleavage, occurring in siltstone and fine-grained schistose rocks is defined by aligned white mica or chlorite laths and strain shadows (Figs. 4.3 B and C). Anastomosing disjunctive cleavage domains wrap around quartz and feldspar phenocrysts in coarse-grained schists and porphyritic volcanic rocks. Throughout the host sequence, a greater proportion of micro-fractured quartz phenocrysts and angular, lozenge-shaped crystal fragments indicate high strain in the volcanic units (eg. Fig. 4.3B). Irregular, anastomosing, S_1-parallel bands of fine-grained polygonal calcite and epidote-chlorite cut across relatively undeformed, coarse-grained fossiliferous domains in the weakly foliated limestone clasts (Fig. 4.3D).

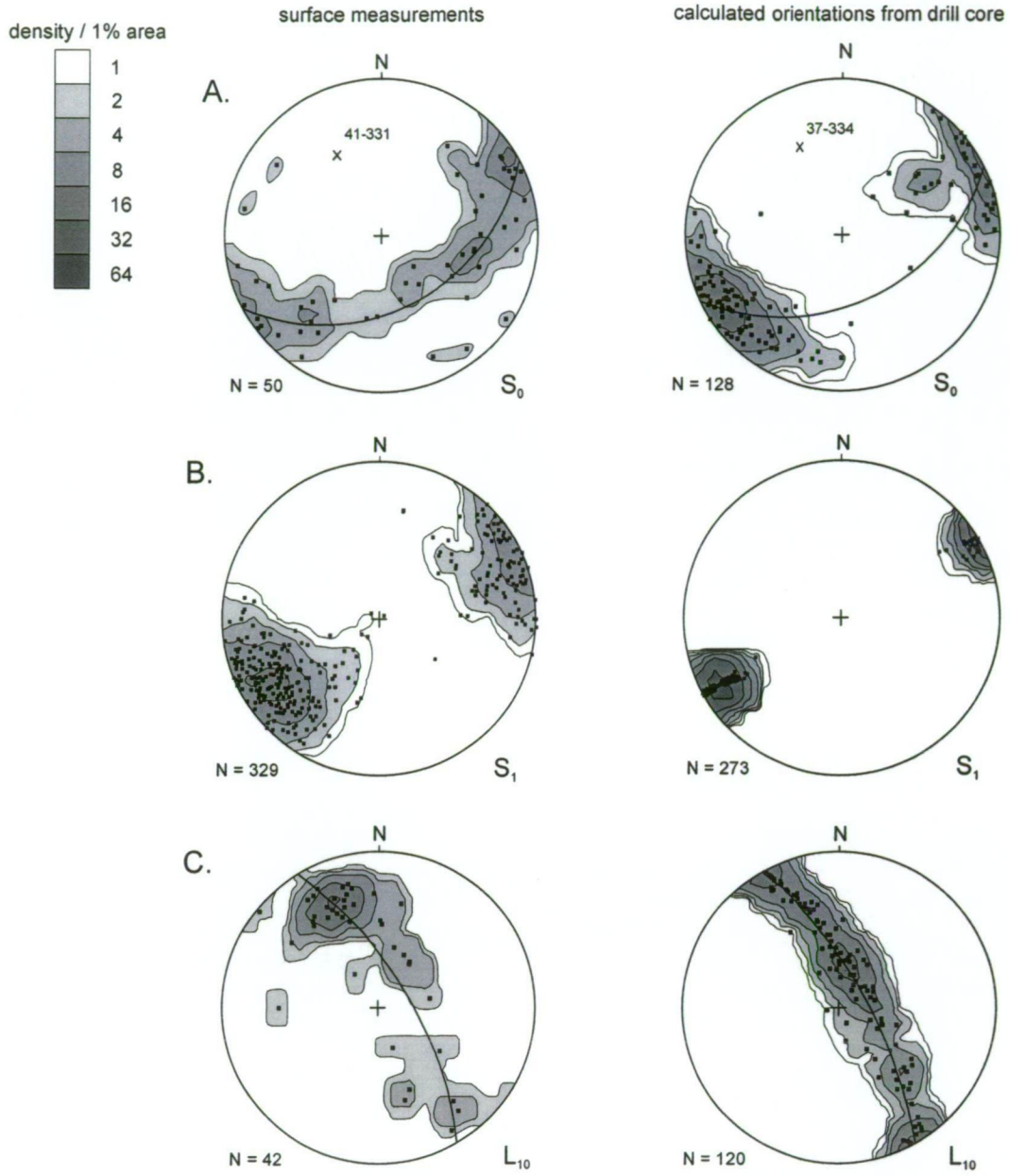

Figure 4.2 Surface and calculated drill core structural fabric orientations plotted on density-contoured equal area stereonets. **A.** Poles to bedding. **B.** Poles to S_1 cleavage. **C.** Calculated L_{10} bedding-first cleavage intersection lineations.

L_{10} bedding-first cleavage intersection lineation

Most calculated surface bedding-cleavage intersection lineations have a similar orientation to the F_1 fold axis (Table 4.4; Fig. 4.2C), suggesting that S_1 is an axial planar foliation. However both surface and drill hole data are distributed on great circles. This scatter is likely to reflect the low angle between bedding and S_1 cleavage on the eastern limb of the regional anticline. Uncertainties in measured and calculated bedding orientations significantly affect the orientation of individual intersection lineations.

Figure 4.3 Structural fabric elements and folds

A Kink folded, calcite-altered quartz crystal-rich sandstone bed in siltstone from the Transitional Unit. TLPD-20, 431 m.

B Strongly sheared quartz-sericite schist characterised by aligned white mica and a smooth, disjunctive S_1 cleavage. Subhedral quartz phenocrysts are associated with symmetrical strain shadows (a). Aggregates of lenticular crystal fragments 'strung out' along cleavage planes (b) are likely to result from the disintegration of pre-existing micro-faulted quartz crystals. TLPD-63, 314 m.

C Strongly-developed, disjunctive S_1 cleavage in a quartz-chlorite schist, defined by discontinuous, wispy domains of aligned chlorite. TLPD-63, 454 m.

D Fossiliferous limestone with a weak disjunctive S_1 cleavage. Anastomosing, cleavage-parallel bands of fine-grained, recrystallised, polygonal calcite cut across coarse-grained fossiliferous limestone domains, which contain crinoid ossicles (c). TLPD-58, 155 m.

E L_1 stretching lineation defined by elongate, oxidised pyrrhotite aggregates on an S_1 cleavage plane in siltstone. The cleavage and stretching lineations are overprinted by anastomosing F_{12} kink bands. TLPD-12, 400 m.

F S-C' fabric developed in siltstone adjacent to a deformed quartz-pyrite vein. The shear bands (C') cut across anastomosing cleavage bands (S_1) of aligned white mica. The shear bands are oblique to the interpreted margin of the Lewis Ponds fault zone. TLPD-65A, 907 m.

G Anastomosing sub-horizontal (1), oblique (2) and sub-vertical (3) F_{12} kink bands on an S_1 cleavage plane, in siltstone. Sub-horizontal bands are overprinted by the sub-vertical kink bands. GR 709510E 6316847N.

H Photomicrograph of F_2 kink folds in quartz-sericite schist, defined by folded S_1 cleavage domains. Hangingwall Siltstone Unit. TLPD-51A, 556 m.

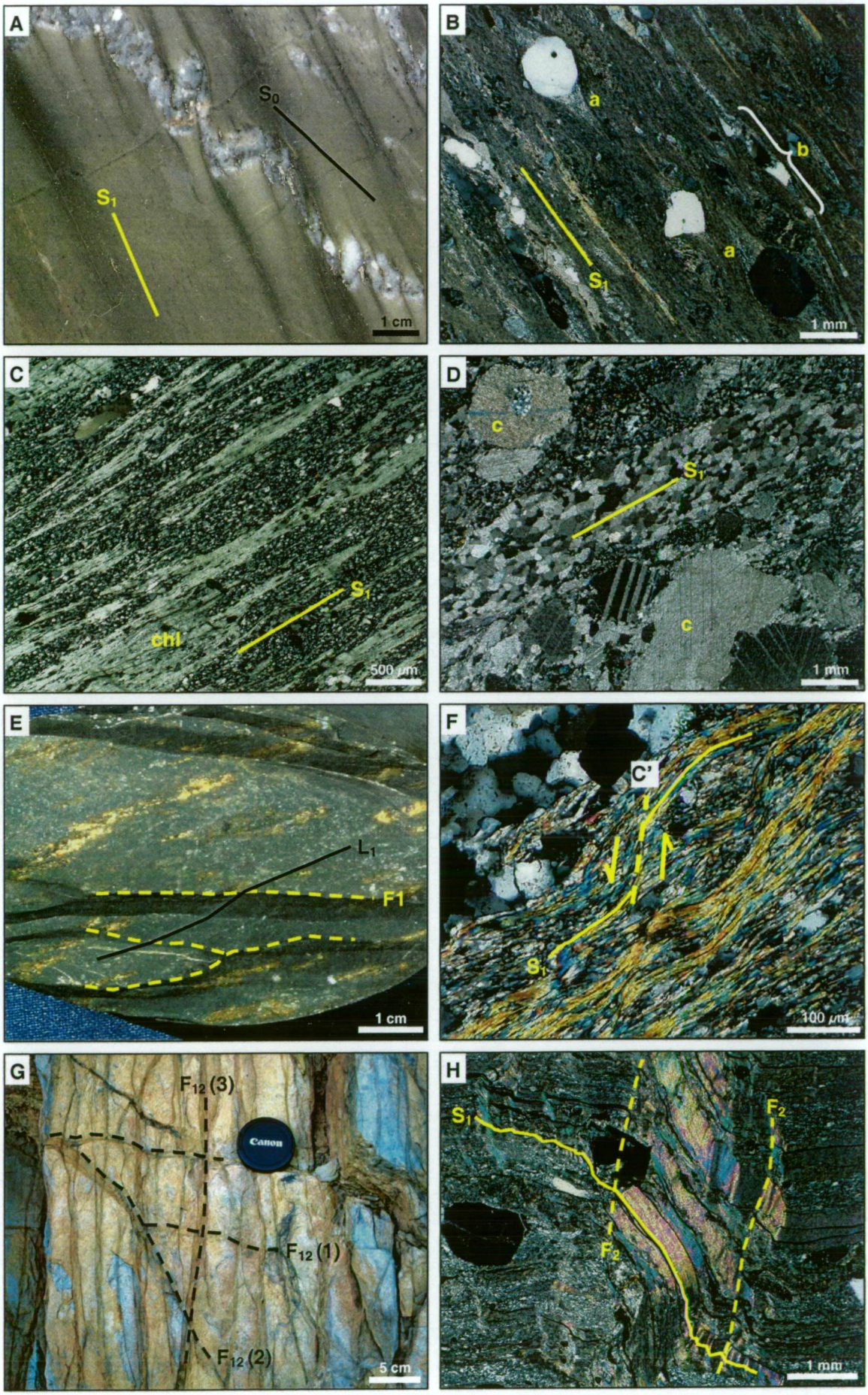
A
S_0
S_1
1 cm
B
a
b
a
S_1
1 mm
C
S_1
chl
500 μm
D
c
S_1
c
1 mm
E
L_1
F1
1 cm
F
C'
S_1
100 μm
G
F_{12} (3)
Canon
F_{12} (1)
F_{12} (2)
5 cm
H
S_1
F_2
F_2
1 mm

Stratigraphic facing and bedding-cleavage relationships

Many sandstone beds in the Transitional Unit and Hangingwall Siltstone Unit have basal load casts and flame structures and/or graded tops (see Chapter 3, sections 3.4 and 3.5). These sedimentary structures indicate the sub-surface stratigraphic facing of the beds. Calculated and observed down-hole bedding-cleavage relationships constrain the vergence direction and therefore, the relative location of fold hinges. Reversals in stratigraphic facing and vergence indicate that small-scale parasitic folds and locally overturned beds occur in the Transitional Unit and Hangingwall Siltstone Unit.

A tight parasitic syncline occurs in the Transitional Unit, in the Main zone footwall (letter *A* in Figs. 4.4 and 4.5). The western limb of the syncline is characterised by west-verging, east-facing stratigraphy. Bedding on the overturned, eastern limb of the syncline verges toward the east and youngs toward the west. Vergence and stratigraphic facing directions could not be obtained from within the thick, massive polymictic breccia unit that hosts Main zone. However, apparent thickening of the limestone-clast breccia unit occurs in the area of the inferred fold hinge.

In the Hangingwall Siltstone Unit, a fault-bound siltstone wedge occurs in the Main zone hangingwall (letter *B* in Figs. 4.4 and 4.5). Sandstone beds within this wedge predominantly young toward the east. The vergence cannot be determined accurately because bedding and cleavage orientations are almost identical.

A fault-bound limestone-dacite unit occurs in the Lewis Ponds fault zone (letter *C* in Figs. 4.4 and 4.5). Sandstone beds in the hangingwall of the Lewis Ponds fault predominantly young toward the east. Bedding on the western side of the limestone-dacite unit verges toward the east and youngs toward the west. This reversal in stratigraphic facing suggests that the quartz-chlorite-sericite schist occurs in the core of a tight anticline, surrounded by a laterally continuous limestone megabreccia lens.

South of Toms zone, stratigraphic facing directions in the Hangingwall Siltstone Unit are highly variable (Fig. 4.6). However, a change in the predominant facing direction of volcaniclastic sandstone beds from east to west indicates the presence of a tight syncline. This syncline occurs in the equivalent stratigraphic position to the Toms zone massive sulfide lens.

L_1 mineral stretching lineation

Elongate pyrrhotite or pyrite blebs define a steep southeast-plunging mineral stretching lineation throughout the host sequence, on S_1 cleavage surfaces (Figs. 4.3E and 4.7A).

Disseminated pyrrhotite is most abundant in the immediate hangingwall and footwall of Main zone. A similarly-oriented, sub-vertical alignment of white mica and chlorite occurs in the Lewis Ponds fault at Toms zone.

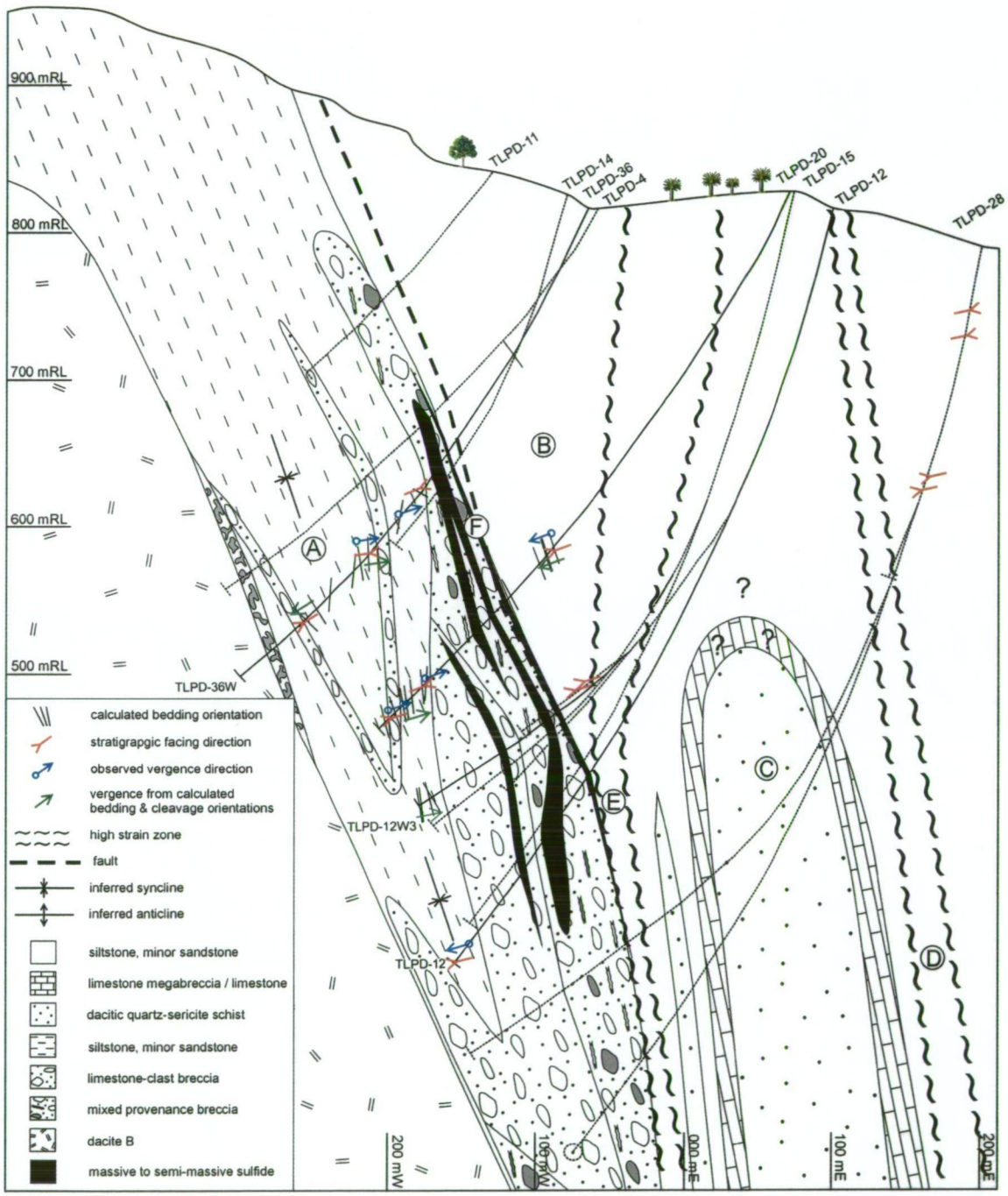

Figure 4.4 Line 1300N section showing observed and inferred structures, stratigraphic facing directions, observed vergence, calculated vergence and calculated bedding orientations (as apparent dips) in the hangingwall and footwall of Main zone. Letters *A* to *F* are referenced in the text.

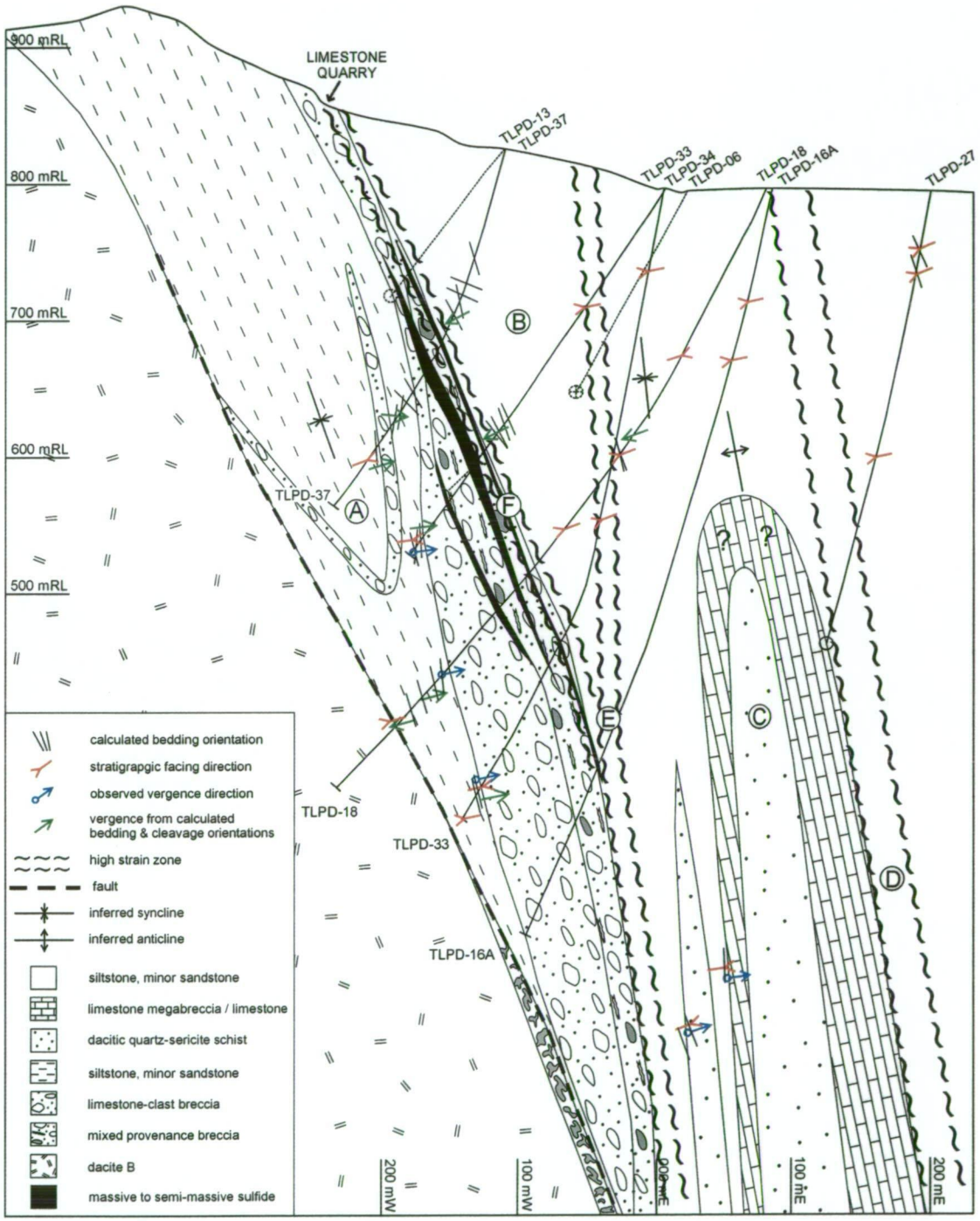

Figure 4.5 Line 1200N section showing observed and inferred structures, stratigraphic facing directions, observed vergence, calculated vergence and calculated bedding orientations (as apparent dips) in the hangingwall and footwall of Main zone. Letters *A* to *F* are referenced in the text.

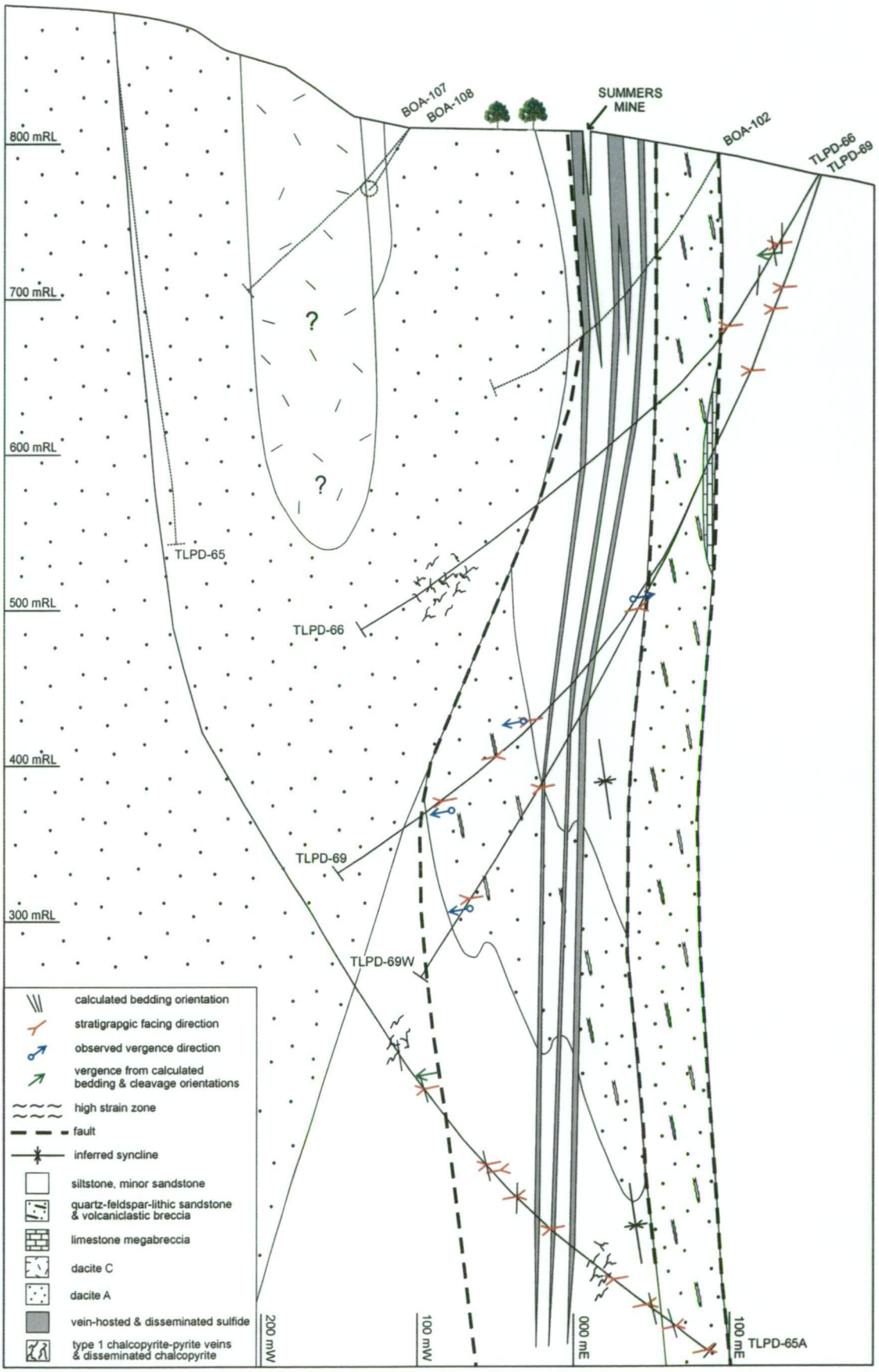

Figure 4.6 Line 200N section showing observed and inferred structures, stratigraphic facing directions, observed vergence, calculated vergence and calculated bedding orientations (as apparent dips), immediately south of Toms zone.

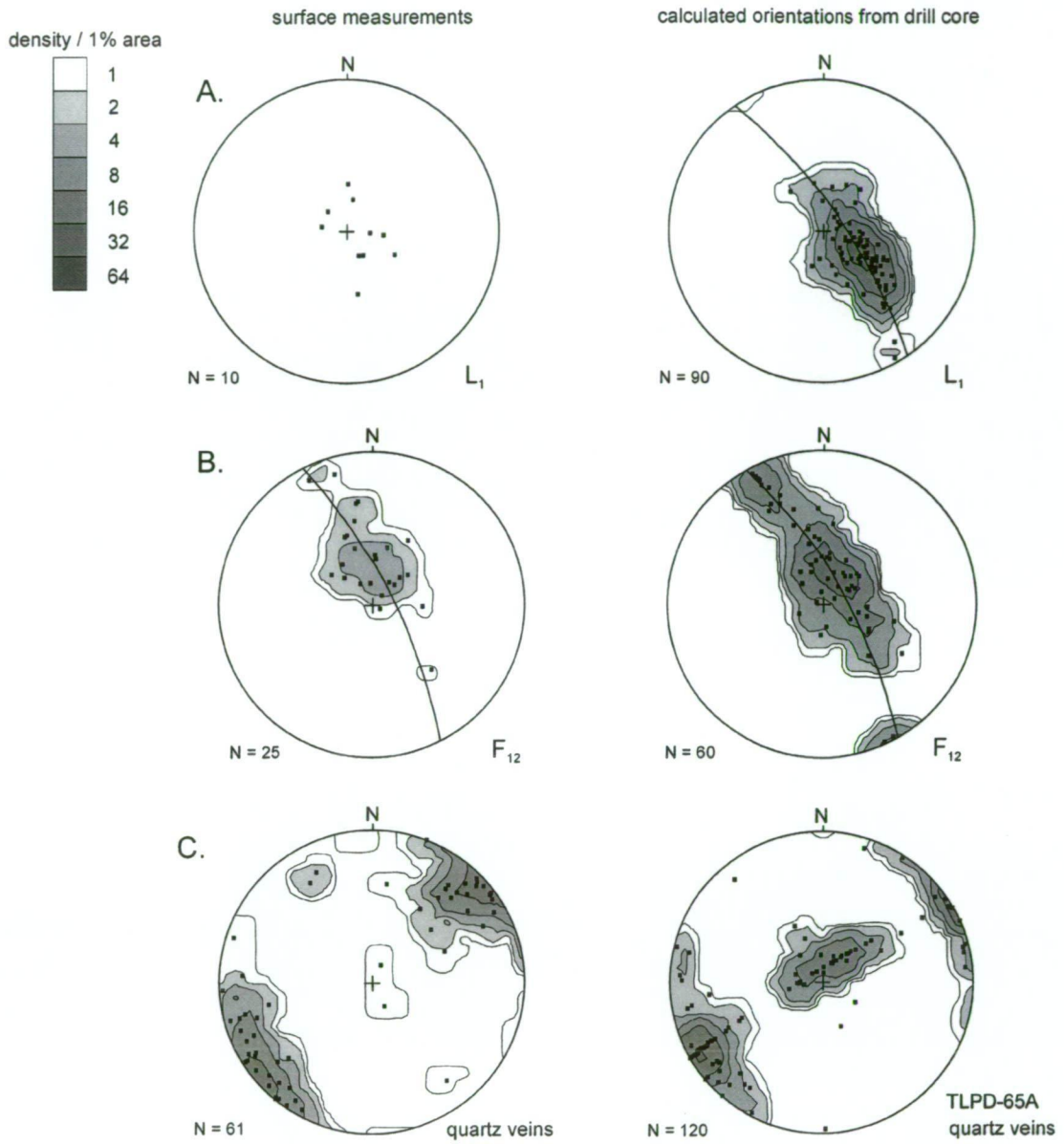

Figure 4.7 Density-contoured equal area steroenets of surface and calculated drill core structural orientation data. **A.** L_1 mineral stretching lineations. **B.** F_{12} kink bands measured on S_1. **C.** Quartz veins plotted as poles. Quartz veins in drill hole TLPD-65A occur in two preferred orientations. Most veins are sub-parallel to the S_1 cleavage and trend 81-060. Another set of sub-horizontal veins trend 11-202.

Late-first generation and second generation structures

Shear fabrics

Highly strained rocks within the Lewis Ponds fault zone are characterised by a sub-vertical, almost mylonitic S_S foliation. However, the S_S shear fabric could not be differentiated from the S_1 axial planar foliation described above. Mineral stretching lineations and kink folds typically plunge steeply toward the southeast. Weakly developed shear bands occur in the Hangingwall Siltstone Unit (Fig. 4.3F). The shear bands are both parallel and oblique to the Lewis Ponds fault.

F_{12} kink bands and F_2 kink folds

Sub-horizontal, oblique, and sub-vertical to vertical, anastomosing kink bands occur throughout the Western Volcanic Succession, Transitional Unit and Hangingwall Siltstone Unit, where small-scale kink folds intersect the S_1 cleavage (Figs. 4.3G and 4.7 B). Closely-spaced kink bands occur in high strain zones. Steeply plunging kink bands typically post-date the sub-horizontal ones. In thin-section, the kink bands are visible within white mica or chlorite-rich domains of the S_1 foliation (Fig. 4.3H). Large 50-100 cm amplitude, southwest verging, sub-horizontal monoclinic folds occur in the limestone quarry (Fig. 4.8). These are defined by kink folded limestone clasts and cleavage.

F_S folds

Sub-vertical, southeast-plunging kink folds occur in the Lewis Ponds fault zone. These structures post-date the S_1 cleavage and syn-D_1 quartz veins. Many have hinges parallel to the steep southwest-trending mineral stretching lineation.

4.4 Faults

Lewis Ponds fault

The Lewis Ponds fault is a 200-250 m wide corridor of steep, NNW-trending, parallel or anastomosing, brittle and ductile structures. In the northern part of the prospect, quartz veins and chlorite-altered siltstone are the only surface expression of the fault. However, a broad high strain zone surrounding Toms mine consists of a sub-vertical cleavage, mineral stretching lineation, kink folds, foliation boudinage and abundant variably deformed, S_1-parallel quartz veins (Fig. 4.9). In drill core, the host rocks are cut by intervals of cataclastic breccia and fault gouge. Fewer kink folds and quartz veins occur in the chlorite-sericite-altered porphyritic dacite south of Toms mine. Here, the high strain zone apparently broadens, becoming less intense in the footwall volcanic succession (Fig. 3.1). However, transfer structures may connect the Lewis Ponds fault to NNW-trending faults occurring immediately south of the prospect which have brought Ordovician rocks into contact with the Mullions Range Volcanics (Fig. 2.5).

The Lewis Ponds fault consists of two strongly deformed intervals at depth. The most easterly of these truncates the top of the limestone megabreccia lens in the structural hangingwall of the massive sulfide deposits (letter *D* in Figs. 4.4 and 4.5). Zones of cataclasite, rock flour and strongly fragmented vein quartz, siltstone and limestone overlie or occur within the limestone megabreccia over a 5-25 m thick interval. S_1 cleavage and F_{12} kink band orientations are highly variable within the fault.

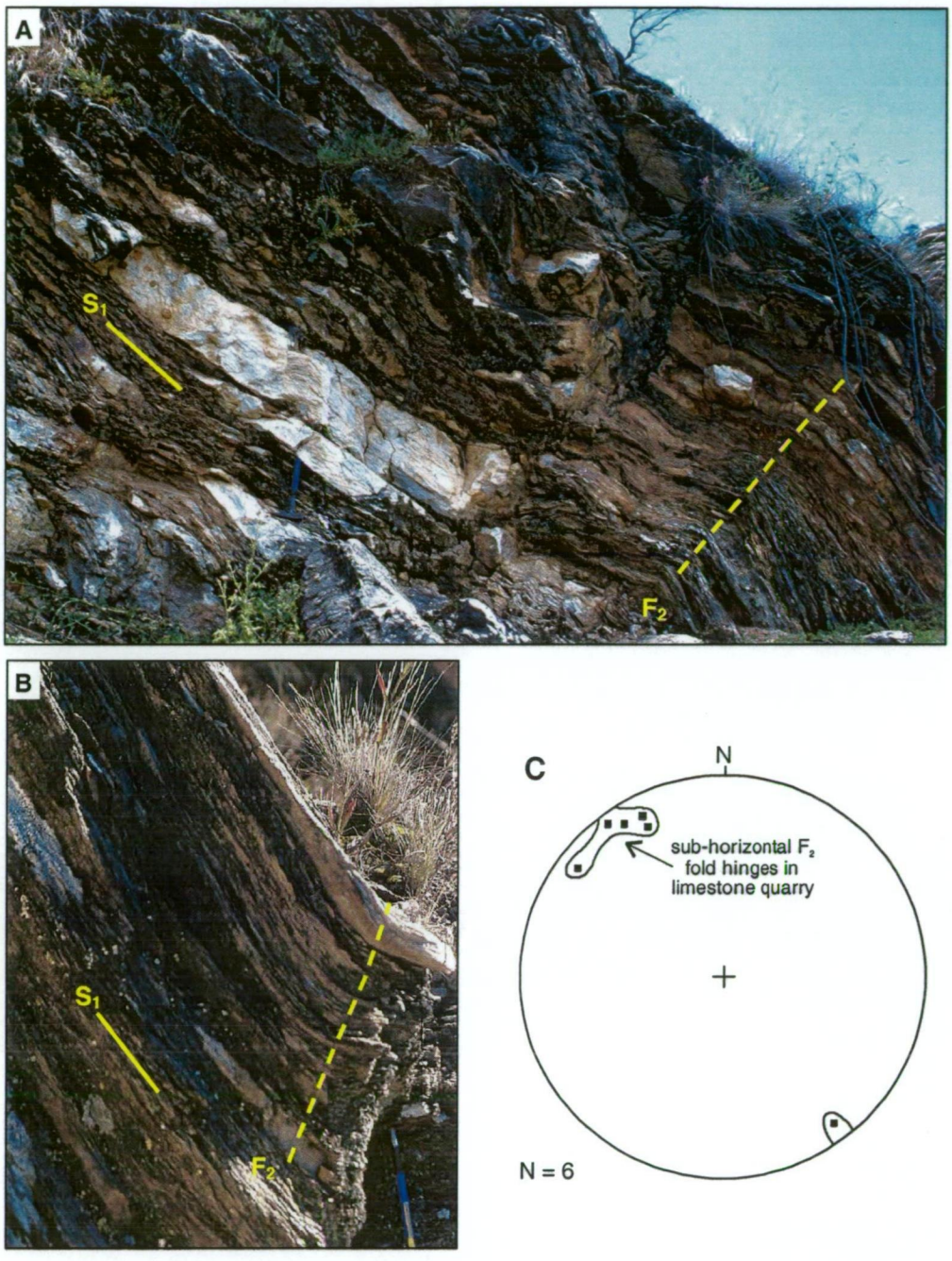

Figure 4.8 Structures exposed in the western wall of the limestone quarry.
A. Angular, blocky and lenticular boulders of recrystallised limestone, oriented sub-parallel to S_1 (40-053). Limestone clasts occur is a strongly foliated matrix of quartz-chlorite-sericite schist. The fabric has been folded into southwest verging, sub-horizontal F_2 kink folds. Hammer for scale.
B. The S_1 cleavage becomes steeper toward the northern side of the quarry (62-059) and limestone clasts, more flattened, suggesting increased strain. The limestone clast occurring at the top of the outcrop has an aspect ratio of approximately 50:1. Pencil for scale. **C.** Northwest-trending F_2 kink fold hinge orientations plotted on an equal area stereonet.

The western high strain zone truncates the polymictic breccia deposits that host Main zone at depth (letter *E* in Figs. 4.4 and 4.5). South of Main zone, the fault splays into numerous parallel to anastomosing shears separated by intervals of siltstone, chlorite ± talc-dolomite-sericite schist and fossiliferous limestone (Fig. 3.10, line 750N section). Alternating limestone and schistose intervals are likely to represent fold or fault repetitions of the same lithologies.

At Lady Belmore zone, disseminated sulfides and boudinaged, kink folded, S_1-parallel quartz-sulfide veins occur in strongly deformed, chlorite-talc-altered rocks.

Kinematic indicators occur throughout the Lewis Ponds fault. These include foliation boudinage, mica fish, carbonate fish, asymmetric strain shadows on quartz phenocrysts and lithic pebbles, asymmetric quartz vein boudins, pyrite porphyroblasts and shear bands (eg. Figs. 4.3F and 4.9A). The majority indicate east-over-west relative displacement across the fault. However, west-over-east shear sense indicators also occur in drill core and outcrops.

A high strain zone separates the Transitional Unit from an eastward facing, fault-bound wedge of the Hangingwall Siltstone Unit in the Main zone hangingwall (letter *F* in Figs. 4.4 and 4.5). The contact between the siltstone and intensely altered, mixed provenance breccia appears conformable in many drill holes. However, strongly deformed intervals occur within the siltstone and the breccia, indicating the presence of a high strain zone. On the surface, limestone clasts exposed in the western wall of the quarry become more attenuated toward the north, consistent with increasing strain (Fig. 4.8). The bedding-parallel structure is interpreted as a lateral branch of the Lewis Ponds fault. It separates westward facing stratigraphy in the Transitional Unit from siltstone and sandstone beds in the Main zone hangingwall that young toward the east. The fault may therefore occur in the hinge zone of a tight, parasitic anticline.

Footwall faults

Numerous faults occur throughout the footwall volcanic succession. A narrow high strain zone that truncates the Western Volcanic Succession south of Toms mine may be a branch of the Lewis Ponds fault (Figs. 3.1 and 4.6). It is associated with quartz veins and anastomosing ferroan magnesite/dolomite veinlets. The associated quartz-sericite alteration assemblage overprints the pervasive chlorite-altered volcanics. Faulted contacts between siltstone and quartz phyric volcanic rocks may also occur at the Little Bell Mount, Britannia and Mount Regan mines (Fig. 3.1).

Interpretation

The Lewis Ponds fault is a 200-250 m wide brittle-ductile shear zone. Its complex anastomosing geometry reflects the presence of competent lithologies such as coherent dacite and massive limestone, surrounded by less competent siltstone. The competent units behaved as rigid objects, with most of the strain focused in the adjacent siltstone. Furthermore, mechanically weak chlorite-sericite-talc-altered rocks locally concentrated the strain around the New Lewis Ponds, Lady Belmore, Main and Toms zones.

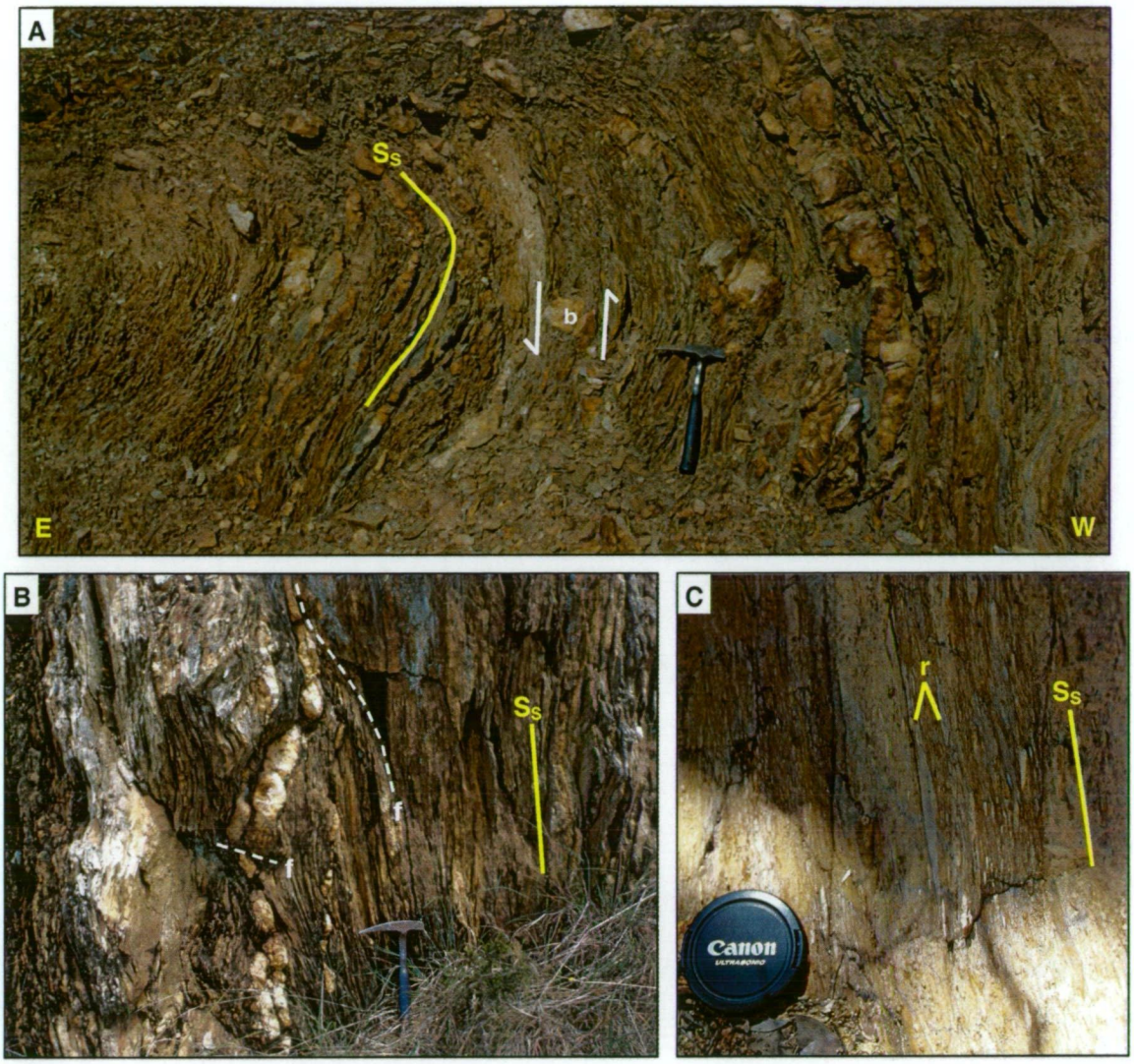

Figure 4.9 Structures in the Lewis Ponds fault zone
A. Outcrop photo showing boudinaged and kink folded, cleavage-parallel quartz veins in strongly sheared, fine-grained sericite-chlorite schist near Toms mine. Asymmetric quartz vein boudin (b) indicates west-over-east relative displacement. Photographed looking south at GR 709968E 6316015N. Hammer for scale. **B.** Kink folded, boudinaged and fractured quartz vein near Toms mine. S_S cleavage has also been boudinaged (f) and kink folded. Photographed looking south at GR 710050E 6315916N. Hammer for scale. **C.** Strongly sheared pebbly-granular, quartz-feldspar-lithic sandstone consisting of elongate, lenticular siliceous pebbles (r) in a fine-grained, quartz crystal-rich matrix. Near GR 710050E 6315916N. Lens cap for scale.

The fault-bound limestone-dacite unit (letter *C* in Figs. 4.4 and 4.5) is interpreted as a possible folded, fault repetition of the Transitional Unit and Western Volcanic succession. It is discordant to bedding in the surrounding Transitional Unit (Figs. 3.1 and 3.9). Quartz phyric rocks occurring between the limestone megabreccia lenses have similar textures and immobile element compositions to lithofacies association A in the Western Volcanic Succession.

The Lewis Ponds fault is parallel to the NNW-trending regional faults, indicating that it is a D_1 structure. Sub-vertical, southeast-dipping mineral stretching lineations, asymmetrical folds and shear sense indicators suggest that it resulted from east-block-up movement with a minor

sinistral component. However, opposing shear sense indicators suggest that normal and reverse displacement occurred at different times either due to fault reactivation or roll-back of the fault.

4.5 Vein generations

Five generations of veins are recognised at Lewis Ponds (Table 4.5). Each generation is characterised by a different morphology, orientation and relationship to the S_1 cleavage.

	Composition	Morphology	Location / host	Age
1A	Ca ± dol-ccp-py-sph-ga-Bi ± po	Isoclinally folded and boudinaged	Toms zone footwall	Pre-D_1 to early-D_1
1B	Qtz-py ± ccp	Isoclinally folded and boudinaged	Toms zone footwall	Pre-D_1 to early-D_1
2	Dol-ccp-py-sph-ga-st ± td ± as	S_1-parallel, pinch & swell structures, boudinaged	Toms zone massive sulfide lens	? Pre-D_1 to late-D_1
3A	Qtz-py ± sph ± ccp ± ga and qtz-po ± sph ± ccp ± ga	S_1-sub-parallel, weakly folded, or well developed pinch & swell structures; massive, banded or crustiform	Lewis Ponds fault zone and Western Volcanic Succession	Early to late-D_1
3B	Ca ± mag-hem	S_1-parallel, weakly folded or well developed pinch and swell structures; transposed and boudinaged in strongly sheared areas	Lewis Ponds fault zone and Hangingwall Siltstone Unit	Early to late-D_1
3C	Carbonate veinlets: mgs, sid, dol, Fe-dol	S_1-parallel, anastomosing, banded internal structure; weakly kink folded	Lewis Ponds fault zone	Early to late-D_1
4	Qtz-ms ± ca ± ab ± py ± ccp ± sph ± ga	S_1-perpendicular, undeformed to weakly kink folded	Lewis Ponds fault zone and Western Volcanic Succession	Late-D_1 / pre-D_2
5	Qtz-py ± sph ± ga	S_1-parallel, undeformed	Lewis Ponds Granite - quartz-feldspar porphyry dykes	Post-D_2,

Table 4.5 Composition, morphology and relative age of veins. Qtz = quartz, ca = calcite, sid = siderite, dol = dolomite, mgs = magnesite, ab = albite, ms = muscovite, ccp = chalcopyrite, py = pyrite, po = pyrrhotite, sph = sphalerite, ga = galena, Bi = native bismuth, st = stannite, td = tetrahedrite, mag = magnetite, hem = hematite.

Isoclinally folded and boudinaged, 1-300 mm wide, type 1 quartz-pyrite and calcite ± dolomite-chalcopyrite-pyrite veins occur in the footwall and hangingwall of Toms zone (Fig. 4.10A and B). These are typically associated with a strong to intense pervasive chlorite halo. The veins contain fractured pyrite with minor sphalerite, galena, native bismuth and pyrrhotite. These paragenetically early veins are overprinted by the S_1 cleavage. They formed prior to, or early during the D_1 deformation.

Boudinaged or anastomosing, 5-500 mm wide, type 2 dolomite veins occur in the Central massive sulfide lens and immediate footwall of Toms zone (Fig. 4.10C). They are parallel to S_1 and sulfide banding. Chalcopyrite, pyrite, sphalerite, galena, tetrahedrite, stannite and arsenopyrite occur in many of the veins, especially in lower parts of the massive sulfide lens. Most veins are boudinaged and kink folded, indicating a pre-tectonic to early syn-tectonic age.

Variably folded and boudinaged, type 3 quartz-sulfide and barren calcite ± magnetite-hematite veins occur throughout the Lewis Ponds fault zone and adjacent footwall volcanics. These massive to crustiform, 1 mm to 1 m wide, planar or anastomosing veins have a preferred orientation parallel or sub-parallel to S_1 and the Lewis Ponds fault (Figs. 4.7C, 4.9 and 4.10D). However, many veins mapped in the footwall volcanic succession trend northwest rather than NNW, possibly indicating a separate generation (Fig. 3.2). Many veins contain pyrite-sphalerite-chalcopyrite-galena or pyrrhotite-sphalerite-chalcopyrite-galena assemblages.

Type 3B calcite veins are restricted to the quartz phyric volcanic rocks in the Lewis Ponds fault zone and carbonaceous mudstone, south of Toms mine (Fig. 4.10E and F). Isoclinally folded and transposed veins with pinch-and-swell structures occur in quartz-chlorite-sericite schist. These become less abundant away from the fault-bound limestone megabreccia lenses. Pyrite has replaced the euhedral magnetite crystals in carbonate veins that are overprinted by younger quartz-pyrite veins. Type 3C Fe, Mn or Mg carbonate veinlets locally constitute 20% of the rock in the Lewis Ponds fault zone. These closely spaced, 0.1-1 mm thick, anastomosing, cleavage-parallel veinlets and lenses typically surround type 3A quartz veins.

Type 3A, B and C veins are interpreted as syn-tectonic shear or extension veins, that formed at a low angle to the major NNW-trending structures during D_1. Some may represent pre-D_1 veins rotated into the flattening plane during subsequent deformation. The type 3 veins are likely to have resulted from periodic brittle shear failure and extension in and around the Lewis Ponds fault.

Undeformed to weakly kink folded, 1-20 mm wide, type 4 quartz ± carbonate ± muscovite veins occur in drill core from the Lewis Ponds fault zone and footwall volcanic succession. These sub-horizontal extension veins have a preferred orientation of 15-218, perpendicular to S_1 (Fig. 4.7C). In drill core, weakly deformed type 4 veins cut across the type 3 quartz and calcite veins. Although generally barren, some of the veins contain chalcopyrite or sphalerite and galena in addition to pyrite. The S_1 cleavage is deflected around many of the weakly deformed veins, indicating they formed late during D_1, simultaneously with cleavage development (Fig. 4.10G).

Figure 4.10 Vein morphology, compositions and cross-cutting relationships

A Type 1A, isoclinally folded and boudinaged, pre-D_1 to early-D_1 calcite-chalcopyrite-pyrite vein cut by a late-D_1 weakly folded type 4 quartz-pyrite vein. Note remobilised sulfides along the margins of the late cross-cutting vein. TLPD-66, 375 m, Toms zone footwall.

B Type 1B, pre-D_1 to early-D_1, boudinaged quartz-pyrite veinlets which are oblique to the S_1 cleavage. TLPD-65A, 803 m, Toms zone footwall.

C Type 2 boudinaged, pre-D_1 to syn-D_1 dolomite-chalcopyrite vein occurring in banded polymetallic massive sulphide. The vein also contains minor pyrite, sphalerite, stannite, galena and tetrahedrite. TLPD-51A, 479 m, Toms Central lens.

D Anastomosing type 3A and type 4 quartz veins and veinlets in silicified siltstone, Toms zone footwall. The largest vein contains disseminated pyrite, sphalerite, galena and chalcopyrite. TLPD-67B, 742 m.

E Type 3B, S_1-parallel, syn-D_1 calcite-magnetite-hematite vein with pinch-and-swell structure, from the fault-bound stratigraphic unit. The euhedral pyrite crystals, which partly pseudomorph magnetite crystals, are associated with a late-D_1 cross-cutting quartz-pyrite vein, not in the field of view. TLPD-27, 468 m.

F Type 3B, early-D_1, isoclinally folded, S_1-parallel calcite veinlets in mudstone cut by a later, S_1-perpendicular calcite veinlet. TOD-10, 365 m.

G Type 4, late syn-D_1, weakly folded quartz-muscovite-pyrite-chalcopyrite vein. Note deflection of S_1 across the vein and the cross-cutting fractures, indicating that it formed simultaneously with the S_1 cleavage. TLPD-46A, 334 m, Toms zone footwall.

H Type 5, post-D_2 quartz vein which cuts across a non-foliated quartz-feldspar porphyry dyke in the Western Volcanic Succession. It contains minor galena (ga), sphalerite (sph) and pyrite (py). TLPD-67B, 905 m, Toms zone footwall.

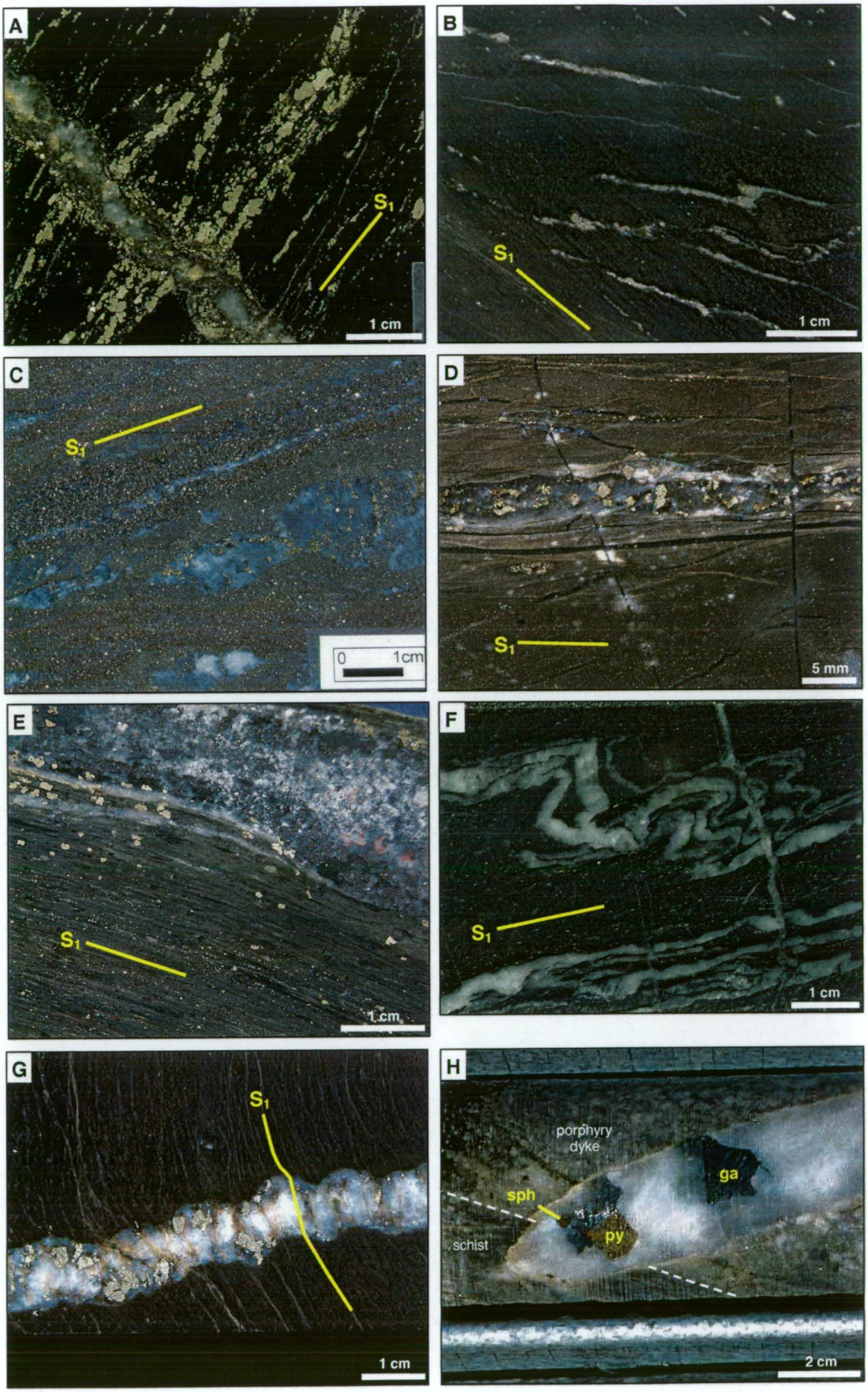
A
S1
1 cm
B
S1
1 cm
C
S1
0 1cm
D
S1
5 mm
E
S1
1 cm
F
S1
1 cm
G
S1
1 cm
H
porphyry
dyke
ga
sph
py
schist
2 cm

Type 5 quartz-pyrite veins cut across non-foliated quartz-feldspar porphyry dykes in the Toms zone footwall (Fig. 4.10H). They are typically associated with broad (up to 3 cm), sericite-biotite halos in the adjacent host rock. Some of the veins contain coarse-grained sphalerite, chalcopyrite and galena. They are interpreted to post-date the D_2 deformation.

In addition to those described above, barren, anastomosing carbonate veins with no preferred orientation cut limestone clasts in the Transitional Unit and pervasive dolomite-altered rocks hosting the massive sulfide. Their timing is apparently not constrained to any particular fabric or deformation event.

Interpretation of syn-tectonic veins

Cox (2000) and Cox et al., (1991) summarised the processes involved in formation of syn-tectonic vein arrays. At high crustal levels, rapid episodic slip events within shear zones lead to transient increases in fault permeability. Fluid pressures are required to exceed the lithostatic lode to reactivate high-angle reverse faults. Following failure, shear stresses acting along the faults are significantly reduced, allowing hydrothermal fluids to circulate and precipitate veins. Once the fracture network is sealed, fluid pressure and differential stress gradually rise again. This cycle of permeability creation through brittle failure and permeability destruction by self-sealing veins was termed *fault-valve* behaviour by Sibson et al. (1988).

Arrays of variably deformed sub-vertical (type 3) shear and extension veins and less abundant, weakly deformed, sub-horizontal (type 4) extension veins, occur throughout the Lewis Ponds fault zone and adjacent footwall volcanics. The sub-vertical veins probably resulted from periodic brittle shear failure and extension at a low angle to the direction of maximum compressive stress along pre-existing planes of weakness, prior to or during development of the S_1/S_S cleavage (Fig. 4.11A-C). The late, cross-cutting, type 4 extension veins are interpreted to reflect fault-valve behaviour associated with episodic brittle failure at a high angle to the direction of maximum compressive stress due to high fluid pressure (Fig. 4.11D and E). Many type 3 and 4 veins contain small amounts of chalcopyrite, sphalerite and galena. If the Lewis Ponds fault is linked to a low-angle detachment surface, as proposed by Glen (1998), fluids sourced from deeper crustal levels beneath the Late Silurian felsic volcanic pile may have been tapped.

The morphology and cross-cutting relationships of syn-tectonic veins at Lewis Ponds are similar to vein arrays documented in the Kambalda area of Western Australia. Nguyen et al. (1998) interpreted a transition from brittle shear failure to more ductile deformation and

Figure 4.11 Model for the formation and progressive deformation of syn-tectonic veins at Lewis Ponds shown as schematic cross-sections and a Mohr circle diagram. Based in part on the 'fault-valve' model proposed by Sibson et al. (1988).
σ_1 = direction of maximum compressive stress at a high angle to the shear zone
σ_3 = direction of minimum compressive stress at a low angle to the shear zone
T_C = tensile strength across cohesionless pre-fractured/cleaved rock
T_R = original tensile strength of the rock
P_F = fluid pressure

A and B. Brittle shear failure at a high strain rate and low angle to the direction of maximum compressive stress. The presence of pre-existing planes of weakness, such as fractures or the S_1 cleavage reduces the cohesion and tensile strength of the rock. Brittle shear failure, represented by Mohr circles A and B, may result in the formation of sub-vertical shear and extension veins along fracture planes and in small dilational jogs.

C. Repeated brittle failure and sealing of the fractures over time produces an array of progressively deformed veins. Boudinage results from a competency contrast between the veins and adjacent chlorite-sericite-altered host rock. With further incremental strain, the oldest veins are completely boudinaged and surrounded by strain shadows. The foliation may also be kink folded and boudinaged.

D. Once cohesion is attained in the fault zone, local areas of high fluid pressure may cause effective stresses to exceed the tensile strength of the rock, allowing brittle failure to occur at a high angle to the direction of maximum compressive stress (Mohr circle D). This produces late sub-horizontal extension veins (cross-section D).

E. Mohr circle E shows possible effective stress conditions immediately following brittle failure at a high angle to the direction of maximum compressive stress. With increasing fluid pressure, the Mohr circle moves toward the left, ultimately resulting in brittle failure (D) and the formation of extension veins under transient conditions of low effective normal stress.

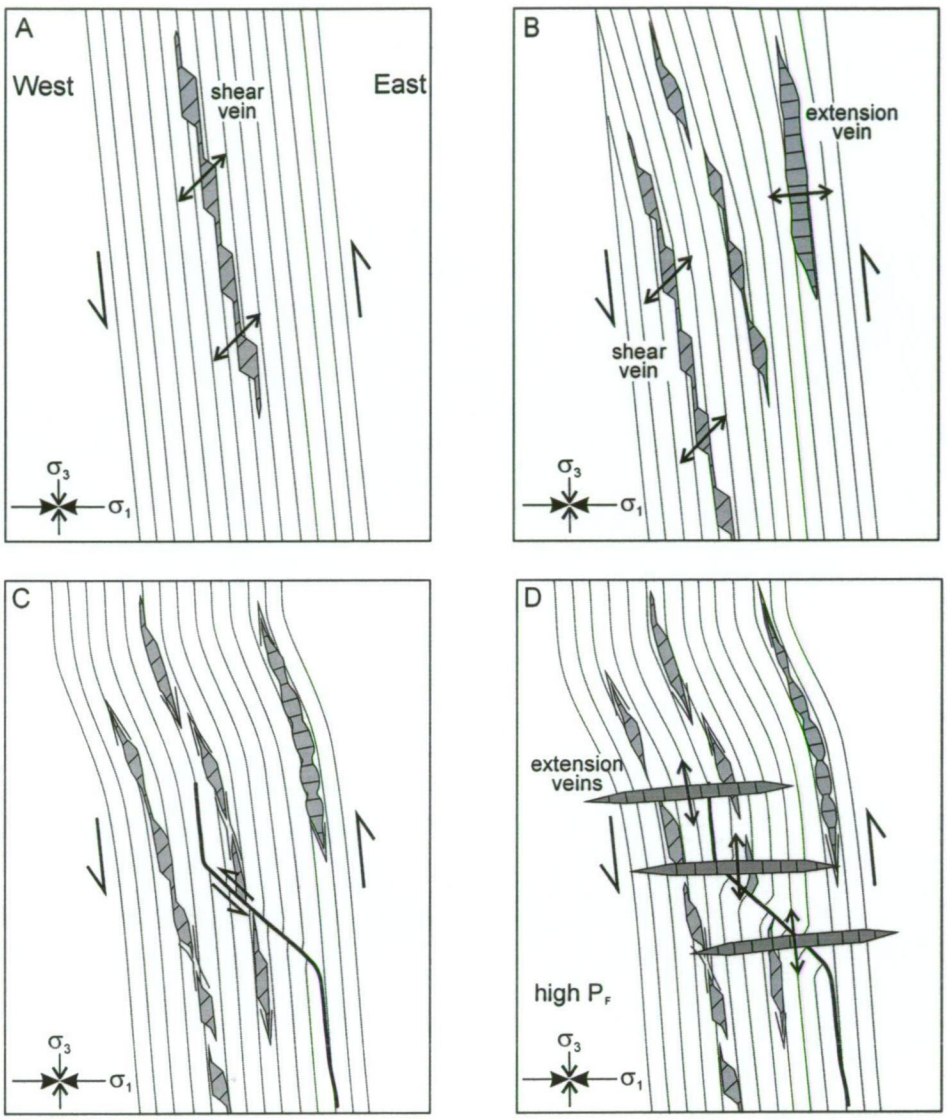
A
West
East
shear vein
σ3
σ1
B
extension vein
shear vein
σ3
σ1
C
σ3
σ1
D
extension veins
high PF
σ3
σ1

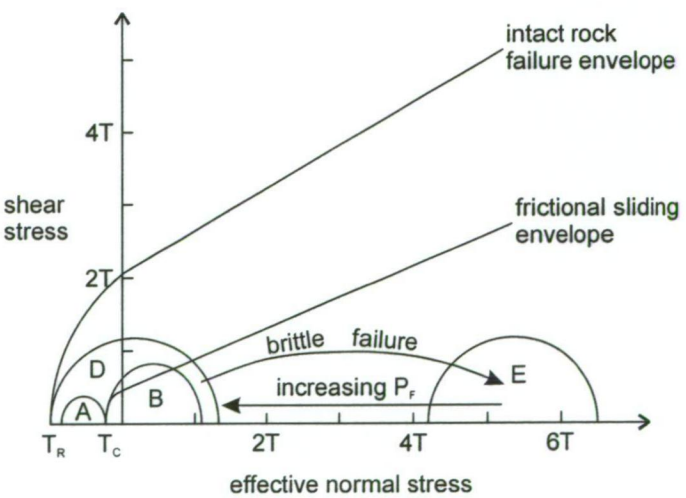
intact rock failure envelope
frictional sliding envelope
shear stress
4T
2T
brittle failure
increasing PF
D
B
A
E
TR
TC
2T
4T
6T
effective normal stress

foliation development, followed by brittle deformation and fault-valve behaviour associated with increased fluid pressure and overall decreased shear stresses at the Revenge gold mine. The cleavage and syn-tectonic veins at Lewis Ponds are similarly interpreted to record increased fluid pressure and a transition from ductile to brittle behaviour.

4.6 Structures within the massive sulfide lenses

This section outlines macroscopic and microscopic structures occurring in the massive sulfide lenses. Structures resulting from ductile deformation are strongly developed in Main and Toms zones. However, structures attributed to brittle behaviour occur mainly in Toms zone. Massive sulfide bands in Main zone are sub-parallel or parallel to the S_1 cleavage. Elongate aggregates of pyrrhotite, chalcopyrite, sphalerite, mica and quartz fibres define the S_1 cleavage (Fig. 4.12). In schositose rocks, unevenly spaced, anastomosing cleavage bands, containing strongly aligned chlorite, phlogopite and talc crystals, wrap around structurally competent, rigid dolomite-quartz-sulfide domains (Fig. 4.12B). Pyrite-sphalerite aggregates, carbonate-quartz clasts and rounded porphyroblasts are typically associated with talc, dolomite or quartz fibre strain shadows (eg. Fig. 4.12C and D). Quartz veins, folds and transposed layering are rarely observed (eg. Fig. 4.12E and F). However, pinch-and-swell structures occur between pyrite and sphalerite-rich massive sulfide bands.

Fossiliferous limestone, siltstone and dacite pebbles in the polymictic breccia and pebbly-granular sandstone deposits are elongate and lenticular (Figs. 3.12A and 3.13B). In the limestone quarry, the clasts become more flattened and boudinaged toward the north, where there is an apparent increase in strain (Fig. 4.8B). Weakly deformed clasts generally have more equant shapes (eg. Fig. 3.16A).

Toms zone is overprinted by brittle and ductile structures. The massive sulfide lens and its constituent pyrite and sphalerite-galena-rich bands are sub-parallel to S_1. However, the cleavage and sulfide band orientations have been re-oriented around open to isoclinal F_S kink folds (Fig. 4.13A, C and D). Fe-carbonate gash veins and small accommodation tear faults occur in the structurally thickened fold hinges. The kink folds are attributed to late-D_1 shearing or reactivation of the Lewis Ponds fault during D_2.

Pinch-and-swell structures, occurring throughout the Toms massive sulfide lens reflect competency differences between sulfide minerals and the quartz, dolomite, talc or chlorite gangue. Anastomosing pyrite, sphalerite galena and chlorite bands wrap around isolated quartz and dolomite boudins (Fig. 4.13B). These represent either deformed, boudinaged veins or 'islands' of mechanically strong, intensely altered host rock.

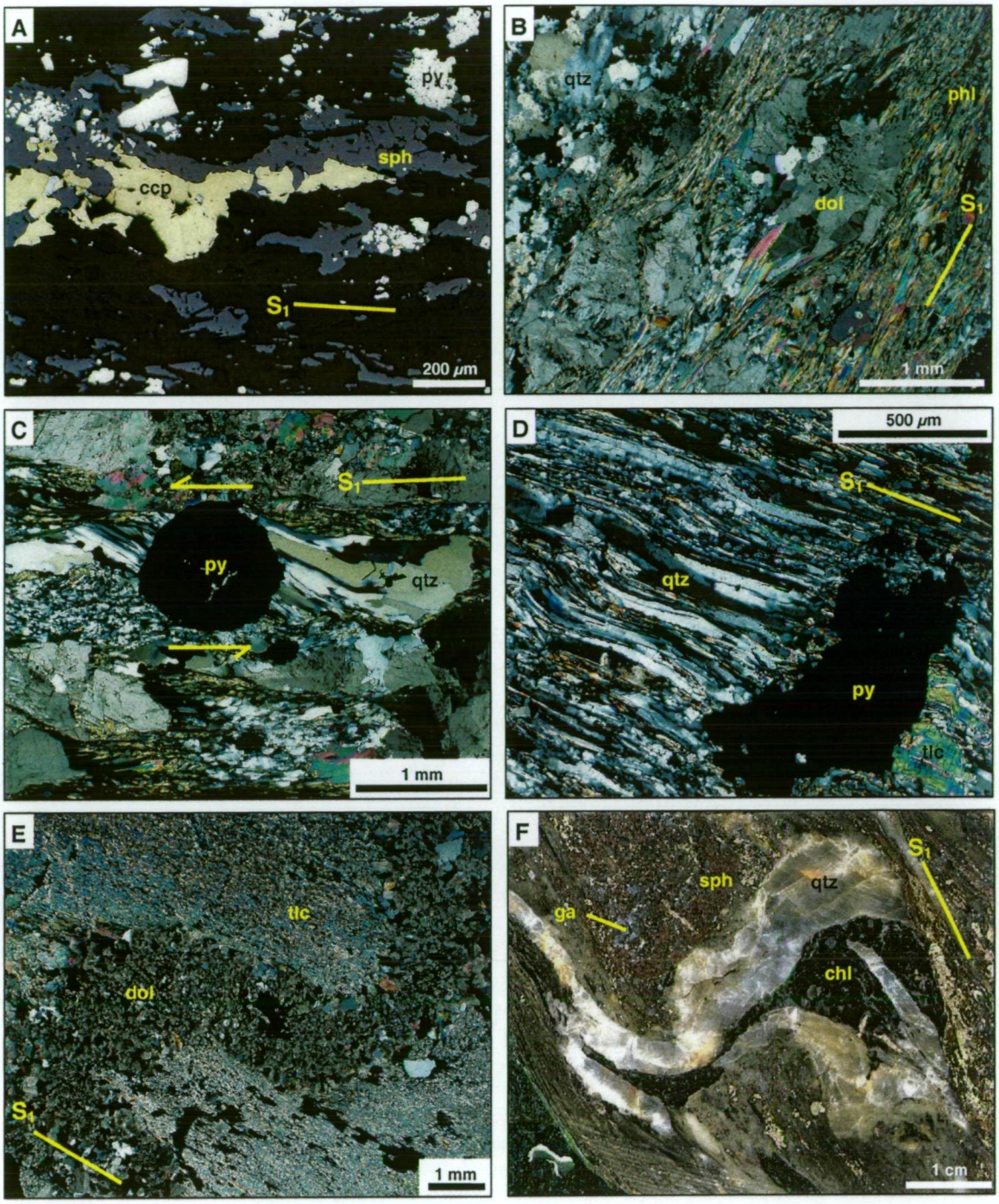

Figure 4.12 Main zone structures
A. Photomicrograph of elongate, S_1-parallel chalcopyrite and sphalerite aggregates in the matrix of a strongly foliated limestone-clast breccia. TLPD-12W3, 439 m. Reflected light. **B.** Strongly aligned phlogopite crystals wrapping around dolomite-quartz domains. TLPD-18, 373 m. Transmitted light. **C.** Asymmetric quartz fibre strain shadow adjacent to a rounded pyrite porphyroblast, indicating relative sense of shear. TLPD-12, 503 m. Transmitted light. **D.** Quartz fibres and a talc strain shadow adjacent to a pyrite aggregate. TLPD-12, 428 m. Transmitted light. **E.** Tightly folded dolomite band in talc schist. TLPD-18, 373 m. Transmitted light. **F.** Folded and boudinaged quartz-chlorite vein. Coarse-grained galena and sphalerite occur in the fold hinges. TLPD-12, 457 m.

Abbreviations: ccp = chalcopyrite, sph = sphalerite, py = pyrite, qtz = quartz, phl = phlogopite, tlc = talc, ga = galena, chl = chlorite.

Figure 4.13 Toms zone structures

A Folded massive quartz-pyrite bands separated by chlorite and quartz-sericite layers. Accommodation tear faults, boudinaged layering and Fe-carbonate gash veins occur in the structurally thickened fold hinges. TLPD-53, 295 m.

B Dolomite-quartz and dolomite-talc boudins occurring in banded pyrite-sphalerite-rich massive sulphide. TLPD-51A, 477 m.

C Kink folds in chlorite-dolomite-talc schist. TLPD-51AW2, 428 m.

D Elongate S_1-parallel chalcopyrite, sphalerite and tetrahedrite aggregate or veinlet in massive sulphide. Note the F_2 kink fold. TLPD-51A, 489 m.

E Recrystallised pyrite aggregate overprinted by anastomosing and orthogonal brittle fractures. The fractures are filled by ductile minerals including chalcopyrite, galena and sphalerite. TLPD-51A, 488 m.

F Cataclastic massive sulfide breccia consisting of 1-40 mm wide, rounded to very angular and splintery, rotated massive sulfide clasts in a vuggy quartz matrix. Clasts are corroded and partly overprinted by the quartz. TLPD-49, 264 m.

Abbreviations: qtz = quartz, py = pyrite, chl = chlorite, Fe-carb = Fe carbonate, tlc = talc, dol = dolomite, sph = sphalerite, ccp = chalcopyrite, td = tetrahedrite, ga = galena.

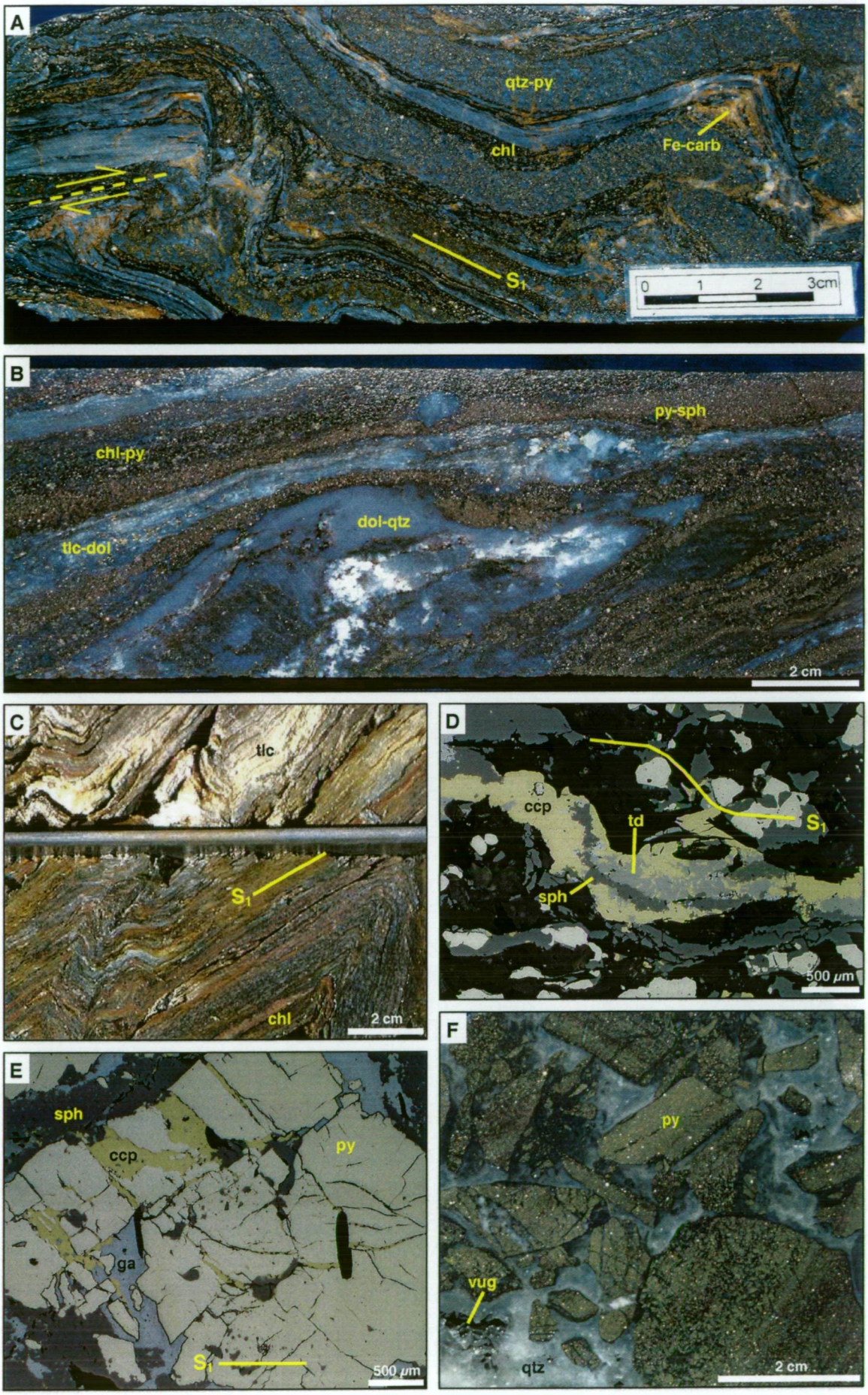
A
qtz-py
chl
Fe-carb
S_1
0 1 2 3cm
B
py-sph
chl-py
dol-qtz
tlc-dol
2 cm
C
tlc
S_1
chl
2 cm
D
ccp
td
S_1
sph
500 μm
E
sph
ccp
py
ga
S_1
500 μm
F
py
vug
qtz
2 cm

The cleavage is strongly developed in chlorite-dolomite-talc-rich areas and weak within polymetallic massive sulfide bands. Aligned mica laths and elongate, typically anastomosing chalcopyrite, galena, sphalerite, pyrrhotite and tetrahedrite aggregates define the S_1 foliation (Fig. 4.13D). Pyrite and arsenopyrite grains are undeformed or cut by brittle fractures. Some of these fractures have been filled with chalcopyrite, sphalerite and galena (Fig. 4.13E).

Breccia textures occur rarely in the massive sulfide at Toms zone (Fig. 4.13F). The breccia comprises 5-80 mm wide, rounded and very-angular clasts of pyrite-rich massive sulfide in a vuggy quartz matrix. Quartz partly overprints the corroded massive sulfide clasts. The occurrence of randomly-oriented, splintery and rounded massive sulfide clasts in a vuggy quartz matrix indicate that the breccia developed in situ. These textures probably resulted from cataclasis in areas where brittle structures cut the massive sulfide lens. Quartz precipitated in open spaces between the massive sulfide clasts.

4.7 Structural history of Lewis Ponds

Prior to the D_1 deformation, the Lewis Ponds host sequence consisted of (in stratigraphic order) quartz-plagioclase phyric volcanics overlain by polymictic breccia, pebbly-granular, quartz crystal-rich sandstone and massive siltstone and mudstone. D_1 was a strong deformation characterised by east-west horizontal compression. This resulted in the formation of NNW-trending, open to tight cylindrical folds and steeply dipping, sinistral reverse faults, an axial planar disjunctive cleavage and southeast-plunging mineral stretching lineation. The compression also caused tight to isoclinal folding of beds in the Transitional Unit and paragenetically early veins in the Toms zone footwall.

Strain was partitioned into brittle and ductile structures within the Hangingwall Siltstone Unit, Transitional Unit and Western Volcanic Succession. The presence of thick, massive limestone lenses and mechanically strong coherent dacite surrounded by less competent siltstone and chlorite-talc-sericite-altered rocks produced complex anastomosing fault geometries with structural repetition in the fault-bound stratigraphic unit. Shearing also occurred within the intensely altered polymictic breccia deposits that host Main zone. Opposing shear sense indicators are consistent with normal and reverse displacement, indicating either reactivation or late reversal in movement across the Lewis Ponds fault.

Five generations of veins are recognised at Lewis Ponds. Type 1 and 2 veins were probably emplaced prior to D_1. High strain rates and periodic shear failure at a low angle to the direction of maximum compressive stress resulted in arrays of variably deformed, type 3, sub-vertical shear or extension veins in the Lewis Ponds fault zone and adjacent footwall volcanic

succession. These accompanied ductile deformation and cleavage development. Episodic brittle failure, at a high angle to the direction of maximum compressive stress produced the late, type 4, sub-horizontal extension veins observed in drill core. Brittle failure occurred in local areas where elevated fluid pressure exceeded the tensile strength of the rock. The weakly deformed, type 4 veins indicate a decrease in overall strain rate, recovery of cohesion within the fault and high fluid pressure. Type 5 veins precipitated after intrusion of the Lewis Ponds granite and non-foliated quartz-plagioclase porphyry dykes.

The weak D_2 deformation, possibly accompanying late reactivation or roll-back of the Lewis Ponds fault, produced sub-horizontal and sub-vertical kink bands and kink folds in the host sequence. These weakly developed structures are most common in highly strained, phylosilicate-altered rocks. Kink bands occur throughout the Hangingwall Siltstone Unit and Transitional Unit. Southwest verging kink folds in the limestone quarry overprint the S_1 cleavage and highly attenuated limestone clasts.

Toms zone was overprinted by brittle and ductile structures associated with shearing along the Lewis Ponds fault. Boudins and pinch-and-swell structures resulted from competency differences between the massive sulfide and gangue minerals. Chalcopyrite, sphalerite, tetrahedrite and pyrrhotite formed elongate, cleavage-parallel blebs within mica-rich domains. Cataclastic breccia resulted from brittle deformation of the massive sulfide.

Main zone was not significantly affected by brittle shear failure within the Lewis Ponds fault. The S_1 cleavage resulted from alignment of chlorite, talc and white mica in phyllosilicate-rich domains. Quartz fibres grew in dilatant strain shadows adjacent to quartz, plagioclase and pyrite crystals. Limestone, siltstone, mudstone and dacite clasts in the polymictic breccia deposits were flattened, kink folded and boudinaged.

Brittle and ductile structures are more strongly developed in Toms zone than Main zone, suggesting that the massive sulfide lenses were emplaced prior to shearing along the Lewis Ponds fault. Variations in sulfide textures and compositions and lateral metal zonation also support this argument (see Chapter 7, sections 7.8 to 7.11). Strain was concentrated in the chlorite-talc and sericite-altered rocks. However, the relative timing of cleavage development and formation of compositional banding in the massive sulfide lenses is poorly constrained because the two fabrics appear sub-parallel and underground exposures are not available. The S_1 cleavage may have overprinted primary compositional layering in the massive sulfide.

This study highlights the possibility of structural repetition in the massive sulfide lenses at Lewis Ponds. Reversals in stratigraphic facing direction and vergence indicate that tight,

parasitic folds occur in the host sequence, east of the regional-scale anticline. These folds occur within and adjacent to the Lewis Ponds fault. Limestone-clast breccia, quartz-chlorite-sericite schist and volcaniclastic sandstone deposits in the Transitional Unit and Hangingwall Siltstone Unit are structurally thickened in the hinge zone of the folds. The massive sulfide lens at Toms zone is dissected by brittle faults, syn-tectonic quartz veins and high strain zones. At Toms zone, diamond drill holes intersected a single massive sulfide lens, or numerous thinner massive sulfide lenses, separated by strongly deformed, intensely altered rock. This indicates that fault repetition may occur in the massive sulfide lens at Toms zone.

4.8 Regional correlations

Large-scale, NNW-trending second generation faults and folds predominate in the Mumbil Group northeast of Orange (Fig. 2.5). Plunge changes and small amplitude symmetrical F_2 folds have been cited as evidence for pre-existing latitudinal folds (Glen and Watkins, 1994; Glen, 1998). Mumbil Group rocks are dismembered by a complex system of N to NNW striking faults in the Mullions Range imbricate zone (Fig. 4.14). Some of these are associated with local mylonite formation, sub-horizontal kink folds and both older-over-younger and younger-over-older stratigraphic relationships (Glen and Watkins, 1994; Glen, 1998).

First generation structures resulting from meridional compression have been recognised within the Lachlan Transverse Zone (Fig. 2.5). The LTZ is interpreted as an area of decreased regional metamorphic grade and D_2 intensity (Glen and Watkins, 1994; Glen and Wyborn, 1997). However, not all WNW-trending structures correspond to the proposed D_1 deformation. Scott (1999) interpreted a fault occurring near Big Bald Hill (located 4.5 km southwest of Lewis Ponds) as a lateral ramp segment of a fault resulting from east to northeast-directed extension, due to the presence of normal shear sense indicators and northeast plunging stretching lineations.

The first generation WNW and W-trending structures apparently do not occur at Lewis Ponds. Therefore D_1 in this study equates to the D_2 deformation of Glen and Watkins (1994). The strong S_1 cleavage is likely to have obliterated earlier foliations and fabrics. D_2 kink bands and kink folds overprint S_1 and possibly result from late reactivation of the Lewis Ponds fault. Similar structures are associated with NNW-trending faults elsewhere in the Orange district (Glen, 1998).

Structural analysis of the Lewis Ponds prospect highlights a number of discrepancies with previous mapping carried out by the Geological Survey of New South Wales (Fig. 4.14A and B). Timing and structural relationships between the footwall volcanic succession (Mullions

Range Volcanics) and overlying, tightly folded sedimentary rocks (Anson Formation) are complex and variable. The shallow emplacement of porphyritic dacite bodies into unconsolidated sediment produced irregular peperitic contacts in the Main zone footwall (see Chapter 3; section 3.3). However, sedimentary units occurring higher in the stratigraphy contain reworked epiclastic material, deposited after volcanism had ceased in the area.

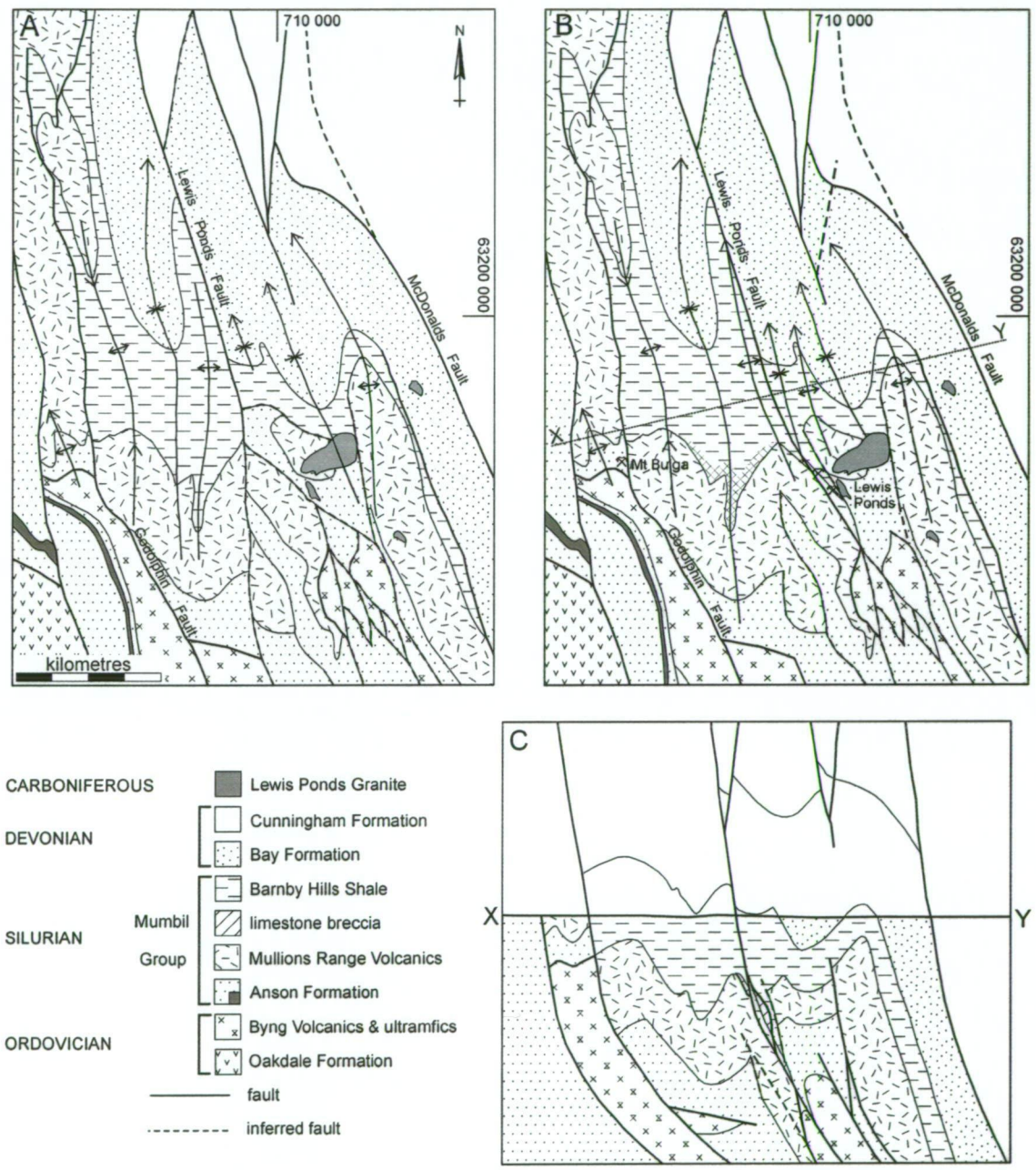

Figure 4.14 Mullions Range imbricate zone
A. Geology map of the Lewis Ponds – Mt Bulga area as it appears on the Orange 1:100 000 map sheet. **B.** Modified map showing preferred position of the Lewis Ponds fault and fold hinges occurring to the west. Note continuation of the Barnby Hills Shale east of Lewis Ponds. The cross-hatched area between the Lewis Ponds and Mt Bulga deposits is a prospective target area for base metal sulfide occurrences. Based in part on interpretation of prospect-scale structures. **C.** Interpreted cross-section based on modified geology map.

Field mapping and drill core logging failed to locate an extensive fault marked on the Orange 1:100 000 map separating the Mullions Range Volcanics and Anson Formation at Lewis Ponds (Fig. 4.14A). The unconformable contact is characterised by only minor deflection of the S_1 cleavage due to a competency contrast between lithologies. However, local faults truncate the footwall volcanic succession in Main zone and south of Toms zone.

At Lewis Ponds, the siltstone, sandstone and polymictic breccia host rocks appear to post-date emplacement of the Mullions Range Volcanics. However, the Geological Survey of New South Wales have included these lithologies in the Anson Formation, which is elsewhere interpreted to stratigraphically underlie the Mullions Range Volcanics because:

- fine-grained sedimentary rocks occur in the core of the Mullions Range Anticline; and
- the basal mixed provenance conglomerate member of the Anson Formation includes basalt, basaltic-andesite and ultramafic clasts derived from the underlying Ordovician volcanic rocks (Pogson and Watkins, 1998).

The siltstone and breccia deposits hosting the massive sulfide lenses at Lewis Ponds should therefore be included in the unit stratigraphically overlying the Mullions Range Volcanics - the Barnby Hills Shale (Fig 4.14 B and C).

Previous maps indicate that the Lewis Ponds fault truncates the hinge zone of a regional-scale anticline occurring immediately west of the Lewis Ponds massive sulfide deposits (Fig. 414A). However, this fault occurs further to the east, where it truncates the adjacent syncline (Figs. 3.1 and 4.14B).

The Lewis Ponds host rocks probably continue on the western limb of the regional-scale anticline (Fig.4.14B). These predominantly fine-grained sedimentary rocks may extend as far west as the Mt Bulga deposit, where massive sulfide occurs in a similar host sequence of siltstone, rhyolite and dacite (Chisholm, 1976). Mt Bulga has an indicated resource of 850 000 t, grading 3.6% Zn, 1.0% Pb, 1.0% Cu, 2.5 g/t Ag and 0.4 g/t Au (Stevens, 1974). The area between the two base metal deposits is therefore a highly prospective target for massive sulfide occurrences, especially in the regional fold hinges.

CHAPTER 5

ALTERATION MINERALOGY AND DISTRIBUTION

5.1 Introduction

Secondary mineral assemblages at Lewis Ponds result from a complex history of diagenesis, hydrothermal alteration, fault-controlled fluid flow, cleavage development, regional greenschist facies metamorphism and post-tectonic granite emplacement. The extent of initial fluid-rock interaction was influenced by primary porosity and permeability in the volcanic and sedimentary units. Reactions between the hydrothermal fluid and host sequence produced discrete mineral assemblages depending on the temperature, fluid chemistry and lithology. The distribution and intensity of these assemblages reflects the overall fluid-rock ratio and proximity to fluid pathways such as faults or permeable units.

A dolomite-chlorite-talc envelope surrounds the massive sulfide lenses at Lewis Ponds. This unusual Mg-rich, carbonate-bearing assemblage is spatially associated with polymictic breccia and siltstone in Main and Toms zones respectively. Carbonate alteration has been documented in the host sequence of numerous eastern Australian VHMS deposits including Henty, Lyell Comstock, Hercules, Rosebery and Thalanga (Khin Zaw and Large, 1992; Halley and Roberts, 1997; Corbett, 2001; Herrmann and Hill, 2001; Large et al., 2001c). Early studies of these deposits concluded that carbonate resulted from sea floor exhalation of hydrothermal fluids (eg. Large and Both, 1980; McLeod and Stanton, 1984; Halley and Roberts, 1997). More recently, authors consider the carbonate-bearing assemblages to indicate sub-sea floor mixing between hydrothermal fluids and seawater in the unconsolidated volcanics (Khin Zaw and Large, 1992; Herrmann and Hill, 2001; Large et al., 2001a) or fluid-rock interactions involving pre-existing carbonate (Callaghan, 2001). Herrmann and Hill (2001) interpreted the dolomite-chlorite-tremolite assemblage at Thalanga, north Queensland as metamorphosed, altered rhyolite based on immobile element and isotope compositions.

In this chapter, the distribution and intensity of diagenetic, hydrothermal and metamorphic mineral assemblages within the Lewis Ponds host sequence are used to establish paragenetic relations. Factors influencing the distribution of hydrothermal and metamorphic mineral assemblages are considered in the interpretation section. Lithogeochemical trends associated with the alteration zones are summarised in the following chapter.

5.2 Methods

The study of alteration and metamorphic mineralogy at Lewis Ponds involved: petrological examination of thin sections, core samples and surface rock samples; short wavelength infrared (SWIR) spectral analysis; staining; and microprobe mineral analysis.

Drill core and surface rock samples were analysed with a portable infrared mineral analyser (PIMA) spectrometer at the Centre for Ore Deposit Research to determine white mica, chlorite, carbonate and clay compositions. Comparisons were made with the short wavelength infrared spectra of reference minerals using *The Spectral Geologist* software. Results from the PIMA study were checked using microprobe analyses, thin section descriptions, HCl acid tests and staining (see below).

The PIMA is a useful field-based tool for fast identification of clays, fine-grained micas and carbonates. The instrument measures mineral reflectance in the short wavelength infrared (SWIR) range from 1300 to 2500 nanometres on clean, dry rock surfaces. Each mineral produces a different short wavelength spectrum characterised by distinctive absorption features corresponding to H_2O, OH, CO_2 and NH_4 covalent bonds and AlOH, MgOH and FeOH ionic bonds (Thompson et al., 1999). In VHMS deposits, the compositions and relative abundance of white mica and chlorite may be determined. Herrmann et al. (2001) and Jones (2001) identified a trend from distal phengitic white mica to orebody-proximal sodic muscovite using SWIR spectral analysis at the Rosebery and Myra Falls deposits respectively.

Microprobe analyses of selected samples and detailed petrological thin section descriptions complimented the SWIR study. Numerous samples were stained with sodium cobaltinitrite or a solution of alizarin red and potassium ferricyanide to test for K-feldspar and ferroan dolomite respectively.

Polished thin sections were carbon coated and analysed by a Cameca SX-50 electron microprobe at the University of Tasmania's Central Science Laboratory to determine mica, carbonate and clay compositions. Traverses across zoned dolomite crystals allowed identification of lateral variations in mineral chemistry. Microprobe analyses are presented in Appendix 3.

In the following chapter, the terms 'carbonate', 'sericite' and 'feldspar' denote types of alteration assemblages. PIMA analyses indicate the presence of both phengite and muscovite in samples characterised by pervasive sericite. However, fine-grained white micas analysed by the microprobe are phengitic, with Si to tetrahedral Al ratios of greater than 3:1.

5.3 Alteration assemblages in the Mullions Range Volcanics

Coherent and clastic facies in the Mullions Range Volcanics are characterised by weak to moderate pervasive sericite, K-feldspar-quartz-sericite-hematite and chlorite-epidote assemblages. These alteration assemblages have resulted from diagenesis and greenschist facies metamorphism. Perlitic fractures, spherulites, flow-banding, pumice and rarely volcanic glass are preserved in the rocks (Figs. 3.19-3.22). Elongate chlorite and white mica laths define the regional cleavage. The following assemblages were observed in eighteen samples collected during regional traverses of the Mullions Range Volcanics.

Sericite

Fine-grained white mica is the most widespread phyllosilicate, occupying the groundmass or matrix of coherent and clastic facies (eg. Figs. 3.6 and 3.22). The mica has partially to completely replaced plagioclase phenocrysts and glomerocrysts. A fine dusting of sericite overprints glass shards and volcanic lithics in clastic units. Uncompacted pumice clasts with relic tube vesicle textures have been replaced by quartz, sericite and biotite (Fig. 3.22H).

Sericite-K-feldspar-quartz ± magnetite-hematite

Coherent facies in the Mullions Range Volcanics are characterised by K-feldspar-quartz-sericite ± magnetite-hematite alteration of the feldspar phenocrysts and/or groundmass. Euhedral phenocrysts and patches of coarse-grained polygonal quartz occur in a microcrystalline mosaic consisting of fine-grained K-feldspar and quartz. Flow-banded, spherulitic dacite contains radiating aggregates of quartz and feldspar (Fig. 3.22C). The spherulites alternate with microcrystalline or glassy domains. Fine-grained quartz fills vesicles in amygdaloidal rhyolite. Perlitic fractures in coherent feldspar phyric dacite are preserved as overlapping acuate sericite or quartz bands (Fig. 3.22D).

Chlorite-epidote-sericite ± clinozoisite

Chlorite-epidote-altered rocks occur throughout the Mullions Range Volcanics, in clastic and coherent facies (eg. Fig. 3.22G). At Lewis Ponds, aggregates of euhedral to subhedral epidote and aligned chlorite occupy the groundmass of quartz-plagioclase phyric dacite and schistose rocks in the fault-bound stratigraphic unit, Eastern Volcanic Succession and Western Volcanic Succession. Epidote patches also occur throughout the matrix and limestone clasts in the polymictic breccia and megabreccia deposits.

5.4 Hydrothermal alteration assemblages at Lewis Ponds

An asymmetric, semiconformable alteration envelope surrounds the massive sulfide lenses at Lewis Ponds (Figs. 5.1 and 5.2). Chlorite-pyrite and sericite-quartz ± chlorite assemblages extend more than 200 m into the footwall volcanic succession immediately south of Toms zone (Fig. 5.3). Large areas dominated by chlorite and sericite have been documented in the Toms zone footwall (Castle, 1976; Glasson, 1977; Valliant, 1998).

In Main zone, alteration mineral distribution and intensity depends on proximity to the massive sulfide lenses and the lithology (Fig. 5.1). Strong to intense pervasive chlorite, dolomite-chlorite-talc, quartz-dolomite-chlorite and calcite-chlorite-sericite assemblages occur in the polymictic breccia and sandstone deposits, whereas siltstone and the footwall volcanic rocks are overprinted by a weak to moderate pervasive sericite-rich assemblage.

Texturally destructive, dolomite-chlorite-talc, chlorite-pyrite, quartz-dolomite-chlorite and quartz-sericite ± hyalophane assemblages host the massive sulfide in Main and Toms zones (Table 5.1). These assemblages are surrounded by an asymmetric, 100-200 m thick phyllosilicate halo characterised by texturally destructive chlorite-pyrite, grading outward into moderate to strong pervasive chlorite or sericite-quartz ± chlorite in the footwall volcanics.

Assemblage	Intensity, pervasiveness	Location/host	Interpretation
Dolomite-chlorite-talc	Intense, patchy to pervasive	Main & Toms zones	Diagenetic & Hydrothermal
Quartz-sericite ± hyalophane	Texturally destructive, pervasive	Toms zone footwall	Hydrothermal
Quartz-dolomite-chlorite	Texturally destructive, pervasive	Main zone	Hydrothermal
Chlorite-sericite-pyrite	Strong to intense, pervasive	Footwall of Main & Toms zones	Hydrothermal
Sericite-chlorite ± calcite ± quartz, sericite-quartz ± chlorite	Moderate to strong, pervasive	Hangingwall & footwall of Main & Toms zones	Hydrothermal
Calcite-sericite-chlorite	Strong to intense, pervasive, texturally destructive	Main zone footwall	Diagenetic & hydrothermal
Magnetite-hematite	Moderate, locally intense pervasive alteration	Fault-bound stratigraphic unit	Metamorphic, hydrothermal or fault-related

Table 5.1 Hydrothermal alteration assemblages at Lewis Ponds listed in order of proximity to the massive sulfide lenses.

Alteration mineral assemblages are weakly developed in the hangingwall. A strong pervasive chlorite-sericite-pyrite assemblage extends several metres into the siltstone overlying Main zone (Fig. 5.1). Schistose volcanics in the fault-bound stratigraphic unit are overprinted by

calcite-magnetite-hematite veins, disseminated magnetite and moderate to intense pervasive chlorite-epidote-sericite and sericite-biotite assemblages, extending the entire length of the prospect.

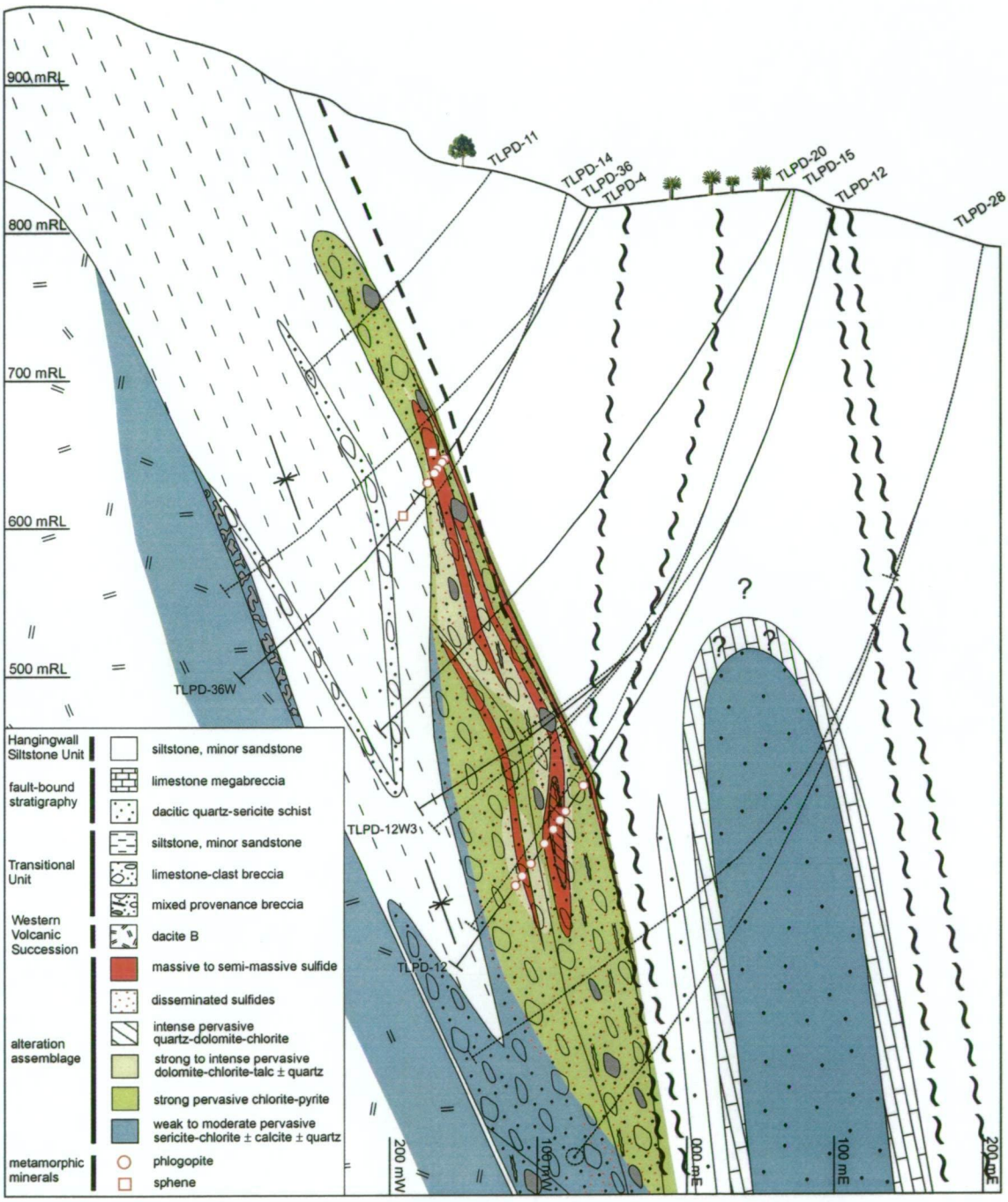

Figure 5.1 Main zone hydrothermal alteration and metamorphic mineral assemblages. Line 1300N section.

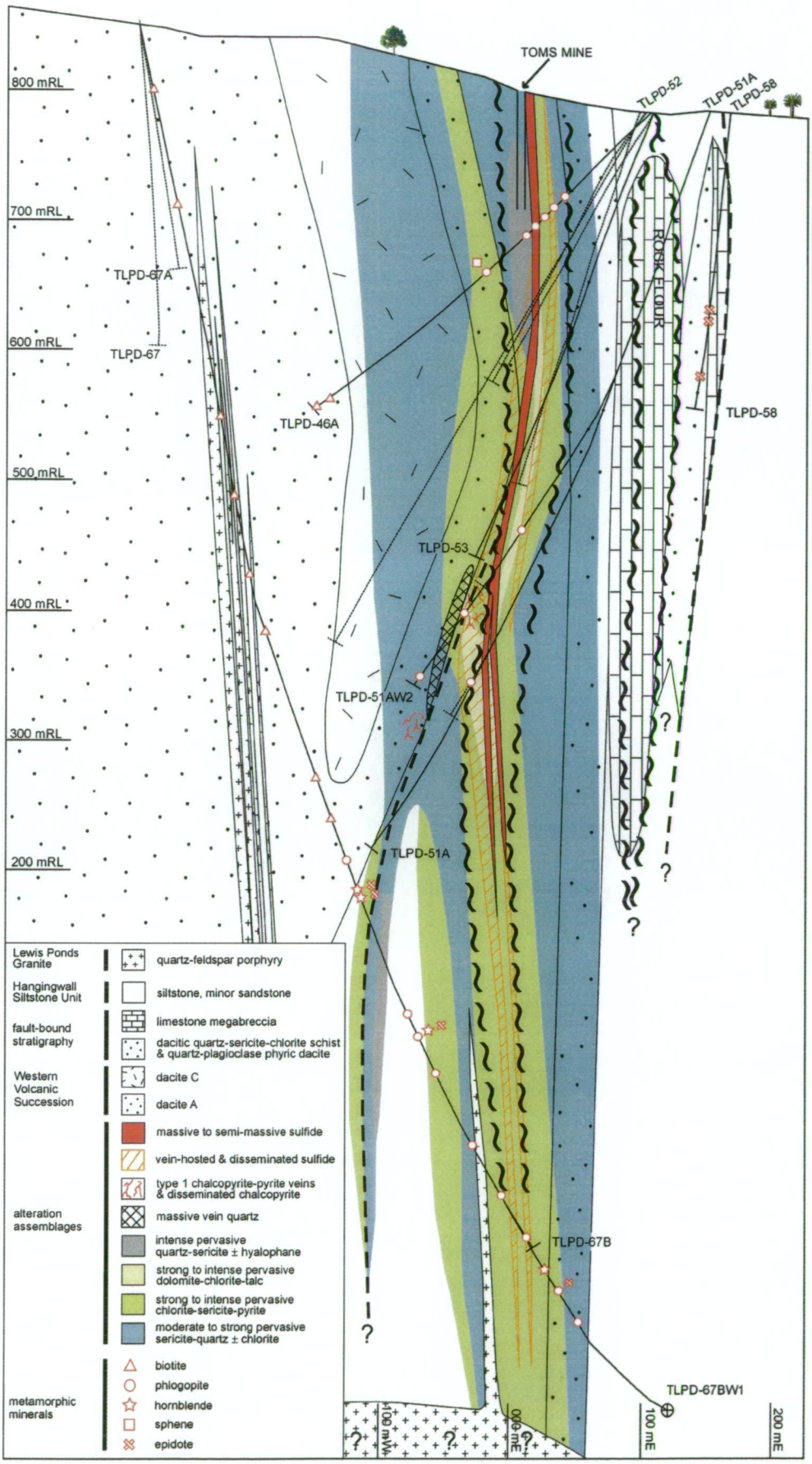

Figure 5.2 Toms zone hydrothermal alteration and metamorphic mineral assemblages. Line 425N section.

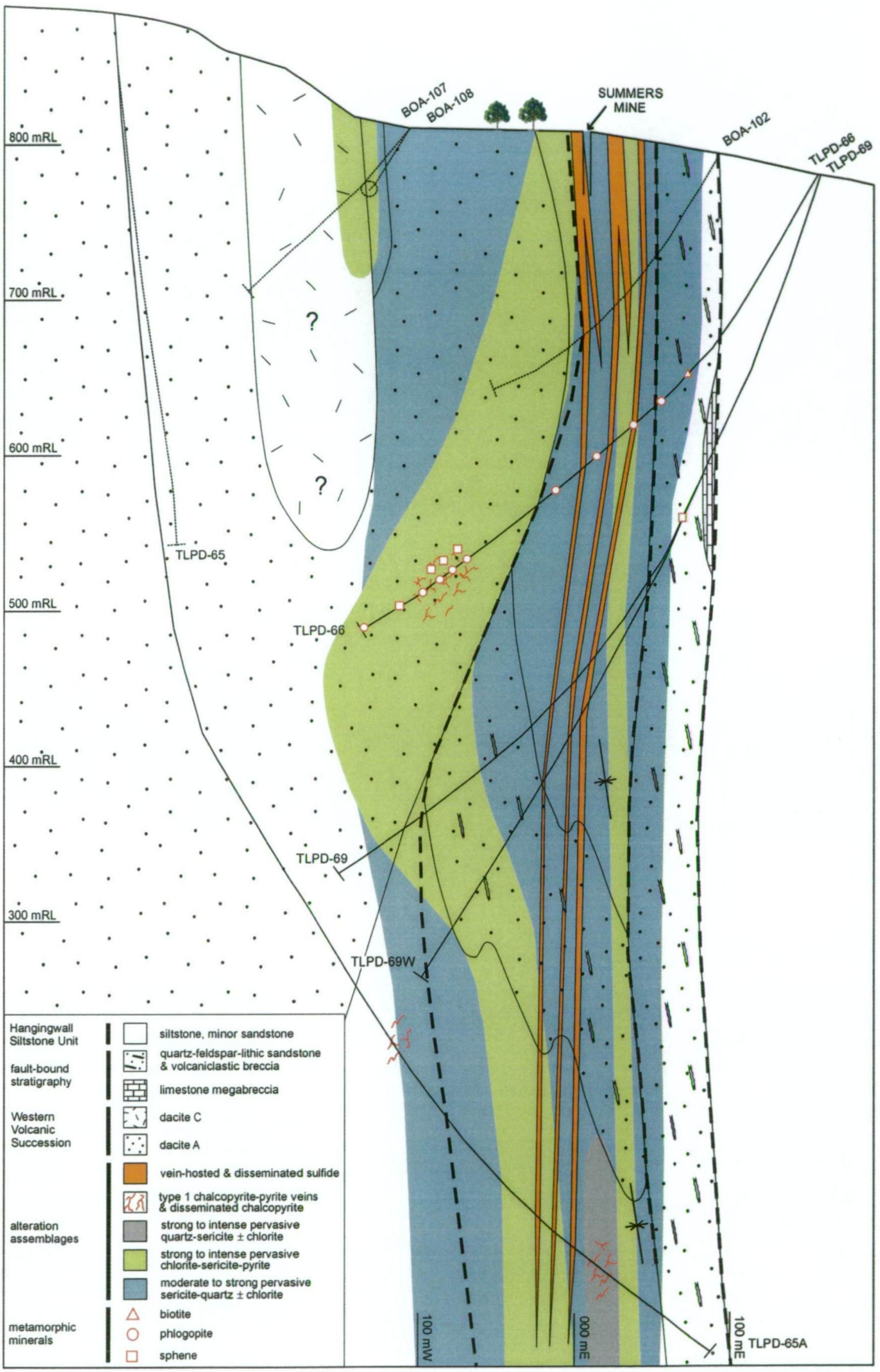

Figure 5.3 Hydrothermal alteration and metamorphic mineral assemblages from south of Toms zone. Line 200N section.

Dolomite-chlorite-talc

A 10-75 m thick, dolomite-chlorite-talc envelope surrounds the massive sulfide lens in Main zone. This assemblage is restricted to the mixed provenance breccia and pebbly-granular sandstone units (Fig. 5.1). Intensity varies from texturally destructive replacement of the breccia and sandstone to patchy, partial replacement of the matrix and the preservation of primary clasts (Fig. 5.4A-D). Dolomite also occurs in the fine-grained deposits hosting Toms zone (Fig. 5.2) and in patches along the Lewis Ponds fault. The following assemblages are recognised: dolomite-chlorite-talc-altered polymictic breccia and pebbly-granular sandstone; texturally destructive vuggy dolomite with quartz, calcite, chlorite, talc and sulfide patches; massive talc; and texturally destructive dolomite-chlorite-quartz ± talc ± phlogopite schist. Intervals of massive talc and dolomite-quartz-chlorite schist occur within Main zone and the Lewis Ponds fault zone. Altered polymictic breccia and vuggy dolomite are restricted to the massive sulfide lenses in Main and Toms zones.

Alteration intensity and mineral assemblages vary throughout the polymictic breccia and sandstone deposits in Main zone. Clasts, crinoid fossils and detrital volcanic quartz crystals are recognisable in strongly altered rocks (Fig. 5.4A, B, C and E). Very fine-grained dolomite, chlorite, talc and hematite have replaced the calcite in fossiliferous limestone clasts (Fig. 5.4B). Chlorite, sericite and dolomite occur in the groundmass of porphyritic dacite pebbles. Weakly altered mudstone, siltstone and felsic volcanic lithics contain dolomite, sericite and disseminated pyrite (Fig. 5.4C and E). Sphalerite, pyrite, rutile dolomite, chlorite, phlogopite and quartz-sulfide patches occur in the breccia matrix. Dolomite occurs as aggregates of anhedral crystals (Fig. 5.4F), spheroids (Fig. 5.4G) and euhedral rhombs (see section 5.8 for detailed descriptions).

The schistose rocks are characterised by dolomite, quartz and sulfide aggregates, surrounded by anastomosing and rarely folded, cleavage bands of chlorite, phlogopite and talc (Fig. 5.4D). These cleavage bands cut across pre-existing pyrite-sphalerite aggregates. Within cleavage bands, the very fine-grained phyllosilicates are strongly aligned with the regional foliation or local shear fabric. Chlorite, phlogopite, and talc occur less abundantly within the dolomite-quartz-sulfide domains. However, the talc is generally coarser-grained and randomly-oriented. Talc and quartz fibres commonly occupy strain shadows adjacent to sulfide aggregates, carbonate-quartz clasts and euhedral pyrite crystals. The dolomite-chlorite-talc schist alternates with intervals of massive, vuggy dolomite and dolomite-chlorite-talc-altered breccia.

Vuggy dolomite is characterised by medium to coarse-grained, euhedral to anhedral crystals and spheroids of dolomite in a very fine-grained dolomite matrix. Quartz, talc, calcite, chlorite, pyrite, sphalerite and galena have filled vugs and channels in the dolomite (Fig. 5.5).

Figure 5.4 Dolomite-chlorite-talc assemblage

A Intensely altered limestone-clast breccia consisting of patchy dolomite-chlorite-talc-altered pebbles (a) surrounded by chlorite schist. Transitional Unit. TLPD-45, 257 m.

B Intensely altered fossiliferous limestone clast characterised by very fine-grained dolomite with minor talc, hematite and chlorite patches. Note preservation of crinoid ossicle (c). Transitional Unit. TLPD-45, 261 m.

C Matrix-supported polymictic volcaniclastic breccia containing sub-rounded to sub-angular siltstone or felsic volcanic pebbles (*a*) and quartz porphyry pebbles (*b* & *c*) in a matrix entirely replaced by very fine-grained dolomite. Minor patches of talc and chlorite occur throughout the dolomite-altered matrix. Pebble *c* is characterised by an intense pervasive chlorite-dolomite assemblage, resulting in the dark colouration, whereas weakly altered clasts *a* and *b* are overprinted by minor chlorite, dolomite and phengite. Main zone, Transitional Unit. TLPD-33, 379 m.

D Dolomite-chlorite-talc schist. Irregular dolomite-quartz patches surrounded by discontinuous anastomosing cleavage-bands of aligned Mg-chlorite, phlogopite and talc. Disseminated fine-grained pyrite throughout. Main zone, Transitional Unit. TLPD-37, 166 m.

E Photomicrograph of weakly altered siliceous pebbles (*a*) and euhedral volcanic quartz crystals in a very fine-grained dolomite-altered matrix. Siliceous clasts are overprinted by disseminated pyrite and phengite patches. TLPD-33, 379 m.

F Fine-grained dolomite mosaic consisting of anhedral inclusion-rich crystals with curved and serrated, non-planar margins. Polymodal size distribution. Main zone, Transitional Unit. TLPD-12, 440 m.

G Dolomite spheroid characterised by wedge-shaped zoned dolomite crystals with strong radial extinction surrounding very fine-grained dolomite in the core. TLPD-36W, 214 m.

Abbreviations: dol = dolomite, tlc = talc, chl = chlorite, hem = hematite.

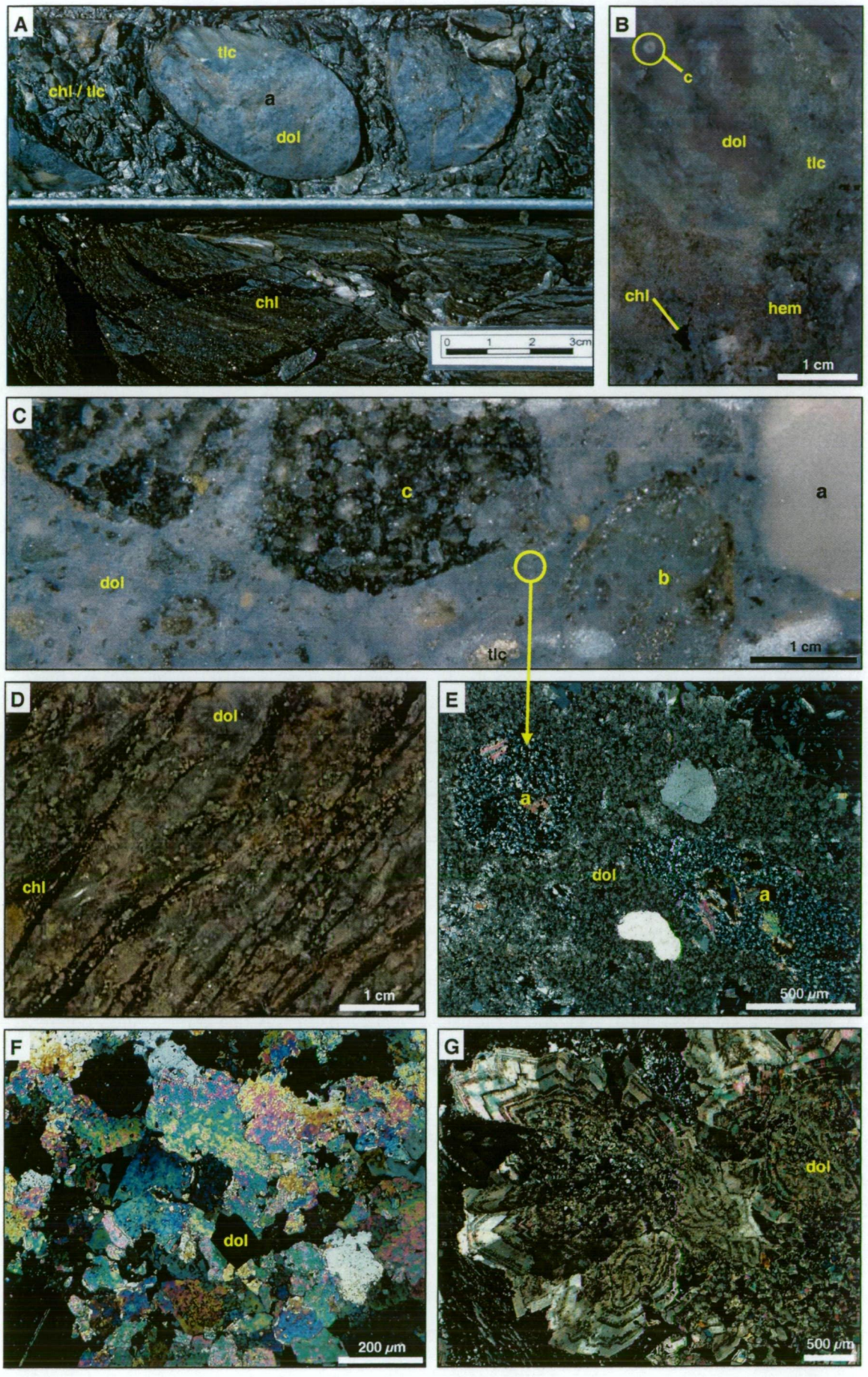
A
tlc
chl / tlc
a
dol
chl
0 1 2 3cm
B
c
dol
tlc
chl
hem
1 cm
C
c
a
dol
b
tlc
1 cm
D
dol
chl
1 cm
E
a
dol
a
500 µm
F
dol
200 µm
G
dol
500 µm

Figure 5.5 Dolomite textures

A Massive vuggy dolomite consisting of vugs and channels filled with clear, amorphous quartz. Transitional Unit. TLPD-33, 389 m.

B Quartz- and calcite-filled vugs in very fine-grained dolomite. Inward-facing prismatic quartz crystals result from unimpeded growth into a fluid-filled cavity. Main zone hangingwall, Transitional Unit. TLPD-12, 440 m.

C Photomicrograph of a vug filled with pyrite, sphalerite and clear, rhombic dolomite crystals. The vug is surrounded by inward facing prismatic dolomite crystals and very fine-grained dolomite. Unimpeded growth of rhombic dolomite crystals was followed by simultaneous deposition of pyrite, sphalerite and dolomite to fill the vug. Plane polarized light. TLPD-12, 440 m.

D Vuggy dolomite sample consisting of zoned euhedral dolomite crystals and aggregates of very fine-grained dolomite lined with chlorite and surrounded by clear, platy calcite. Calcite and chlorite precipitated around the zoned dolomite crystals and fine-grained dolomite to fill the remaining space. Main zone, Transitional Unit. TLPD-12, 493 m.

E Elongate patch of very fine-grained talc surrounded by inward-facing rhombic dolomite crystals and very fine-grained dolomite. TLPD-33, 405 m.

F Photomicrograph of chlorite-filled vug surrounded by very fine-grained dolomite and disseminated euhedral pyrite crystals. Main zone footwall. TLPD-36W, 206 m.

G Very fine-grained dolomite cut by anastomosing white dolomite veins. Irregular, angular patches of chlorite and talc occur throughout the dolomite matrix. Toms zone Central massive sulfide lens, Hangingwall Siltstone Unit. TLPD-51A, 484 m.

H Pseudobreccia consisting of angular chlorite patches in a matrix of very fine-grained vuggy dolomite. Concentric bands in the dolomite matrix result from unidirectional growth. TLPD-33, 409 m.

Abbreviations: dol = dolomite, qtz = quartz, ca = calcite, py = pyrite, sph = sphalerite, chl = chlorite, tlc = talc.

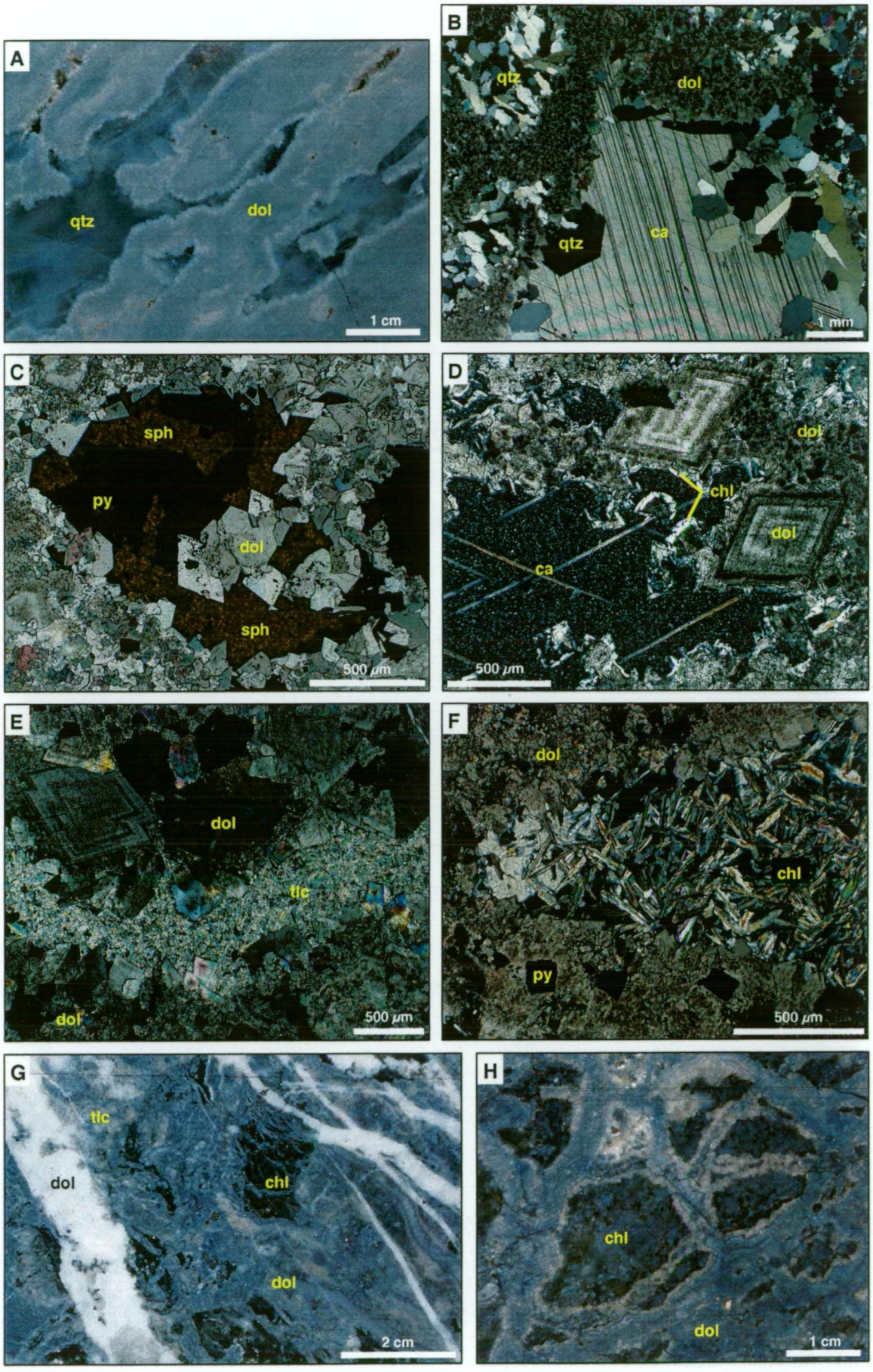
A
qtz
dol
1 cm
B
qtz
dol
qtz
ca
1 mm
C
sph
py
dol
sph
500 μm
D
dol
chl
dol
ca
500 μm
E
dol
tlc
dol
500 μm
F
dol
chl
py
500 μm
G
tlc
dol
chl
dol
2 cm
H
chl
dol
1 cm

The vugs are lined with inward facing quartz and dolomite crystals, chlorite laths and fine-grained quartz, indicating unidirectional, unimpeded growth into open cavities. Anastomosing dolomite veins and veinlets containing minor phengite, pyrite and sphalerite cut across the carbonate-altered rock (Fig. 5.5G). Pseudobreccia textures occur where very fine-grained dolomite surrounds angular chlorite patches (Fig. 5.5H).

Quartz-sericite ± hyalophane and quartz-dolomite-chlorite

Thin (5-20 m) lenses of intensely silicified rock occur within the massive sulfide lenses or in the immediate footwall (Figs. 5.1-5.3). In Main zone, patchy silicified intervals alternate with massive sulfide. The rock comprises phengitic muscovite, chlorite, dolomite and coarse-grained quartz in a microcrystalline quartz mosaic (Fig. 5.6A). In Toms zone, the quartz-sericite assemblage includes 5-10 modal % euhedral or poikiloblastic hyalophane crystals (barium feldspar; Fig. 5.6B). This assemblage, observed only in two thin sections, corresponds to anomalous whole rock Ba concentrations in the Toms zone footwall. Anastomosing quartz and carbonate veinlets cut across the silicified rocks.

Chlorite-sericite-pyrite (chlorite >> sericite)

Chlorite with subordinate sericite and pyrite surrounds the dolomite and quartz-bearing assemblages (Figs. 5.1-5.3). Dark green to black chlorite occurs throughout the polymictic breccia matrix in Main zone. The chlorite envelope becomes more widespread to the south, where it extends 150 m into the footwall volcanic succession and 50 m into hangingwall siltstone immediately south of Toms zone (Fig. 5.3). Here, chlorite occupies the groundmass or matrix of quartz phyric volcanic rocks and siltstone. Chlorite abundance decreases from 90 modal % at the top of the footwall volcanic succession to 15% with distance from the Toms massive sulfide lens. Chlorite selvages locally surround calcite-chalcopyrite-pyrite veins in the Toms zone footwall. Two types of chlorite occur in thin section. Intensely altered rocks are characterised by fibrous, radial aggregates of chlorite with no preferred orientation (Fig. 5.6C). Fine-grained, aligned chlorite laths define the S_1 cleavage in strongly altered rocks away from these areas (Fig. 5.6D). The preservation of primary chlorite may reflect inhomogeneous strain or the presence of mechanically strong lithologies and lithic clasts within the rocks.

Sericite-chlorite ± calcite and sericite-quartz ± chlorite (sericite > chlorite)

A weak to moderate pervasive sericite-chlorite ± calcite assemblage occurs in the footwall volcanics at Main zone (Fig. 5.1). Sericite-quartz ± chlorite also occurs in a 250 m thick symmetrical envelope that surrounds chlorite-altered rocks at Toms zone (Fig. 5.2). This assemblage extends into the footwall volcanic succession and Hangingwall Siltstone Unit.

Very fine-grained white mica and chlorite partly to completely overprint plagioclase phenocrysts and the microcrystalline groundmass in quartz-plagioclase phyric dacite. Feldspar destructive sericite assemblages occur only in the hangingwall and footwall of Toms zone. White mica in the Main zone footwall lacks a preferred orientation, whereas fine-grained laths occurring throughout quartz phyric volcanic and pelitic rocks in Toms and Lady Belmore zones are strongly aligned with the S_1 cleavage (Fig. 5.6E)

False-clastic textures are common in the quartz-feldspar phyric dacite (B) underlying Main zone. Elongate, cleavage-parallel chlorite pseudoclasts with sharp or wispy margins are surrounded by quartz-sericite-altered domains. Coherent porphyritic textures occur within the chlorite patches. Allen (1988) interpreted this type of pseudobreccia to result from two phase alteration involving fracture-controlled silicification of coherent lava, followed by phyllosilicate growth between the silicified domains.

Calcite-sericite-chlorite

The strong pervasive calcite-sericite-chlorite assemblage is restricted to fossiliferous quartz crystal-rich sandstone and pebbly-siltstone beds underlying Main zone. Patches of fine-grained polygonal calcite and large platy calcite crystals occur throughout the matrix (Fig. 5.6F). Some of these represent crinoid fossils, shell fragments and recrystallised limestone clasts. Aligned chlorite and sericite laths define the S_1 cleavage.

Magnetite-hematite

Disseminated and vein-controlled magnetite crystals occur throughout the Western Volcanic Succession, Transitional Unit and Hangingwall Siltstone Unit. These are commonly corroded and partly altered to hematite. Cleavage-parallel calcite-magnetite-hematite veins in the fault-bound stratigraphic unit become less abundant away from the limestone lenses. Anastomosing, cleavage-parallel, magnetite-hematite bands also cut the limestone megabreccia.

Jasper lenses

Discontinuous, 10-15 m wide jasper lenses occur along the western contact of the Eastern Volcanic Succession (Fig. 3.1). A jasper lens also occurs at the upper contact of the Western Volcanic Succession near the Ceasars workings. The rock comprises fine-grained polygonal quartz with minor disseminated hematite and martitised euhedral magnetite crystals (Fig 5.6G). Sphalerite veinlets cut the jasper in places. Where this occurs, adjacent magnetite crystals are partly altered to sphalerite and/or hematite (Fig. 5.6H). The jasper consists of 85 wt % SiO_2, 15 wt % Fe_2O_3 5-35 ppm Ba, V, Ni, Cu, and Zn and 1.7 ppm Tl (sample LPD014, Appendix 4). Rock chip samples contain up to 900 ppm Zn (Tri Origin, unpublished data).

Figure 5.6 Hangingwall and footwall alteration assemblages

A Intense pervasive quartz-dolomite-chlorite assemblage. Consists of chlorite laths and poikilitic dolomite patches in a very fine-grained, equigranular quartz mosaic. Main zone, Transitional Unit. TLPD-12, 465 m.

B Ba-rich, silicified rock from Toms zone footwall consisting of poikilitic hyalophane crystals and minor phengite in a very fine-grained equigranular quartz mosaic. Hangingwall Siltstone Unit. TLPD-46A, 134 m.

C Texturally destructive chlorite-phlogopite assemblage characterised by medium-grained, fibrous, typically radiating, chlorite and phlogopite laths which have not been recrystallised during metamorphism. Western Volcanic Succession. TLPD-66, 267 m.

D Quartz-chlorite schist consisting of fine-grained chlorite laths aligned with the S_1 cleavage. Western Volcanic Succession. TLPD-63, 454 m.

E Quartz-sericite schist dominated by fine-grained phengite aligned with the S_1 cleavage. Western Volcanic succession. TLPD-63, 284 m.

F Intense pervasive calcite-chlorite-sericite assemblage in quartz crystal-rich sandstone from Main zone footwall. Some of the calcite patches may represent recrystallised primary limestone clasts. Transitional Unit, TLPD-36W, 277 m.

G Jasper from the western contact of the Eastern Volcanic succession consisting of disseminated magnetite and hematite in an equigranular quartz mosaic. LPD014, GR 710242E 6315970N.

H Photomicrograph of jasper cut by an anastomosing sphalerite veinlet. Martitised euhedral magnetite crystals, adjacent to the veinlet are partly replaced by hematite and sphalerite. Toms zone hangingwall. LPD014.

Abbreviations: qtz = quartz, dol = dolomite, chl = chlorite, phg = phengite, hly = hyalophane, ca = calcite, mag = magnetite, hem = hematite, sph = sphalerite.

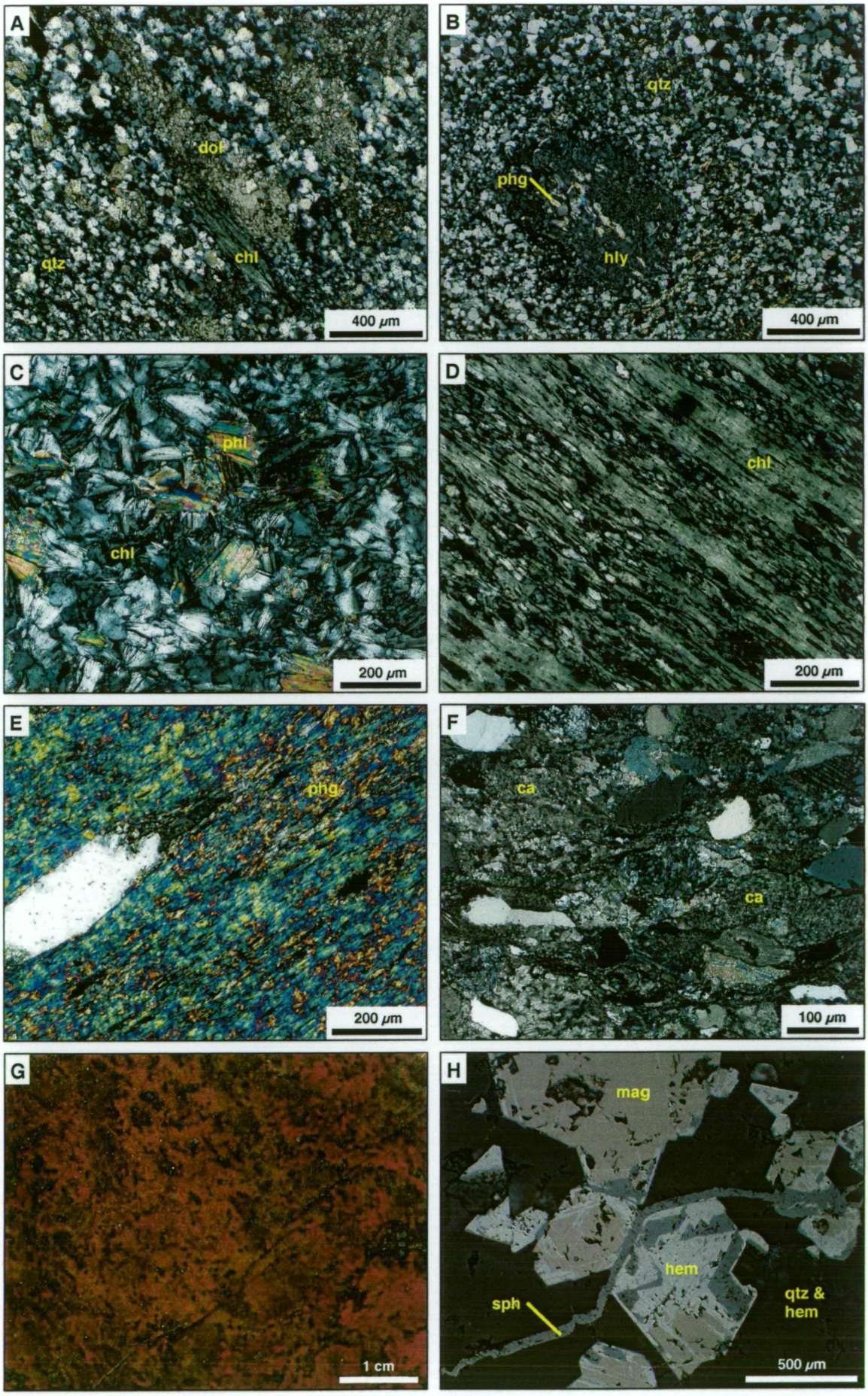
A
dol
qtz
chl
400 μm
B
qtz
phg
hly
400 μm
C
phl
chl
200 μm
D
chl
200 μm
E
phg
200 μm
F
ca
ca
100 μm
G
1 cm
H
mag
hem
sph
qtz &
hem
500 μm

5.5 Fault-controlled and deformation-related assemblages

Hydrothermal alteration assemblages attributed to the D_1 deformation are confined to the Lewis Ponds fault zone and host rock adjacent to type 3A quartz veins. The variably deformed, cleavage-parallel, type 3A quartz-sulfide veins resulted from periodic brittle shear failure and extension (see Chapter 4, section 4.5). The veins are surrounded by quartz-sericite-carbonate selvages, that overprint pre-existing chlorite and sericite assemblages.

Patches of fine-grained talc occur in chlorite-sericite-altered schistose rocks in Toms zone, Lady Belmore zone and New Lewis Ponds (Fig. 3.1). Talc is most abundant in the breccia and sandstone units in Main zone, adjacent to the Lewis Pond fault. These massive intervals represent intensely altered, polymictic breccia. The massive talc occurs with dolomite.

Iron, Mn and Mg carbonates occur in closely spaced, 0.1-1 mm thick, anastomosing cleavage-parallel, type 3C veinlets, carbonate lenes and rare tectonic fish adjacent to the type 3A quartz veins (Fig. 5.8A-C). The carbonate veins are considered an alteration type due to their abundance throughout the Lewis Ponds fault zone. They are composed of very fine-grained dusty inclusion-rich or clear dolomite, ferroan-dolomite, siderite or sidero-magnesite crystals (Fig. 5.7, Appendix 3). Most have banded, crustiform internal textures characteristic of a crack-seal mechanism of formation. The deformed veins are truncated by F_{12} kink bands, indicating that they precipitated prior to the D_2 deformation.

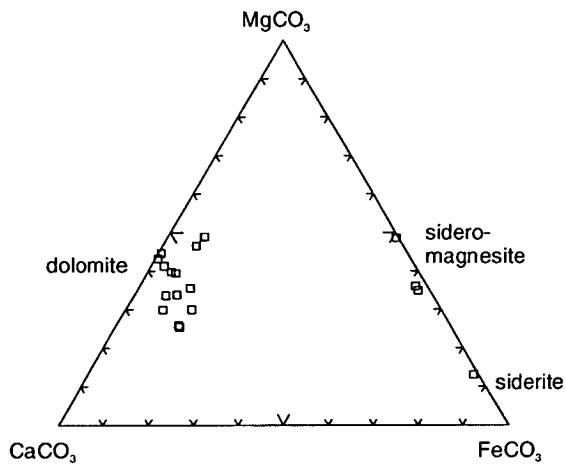

Figure 5.7 Triangular diagram showing composition of type 3C carbonate veinlets occurring in the Lewis Ponds fault zone. Based on 18 microprobe analyses.

5.6 Metamorphic assemblages

The following section outlines mineral assemblages that post-date hydrothermal activity at Lewis Ponds. These typically overprint the S_1 cleavage or non-foliated quartz-feldspar porphyry dykes.

Figure 5.8 Metamorphic and fault-related alteration assemblages

A Anastomosing, weakly kink folded, cleavage-parallel magnesite veinlets in a chlorite matrix. Toms zone footwall. TLPD-51AW2, 406 m.

B Type 3A cleavage-parallel quartz vein with pinch and swell structure, associated with intense pervasive quartz-sericite assemblage and magnesite veinlets in the adjacent siltstone. Toms zone footwall, Hangingwall Siltstone Unit. TLPD-51AW2, 424 m.

C Photomicrograph of tectonic fish composed of dolomite, cutting a deformed quartz veinlet. Crustiform texture results from precipitation of dolomite in a dilation zone opened during shearing. Western Volcanic Succession. TLPD-66, 311 m.

D Photomicrograph of aligned, pale brown Mg-F-rich phlogopite occurring in anastomosing cleavage bands that wrap around dolomite-quartz domains. Main zone, Transitional Unit. TLPD-12, 503 m. Plane Polarised Light.

E Photomicrograph of cleavage-aligned, pale red-brown Fe-Ti-rich phlogopite surrounded by chlorite. Associated with type 1A calcite-chalcopyrite-pyrite veins. Toms zone footwall, Western Volcanic Succession. TLPD-66, 374 m. Plane polarised light.

F Quartz-feldspar porphyry dyke characterised by weak pervasive sericite-chlorite-biotite assemblage. Primary biotite phenocrysts (bt 1) have been partly replaced by chlorite and white mica. Toms zone footwall. TLPD-67B, 440 m. Plane polarised light.

G Hornblende-dolomite-epidote assemblage comprising hornblende laths with no preferred orientation, and minor epidote. Toms zone footwall. TLPD-67B, 687 m.

H Photomicrograph of a rounded sericite-chlorite aggregate possibly replacing a cordierite porphyroblast. The internal alignment of phengite is oblique to the S1 cleavage orientation in the surrounding siltstone. TLPD-67B, 841 m.

Abbreviations: chl = chlorite, mgs = magnesite, qtz = quartz, phg = phengite, dol = dolomite, phl = phlogopite, bt = biotite, fsp = plagioclase, hbl = hornblende, ep = epidote.

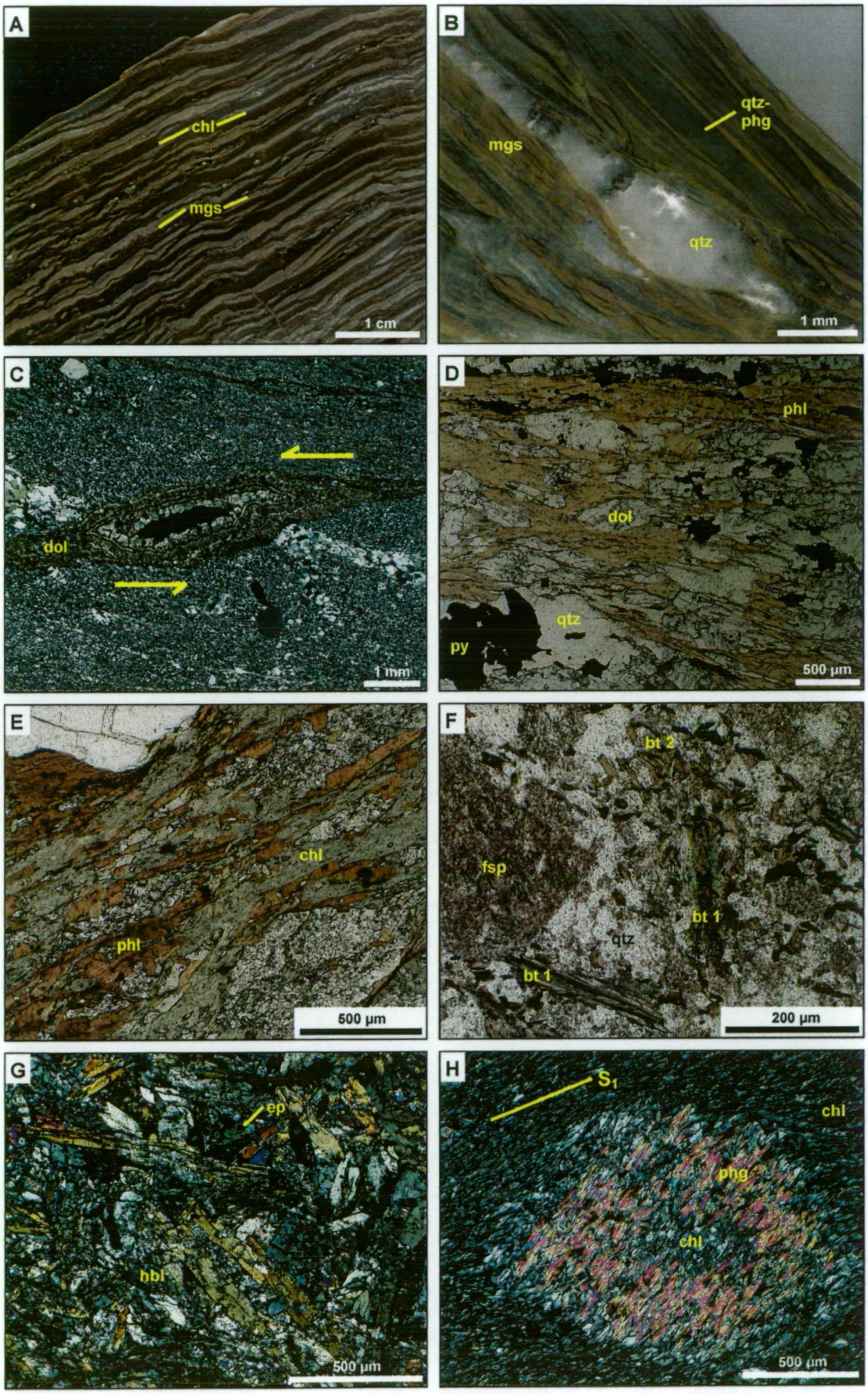
A
chl
mgs
1 cm
B
mgs
qtz-
phg
qtz
1 mm
C
dol
1 mm
D
phl
dol
qtz
py
500 µm
E
chl
phl
500 µm
F
bt 2
fsp
bt 1
qtz
bt 1
200 µm
G
ep
hbl
500 µm
H
S1
chl
phg
chl
500 µm

Biotite, phlogopite and sphene

Biotite occurs south of Main zone in the Western Volcanic Succession, Hangingwall Siltstone Unit and quartz-feldspar porphyry dykes. Phlogopite and sphene, however are confined to the dolomite-chlorite-talc and chlorite-sericite-pyrite envelopes surrounding the two massive sulfide zones (Figs. 5.1-5.3). Pale brown to red-brown phlogopite and red-brown to green biotite occur throughout the matrix or groundmass of clastic and coherent rocks (Fig. 5.8D and E). Phlogopite in Main zone is very pale and easily mistaken for white mica. Biotite and phlogopite laths are randomly oriented or aligned with the S_1 cleavage. They have partially to completely replaced aligned chlorite in strongly foliated rocks. The mica occupies strain shadows on quartz and feldspar crystals in weakly altered rocks. Type 1 and 3 veins are locally associated with 0.5-3 mm wide selvages of biotite or phlogopite overprinting earlier chlorite.

Non-foliated quartz-feldspar porphyry dykes are characterised by a weak, patchy to pervasive sericite-biotite-chlorite assemblage. Fine-grained white mica and pale green biotite occurs throughout the groundmass (Fig. 5.8F). Chlorite and white mica typically overprint the large primary biotite phenocrysts.

Hornblende-dolomite-epidote

Hornblende-dolomite-epidote patches occur rarely in the footwall and hangingwall of Toms zone (Fig. 5.8G). The intensely altered, fine-grained sedimentary rocks comprise elongate dolomite patches and disseminated pyrite in a matrix dominated by bluish-green hornblende with no preferred orientation and minor epidote. The hornblende compositions are characterised by 1.5 tetrahedral Al atoms substituting for Si (Appendix 3). The Hornblende may have resulted from reactions involving epidote and chlorite (Yardley, 1989).

Cordierite

Fine-grained sedimentary rocks hosting Toms zone rarely contain irregular rounded phyllosilicate patches. The 1-5 mm wide aggregates of aligned phengite and chlorite occur in a chlorite-altered matrix with secondary biotite (Fig. 5.8H). The internal fabric is oblique to S_1 in the surrounding matrix. These irregular patches may represent retrogressed cordierite porphyroblasts, which overprinted the S_1 cleavage.

5.7 Geochemistry of hydrothermal and metamorphic minerals

The following section presents the results of the microprobe analyses of phyllosilicate and carbonate minerals at Lewis Ponds.

Dolomite

The dolomite and ferroan-dolomite contains 33-43 wt % $MgCO_3$, 51-61 wt % $CaCO_3$, 0.2-7 wt % $MnCO_3$, 0-7 wt % $FeCO_3$, up to 2300 ppm $ZnCO_3$ and 4200 ppm $SrCO_3$ (Appendix 3). Unusually high Mn concentrations in several analyses from Main zone may result from mineral inclusions. The dolomite compositions do not reflect lithology because there are no systematic variations between Main and Toms zones. Euhedral dolomite crystals have highly variable $CaCO_3$, $MgCO_3$, $MnCO_3$, and $FeCO_3$ contents within and between samples (Appendix 3). Cores are depleted in $FeCO_3$ and enriched or depleted in $MnCO_3$ relative to the outer rims (Fig. 5.9). However, compositions do not vary systematically between zoned crystals, suggesting that the dolomite nuclei may have precipitated at different times.

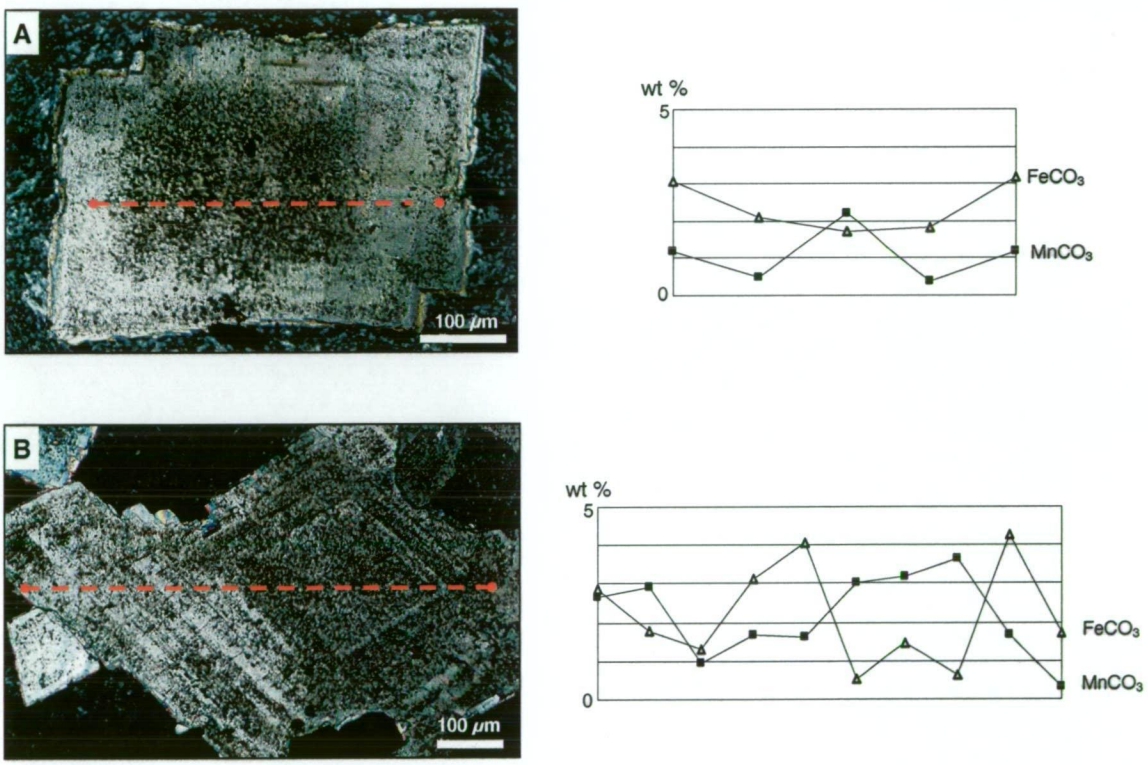

Figure 5.9 Microprobe traverses of zoned dolomite rhombs in Main (A) and Toms (B) zones showing variations in $FeCO_3$ and $MnCO_3$ concentrations. A = TLPD-33, 390 m, B = TLPD-51A, 484 m.

Chlorite

Chlorite crystals in the polymictic breccia in Main zone contain 7.0 to 8.5 Mg cations. They have Mg numbers 100[Mg/(Fe + Mg)], that range from 80 to 90 (Fig. 5.10). Chlorite laths occurring in the siltstone and footwall volcanics in Toms zone have 5.3 to 8.6 Mg cations and variable Mg numbers, ranging from 59 to 92. Lewis Ponds chlorite compositions are therefore closer to the chlinochlore, $(Mg_{10}Al_2)(Si_6Al_2O_{20}(OH)_{16}$, end-member than the chamosite, $(Fe^{2+}{}_{10}Al_2)(Si_6Al_2O_{20}(OH)_{16}$ end-member.

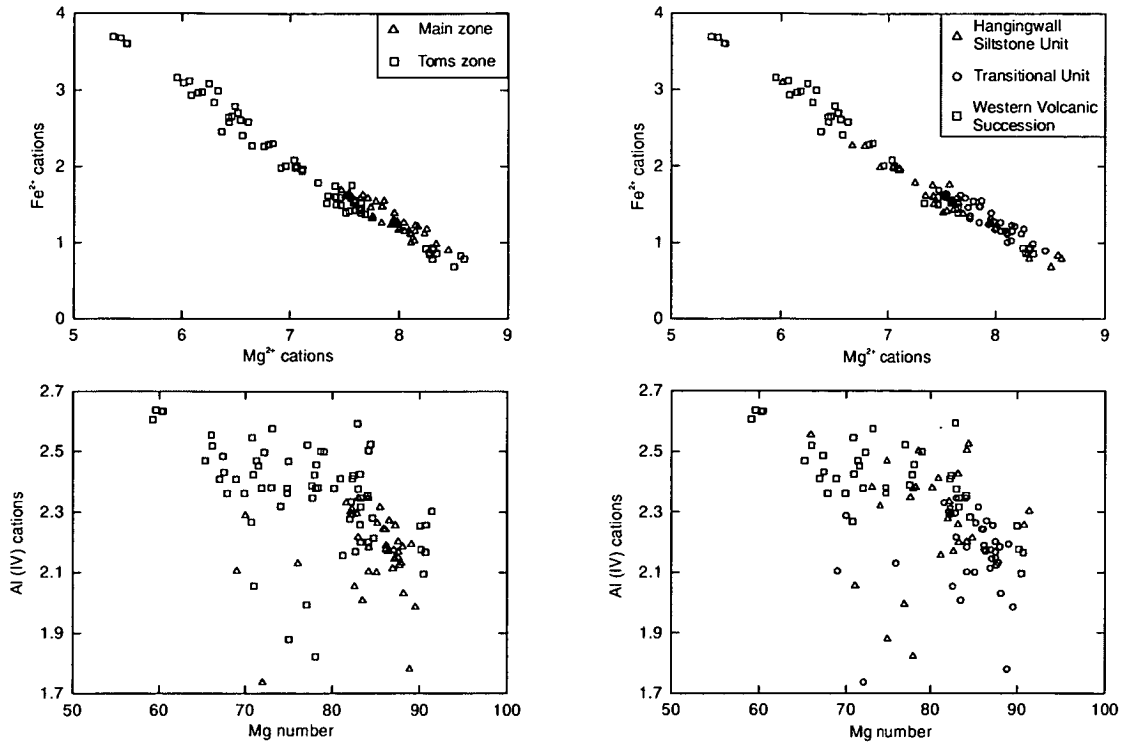

Figure 5.10 Chlorite compositions plotted in terms of mineralised zone and stratigraphic location. Based on 107 microprobe analyses.

SWIR spectral analysis provided inaccurate estimates of chlorite compositions from the footwall and hangingwall. No positive correlation exists between Mg numbers obtained from chlorite microprobe analyses and the MgOH absorption feature measured on the same samples by the PIMA (Fig. 5.11). The MgOH spectral feature may be affected by Mg-carbonates or AlOH features occurring in white mica. These observations are consistent with Herrmann et al. (2001), who found the instrument unreliable at estimating chlorite compositions in mixtures of chlorite and white mica.

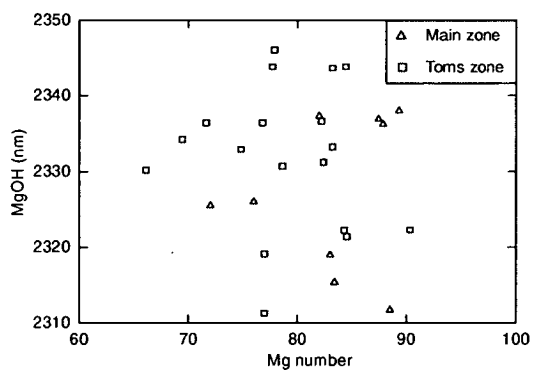

Figure 5.11 Chlorite Mg number versus MgOH short wavelength absorption features measured by the electron microprobe and PIMA respectively.

White mica

The fine-grained white mica contains 2-4 octahedral Al cations and up to 2 K cations and 0.1 Ba cations (Fig. 5.12). These compositions are consistent with phengitic muscovite (Bailey, 1984; Deer et al., 1992). Phengite compositions do not vary systematically between

host lithologies (Fig. 5.12). However, white micas occurring in syn-tectonic quartz veins generally contain less Mg, Si and K and more Na and Al(VI) than pervasive sericite surrounding the massive sulfide lenses.

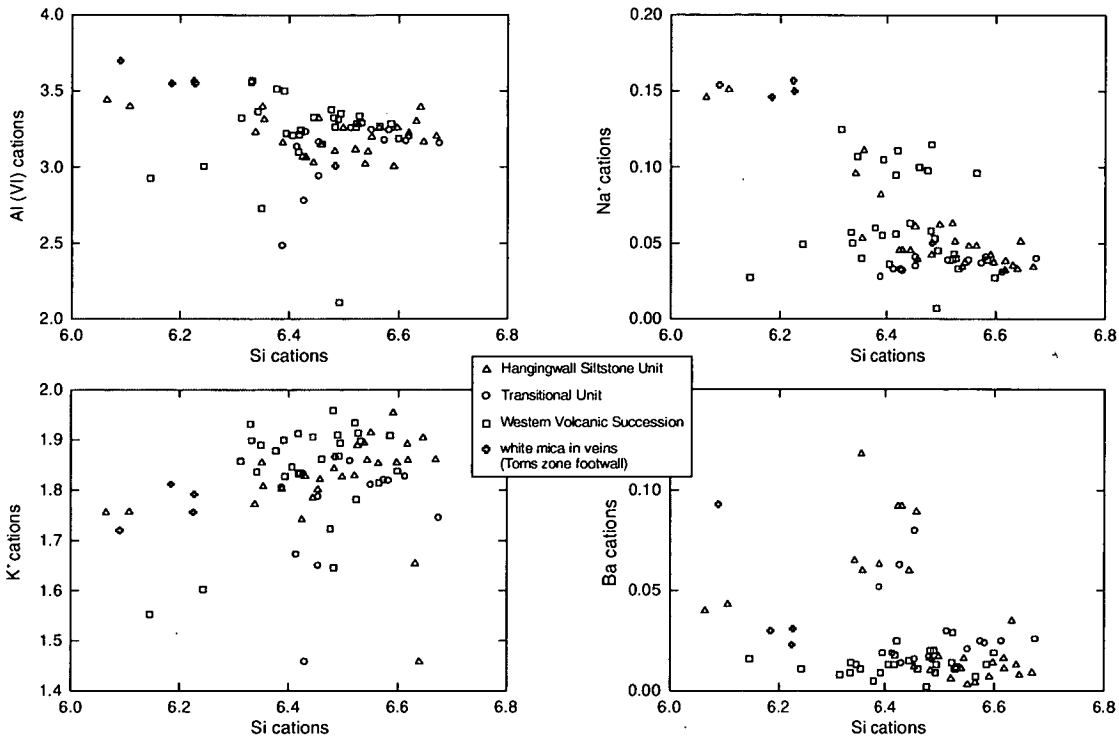

Figure 5.12 White mica compositions plotted in terms of stratigraphic unit. 5 analyses are from type 3A and type 4 quartz veins occurring in the Toms zone footwall. Based on 73 microprobe analyses.

Phlogopite and biotite

Microprobe analyses yielded highly variable phlogopite and biotite compositions, depending on lithology and proximity to the massive sulfide lenses (Fig. 5.13). Phlogopite grains in the breccia deposits in Main zone have higher F and Mg and lower Al, Fe and Ti concentrations than those in the volcanic and siltstone units in Toms zone. The inverse relationship between F and Fe concentration is known as Fe-F avoidance (Munoz, 1984). Biotite grains have higher Fe and Ti concentrations than phlogopite, reflecting substitution for Al in octahedral sites.

5.8 Interpretation

Diagenetic alteration of the Mullions Range Volcanics

Perlitic fractures, spherulites, glass shards and pumice indicate that glassy domains formerly occurred in the coherent and clastic facies of the Mullions Range Volcanics. Phyllosilicate assemblages (sericite, sericite-K-feldspar-quartz ± magnetite-hematite and chlorite-epidote) have overprinted glassy and non-glassy domains. Quartz and sericite fill primary pore spaces including vesicles in coherent rhyolite and tube pumice clasts. The epidote and clinozoisite

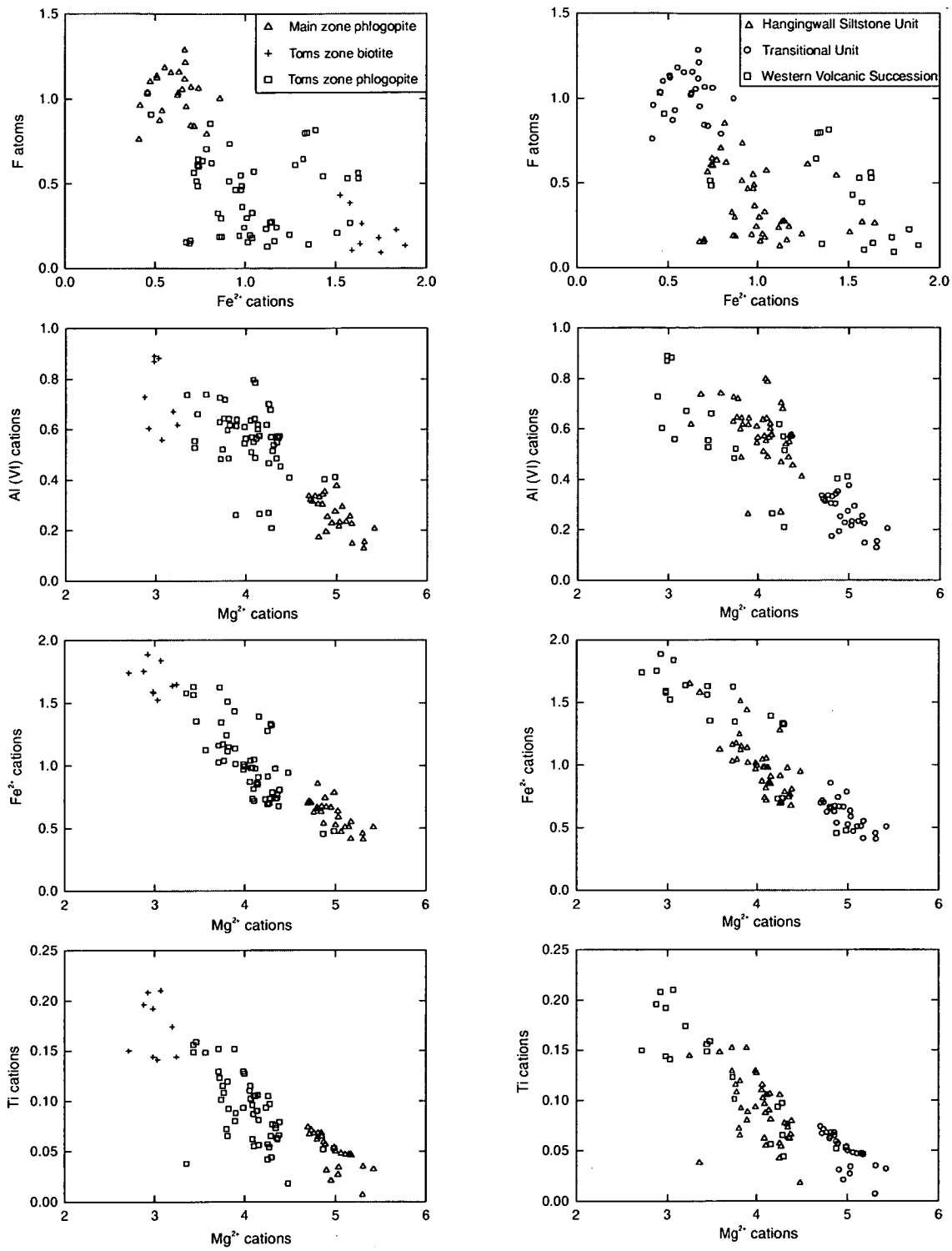

Figure 5.13 Biotite and phlogopite compositions plotted in terms of mineralised zone and stratigraphic unit. Based on 87 microprobe analyses.

are likely to result from low temperature diagenesis or metamorphism of calcium-bearing lithologies such as limestone or plagioclase phyric volcanic rocks. Recrystallisation and alignment of the chlorite and sericite during deformation produced the regional cleavage. Volcanic glass is metastable and therefore susceptible to hydration and devitrification during cooling and diagenesis (Lofgren, 1971; McPhie et al., 1993). Devitrification involves crystal nucleation and the development of a granular microcrystalline groundmass containing quartz

and K-feldspar. Hydration results from the absorption of water, which consequently modifies the glass structure. Perlitic cracks are attributed to either hydration of the glass or stress release during cooling (Doyle, 2001).

Sericite, chlorite-epidote and sericite-K-feldspar-quartz assemblages occurring in the Mullions Range Volcanics probably resulted from devitrification, diagenesis and low-temperature metamorphism of clastic and coherent rocks. Phyllosilicate-bearing assemblages have replaced the primary diagenetic clays, zeolites and chlorite that lined vesicle walls and altered glassy domains (Noh and Boles, 1989; Gifkins and Allen, 2001).

Dolomite textures

Figure 5.15 summarises the five dolomite textures recognised at Lewis Ponds. Type 1 dolomite occurs in most sulfide-bearing, carbonate altered rocks. It is characterised by a unimodal mosaic of very fine-grained (<0.2 mm) clear or dusty, subhedral to anhedral crystals. In Main zone, irregular patches of type 1 dolomite occur within pyrite and sphalerite aggregates (Fig. 5.14). Contacts between the sulfide and surrounding type 1 dolomite matrix are also highly irregular.

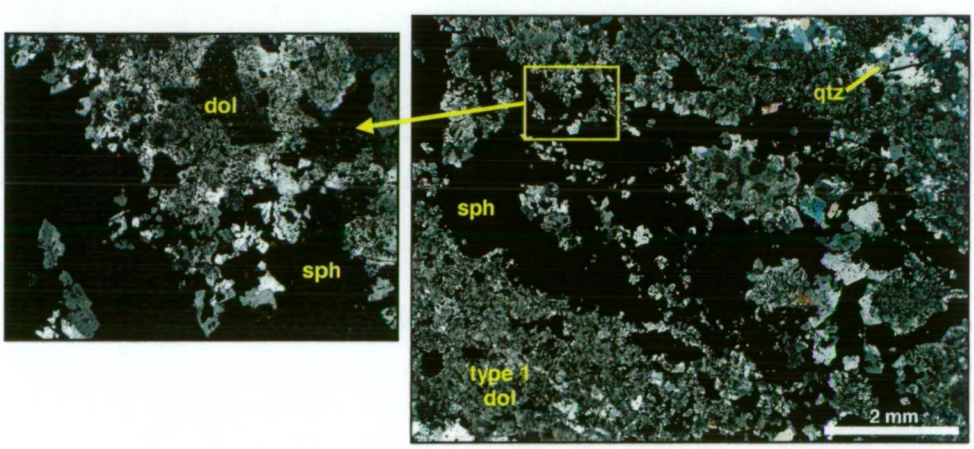

Figure 5.14 Honeycomb texture consisting of an irregular aggregate of massive sphalerite (sph) with minor galena, pyrrhotite and pyrite surrounded by very fine-grained type 1 dolomite (dol) and quartz (qtz). Irregular patches of type 1 dolomite also occur within the sphalerite. Main zone, Central massive sulfide lens. TLPD-18, 365 m. Transmitted light.

The type 1 dolomite is interpreted to pre-date deposition of the massive sulfide in Main zone. Fragments of wall rock occurring within irregular patches of pyrite and sphalerite indicate corrosion of the massive dolomite by the mineralising fluid. Amthor and Friedman (1991) interpreted aggregates of very fine-grained dolomite as an early replacement texture. The small crystal size results from either a high density of nucleation sites or high level of supersaturation regardless of temperature (Sibley and Gregg, 1987). The unimodal size distribution may indicate a single nucleation event with uniform growth rates.

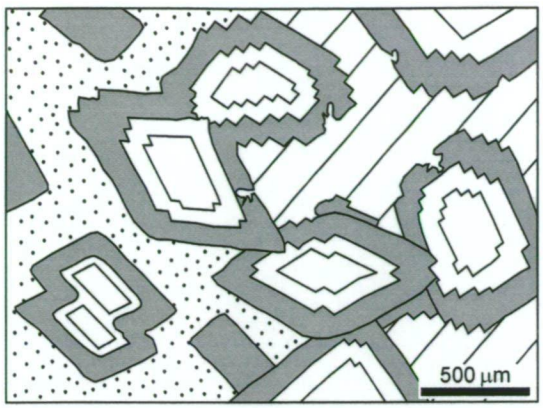

Type 1 (represented by dots) - mosaic of very fine- to fine-grained (<0.2 mm) dusty subhedral to anhedral crystals, eg. Fig. 5.5F. Unimodal size distribution.

Type 2 - clear or zoned medium- to very coarse-grained (0.2-1.5 mm) euhedral to subhedral crystals occurring individually or in aggregates with planar or 'compromise' boundaries, eg. Fig. 5.5C, D and E and 5.9. Unimodal to polymodal size distribution.

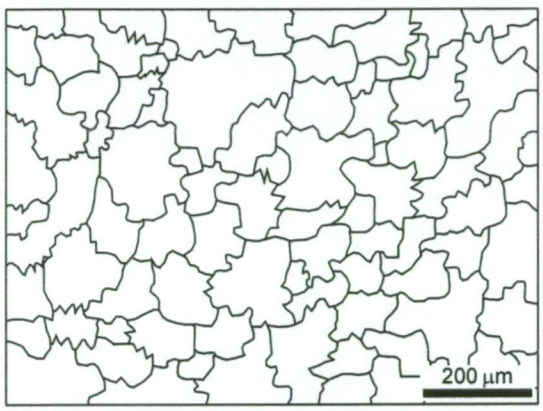

Type 3 - mosaic of medium- to coarse-grained (0.2-1 mm) clear or dusty, anhedral crystals with non-planar margins and undulatory extinction, eg. Fig. 5.4F. Polymodal size distribution.

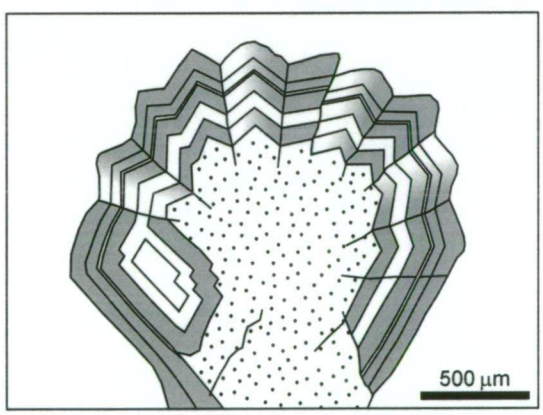

Type 4 - 1-4 mm wide spheroids consisting of wedge-shaped laths of zoned dolomite with strong undulatory extinction, eg. Fig. 5.4G. Fine-grained type 1 dolomite typically occurs in the core (shown as dots). The spheroids partly overprint type 2, zoned rhombic dolomite crystals.

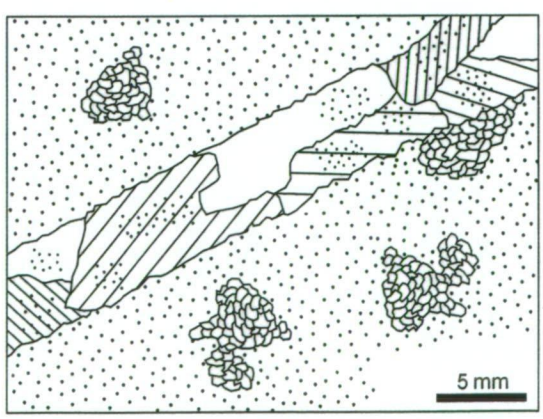

Type 5 - very coarse grained (2-8 mm) anhedral dusty crystals occurring in veins, eg. Fig. 5.5G. Partly overprinted by type 1 dolomite. Polymodal size distribution.

Here the vein is surrounded by type 1 dolomite (shown as dots) and patches of type 3 dolomite.

Figure 5.15 Types of dolomite occurring at Lewis Ponds.

Type 2 dolomite consists of medium- to very coarse-grained (0.2-1.5 mm), euhedral to subhedral rhombs with planar, typically corroded margins or 'compromise' boundaries and sharp to weakly undulatory extinction (Fig. 5.15). Zoned rhombs have a dusty, inclusion-rich core surrounded by 5-200 μm wide, alternating clear and dusty bands. Patches of rhombic crystals with a unimodal or polymodal size distribution occur in a matrix of very fine-grained, type 1 dolomite. Aggregates of inward-facing rhombic dolomite crystals commonly line vugs and channels filled with quartz, calcite, chlorite, pyrite or sphalerite (Fig. 5.5C-F). Clear and zoned, type 2 dolomite rhombs surround patches and disseminations of pyrite, sphalerite and galena throughout the mineralised, Main zone host rocks (eg. Fig. 5.5C).

Type 2 dolomite is interpreted to have precipitated prior to and during mineralisation in Main zone. Medium to coarse-grained rhombic crystals occur within and adjacent to pyrite, galena and sphalerite aggregates in the dolomite-altered, breccia and pebbly-granular sandstone deposits. Individual or coalesced euhedral rhombs result from in situ, simultaneous growth at different nucleation sites over an extended period. They generally form at low temperatures or low levels of supersaturation (Gregg and Sibley, 1984; Rao, 1997). The growth rate and nucleation kinetics depend on the level of supersaturation, type of substrate and fluid composition (Sibley and Gregg, 1987) and the involvement of impurities such as Fe^{2+} ions (Gregg and Sibley, 1984; Meyer, 1984). Consequently, coarsely crystalline euhedral dolomite also forms at higher temperatures. Variations in the growth rate, fluid composition or numerous crystallisation episodes produces zoned crystals with a polymodal size distribution. Growth of the dolomite ceases when the majority of intercrystalline space had been consumed or conditions prevent diffusion through the substrate or delivery of cations to the growing crystals.

Type 3 consists of polymodal aggregates of medium- to coarse-grained (0.2-1 mm) inclusion-rich, anhedral dolomite crystals with serrated or curved, non-planar margins and undulatory extinction (Figs. 5.4F and 5.15). These occur in a fine-grained dolomite matrix. This texture has been referred to as xenotopic dolomite (Gregg and Sibley, 1984). Anhedral crystals with non-planar interfaces result from high temperature (>50°C) dolomitisation of limestone or recrystallisation of pre-existing dolomite (Gregg and Sibley, 1984). The undulatory extinction reflects a distorted crystal lattice due to asymmetric growth (see discussion on following page).

Elongate, wedge-shaped anhedral dolomite crystals occurring in 1-4 mm wide, spheroidal aggregates define type 4 dolomite (Figs. 5.4G and 5.15). The curved crystals are characterised by anhedral or euhedral outer terminations and undulatory (radial) extinction. Very fine-grained type 1 dolomite typically occurs in the core of the spheroids.

The spheroids result from rapid asymmetric growth from a single nucleus at high temperatures. Alternating clear and inclusion-rich bands indicate variations in the growth rate, diffusion rate, fluid composition and level of supersaturation. The radial habit, dusty appearance and strong undulatory extinction is analogous to radiaxial calcite (Kendall, 1985) and saddle dolomite (Radke and Mathis, 1980). Asymmetric growth and distortion of the crystal lattice is attributed to crystal-splitting due to the interference of dissolved species or growth from highly supersaturated fluids (Radke and Mathis, 1980; Kendall, 1985). Saddle dolomite commonly occurs as a void-filling cement or replacement carbonate in hydrocarbon reservoirs and base-metal sulfide deposits. It forms at temperatures of 60-150°C (Radke and Mathis, 1980).

Type 5 dolomite occupies anastomosing veins and veinlets in Toms zone (Figs. 5.5G and 5.15). The large (2-8mm), dusty, anhedral crystals have irregular serrated, nonplanar margins and sharp extinction. Veins formed after brittle fractures opened in the carbonate-altered rock. These were transient conduits characterised by high permeability and fluid flow. Anhedral dolomite crystals are interpreted to result from high temperature (>50°C) fluids. The large crystal size suggests high growth rates relative to nucleation rate within the fractures (Sibley and Gregg, 1987).

Carbonate alteration assemblages

Hydrothermal alteration in Main zone involved partial to complete replacement of the mixed provenance breccia, limestone-clast breccia and quartz crystal-rich sandstone by dolomite, calcite, Mg-chlorite, talc, quartz, white mica and sulfides. Limestone clasts are preserved as calcite patches in weakly altered areas. Relict crinoid fossils occur in even the most intensely altered rocks, where dolomite, chlorite and talc have replaced the calcite (Fig. 5.4B). Sharp irregular contacts between dolomite-quartz and chlorite-talc-phlogopite domains may represent former clast margins. However many of these contacts are parallel to the S_1 cleavage and therefore structurally controlled. The dolomite-quartz-chlorite schist is a texturally destructive assemblage that has replaced fine or coarse-grained lithologies.

Alteration intensity in the polymictic breccia deposits partly reflects the initial clast composition. Chlorite, dolomite and talc occur throughout the groundmass of intensely altered quartz porphyry pebbles. The chlorite has probably replaced Al-bearing, diagenetic clays and micas. Perlitic fractures may have promoted diagenetic alteration of the groundmass in porphyritic dacite clasts (eg. Fig. 3.14G). In contrast, a weak patchy sericite-dolomite-pyrite assemblage overprints the felsic volcanic, siltstone and mudstone pebbles because they are predominantly composed of fine-grained quartz with little clay.

The Toms zone host rocks are characterised by vuggy dolomite-chlorite-talc and dolomite-quartz-chlorite schist. The texturally destructive assemblages probably overprint siltstone or fine-grained sandstone because polymictic breccia does not host the Toms massive sulfide lens.

The dolomite-chlorite-talc and calcite-sericite-chlorite assemblages resulted from selective replacement of limestone clasts, cementation in open cavities, massive replacement of the matrix and precipitation in fractures. Circulation of hydrothermal fluids through the substrate was therefore strongly dependent on secondary porosity, permeability and rock type. Rapid, episodic fluid flow along transient interconnected fractures produced the veins.

Carbonate-bearing assemblages typically form at the periphery of stratiform Pb-Zn deposits such as Thalanga (Herrmann and Hill, 2001), Rosebery (Large et al., 2001c) and Mt Chalmers (Large and Both, 1980). Herrmann and Hill (2001) suggested that rhombic and spheroidal textures in the Thalanga dolomites developed at an early hydrothermal stage. Spheroids, rhombs and anhedral dolomite crystals grow during 60-150°C dolomitisation of carbonate-rich sediments (Radke and Mathis, 1980; Gregg and Sibley, 1984). In low salinity fluids with constant pH and X_{CO2}, carbonate solubility decreases with increasing temperature (Rimstidt, 1997), causing carbonate minerals to precipitate.

Dolomite and calcite surrounding Main and Toms zones may have precipitated during diagenesis and low temperature hydrothermal alteration. The carbonates rapidly filled pore spaces in the sediment and overprinted diagenetic clays. Zoned euhedral dolomite rhombs resulted from unimpeded growth into open cavities or replacement of the surrounding matrix. Dolomitisation increased permeability in the host sediment by creating secondary pore spaces.

Quartz, calcite, chlorite, talc, pyrite and sphalerite filled secondary vugs, channels and intercrystalline spaces in the dolomite at Lewis Ponds (Fig. 5.5). Amthor and Friedman (1991) suggested that secondary vugs and channels result from dissolution and enlargement of intercrystalline porosity. Porous dolomite successions host stratabound Pb-Zn-Ag-rich sulfide lenses in Irish-style and Mississippi Valley Type deposits (Sverjensky, 1981; Hitzman et al., 2002; Peace et al., 2003).

Talc is unusual in volcanic-hosted massive sulfide deposits. Extensive talc-bearing alteration assemblages have been documented at Mount Chalmers, Central Queensland (Large and Both, 1980); Woodlawn, New South Wales (McLeod and Stanton, 1984; McKay, 1989); Mattabi Lake, Abitibi District, Canada (Costa et al., 1983); Stirling, Cape Breton Island, Nova Scotia (Kontak, 1999); Onedin prospect, northwestern Australia (Orth, 2002) and numerous deposits in the Eastern Desert of Egypt (Botros, 2003).

Talc occurs within the massive sulfide lenses, in the immediate footwall or in local shear zones. Talc-bearing VHMS deposits have a number of similar features (Large, 1977; Costa et al., 1983; McLeod and Stanton, 1984; McKay, 1989; Bodon and Valenta, 1985; Kontak, 1999; Herrmann and Hill, 2001; Botros, 2003). 1. They commonly occur in bimodal volcanic successions and mixed silicic and intermediate volcanic successions or in close proximity to genetically unrelated mafic/ultramafic rocks. 2. The talc is intergrown, or associated with base metal sulfides and other Mg- and Ca-bearing minerals including phlogopite, Mg-chlorite, actinolite, tremolite, stipnomelane, dolomite and calcite. 3. The compositions of talc, chlorite, phlogopite and sericite in the footwall may vary systematically with proximity to the massive sulfide lens. Costa et al. (1983) and McKay (1989) suggested that talc resulted from incorporation of seawater Mg by intermittent turbulent mixing of brine pools with the overlying marine water.

Talc forms by direct precipitation from hydrothermal fluids, replacement of clays, low-grade metamorphism and hydrothermal alteration of mafic rocks and contact or regional metamorphism of calcareous rocks (McLeod and Stanton, 1984; Deer et al., 1992). It typically forms by the following decarbonation reaction during metamorphism and hydrothermal alteration:

$$3CaMgCO_3 + 4SiO_2 + H_2O = Mg_3Si_4O_{10}(OH)_2 + 3CaCO_3 + 3CO_{2(g)} \quad \text{(Yardley, 1989)} \qquad (1)$$

dolomite quartz talc calcite

Reaction 1 occurs at less than 400°C in shallow environments with low confining pressures of approximately 1 000 bars (Slaughter et al., 1975). Although talc at Lewis Ponds is spatially associated with dolomite, the lack of associated calcite (a product of Reaction 1) suggests that talc may have precipitated directly from a low temperature Mg-rich hydrothermal or metasomatic fluid, or that the calcite was involved in other reactions. The relatively coarse-grained, randomly-oriented talc, preserved within dolomite-quartz-sulfide domains probably formed prior to the S_1 cleavage and S_S shear fabric.

The occurrence of talc, Mg-chlorite and phlogopite indicates abundant Mg, Al and K in the hydrothermal fluid and/or proximal carbonate-bearing host rocks at Lewis Ponds. High Ca concentrations in the limestone-bearing facies may have favoured the formation of tremolite at higher metamorphic grades because talc reacts with quartz and calcite or dolomite to produce tremolite at temperatures of greater than 400°C (Slaughter et al. 1972; Yardly, 1989). The preferential formation of talc rather than tremolite at lower temperatures may also indicate low CO_2 concentrations in the fluid. Carbonate-tremolite assemblages occur at Garpenberg, Sweden (Vivallo, 1985) and Thalanga, northern Queensland (Herrmann and Hill, 2001). However, since no tremolite was observed at Lewis Ponds, peak metamorphic temperatures were probably less than 400°C.

Quartz-sericite ± hyalophane and quartz-dolomite-chlorite

The intense, texturally destructive silicified zones probably result from high fluid flux accompanying massive sulfide deposition or the emplacement of syn-tectonic quartz veins. Some of the quartz-rich lenses surrounding cleavage-parallel veins in the Toms zone footwall overprint earlier hydrothermal chlorite-sericite assemblages. Similar quartz-rich lenses have been documented in stratabound (eg. Large et al., 2001c) and pipe-like (eg. Gemmell and Fulton, 2001) alteration systems. Thermodynamic modelling suggests that the siliceous core of the footwall alteration plume at Hellyer formed at approximately 350°C (Schardt et al., 2001).

Phyllosilicate-bearing assemblages

Footwall alteration assemblages vary significantly between the two mineralised zones. In Toms zone, chlorite overprinting the footwall volcanic succession grades into a sericite-quartz-rich assemblage. Chlorite, phengite, biotite and phlogopite compositions become progressively enriched in Fe away from the massive sulfide lens (Fig. 5.16). Proximal phyllosilicates contain higher average Mg, Ba and F concentrations. In contrast, the chlorite envelope surrounding Main zone only occurs in the polymictic breccia and pebble-granular sandstone deposits. The underlying quartz-plagioclase phyric dacite is overprinted by a weak to moderate pervasive sericite-chlorite-calcite assemblage. There are no progressive changes in mineral composition in the immediate footwall to Main zone.

Mineralogical trends in the Toms zone footwall rocks are similar to eastern Australian VHMS deposits. Sericite-rich assemblages surround stratabound chlorite envelopes at Rosebery (Large et al., 2001c), Thalanga (Herrmann and Hill, 2001), Currawong (Allen, 1992; Bodon and Valenta, 1995) and Captains Flat (Davis, 1990). In pipe-like alteration systems, chlorite grades laterally into sericite-quartz away from the silicious core (Large, 1992; Gemmell and Fulton, 2001). Systematic variations in chlorite Mg number have been documented at VHMS deposits in Australia, Japan and Canada (Urabe and Scott, 1983; Urabe et al., 1983; McLeod and Stanton, 1984; McLeod et al., 1987; Paulick et al., 2001). Rosebery is a notable exception, since there is no obvious relationship between alteration intensity and chlorite composition (Large et al., 2001c).

Mineral zonation in the footwall of VHMS deposits is controlled by fluid composition, temperature, redox state, and fluid/rock ratio (Walshe and Solomon, 1981; Galley, 1995; Schardt et al., 2001). The alteration assemblages result from progressive fluid-rock interaction and chemical evolution of the hydrothermal fluid. Thermodynamic and oxygen isotope modelling of footwall alteration predicts that chlorite precipitates from high temperature (250-300°C), weakly acidic (4.5-5.5), Mg-bearing fluids while lower temperature (<250°C),

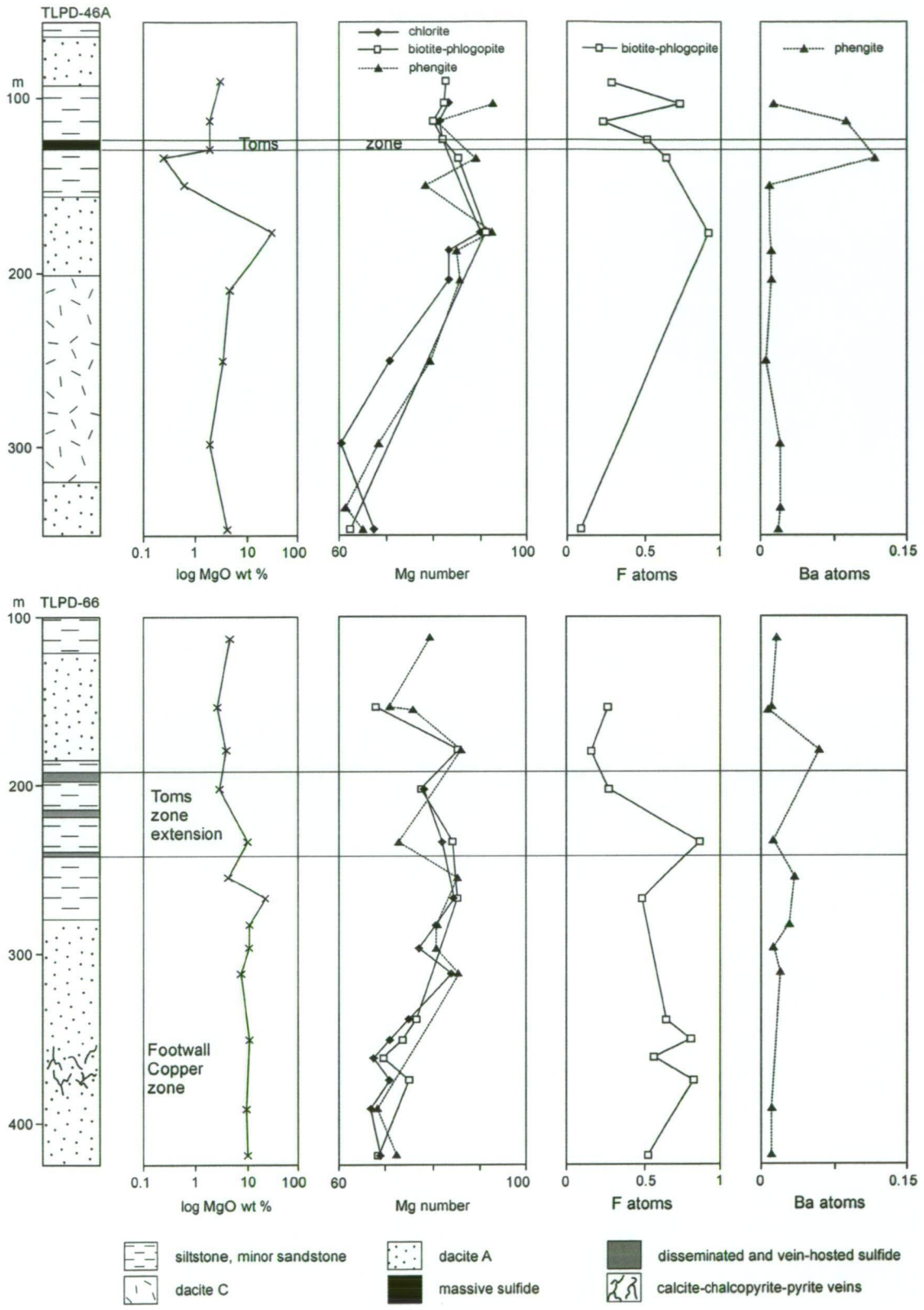

Figure 5.16 Drill logs showing lithology, whole rock MgO concentration and systematic variations in chlorite, phlogopite, biotite and phengite composition in the Toms zone footwall. Whole rock MgO concentration and Mg number, F and Ba content in the micas decrease away from the massive sulfide lens or vein-hosted sulfides. These trends are less pronounced in TLPD-66, where the chlorite-pyrite envelope extends more than 150 m into the footwall volcanic succession. Based on individual microprobe analyses from the fault-bound stratigraphic unit, Transitional Unit and Western Volcanic Succession.

more acidic (4-4.5) fluids produce the surrounding sericite-quartz zones (Urabe et al., 1983; Gemmell and Fulton, 2001; Schardt et al., 2001). Chlorite occurs with dolomite and talc in the polymictic breccia and siltstone deposits in Main and Toms zones. This chlorite may result from near neutral fluids passing through the carbonate-bearing host rocks. Thermodynamic modelling of the Hellyer footwall alteration plume indicates that hydrothermal fluids with high pH stabilise Mg-chlorite precipitation at lower temperatures (<200°C; Schardt et al., 2001).

Jasper lenses

The jasper may represent chemical sediment, altered host rock or quartz-magnetite-hematite veins formed during hydrothermal or deformation-related activity. The jasper contains anomalous Cu, Zn, and Tl concentrations. Immobile element concentrations are significantly lower (below XRF detection limits) than the surrounding siltstone and dacite. The Valliant and Meares (1998) facies model for Lewis Ponds featured a continuous jasper horizon. Their interpretation assumed that a conformable contact separated the Eastern Volcanic Succession from the structurally underlying siltstone. However, poor outcrop prevented accurate observation of the contact during this study. Castle (1976) proposed that the western margin of the Eastern Volcanic Succession was truncated by a NNW-trending fault (Fig. 4.1). More work is required to interpret the formation of the jasper lenses.

Metamorphic assemblages

Regional greenschist facies metamorphism produced biotite throughout the Mullions Range Volcanics and Anson Formation, east of Orange. Cordierite, sphene and randomly oriented biotite, hornblende and phlogopite laths post-date the S_1 cleavage in the Lewis Ponds host rocks. These minerals also overprint pre-existing aligned chlorite and white mica. Secondary biotite in southern and eastern areas of the prospect may result from localised contact metamorphism accompanying emplacement of the Lewis Ponds granite and non-foliated quartz-feldspar porphyry dykes or a later regional metamorphic event.

The first appearance of biotite together with muscovite results from the following reaction, occurring at 300-400°C:

chlorite + K-feldspar = biotite + muscovite + quartz + H_2O (Spear, 1993) (2)

Since K-feldspar does not usually occur in pelitic rocks, biotite also forms by:

chlorite + phengite = biotite + phengite-poor muscovite + quartz + H_2O (Yardley, 1989) (3)

Although chlorite is consumed by Reactions 2 and 3, the remaining phyllosilicates may become enriched in Mg^{2+} due to preferential diffusion of Fe^{2+} into biotite. Therefore, chlorite compositions may be reset during deformation and metamorphism.

Secondary phlogopite replaces pre-exiting mica during high-grade regional metamorphism or precipitates directly from low temperature (eg. <250°C), F-Mg-bearing hydrothermal fluids. It occurs in metamorphosed limestone or Al-poor pelites (Deer et al., 1962; Kearns et al., 1980; Spear, 1993), contact aureoles surrounding intrusions (Rice, 1977) and active geothermal systems (Belkin et al., 1988; Carman, 1994). High fluorine concentrations increase thermal stability of the phlogopite-calcite-quartz assemblage, allowing the mineral to exist in amphibolite to granulite facies rocks (Kearns et al., 1980; Munoz, 1984; Abercrombie et al., 1987).

At Lewis Ponds, phlogopite was probably stabilised at relatively low temperatures due to high Mg and/or F concentrations in the dolomite and chlorite envelopes surrounding the massive sulfide lenses. Higher F concentrations in the Main zone phlogopite may reflect original composition of the carbonate-rich host rocks.

Phyllosilicate compositions at Toms zone vary systematically with whole rock geochemistry, alteration intensity and proximity to the massive sulfide lens (Fig. 5.16). Identical trends occur in chlorite, phengite, biotite and phlogopite Mg number. Proximal phyllosilicates are enriched in Mg, F and Ba. Chlorite and phlogopite occurring in the Main zone host rocks have higher Mg concentrations than phyllosilicates in the siltstone and volcanic rocks in Toms zone, suggesting that whole rock compositions also depend on the original lithology.

5.9 Paragenesis

Spatial and paragenetic relationships among alteration and metamorphic minerals are summarised in Figures 5.17 and 5.18. Diagenesis of the Mullions Range Volcanics involved devitrification, hydration and development of perlitic fractures in the glassy domains of coherent facies and porphyritic rhyolite clasts. Early clays occurring throughout coherent and clastic facies were replaced by K-feldspar, sericite and chlorite. Plagioclase crystals in clastic and coherent rocks were partly overprinted by fine-grained white mica. Calcite and dolomite may have precipitated in the polymictic breccia and fossiliferous quartz crystal-rich sandstone deposits, due to reactions involving cold seawater.

Low temperature hydrothermal activity resulted in dolomite-altered limestone clasts and dolomite cement throughout the polymictic breccia, sandstone and siltstone (Figs. 5.17 and 5.18). Quartz, dolomite, calcite, Mg-chlorite, talc and sulfides filled secondary porosity (vugs and channels) and replaced the dolomite matrix. The clasts were overprinted by patchy to pervasive chlorite-dolomite-talc-pyrite assemblages. Dolomite-sulfide textures occurring throughout Main zone indicate that dolomite precipitated both before and during mineralisation.

The distribution of alteration minerals in the breccia and sandstone deposits was predominantly controlled by clast type and permeability.

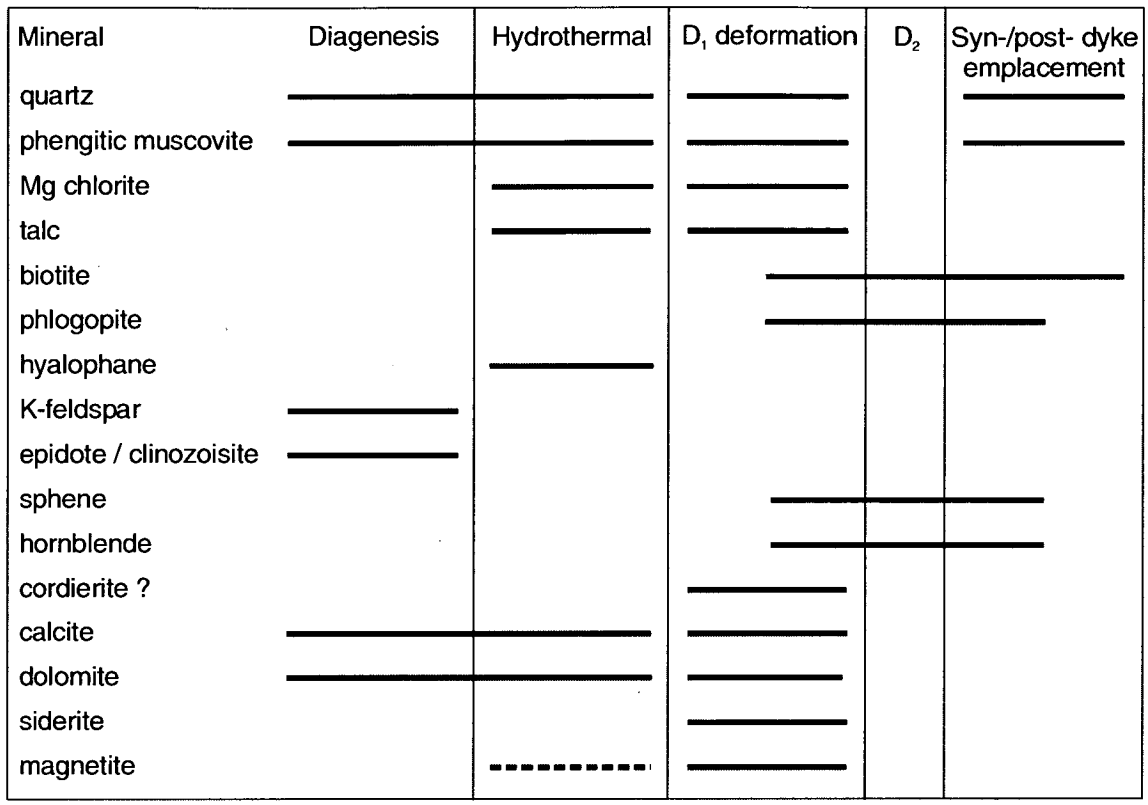

Figure 5.17 Paragenesis of diagenetic, hydrothermal and metamorphic minerals.

Sericite-chlorite-calcite, chlorite-pyrite and sericite-quartz ± chlorite assemblages developed throughout the breccia deposits and footwall volcanics at higher temperatures and fluid-rock ratios (Figs. 5.17 and 5.18). Patchy lenses of texturally destructive quartz-sericite and quartz-dolomite-chlorite formed in the mineralised host rocks. However, some of these silicified zones may be attributed to later fault-related activity.

Quartz-sulfide shear and extension veins resulted from episodic brittle failure in and around the Lewis Ponds fault zone. Many of the larger veins are associated with quartz-sericite and magnesite, siderite or dolomite selvages. Massive talc precipitated along the fault and in the adjacent polymictic breccia deposits, replacing dolomite-altered fossiliferous limestone clasts and the breccia matrix.

Regional greenschist facies metamorphism and cleavage development involved recrystallisation of pre-existing phyllosilicates and growth of new minerals throughout the host sequence. Biotite overprinted sericite in quartz phyric volcanic rocks and non-foliated quartz-feldspar porphyry dykes south of Main zone. Phlogopite formed in the chlorite and dolomite

envelopes surrounding the massive sulfide lenses and replaced pre-existing chlorite. Sphene, epidote and hornblende grew in areas enriched in Ca and Mg.

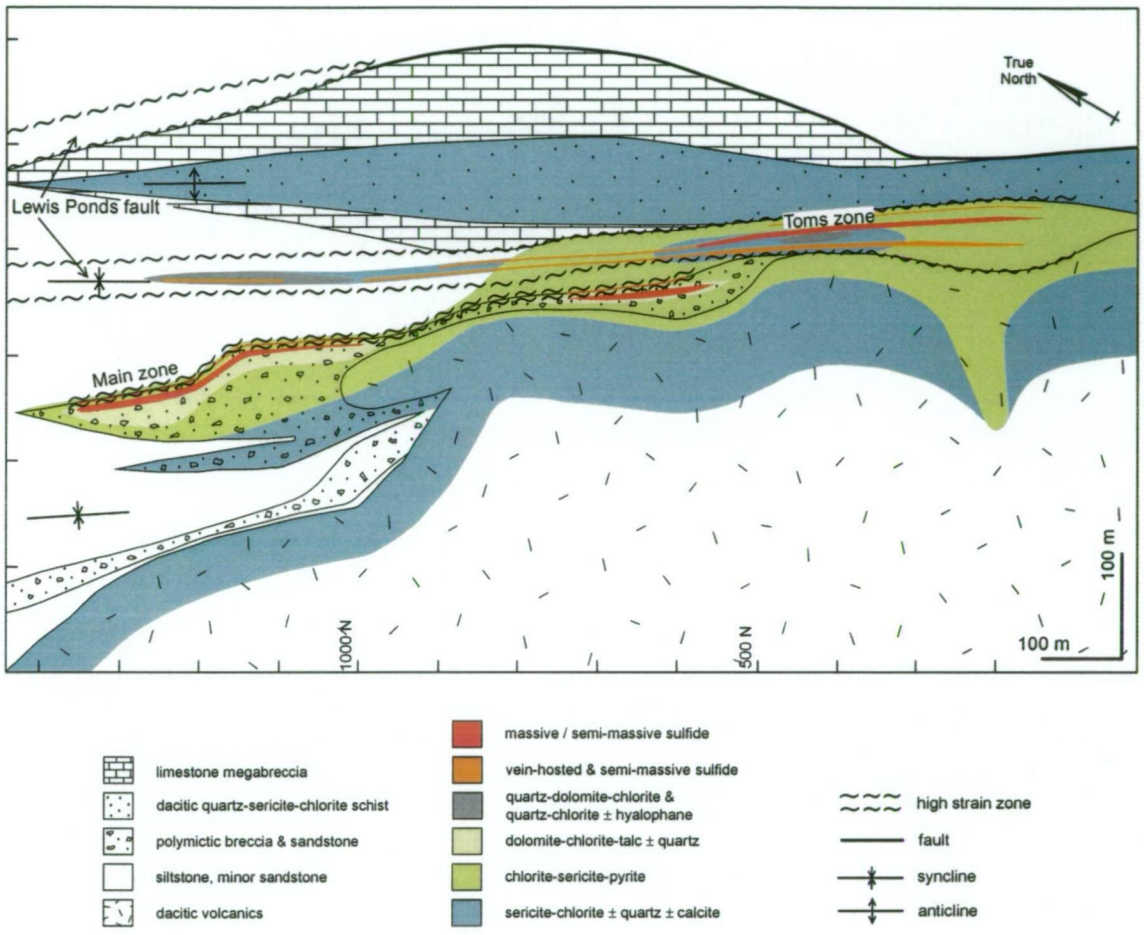

Figure 5.18 Alteration model showing spatial distribution of hydrothermal alteration assemblages at Lewis Ponds. Based on interpreted 600 mRL level plan, compiled from drill hole data.

CHAPTER 6

LITHOGEOCHEMISTRY

6.1 Introduction

Hydrothermal fluid-rock interactions produce distinct alteration mineral zonation in submarine volcanic successions. Lithogeochemical studies have traditionally focussed on:

- separating altered volcanic successions into magmatic affinity groups and rock types (Crawford et al., 1992; Barrett and MacLean, 1994; Barrett et al., 1996);
- determining mass changes in altered volcanic rocks (Barrett and MacLean, 1994; Herrmann and Hill, 2001);
- defining the extent of proximal alteration halos (Gemmell and Fulton, 2001; Large et al., 2001c);
- interpreting the composition and thermal characteristics of the fluid (Sangster and Scott, 1976; Galley, 1995); and
- modelling fluid-rock interactions in the source rocks (Stolz and Large, 1992; Callaghan, 2001).

The regional application of quantitative lithogeochemical techniques serves to delineate prospective areas, favourable horizons and large-scale alteration halos (Galley, 1995; Brauhart et al., 2001). Recent studies have developed methods for vectoring in to massive sulfide deposits by identifying proximal and distal geochemical gradients in whole rock and stable isotope geochemistry and mineral compositions (eg. Large et al., 2001a).

In this chapter, mass balance calculations, alteration indices and element ratios are used to quantify the intensity and spatial extent of hydrothermal alteration in the Lewis Ponds host sequence, thereby determining the nature of the mass changes. A geochemical model is presented for Lewis Ponds based on lithogeochemical trends associated with the massive sulfide lenses. Some of the alteration indices and element ratios are useful exploration vectors for identifying carbonate and volcanic-hosted massive sulfide deposits at the regional scale.

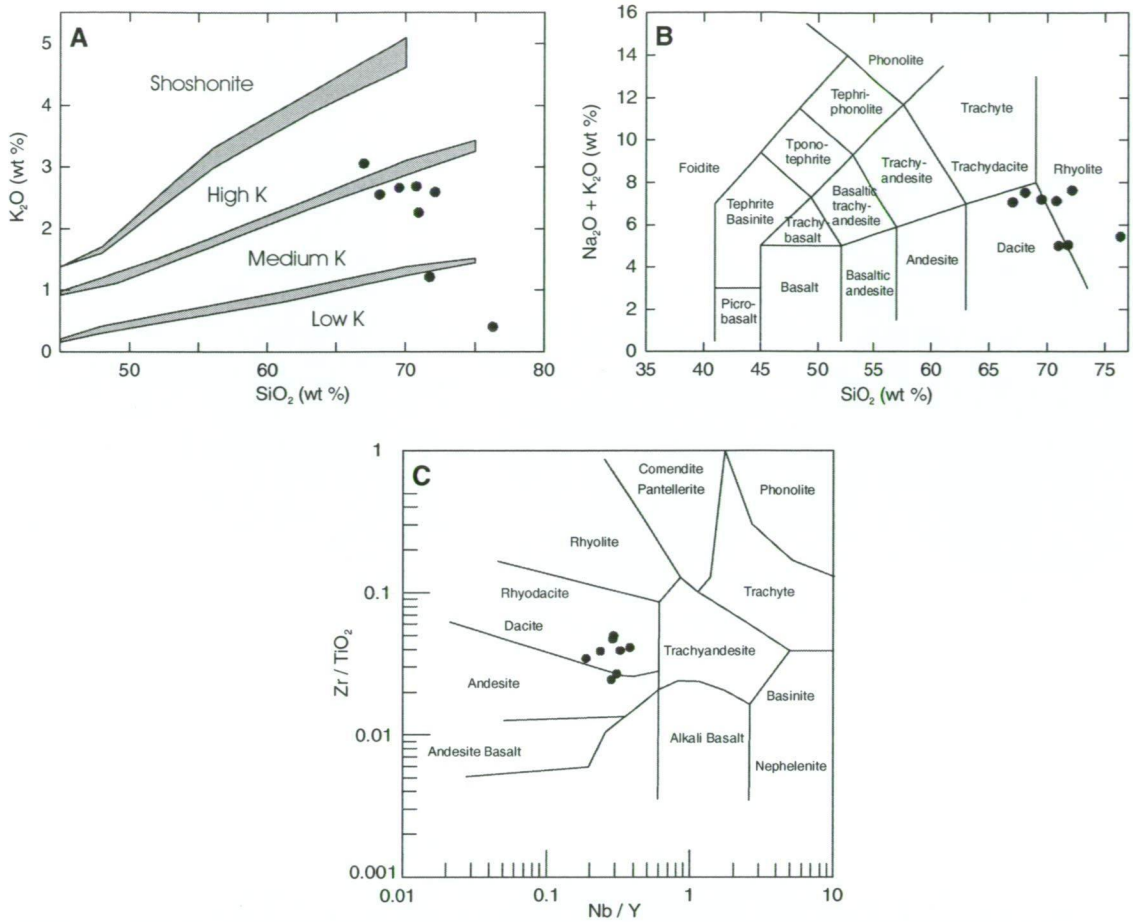

Figure 6.1 Geochemistry of least altered rocks from the Mullions Range Volcanics, including five samples from this study, two from Tri Origin (listed on page 13 of Appendix 4) and sample ORMS0310 from the Geological Survey of New South Wales database. **A.** SiO_2 versus K_2O diagram using the subdivisions outlined in Rollinson (1993). **B.** SiO_2 versus total alkali ($Na_2O + K_2O$) diagram (after Le Maitre, 1989). **C.** Nb/Y versus Zr/TiO_2 discrimination diagram (after Winchester and Floyd, 1977). Variable SiO_2, Na_2O and K_2O concentrations result from weak diagenetic or hydrothermal alteration.

X-Y scatter plots of compatible-incompatible and compatible-compatible immobile element pairs are useful for identifying individual units and quantifying mass changes in altered volcanic successions (Crawford et al., 1992; Herrmann and Hill, 2001). Net mass gains and losses of mobile components produce highly-correlated ($r \cong 0.85$ to 0.99) linear trends, passing through the origin and precursor compositions due to immobile element dilution or concentration (MacLean, 1990; MacLean and Barrett, 1993; Barrett et al., 1996). In multiple precursor systems, an array of lines result from hydrothermal alteration of a fractionated magmatic series (MacLean and Barrett, 1993).

The footwall volcanic succession at Lewis Ponds consists of three lithofacies associations; A, B and C, distinguishable in drill core by the abundance and size of the phenocrysts (Chapter 3, section 3.3). The variably altered rocks have similar Zr/TiO_2 and Nb/Y values to least altered rocks in the Mullions Range Volcanics, indicating that Zr, Ti, Y and Nb were relatively immobile during hydrothermal alteration (Fig. 6.2). Although samples contain visible quartz phenocrysts, they predominantly plot as dacite on immobile element discrimination diagrams.

Sample compositions lie along three linear trends on immobile element X-Y scatter plots, with correlation coefficients (r) generally greater than 0.85 (Fig. 6.3). Least altered rocks define an approximate fractionation trend of decreasing TiO_2 and Cr and increasing Zr. Quartz-feldspar porphyry clasts from the overlying polymictic breccia unit occur on the same alteration line as lithofacies association B. Figure 6.3 demonstrates that Zr, TiO_2, Cr, Sc and V were immobile in the footwall volcanic succession. Variability of Al_2O_3, Y and Nb concentrations may reflect primary chemical heterogeneities in the volcanic units or remobilisation during hydrothermal alteration.

Immobile element concentrations in strongly foliated, quartz phyric rocks from the fault-bound stratigraphic unit and Eastern Volcanic Succession also define an alteration line (Fig. 6.4). Comparisons of this line to those of the footwall volcanic succession indicate that quartz phyric dacite in the structural hangingwall of Lewis Ponds has a similar immobile element composition and probably magmatic affinity to lithofacies association A.

6.5 Alteration indices and element ratios

Lithogeochemical indices and element ratios have been developed to quantify alteration zonation and changes in alteration intensity associated with VHMS deposits.
Ishikawa *Alteration Index*:

$$AI = \frac{100(K_2O + MgO)}{(K_2O + Na_2O + MgO + CaO)} \qquad \text{varies from 0 to 100} \qquad (1)$$

The alteration index (Equation 1), defined by Ishikawa (1976), quantifies phyllosilicate alteration of footwall volcanic rocks. Sericite and chlorite progressively replace plagioclase phenocrysts and glassy domains in the groundmass by the following reactions:

$$\underset{\text{albite}}{3NaAlSi_3O_8} + K^+ + 2H^+ = \underset{\text{sericite}}{KAl_3Si_3O_{10}(OH)_2} + \underset{\text{quartz}}{6SiO_2} + 3Na^+ \quad \text{(Large et al., 2001b)} \qquad (2)$$

$$2KAl_3Si_3O_{10}(OH)_2 + 3H_4SiO_4 + 9Fe^{2+} + 6Mg^{2+} + 18H_2O =$$
$$\underset{\text{sericite}}{} \qquad \underset{\text{chlorite}}{3Mg_2Fe_3Al_2Si_3O_{10}(OH)_8} + 2K^+ + 28H^+ \qquad (3)$$

The replacement of albite by sericite (Equation 2) involves addition of K_2O and removal of Na_2O in outer parts of the hydrothermal system. This may produce district-scale quartz-sericite assemblages (eg. Eastoe et al., 1987; Brauhart et al., 2001). Chlorite results from higher temperature MgO and FeO metasomatism and replacement of sericite (Equation 3) adjacent to the massive sulfide body (Urabe et al., 1983; Large, 1992; Gemmell et al., 1998; Schardt et al., 2001).

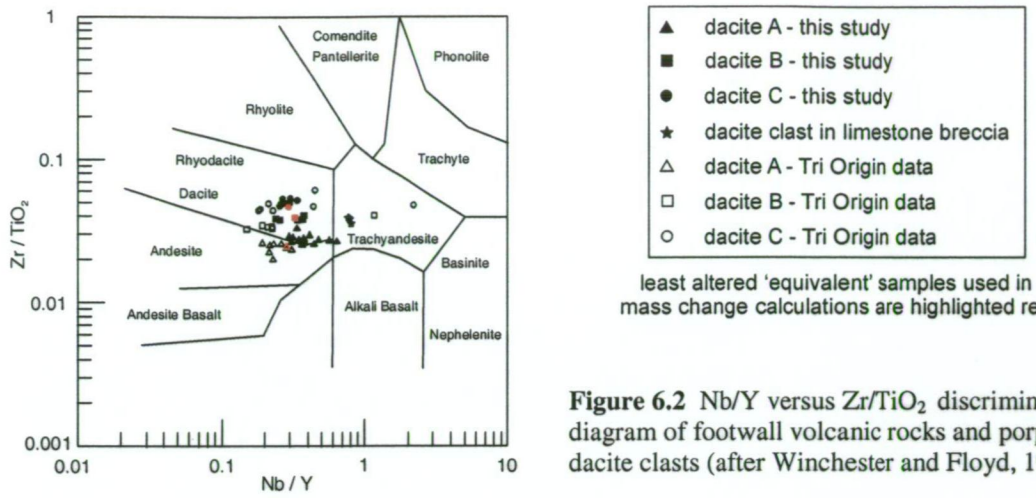

Figure 6.2 Nb/Y versus Zr/TiO_2 discrimination diagram of footwall volcanic rocks and porphyritic dacite clasts (after Winchester and Floyd, 1977).

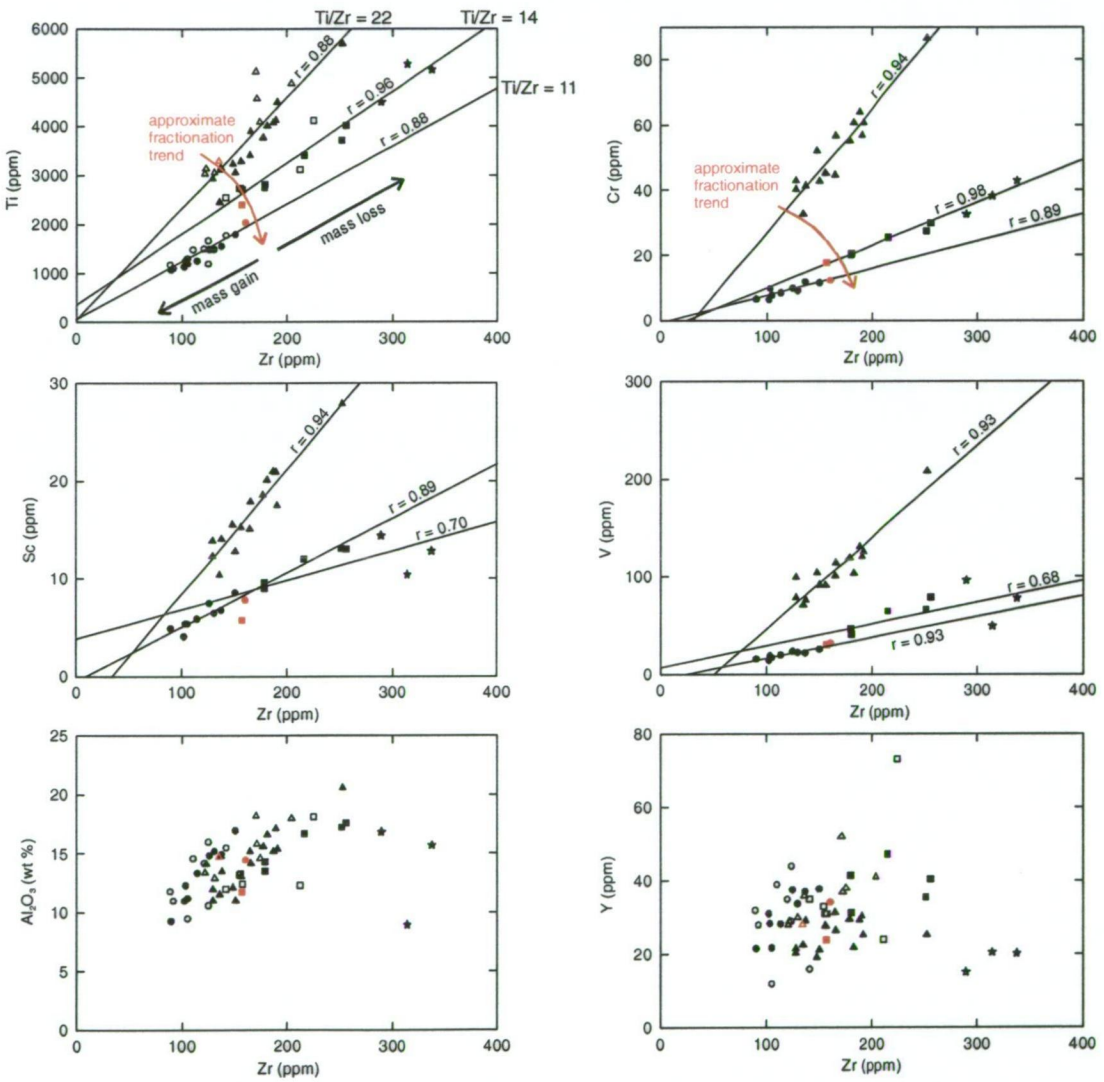

Figure 6.3 Immobile element composition of footwall volcanics and porphyritic dacite clasts. Samples from lithofacies associations A, B and C lie along three highly correlated linear trends which extend toward the origin. The spread of data reflects concentration or dilution of immobile elements by mass exchange of mobile components during hydrothermal alteration. Least altered equivalent rocks (highlighted in red) define a fractionation trend of decreasing TiO_2 and Cr and increasing Zr. Strongly altered porphyritic dacite pebbles in the limestone-clast breccia have a similar magmatic affinity to dacite B. Calculated linear regression lines and correlation coefficients are shown. Note that Cr, Sc and V analyses are not available for whole rock compositions provided by Tri Origin. Based on 54 XRF analyses from the Western Volcanic Succession and 3 from the Transitional Unit.

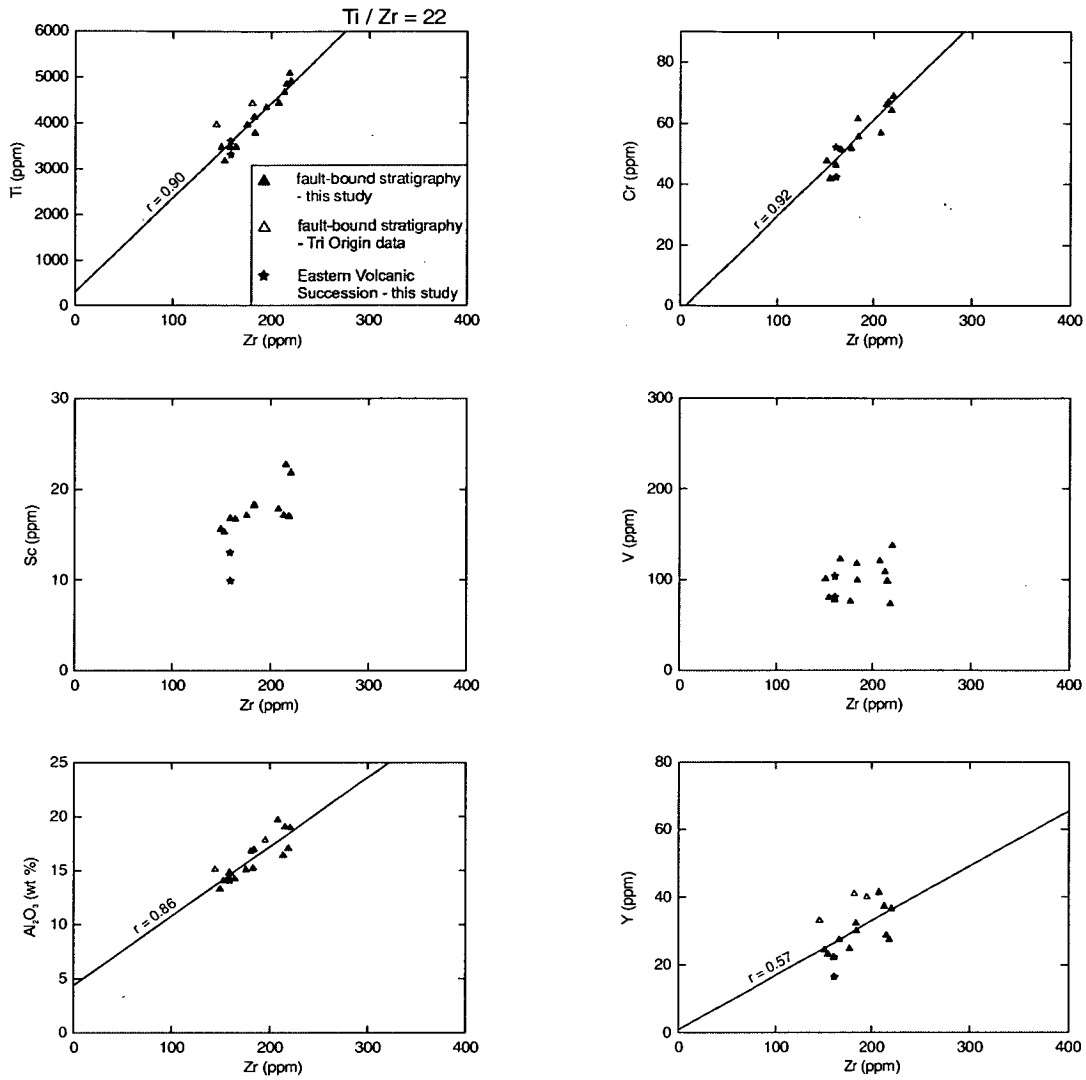

Figure 6.4 Immobile element geochemistry of volcanic rocks in the structural hangingwall. Samples define an alteration trend corresponding to lithofacies association A in the footwall volcanic succession. Calculated linear regression lines and correlation coefficients are shown. Based on 17 XRF analyses.

Iron and Mg-bearing minerals such as chlorite, dolomite, siderite, and pyrite dominate proximal alteration assemblages in VHMS deposits (McLeod and Stanton, 1984; Herrmann and Hill, 2001; Large et al., 2001c). Chlorite surrounds and partly overprints the siliceous core underlying mound-style deposits such as Hellyer, north western Tasmania (Gemmell and Fulton, 2001). Conformable chlorite and carbonate envelopes are strongly developed in the immediate footwall or hangingwall of stratabound massive sulfide lenses (eg. Herrmann and Hill, 2001; Large et al., 2001c). The Chlorite-Carbonate-Pyrite Index (Equation 4) was developed to quantify the addition of FeO and MgO (Large et al., 2001b).

Chlorite-Carbonate-Pyrite Index:

$$CCPI = \frac{100(MgO + FeO)}{(MgO + FeO + Na_2O + K_2O)} \qquad \text{varies from 1 to 100} \qquad (4)$$

Other whole rock lithogeochemical vectors applied to VHMS deposits include the S/Na_2O and Ba/Sr ratios (eg. Large et al., 2001c). The S/Na_2O ratio increases by three or four orders of magnitude in host rock surrounding massive sulfide lenses due to disseminated sulfides and chlorite-sericite alteration of the footwall volcanics. Barium substitutes for Al in white micas, whereas Sr occurs in albite (Deer et al., 1992; Large et al., 2001c). Therefore elevated Ba/Sr ratios result from feldspar destructive sericite alteration of plagioclase phenocrysts and glassy domains. Low Ba/Sr ratios may indicate carbonate alteration because Sr also substitutes for Ca in carbonate.

6.6 Geochemistry of alteration halos

The following section summarises whole rock geochemical trends associated with the two massive sulfide zones at Lewis Ponds. Lithogeochemical data are presented as logs (Figs. 6.5, 6.6 and 6.8) and contoured cross-sections (Fig. 6.7).

Main zone

The broad asymmetric alteration halo surrounding Main zone consists of >1.5 wt % S, >100 ppm As, Cu, Pb and Zn, 4-30 ppm Tl and >20 ppm Ni. Polymictic breccia and pebbly-granular sandstone units hosting the massive sulfide lenses are characterised by:

- AI values ranging from 32 to 98 (Fig. 6.5);
- variable CaO (2-35 wt %), MgO (3-21 wt %) and Fe_2O_3 (0-15 wt %) concentrations;
- high CCPI (>80) and S/Na_2O (>2) values; and
- generally low SiO_2 (40 wt % avg.), K_2O (1.5 wt % avg.) and Ba (<250 ppm).

AI and CCPI values, in the overlying and underlying siltstone increase systematically from 60 to 97 toward the massive sulfide lens and Ba/Sr varies from 10 to 275 (Fig. 6.5). Quartz-plagioclase phyric dacite in the footwall volcanic succession has higher average Na_2O and Sr concentrations than the overlying siltstone. However, AI and CCPI values are significantly lower in the footwall volcanic rocks.

High AI, CCPI and S/Na_2O values coincide with chlorite-pyrite, dolomite-chlorite-talc and sulfide-dominant assemblages occurring in the altered polymictic breccia, sandstone and siltstone surrounding the Main zone Central massive sulfide lens. Lower AI and Ba/Sr values in the breccia deposits reflect variable CaO and Sr concentrations due to the limestone clasts and patchy carbonate-altered matrix. Relatively high Na_2O and Sr concentrations and low AI values in the footwall dacite (lithofacies association B) indicate the preservation of plagioclase phenocrysts.

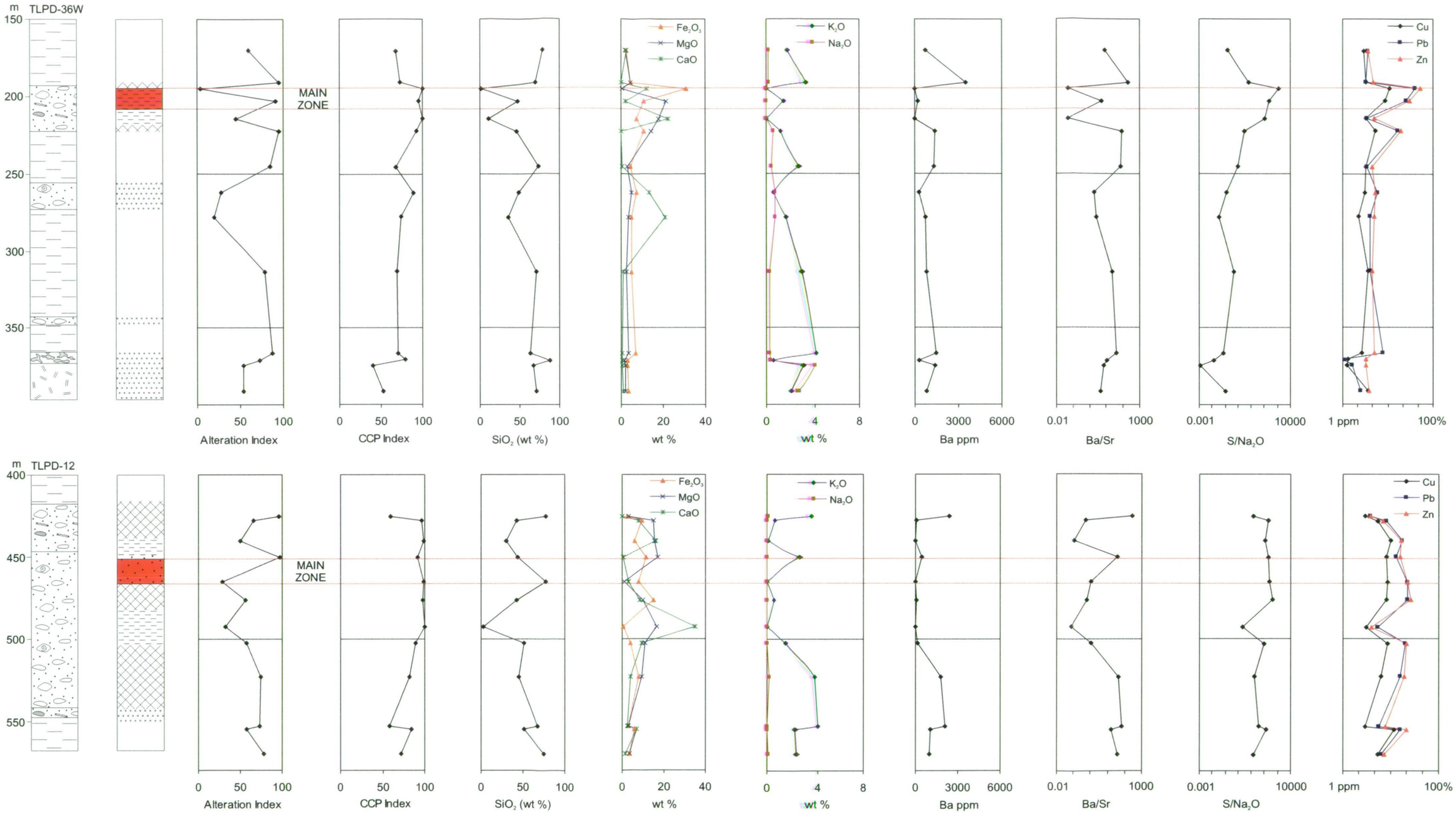

Figure 6.5 Lithogeochemical trends associated with Main zone. Drill logs showing lithology, alteration assemblages, element abundance and AI, CCPI, Ba/Sr and S/Na_2O values. TLPD-36W extends from the Hangingwall Siltstone Unit into the footwall, Western Volcanic Succession. Section from TLPD-12 only occurs in the Transitional Unit.

Toms zone

Toms zone is associated with a strongly-developed, asymmetric alteration envelope that extends from the hangingwall to the footwall volcanic rocks (Figs. 6.6 and 6.7). AI and CCPI values progressively increase from 50 to 99 with alteration intensity, toward the massive sulfide lens. Barium, SiO_2 and S/Na_2O values also increase systematically within this envelope. Anomalous Zn (100-500 ppm) and Ba/Sr (>10) values extend more than 100 m into the footwall volcanic succession (Fig. 6.7). Dolomite-chlorite-talc-altered rocks hosting the massive sulfide lens have relatively low SiO_2, K_2O and Ba concentrations and low AI values (Fig. 6.6). Higher average K_2O and Na_2O concentrations occur in the hangingwall and footwall volcanic rocks due to pervasive sericite and variable preservation of plagioclase phenocrysts (Figs. 6.6 and 6.7).

Immediately south of Toms zone, the quartz-sulfide veins, disseminated sulfides and calcite-chalcopyrite-pyrite veins are surrounded by a broad alteration envelope consisting of 4-22 wt % MgO, 2-10 wt % Fe_2O_3, 0-4 wt % K_2O and less than 0.5 wt % Na_2O (Fig. 6.8). AI values within the alteration envelope range from 90 to 99. CCPI values are considerably higher in the footwall (80-97) than in the hangingwall (40-61).

Lithogeochemical indices and element ratios associated with Toms zone reflect alteration mineralogy and proximity to the massive sulfide lens. High AI, CCPI and S/Na_2O values result from extensive, feldspar destructive chlorite and sericite alteration of the footwall and hangingwall volcanic rocks. Anomalous Ba concentrations (0.2-2 wt %) coincide with quartz-sericite ± hyalophane assemblages occurring in the immediate footwall (see Chapter 5, section 5.4). As with Main zone, the dolomite-chlorite-talc assemblage hosting the massive sulfide is characterised by relatively low AI values due to the predominance of dolomite (CaO occurs in the denominator in Equation 1).

The *box plot* is a simple graphical representation of hydrothermal and diagenetic alteration trends in coherent volcanic units (Large et al., 2001b). Changes in AI and CCPI reflect the alteration intensity and the relative abundance of alteration minerals. Least altered rocks at Lewis Ponds plot within a box, arbitrarily defined by AI = 20-60 and CCPI = 15-50 (Fig. 6.9). Volcanic rocks in the Toms zone footwall (dacite A and C) extend radially from the least altered box to higher AI and CCPI values depending on the relative abundance of chlorite and sericite, ie. the intensity of plagioclase destructive phyllosilicate alteration. In Main zone, lower AI and CCPI values in volcanic rocks at the top of the footwall volcanic succession (dacite B) reflect moderate to strong pervasive sericite-chlorite-calcite alteration of the groundmass and the preservation of plagioclase phenocrysts.

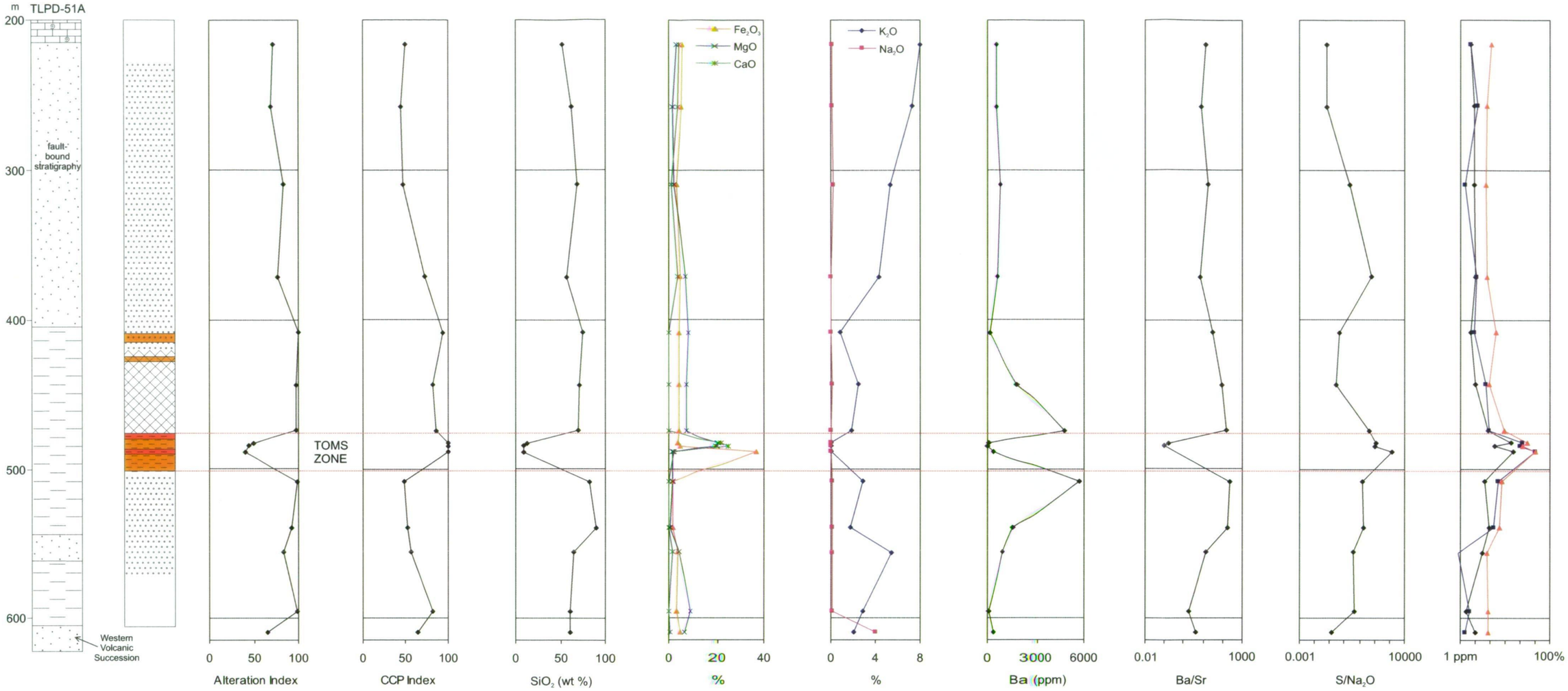

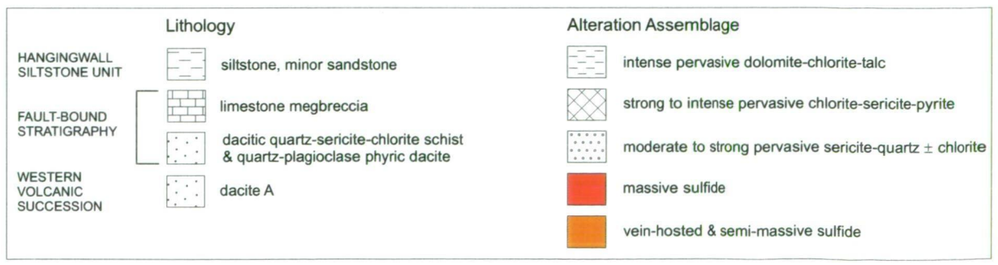

Figure 6.6 Lithogeochemical trends associated with Toms zone. Drill logs showing lithology, alteration assemblages, element abundance and AI, CCPI, Ba/Sr and S/Na_2O values in TLPD-51A.

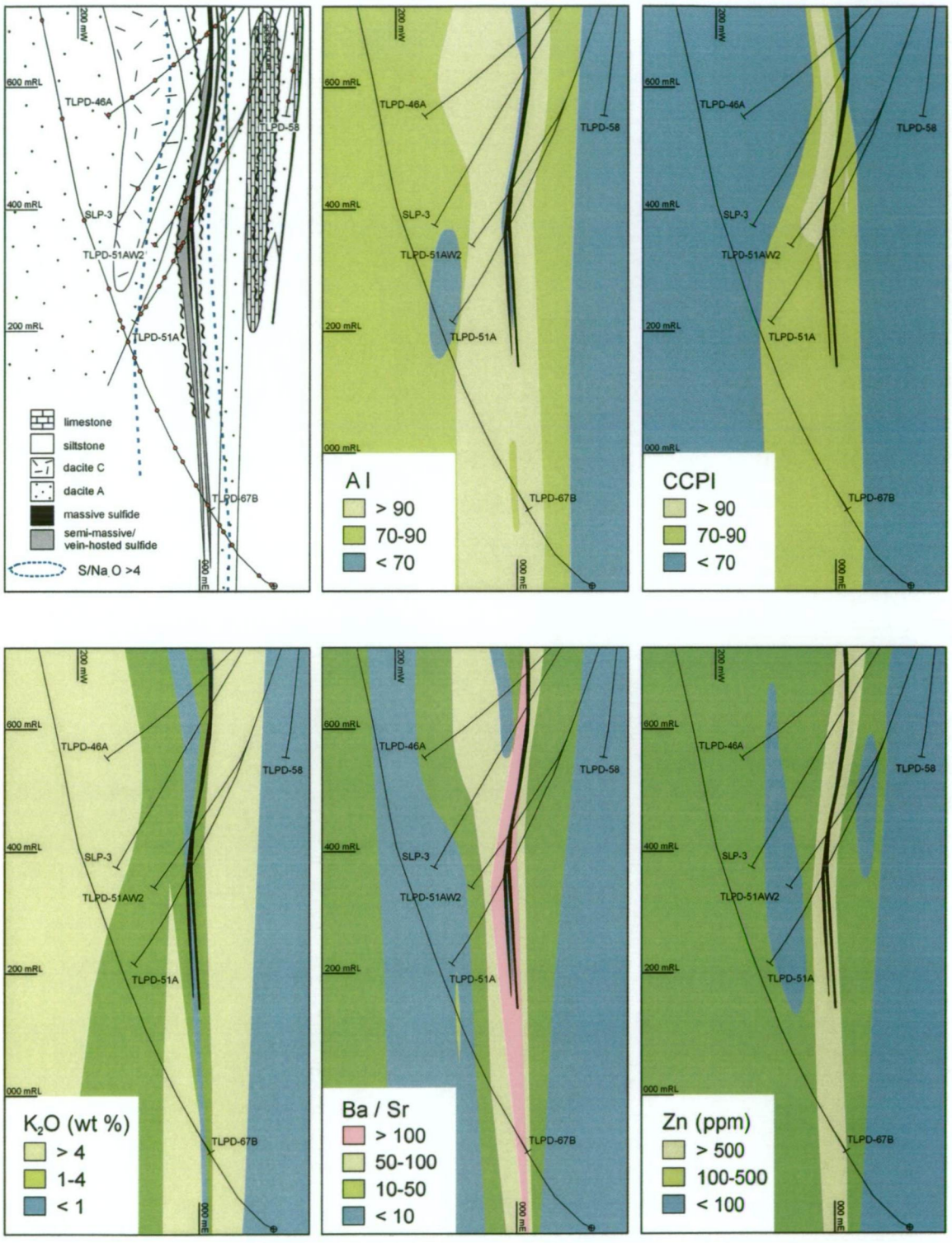

Figure 6.7 Contoured cross-sections illustrating spatial variations in Alteration Index, Ba/Sr, S/Na_2O and Chlorite-Carbonate-Pyrite Index values and K_2O and Zn concentrations associated with Toms zone. Based on 49 whole rock analyses from this study and four unpublished analyses from Tri Origin. Drill core sample locations are shown as red dots on the lithological section. The highest AI, CCPI, Ba/Sr, S/Na_2O and Zn values occur in host rocks immediately surrounding the Toms Central massive sulfide lens. Dolomite-bearing alteration assemblages account for the low AI and Ba/Sr values. The highest K_2O concentrations occur in the hangingwall and footwall volcanic successions, where alteration mineral assemblages contain phengitic white mica.

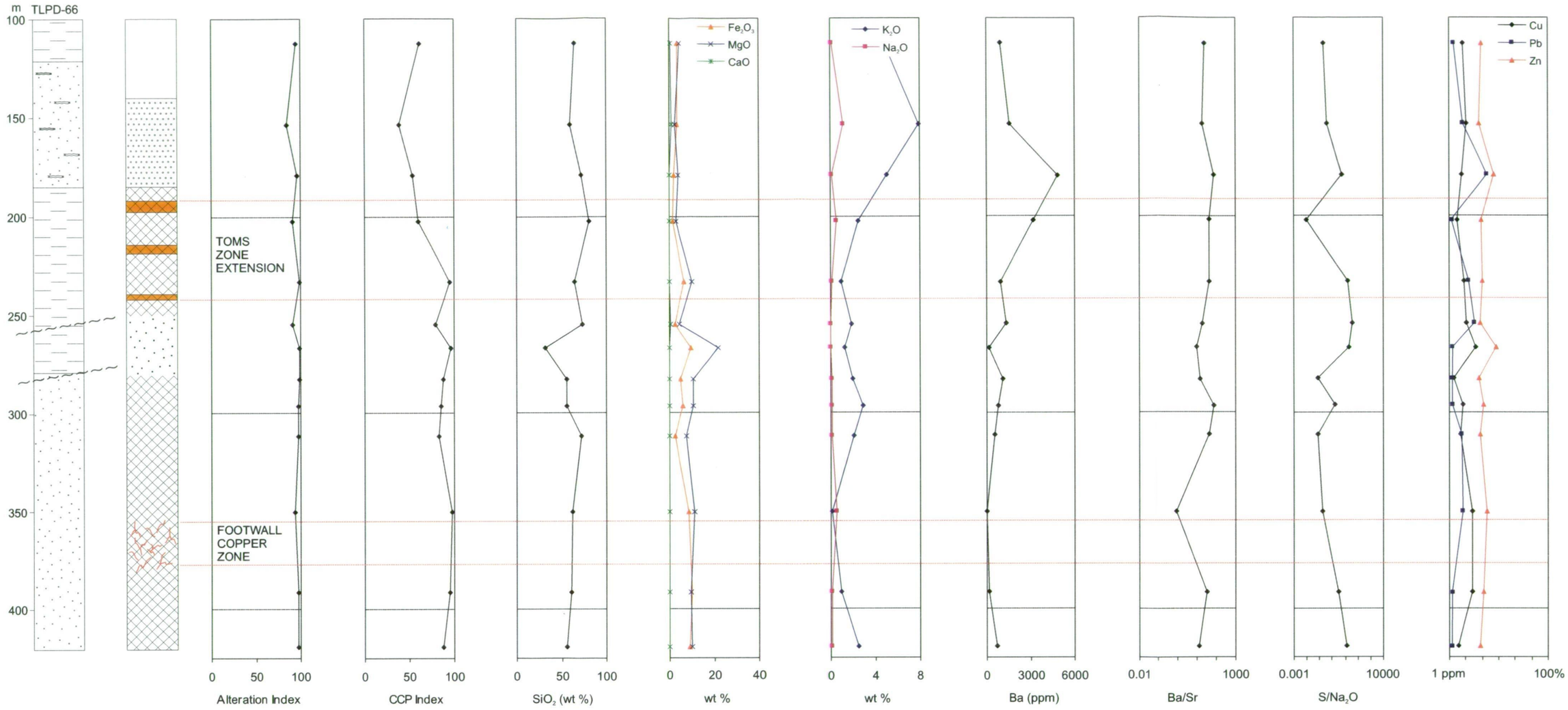

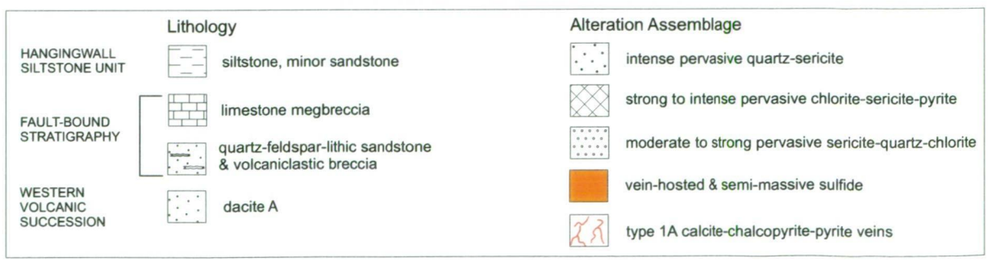

Figure 6.8 Lithogeochemical trends associated with the Footwall Copper zone. Drill logs showing lithology, alteration assemblages, element abundance and AI, CCPI, Ba/Sr and S/Na_2O values in TLPD-66.

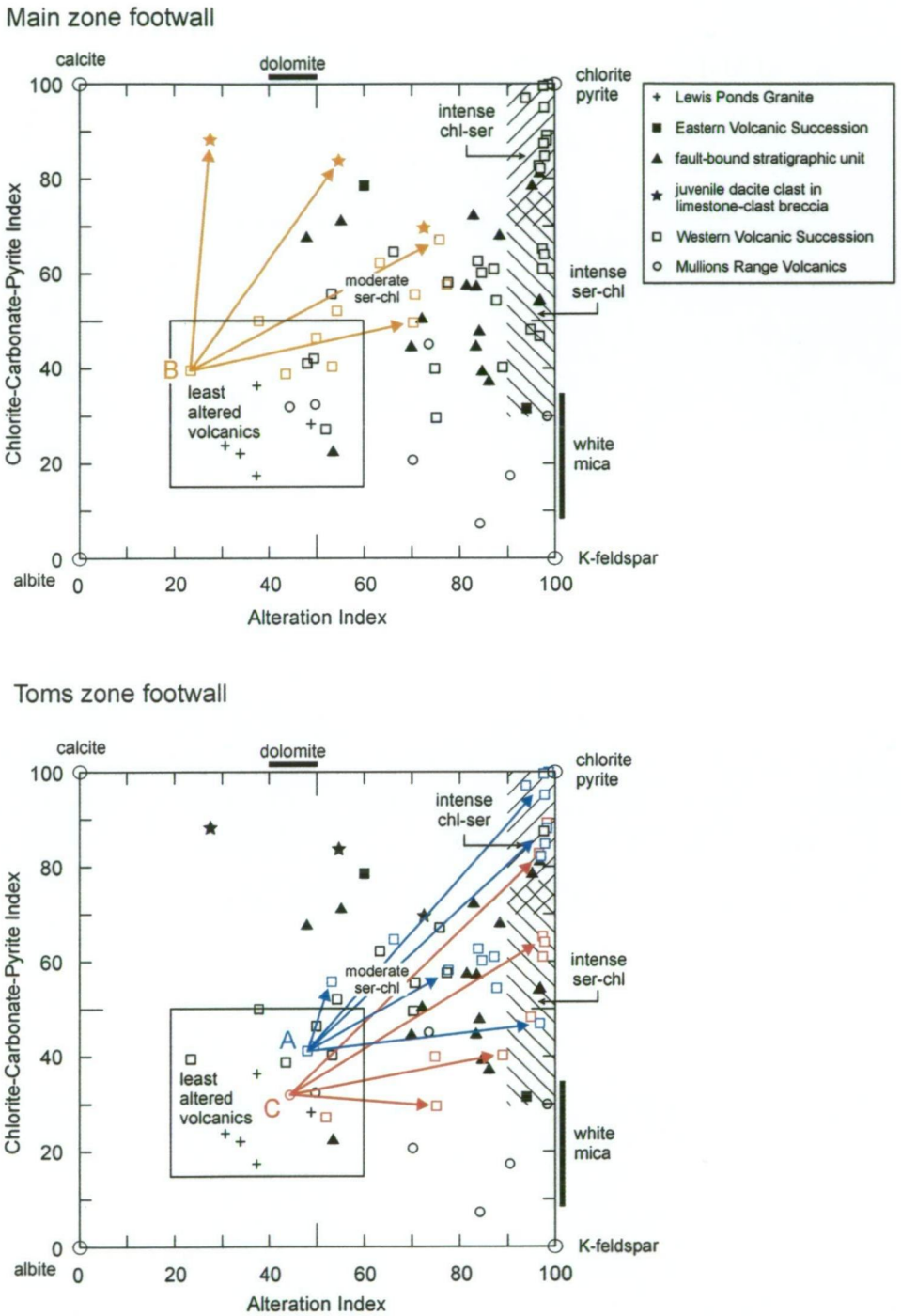

Figure 6.9 Box plots illustrating footwall hydrothermal alteration trends in dacite A (blue), dacite B (orange) and dacite C (red). The common hydrothermal minerals, chlorite, sericite, dolomite and calcite plot along the right hand AI axis and upper CCPI axis. Least altered rocks occur in a box arbitrarily defined by AI = 20-60 and CCPI = 15-50. Data from the Toms zone footwall (dacite A and dacite C) extend radially toward the right hand side of the diagram due to variations in chlorite and sericite abundance throughout the groundmass. Quartz-plagioclase phyric dacite in the Main zone footwall (dacite B) has lower AI and CCPI values due to moderate to strong pervasive sericite-chlorite-calcite alteration of the groundmass. Abbreviations: chl = chlorite and ser = sericite.

6.7 Mass changes in altered dacite

Mass changes are determined for each mobile element using the relative amount of dilution or concentration of an immobile component such as Zr (MacLean and Barrett, 1993; Barrett and MacLean, 1994). Equation 5 compares the concentrations of mobile elements in an altered rock to those of an equivalent precursor. This method requires an accurate estimation of the precursor composition. However, many deposit-scale studies compare variably altered rocks to the least altered equivalent rather than an unaltered precursor (eg. Herrmann and Hill, 2001).

$$\text{Absolute mass change} = \left[\left(\frac{Zr^o}{Zr^a}\right)C^a\right] - C^o \qquad \text{(MacLean and Barrett, 1993)} \qquad (5)$$

where: Zr^o = wt % concentration of Zr in precursor rock

Zr^a = wt % concentration of Zr in altered rock

C^o = wt % concentration of mobile component in precursor rock

C^a = wt % concentration of mobile component in altered rock

Coherent samples with the lowest combined AI + CCPI value were considered the least altered equivalents of the dacite (Table 6.1). These samples contained weak pervasive sericite-biotite or sericite-chlorite-calcite assemblages. Mass changes in the Main zone footwall were calculated using coherent dacite and porphyritic dacite pebbles in the footwall volcanic succession and limestone-clast breccia unit. Immobile element ratios indicate that the clasts have similar magmatic affinities to lithofacies association B (Fig. 6.2). Samples of dacite A and C provided the basis for determining mass changes in the Toms zone footwall and hangingwall volcanics. Mass changes were not calculated for alteration assemblages in the sedimentary rocks because immobile element concentrations are highly variable (Appendix 4).

Footwall unit	Sample	AI	CCPI	AI + CCPI	Ba/Sr	S/Na_2O
Dacite A	LP67B651	48	41	89	1.6	-
Dacite B	LP43386	23	40	63	0.38	<0.002
Dacite C	MRV24	44	32	76	3.2	<0.002

Table 6.1 Least altered porphyritic dacite samples from the footwall volcanic succession used in mass change calculations. LP67B561 is a Tri Origin drill core sample from the Toms zone footwall. LP43386 and MRV24 are drill core and surface samples analysed at the University of Tasmania. Elevated Ba/Sr ratios in LP67B651 and MRV24 indicate the occurrence of minor sericite and/or biotite. Sulfur was below XRF detection limits in LP43386 and MRV24.

Mass changes in selected samples from the footwall and hangingwall dacites are presented in Table 6.2 and Figure 6.10. Hydrothermal alteration in the Main zone footwall resulted in CaO, MgO, Fe_2O_3 and K_2O enrichment and depletion of SiO_2, Al_2O_3 and Na_2O. This produced net losses of 0-40 g/100g in the coherent dacite and 40-60 g/100g in the porphyritic dacite clasts. Primary variations in plagioclase phenocryst abundance may account for the apparent depletion of Al_2O_3, which is usually considered immobile (Winchester and Floyd, 1977).

	Main zone footwall ← massive sulfide lens			Toms HW	Toms zone footwall ← massive sulfide lens				
g/100g	LP36W262 dacite clast	LP36W374 dacite B	LP36W391 dacite B	LP46A090 dacite A	LP46A177 dacite A	LP46A210 dacite C	LP46A250 dacite C	LP46A297 dacite C	LP46A346 dacite A
SiO_2	-52.1	-34.7	-14.1	-4.5	-52.5	16.0	14.1	46.8	-14.4
TiO_2	0.0	0.0	0.0	0.0	0.0	0.0	0.0	0.0	0.0
Al_2O_3	-7.2	-1.0	0.1	-2.8	-3.8	4.6	4.3	4.6	-3.2
Fe_2O_3	1.4	-0.4	0.8	-0.7	0.4	1.7	1.2	1.1	1.5
MgO	0.9	-0.2	0.5	0.4	13.4	4.4	2.9	1.4	0.9
CaO	5.7	-0.7	-0.1	-0.4	-0.4	-0.1	-0.1	0.1	-0.4
Na_2O	-4.6	-2.6	-2.7	-4.9	-4.9	-4.9	-4.9	-4.9	-3.8
K_2O	-0.1	1.5	1.6	1.6	-2.5	2.4	2.2	3.6	1.2
MnO	0.2	0.0	0.0	0.0	0.0	0.1	0.1	0.0	0.0
P_2O_5	0.0	0.0	0.0	0.0	-0.1	0.1	0.0	0.2	0.0
S	0.0	0.0	0.3	0.5	0.0	0.5	0.1	0.0	0.3
Ba	0.0	0.1	0.1	0.2	0.0	0.1	0.1	0.1	0.1
Cu	0.0	0.0	0.0	0.0	0.0	0.0	0.0	0.0	0.0
Pb	0.0	0.0	0.0	0.0	0.0	0.0	0.0	0.0	0.0
Zn	0.0	0.0	0.0	0.0	0.0	0.0	0.2	0.0	0.0
Net change	-55.7	-38.1	-13.4	-10.6	-50.4	24.8	20.0	53.0	-17.9

Table 6.2 Absolute mass changes in hangingwall and footwall quartz phyric dacite samples based on comparison of least altered rocks in Table 6.1 with whole rock compositions from two drill holes: TLPD-36W and TLPD-46A (all in g/100g). Calculated using Equation 5 (MacLean and Barrett, 1993; Barrett and MacLean, 1994). Positive values indicate mass gains. MgO additions in the Toms zone footwall vary with proximity to the massive sulfide lens.

Hydrothermal alteration in Toms zone involved additions of MgO, Fe_2O_3 and K_2O with losses of CaO and Na_2O (Fig. 6.10). Calcium enrichment occurred in parts of the hangingwall due to the emplacement of syn-tectonic calcite veins. The removal of SiO_2 from dacite A contributed to net losses of 0-50 g/100g in the Toms zone hangingwall and footwall. However, significant additions of Fe_2O_3 and MgO to chlorite-altered rocks surrounding the Footwall Copper zone resulted in small gains of 1-2 g/100g. In contrast, dacite C gained 0-75 g/100g due mainly to SiO_2 enrichment in the immediate footwall of Toms zone.

Trace element exchanges were similar in the footwall volcanic rocks of both mineralised zones. Mass changes involved additions of Ba (0-3000 g/10^6g), Zn (0-480 g/10^6g), Ni (0-20 g/10^6g) and As (0-12 g/10^6g) and removal of 50-250 g/10^6g of Sr (Fig. 6.10). Hydrothermal alteration resulted in Cu, Pb, Sc, Ce, Y and Nd enrichment or depletion relative to the least altered rocks. However, only Ba contributed significantly to the overall net mass changes.

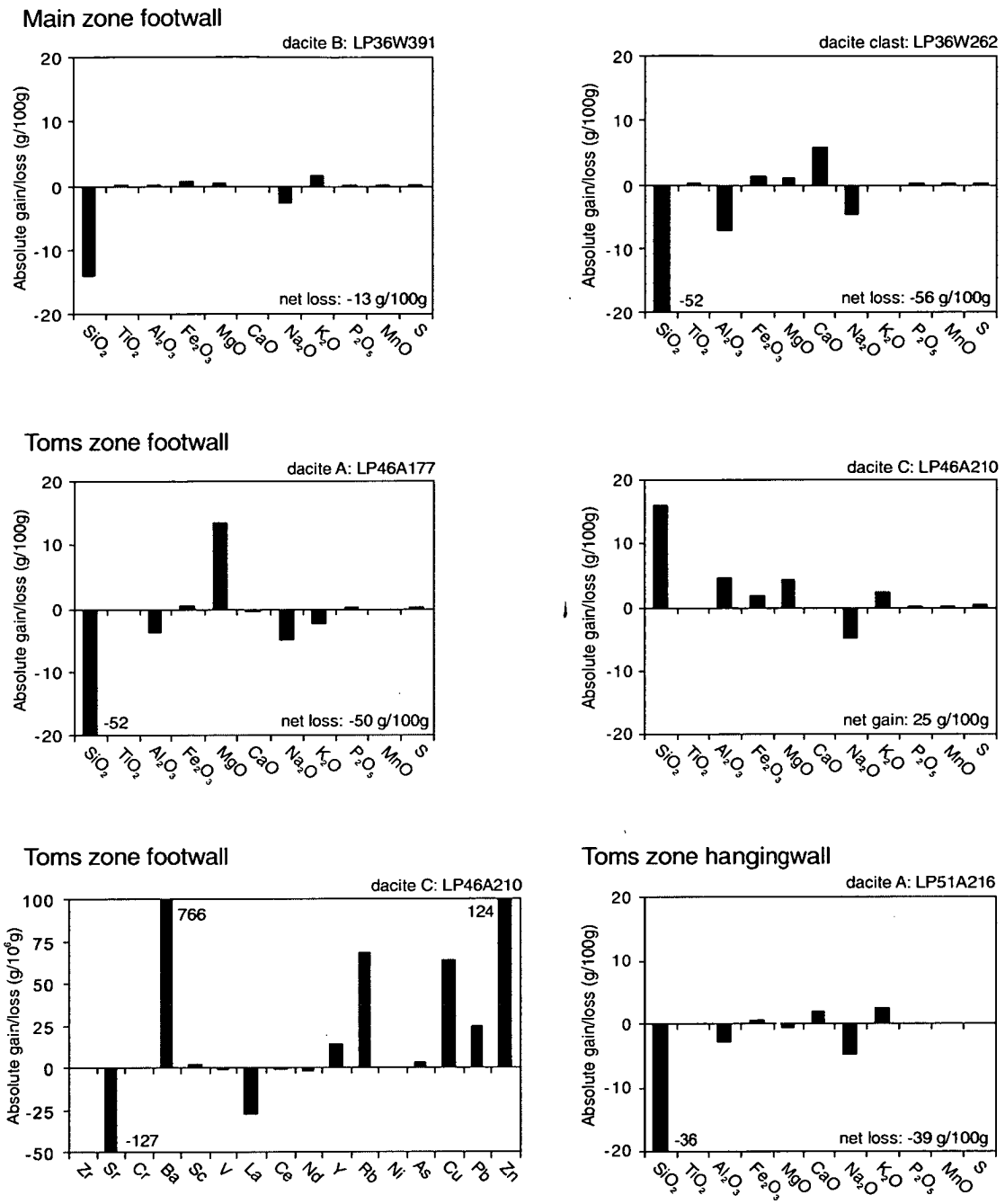

Figure 6.10 Mass changes in selected footwall and hangingwall dacite samples from Main and Toms zones. Calculated using Equation 5. Mass change data are listed in Appendix 4.

Coherent dacite at the top of the footwall volcanic succession and porphyritic dacite clasts in the polymictic breccia unit underwent the largest net mass changes at Lewis Ponds due to enrichment of MgO and enrichment or depletion of SiO_2 during hydrothermal alteration and mineralisation. Calculated absolute mass changes in the Toms zone footwall compare closely with those in the footwall chlorite and sericite zones at Hellyer, north western Tasmania (Gemmell and Fulton, 2001) and Thalanga, north Queensland (Herrmann and Hill, 2001). Although net mass changes do not vary systematically with proximity to the Toms massive sulfide lens, progressive increases in chlorite abundance correspond to larger amounts of MgO added (Table 6.2). Similarly, the amount of K_2O added varies with sericite abundance. The

trend of increasing MgO addition toward the massive sulfide lens does not occur in the footwall volcanic succession at Main zone.

6.8 Geochemical model

Variations in whole rock element abundance, lithogeochemical indices and mineral chemistry provide useful exploration tools for vectoring in on regional and proximal alteration haloes surrounding massive sulfide lenses. The alteration halo associated with Main zone extends into massive siltstone directly overlying and underlying the polymictic breccia deposits (Fig 6.11). However, lithogeochemical trends are more strongly developed in the altered footwall volcanic succession south of Main zone.

Element abundance

Breccia, sandstone and siltstone facies hosting the massive sulfide lenses at Lewis Ponds are enriched in MgO, Fe_2O_3, CaO, Ba, Sr, S, As, Cu, Pb and Zn. However, relatively high Sr and CaO concentrations occurred in the limestone-clast breccia and sandstone prior to hydrothermal alteration. Main zone is associated with a Tl halo (2-30 ppm) of at least 30 to 100 m thickness. Anomalous Ba concentrations (0.2-2 wt %; Fig. 6.11) in Main and Toms zones correspond to a symmetrical halo containing hyalophane ($Ba,K,Na(Al,Si)_4O_8$) and/or Ba-rich white micas. Extensive areas of K_2O enrichment and Na_2O and CaO depletion occur in the footwall and hangingwall volcanic successions at Toms zone (Fig. 6.11). High Ba/Sr and S/Na_2O values in these units reflect feldspar-destructive sericite and chlorite alteration assemblages and disseminated sulfides.

Alteration indices

Alteration indices vary systematically with proximity to the massive sulfide lenses. AI and CCPI values in the footwall volcanic and sedimentary rocks progressively increase from 70 to 90 within 200 to 300 m of Toms zone and 50 m of Main zone (Fig. 6.11). High AI and CCPI values in the Toms zone footwall correspond to widespread feldspar destructive, chlorite and sericite alteration of the porphyritic dacite. Low AI values within the Toms Central massive sulfide lens reflect dolomite alteration of the fine-grained sedimentary host rocks.

Alteration indices are of limited use in Main zone because the proximal alteration halo occurs only in coarse-grained sedimentary rocks. Lower average AI values reflect the carbonate-bearing alteration assemblages and the limestone-bearing, polymictic breccia and sandstone deposits. Elevated AI and CCPI values in the Main zone host rocks are attributed to chlorite-pyrite and dolomite-chlorite-talc alteration assemblages in the breccia and sandstone matrix.

The preservation of plagioclase phenocrysts accounts for the lower AI and CCPI values in the weakly altered footwall volcanic rocks (Fig. 6.11).

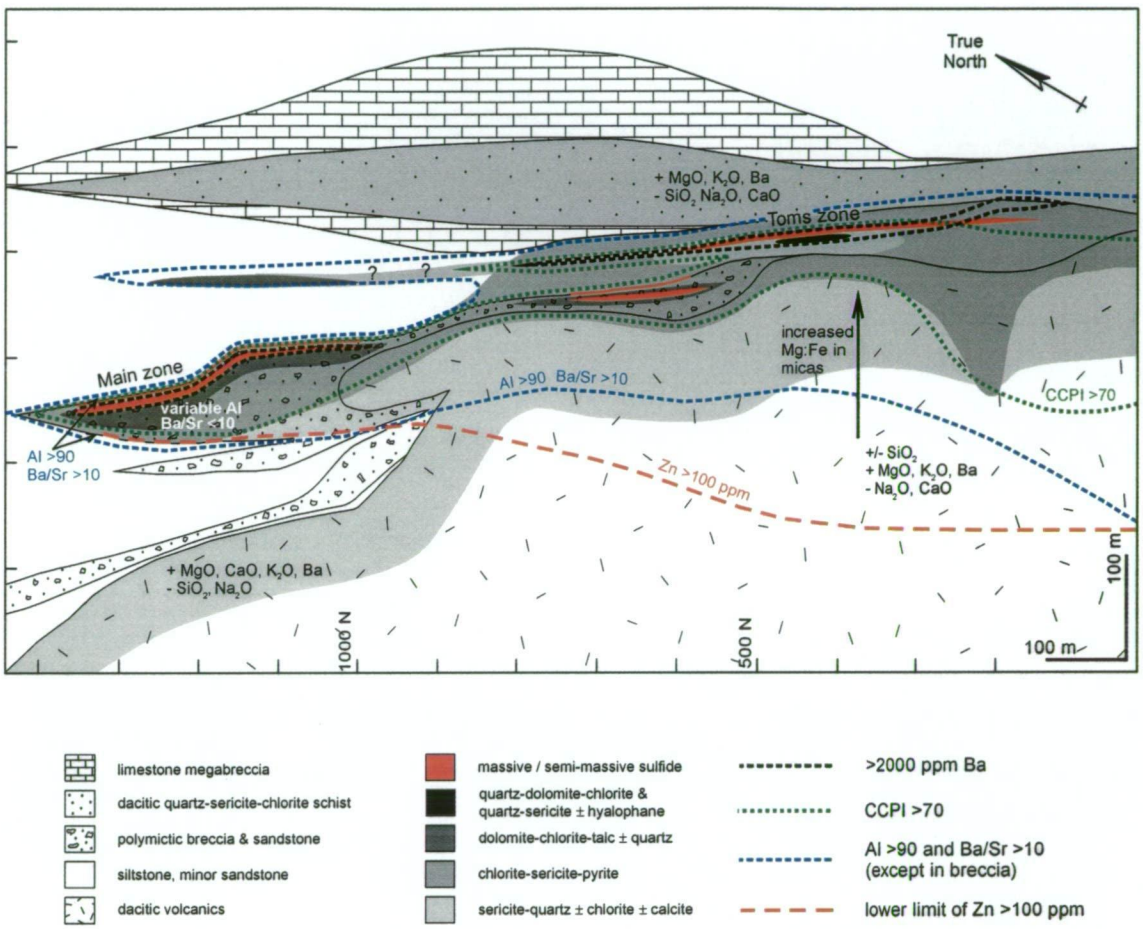

Figure 6.11 Geochemical model for Lewis Ponds illustrating mass changes in hangingwall and footwall volcanics and lithogeochemical trends associated with the massive sulfide lenses. Main and Toms zones are surrounded by a halo of high Alteration Index (>90), Chlorite-Carbonate-Pyrite Index (>70) and Ba/Sr (>10) values and high Ba concentrations (> 2000 ppm). However, lower average AI and Ba/Sr values occur in the carbonate-altered polymictic breccia, sandstone and siltstone deposits hosting the massive sulfide lenses, due to calcite and dolomite. Systematic variations in mica compositions occur only in the Toms zone footwall. Coherent dacitic volcanic rocks in the Main zone footwall are only weakly altered. Compiled from drill hole logs and whole rock geochemical data.

Mineral chemistry

The compositions of primary and recrystallised micas in the Toms Zone footwall correlate strongly with whole rock lithogeochemical trends associated with the massive sulfide lens (Fig. 5.16). Chlorite, phengite phlogopite and biotite Mg numbers progressively increase from 55 in the sericite-quartz ± chlorite envelope to 92 in the chlorite-pyrite zone. Proximal white mica and phlogopite grains contain higher average Ba and F concentrations than those in the surrounding sericite-quartz ± chlorite envelope. In contrast, alteration minerals occurring in the breccia and sandstone units in Main zone have relatively uniform compositions.

6.9 Summary

The asymmetric, stratabound alteration halo surrounding Main zone has:

- high AI, CCPI, Ba/Sr and S/Na_2O values; and
- variable, but generally high MgO, CaO, Fe_2O_3, Ba, Sr, S, As, Ni, Cu, Pb Zn and Tl concentrations.

However, the carbonate-rich breccia and sandstone facies have lower average AI and Ba/Sr values due to the occurrence of dolomite and calcite. Mass changes in the porphyritic dacite clasts and weakly altered footwall volcanic succession (dacite B) involved additions of MgO, Fe_2O_3, CaO and K_2O with removal of SiO_2 and Na_2O, producing net losses of 0-60 g/100g.

The asymmetric, semiconformable alteration envelope surrounding Toms zone is associated with strongly developed lithogeochemical gradients in the footwall. The chlorite-sericite-altered sedimentary host rocks are characterised by:

- high AI, CCPI, Ba/Sr and S/Na_2O values; and
- high MgO, CaO, Fe_2O_3, Ba, S, As, and Zn concentrations.

Hydrothermal alteration of the footwall and hangingwall volcanics resulted in MgO, Fe_2O_3, K_2O and Ba enrichment and Na_2O, CaO and Sr depletion. The addition of SiO_2 to dacite C contributed to overall net gains of 0-75 g/100g. The leaching of SiO_2 from dacite A led to net losses of 0-50 g/100g except in the Footwall Copper zone, where SiO_2 depletion was offset by significant additions of MgO and Fe_2O_3.

Elevated AI values (>70) and whole rock Zn concentrations (>100 ppm) in the Toms zone footwall are a useful proximity guide to the massive sulfide lens. A feldspar destructive alteration envelope characterised by pervasive chlorite and sericite extends more than 300 m into the footwall immediately south of Toms zone. These exploration vectors may assist in exploring for massive sulfide deposits elsewhere in the Mullions Range Volcanics and eastern Lachlan Fold Belt.

CHAPTER 7

GEOLOGY AND GEOCHEMISTRY OF THE MINERALISED ZONES

7.1 Introduction

The Lewis Ponds indicated resource includes two stratabound lenses of polymetallic massive sulfide. Main zone is hosted in mixed provenance breccia and pebbly-granular sandstone. It comprises a 10-15 m thick, Central massive to semi-massive sulfide lens and two smaller lenses (Fig. 7.1; Table 7.1). These occur in a 20-100 m thick envelope of disseminated sulfides that extends over 800 m strike length. Toms zone occurs in the overlying siltstone, along strike south of Main zone (Fig. 7.1). The 5 m thick, Toms Central massive sulfide lens passes laterally into disseminated sulfides and variably deformed, cleavage-parallel, quartz-sulfide veins. These veins also occur in the immediate hangingwall and footwall of the lens. Toms zone has significantly higher overall Zn, Pb, Cu and Ag grades than Main zone (Table 1.2). Lower average grades in Main zone reflect intercalation of massive sulfide bands with disseminated sulfides in the breccia matrix (Valliant and Meares, 1998).

The two massive sulfide zones have been structurally modified (see Chapter 4). Toms zone occurs within the Lewis Ponds fault (Fig. 7.1). Strongly foliated rocks, characterised by abundant shear and extension veins host the Toms Central massive sulfide lens. In contrast, the Main zone Central lens occurs west of the Lewis Ponds fault. However, the chlorite-dolomite-talc-altered Main zone host rocks are truncated by the fault at 200-600 m depth (Fig. 3.10).

In addition to the 5.7 Mt resource at Lewis Ponds, vein-hosted and disseminated sulfides occur at numerous abandoned mines (Fig. 3.1). Quartz-chalcopyrite veins in the footwall volcanic succession, south of Toms mine have been interpreted as deformed stringers (Valliant and Meares, 1998) and shear-controlled veins (Shepherd, 1972; Glasson, 1977; Parton, 1981). In the following chapter, the Little Bell Mount, Big Bell, Britannia and Mt Regan areas are collectively referred to as the *footwall copper zone*. The Lady Belmore and New Lewis Ponds zones occur within the Lewis Ponds fault (Fig. 7.1).

This chapter provides a description of the stratigraphic location, distribution, mineralogy, textures and geochemistry of the mineralised zones at Lewis Ponds. Primitive and diagenetic sulfide textures are differentiated from those resulting from deformation and metamorphism.

Assays, microprobe analyses and whole rock compositions are used to constrain trace element distribution among sulfides and metal abundance throughout the mineralised zones.

	Thickness	Length	Sulfide associations
Main zone:			
Hangingwall lens	1-5 m	800 m	- Banded pyrite-sphalerite-galena - Semi-massive sulfide
Central lens	10-15 m	200 m	- Massive to banded pyrite-sphalerite-galena and pyrrhotite-chalcopyrite - Semi-massive sulphide - Pyrite-altered limestone clasts
Southern lens	8-10 m	100 m	- Banded pyrite-sphalerite-galena - Semi-massive to disseminated sulphide
Footwall zone	20-100 m	800 m	- Disseminated sulphides in breccia matrix and rare massive pyrite-sphalerite-galena bands
Toms zone:			
Hangingwall zone	2.5-5 m	200 m	- Massive pyrite - Type 3A quartz-sulfide veins
Central lens	5-10 m average 5	200 m	- Banded pyrite-sphalerite-galena, - Massive pyrite, - Type 2 dolomite-chalcopyrite-sphalerite-galena-stannite veins
Footwall zone	5-30 m	200 m	- Semi-massive to disseminated sulfide - Type 3 carbonate and quartz-chalcopyrite veins
Footwall Copper zone:			
	25-300 m	~2 000 m	- Type 1A carbonate-chalcopyrite-pyrite veins - Type 1B and type 3A quartz-chalcopyrite-pyrite veins - Disseminated chalcopyrite-pyrite
New Lewis Ponds zone:			
	5-20 m	150 m	- Banded pyrite-sphalerite-galena - Type 3A quartz-pyrite-sphalerite-galena veins
Lady Belmore zone:			
	50 m	300 m	- Type 3A quartz-pyrite-sphalerite-galena veins - Type 3A quartz-pyrrhotite-sphalerite-chalcopyrite veins - Arsenopyrite-pyrite-rich carbonate bands/veinlets - Disseminated sulfide

Table 7.1 Mineralised zones at Lewis Ponds. Refer to Figure 7.1 on following page for location of mineralised zones in the host sequence.

7.2 Methods

This study involved petrological observations and analysis of new and acquired analytical data. Microscopic textures, paragenetic relationships and modal sulfide abundance were determined from polished thin sections during a detailed petrological study of available mineralised samples.

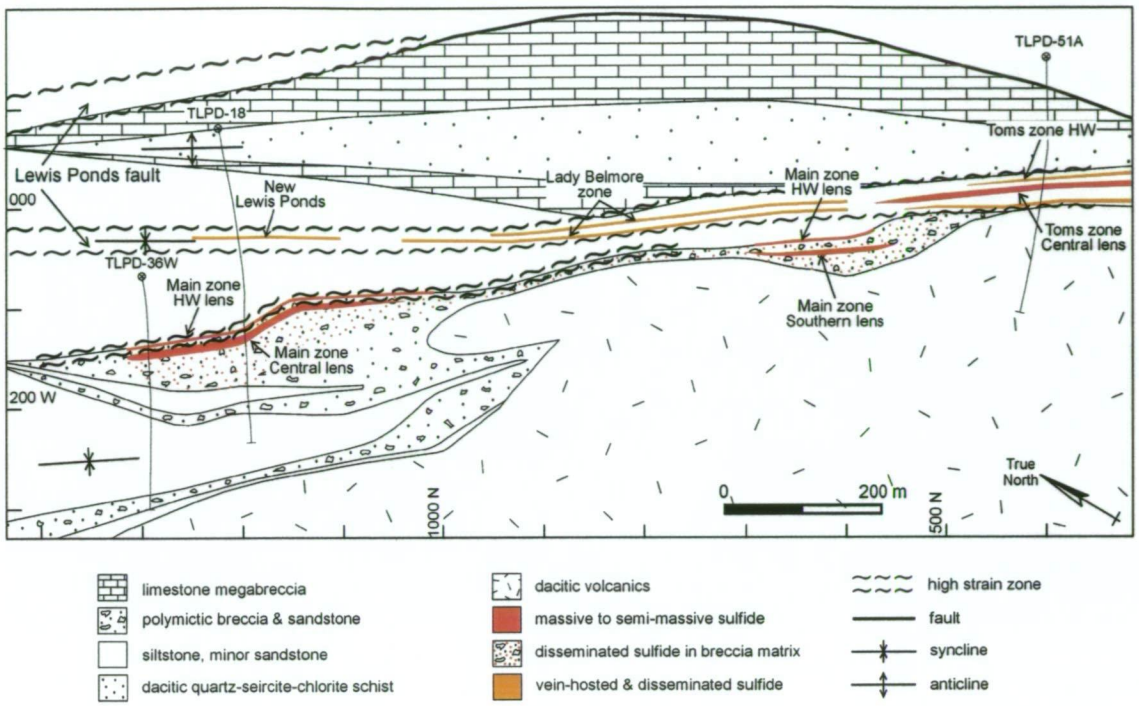

Figure 7.1 Interpreted 600 m RL level plan showing distribution of mineralised zones. Compiled from drill hole data. Diamond drill holes TLPD-18, TLPD-36W and TLPD-51A are projected onto the level plan for reference to logs in Figures 7.2, 7.3 and 7.4.

Tri Origin provided assay data from diamond drill core and rock chip samples. Routine assays of Cu, Pb, Zn, Au and Ag were carried out on predominantly one metre drill core intervals and analysed by Australian Laboratory Services, between 1992 and 1997. Tri Origin also supplied assays from older holes, drilled by previous exploration companies. Copper, Pb, Zn, Au and Ag assays were gridded and contoured as long sections in *Surfer* version 7. The uneven distribution and wide spacing of data meant that the 'natural neighbour' gridding method was more appropriate than conventional kriging. A ten metre grid spacing was chosen. Assays included in the metal contoured long sections were manually selected from diamond drill hole intersections of the massive sulfide lenses.

XRAL Laboratories, Ontario conducted multi-element analysis on selected drill holes; six from Main zone, three from Toms zone and five holes drilled by previous companies. One metre intervals were re-analysed for Cu, Pb, Zn, Au and Ag, using conventional fire assay and atomic absorption techniques. XRAL also analysed for the following trace elements: Cd, As, Sb, Sn, Hg, Ba, Co, W, Bi, Mo and Te, using X-Ray Fluorescence and Atomic Absorption Spectroscopy. The trace element data used in this study were contained in unpublished company reports: Perkins (1995; 1996).

Approximately 230 microprobe analyses were carried out to identify unknown minerals and compare sulfide compositions. The major and trace element compositions of sphalerite,

galena, tetrahedrite, stannite, pyrite, pyrrhotite, arsenopyrite, chalcopyrite and electrum were determined in selected samples using the Cameca SX-50 electron microprobe at the University of Tasmania's Central Science Laboratory. Long count times (eg. 120 sec) and high beam current (50-60 nA) enabled lower, unconventional detection limits for trace elements in the sulfides. Dr. David Steele, Electron Microscopy Facility, used the background count times, sample count times, sensitivity and beam current to calculate approximate detection limits for most of the elements analysed during this study. Microprobe data and the detection limits are listed in Appendix 5. Tri Origin provided 385 additional microprobe analyses of sphalerite, galena, tetrahedrite and stannite from seven polished thin sections.

7.3 Main zone

Main zone consists of three stratabound massive to semi-massive sulfide lenses, dipping 70-051 (Fig. 7.1, Table 7.1). The 10-15 m thick Central lens extends from 150 to 550 m depth (Fig. 5.1). It constitutes the total indicated resource for Main zone of 4.9 Mt. The Southern massive sulfide lens occurs in the Toms zone footwall and is truncated by the Lewis Ponds fault. A thin, discontinuous Hangingwall lens overlies the Central and Southern lenses. These massive and semi-massive sulfide lenses occur within a broad envelope of disseminated sulfides that extends over 800 m strike length.

A two metre wide gossan crops out discontinuously north of Spicers mine, up-plunge from the Central lens (Fig. 3.1). The gossan consists of Fe-oxide domains with extensive boxwork texture, intercalated with siliceous bands. Anomalous assays in shallow, reversed circulation drill holes, including 2 m at 9% Cu (TLPRC-01) and 3 m at 4 g/t Au (TLPRC-02) probably indicate supergene Cu-Au enrichment in this area. Ferrugenous, puggy zones occur in the walls of the abandoned limestone quarry. Shepherd (1972) described these as high grade pods of cerussite and smithsonite. Rock chip sampling carried out by Homestake yielded up to 3.0% Zn, 2.8% Pb, 410 ppm As, 103 ppm Ag and 1.6 ppm Au in the quarry walls (unpublished company data).

The Hangingwall, Central and Southern lenses occur in the mixed provenance breccia and pebbly-granular sandstone unit (Figs. 7.2 and 7.3). Unevenly distributed, five millimetre to five metre thick massive pyrite or banded pyrite-sphalerite-galena intervals and disseminated sulfides occur in chlorite-dolomite-talc schist or strongly altered breccia. Irregular, patchy zones of massive chalcopyrite and pyrrhotite locally overprint the pyrite, sphalerite and galena bands (Fig. 7.3B). The discontinuous, 1-5 m thick Hangingwall lens occurs in strongly sheared rocks, near the stratigraphic base of the mixed provenance breccia deposit (Fig. 7.2). It is characterised by banded pyrite-sphalerite-galena, massive pyrite and semi-massive sulfide.

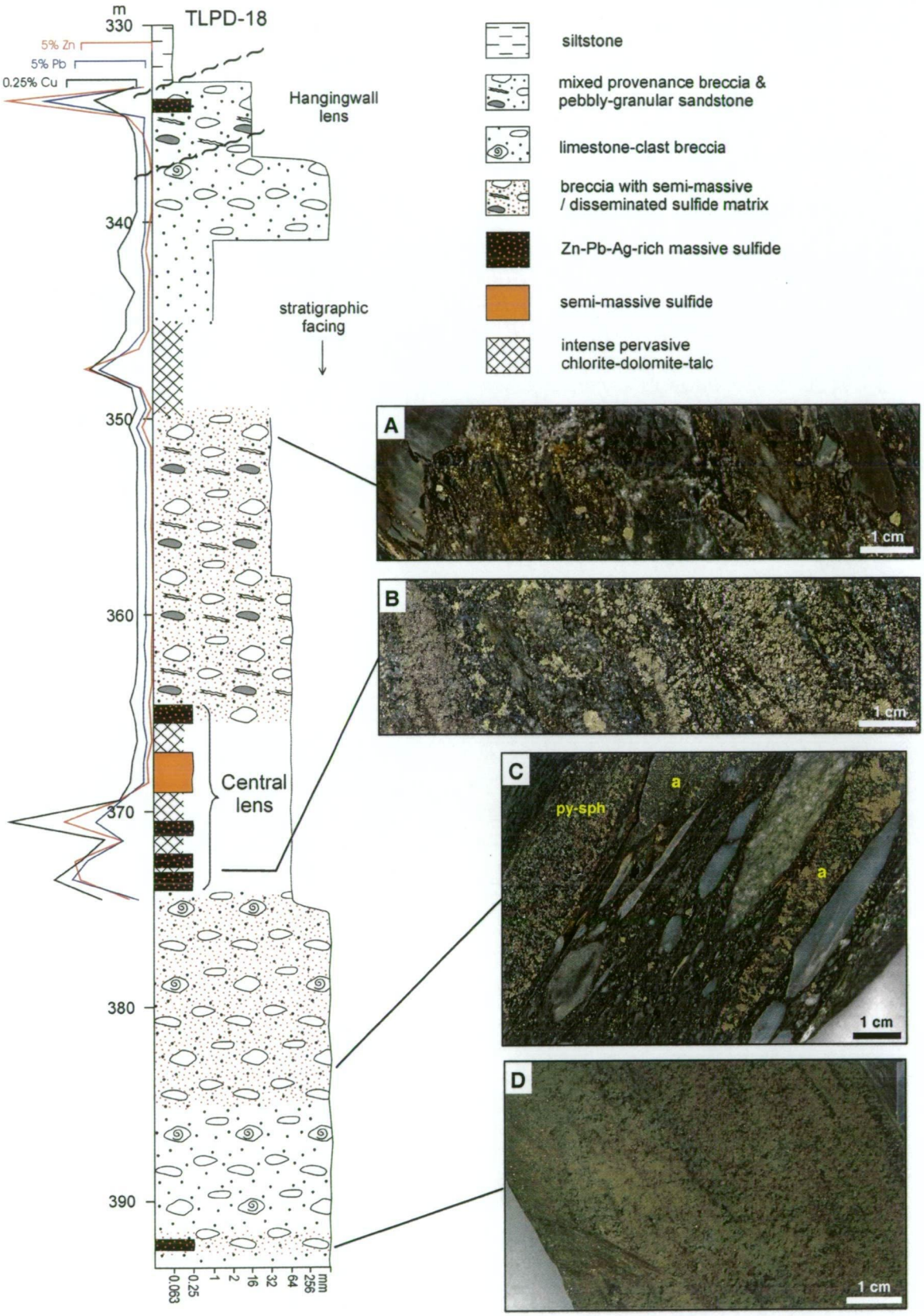

Figure 7.2 Drill log showing Main zone Hangingwall and Central lenses hosted in mixed provenance breccia. Assays are plotted on the left hand side. **A.** Disseminated pyrite in matrix-supported polymictic breccia. 351 m. **B.** Banded massive sulfide comprising pyrite and sphalerite-galena bands. 373 m **C.** Matrix-supported, limestone-clast breccia cut by a massive pyrite-sphalerite-galena band. Two limestone clasts (a) have been overprinted by pyrite and sphalerite. 383 m. **D.** Massive pyrite-sphalerite band in limestone-clast breccia. 392 m.

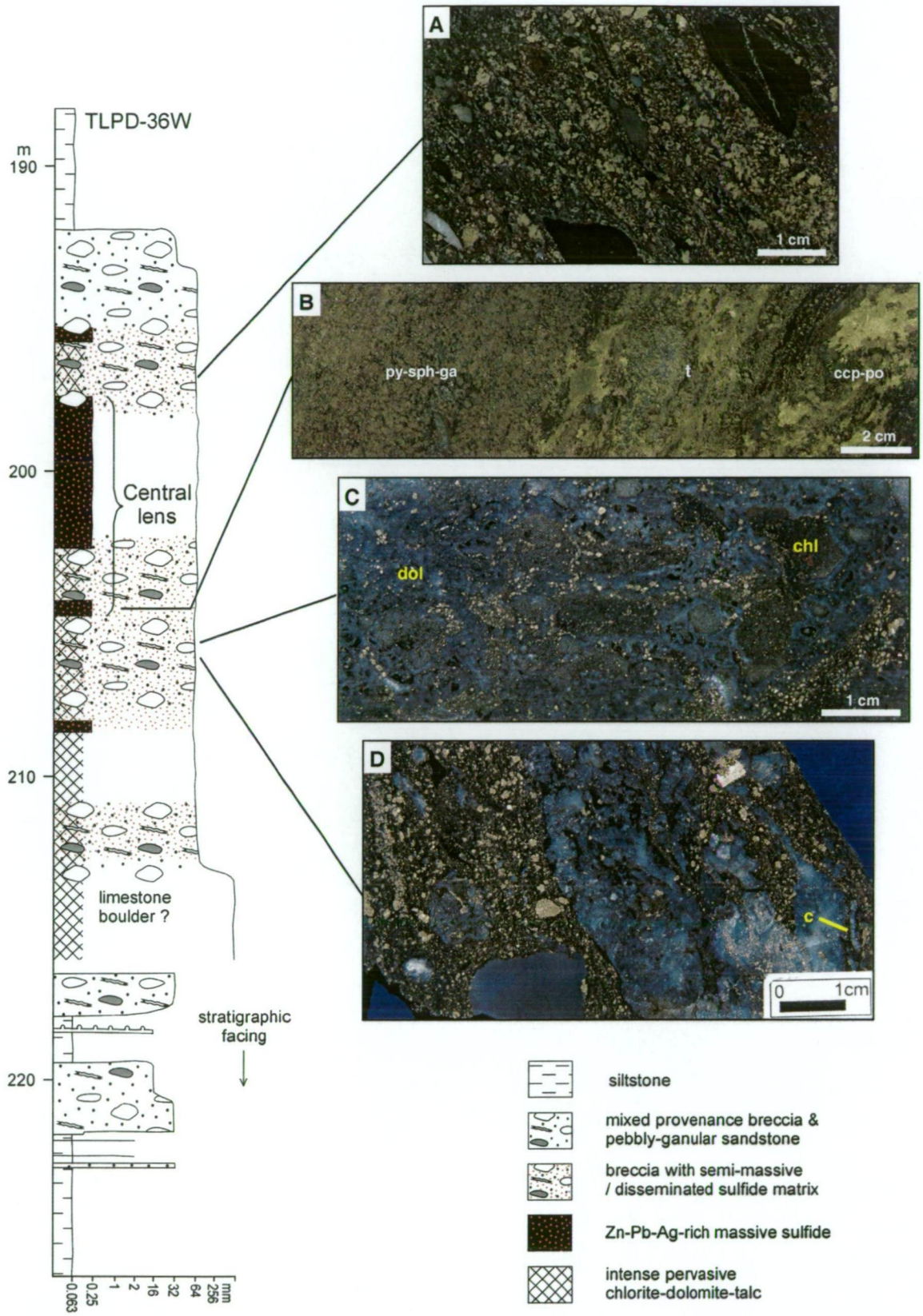

Figure 7.3 Drill log of Main zone Central lens hosted in the mixed provenance breccia. **A.** Disseminated pyrite, sphalerite and galena in granular-sandy mudstone matrix. 197 m. **B.** Banded pyrite-sphalerite-galena and massive pyrrhotite-chalcopyrite. A transitional zone (t) occurs between the two assemblages where chalcopyrite and pyrrhotite have overprinted the banded massive sulfide. 204 m. **C.** Disseminated pyrite in massive vuggy dolomite with angular chlorite patches. 206 m. **D.** polymictic breccia consisting of siltstone and fossiliferous limestone clasts in a chlorite-altered mudstone matrix with disseminated pyrite. The limestone clast has been partly replaced by patchy dolomite, Mg-chlorite and disseminated pyrite. Note preserved crinoid stem fragment (c). 207 m.

The Main zone footwall consists of patchy, disseminated sulfides and rare, cleavage-parallel, massive pyrite-sphalerite lenses (Figs. 7.2 and 7.3). These occur throughout the limestone-clast breccia, pebbly-siltstone and quartz crystal-rich sandstone beds. Disseminated pyrite overprints some of the limestone pebbles (Fig. 7.2C). Modal sulfide abundance decreases progressively from 30% at the top of the Footwall zone to <5% at the bottom. Base metal sulfides do not occur in the adjacent siltstone beds.

7.4 Toms zone

Toms zone consists of a 5 m thick Central massive sulfide lens that extends from surface to 500 m depth (Fig. 5.2, Table 7.1) and dips steeply to the northeast (88-030) or southwest (80-210). The indicated resource is currently 0.8 Mt. The uppermost 100 m were predominantly mined out between 1887 and 1921 (Department of Mines, annual reports, 1887-1930). Diffuse hangingwall and footwall zones of disseminated and vein-hosted sulfide surround the Central lens.

Gossan crops out discontinuously for 500 m strike length, south of Toms mine (Fig. 3.1). The steeply dipping, one metre wide gossan consists of massive hematite with minor goethite and quartz. A rock chip sample from the collapsed stope near Toms mine assayed 3 125 ppm Zn, 8 500 ppm Pb, 3 000 ppm Cu and 45 ppm Ag (Cominco Exploration report, 1969).

The Toms zone Central lens consists of fine to very coarse-grained massive pyrite and banded pyrite-sphalerite-galena (Fig. 7.4). Pyrite-chlorite, pyrite-sphalerite and sphalerite-galena-tetrahedrite bands occur in a quartz-dolomite-chlorite matrix. The massive sulfide bands wrap around dolomite boudins and kink folded or boudinaged dolomite-chalcopyrite-pyrite veins. Below 300 m depth, two or more, narrow massive sulfide lenses separated by intervals of quartz-chlorite-sericite schist or dolomite-chlorite-talc, suggest possible fold or fault repetition of the Central lens (Fig. 7.4). Cleavage-parallel, deformed, type 3 and 4 quartz-sulfide veins and disseminated sulfides predominate along strike and down plunge from the Central lens. These 1-20 mm thick, closely spaced, anastomosing veins typically occur in two or three groups over a 50 m interval. The veins contain minor sphalerite, galena and chalcopyrite together with pyrite or pyrrhotite.

The Hangingwall sulfide zone is characterised by massive pyrite, disseminated sulfides and variably deformed, anastomosing type 3 and 4 quartz-pyrite-sphalerite-galena veins. These veins extend along the Lewis Ponds fault to the Lady Belmore and New Lewis Ponds zones (Fig. 7.1).

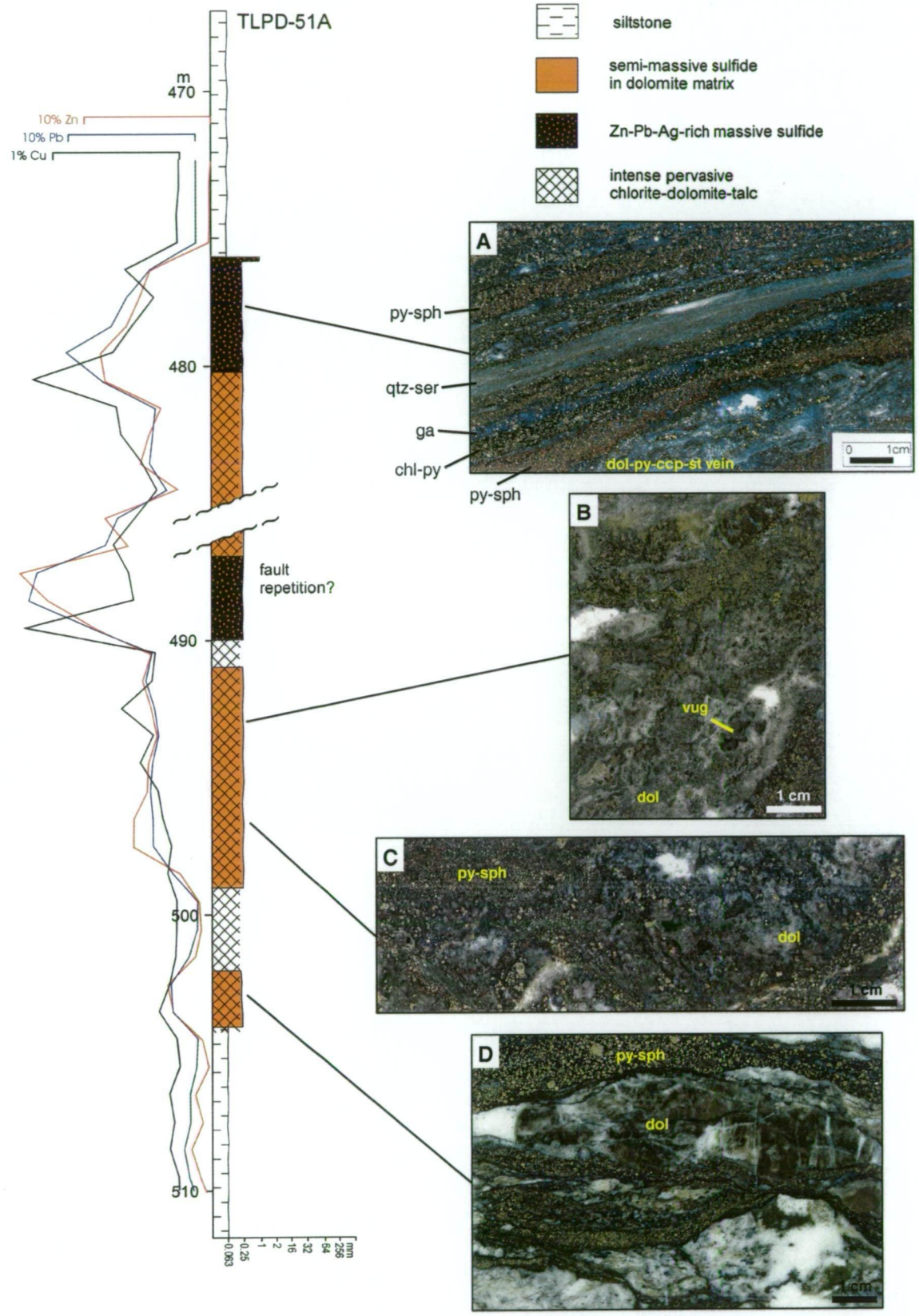

Figure 7.4 Drill log of Toms zone Central lens. Assays are plotted on the left hand side. **A.** Banded massive sulfide consisting of pyrite, sphalerite, galena and chlorite-rich bands, cut by a type 2 dolomite-chalcopyrite-sphalerite-stannite vein. 477 m. **B.** Disseminated pyrite, chalcopyrite, sphalerite and galena in vuggy dolomite matrix. 492 m. **C.** Semi-massive sulfide in a dolomite, chlorite and talc matrix. 496 m. **D.** Anastomosing quartz-pyrite-sphalerite bands surrounding dolomite boudins. 503 m. Abbreviations: py = pyrite, sph = sphalerite, ga = galena, ccp = chalcopyrite, chl = chlorite, ser = sericite, dol = dolomite.

7.5 Footwall Copper zone

The Footwall Copper zone occupies a 2 000 x 700 m area of the Western Volcanic Succession south of Toms mine (Fig. 3.1). Discordant, north-trending soil geochemical anomalies consisting of 400-1 500 ppm Cu occur in this area (Fig. 1.2). Abandoned workings are located within porphyritic dacite or along sheared contacts between siltstone and dacite at the Big Bell, Little Bell Mount, Britannia and Mount Regan Cu mines. These areas are characterised by discontinuous gossan outcrops, 5-100 cm wide, cleavage-parallel quartz-pyrite ± chalcopyrite veins and patches of pyrite, chalcopyrite, chalcocite, malachite and azurite in chlorite-altered siltstone and volcanic schist (Shepherd, 1972; Parton, 1981; this study).

In drill core south of Toms mine, 2-50 mm wide type 1 carbonate-chalcopyrite-pyrite and quartz-pyrite veins occur in chlorite-phlogopite-altered dacitic schist (Fig. 7.5A) or the overlying siltstone. Many veins are isoclinally folded, indicating that they predate cleavage development (eg. Fig. 4.10A and B). The carbonate veins contain minor sphalerite, galena, pyrrhotite and native bismuth in addition to chalcopyrite. Drill hole intersections of the Footwall Copper zone include 4 m at 1.7 % Cu (TLPD-66) and 3 m at 3.9 % Cu (TOD-2). These intervals contained less than 0.1 ppm Au and 20 ppm Ag (Tri Origin assays).

7.6 New Lewis Ponds and Lady Belmore zones

New Lewis Ponds and Lady Belmore (named after the abandoned mines) are located within the Lewis Ponds fault zone (Figs. 3.1 and 7.1). The Lady Belmore zone consists of disseminated sulfides, arsenopyrite-pyrite-rich carbonate bands/veinlets, groups of cleavage-parallel, type 3 and type 4 quartz ± sulfide veins and minor 5-50 cm thick, massive to semi-massive sulfide bands in chlorite-carbonate-talc-altered rock (Table 7.1; Fig. 7.5B). The kink folded and boudinaged veins contain chalcopyrite, sphalerite, galena and pyrite or pyrrhotite.

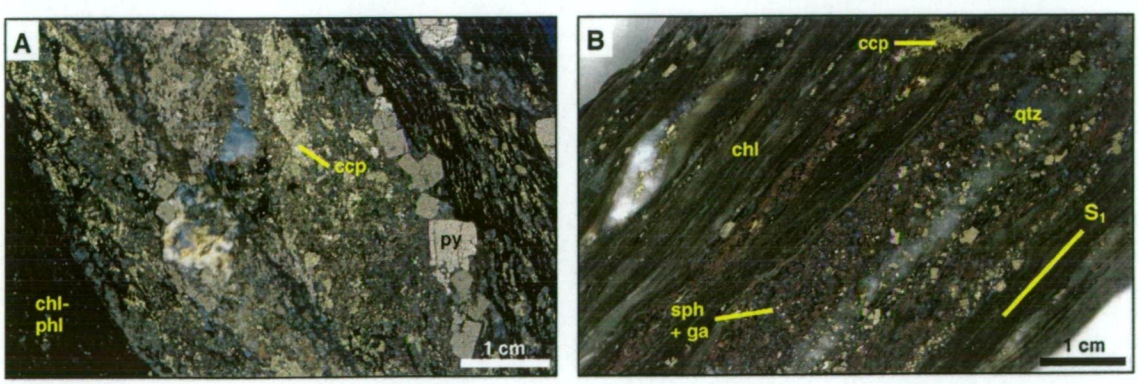

Figure 7.5 **A.** Type 1A calcite-chalcopyrite-pyrite vein in chlorite schist. The vein contains minor Se-Bi-rich galena, sphalerite, pyrrhotite and native bismuth. Footwall Copper zone, TLPD-66, 374 m. **B.** Cleavage-parallel, type 3A, quartz-pyrite-sphalerite-chalcopyrite-galena veins and disseminated pyrite and chalcopyrite in chlorite schist. Lady Belmore zone, TLPD-69, 411 m. Abbreviations: chl = chlorite phl = phlogopite, ccp = chalcopyrite, py = pyrite, sph = sphalerite, ga = galena.

Massive to semi-massive sulfide lenses were reported in Tri Origin drill logs at New Lewis Ponds. Samples obtained from mullock heaps adjacent to the New Lewis Ponds mine consisted of fine-grained, massive to banded pyrite-sphalerite-galena-chalcopyrite in a vein quartz matrix. In drill core, the New Lewis Ponds zone consists of disseminated and vein-hosted sulfides in chlorite-talc schist.

7.7 Sulfide mineralogy and textures

The massive sulfide in Main zone and Toms zone consists of pyrite, sphalerite and galena with subordinate chalcopyrite, tetrahedrite and arsenopyrite (Table 7.2). Stannite, tennantite, pyrargyrite and electrum are rarely observed. Pyrrhotite occurs in association with sphalerite, chalcopyrite or pyrite in the Main zone Central lens and Toms zone footwall. The massive sulfide has textural and mineralogical banding, sub-parallel to the regional S_1 cleavage. Very fine-grained pyrite ± arsenopyrite bands alternate with sphalerite-galena-tetrahedrite bands (eg. Fig. 7.4A). The base metal layers consist of fine to very coarse-grained (up to 2 mm), corroded subhedral pyrite crystals and cuspate galena grains enclosed in sphalerite. Base metal bands in Main zone are overprinted by massive pyrrhotite and chalcopyrite (Fig. 7.3B).

Mineral	Main zone	Toms zone	FW Cu zone	Lady Belmore	New Lewis Ponds
Pyrite	m	m	n	n	m
Sphalerite	m	m	t	n	n - m
Galena	n	n	t	t	t
Chalcopyrite	t	t	n	t	t
Tetrahedrite	t - n	n		r	
Tennantite		r			
Arsenopyrite	t	n		t	r
Pyrrhotite	n	r	t	n	
Stannite	r	t			
Digenite			r		
Pyrargyrite	r	r		r	
Native bismuth			t		
Bi-Se sulfide			r		
Electrum	r				
Quartz	t - n	n	t - n	n	n
Dolomite	n - m	n - m	t		
Calcite	t - n		n	t	
Chlorite	n - m	t	m	t	t
Talc	t	r		t	t

Table 7.2 Relative modal abundance of minerals observed during this study in the mineralised zones. Abbreviations: m = >10%, n = 1-10%, t = <1%, r = rarely observed. Estimations are based on point counts and petrological observations.

Type 1A veins in the Toms zone footwall (eg. Figs.4.10A and 7.5A) consist of chalcopyrite, pyrite, sphalerite, galena, pyrrhotite, native bismuth and rare Bi-Se sulfides in a fine-grained matrix of calcite, dolomite, quartz, chlorite and phlogopite. Pyrite occurs as corroded,

euhedral crystals and irregular lattices. Chalcopyrite, native bismuth and galena fill brittle fractures in the pyrite aggregates. An emulsion of small (<75 μm), rounded native bismuth blebs and galena occur in large chalcopyrite grains. Sphalerite aggregates contain small inclusions of chalcopyrite as oriented intergrowth and emulsion textures.

Boudinaged or anastomosing, type 2 dolomite veins occur within the massive sulfide in Toms zone (Figs. 4.10C and 7.4A). The dolomite veins consist of large chalcopyrite aggregates and minor tetrahedrite, sphalerite, galena, arsenopyrite, stannite and pyrite in a fine to medium-grained dolomite matrix. Small (< 200 μm) rounded or angular grains of stannite occur within larger chalcopyrite and sphalerite aggregates. Chalcopyrite surrounds corroded, euhedral to subhedral pyrite crystals and sphalerite grains at the vein margins. These textures indicate that chalcopyrite partly replaced the adjacent base metal sulfide bands.

The Lady Belmore zone and outer parts of Toms zone are dominated by type 3A quartz veins and disseminated sulfides (eg. Fig. 7.5B). Many veins consist of 0.05-5 mm euhedral pyrite crystals and cuspate galena grains surrounded by large sphalerite aggregates, in a microcrystalline quartz matrix. Others contain pyrrhotite, chalcopyrite and sphalerite with minor galena and no pyrite.

Pyrite

The following types of pyrite occur at Lewis Ponds:

- microcrystals (< 5 μm) and very fine-grained (5 μm - 0.1 mm) euhedra;
- fine to very coarse-grained (0.1-2 mm) euhedra;
- recrystallised or annealed aggregates; and
- large (0.5-1.5 mm) rounded porphyroblasts.

Very fine to medium-grained euhedra, dispersed microcrystals and recrystallised aggregates are the most common types of pyrite in Main zone (eg. Fig. 7.6A). The microcrystals occur in framboidal, spongy, concentrically banded and bladed aggregates. Large masses of recrystallised pyrite contain minor amounts of sphalerite, galena, chalcopyrite and tetrahedrite. Rare, 0.5-1.5 mm wide porphyroblasts with ragged margins and no internal fabric occur in the dolomite-chlorite-talc schist (Fig. 7.6B). Asymmetric quartz fibre strain shadows and lack of internal fabric indicate that many porphyroblasts formed prior to the S_1 cleavage.

In contrast, Toms zone is dominated by fine to very coarse-grained, typically corroded pyrite euhedra (Fig. 7.6C) and large pyrite aggregates. Pyrite aggregates are extensively micro-fractured. Type 1A veins contain aggregates of recrsytallised pyrite, partly corroded euhedra

and irregular lattices that fill intercrystalline spaces or mineral cleavage planes in the matrix (Fig. 7.6D-E). Fine to very coarse-grained pyrite euhedra occur in types 3 and 4 quartz veins.

Sphalerite

Sphalerite is a major constituent of the massive sulfide at Lewis Ponds (up to 35 modal %). Large, irregular sphalerite aggregates surround pyrite euhedra and rounded to angular chalcopyrite, tetrahedrite, galena and pyrrhotite grains (eg. Fig. 7.6F-H). Elongate, cleavage-parallel sphalerite aggregates also occur in banded massive sulfide. Quartz and dolomite veins contain large grains of sphalerite.

Galena

Galena occurs as small, very angular, cuspate aggregates surrounded by pyrite, pyrrhotite, sphalerite, tetrahedrite or chalcopyrite (eg. Fig. 7.6F). Galena-rich bands in the massive sulfide in Toms zone consist of elongate, cleavage-parallel aggregates. Galena also occurs in fractures that cut across recrystallised pyrite aggregates.

Chalcopyrite

The massive sulfide lenses, quartz veins and carbonate veins contain minor to trace amounts of chalcopyrite. Large chalcopyrite aggregates surround pyrite, sphalerite, galena, tetrahedrite or stannite. Chalcopyrite also occurs in brittle fractures. Small (< 50 μm), rounded, dispersed inclusions rarely occur as emulsion and oriented intergrowth textures in sphalerite. Trails of chalcopyrite blebs are parallel to grain boundaries (Fig. 7.6G) or cleavage planes (Fig. 7.6H) in the sphalerite. Many chalcopyrite blebs appear to have segregated toward grain boundaries, mineral cleavage planes or fractures during deformation and recrystallisation of the sphalerite. This texture, commonly referred to as 'chalcopyrite disease' is also attributed to exsolution during cooling (Ramdohr, 1979; Solomon and Gaspar, 2001) or partial replacement of the sphalerite by chalcopyrite (Barton, 1978; Eldridge et al., 1983; Deer et al., 1992).

Tetrahedrite-tennantite

Tetrahedrite is a minor component of the massive sulphide in Main and Toms zones (up to 2 modal %). Trace amounts occur in semi-massive sulfide and type 2 dolomite veins. Rare tennantite grains were identified in samples from the Toms Central lens by microprobe analyses. The more abundant minerals such as sphalerite, chalcopyrite and galena typically surround large (0.02-1.2 mm) anhedral tetrahedrite grains (Fig. 7.6F). Elongate blebs of tetrahedrite locally define the S_1 cleavage. Dispersed tetrahedrite inclusions occur with chalcopyrite and arsenopyrite as an emulsion texture in type 2 veins (Fig. 7.6I).

Figure 7.6 Photomicrographs of sulfides I

A Very fine-grained pyrite euhedra and recrystallised pyrite aggregates surrounded by galena and sphalerite. Main zone Central lens. TLPD-18, 365 m.

B Rounded pyrite porphyroblast with ragged margins occurring in chlorite-phlogopite-talc schist. Main zone Hangingwall lens. TLPD-12, 450 m.

C Medium-grained, corroded subhedral pyrite crystals surrounded by sphalerite. Toms zone Central lens. TLPD-51A, 482 m.

D Atoll texture consisting of a corroded euhedral pyrite crystal surrounded by chalcopyrite. Type 1A calcite-chalcopyrite-pyrite vein. TLPD-70, 127 m.

E Pyrite filling interstitial spaces and rhombic cleavage planes in calcite aggregate. Type 1A calcite-chalcopyrite-pyrite vein. TLPD-66, 374 m.

F Massive sulfide consisting of anhedral tetrahedrite, chalcopyrite, pyrrhotite, sphalerite and galena aggregates and rare pyrargyrite. Main zone Central lens, TLPD-18, 365 m.

G Chalcopyrite inclusions occurring near grain boundaries in a recrystallised sphalerite aggregate. Main zone Central lens, TLPD-18, 365 m.

H Oriented intergrowth, emulsion texture consisting of dispersed chalcopyrite inclusions in sphalerite. Type 1A calcite-chalcopyrite-pyrite vein. TLPD-66, 361 m.

I Irregular intergrowth of chalcopyrite, tetrahedrite and arsenopyrite with minor sphalerite and galena. Type 2 dolomite-chalcopyrite-sphalerite-stannite vein. Toms zone Central lens. TLPD-51A, 488 m.

Abbreviations: sph = sphalerite, ga = galena, py = pyrite, ccp = chalcopyrite, ca = calcite, td = tetrahedrite, po = pyrrhotite, pg = pyrargyrite, as = arsenopyrite.

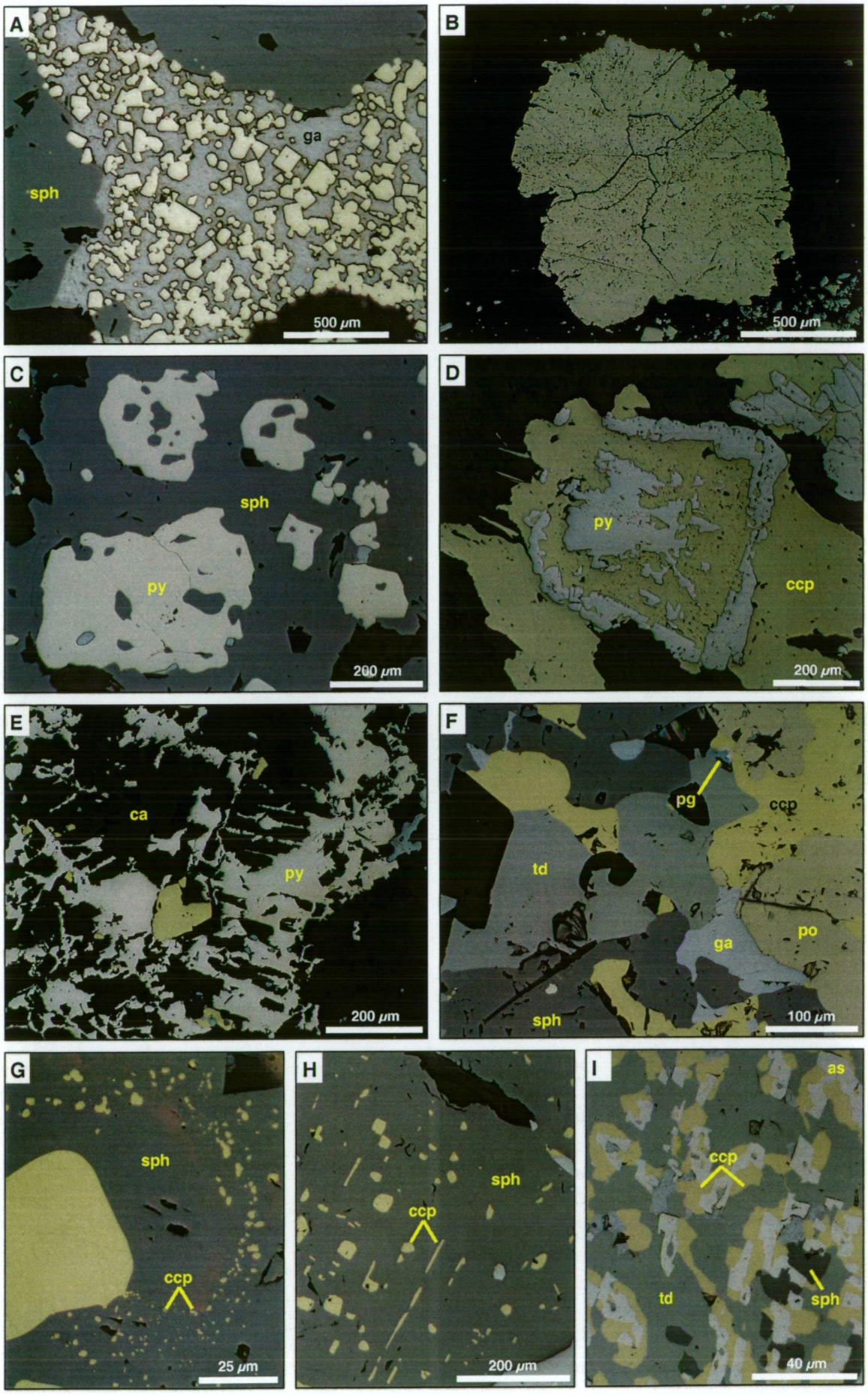
A
ga
sph
500 μm
B
500 μm
C
sph
py
200 μm
D
py
ccp
200 μm
E
ca
py
200 μm
F
pg
ccp
td
po
ga
sph
100 μm
G
sph
ccp
25 μm
H
sph
ccp
200 μm
I
as
ccp
td
sph
40 μm

Arsenopyrite

Arsenopyrite is most abundant in the Toms Central lens (locally up to 5 modal %). Trace amounts occur in Main and Lady Belmore zones as disseminations or arsenopyrite-pyrite-rich bands. Euhedral to subhedral rhombs (Fig. 7.6I), recrystallised aggregates and very-angular splintery laths are the most common forms of arsenopyrite.

Pyrrhotite

Numerous types of pyrrhotite occur in the host sequence and mineralised zones. Elongate crystals up to 10 mm long define the L_1 stretching lineation (see Chapter 4, Fig. 4.3E). These are dispersed throughout siltstone and sandstone units in the Hangingwall Siltstone Unit and Transitional Unit. Large anhedral aggregates or small (<50 μm) inclusions of pyrrhotite are associated with pyrite, chalcopyrite and sphalerite in type 3A quartz veins and in Main zone massive sulfide (Fig. 7.7A). Corroded, acicular and tabular, 100-2000 μm long, pyrrhotite laths occur in semi-massive sulfide throughout Main zone (Fig. 7.7B). Some of these bladed crystals have an orthorhombic crystal form, indicating pseudomorphic replacement of an orthorhombic mineral such as barite or anhydrite (Fig. 7.7B inset).

Stannite

Trace amounts of stannite occur in the polymetallic massive sulfide in association with chalcopyrite and/or sphalerite (Fig. 7.7C). Stannite is most abundant in type 2 dolomite-chalcopyrite veins in the Toms Central massive sulfide lens. Dispersed, rounded or angular inclusions occur in large chalcopyrite aggregates or in tetrahedrite and sphalerite to a lesser extent. Rounded blebs and lamellae typically define myrmekitic and oriented intergrowth, emulsion textures in sphalerite aggregates (Fig. 7.7D).

Digenite

Digenite rarely surrounds large chalcopyrite aggregates in quartz veins south of Toms zone (Fig. 7.7E). The mineral, found immediately beneath the weathered zone, probably resulted from oxidation of chalcopyrite.

Pyrargyrite

Pyrargyrite occurs rarely in the Main zone Central lens and Lady Belmore zone. Small 15-100 μm, rounded or angular pyrargyrite grains occur within tetrahedrite aggregates (Fig. 7.7F) or along the margins of tetrahedrite and chalcopyrite grains. The pyrargyrite contains 60-64 wt % Ag, 21-24 wt % Sb and trace amounts of Zn, Fe, Co, Mo and Sn (microprobe analyses in Appendix 5).

Figure 7.7 Photomicrographs of sulfides II

A Massive pyrrhotite, chalcopyrite and sphalerite from Main zone Central lens. TLPD-12, 457 m.

B Partly corroded, bladed pyrrhotite crystals surrounded by sphalerite and galena.
Inset photo: Orthorhombic bladed pyrrhotite crystal, looking down the long axis of the crystal. Main zone Central lens. TLPD-18, 365 m.

C Massive sulfide from Toms Central lens consisting of chalcopyrite, tetrahedrite, pyrite, galena, stannite, sphalerite and arsenopyrite. TLPD-51A, 488 m.

D Emulsion texture characterised by oriented intergrowths of stannite in sphalerite. Type 2 dolomite-chalcopyrite-pyrite-stannite vein in Toms Central lens. TLPD-51A, 488 m.

E Chalcopyrite rimmed by digenite. Type 1 quartz-chalcopyrite vein occurring south of Toms zone. TLPD-70, 69 m.

F Anhedral pyrargyrite bleb surrounded by tetrahedrite and chalcopyrite. Main zone Central lens. TLPD-18, 365 m.

G Emulsion texture characterised by native bismuth and galena surrounded by chalcopyrite. Type 1A calcite-chalcopyrite-pyrite vein. Toms zone footwall. TLPD-66, 374 m

H Small, 0.2 mm electrum grain surrounded by galena, chalcopyrite, pyrrhotite and pyrite. The electrum contains 58 wt % Ag, 37 wt % Au and 5 wt % Hg. Main zone Central lens. TLPD-18, 365 m.

Abbreviations: py = pyrite, sph = sphalerite, ccp = chalcopyrite, po = pyrrhotite, ga = galena, st = stannite, td = tetrahedrite, as = arsenopyrite, dg = digenite, pg = pyrargyrite, Bi = native bismuth, el = electrum.

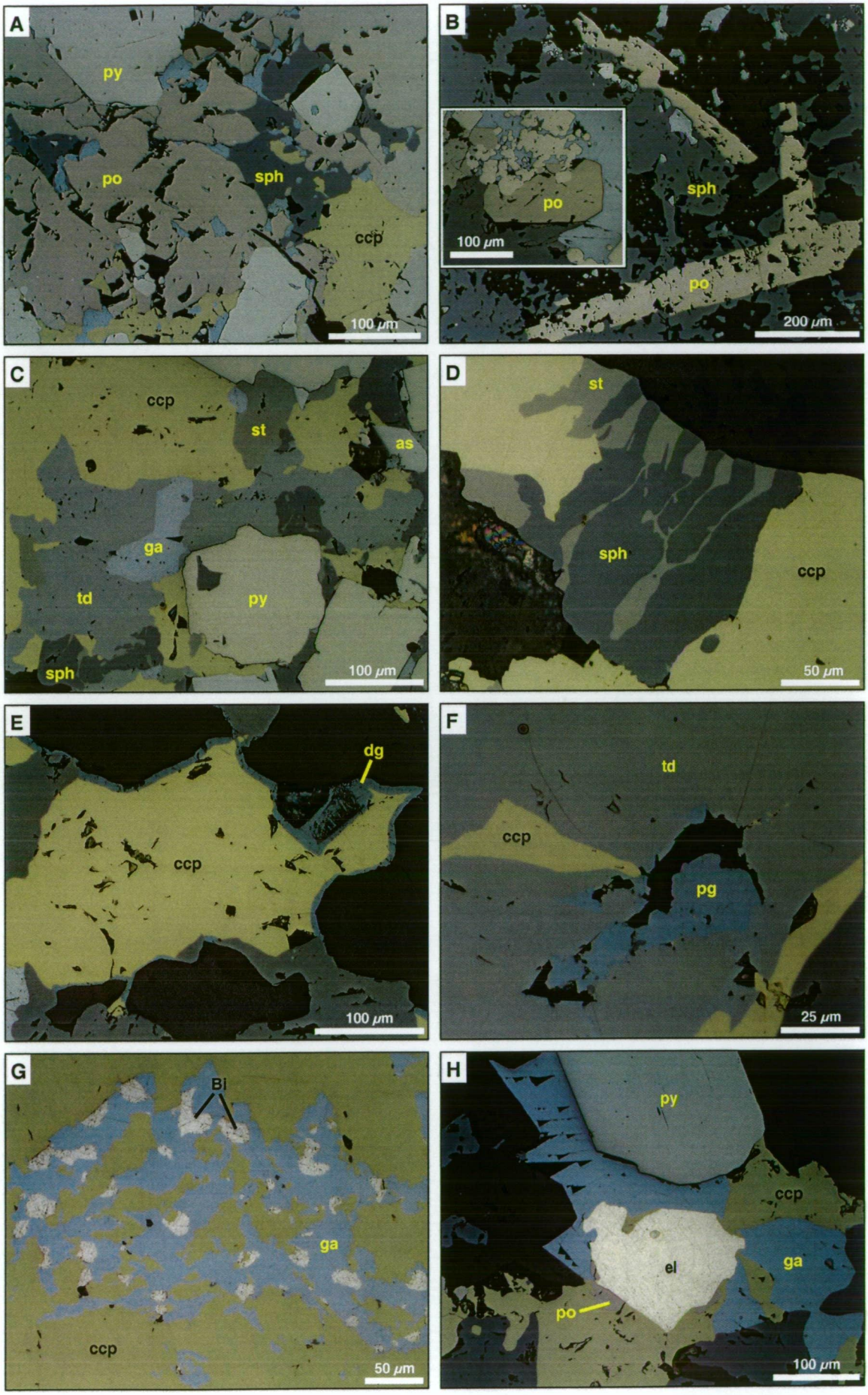
A
py
po
sph
ccp
100 μm
B
po
100 μm
sph
po
200 μm
C
ccp
st
as
ga
td
py
sph
100 μm
D
st
sph
ccp
50 μm
E
dg
ccp
100 μm
F
td
ccp
pg
25 μm
G
Bi
ga
ccp
50 μm
H
py
ccp
el
ga
po
100 μm

Native bismuth and Bi-bearing sulfides

Native bismuth and rare Bi-bearing sulfides ($Pb_7Bi_2S_{10}$) occur in type 1A carbonate veins in the Toms zone footwall. Small, 5-75 μm, rounded inclusions of native bismuth are dispersed throughout galena aggregates as an emulsion texture in chalcopyrite (Fig. 7.7G). Bismuth also occurs in brittle fractures within large masses of pyrite or chalcopyrite. The mineral contains >99 wt % Bi and up to 1030 ppm Sb and 700 ppm Se (Appendix 5).

Electrum

A 0.2 mm wide electrum grain identified in a sample from Main zone (Fig. 7.7H) contains 37 wt % Au, 58 wt % Ag and 5 wt % Hg. It has a uniform composition across the grain.

7.8 Primitive sulfide textures

Various textures resulting from primary crystallisation of Fe-sulfides occur at Lewis Ponds. Framboidal, spongy, concentrically banded, bladed, dendritic and reticulate textures are common in semi-massive sulfide areas of Main zone and rarely in Toms zone. These textures have been infilled and partly replaced by base metal sulfides.

Framboids, spongy pyrite and atoll structures

Pyrite framboids occur in the matrix of polymictic breccia, quartz crystal-rich sandstone and siltstone deposits in Main zone. They are most abundant (locally up to 20 modal %) in polymetallic or pyrite-rich semi-massive sulfide samples. The variably recrystallised and deformed framboids have diameters that ranging from 4 to 70 μm and average diameters of 12 to 13 μm (Table 7.3). They are composed of cubic, pyritohedral or octahedral pyrite microcrystals, loosely or densely packed into a spherical aggregate (Fig. 7.8A-B). Deformed framboids are surrounded by elongate, cleavage-parallel base metal sulfide aggregates or chlorite pressure shadows in highly strained rocks.

Sample	N	Diameter (μm)	Mean (μm)	St. Dev.	Skewness
LP12450	394	6-40	12.9	3.7	1.4
LP36W195	506	4-66	13.6	5.1	3.1
LP36W281	573	5-28	13.3	3.6	0.3
LP44243	449	4-27	12.0	3.4	0.8

Table 7.3 Framboid size distribution, measured on polished thin sections using a digitising stage.

Many framboids have been partly to completely replaced by pyrrhotite, sphalerite, chalcopyrite, galena, stannite, or a combination of sulfides (Fig. 7.8C-J). Galena occupies interstitial spaces between pyrite microcrystals (Fig. 7.8B). Atoll structures consist of

Figure 7.8 Framboidal textures in Main zone

A Loosely packed framboidal aggregate of pyritohedrons in a dolomite matrix. TLPD-36W, 195 m.

B Framboid consisting of pyrite microcrystals densely packed into a spherical aggregate with minor interstitial galena. TLPD-36W, 195 m.

C Chalcopyrite pseudomorphs of pyrite framboids, surrounded by botryoidal pyrite band. TLPD-36W, 195 m.

D Framboids? replaced by sphalerite and stannite emulsion. TLPD-36W, 195 m.

E Recrystallised pyrite framboids partly replaced by galena and enclosed in a large sphalerite mass. TLPD-36W, 197 m.

F Recrystallised framboid relic? consisting of chalcopyrite in the core and galena in the rim. TLPD-36W, 195 m.

G & H Pyrite framboids overgrown by galena and coarser grained pyrite. Galena has filled interstitial spaces between the pyrite microcrystals. TLPD-18, 365 m and TLPD-36W, 202 m.

I Irregular, spongy mass of very fine-grained pyrite, galena and arsenopyrite. TLPD-36W, 195 m.

J Framboidal aggregates pseudomorphed by pyrrhotite. Occurs in the matrix of a thin pebbly-siltstone bed. Main zone footwall. TLPD-36W, 281 m.

K Relict framboidal aggregate consisting of galena and sphalerite patches rimmed by pyrite. TLPD-36W, 195 m.

L Dispersed atoll structures and framboids (fr) in a fine-grained chlorite matrix. The atolls comprise a central core of recrystallised pyrite microcrystals and galena, sphalerite or chalcopyrite surrounded by pyrite. TLPD12, 450 m.

M Unaltered recrystallised pyrite framboids enclosed in a chalcopyrite band. TLPD-36W, 195 m.

Abbreviations: dol = dolomite, ccp = chalcopyrite, sph = sphalerite, st = stannite, ga = galena, py = pyrite, po = pyrrhotite, chl = chlorite.

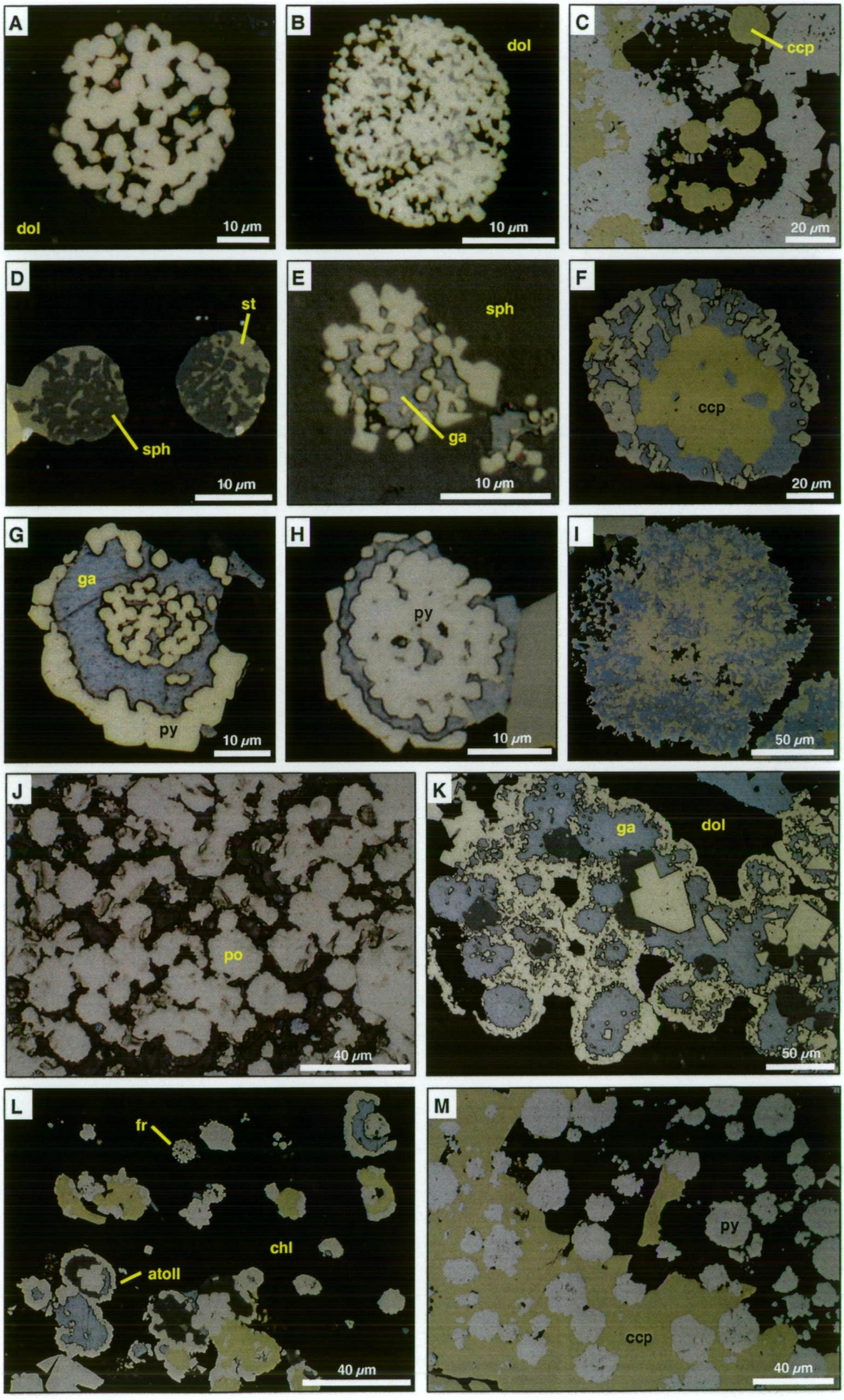
A
dol
10 μm
B
dol
10 μm
C
ccp
20 μm
D
st
sph
10 μm
E
sph
ga
10 μm
F
ccp
20 μm
G
ga
py
10 μm
H
py
10 μm
I
50 μm
J
po
40 μm
K
ga
dol
50 μm
L
fr
chl
atoll
40 μm
M
py
ccp
40 μm

rings of recrystallised pyrite surrounding a central core of sphalerite, galena, chalcopyrite, pyrite microcrystals or framboids (Fig. 7.8K and L). Individual framboidal relics and ring structures occur within large masses of sphalerite, galena chalcopyrite and coarse-grained pyrite (eg. Fig. 7.8E and M).

Large (up to 2.5 mm width), irregular spongy aggregates of pyrite microcrystals also occur in the Main zone massive sulfide (Fig 7.8I). These contain minor interstitial galena, sphalerite and arsenopyrite. Dolomite, sphalerite, pyrrhotite and coarser grained, euhedral pyrite typically surround the spongy aggregates.

Bladed, dendritic and reticulate textures

Bladed textures involving pyrrhotite, pyrite, arsenopyrite, galena, chalcopyrite and quartz occur in the Main zone Central lens and rarely in Toms zone. Corroded, acicular or tabular pyrrhotite crystals are the most common bladed mineral (Fig. 7.7B). Some of these are probably pseudomorphs of barite or anhydrite (Fig. 7.7B inset). Many bladed pyrrhotite crystals have been partly replaced by pyrite, sphalerite and galena (Fig. 7.9A-C). Quartz pseudomorphs of twinned sulfate crystals rarely occur in Main zone (Fig. 7.9D). Aggregates of acicular or bladed pyrite and pyrrhotite crystals are arranged in 100-500 μm wide radial dendritic patterns (Fig. 7.9E-F) or reticulate networks (Fig. 7.9G-H), with interstitial sphalerite, galena and chalcopyrite.

Concentrically banded, vuggy and crustiform textures

Vuggy, crustiform and concentrically banded or botryoidal textures occur throughout the Main zone and rarely Toms zone Central lenses in semi-massive and massive sulfide. Very fine-grained dog-tooth pyrite encrustations and narrow, pyrite bands occur around the margins of large sphalerite, galena, chalcopyrite and tetrahedrite masses (Fig. 7.10A-B) and dolomite-filled vugs (Fig. 7.10C-D). Stannite, chalcopyrite, sphalerite, galena and dolomite bands alternate with the pyrite bands and framboidal pyrite aggregates (Fig. 7.10E-H). Some of the pyrite bands surround a central core of galena, sphalerite or chalcopyrite (eg. 7.10F).

Interpretation of primitive sulfide textures

The framboidal, bladed, botryoidal and spongy textures pre-date deformation and metamorphism of the massive sulfide at Lewis Ponds. They commonly occur in well preserved or strongly deformed, ancient VHMS deposits (Eldridge et al., 1983; England and Ostwald, 1993; McArthur, 1996; Peter et al., 1999; Martin, 2002) and modern sea floor sulfide mounds in back-arc basins (Halbach et al., 1993) and sediment-covered ocean rift valleys (Zierenberg et al., 1993; Duckworth et al., 1994).

Figure 7.9 Bladed textures in Main and Toms zones

A Corroded, tabular pyrrhotite crystal partly replaced by galena and overgrown by a large sphalerite mass. Some of the replacement has occurred along mineral cleavage planes. Main zone Central lens. TLPD-18, 365 m.

B Bladed pyrrhotite overgrown and partly replaced by galena and recrystallised pyrite. Main zone Central lens. TLPD-18, 365 m.

C Bladed pyrrhotite encrusted with a dendritic aggregate of bladed crystals pseudomorphed by galena and pyrite. Main zone Central lens. TLPD-18, 365 m.

D Rectangular aggregates of fine-grained quartz as pseudomorphs of twinned, bladed crystals, in a very fine-grained dolomite matrix. TLPD-18, 365 m. Main zone Central lens. Plane polarised light.

E Dendritic aggregate of acicular pyrite crystals infilled with chalcopyrite, sphalerite and galena and overgrown by pyrite around the margin. Crystals grew outward from the mass of pyrite microcrystals at the right-hand side of the photomicrograph. Limestone-clast breccia matrix, Main zone footwall. TLPD-12, 490 m.

F Possible dendritic aggregate of bladed crystals preserved in massive pyrite and galena. Toms zone Central lens. TLPD-51A, 488 m.

G Irregular network of acicular spongy crystals pseudomorphed by very fine-grained pyrite and arsenopyrite, and infilled with sphalerite. Mixed provenance breccia matrix, Main zone Central lens. TLPD-36W, 207 m.

H Reticulate and dendritic network of bladed, acicular pyrite crystals infilled with sphalerite, chalcopyrite and galena. Limestone-clast breccia matrix, Main zone footwall. TLPD-12, 490 m.

Abbreviations: po = pyrrhotite, sph = sphalerite, ga = galena, py = pyrite, qtz = quartz, dol = dolomite, ccp = chalcopyrite, as = arsenopyrite.

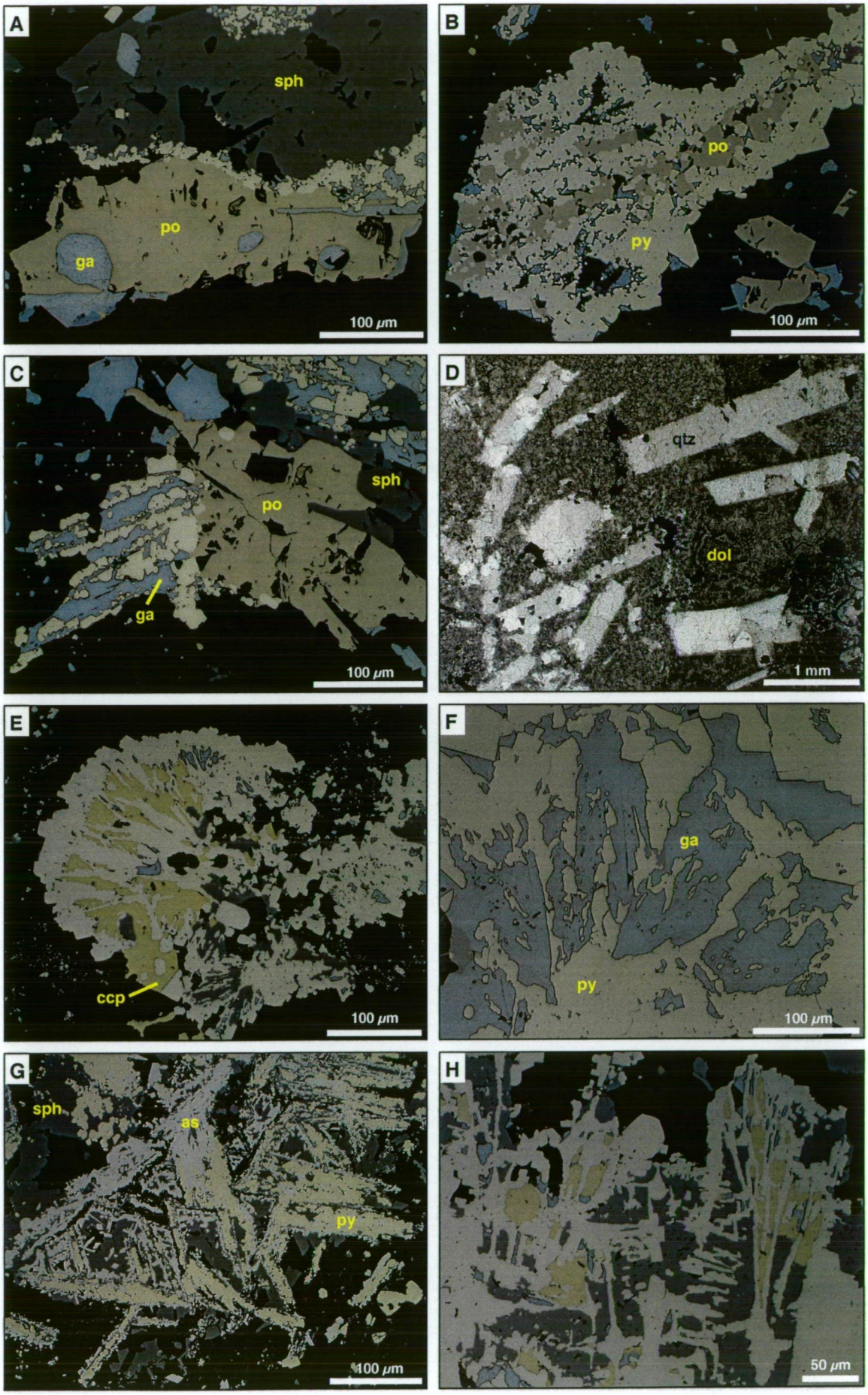
A
sph
po
ga
100 μm
B
po
py
100 μm
C
sph
po
ga
100 μm
D
qtz
dol
1 mm
E
ccp
100 μm
F
ga
py
100 μm
G
sph
as
py
100 μm
H
50 μm

Figure 7.10 Concentrically banded and crustiform textures in Main and Toms zones

A Vuggy massive sulfide consisting of chalcopyrite, tetrahedrite and botryoidal galena-sphalerite masses lined with pyrite, and bladed chalcopyrite pseudomorphs encrusted with very fine-grained dog-tooth pyrite. Main zone Central lens. TLPD-36W, 195 m.

B Concentric circular bands of pyrite rimming a large botryoidal sphalerite mass. Main zone Central lens. TLPD-36W, 197 m.

C Dolomite-filled vugs lined with pyrite and surrounded by massive sphalerite-pyrite. A framboid relic has been preserved in the pyrite (fr). Main zone Central lens. TLPD-36W, 195 m.

D Dolomite-filled vug lined with very fine-grained dog-tooth pyrite, in massive chalcopyrite-galena. Main zone Central lens. TLPD-36W, 195 m.

E Semi-massive sulfide characterised by concentric framboidal pyrite (A) and microcrystalline pyrite (B) bands in a dolomite matrix, partly infilled and replaced by chalcopyrite parallel to the banding (C). Main zone Central lens. TLPD-36W, 195 m.

F Concentric pyrite and galena bands surrounding a central core of galena. Main zone Central lens. TLPD-36W, 195 m.

G Botryoidal pyrite aggregate characterised by alternating pyrite and dolomite bands. Chalcopyrite partly infills some of the bands. Main zone Central lens. TLPD-36W, 195 m.

H Relict botryoidal pyrite aggregate partly infilled by galena. Toms zone Central lens. TLPD-67B, 965 m.

Abbreviations: dol = dolomite, td = tetrahedrite, ga = galena, ccp = chalcopyrite, sph = sphalerite, py = pyrite, qtz = quartz.

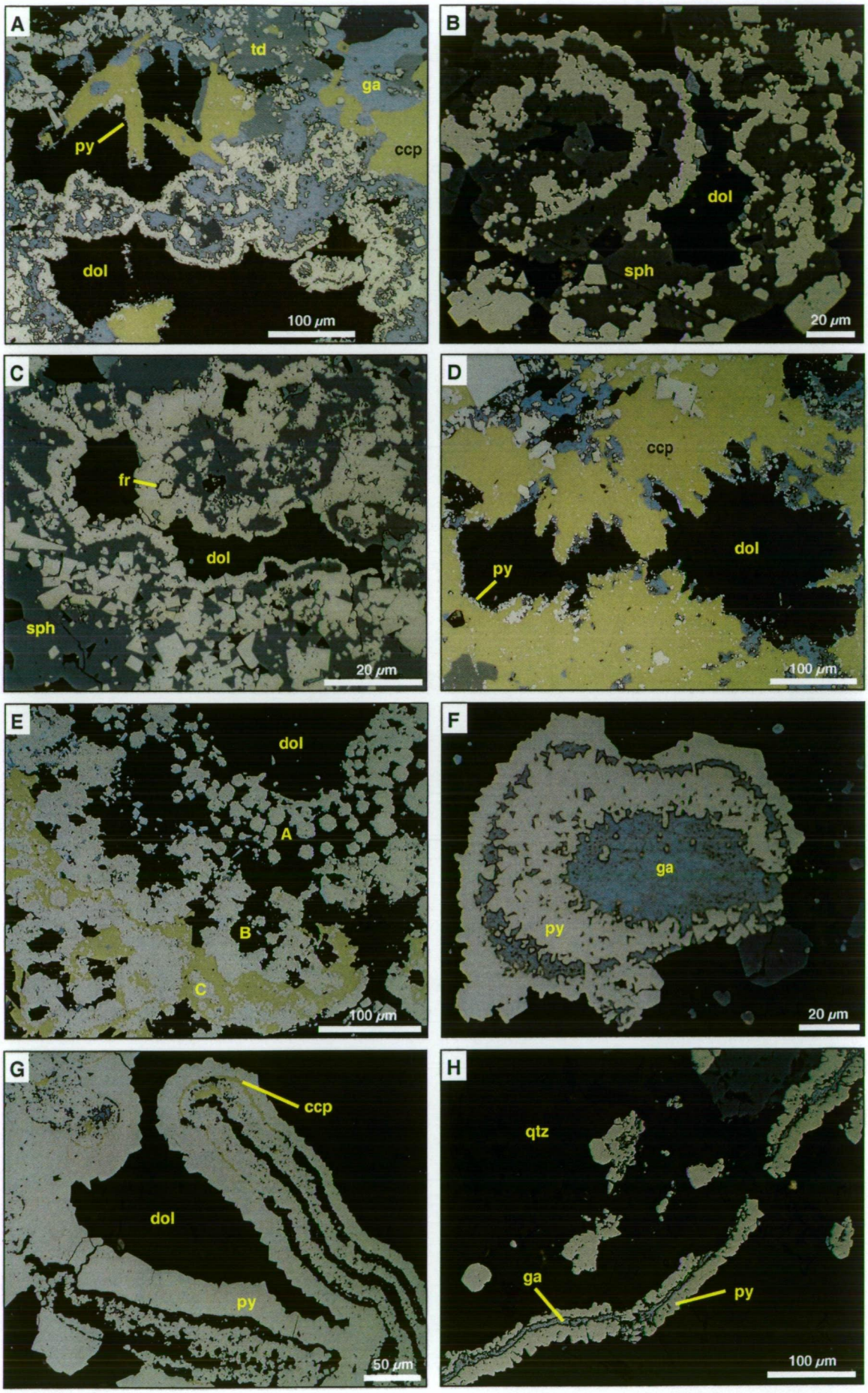
A
td
ga
py
ccp
dol
100 μm
B
dol
sph
20 μm
C
fr
dol
sph
20 μm
D
ccp
dol
py
100 μm
E
dol
A
B
C
100 μm
F
ga
py
20 μm
G
ccp
dol
py
50 μm
H
qtz
ga
py
100 μm

Paragenetically early, primitive sulfide textures provide information about the mechanisms of sulfide deposition and chemistry of the mineralising fluid.

Fine-grained primitive sulfide textures, including dispersed microcrystals and spongy, framboidal, dendritic and reticulate aggregates of pyrite and pyrrhotite result from quenching of a reduced fluid, highly supersaturated in Fe and S species (Paradis et al., 1988; Mullin, 1993; Rimstidt, 1997; Solomon and Gaspar, 2001). The very fine grain size indicates rapid nucleation and limited growth of the crystals (Herzig and Hannington, 1995). Butler and Rickard (2000) synthesised framboids by oxidising mackinawite (FeS) in a weakly acidic solution containing H_2S, without oxygen. The early metastable phases including amorphous FeS, makinawite and hexagonal pyrrhotite rapidly transform into pyrite, marcasite or pyrrhotite by low temperature sulfidation reactions, provided $H_2S_{(aq)}$ is present (Schoonen and Barnes, 1991).

Framboids may form in the water column or anoxic, unconsolidated sediment several centimetres beneath the sea floor (Wilkin and Barnes, 1997). Wilkin et al. (1996) demonstrated that iron sulfide microcrystals, precipitating in sediments beneath oxygenated water, produce framboids that are more variable in size than those growing in the water column of anoxic basins due to longer growth times. The relatively large framboids occurring at Lewis Ponds (Table 7.3) may result from very rapid diffusion rates through the substrate, an extended period of microcrystal growth, or precipitation of secondary diagenetic or hydrothermal pyrite overgrowths.

Bladed crystals of barite, anhydrite, sphalerite or hexagonal pyrrhotite occur in well preserved, modern and ancient VHMS deposits. These paragenetically early minerals are commonly pseudomorphed by quartz, carbonate, pyrite, chalcopyrite, pyrrhotite and marcasite (Paradis et al., 1988; Sharpe, 1991; Goodfellow and Franklin, 1993; Halbach et al., 1993; McArthur, 1996). Euhedral, bladed barite, pyrite, chalcopyrite and hexagonal pyrrhotite crystals occur in sea floor sulfidic muds and black smoker chimney fragments associated with sediment-covered mid-ocean rifts (Oudin et al., 1981; Davis et al., 1987; Goodfellow and Franklin, 1993; Zierenberg et al., 1993). The bladed crystals form open networks partly infilled by sphalerite, isocubanite and chalcopyrite. Bladed sulfate crystals commonly occur in ocean-rift (Davis et al., 1987) or back-arc (Eldridge et al., 1983; Halbach et al., 1993) environments.

The vuggy, concentrically banded, botryoidal and encrustation textures resulted from replacement of the fine-grained dolomite matrix and unimpeded, unidirectional growth into open cavities. Botryoidal pyrite or marcasite occurs in many modern and ancient VHMS

deposits (eg. Eldridge et al., 1983; Halbach et al., 1993; Bodon and Valenta, 1995; Solomon and Gaspar, 2001; Martin, 2002). Base metal sulfides may preferentially replace some of the older pyrite bands. Solomon and Gaspar (2001) interpreted dome-like, banded pyrite textures at Hellyer, western Tasmania to indicate progressive unidirectional growth into cavities. Botryoidal textures, commonly referred to as *colloform* textures, are thought to result from homogenous nucleation of colloidal particles in a highly supersaturated solution (Saunders, 1990; Rollinson, 1993).

Primitive Fe-sulfide textures at Lewis Ponds indicate rapid quenching of a reduced, highly supersaturated fluid prior to the base metal mineralising event. The bladed pyrrhotite crystals are probably pseudomorphs of barite or anhydrite. Pyrite framboids, pyrrhotite blades with an orthorhombic crystal form and botryoidal pyrite textures predominantly occur in the matrix of the tightly folded polymictic breccia unit hosting Main zone. These extremely poorly-sorted deposits probably allowed hydrothermal fluids to circulate through a permeable matrix. The surrounding chlorite, dolomite and quartz protected framboidal, bladed and botryoidal aggregates from recrystallisation during deformation and metamorphism.

7.9 Textures resulting from deformation and metamorphism

The massive sulfide at Lewis Ponds is characterised by recrystallised/annealed textures that overprinted primitive sulfide textures during deformation and metamorphism. Fractured pyrite and cataclastic breccia predominantly occur in the Toms zone Central lens, Lady Belmore zone and pre-tectonic to early syn-tectonic veins.

Annealed textures are strongly developed in the banded massive sulfide in Toms zone. Aggregates of pyrite have 120° interfacial angles between adjacent crystals (Fig. 7.11A). Cuspate grains of interstitial galena, chalcopyrite and sphalerite occur along the pyrite grain boundaries. The base metal bands consist of fine to very coarse-grained pyrite euhedra and cuspate grains of galena, chalcopyrite and tetrahedrite, surrounded by large aggregates of sphalerite (Fig. 7.11B). The subordinate sulfides are rounded where galena and chalcopyrite are the predominant enclosing phase (eg. Fig. 7.11C).

Textures resulting from ductile deformation of the massive sulfide and syn-tectonic quartz veins include kink folds, boudins, pinch-and-swell structures and microscopic flattening fabrics. These textures occur in Main, Toms and Lady Belmore zones. Elongate, kink folded blebs of chalcopyrite, tetrahedrite, galena and pyrrhotite define the regional cleavage (eg. Fig. 7.11 D). Kink folds, pinch-and-swell structures and boudins occur throughout the Toms zone and rarely Main zone Central lenses (Figs. 4.12 and 4.13).

Figure 7.11 Textures resulting from metamorphism and deformation

A Fractured aggregate of annealed pyrite characterised by 120° interfacial angles between adjacent crystals. Toms zone hangingwall. TLPD-51AW2, 355 m.

B Annealed textures in a base metal band consisting of cuspate galena grains where sphalerite is the predominant phase, and rounded sphalerite grains where galena is the predominant phase. Toms zone Central lens. TLPD-51A, 479 m.

C Annealed massive pyrrhotite-galena-sphalerite characterised by rounded pyrrhotite blebs in galena. Main zone Central lens. TLPD-18, 365 m.

D Elongate pyrrhotite grains in sphalerite, aligned with the S_1 flattening orientation. Type 3A quartz-sphalerite-pyrrhotite-chalcopyrite vein, Lady Belmore zone. TLPD-63, 415 m.

E Anastomosing fractures in pyrite-arsenopyrite aggregates. Fractures end abruptly at the margin of the large chalcopyrite-galena-sphalerite mass in the centre of the photomicrograph. Toms zone Central lens. TLPD-51A, 479 m.

F Fractures developed along grain boundaries in annealed, coarse-grained pyrite. Fractures are filled with galena and chalcopyrite. Toms zone Central lens. TLPD-51A, 488 m.

G Orthogonal fractures in pyrite, parallel to the mineral cleavage planes. Toms zone Central lens. TLPD-46A, 126 m.

H In situ cataclastic breccia resulting from intense brittle fracturing of pyrite and arsenopyrite aggregate. Toms zone Central lens. TLPD-46A, 126 m.

Abbreviations: ga = galena, ccp = chalcopyrite, sph = sphalerite, po = pyrrhotite, as = arsenopyrite.

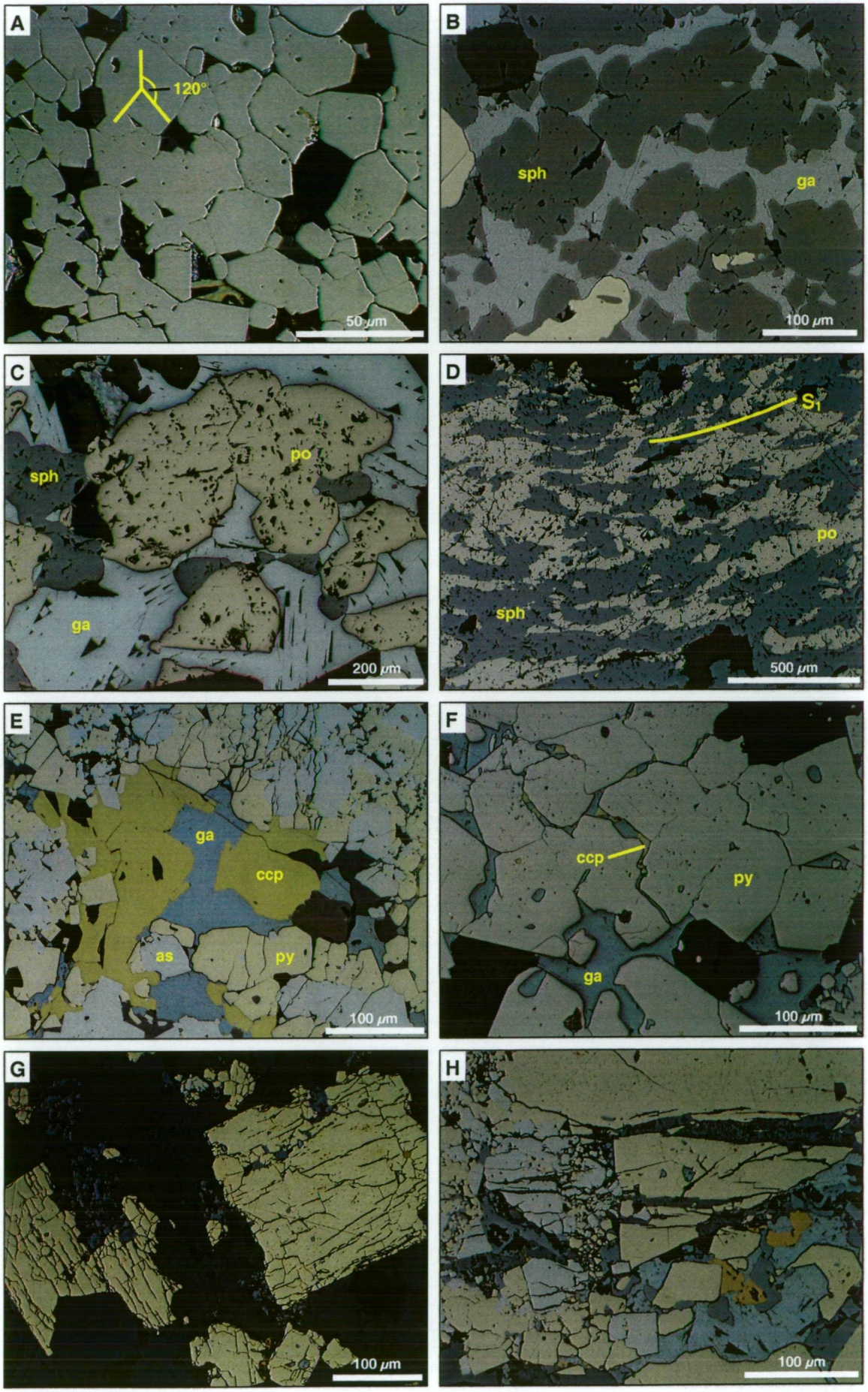
A
120°
50 μm
B
sph
ga
100 μm
C
sph
po
ga
200 μm
D
S1
po
sph
500 μm
E
ga
ccp
as
py
100 μm
F
ccp
py
ga
100 μm
G
100 μm
H
100 μm

Orthogonal, dendritic and anastomosing fracture networks occur in pyrite and arsenopyrite aggregates in Toms zone (Fig 7.11E-H). These are parallel to the tectonic cleavage, grain boundaries or mineral cleavage planes. Ductile minerals such as chalcopyrite and galena have filled the brittle fractures (Fig. 7.11F). Microscopic to macroscopic areas of in situ cataclastic breccia occur throughout Toms zone, where brittle structures cut across the massive sulfide (Figs. 4.13F and 7.11G).

Interpretation of annealed textures

Regional deformation and metamorphism cause significant textural modification of massive sulfide. Annealing involves the rearrangement of grain boundaries to reduce free energy resulting from plastic deformation of the crystal lattice. This is achieved by decreasing the surface area, thereby increasing grain size (Stanton, 1972). In monomineralic aggregates, 120° interfacial angles develop when textural equilibrium exists between adjacent grains (Stanton, 1965).

In aggregates of two or more sulfides, the minor phase segregates along grain boundaries of the more abundant mineral. Cuspate galena grains occur where sphalerite is the most abundant phase. Rounded tetrahedrite, chalcopyrite and pyrrhotite grains occupy interstitial spaces in large galena aggregates. Euhedral pyrite crystals develop in the base metal bands because their surface energies are significantly lower than the surrounding base metal sulfide (Stanton, 1965).

7.10 Sulfide Geochemistry

In the following section, whole rock geochemistry of selected samples, microprobe analyses of sulfides and modal sulfide abundance are used to compare the major and trace element distribution among sulfides in each of the mineralised zones.

Whole rock geochemistry

Individual and averaged whole rock geochemical analyses from the mineralised zones are presented in Tables 7.4 and 7.5. The Lewis Ponds massive sulfide is enriched in Fe, S, Cu, Pb, Zn, As, Ag, Sb, Sn, Cd, Hg, Au, Bi and Se, relative to the surrounding, intensely altered host rock. Toms zone has higher and more variable Zn, Pb, Cu, Ag, Sb, Sn, Cd, Bi, Mo and Ba concentrations than Main zone. These differences in whole rock geochemistry partly reflect the more massive nature of the Toms zone Central lens and fine-grained sedimentary host rock. Main zone occurs in poorly-sorted polymictic breccia and pebbly-granular sandstone. The Main zone Central lens has higher average As and Au concentrations than Toms zone.

Disseminated pyrite-rich rocks in Main and Toms zones are characterised by higher Ni and Cr concentrations than the massive sulfide. Whole rock geochemical data is not available for the New Lewis Ponds, Lady Belmore, and Footwall Copper zones.

	Main zone				Toms zone		
Sample:	LP12450	LP12465	LP12476	LP36W195	LP51A482	LP51A484	LP51A488
Major (wt %)							
SiO_2	44.33	77.94	42.28	1.03	13.16	9.47	8.28
TiO_2	0.38	0.04	0.05	-0.01	-0.01	0.09	0.02
Al_2O_3	11.81	0.69	1.61	0.02	1.02	2.05	0.18
MgO	17.35	1.11	10.22	0.45	20.20	19.58	1.49
CaO	0.37	2.81	8.54	12.64	21.08	24.16	2.24
Na_2O	-0.05	-0.05	-0.05	-0.05	-0.05	-0.05	-0.05
K_2O	2.71	0.03	0.60	-0.01	-0.01	0.01	0.04
MnO	0.08	0.05	0.27	0.66	1.36	0.87	0.14
P_2O_5	0.27	0.01	0.08	0.04	0.1	0.08	0.16
S	5.06	6.41	9.84	32.50	3.36	2.86	37.30
Fe_2O_3	11.67	7.89	15.34	30.93	3.48	4.50	36.57
Zn	0.43	1.18	1.72	13.75	2.72	1.41	10.60
Pb	0.22	1.14	1.12	6.51	1.43	1.06	10.32
Cu	0.05	0.06	0.05	0.13	0.26	0.02	0.33
Total	94.75	99.39	91.75	98.68	68.21	66.19	107.7
LOI	8.42	6.89	17.85	13.5	27.59	34.68	24.62
Trace (ppm)							
As	5 323	330	1 392	11 200	37	183	7 800
Ba	454	32	67	12	71	23	380
Ag	na	na	39	403	101	na	730
Sb	na	na	67	815	107	na	1 090
Sn	na	na	8	240	62	na	376
Cd	na	na	44	202	67	na	265
Cr	419	19	100	5	-1	-1	12
Ni	118	14	38	25	5	-1	4
Se	2	4	6	na	na	-1	na
Bi	-2	5	-2	-2	-2	-2	-2

Table 7.4 Whole rock analyses of disseminated sulfide and massive sulfide samples from Toms zone and Main zone (this study). Negative numbers are below XRF detection limits. Low totals in LP12450, LP12476, LP51A482 and LP51A484 result from high ignition losses due to CO_2 in carbonates and oxidation of SO_2 in sulfides (Potts, 1987). LP51A488 has a high total (>100%) because total iron is expressed as Fe_2O_3 rather than FeS. Na = not analysed.

	Main zone Central lens				Toms zone Central lens		
Drill Hole	TLPD-3	TLPD-12	TLPD-21	TLPD-34W	TLPD-49	TLPD-51AW1	TLPD-51AW2
Interval (m)	177-189	453-483	435-446	241-250	261-267	475-480	388-395
Major (wt %)							
Zn	2.51	7.16	3.70	1.91	6.60	8.80	13.76
Pb	1.19	4.65	2.38	0.95	2.22	7.11	8.36
Cu	0.11	0.21	0.24	0.10	0.20	0.56	0.27
Trace (ppm)							
As	1 461	3 893	2 162	2 072	3 242	1 300	1 823
Ba	na	114	344	348	252	7 141	2 202
Ag	64	151	127	57	72	450	176
Sb	344	662	129	108	206	1 330	751
Sn	41	62	45	30	110	210	77
Cd	79	182	94	56	204	225	338
Co	15	13	na	na	na	na	na
Bi	12.1	na	7.8	10.5	39.5	5.3	6.5
Mo	2	6	na	na	5	15	11
Au	1.89	4.27	3.17	1.40	1.34	4.89	1.83
Hg	8.4	20.7	12.1	7.77	8.4	12.6	20.8
Te	na	na	0.41	0.17	0	0	0.02

Table 7.5 Major and trace element composition of the Central massive sulfide lenses expressed as numerical averages of one metre samples from selected drill hole intervals. Data occurs in unpublished company reports: Perkins (1995; 1996). Analyses were carried out by XRAL Laboratories, Ontario. Na = not analysed. All major and trace element concentrations were significantly higher than the minimum detection limits except for Te.

Figure 7.12 presents the whole rock, major and trace element composition of one metre samples from the massive sulfide lenses. Moderate to strong positive correlations exist between all of the elements plotted. However, whole rock compositions are more variable in Toms zone than Main zone. Two discrete linear trends occur on the Ag-Pb, Au-As, Hg-Au, Hg-Zn, Hg-Sn and Bi-Pb scatter plots. The Toms zone Central massive sulfide lens has consistently higher Zn:Hg, Sn:Hg and Pb-Bi ratios than Main zone. This may indicate that galena grains in Toms zone generally have lower Bi concentrations and that sphalerite grains have lower Hg or higher Zn concentrations than those in Main zone. The linear trends in Figure 7.12 are attributed to variations in the relative modal abundance and composition of tetrahedrite, galena, arsenopyrite, electrum, sphalerite and stannite.

The whole rock geochemical trends are consistent with observed sulfide mineralogy and indicate that:

- Au is associated with Hg, As and Cu;
- Ag occurs with Pb and Sb;
- Zn and Sn-bearing minerals contain Cd and Hg; and
- Bi occurs in Pb-bearing minerals.

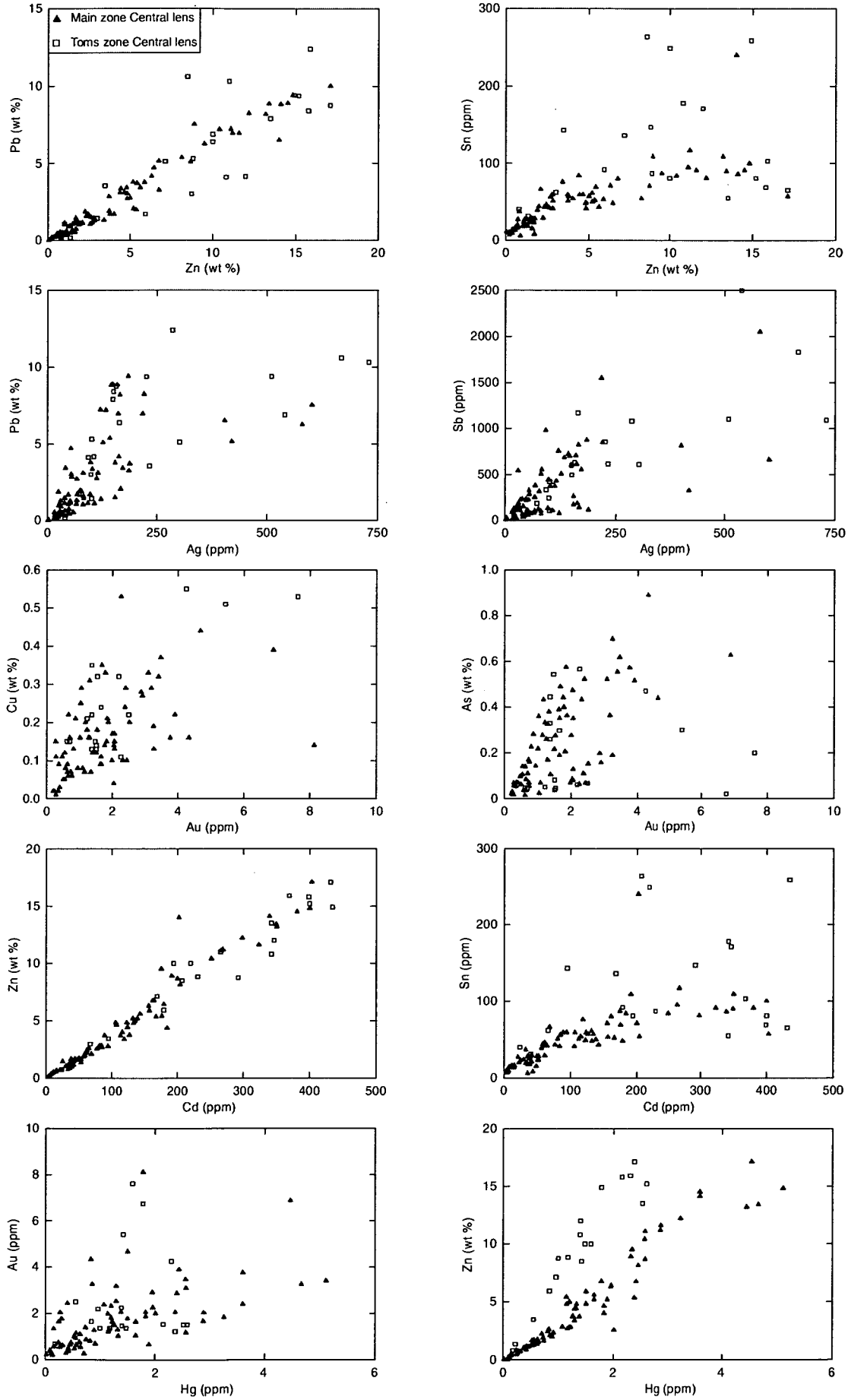

Figure 7.12 Scatter plots of whole rock geochemical data from the Central massive sulfide lenses.

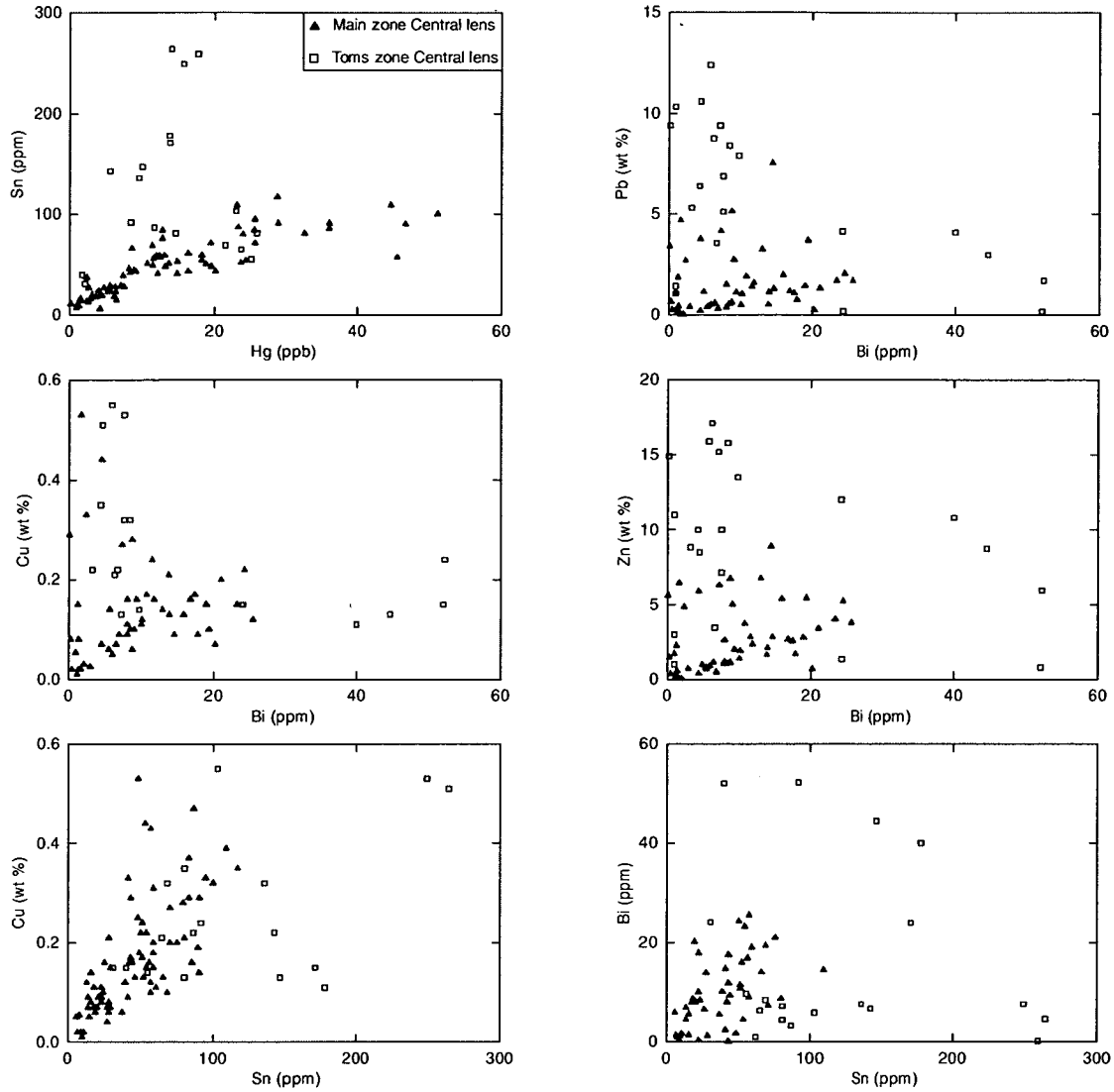

Figure 7.12 continued. Scatter plots of whole rock geochemical data from the Central massive sulfide lenses at Main and Toms zones. Based on 96 unpublished analyses taken over one metre intervals from drill holes: TLPD-3, TLPD-12, TLPD-21, TLPD-34W, TLPD-49, TLPD-51AW1 and TLPD-51AW2 (Perkins 1995; 1996) and 8 samples from this study.

Sulfide mineral compositions

Pyrite

The pyrite contains up to 0.9 wt % As, 4 370 ppm Co, 3 170 ppm Zn, 2 320 ppm Bi, 1 140 ppm Ag, 910 ppm Mn, 520 ppm Cu, and 360 ppm Ni (Table 7.6; Appendix 5). These elements are interpreted to occur as non-stoichiometric lattice substitutions for Fe or sub-microscopic arsenopyrite, sphalerite, tetrahedrite, galena and chalcopyrite inclusions within the pyrite. Gold, Bi, Co and Ni concentrations were mostly at or below microprobe detection limits. Framboidal and spongy pyrite aggregates in Main zone have higher average As, Ag and Mn concentrations than the recrystallised pyrite in Toms zone.

Zone	N	Co (ppm)	Ni (ppm)	Cu (ppm)	Zn (ppm)	As (ppm)	Ag (ppm)
Main	10	<120 – 4 370	<150 – 170	<250 – 340	<250 – 3 170	600 – 8 830	<90 – 490
Toms	5	<120	<150	<250 – 320	<250 – 2 250	<70 – 1 350	<90
Lady Belmore	4	<120	<150	<250 – 520	<250	<70 – 2 380	<90 – 1 140
FW Copper	6	<120 – 380	<150 - 360	<250	<250	<70	<90 – 140

Table 7.6 Pyrite trace element compositions. Based on 25 microprobe analyses from 11 polished thin sections. Detection limits: 120 ppm Co, 150 ppm Ni, 250 ppm Cu, 250 ppm Zn, 70 ppm As, 90 ppm Ag.

Sphalerite

Sphalerite trace element compositions are highly variable (Table 7.7; Appendix 5). The Cu and Ag probably occur in sub-microscopic chalcopyrite, tetrahedrite and galena inclusions. Unpublished microprobe data provided by Tri Origin indicate that the Fe and Zn concentrations do not vary significantly within individual samples or polished thin sections. Average Mn concentrations in the sphalerite are higher in Toms zone than other mineralised zones (Fig. 7.13). Sphalerite grains in the Footwall Cu zone generally contain more Cd than those in the massive sulfide lenses. Iron and Zn concentrations do not vary systematically between the mineralised zones at Lewis Ponds (Fig. 7.13).

Zone	N	Fe (wt %)	Cu (ppm)	Mn (ppm)
Main	23	3.4 – 7.4	<250 – 1 330	80 – 1 590
Toms	15	0.1 – 6.8	<250 – 4 280	<50 – 2 570
Lady Belmore	2	6.4 – 6.9	<250	770 – 1 180
FW Copper	8	3.2 – 7.3	<250 – 1 910	430 – 2 020
	N	Cd (ppm)	Ag (ppm)	Hg (ppm)
Main	23	<90 – 2 290	<290 – 2 730	<260 - 670
Toms	15	<90 – 2 090	<290 – 3 780	<260
Lady Belmore	2	<90 – 1 780	<290 – 2 040	<260
FW Copper	8	<90 – 3 380	<290 – 1 650	<260

Table 7.7 Sphalerite compositions. Based on 48 microprobe analyses from 34 polished thin sections. Detection limits: 180 ppm Fe, 250 ppm Cu, 50 ppm Mn, 90 ppm Cd, 290 ppm Ag, 260 ppm Hg.

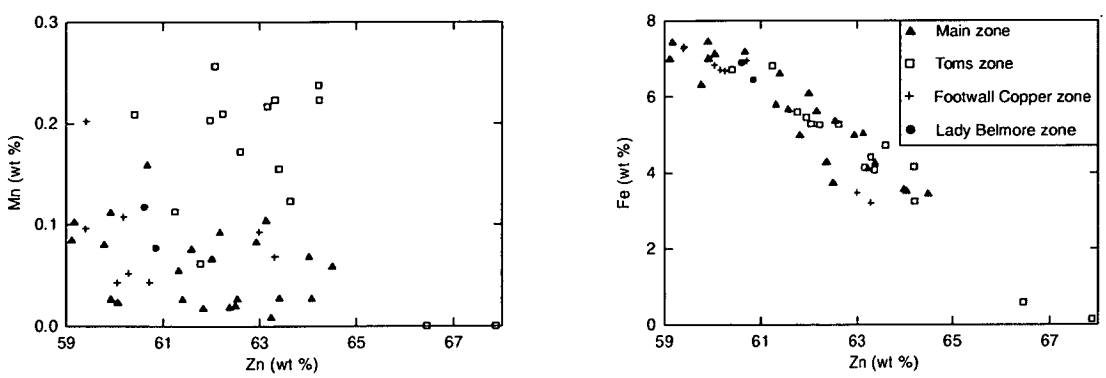

Figure 7.13 Sphalerite compositions from Main, Toms, Lady Belmore and Footwall Copper zones. Detection limit for Mn is 50 ppm.

Significant amounts of Fe, Mn and Cd may substitute for Zn in sphalerite (Deer et al., 1992). Huston et al., (1995) interpreted that Cu, Ag, Ni, In, Mo, and Te also substitute into the sphalerite lattice. High temperature (400-800°C) experiments determined that Mn and Cd concentrations in sphalerite and wurtzite are strongly dependent on temperature and pressure (Bethke and Barton, 1971; Kubo et al., 1992). Since Mn occurs in numerous oxidation states, the activity of Mn in hydrothermal fluids also varies with fO_2 (Mishra and Mookherjee, 1988). Therefore, the Mn content of sphalerite at Lewis Ponds may also indicate variations in the chemistry and temperature of the hydrothermal fluid.

Galena

The galena contains up to 2.4 wt % Se, 2.0 wt % Bi, 2.2 wt % Ag, 9 010 ppm Fe, 1 910 ppm Sb and 550 ppm Te (Table 7.8 and Appendix 5). Antimony, Te and Bi were not included in all of the microprobe analyses. Galena grains occurring in type 1A carbonate-chalcopyrite-pyrite veins in the Footwall Copper zone have significantly higher (up to 100x) the Se, Ag, Bi and Fe concentrations than those in the massive sulfide (Table 7.8; Fig. 7.14). The galena grains in Toms zone generally contain less Fe than those in Main zone and the Footwall Copper zone. Trace amounts of Fe, Ag, Sb and Bi may occur as stoichiometric substitutions for Pb or non-stoichiometric mineral inclusions such as pyrite, argentite and tetrahedrite (Deer et al., 1992). Selenium and Te readily substitute for S as a complete solid solution between galena (PbS), clausthalite (PbSe) and altaite (PbTe).

Zone	N	Fe (ppm)	Ag (ppm)	Se (ppm)	N	Bi (ppm)
Main	20	<280 – 9 010	870 – 4 290	<260 – 2 620	2	2 550 – 2 840
Toms	16	<280 – 5 140	2 060 – 5 050	330 – 19 030	2	2 710 – 2 800
Lady Belmore	3	<280 – 4 860	300 – 6 000	<260 – 13 390	0	-
Footwall Cu	17	<280 – 6 680	5 140 – 8 950	7 600 – 23 890	14	13 700 – 19 900

Table 7.8 Galena trace element compositions. Based on microprobe analyses from 32 thin sections. Detection limits: 280 ppm Fe, 200 ppm Ag, 260 ppm Se, 300 ppm Bi.

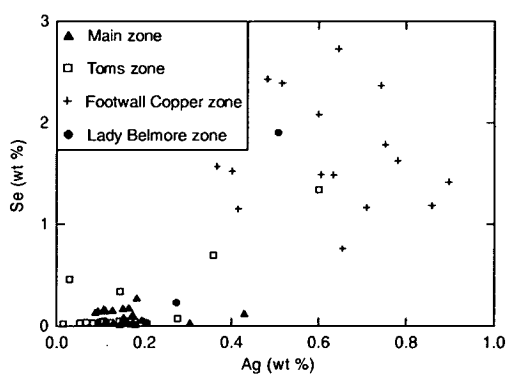

Figure 7.14 Galena compositions from Main, Toms, Lady Belmore and Footwall Copper zones.

Chalcopyrite

The chalcopyrite grains analysed during this study contain up to 6 790 ppm Zn, 1 250 ppm Sn, 990 ppm Ag and 590 ppm Se (Table 7.9; Appendix 5). These elements may occur as sphalerite, stannite, tetrahedrite and galena mineral inclusions or as lattice substitutions for Cu and S. Chalcopyrite grains occurring in the Main zone Central massive sulfide lens and Footwall Copper zones have higher average Ag concentrations than those in Toms zone.

Zone	N	Zn (ppm)	Ag (ppm)	Se (ppm)
Main	4	<250 – 1 780	<90 – 990	<260 – 590
Toms	3	<250 – 6 790	<90	<260 – 190
Footwall Cu	11	<250 – 590	<90 – 560	<260 – 500

Table 7.9 Chalcopyrite trace element compositions. Based on 18 microprobe analyses from 9 polished thin sections. Detection limits: 250 ppm Zn, 90 ppm Ag, 260 ppm Se.

Tetrahedrite and tennantite

The major and trace element compositions of tennantite and tetrahedrite grains are presented in Table 7.10. Coupled substitutions occur between the following sets of elements: Cu-Ag, Fe-Zn and Sb-As (Fig. 7.15). The Sb/(Sb+As+Bi) values vary from 0.4 to 1.0 and Ag/(Ag+Cu) values vary from 0.05 to 0.5 (Fig. 7.15). The tetrahedrite contains significant amounts of Ag (6-28 wt %), Sb (12-28 wt %) and Cu (17-36 wt %). Nickel, Te, Au, Hg, Pb and Bi concentrations were mostly below microprobe detection limits. The trace element compositions of the tetrahedrite sulfosalts do not vary systematically between mineralised zones or within individual samples at Lewis Ponds.

Zone	N	Sb (wt %)	Cu (wt %)	Ag (wt %)	Fe (wt %)
Main	25	25.3 – 27.6	18.7 – 36.1	3.1 – 26.9	4.3 – 5.6
Toms	19	12.1 – 27.7	22.3 – 35.4	7.6 – 21.6	4.7 – 5.5
Lady Belmore	2	26.2	17.7 – 18.4	27.1 – 28.3	5.3
	N	Zn (wt %)	As (ppm)	Cd (ppm)	Se (ppm)
Main	25	0.5 – 2.8	<180 – 22 450	<180 – 630	<200 – 560
Toms	19	1.2 – 1.9	<180 – 111 250	<180 – 480	<200 – 800
Lady Belmore	2	1.0 – 1.2	<180	<180 – 260	<200 – 240

Table 7.10 Tetrahedrite and tennantite major and trace element compositions. Based on 46 microprobe analyses in 17 polished thin sections. Detection limits: 200 ppm Sb, 200 ppm Cu, 210 ppm Ag, 140 ppm Fe, 170 ppm Zn, 180 ppm As, 180 ppm Cd, 200 ppm Se.

Tetrahedrite-tennantite sulfosalts are represented by the following general formula:
$(Cu,Ag)_6\ [Cu_{2/3}(Fe,Zn,Cd,Hg,Pb)_{1/3}]_6\ (Sb,As,Bi)_4\ (S,Se)_{13}$ (Sack and Loucks, 1985).
The compositions of tetrahedrite and tennantite minerals at Lewis Ponds, when normalised to four Sb+As+Bi atoms, are summarised as:
$(Cu_{1.1\text{-}5.5}Ag_{0.5\text{-}4.8})_6\ (Cu_{3.9\text{-}4.3}Fe_{1.2\text{-}1.8}Zn_{0.1\text{-}0.7})_6\ (Sb_{1.6\text{-}4}As_{0\text{-}2.4})_4\ S_{13}$.

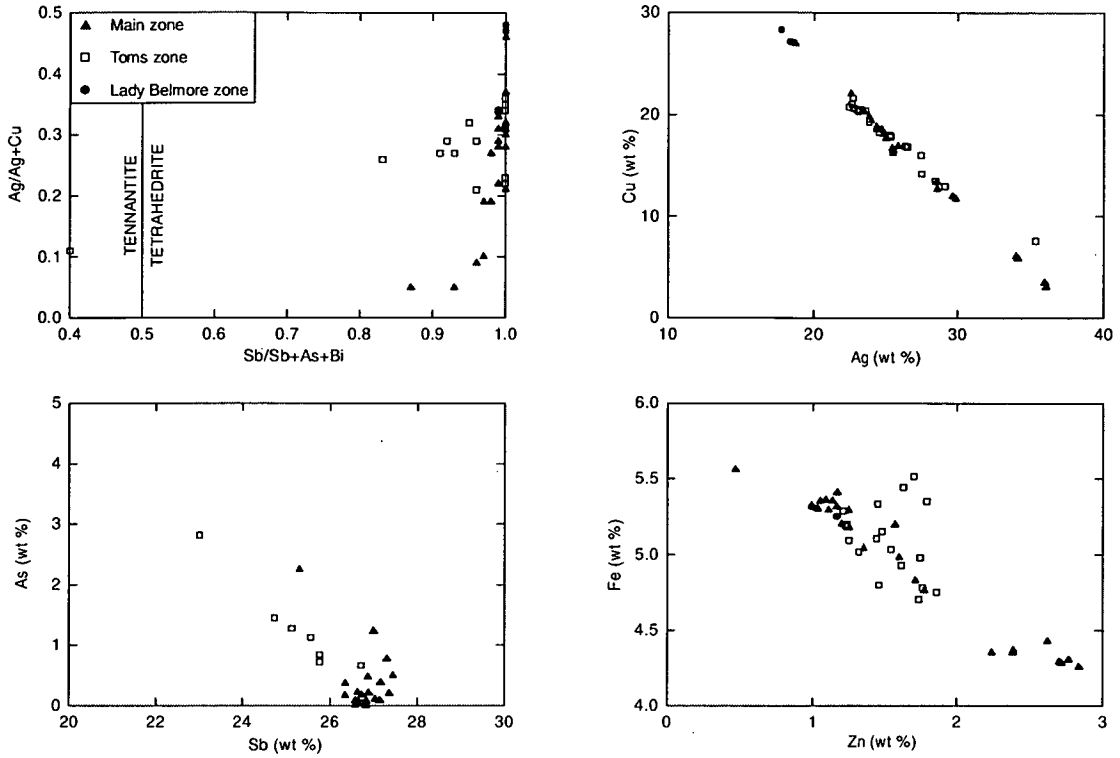

Figure 7.15 Tetrahedrite-tennantite compositions from Main, Toms and Lady Belmore zones. Detection limits: 210 ppm Ag, 200 ppm Sb, 180 ppm As, 170 ppm Zn, 140 ppm Fe and 240 ppm Hg. Based on 46 analyses.

Stannite

At Lewis Ponds, stannite has the general formula, $Cu_{1.9\text{-}2.0}(Fe_{0.8\text{-}0.9},Zn_{0.1\text{-}0.4})SnS_4$, when normalised to four S+Se+Te atoms. The stannite contains up to 5 750 ppm Mo, 3 310 ppm Te, 1 890 ppm Se, 1 110 ppm Cd, 890 ppm As and 440 ppm Ag. (Table 7.11; Appendix 5).

Zone	N	Zn (wt %)	Cd (ppm)	Ag (ppm)	As (ppm)	Te (ppm)	Se (ppm)
Main	6	1.9 – 5.5	<520 – 1 110	<350 – 440	<380 – 480	<320 - 2 170	<280 – 1 860
Toms	19	1.9 – 4.6	<520 – 860	<350	<380 – 890	<320 - 3 310	<280 – 1 890

Table 7.11 Stannite trace element compositions expressed as wt % and ppm. Based on 25 microprobe analyses from 10 polished thin sections. Detection limits: 470 ppm Zn, 520 ppm Cd, 350 ppm Ag, 380 ppm As, 320 ppm Te, 280 ppm Se.

A solid solution exists between stannite, chalcopyrite and sphalerite. Zinc and Cu sulfide readily dissolve into stannite at high temperatures (Ramdohr, 1979). Experimental studies have determined that sphalerite precipitated in equilibrium with stannite may contain up to 1.7 wt % Sn at 500°C (Nekrasov et al., 1981). The Sn content of sphalerite increases with temperature and decreases with S activity. During slow cooling, sphalerite, chalcopyrite and stannite grains dissociate into the component sulfides, resulting in the characteristic intergrowth textures (eg. Fig. 7.7D). Rapid cooling prevents exsolution of stannite from Sn-rich sphalerite (Nekrasov et al., 1981).

Whole rock geochemistry and trace element distribution among sulfides

Manganese (Mn)

Manganese occurs as a major element in the dolomite (to 7 wt % $MnCO_3$) and a trace element in the sphalerite, pyrite and pyrrhotite (Appendix 5). Sphalerite grains in Toms zone have higher Mn concentrations than those in Main zone (Fig. 7.13). However, primitive sulfides in Main zone, including pyrite framboids and bladed pyrrhotite crystals contain more Mn than the recrystallised sulfides. Therefore, trends in whole rock Mn content depend on the relative abundance of pyrite, pyrrhotite, sphalerite and dolomite and the amount of recrystallisation.

Arsenic (As) and Antimony (Sb)

Significant amounts of As occur in the arsenopyrite (40 wt %) and tetrahedrite (0-11 wt %). Arsenic also occurs as sub-microscopic arsenopyrite inclusions or non-stoichiometric substitutions for Fe in pyrite and stannite (Tables 7.6-7.11; Appendix 5). Pyrite grains in Main zone have significantly higher average As concentrations than those in Toms Zone and the Footwall Copper zone. Therefore, although arsenopyrite and tetrahedrite are more abundant in Toms zone, the higher, more variable whole rock As concentrations in Main zone are attributed to arsenian pyrite compositions, because pyrite is the most abundant sulfide.

Antimony occurs in tetrahedrite, tennantite, pyrargyrite and galena. Antimony concentrations in these minerals do not vary systematically between the mineralised zones. However, Toms zone has higher average whole rock Sb concentrations than Main zone. This variation reflects a greater modal abundance of galena and tetrahedrite in the Toms Central lens.

Silver (Ag)

Silver is a major element in the tetrahedrite, tennantite and pyrargyrite. Trace amounts occur in galena, sphalerite, pyrite and chalcopyrite as mineral inclusions or lattice substitutions (Tables 7.6-7.10; Appendix 5). The massive sulfide contains up to 8 modal % galena and 2 modal % tetrahedrite. Rare Ag sulfosalts such as pyrargyrite do not contribute significantly to the total Ag content. Pyrite grains in Main zone contain more Ag than the those in Toms zone. Silver concentrations in tetrahedrite and galena do not vary systematically between the two massive sulfide zones. Toms zone therefore has higher overall Ag grades than Main zone because tetrahedrite and galena are more abundant in the massive sulfide.

Cadmium (Cd)

Cadmium occurs in the sphalerite, stannite and tetrahedrite (Tables 7.7, 7.10 and 7.11). Substitution of Cd for Zn in sphalerite and stannite accounts for the strong positive correlation

between Cd, Zn and Sn in whole rock analyses from Main and Toms zones (Fig. 7.12). Cd concentrations in the sphalerite and stannite do not vary systematically between the mineralised zones. Whole rock Cd concentrations appear to reflect the abundance of these sulfides.

Nickel (Ni) and Cobalt (Co)

Trace amounts of Ni (<150 - 2 770 ppm) and Co (to 1 420 ppm) occur in the pyrite, pyrrhotite, pyrargyrite and tetrahedrite (Appendix 5). However, pyrite and pyrrhotite contain significantly higher Co and Ni concentrations than the other minerals. Pyrite is the most abundant sulfide at Lewis Ponds. Pyrrhotite occurs throughout Main zone and in the Toms zone footwall. In these areas, whole rock Ni concentrations typically vary from 25 to 350 ppm. Nickel concentrations are significantly lower in the polymetallic massive sulfide than in areas of disseminated sulfide due to dilution of pyrite and pyrrhotite by sphalerite, galena and tetrahedrite.

Tin (Sn)

Tin occurs in sphalerite (<170 – 260 ppm) and chalcopyrite (<170 – 1 250 ppm) in addition to stannite (Appendix 5). Positive correlations exist between Sn, Zn, and Cu in whole rock analyses. The variation in whole rock Sn concentrations between mineralised zones (Fig.7.12) probably reflects the relative modal abundance of stannite, chalcopyrite and sphalerite. Most of the visible stannite in Toms zone occurs in type 2 dolomite-chalcopyrite-pyrite veins. These veins do not occur in the Main zone Central massive sulfide lens.

Bismuth (Bi)

Trace amounts of Bi occur throughout the massive sulfide lenses in galena, tetrahedrite, pyrite and chalcopyrite (Appendix 5). Bi may also substitute into the lattice of sphalerite (Deer et al., 1992). These observations account for the strong positive correlation between Bi, Pb, Cu and Zn in whole rock analyses (Fig. 7.12). Native bismuth and Bi-Se-rich galena occur in type 1A calcite-chalcopyrite-pyrite veins in Footwall Copper zone. However, these minerals were not observed in either massive sulfide zone.

Gold (Au) and Mercury (Hg)

A strong positive correlation exists between Hg, Zn, Au and Sn in whole rock compositions (Fig. 7.12). The highest Hg concentrations occur in sphalerite (670 ppm) and electrum (5.6 wt %). Mercury and Au concentrations in pyrite, pyrrhotite and tetrahedrite were mostly below microprobe detection limits. Some of the Au occurs in electrum (eg. Fig 7.7H). The remainder probably occurs in pyrite and sphalerite. Higher overall Zn:Hg ratios in the Toms zone massive sulfide may reflect lower average Hg concentrations in the sphalerite.

7.11 Metal distribution and zonation

Main zone

The Main zone Central lens is characterised by irregularly distributed massive sulfide and shows no systematic vertical or lateral variations in metal content. Thicker intervals of massive sulfide occur in upper parts of the Central lens and in the Hangingwall lens. Zinc, Pb, Cu, Ag and Au grades are highly erratic. However, the highest Au ± Zn, Ag, Sb and Hg grades generally occur toward the top of the Central lens and throughout the Hangingwall lens in numerous drill holes. Metal contoured long sections of the Central lens define an area of greater than 2 wt % Zn, 2 wt % Pb, 0.2 wt % Cu, 80 ppm Ag and 2 ppm Au, extending over 200 m strike length and from 700 to 400 m RL (Fig 7.16). High-grade massive sulfide occurs within a broad envelope grading 1 wt % Zn, 0.5 wt % Pb, 0.1 wt % Cu and 40 ppm Ag, with Zn ratios of 60-75.

In the Main zone footwall, massive to disseminated sulfide occurs in the matrix of the mixed provenance breccia, limestone-clast breccia and pebbly-granular sandstone deposits. However, these do not constitute a discrete lens. Intervals of massive siltstone are weakly altered and devoid of base metal sulfides.

Toms zone

Metal concentrations vary from the structural footwall to the hangingwall of the Toms Central lens. Copper (Fig. 7.4), ± Ag, Sb, Sn and Mo are relatively enriched in the lowest one to two metres of the massive sulfide lens. High Cu grades also extend into the immediate footwall. Whole rock Bi concentrations progressively increase upward through the Central massive sulfide lens, whereas Sn, Sb and Mo appear to decrease. The high Cu and Sn grades probably reflect a greater abundance of disseminated chalcopyrite and type 2 dolomite-chalcopyrite-pyrite-stannite veins.

Metal contoured long sections of the Toms Central lens outline a patchy area of greater than 4 wt % Zn, 2 wt % Pb, 0.2 wt % Cu, 80 ppm Ag and 0.5 ppm Au, extending over 200 m strike length and from 750 to 300 m RL (Fig. 7.17). This occurs within a 400-500 m long, low grade envelope of greater than 1 wt % Zn, 0.5 wt % Pb, 20 ppm Ag and 0.5 ppm Au. Zinc is evenly distributed throughout the lens. However, higher overall Ag, Pb and Cu concentrations occur at depths below 400 m RL. Shallower parts of the Central lens are characterised by pyrite-sphalerite-rich massive sulfide.

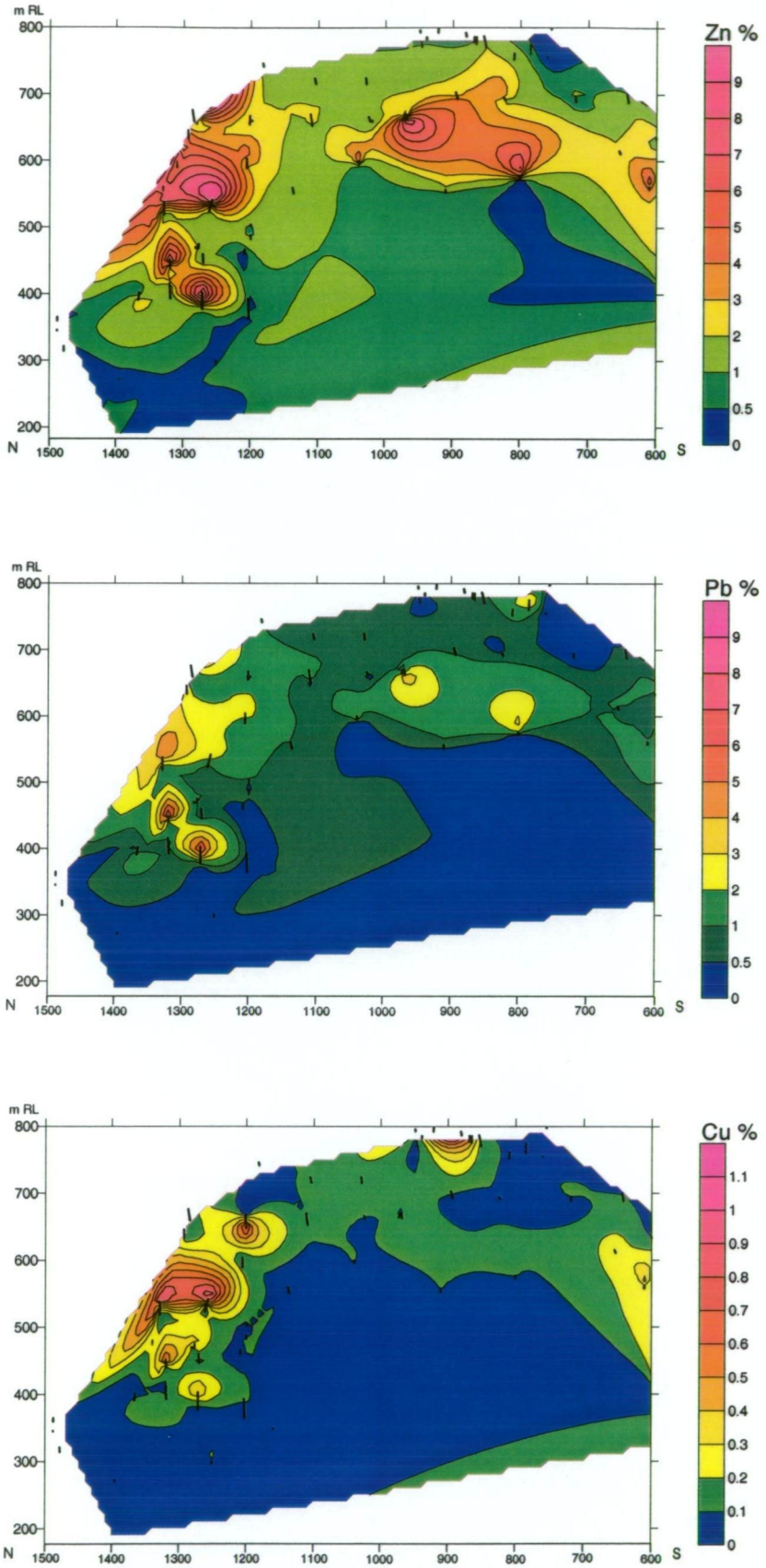

Figure 7.16 Metal contoured long sections of the Main zone Central lens based on 590 assays. Gridded at 10 m line spacing using the 'natural neighbour' gridding method in *Surfer* version 7.0. 'Bulls-eyes' result from the uneven distribution of assays and are not representative of the true metal distribution. Data points are represented by small black dots and lines. Viewed looking toward the hangingwall.

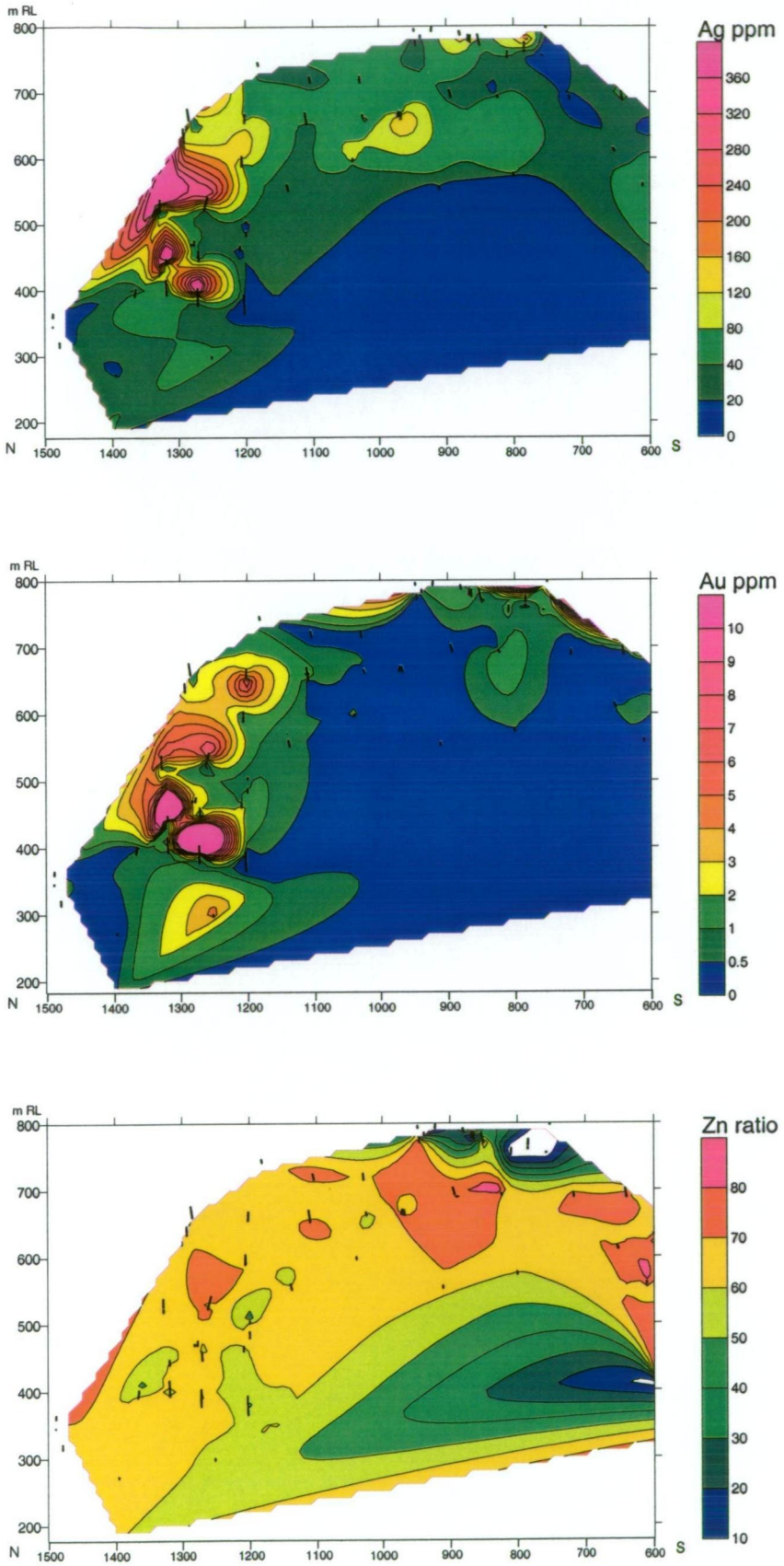

Figure 7.16 continued.

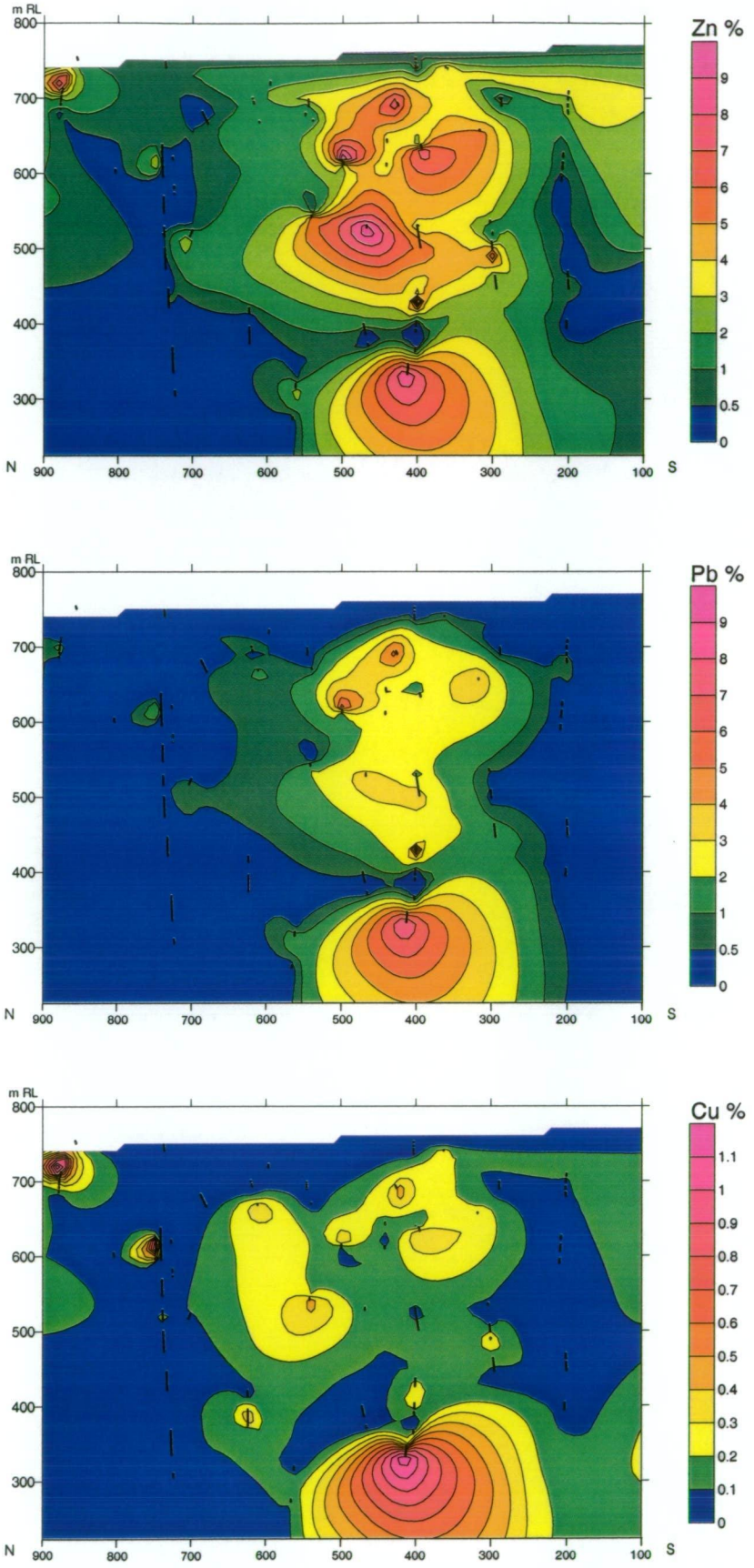

Figure 7.17 Metal contoured long sections of the Toms zone Central lens based on 614 assays. Gridded at 10 m line spacing using the 'natural neighbour' gridding method in *Surfer* version 7.0. 'Bulls-eyes' result from the uneven distribution of assays and are not representative of the true metal distribution. Data points are represented by small black dots and lines. Viewed looking toward the hangingwall.

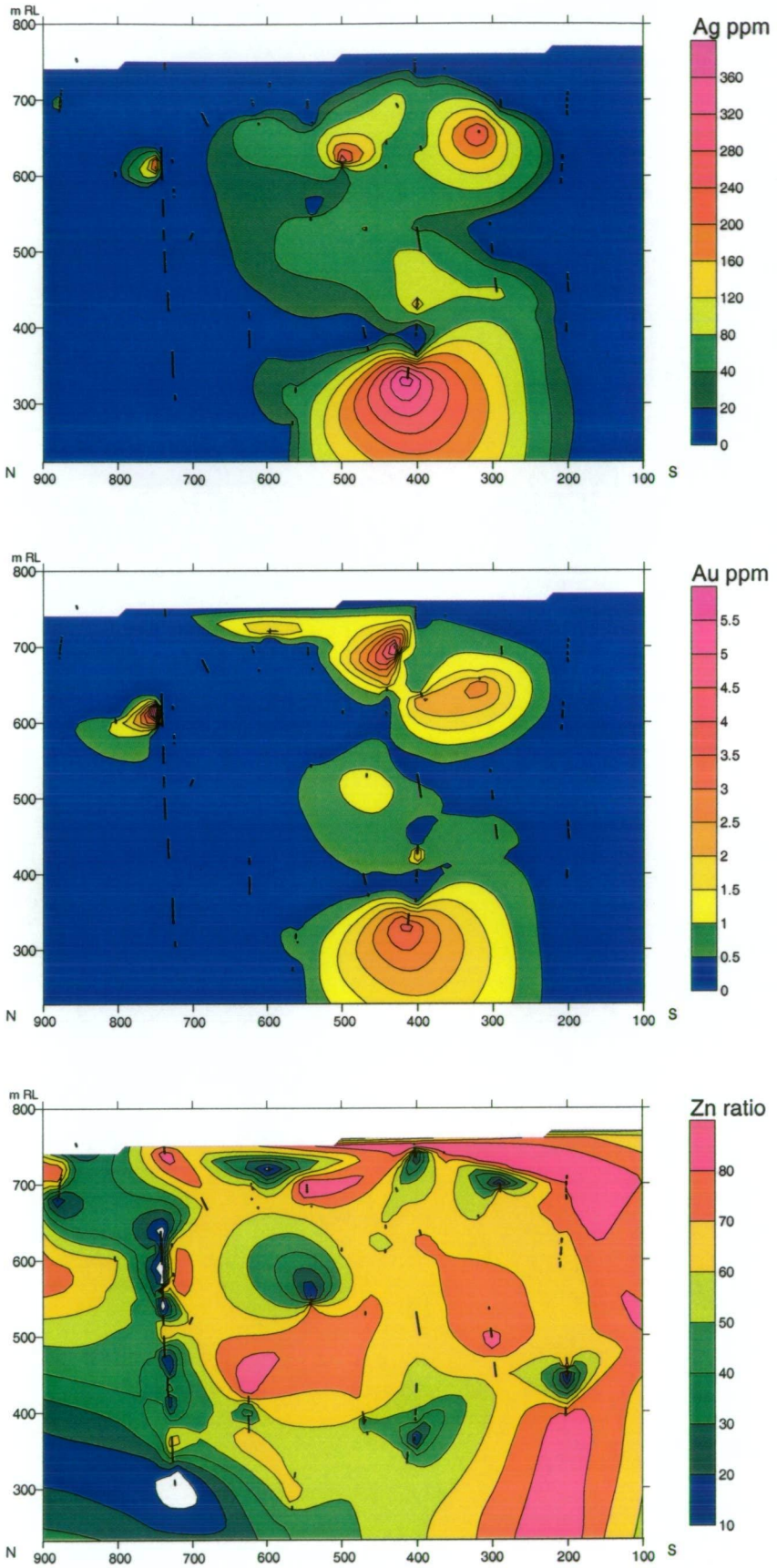

Figure 7.17 continued.

Lewis Ponds fault zone

Overall metal grades within the Lewis Ponds fault zone are variable and highly depleted relative to the massive sulfide lenses. Available assays indicate that the area between Main zone and Toms zone has average grades of 0.5-1 wt % Zn, 0.2-0.4 wt % Pb, 0.04-0.1 wt % Cu, 6-19 ppm Ag and 0.1-0.4 ppm Au (Fig. 7.18). Copper, Au and Zn anomalies extend along the fault for 700-800 m from Toms zone to New Lewis Ponds. Relatively high Au grades occur adjacent to Main, Lady Belmore and Toms zones. There is a strong Au-As association within parts of the Lady Belmore zone. These intervals are characterised by numerous cleavage-parallel arsenopyrite-pyrite-rich carbonate veinlets and have overall Au grades of 1-4 ppm. A significant proportion of assays from the Lewis Ponds fault zone were at or below detection limits (up to 50% for Cu and Au).

Effect of deformation and metamorphism on metal distribution

Thermal metamorphism involves textural and mineralogical changes to rocks. However, processes of solid-state, mechanical transfer do not significantly modify the overall grade and bulk composition of sulfide-bearing rocks (Marshall et al., 2000). Annealing and recrystallisation typically involves expulsion of non-stoichiometric elements and mineral inclusions from pyrite, chalcopyrite, and sphalerite (eg. Huston et al., 1995). Sulfur activity increases in pyrite-pyrrhotite assemblages during high temperature (> 300°C) prograde metamorphism, resulting in progressive corrosion and pseudomorphic replacement of pyrite by pyrrhotite (Craig and Vokes, 1993). This may be accompanied by increased FeS concentrations in coexisting sphalerite (Sangster and Scott, 1976). Fluid flow through transient fracture networks in a shear zone has a greater potential to upgrade or disperse the massive sulfide. Remobilisation may occur over tens to hundreds of metres (Marshall and Gilligan, 1993; Marshall et al., 2000).

Huston et al. (1995) determined that elements occurring in mineral inclusions or as non-stoichiometric substitutions (eg. Cu, Zn, Ag, As, Au and Mo) are removed from pyrite crystals during metamorphic and hydrothermal recrystallisation. However, elements occurring as stoichiometric substitutions for Fe (Ni, Co) or S (Se) remain in the lattice and provide information about the chemistry and temperature of the hydrothermal fluid. Mercury, Se and Ag are interpreted to occur predominantly as lattice substitutions in sphalerite, galena and tetrahedrite respectively (Deer et al., 1992; Huston et al., 1995).

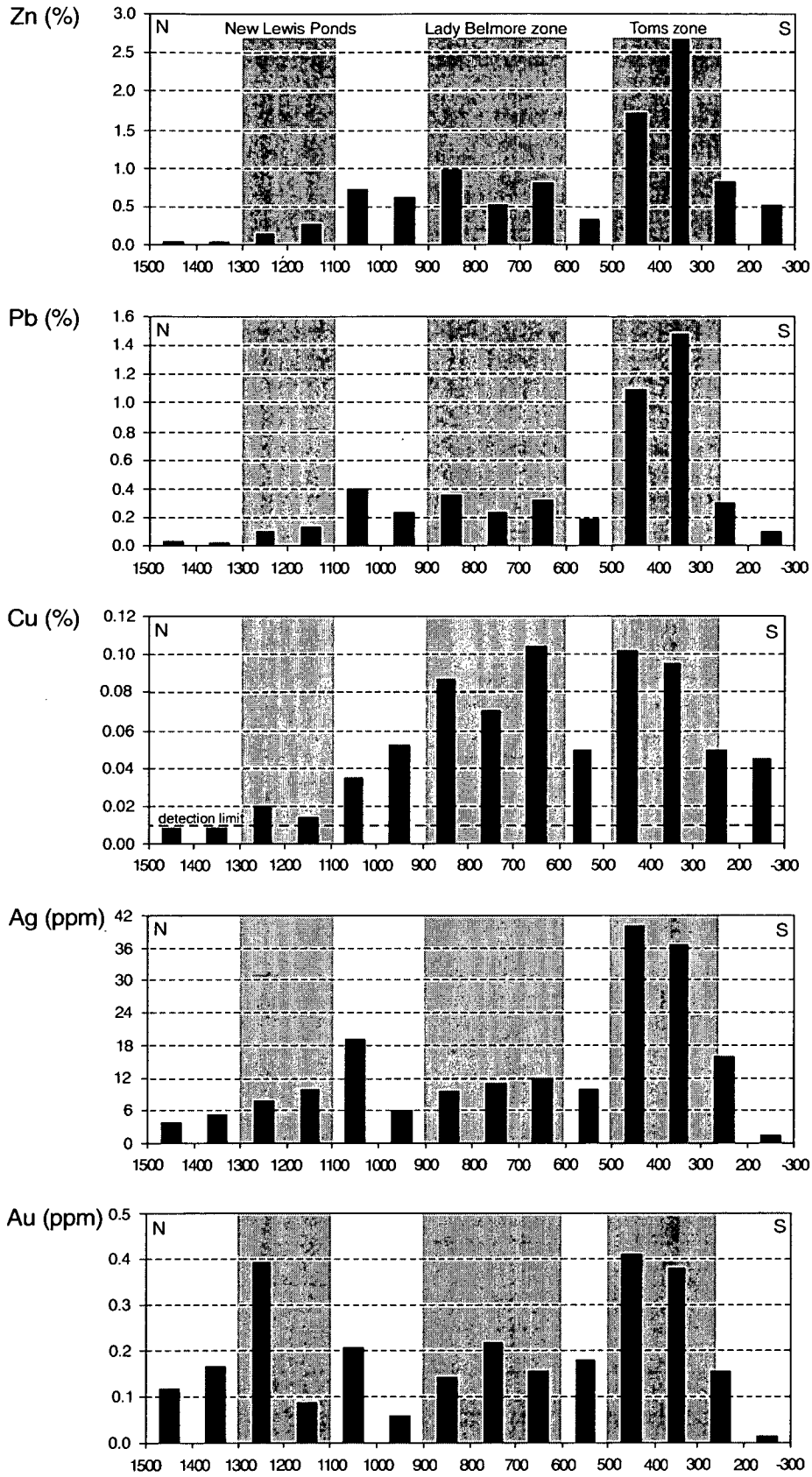

Figure 7.18 Bar graphs showing average Zn, Pb, Cu, Ag and Au grades within the Lewis Ponds fault, averaged over 100 m intervals. Includes all available assay data extending from 100 m east of the baseline to 75 m west of the baseline. All assays at or below the detection limits (0.01% Cu, Pb, Zn; 0.01 ppm Au and 1 ppm Ag) have been assigned half the value of the detection limit for consistency.

Trace element concentrations in pyrite, sphalerite, galena and chalcopyrite vary between mineralised zones at Lewis Ponds. Sphalerite grains in Toms zone have higher average Mn concentrations than those in Main zone. Frabmboidal and spongy pyrite aggregates in Main zone contain more As and Mn than recrystallised pyrite in Toms zone. Galena, sphalerite and chalcopyrite grains in the Footwall Copper zone have significantly higher Se, Ag, Bi and Cd concentrations than those in the massive sulfide.

These variations in sulfide mineral composition are interpreted to reflect the chemistry and temperature of the mineralising fluid(s). Massive sulfide in Toms zone is coarser grained and more strongly annealed than in Main zone. Therefore, recrystallisation, annealing and the rearrangement of grain boundaries in the Toms zone massive sulfide probably accounts for the lower average As, Ag, and Fe content in pyrite, chalcopyrite and galena respectively.

Pyrrhotite pseudomorphs of pyrite rarely occur in the Transitional Unit and Hangingwall Siltstone Unit. Pyrrhotite has replaced pyrite framboids (eg. Fig. 7.8J) and euhedral pyrite crystals. The pyrrhotite may have resulted from an increase in S activity during prograde regional greenschist facies metamorphism.

Remobilisation has occurred along the Lewis Ponds fault and in the adjacent footwall volcanics. Syn-tectonic quartz-sulfide veins surround the Central massive sulfide lens at Toms zone. Numerous centres dominated by disseminated and vein-hosted sulfides occur along the fault at the New Lewis Ponds and Lady Belmore zones. NNW-trending quartz-chalcopyrite veins occupy a large area of the Western Volcanic Succession, south of Toms mine. Initial migration of sulfides along the Lewis Ponds fault was probably limited by low fluid flux, since the majority of syn-tectonic, cleavage-parallel quartz veins (type 3A) resulted from brittle shear failure and extension only (see Chapter 4, section 4.5). However, the late sub-horizontal, type 4 quartz-sulfide veins developed in response to brittle failure when fluid pressures exceeded the lithostatic load. Many syn-tectonic quartz veins contain chalcopyrite, sphalerite and galena. Therefore significant remobilisation of the massive sulfide in Main and Toms zones may have occurred under these conditions.

7.12 Paragenesis

Figure 7.19 summarises paragenetic relationships between sulfide minerals and the textural evolution of the massive sulfide at Lewis Ponds.

1. Development of primitive textures

Dispersed nuclei and bladed, acicular minerals crystallised rapidly from a highly supersaturated fluid in the breccia, sandstone and siltstone matrix. Primary growth of iron (II) monosulfide nuclei was probably limited by the diffusion rate, fluid supply and occurrence of a suitable substrate. Progressive growth of the bladed crystals and microcrystals led to the formation of spongy, framboidal, banded, botryoidal, crustiform, dendritic and reticulate aggregates. Pyrite and pyrrhotite probably replaced the early sulfate minerals and metastable iron (II) monosulfide phases. Dendritic and reticulate networks of bladed crystals and aggregates of micrcocrystals provided a substrate for the subsequent growth of interstitial base metal sulfides.

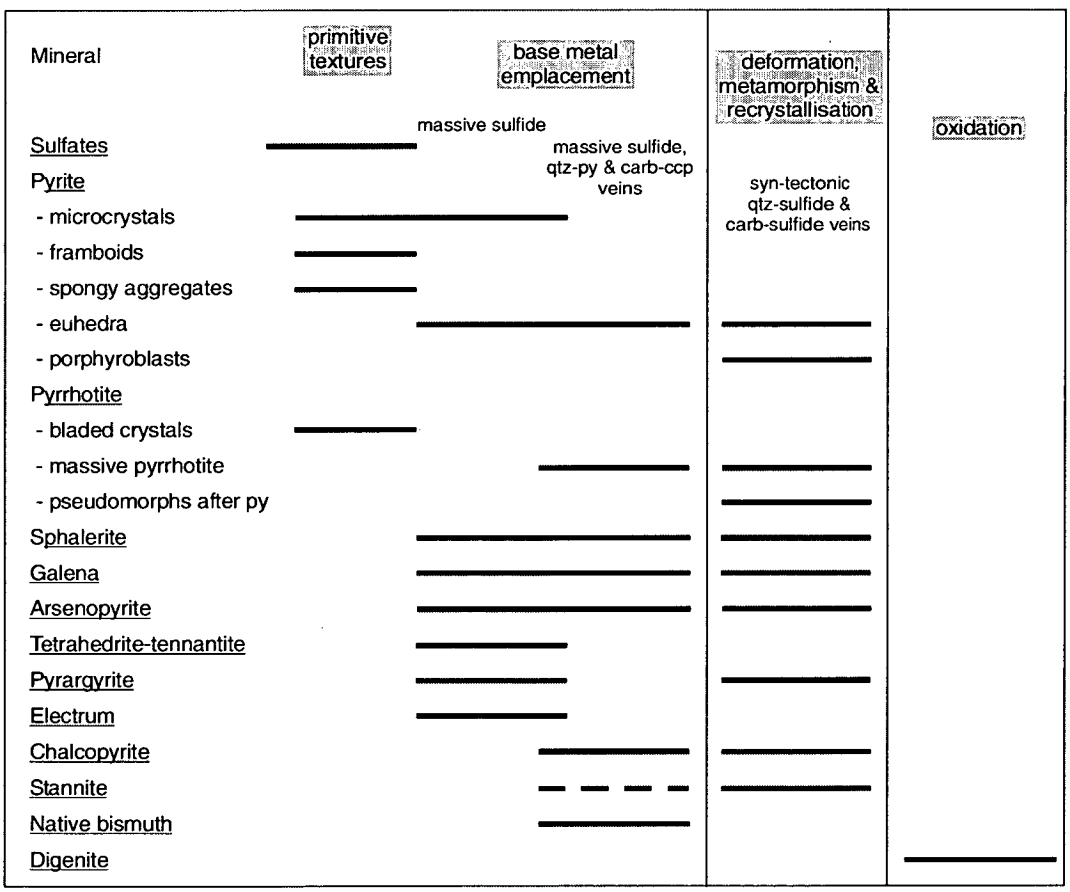

Figure 7.19 Paragenesis of sulfide minerals.

2. Emplacement of massive sulfide lenses and type 1 veins

Primitive textures of pyrite and pyrrhotite were overgrown and infilled by base metal sulfides. Chalcopyrite, sphalerite, galena, tetrahedrite and pyrite partly replaced the fine-grained dolomite matrix. The unimpeded growth of sulfides into secondary pore spaces produced vuggy, botryoidal and crustiform textures. Chalcopyrite, pyrite, Se-Bi-rich galena, sphalerite and native bismuth precipitated in type 1A carbonate veins in the Toms zone footwall. Type 2 dolomite veins, containing chalcopyrite, sphalerite, tetrahedrite, arsenopyrite and stannite were emplaced into lower parts of the Toms Central massive sulfide lens. A chalcopyrite ± pyrrhotite assemblage partly overprinted sphalerite, galena and pyrite bands in the massive sulfide at Main zone.

3. Deformation and metamorphism

The massive sulfide was overprinted by brittle and ductile structures during the D_1 deformation. Type 3 and type 4, shear and extension quartz ± sulfide veins developed in response to brittle failure of the host rocks at low and high angles to the direction of maximum compressive stress. Microfractures formed throughout aggregates of pyrite and arsenopyrite in the Toms Central massive sulfide lens. Fracture orientations reflected the flattening direction, grain boundaries and mineral cleavage planes. Ductile sulfides such as chalcopyrite, tetrahedrite and sphalerite were flattened into elongate, cleavage-parallel aggregates and were later kink folded.

Prograde greenschist facies metamorphism annealed the massive sulfide and produced coarser grained pyrite, with 120° interfacial angles between adjacent grains. Annealed and recrystallised textures developed throughout the Toms zone Central lens and Main zone to a lesser extent. These textures overprinted the paragenetically early bladed, framboidal, spongy and botryoidal aggregates of pyrite and pyrrhotite. Tetrahedrite, stannite, galena, sphalerite and chalcopyrite were segregated along grain boundaries of the pyrite. Expulsion of mineral inclusions and non-stoichiometric elements during metamorphic recrystallisation resulted in lower average As, Ag and Fe concentrations in pyrite, chalcopyrite and galena in Toms zone. Some of the framboids and euhedral crystals of pyrite converted to pyrrhotite.

CHAPTER 8

STABLE AND RADIOGENIC ISOTOPE GEOCHEMISTRY

8.1 Introduction

In this chapter, stable isotopes, radiogenic isotopes, fluid inclusions and metal ratios are used to predict the composition temperature and source of the fluids responsible for hydrothermal alteration and massive sulfide deposition at Lewis Ponds. Part A deals with fluid chemistry during low temperature hydrothermal alteration of the polymictic breccia and siltstone, prior to and during mineralisation. Part B considers the source of metals and S in the mineralising fluid.

8.2 Methods

This study uses fluid inclusion, S isotope and C-O isotope data acquired during this study, together with geochemical data obtained from other sources. Graham Carr, CSIRO division of Exploration and Mining, provided six well constrained Pb isotope analyses from pre-Tri Origin diamond drill holes at Lewis Ponds. Fourteen S isotope analyses were obtained from the Geological Survey of New South Wales. Diamond drill hole assays were provided by Tri Origin.

The $\delta^{13}C_{PDB}$ and $d^{18}O_{VSMOW}$ values of calcite and dolomite were measured using the CO_2 extraction technique outlined in Swart et al. (1991) and a stable isotope mass spectrometer at the University of Tasmania, Central Science Laboratory. Fine-grained carbonate powder was extracted from samples using a dentist's drill. The sixty-seven samples submitted for C-O isotope analysis included: fossiliferous limestone from the Anson Formation and Mullions Range Volcanics; recrystallised limestone clasts from the polymictic breccia and fault-bound stratigraphic unit at Lewis Ponds; hydrothermal dolomite surrounding the massive sulfide lenses; patchy and pervasive hydrothermal calcite; and calcite and dolomite veins.

Three moderately coarse-grained, vuggy dolomite samples, containing abundant liquid-vapour fluid inclusions were chosen for heating and freezing experiments to determine the homogenisation temperature (T_h) and freezing point depression or final melting temperature (θ) of the inclusions; two from Main zone and one from Toms zone. The thick (100 μm) wafers

were cut into smaller pieces and placed, individually in a sealed Linkam fluid inclusion stage for the experiments. Results are listed in Appendix 7.

Sulfur isotope compositions were obtained using the SO_2 combustion method of Robinson and Kusakabe (1975). Sample preparation involved carefully drilling out 8-30 mg of pyrite, pyrrhotite, galena, sphalerite and chalcopyrite from relatively coarse-grained, mineralised rocks using a dentist's drill. These samples were submitted for S isotope analysis at the University of Tasmania, Central Science Laboratory. The results are listed in Appendix 8.

8.3 PART A – carbon-oxygen isotopes and fluid inclusions

The Lewis Ponds host sequence contains abundant primary (sedimentary) and secondary (diagenetic or hydrothermal) carbonate. Fossiliferous limestone-bearing breccia and sandstone occur in Main zone. Fault-bound limestone megabreccia lenses structurally overlie both mineralised zones. A proximal, texturally destructive dolomite-chlorite-talc assemblage surrounds the massive sulfide lenses in Main and Toms zones. Calcite and dolomite veins occur throughout the Lewis Ponds fault and the adjacent footwall volcanic succession.

The relative timing of dolomitisation at Lewis Ponds is well constrained. Sulfide-dolomite textures in Main zone resulted from partial dissolution of the fine-grained dolomite matrix by the mineralising fluid (see Chapter 5, Fig. 5.14). Dolomite also fills secondary pore spaces in the polymictic breccia and massive sulfide (see Chapter 7, Fig. 7.10). The dolomite is spatially associated with primitive sulfide textures including pyrite framboids and acicular pyrrhotite crystals. Therefore, dolomite precipitated prior to and during sulfide mineralisation. Fracture-controlled hydrothermal fluids circulating through the Lewis Ponds fault during the D_1 deformation may have modified the isotopic composition of dolomite in Toms zone.

The purpose of PART A is to: investigate the effects that hydrothermal fluid-rock interactions had on the isotopic composition of the fossiliferous limestone; and determine the possible temperature, composition and source of the fluid from which the dolomite precipitated. The isotopic composition of carbonates depends on the 1) initial isotopic composition of the fluid and reactive host rock, 2) temperature, 3) relative proportion of aqueous C species and 4) amount of CO_2 degassing (Zheng, 1990; Zheng and Hoefs, 1993). In this chapter, two isotopic exchange processes are modelled using mass balance equations and variables 1, 2 and 3, defined above, to predict the isotopic composition of hydrothermal carbonates.
The first isotopic exchange process involves reacting a hydrothermal fluid with pre-existing carbonate (fluid-rock interaction models). In the fluid mixing models, two fluids of differing isotopic composition and temperature are mixed.

Introduction to carbon and oxygen isotope geochemistry

Carbon and O isotopes behave differently to one another in hydrothermal fluids. Minerals precipitating from a fluid attain equilibrium with $\delta^{18}O_{fluid}$ under most temperature and pH conditions. $\delta^{18}O_{fluid}$ does not vary during mineral precipitation because the relative amount of O removed from the fluid is negligible (Ohmoto, 1986). However, $\delta^{13}C_{fluid}$ is strongly dependent on the relative proportions of aqueous C species involved. Mineral precipitation may remove significant amounts of C, causing large variations in $\delta^{13}C_{fluid}$ and therefore, $\delta^{13}C_{carbonate}$ (Ohmoto, 1986).

The common C species in fluids are $H_2CO_{3(aq)}$, $HCO_3^-{}_{(aq)}$, $CO_3^{2-}(aq)$, $CO_{2(g,aq)}$ and $CH_{4(g,aq)}$. Temperature, pH and oxygen fugacity determine the relative proportion of oxidised and reduced ionic C species in hydrothermal fluids (Ohmoto and Rye, 1979). The predominant C-bearing species in seawater is $HCO_3^-{}_{(aq)}$ (Ripperdan, 2001). In hydrothermal fluids ≥100°C, the amount of $HCO_3^-{}_{(aq)}$ is negligible compared to $H_2CO_{3(aq)}$ (Ohmoto, 1986). The total amount of dissolved carbon dioxide and bicarbonate ($H_2CO_{3\ apparent}$) is the sum of the molar concentrations of $CO_{2(aq)}$ and $H_2CO_{3(aq)}$. However, since the isotopic fractionation factors between $CO_3^{2-}{}_{(aq)}$ and $CO_{2(g)}$ are significantly less than those between $CO_{2(g)}$ and $CH_{4(g,aq)}$ at temperatures above 100°C, the following approximation is made:

$$\delta^{13}C_{H_2CO_3(apparent)} \cong \delta^{13}C_{CO_2} \quad \text{(Ohmoto 1972)} \qquad (1)$$

Hydrothermal fluids may also acquire a component of organic C by oxidation reactions. Oxidation of organic CH_4 to CO_2 produces a zone of coupled sulfate reduction – methane oxidation in sediments containing bacteria (Burns, 1998). The resulting range of $\delta^{13}C_{CO2}$ values (-10‰ to -35‰; Ohmoto and Rye, 1979), is considerably lower than $\delta^{13}C_{CO2}$ values predicted from thermodynamic equilibria due to kinetic effects. Final $\delta^{13}C$ values therefore depend on the rate of isotopic exchange between CH_4 and CO_2 (Ohmoto, 1986).

The isotopic composition of carbonate depends on fractionation between the minerals and fluid; and the temperature, pH, oxygen fugacity and isotopic composition of the fluid (Ohmoto and Rye, 1979; Ohmoto, 1986). The fractionation factors relative to temperature are calculated using Equation 2 for O (Ohmoto and Rye, 1979), Equation 3 for C (Ohmoto and Goldhaber, 1997) and the coefficients listed in Table 8.1.

$$1000\ln\alpha = A + \frac{B(10^3)}{T} + \frac{C(10^6)}{T^2} + D \qquad \text{where T(°K)} \qquad (2)$$

$$1000\ln\alpha = A + \frac{B(10^3)}{T} + \frac{C(10^6)}{T^2} + \frac{D(10^9)}{T^3} + E \qquad \text{where T(°K)} \qquad (3)$$

	A	B	C	D	E	Temperature range
$\Delta^{18}O_{ca - H_2O}$	-2.89	0	2.78	0		0-500°C
$\Delta^{18}O_{dol - H_2O}$	-2.0	0	3.2	0		300-510°C
$\Delta^{13}C_{ca - CO_2}$	2.962	-11.346	5.358	-0.388	0	<600°C
$\Delta^{13}C_{dol - CO_2}$	3.132	-11.346	5.538	-0.388	0	<600°C
$\Delta^{13}C_{dol - HCO_3^-}$	38.832	-31.506	7.698	-0.388	0	<290°C

Table 8.1 Fractionation coefficients for carbonate minerals from Northorp and Clayton (1966) Friedman and O'Neil (1977) and Ohmoto and Goldhaber (1997). ca = calcite, dol = dolomite.

Results of carbon-oxygen isotope study at Lewis Ponds

Results of the C-O isotope study at Lewis Ponds are presented in Figures 8.1, 8.2 and Table 8.2.

	Sample description	N	Mineral	$\delta^{18}O_{VSMOW}$ (‰)	$\delta^{13}C_{VPDB}$ (‰)
	Regional fossiliferous limestone	3	Ca	24 to 28	2 to 5
Lewis Ponds	Recrystallised limestone clasts	27	Ca	11 to 20	-5 to 2
	Dol-altered limestone clasts	7	Dol	11 to 16	-11 to -1
	Intense pervasive dol (Main zone)	13	Dol	11 to 15	-11 to 1
	Intense pervasive dol (Toms zone)	6	Dol	8 to 11	-7 to -1
	Dol-ccp-sph-st veins (Toms zone)	5	Dol	6 to 13	-9 to -3
	Ca-ccp-py veins (FW Copper zone)	2	Ca	9	-3 to -1
	Intense patchy / pervasive ca	4	Ca	10 to 11	-5 to -1

Table 8.2 Range of $\delta^{18}O$ and $\delta^{13}C$ values in primary and secondary carbonate from the Lewis Ponds host sequence and fossiliferous limestone lenses from the Mullions Range Volcanics and Anson Formation. Refer to Figure 3.18 for locations of regional limestone samples. Mineral abbreviations: ca = calcite, dol = dolomite, ccp = chalcopyrite, sph = sphalerite, py = pyrite, st = stannite.

The isotopic compositions of primary and secondary carbonate in the Lewis Ponds host sequence are significantly lighter than the regional limestone (Table 8.2). Data obtained during this study indicate that limestone in the Mullions Range Volcanics and Anson Formation has high $\delta^{18}O_{VSMOW}$ (24-28‰) and $\delta^{13}C_{VPDB}$ (2-5‰) values. At Lewis Ponds, limestone clasts in the Transitional Unit and fault-bound stratigraphic unit have variable, generally lower $\delta^{18}O_{VSMOW}$ values of 11 to 20‰ and $\delta^{13}C_{VPDB}$ values of -5 to 2‰. Pervasive carbonate surrounding the massive sulfide lenses, dolomite-altered limestone clasts in Main zone and carbonate-sulfide veins in Toms zone are enriched in light C isotopes. The $\delta^{13}C_{VPDB}$ values range from -11 to 0‰ and $\delta^{18}O_{VSMOW}$ values range from 6 to 16‰. Toms zone dolomite has lighter average O isotope compositions than dolomite in Main zone. In summary, $\delta^{18}O_{VSMOW}$ and $\delta^{13}C_{VPDB}$ values in primary and secondary carbonate at Lewis Ponds decrease toward the mineralised zones (Fig. 8.2).

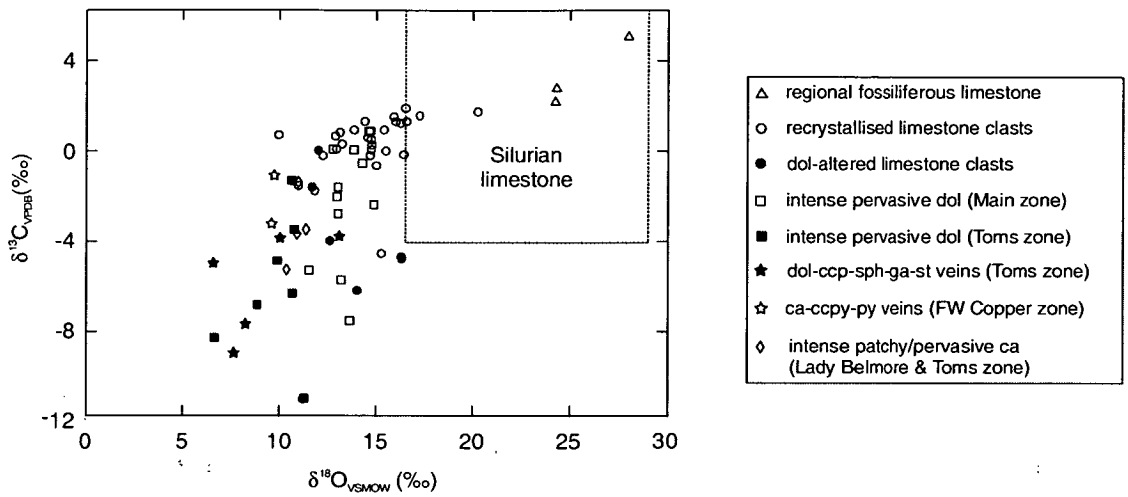

Figure 8.1 C-O isotopes in primary and secondary carbonate at Lewis Ponds and fossiliferous limestone lenses from the Mullions Range Volcanics and Anson Formation. Based on 67 analyses. Field of Silurian marine and freshwater carbonate is from figures 4 and 5 in Veizer and Hoefs (1976).

Temperature, salinity and isotopic composition of dolomite-forming fluid

Fluid inclusions constrain the temperature, salinity and composition of hydrothermal fluids. At Lewis Ponds, medium to coarse-grained, zoned rhombic dolomite crystals contain abundant two phase, liquid-vapour inclusions (Fig. 8.3). These occur in the proximal dolomite-chlorite-talc assemblage associated with the two massive sulphide lenses (see Chapter 5, section 5.4). The rhombic, rectangular or amoeboid fluid inclusions range from one to sixteen micrometres length. Individual inclusions commonly occur in trails, parallel to growth and cleavage planes. Gas bubbles occupy 5-30% of the total volume of the inclusion.

The zoned dolomite crystals occur within structurally competent, rigid patches or lenses of dolomite, with most of the strain focussed in the surrounding chlorite-phlogopite-talc-sulfide-altered polymictic breccia matrix. They are interpreted to have precipitated during diagenesis and low temperature hydrothermal alteration. Dolomite-sulfide textures in Main zone (eg. Figs. 5.5C and 5.14) indicate that the dolomite formed prior to and during mineralisation. The fluid inclusions are therefore likely to contain fluids trapped during diagenetic and hydrothermal alteration of the poylmictic breccia and siltstone deposits.

Minimum trapping temperatures were calculated using the equation: $T = T_h + q$, (4)
where T_h is the homogenisation temperature and q is a pressure correction factor (Roedder, 1984, p. 262) to account for the overlying water column. Assuming that Lewis Ponds formed at 200 to1 000 m water depth and 2 to 10 MPa pressure, the pressure correction factor varies from 2 to 10°C. Therefore, minimum trapping temperatures of fluid inclusions in Main zone range from 166°C to 232°C and fluid inclusions in the dolomite in Toms zone range from 170°C to 232°C (Table 8.3). Homogenisation temperatures have standard deviations of 5 to 5.5. The fluid inclusions generally did not stretch or decrepitate during heating experiments.

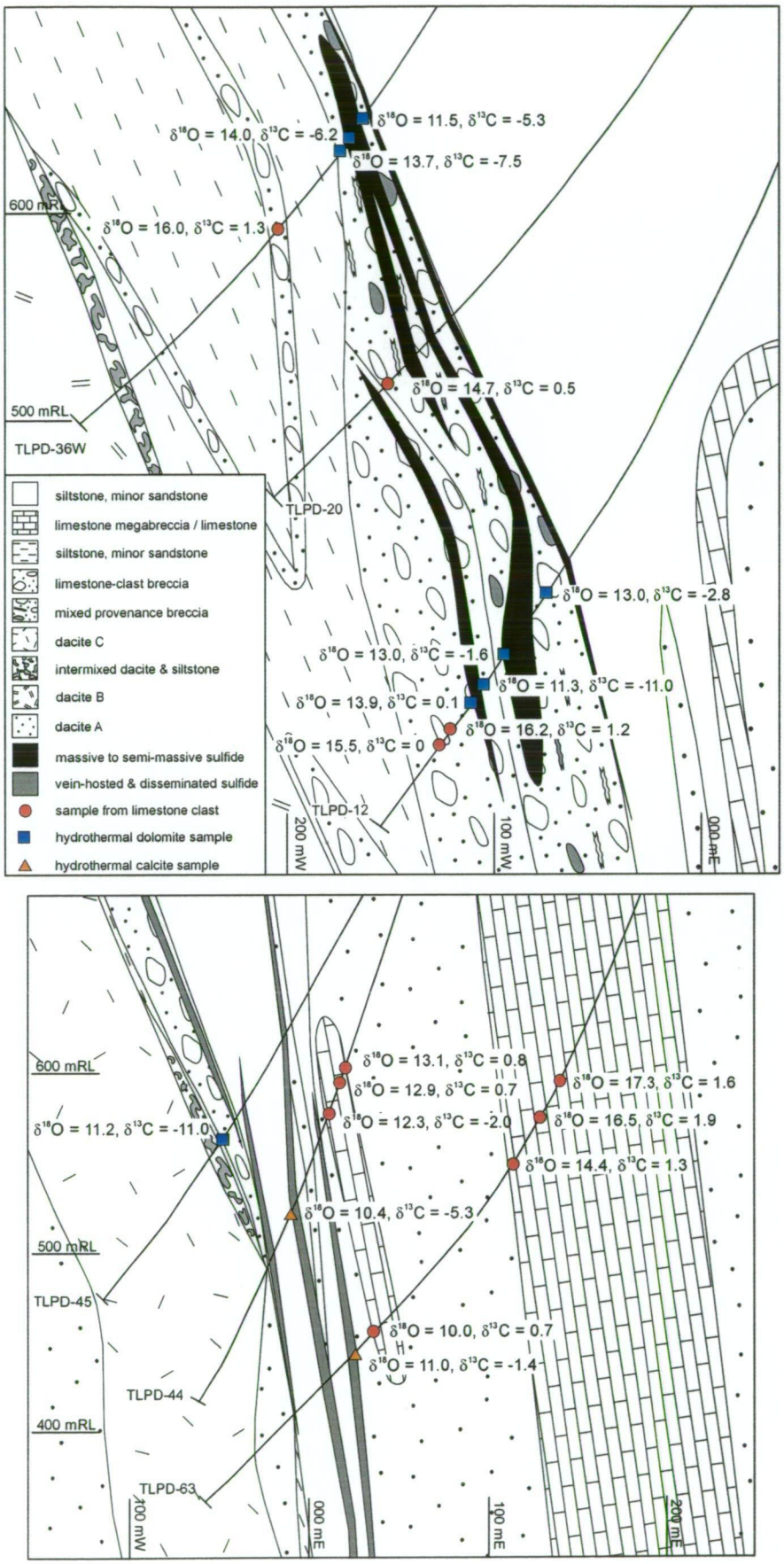

Figure 8.2 Spatial distribution of $\delta^{18}O_{VSMOW}$ and $\delta^{13}C_{VPDB}$ values in limestone clasts, massive dolomite and dolomite-altered limestone clasts in Main zone and Lady Belmore zone. Line 1300 m N section (top) and line 750 m N section (bottom).

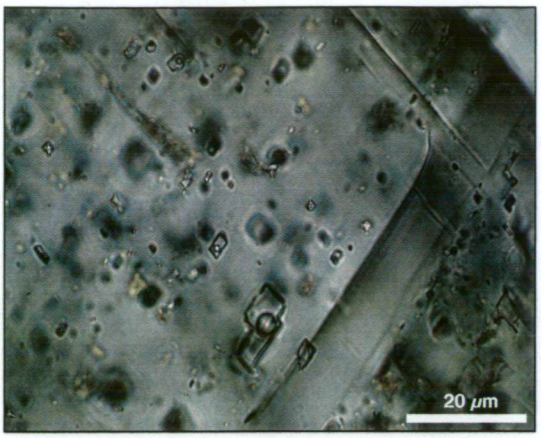

Figure 8.3 Photomicrograph of primary two phase fluid inclusions in zoned rhombic dolomite crystal. TLPD-12, 493 m.

Sample	Size (μ)	Salinity (equiv wt % NaCl)				Pressure corrected homogenisation temp.			
		N	Range	Mean	SD	N	Range	Mean	SD
LP12493	2 – 13	59	2.9 – 7.7	4.2	1.0	40	166 – 198°C	180°C	5.2
LP36W214	1 – 16	55	1.6 – 5.8	4.1	1.0	58	170 – 232°C	183°C	5.5
LP51A484	2 – 13	53	1.4 – 7.3	3.9	1.0	41	170 - 232°C	187°C	5.5

Table 8.3 Data from fluid inclusions in rhombic dolomite crystals. The pressure correction factor added to homogenisation temperatures is 10°C for 1 000 m depth below sea level. Samples LP12493 and LP36W214 are from Main zone. LP51A484 is from Toms zone.

Salinities in equivalent weight percent NaCl (w_s) were calculated using the equation:

$$w_s = (1.76958 \times \theta) - (4.2384 \times 10^{-2}\theta) + (5.2778 \times 10^{-4}\theta^3) \quad \text{(Potter II et al., 1978)} \quad (5)$$

where θ is the freezing point depression in °C. Fluid inclusions in the dolomite at Lewis Ponds have salinities that range from 1.4 to 7.7 eqiv wt % NaCl (Table 8.3). The average salinities are similar to modern seawater: 3.2 wt % NaCl (Roedder, 1984; Lydon, 1988). However, the fluid inclusions at Lewis Ponds probably contain Mg^{2+}, Ca^{2+}, HCO_3^- and H_2CO_3 ions in addition to NaCl since they occur within dolomite.

Given the pressure corrected homogenisation temperatures, the isotopic composition of the fluid from which the dolomite precipitated was calculated using equations 6 and 7:

$$\delta^{18}O_{fluid} = \delta^{18}O_{dolomite} - \Delta^{18}O_{H_2O}^{dolomite} \quad (6)$$

$$\delta^{13}C_{fluid} = \delta^{13}C_{dolomite} - \Delta^{13}C_{CO_2}^{dolomite} \quad (7)$$

where:

$\Delta^{18}O_{H_2O}^{dolomite}$ = fractionation factor between secondary dolomite and H_2O

$\Delta^{13}C_{CO_2}^{dolomite}$ = fractionation factor between secondary dolomite and CO_2

$\delta^{18}O_{dolomite}$ = $\delta^{18}O$ of secondary dolomite

$\delta^{13}C_{dolomite}$ = $\delta^{13}C$ of secondary dolomite

Table 8.4 presents calculated fluid compositions for the three samples.

Sample	Mean T_h (°C)	$\delta^{18}O_{dolomite}$ (‰)	$\delta^{13}C_{dolomite}$ (‰)	$\delta^{18}O_{fluid}$ (‰)	$\delta^{13}C_{fluid}$ (‰)
LP12493	180	11.3	-11.0	-2.3	-13.6
LP36W214	183	13.7	-7.5	0.3	-10.2
LP51A484	187	10.6	-1.3	-2.5	-4.0

Table 8.4 Calculated isotopic fluid compositions based on average pressure corrected fluid inclusion homogenisation temperatures listed in Table 8.3 and the measured $\delta^{18}O_{VSMOW}$ and $\delta^{13}C_{VPDB}$ values in the dolomite. Calculated using Equations 6 and 7.

Fluid inclusions from Lewis Ponds fall into the range of relatively low temperature (<350°C), low salinity (<10 NaCl equiv wt %) inclusions occurring in Japanese and eastern Australian VHMS deposits (eg. Pisutha-Arnond and Ohmoto, 1983; Roedder, 1984; Khin Zaw and Large, 1992). However, the extent to which syn-tectonic or metamorphic fluids modified these inclusions is difficult to determine. If dolomite precipitated prior to mineralisation, during diagenesis and low temperature hydrothermal activity, a greater range in homogenisation temperatures may be expected.

Interpretation of carbon-oxygen isotopes at Lewis Ponds

The wide distribution of $\delta^{13}C$ values at Lewis Ponds probably reflects isotopic exchange reactions involving carbonate minerals and aqueous C species. In Main zone, hydrothermal alteration of pre-existing fossiliferous limestone clasts and diagenetic carbonate assemblages could have involved precipitation of secondary calcite and/or dolomite. Alternatively, the intense, texturally destructive hydrothermal dolomite assemblage in Main and Toms zones may have resulted from mixing between seawater and a hydrothermal fluid. These two possible isotopic exchange processes are tested in the following sections.

The hydrothermal fluid, from which the dolomite precipitated may have contained $H_2CO_{3(aq)}$, $HCO_3^-{}_{(aq)}$, $CO_3^{2-}{}_{(aq)}$ and $CH_{4(aq)}$ molecules. However, $HCO_3^-{}_{(aq)}$ predominates in low temperature (<100°C), alkaline hydrothermal fluids and H_2CO_3/CO_2 predominates in higher temperature, more acidic fluids (Ohmoto, 1972, 1986; Large et al., 2001d). Since $\delta^{13}C_{H2CO3\ (apparent)} \cong \delta^{13}C_{CO2}$ (Ohmoto, 1972), fractionation factors involving carbonate minerals and $CO_{2(aq)}$ are used in the following models. Results of the fluid modelling are presented in Appendix 6.

Fluid-rock interaction models

When limestone undergoes hydrothermal alteration, $H_2CO_{3(aq)}$, $HCO_3^-{}_{(aq)}$ and $CO_{2(aq)}$ may be removed by dissolution or thermal decarbonation (Ohmoto, 1986). The resulting $\delta^{13}C_{fluid}$,

from which secondary carbonate precipitates, depends on the initial $\delta^{13}C$ of the limestone, the relative proportions of aqueous C species, the fractionation factors and the amount of decomposition (Ohmoto, 1986).

The isotopic composition of secondary carbonate is determined by the general mass balance equation:

$$W\delta^{i}_{fluid} + R\delta^{i}_{rock} = W\delta^{f}_{fluid} + R\delta^{f}_{rock}, \quad (8)$$

where *W* and *R* denote the atomic percentage of isotopes in the fluid and rock respectively; and *i* and *f* represent the initial and final isotopic composition (Taylor, 1977). Zheng and Hoefs (1993) applied this equation to fluid-rock interaction models in open (Equations 9 and 10) and closed (Equations 11 and 12) systems. In an open system, fluid is replenished by fluid with the same initial isotopic composition and temperature. Closed systems are characterised by continuous equilibrium between the fluid and rock (Taylor, 1987; Zheng and Hoefs, 1993).

$$\delta^{18}O_{carb} = (\delta^{18}O^{i}_{fluid} + \Delta^{18}O^{carb}_{H_2O}) - (\delta^{18}O^{i}_{fluid} + \Delta^{18}O^{carb}_{H_2O} - \delta^{18}O^{i}_{calcite})e^{-W/R} \quad (9)$$

$$\delta^{13}C_{carb} = (\delta^{13}C^{i}_{fluid} + \Delta^{13}C^{carb}_{CO_2}) - (\delta^{13}C^{i}_{fluid} + \Delta^{13}C^{carb}_{CO_2} - \delta^{13}C^{i}_{calcite})e^{-W/R}X_{CO_2} \quad (10)$$

$$\delta^{18}O_{carb} = \frac{\delta^{18}O^{i}_{calcite} + W/R(\delta^{18}O^{i}_{fluid} + \Delta^{18}O^{carb}_{H_2O})}{(1 + W/R)} \quad (11)$$

$$\delta^{13}C_{carb} = \frac{\delta^{13}C^{i}_{calcite} + W/RX_{CO_2}(\delta^{13}C^{i}_{fluid} + \Delta^{13}C^{carb}_{CO_2})}{(1 + W/RX_{CO_2})} \quad (12)$$

where:

$\delta^{18}O_{carb}$ = $\delta^{18}O$ of secondary carbonate

$\delta^{13}C_{carb}$ = $\delta^{13}C$ of secondary carbonate

$\delta^{18}O^{i}_{calcite}$ = initial $\delta^{18}O$ of fossiliferous limestone

$\delta^{13}C^{i}_{calcite}$ = initial $\delta^{13}C$ of fossiliferous limestone

$\delta^{18}O^{i}_{fluid}$ = initial $\delta^{18}O$ of fluid

$\delta^{13}C^{i}_{fluid}$ = initial $\delta^{13}C$ of fluid

X_{CO_2} = mole fraction of CO_2 in fluid

$\Delta^{18}O^{carb}_{H_2O}$ = fractionation factor between secondary carbonate and H_2O

$\Delta^{13}C^{carb}_{CO_2}$ = fractionation factor between secondary carbonate and CO_2

W/R = atomic ratio of water to rock during interaction

Figure 8.4 illustrates the theoretical isotopic composition of secondary calcite and dolomite precipitated by fluid-rock interactions involving unaltered, regional fossiliferous limestone ($\delta^{18}O_{VSMOW}$ = 24.25‰, $\delta^{13}C_{VPDB}$ = 2.5‰) and a H_2CO_3/CO_2-bearing hydrothermal fluid (A).

The composition of fluid A ($\delta^{18}O$ = -2‰, $\delta^{13}C$ = -9‰) and the temperature range (150-250°C) are constrained by the fluid inclusion data and calculated isotopic fluid compositions presented in Tables 8.3 and 8.4.

A - calcite precipitation

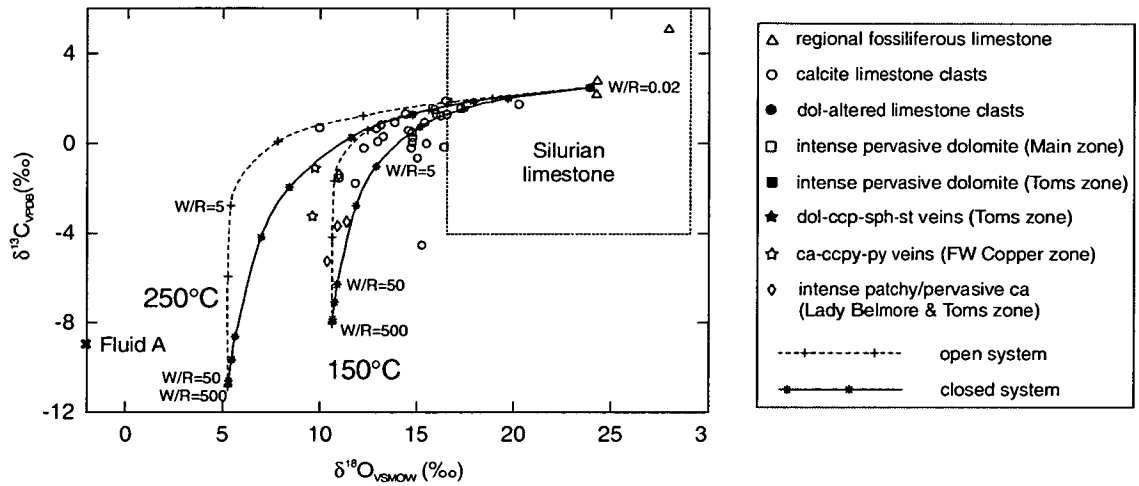

B - dolomite precipitation

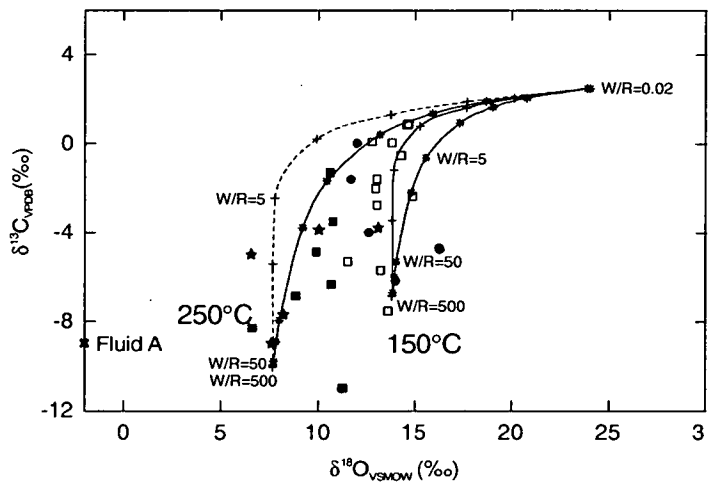

Figure 8.4 **A.** Modelled covariance trends of calcite precipitated by reacting a hydrothermal fluid ($\delta^{18}O$ = -2‰, $\delta^{13}C$ = -9‰) at 150°C and 250°C with unaltered, fossiliferous limestone or diagenetic carbonate ($\delta^{18}O$ = 24.25‰, $\delta^{13}C$ = 2.5‰) in an open and closed system. Calculated using Equations 9 to 12. **B.** Modelled covariance trends of dolomite precipitated by reacting a hydrothermal fluid ($\delta^{18}O$ = -2‰, $\delta^{13}C$ = -9‰) at 150°C and 250°C with unaltered limestone or diagenetic carbonate as above, in an open and closed system. The modeled dolomite compositions become progressively enriched in light C and O isotopes with increasing water-rock ratio.

Fluid-rock interaction at 150-250°C and water/rock ratios of 0.5 to 5 may account for the isotopic composition of limestone clasts in the Lewis host sequence. The observed compositions vary with proximity to the massive sulfide lenses (eg. Fig 8.2) and therefore are likely to reflect increased water/rock ratios. In this model, calcite veins and intense pervasive calcite assemblages precipitated from a higher temperature fluid (>250°C). The massive dolomite in Main and Toms zone may have resulted from fluid-rock interactions involving the

regional fossiliferous limestone and a hydrothermal fluid at 150-250°C and water/rock ratios of 2 to 100. The modelled isotopic compositions have a similar range of $\delta^{13}C$ and $\delta^{18}O$ values to the Lewis Ponds dolomites. A simple fluid-rock interaction model involving alteration of fossiliferous limestone clasts in the carbonate-bearing host sediment and precipitation of secondary carbonate over a temperature range of 150-250°C may therefore account for the observed distribution of $\delta^{18}O$ and $\delta^{13}C$ values.

Fluid mixing models

Fluid mixing is an efficient mechanism of precipitating hydrothermal carbonates, at or below the seafloor, in porous volcanic successions. Recent studies have indicated that the VHMS-related carbonates result from mixing between seawater and a hydrothermal fluid (Khin Zaw and Large, 1992; Goodfellow et al., 1993; Callaghan, 2001; Herrmann and Hill, 2001). Zheng and Hoeffs (1993) modelled the isotopic composition of fluid mixtures and the resulting carbonates by varying the relative proportion of two different fluids (A and B) and specifying the relative C contents in the two fluids (P). Equations 13 and 14 (Zheng and Hoefs, 1993) were used to determine the composition of secondary, hydrothermal dolomite precipitated from the fluid mixture. This study employed a simple linear fluid mixing model, similar to that of Williams (2000). For example, the temperature of a mixture containing half of fluid A and B will be half-way between the initial temperature of each fluid. The results are listed in Appendix 6.

$$\delta^{18}O_{dolomite} = \delta^{18}O_b + \Delta^{18}O_{H_2O}^{dolomite} + X_a(\delta^{18}O_a - \delta^{18}O_b) \quad (13)$$

$$\delta^{13}C_{dolomite} = \frac{X_a(\delta^{13}C_a + \Delta^{13}C_a^{dolomite}) + P(1-X_a)(\delta^{13}C_b + \Delta^{13}C_b^{dolomite})}{(P + X_a - PX_a)} \quad (14)$$

where:

$\delta^{18}O_{dolomite}$ = $\delta^{18}O$ of secondary dolomite

$\delta^{13}C_{dolomite}$ = $\delta^{13}C$ of secondary dolomite

$\delta^{18}O_a$ = $\delta^{18}O$ of fluid A

$\delta^{13}C_a$ = $\delta^{13}C$ of fluid A

$\delta^{18}O_b$ = $\delta^{18}O$ of fluid B

$\delta^{13}C_b$ = $\delta^{13}C$ of fluid B

X_a = mole fraction of fluid A in the mixed fluid

$\Delta^{18}O_{H_2O}^{dolomite}$ = fractionation factor between secondary dolomite and H_2O

$\Delta^{13}C_{CO_2}^{dolomite}$ = fractionation factor between secondary dolomite and CO_2

P = relative proportion of C in fluids A and B, such that $P = C_b/C_a$

Figure 8.5 presents the theoretical isotopic compositions of dolomite precipitated by mixing three isotopically different hydrothermal fluids at 350°C (fluid B) with a seawater-dominant pore fluid at 100°C (fluid A). The isotopic composition of fluid A ($\delta^{18}O_{VSMOW}$ = -2‰, $\delta^{13}C_{VPDB}$ = -0.5‰), is similar to interstitial pore fluids that have reacted with marine carbonate or volcanic rocks, several hundred metres below the seawater-sediment interface (eg. De Carlo et al., 2001; De Carlo et al., 2002). In the first model (Fig. 8.5A), the hydrothermal fluid is interpreted to be magmatic in origin. The footwall volcanic succession at Lewis Ponds consists of S-type porphyritic dacite intrusions (see Chapter 6, section 6.3). $\delta^{18}O_{VSMOW}$ values in S-type granites (9 to 13‰) are significantly higher than $\delta^{18}O$ values in typical arc-related rocks with I-type affinities (Ohmoto, 1986). $\delta^{13}C_{PDB}$ values probably range from -10 to 2‰ in fluids exsolved from granitic magmas because CO_2 is the predominant C species and $\delta^{13}C_{magmatic\ fluid} \cong \delta^{13}C_{melt}$ (Ohmoto and Rye, 1979). Therefore, the magmatic hydrothermal fluid (fluid B) used in this model had the composition, $\delta^{18}O_{VSMOW}$ = 10‰ and $\delta^{13}C_{VPDB}$ = -9‰. In the second and third models (Fig. 8.5B-C), the initial seawater-dominant hydrothermal fluid ($\delta^{18}O_{VSMOW}$ = 2‰, $\delta^{13}C_{VPDB}$ = -5‰ or –9‰) had reacted extensively with the footwall volcanic rocks and acquired a component of reduced organic C. The isotopic composition of this evolved seawater is similar to vent fluids observed in some modern seafloor hydrothermal systems (eg. de Ronde, 1995; Shanks, 2001).

In the magmatic mixing model (Fig. 8.5A), the modelled dolomite compositions are characterised by higher $\delta^{18}O$ values than most of the actual samples. The modelled dolomite compositions in Figure 8.5B, for P = 0.1 and 1 are similar to observed $\delta^{18}O$ and $\delta^{13}C$ values in Toms zone and indicate that the dolomite may have precipitated from a mixed hydrothermal fluid at 150-350°C. However, the range in modelled fluid compositions does not overlap completely with the calculated fluid compositions for samples LP12493, LP36W214 and LP51A484. The majority of dolomite samples from Main zone plot near the modelled trend line for P = 1, in Figure 8.5C and are consistent with fluid temperatures of 150-225°C. None of the trend lines account for the wide distribution of $\delta^{13}C$ values in the dolomite from Main zone. The modelled fluid compositions presented in Figure 8.5 have higher $\delta^{18}O$ and $\delta^{13}C$ values than the fluid compositions calculated for the dolomite samples, but are best explained by model C.

In summary, the hydrothermal dolomite at Lewis Ponds is more likely to have resulted from mixing between a low temperature, seawater-dominant pore fluid and higher temperature evolved seawater (Fig. 8.5B-C) than by mixing between seawater and a purely magmatic hydrothermal fluid (Fig. 8.5A). The fluid mixing models presented in Figure 8.5 do not fully account for the wide distribution of $\delta^{13}C$ values in the dolomite from Main zone or the calculated isotopic fluid compositions for LP12493, LP36W214 and LP51A484.

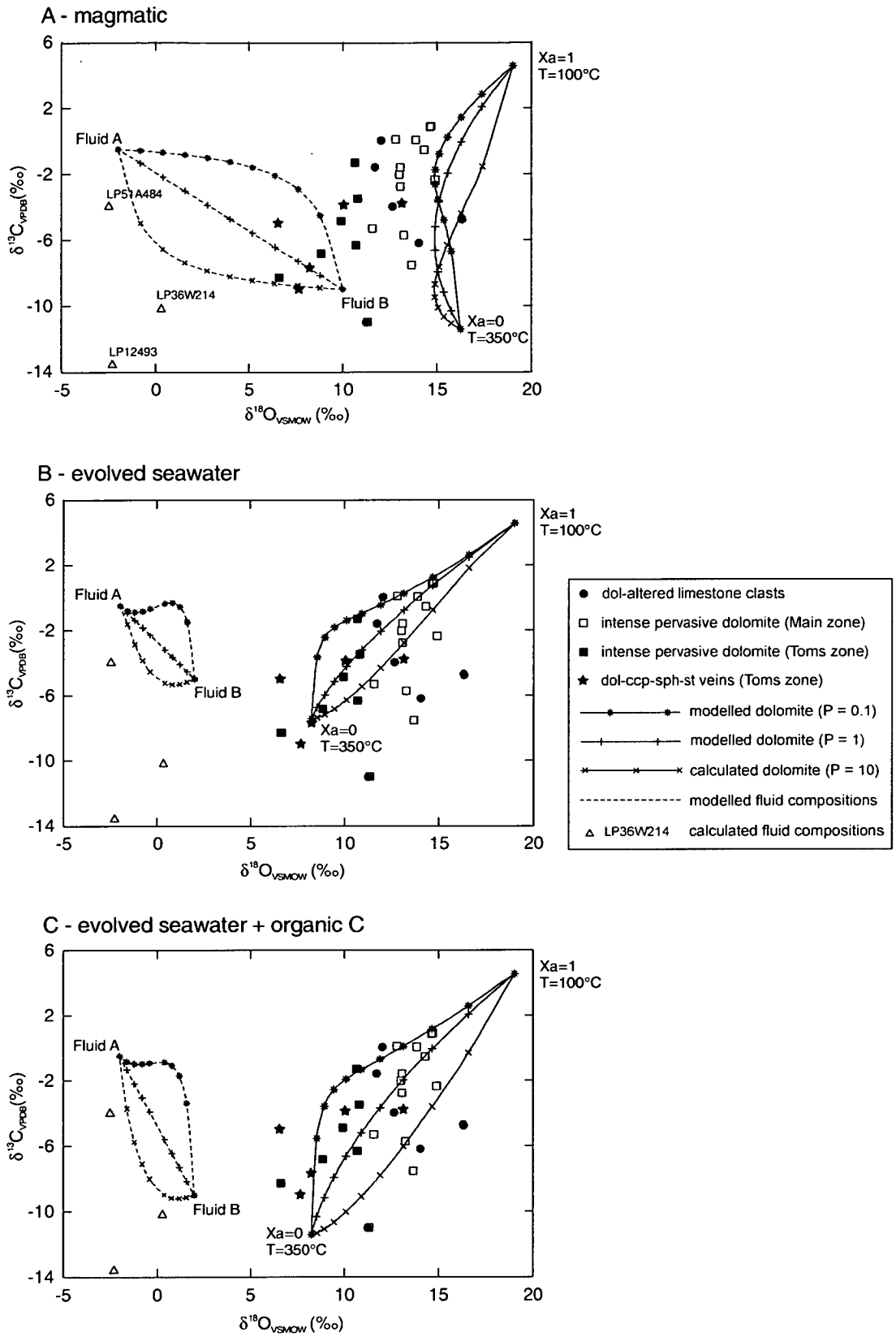

Figure 8.5 Modelled covariance trends of dolomite precipitated by mixing a seawater-dominant pore fluid (fluid A; $\delta^{18}O$ = -2‰, $\delta^{13}C$ = -0.5‰) at 100°C with each of three isotopically different hydrothermal fluids (fluid B) at 350°C. The isotopic compositions of fluid B are $\delta^{18}O$ = 10‰, $\delta^{13}C$ = -9‰ (model A), $\delta^{18}O$ = 2‰, $\delta^{13}C$ = -5‰ (model B), and $\delta^{18}O$ = 2‰, $\delta^{13}C$ = -9‰ (model C). P is the relative proportion of carbon in fluids A and B: 0.01, 1 and 10. Xa is the amount of fluid A in the mixture such that when Xa = 1, the mixture consists entirely of fluid A. In both fluids, CO_2 is the predominant C-bearing species. The isotopic compositions of the modelled fluid mixtures are shown. The triangles represent calculated isotopic fluid compositions for dolomite samples LP12493, LP36W214 and LP51A484.

Discussion: reasons for carbon and oxygen isotopic fractionation in carbonate at Lewis Ponds

The C isotopic compositions of recrystallised fossiliferous limestone clasts in the Lewis Ponds host sequence compare with typical Silurian, marine and freshwater carbonates (Veizer and Hoefs, 1976; Ripperdan, 2001). The narrow range of $\delta^{13}C_{PDB}$ values (-2 to 2‰; except for one sample with -4.5‰) indicates that the limestone may have precipitated in equilibrium with $HCO_{3\,(aq)}^{-}$ in the seawater at approximately 25°C.

Secondary (hydrothermal) carbonates at Lewis Ponds have a relatively wide range in $\delta^{13}C_{PDB}$ values (-11 to 1‰). In contrast, eastern Australian VHMS deposits including South Hercules and Henty, western Tasmania (Khin Zaw and Large, 1992; Callaghan, 2001) and Mt Chalmers, central Queensland (Huston et al., 1999) have a narrow range of $\delta^{13}C_{PDB}$ values (-5 to 1‰). Two possible processes may account for the low $\delta^{13}C_{PDB}$ values at Lewis Ponds: reduction of organic C or decarbonation reactions.

Some of the C isotopic fractionation may result from the incorporation of organic C into the hydrothermal fluid. Eastoe and Nelson (1988) attributed low $\delta^{13}C$ values (-12 to 0‰) in carbonates at the Afterthought-Ingot area, California to mixing of seawater carbonate with oxidised organic C. At Lewis Ponds, dark grey mudstone in the Hangingwall Siltstone Unit may indicate the presence of sulfate-reducing bacteria during diagenesis. However, no other mineralogical or textural evidence exists for oxidation reactions in the host sequence.

Dolomite occurs with talc and quartz in the polymictic breccia and siltstone units, within and adjacent to the Lewis Ponds fault (eg. Figs. 5.4 and 5.5). The talc may have formed by thermal decarbonation reactions involving dolomite and quartz, during hydrothermal alteration or regional metamorphism (see Chapter 5, Equation 1). Decarbonation reactions cause $\delta^{13}C$ values in pre-existing limestone to decrease because ^{13}C preferentially fractionates into $CO_{2(g)}$ (Faure, 1977). Therefore reactions involving the formation of talc may have caused the dolomite to become enriched in lighter C isotopes. This metasomatism possibly occurred during hydrothermal alteration and metamorphism.

The O isotopic compositions of primary and secondary carbonate in the Lewis Ponds host sequence ($\delta^{18}O_{VSMOW}$ = 6 to 20‰) are 5 to 10‰ lower than typical Silurian, marine and freshwater carbonates (Veizer and Hoefs, 1976). Secondary dolomite surrounding Main and Toms zones has a similar range of $\delta^{18}O_{VSMOW}$ values to hydrothermal carbonate in VHMS deposits including South Hercules (Khin Zaw and Large, 1992) and Henty (Callaghan, 1998). Oxygen isotopic fractionation of hydrothermal carbonates in VHMS deposits is attributed to

variations in depositional temperature, between 100°C and 300°C (Huston et al., 1999). The amount of fractionation decreases at higher temperatures (Equation 2).

Massive and vein dolomite samples in Toms zone have lighter, more variable O isotopic compositions than dolomite surrounding Main zone. This variation may indicate higher temperature deposition of dolomite in Toms zone. Alternatively, the dolomite may have re-equilibrated with fracture-controlled fluids, localised along the Lewis Ponds fault during the D_1 deformation.

In conclusion, the distribution of $\delta^{18}O$ and $\delta^{13}C$ values in the Lewis Ponds host sequence may have resulted from fluid-rock interactions involving the limestone-bearing host rocks and a hydrothermal fluid, and/or mixing between seawater-dominant pore fluids at 100°C and evolved seawater at 350°C. Both types of models indicate that the dolomite in Toms zone precipitated at higher temperatures than the dolomite in Main zone, despite little variation in fluid inclusion homogenisation temperatures. Fluid-rock interactions and fluid mixing do not account for the observed variation in $\delta^{13}C$ values or the calculated fluid isotopic compositions for samples LP12493, LP36W214 and LP51A484. Decarbonation reactions or the involvement of reduced organic C may have decreased $\delta^{13}C$ values in the massive dolomite and dolomite-altered limestone clasts in Main zone. The lighter, more variable O isotopic signature of dolomite in Toms zone possibly reflects deposition from a higher temperature fluid or isotopic re-equilibration due to the circulation of younger fracture-controlled fluids within the Lewis Ponds fault zone during the D_1 deformation.

8.4 PART B – sulfur and lead isotopes and metal ratios

The purpose of part B is to use the isotopic composition of sulfides and metal ratios to interpret the composition of the mineralising fluid and the source of metals at Lewis Ponds.

Sulfur isotopes

Sulfur isotopic relationships among co-existing minerals help to constrain the S source, temperature and chemistry of the mineralising fluid and mechanisms of mineral deposition (Ohmoto and Goldhaber, 1997). Sulfur has four isotopes, in order of decreasing abundance: ^{32}S, ^{34}S, ^{33}S and ^{36}S. The isotope ratio of compound *i* is expressed as:

$$\delta^{34}S_i = \left[\left(\frac{R_i}{R_{VCDT}}\right) - 1\right] \times 1000 \quad ‰ \qquad \text{(Ohmoto and Rye 1979)} \qquad (15)$$

where: $R_i = {}^{34}S/{}^{32}S$ of compound *i* and $R_{VCDT} = {}^{34}S/{}^{32}S$ of troilite in the Vienna standard.

Fractionation of S isotopes in hydrothermal systems may occur during phase separation of a fluid from magma, reduction of seawater sulfate, cooling of the fluid, mineral precipitation and mineral dissolution. In high temperature fluids (>400° C), H_2S and SO_2 are the predominant aqueous S species. At lower temperatures (<350° C), fluids may contain H_2S, HS^- and various oxidised sulfate species including SO_4^{2-}, HSO_4^-, $NaSO_4^-$, $CaSO_4$ and $MgSO_4$ (Ohmoto and Rye, 1979). Therefore, S isotope fractionation between minerals and the hydrothermal fluid depends on temperature, pH, oxygen fugacity and $\delta^{34}S$ of the fluid and the precipitation of sulfide or sulfate minerals.

In VHMS deposits, $\delta^{34}S_{VCDT}$ values range from -20 to 27‰ in sulfides and 10 to 40‰ in sulfates (Ohmoto and Rye, 1979; Huston et al., 1999). The small variation within individual deposits and massive sulfide lenses, typically less than 5‰, indicates a relatively homogeneous source area. Possible sources of S include direct input from magmatic fluids, leaching of volcanic rocks, biogenic reduction of seawater sulfate (Sangster, 1968) and inorganic reduction of diagenetic or hydrothermal sulfate (Ohmoto et al., 1983). Sangster (1968) and Large (1992) demonstrated the involvement of reduced seawater sulfate in VHMS deposits through time by correlating average $\delta^{34}S$ values in massive sulfide deposits and contemporaneous marine sulfate deposits. Gemmell and Large (1992) interpreted the distribution of S isotope ratios at Hellyer to indicate evolution of a seawater-dominated hydrothermal fluid into a fluid containing S leached from the volcanic host rocks, as the hydrothermal system intensified.

At Lewis Ponds, $\delta^{34}S_{VCDT}$ values in sulfides vary from 0.1 to 7.4‰ (Table 8.5; Fig. 8.6). Main zone, Toms zone and the quartz-sulfide veins have a similar range of $\delta^{34}S_{VCDT}$ values (0.1 to 5.0‰). Calcite-chalcopyrite-pyrite veins in the Footwall Copper zone are characterised by higher average $\delta^{34}S_{VCDT}$ values (5.7‰).

Location	N	Range $\delta^{34}S_{VCDT}$ (‰)	Average $\delta^{34}S_{VCDT}$ (‰)
Main zone	11	1.7 – 4.9	3.4
Toms zone	8	2.4 – 5.0	4.0
Footwall Copper zone	9	3.9 – 7.4	5.7
syn-tectonic quartz-sulfide veins	9	0.1 – 5.0	3.4
total (includes one other analysis)	38	0.1 – 7.4	4.1

Table 8.5 $\delta^{34}S_{VCDT}$ values from massive sulfide, quartz-sulfide veins and calcite-chalcopyrite veins at Lewis Ponds. Includes 24 analyses from this study and 14 unpublished analyses from the Geological Survey of New South Wales. All data are listed in Appendix 8.

The average S isotopic composition of acid volcanic rocks is 0 ± 3‰ (Ohmoto and Rye, 1979). Late Silurian marine sulfate deposits have $\delta^{34}S_{VCDT}$ values of 25-30‰ (Claypool et al., 1980).

Therefore, the distribution of $\delta^{34}S$ data at Lewis Ponds indicates that the mineralising fluid probably contained a relatively homogeneous mixture of magmatic S derived from the host volcanic rocks or a magmatic fluid, and a minor component of reduced seawater sulfate. Bladed quartz and pyrrhotite pseudomorphs (Fig. 7.9D) indicate that anhydrite or barite may have co-existed with pyrite and pyrrhotite during mineralisation. Sulfides occurring in cleavage-parallel, syn-tectonic quartz veins have a similar range of $\delta^{34}S_{VCDT}$ values (0.1-5.0‰) to the massive sulfide. This indicates that fracture-controlled fluids may have leached S from the host volcanic rocks or pre-existing massive sulfide during the D_1 deformation.

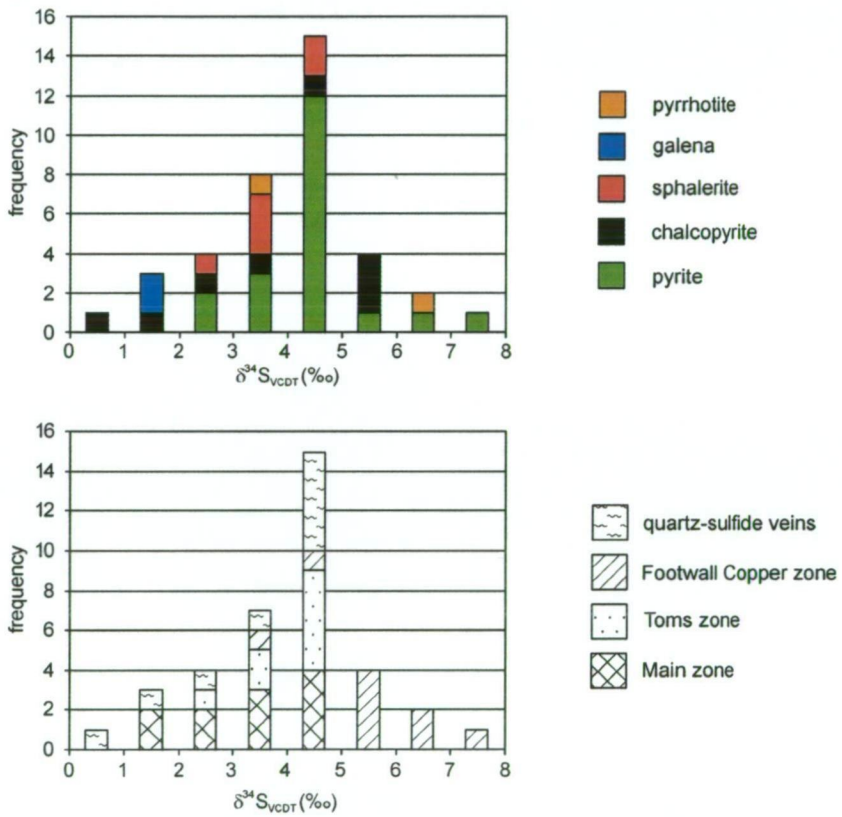

Figure 8.6 Distribution of $\delta^{34}S_{VCDT}$ values at Lewis Ponds plotted in terms of sulfide mineral and location: Main zone, Toms zone, Footwall Copper zone and quartz-sulfide veins in the Lewis Ponds fault. Includes 24 analyses from this study and 14 analyses from the Geological Survey of New South Wales.

Numerous factors may have caused the observed variation in average $\delta^{34}S$ values between the massive sulfide and Footwall Copper zone at Lewis Ponds. A trend of decreasing $\delta^{34}S$ in sulfides from the footwall stockwork zone to the overlying massive sulfide lens occurred at the Shakanai mine, Japan (Kajiwara, 1972) and Iron Mountain mine, California (South and Taylor, 1985). Kajiwara (1972) attributed this trend to increased oxygen fugacity and fluid pH due to a greater contribution of seawater to the hydrothermal fluid. Under equilibrium conditions, sulfides become enriched in light S with increased fluid pH or oxygen fugacity (Ohmoto and Rye, 1979). However, in many modern and ancient sea floor exhalative deposits,

mineralisation occurs by rapid, disequilibrium mixing of hydrothermal fluids with cooler seawater (Ohmoto et al., 1983). Lydon (1996) attributed higher $\delta^{34}S$ values in Cu-rich assemblages to the temperature dependence of the inorganic reduction of seawater sulfate. Alternatively, hydrothermal fluids at Lewis Ponds may have acquired a component of lighter S from the host sedimentary rocks by partial reduction of trace amounts of seawater sulfate occurring in the fossiliferous limestone clasts or incorporation of biogenic S, derived from diagenetic pyrite and pyrrhotite in the Hangingwall Siltstone Unit.

The isotopic compositions of sufides at Lewis Ponds compare with other Silurian base metal and barite deposits in the Hill End and Captains Flat-Goulburn troughs (Table 8.6). $\delta^{34}S$ values in sulfides from the Mt Bulga deposit range from -1.7 to 3.7‰. The Calula deposit also has a small range of values: 4.0-7.6‰. Deposits with higher average $\delta^{34}S$ values including Sunny Corner, Commonwealth, Peelwood and Gurrundah may result from a greater contribution of reduced seawater sulfate to the hydrothermal fluid.

Deposit	Range $\delta^{34}S_{VCDT}$ (‰)	Avg. $\delta^{34}S_{VCDT}$ (‰)	Reference
Mt Bulga	-1.7 to 3.7	1.6	Chisholm (1976)
Sunny Corner	1.7 to 10.7	7.4	Seccombe et al. (1984)
Gurrundah	6.0 to 11.6	9.1	Maier (2002)
Woodlawn	2.8 to 9.2	6.6	Ayres et al. (1979)
Commonwealth	3.1 to 10.1	7.6	References cited in Downes and Seccombe (2000)
Calula	4.0 to 7.6	6.1	
Peelwood	11.9 to 13.7	13.0	

Table 8.6 Sulfur isotopes from massive sulfide and barite deposits in the Hill End Trough and Captains Flat-Goulburn Trough. Refer to Figures 2.5 and 2.6 for the location of these deposits.

Lead isotopes

Ore deposit studies have traditionally used lead isotopes to:

- determine the model age of mineralising events;
- interpret the composition and age of the source reservoir; and
- constrain the geological history of the deposit (Franklin et al., 1981).

Regional-scale studies compare the Pb isotope ratios in sulfides, orthoclase and detrital minerals to identify favourable horizons (Gulson, 1977), evaluate prospects (Delevaux et al., 1967) and determine the source of Pb (Carr et al., 1995) in areas surrounding existing deposits.

Chemical and physical processes responsible for fractionation of U, Pb and Th isotopes include partial melting, separation of a fluid phase from a magma, metamorphism, deformation and weathering (Faure, 1977; Gulson, 1986). During partial melting, U and Th remain in the

melt and become concentrated in evolved silicic rocks relative to primitive rocks (Faure, 1977). Therefore, the crustal and mantle reservoirs are likely to have significantly different Pb isotope ratios due to fractionation and unique geological histories.

Terrain-specific models have been developed to date individual deposits and metallogenic events. Carr et al. (1995) relied on well constrained Pb isotopes from sulfides and igneous rocks together with Ar-Ar ages to construct mixing isochrons between the Lachlan Fold Belt, crustal and mantle growth curves. The following section reviews the results of Carr et al. (1995) and highlights the implications for the source of Pb in Late Silurian massive sulfide deposits such as Lewis Ponds.

Lead isotopes in the Lachlan Fold Belt

The Pb isotope signature of hydrothermal deposits in the LFB appear to reflect the age of the host rock, source of Pb and the type of deposit. Epithermal and porphyry Cu-Au occurrences in the Ordovician shoshonitic volcanics have variable $^{206}Pb/^{204}Pb$ (17.68-18.21) and very low $^{207}Pb/^{204}Pb$ (15.40-15.49) and $^{208}Pb/^{204}Pb$ (37.21-37.83) values. The deposits lie along linear arrays, interpreted to indicate mixing of Pb from two or more mantle reservoirs (Fig. 8.7).

In contrast, Pb-Zn-rich massive sulfide deposits hosted in Late Silurian felsic volcanic rocks have a more radiogenic Pb isotope signature. The restricted range of $^{207}Pb/^{204}Pb$ (15.56-15.63) and $^{208}Pb/^{204}Pb$ (37.95-38.22) values indicates a relatively homogenous crustal source of Pb. At Lewis Ponds, $^{206}Pb/^{204}Pb$ = 18.05-18.08, $^{207}Pb/^{204}Pb$ = 15.56-15.60 and $^{208}Pb/^{204}Pb$ = 37.98-38.07 (Fig. 8.7). The majority of analyses from Lewis Ponds drill core samples plot within a 95% confidence interval ellipse, in the Silurian VHMS field of Carr et al. (1995).

Stratabound massive sulfide deposits in the Hill End and Captains Flat-Goulburn troughs occur in two groups, with model ages of 450-400 Ma (Carr et al., 1995). John Fardy, Peelwood, Sunny Corner and Lewis Ponds plot near the crustal growth curve on the $^{207}Pb/^{204}Pb$ versus $^{206}Pb/^{204}Pb$ diagram. Mt Bulga, Calula, Wisemans Creek, Mt Shorter and Pride of the Hills have lower, less radiogenic $^{207}Pb/^{204}Pb$ and $^{208}Pb/^{204}Pb$ values, and plot along steep, inferred mixing trend lines.

The Late Silurian massive sulphide deposits have a strong crustal Pb isotope signature due to magmatic assimilation of crustal rocks or the circulation of hydrothermal fluids. Deposits with a less radiogenic Pb isotope signature, including Mt Bulga, Calula, Wisemans Creek, Mt Shorter and Pride of the Hills contain a mixture of Pb, sourced from primitive mantle-derived rocks and a homogeneous crustal reservoir.

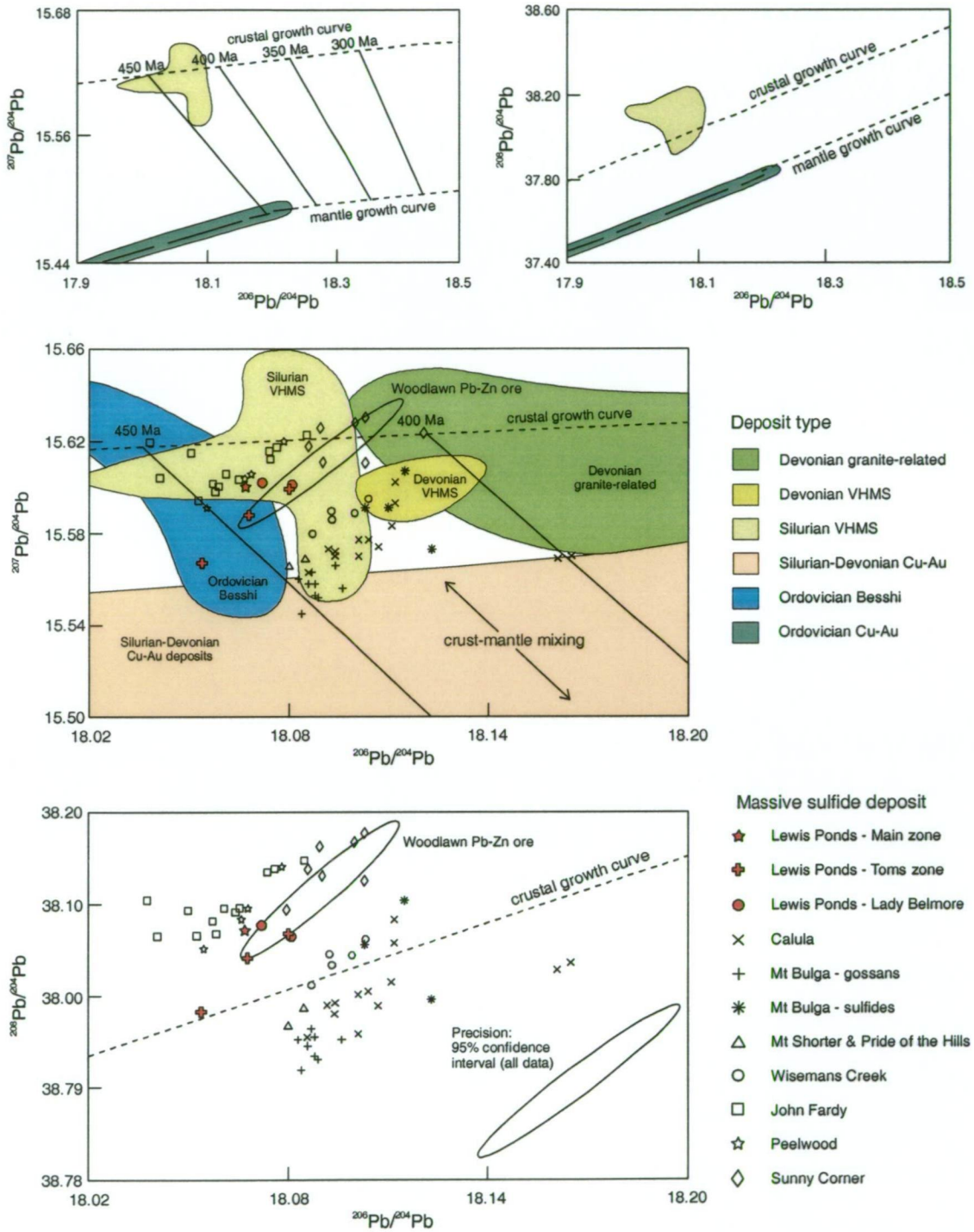

Figure 8.7 Plots of Pb isotope data from polymetallic massive sulfide deposits in the Hill End and Captains Flat-Goulburn troughs combined with the plumbo-tectonic model of Carr et al. (1995) for the Lachlan Fold Belt in New South Wales. Mineral deposit fields are from Carr et al. (1995). Mt Shorter and Pride of the Hills samples are from an unpublished company report. All other data are from Carr et al. (1995). Analyses from Lewis Ponds are highlighted in red. Refer to Figures 2.5 and 2.6 for location of massive sulfide deposits.

Metal ratios and metal distribution

The Zn ratio, 100[Zn/(Zn+Pb)] and Cu ratio, 100[Cu/(Cu+Zn)] allows massive sulfide deposits to be differentiated using the relative metal content (Lydon, 1984; Large, 1992; Antony, 1999). Huston and Large (1987) highlighted the geochemical significance of base metal ratios and their relationship to the mineralising fluid.

Massive sulfide lenses at Lewis Ponds have a restricted range of Zn ratios, with average values of 60 to 68 and standard deviations of less than 11 (Figs. 8.8 and 8.9). Areas dominated by disseminated sulfides and syn-tectonic quartz-sulfide veins, including Lady Belmore zone, New Lewis Ponds, Toms zone hangingwall and the extremities of Toms zone have widely distributed Zn ratios with more variable averages, and higher standard deviations. The assay data define lines of constant Zn ratio on Zn versus Pb scatter plots (Fig. 8.9). Data from the Central massive sulfide lenses occur on a line represented by the equation, $Zn \cong 1.5Pb$. However, trend lines from New Lewis Ponds and Lady Belmore zone have variable orientations given by $Zn = 1.5Pb$ to $Zn = 2.6Pb$.

Similar trends exist in the Cu ratios at Lewis Ponds. The massive sulfide lenses have consistently low average values of 4 to 9 (Fig. 8.10). Copper ratios in the Lady Belmore zone, New Lewis Ponds and outer low-grade extensions of Toms zone are higher and more variable, with average values of 10-30 and standard deviations ranging from 12 to 30. Copper enrichment is greatest in the Footwall Cu zone and Toms zone footwall.

The tight distribution of Zn and Cu ratios in the massive sulfide lenses at Lewis Ponds compare closely with values occurring at Australian and Canadian Zn-Pb-Cu-rich VHMS deposits (Lydon, 1984; Huston and Large, 1987). Huston and Large demonstrated that Zn ratios reflect temperature and salinity of the mineralising fluid. For a given salinity, a solution saturated in Zn and Pb will deposit massive sulfide with a unique ratio at a particular temperature. Assuming the involvement of chloride complexes, Zn ratios in the resulting massive sulfide will decrease with increasing temperature.

At Lewis Ponds, the highly variable Zn ratios occurring in areas dominated by syn-tectonic quartz-sulfide veins partly reflect the extremely low average metal grades; less than 2% combined Cu+Zn+Pb. However, fluctuations in fluid chemistry within the Lewis Ponds fault zone may have controlled the dissolution rate of metals in the source rock and the level of Cu, Pb and Zn saturation in the fluid. Since type 3 and type 4 quartz veins resulted from brittle failure over an extended period, the temperature and salinity of fracture-controlled fluids migrating through the fault zone may have varied considerably.

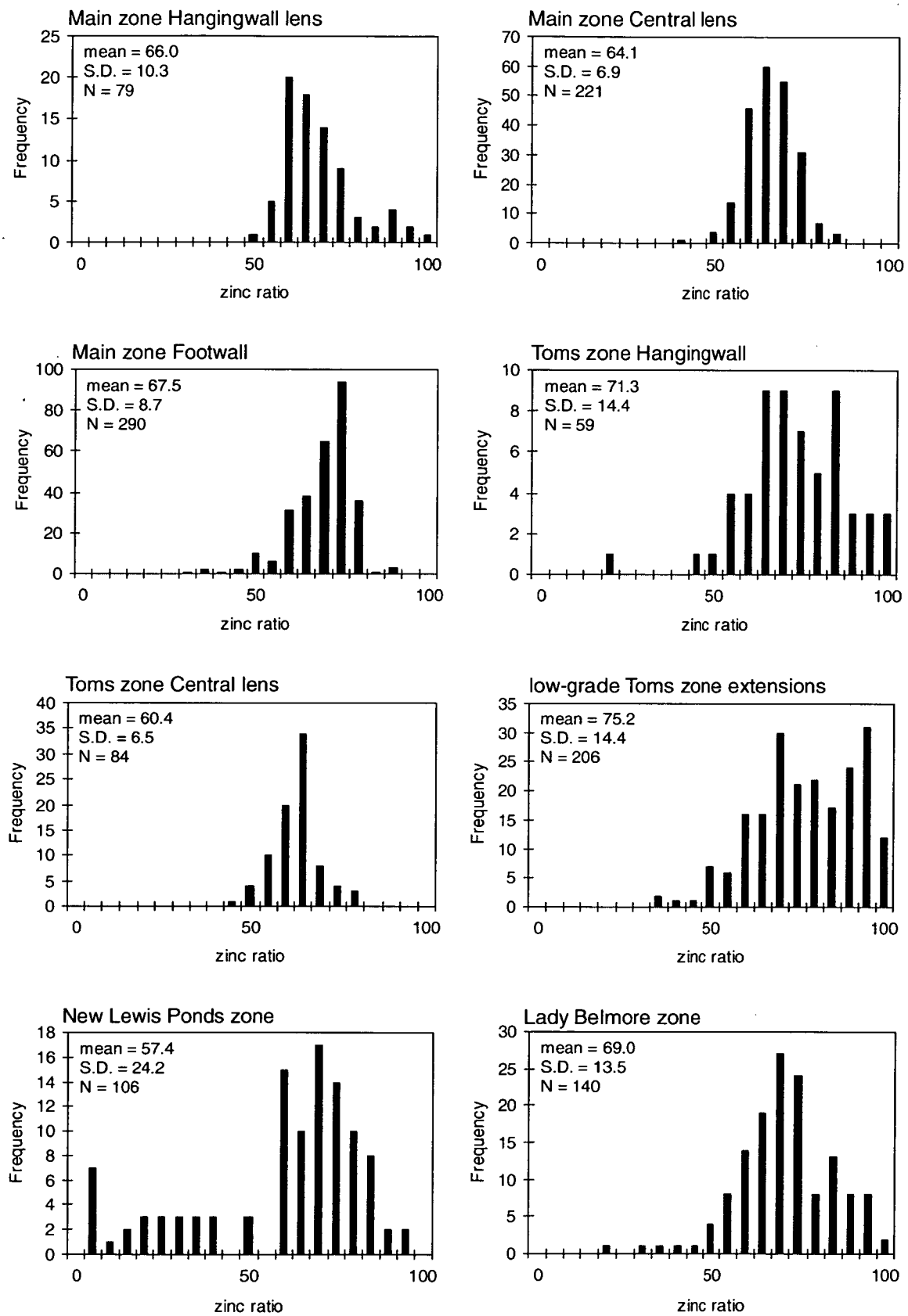

Figure 8.8 Zn ratios from the massive sulfide lenses at Main zone and Toms zone, and from areas of vein-hosted sulfide at Toms zone, Lady Belmore zone and New Lewis Ponds. Only assays grading >0.05% Zn and >0.05% Pb are included. Mean and standard deviation are presented for each mineralised zone.

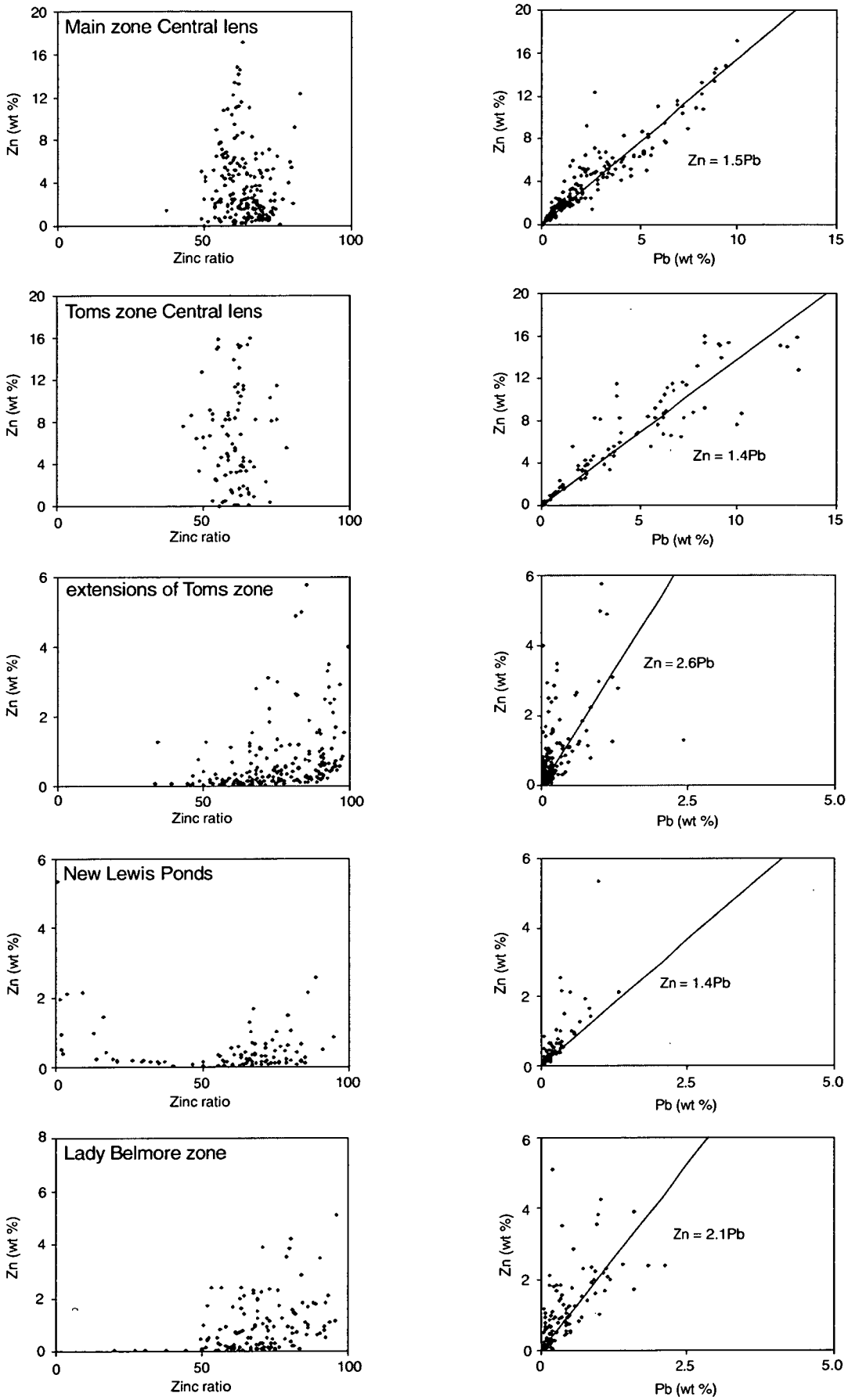

Figure 8.9 Scatter plots of Zn ratio versus total Zn and Pb versus Zn, using the same assay data as in Figure 8.8.

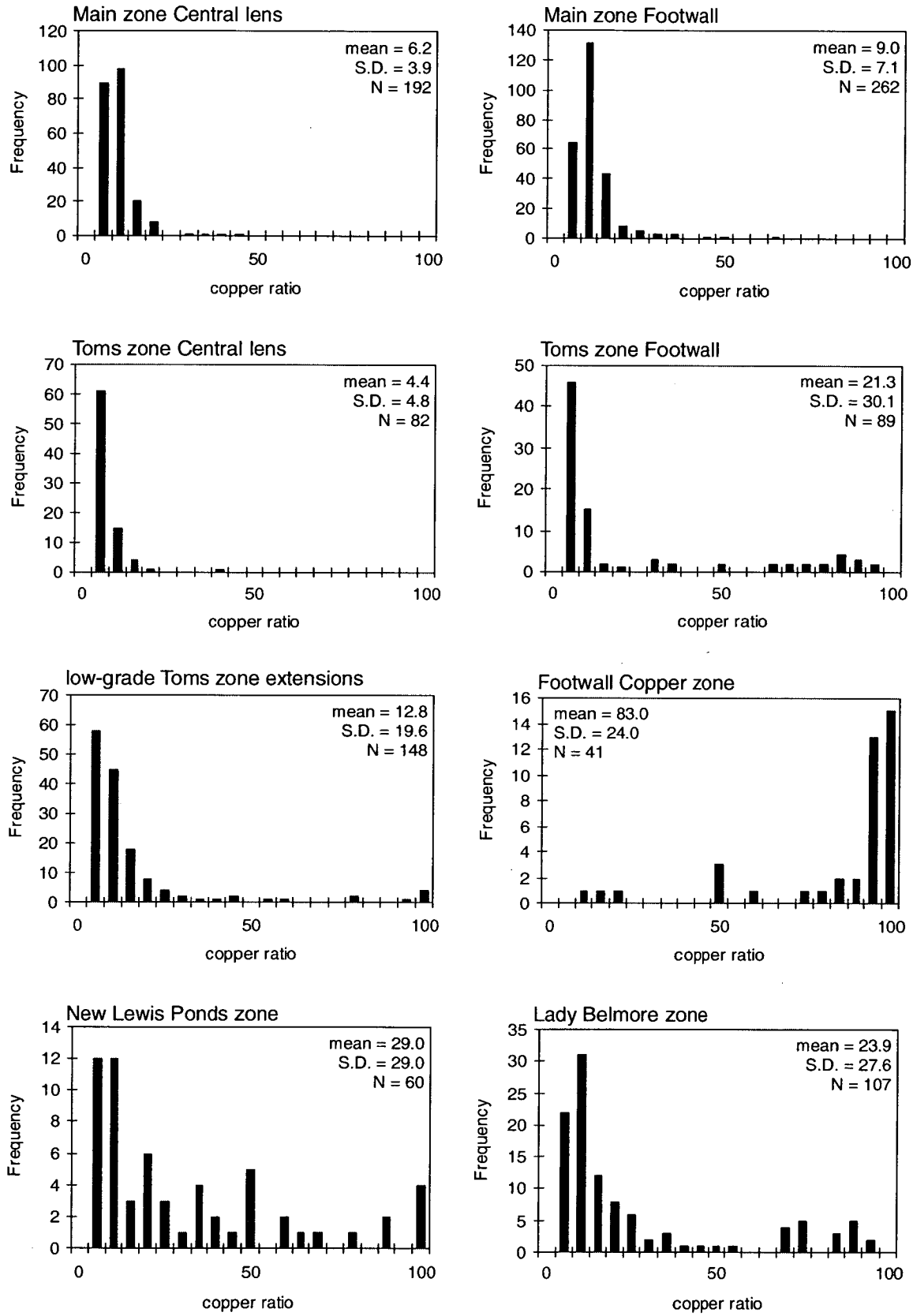

Figure 8.10 Cu ratios from Main zone and Toms zone, and from areas of vein-hosted sulfide in the Toms zone footwall, Lady Belmore zone and New Lewis Ponds. Only assays grading >0.05% Cu and >0.05% Pb are included. Mean and standard deviation are presented for each mineralised zone.

Discussion: source of metals

The massive sulfide lenses in Main and Toms zones have relatively homogenous S and Pb isotopic compositions. Zn-Pb sulfides precipitated from the hydrothermal fluid over a similar range of temperatures, resulting in tightly distributed Zn ratios. Sulfur isotopes indicate that the fluid contained magmatic S and a component of reduced seawater sulfate. The hydrothermal fluid may have therefore leached metals out of the underlying Late Silurian, rhyolitic and dacitic volcanic host rocks. Direct input of a reduced, high temperature magmatic fluid could have also contributed metal chloride complexes to the solution. The chemistry of the mineralising fluid and conditions of massive sulfide deposition are discussed in Chapter 9.

The syn-tectonic quartz-sulfide veins appear to result from younger, fracture-controlled hydrothermal fluids with variable chemistry, migrating through the Late Silurian, volcanic-sedimentary package, during the D_1 deformation (Middle Devonian to Early Carboniferous). Pyrite, sphalerite, galena and chalcopyrite occurring in the veins have similar $\delta^{34}S$ values to the massive sulfide. The S isotopes, metal ratios and overall metal grades indicate that sulfides were leached out of the massive sulfide lenses and mineralised host rocks.

The Pb isotopic signature of Late Silurian, stratabound Zn-Pb deposits in New South Wales reflects the host rock composition and source of metals. Carr et al. (1995) demonstrated that Au-rich massive sulphide deposits, located close to the structural boundary of the sedimentary troughs including Wisemans Creek, Mt Bulga and Calula contain a greater component of mantle-derived Pb than the more radiogenic deposits. This interpretation is consistent with Wyborn et al. (1992), who predicted that Au-rich massive sulfide deposits would occur in areas where Late Silurian hydrothermal systems penetrated into the underlying Ordovician shoshonitic rocks.

CHAPTER 9

GENETIC MODEL AND DISCUSSION

9.1 Introduction

The distribution of hydrothermal alteration mineral assemblages, geochemical trends, sulfide mineralogy and textures in Main and Toms zones indicate that Lewis Ponds is a strongly deformed, stratabound VHMS deposit with characteristics that are intermediate between VHMS and carbonate-hosted replacement deposits. Table 9.1 summarises the major features of the two mineralised zones outlined in previous chapters. Other critical observations that relate to the genesis of the deposits are listed below:

1. The polymictic breccia, pebbly-granular sandstone and siltstone units that host the massive sulfide lenses overlie a thick footwall succession of massive quartz-plagioclase phyric dacite and syn-sedimentary porphyritic dacite intrusions.

2. The massive sulfide lenses are surrounded by an asymmetric, semiconformable hydrothermal alteration envelope characterised by Mg, Fe, S, Ba and K enrichment and Na depletion. Texturally destructive chlorite-dolomite-talc, quartz-dolomite-chlorite and quartz-sericite ± hyalophane assemblages occur within the polymictic breccia, pebbly-granular sandstone and siltstone units.

3. Coherent porphyritic dacite in the immediate footwall of Main zone has not undergone significant hydrothermal alteration or mass change (Table 6.2, Fig. 6.10). However, strong pervasive sericite and chlorite assemblages extend several hundred metres into the footwall volcanic succession south of Main zone (Figs. 5.2 and 5.3). Chlorite-pyrite grades outward into sericite-quartz ± chlorite with distance from the Toms Central lens.

4. Bladed, dendritic, reticulate, botryoidal, spongy and framboidal aggregates of pyrite and pyrrhotite occur throughout the breccia, sandstone and siltstone in Main zone and rarely in Toms zone. These aggregates have been overgrown and partly replaced by base metal sulfides.

5. The Toms Central massive sulfide lens occurs within a 200-250 m wide corridor of anastomosing high strain zones. Quartz-sulfide shear and extension veins surround the massive

sulfide lens. These veins formed by brittle failure and extension in the strongly foliated host rocks, during and after cleavage development (see Chapter 4, section 4.5). Other features resulting from brittle and ductile deformation include pinch-and-swell structures, kink folds, cataclastic breccia, gash veins, tear faults and cleavage-aligned sulfide aggregates.

	Main zone	Toms zone
Overall:		
Size and geometry	10-15 m thick, 500x200 m long Central massive sulfide lens	5 m thick, 600x200 m long Central massive sulfide lens
Type	Stratabound	Fault-bound ± stratabound
Host rock	Polymictic limestone-clast breccia, mixed provenance breccia, pebbly-granular siltstone and sandstone	Siltstone & minor sandstone
Interpreted footwall volcanic facies	Qtz-plag phyric dacite cryptodome and associated peperite facies	Massive dacite & qtz-plag phyric dacite sills
Alteration:		
Envelope geometry and distribution	Asymmetric, conformable, texturally destructive assemblages confined to breccia-sandstone unit	Asymmetric, stratabound, strongly developed, semiconformable to discordant chlorite-sericite envelope extending into footwall volcanic succession
Assemblages	Qtz-dol-chl, dol-chl-tlc and chl-py in breccia unit	Qtz-ser ± hly, dol-chl-tlc and chl-py grading out into ser-qtz ± chl in FW
Element enrichment surrounding massive sulfide lens	Fe, Mg, Ba, Sr, As, S, Tl	Fe, Mg, Ba, Sr, As, S, Zn ± K
Sulfides:		
Observed mineralogy	Py, sph, ga, ccp, td, as, po, st, pg, electrum	Py, sph, ga, ccp, td, as, st, tn, pg
Relative modal abundance	More po than Toms zone	More st, td, sph, ga & as than Main zone
Sulfide associations	Banded py-sph-ga, massive po-ccp, semi-massive to disseminated sulfides, mineralised limestone clasts	Banded py-sph-ga, massive py, semi-massive to disseminated sulfides, qtz-sulfide veins, dol-sulfide veins
Sulfide textures	Primitive textures (framboidal, dendritic, botryoidal, encrustation), vuggy and recrystallised textures	Annealed, coarse-grained sulfides, cataclastic breccia, kink folds and pinch-and-swell structures and rare primitive textures
Metal zonation:		
Lateral (along strike)	None observed	Lower Cu, Pb, Zn & Ag grades along L.P. fault, away from massive sulfide
Vertical (from FW to HW)	Higher Au ± Ag, Sb, Hg grades toward the top of the Central lens and throughout the HW lens	Higher Cu ± Ag, Sb, Sn, Mo grades in the lower 1-2 m of the Central lens; progressive upward increase in Bi

Table 9.1 Comparison of Main zone with Toms zone. Mineral abbreviations: qtz = quartz, plag = plagioclase, dol = dolomite, chl = chlorite, ser = sericite, tlc = talc, hly = hyalophane, py = pyrite, sph = sphalerite, ga = galena, ccp = chalcopyrite, td = tetrahedrite, tn = tennantite, as = arsenopyrite, po = pyrrhotite, st = stannite, pg = pyrargyrite Bi = native bismuth.

6. Type 1 quartz-pyrite and carbonate-chalcopyrite-pyrite veins (see Chapter 4, section 4.5) in the Toms zone footwall and Footwall Copper zone probably represent pre-tectonic stringers. However, the relative timing of vein emplacement and massive sulfide deposition is uncertain as the type 1 veins are displaced along strike from Toms zone, and the host sedimentary rocks are tightly folded (Figs. 5.2 and 5.3). The stringer zone may have formed above syn-volcanic extensional faults within the footwall.

7. Trace element distribution among sulfides varies between the mineralised zones (Table 9.2). Galena grains in the Footwall Copper zone have significantly higher average Se, Ag, Bi and Fe concentrations than those in the massive sulfide. Sphalerite grains in Main zone contain less Mn and Cd than those in Toms zone. These variations are interpreted to reflect the chemistry and temperature of the mineralising fluid (see Chapter 7, sections 7.10 and 7.11).

Mineral		Main zone			Toms zone			FW Copper zone		
		Avg.	N	MDL	Avg.	N	MDL	Avg.	N	MDL
Sphalerite	Cd	540	23	100	420	15	100	1 540	8	100
	Mn	590	23	100	1 640	15	100	880	8	100
Galena	Fe	1 250	20	40	330	16	12	1 200	17	47
	Se	900	20	75	2 030	16	81	16 450	17	100
	Ag	1 700	20	100	1 750	16	100	7 170	17	100
	Bi	2 700	2	100	2 750	2	100	28 760	14	100

Table 9.2 Average trace element concentrations in sulfide minerals (all in ppm). N is the number of microprobe analyses. MDL is the percentage of analyses above the minimum detection limit.

In this chapter, a genetic model for the formation and post-depositional modification of the Lewis Ponds deposits is presented by considering the source of metals, composition and temperature of the hydrothermal fluids and the factors that controlled metal deposition at the trap site. Comparisons are made between Lewis Ponds and other stratabound massive sulfide deposits both within the Lachlan Fold Belt and worldwide.

9.2 Sea floor exhalative or sub-sea floor replacement origin

Main zone

Mineralogical, geochemical and textural evidence presented in chapters 5, 6 and 7 indicate that Main zone formed by lateral fluid flow and sub-sea floor replacement of the permeable, pebbly-granular sandstone and polymictic breccia in the Transitional Unit. Chlorite, dolomite, talc, phlogopite and sulfides occur throughout the sandstone and breccia matrix. Intervals of massive siltstone in the Main zone footwall are weakly altered and devoid of base metal sulfides. A weak to moderate pervasive sericite-chlorite-calcite assemblage has overprinted the footwall volcanic rocks, indicating minimal fluid-rock interaction. Facies variations in the Transitional Unit controlled the distribution of hydrothermal alteration assemblages. The more permeable,

coarse-grained breccia and sandstone units were aquifers for hydrothermal fluids. Chlorite, dolomite, talc and sulfides have partly to completely replaced the lithic clasts and matrix of the breccia. Irregular honeycomb, vuggy, botryoidal and encrustation sulfide-dolomite textures (Figs. 5.5C, 5.14 and 7.10) resulted from dissolution of the massive dolomite and unimpeded growth of dolomite, calcite, quartz, chlorite, talc, sphalerite, pyrite, chalcopyrite, tetrahedrite and galena into open cavities (vugs and channels). Clastic sulfide textures, indicative of erosion and re-working of an exposed massive sulfide lens do not occur in Main zone. Brittle deformation has produced pseudoclastic textures within arsenopyrite and pyrrhotite aggregates.

Toms zone

Toms zone may represent either a sea floor exhalative or sub-sea floor replacement deposit. Siltstone, hosting the Central massive sulfide lens was deposited in a relatively quiet, deep water environment which may have allowed the preservation of a sea floor massive sulfide lens. However, there are no constraints on the relative position of the sea floor during mineralisation at Lewis Ponds. Recrystallisation and annealing would have destroyed any primary clastic sulfide textures. The apparent absence of barite in Toms zone is not necessarily indicative of a sub-sea floor environment of formation because the massive sulfide lens is surrounded by a symmetrical halo of anomalous Ba (0.1-1.9 wt %) and primitive sulfide textures are not preserved. Furthermore, the replacement of bladed barite or anhydrite crystals by pyrrhotite in Main zone, indicates sulfate reduction after deposition of the sediment.

VHMS deposits are commonly overlain by chemical sediments resulting from exhalation of hydrothermal fluids on the sea floor or mixing between hydrothermal fluids and seawater in unconsolidated sediments (Ohmoto et al., 1983; Lydon, 1988; Large, 1992). At Lewis Ponds, jasper lenses crop out discontinuously around the margins of the Western and Eastern volcanic successions (see Chapter 5, section 5.4). Anomalous Zn and Tl concentrations in one sample from the Toms zone hangingwall (LPD014, Appendix 4) may indicate submarine exhalative activity. Very low immobile element concentrations suggest that the jasper does not represent an altered volcanic or sedimentary rock. Jasper occupied a discrete horizon in the Lewis Ponds facies model proposed by Valliant and Meares (1998). However, faults and tight folds separate the jasper from the massive sulfide lenses, thereby limiting any genetic interpretation.

9.3 Temperature and chemistry of the hydrothermal fluids

In the following section, mineral assemblages, textures and paragenetic relationships are used to infer the temperature and pH of the hydrothermal fluids at Lewis Ponds, the redox conditions and the mechanisms of sulfide deposition. These interpretations rely on published thermodynamic modelling studies and genetic models of VHMS deposits. Mineral

assemblages, metal zonation, paragenetic relationships and theoretical thermodynamic models help to constrain the: solubility of metals in hydrothermal fluids; pH, oxidation and temperature conditions from which metals precipitate; and partitioning of trace elements among sulfides.

Temperature of the fluids

Fluid inclusions provide the most direct evidence for the temperature of mineralising fluids. These were rarely preserved in the strongly deformed and recrystallised massive sulfide at Lewis Ponds. However, zoned dolomite crystals occurring in the mineralised host rocks contain primary two phase liquid-vapour inclusions with pressure corrected homogenisation temperatures of 166-232°C (for 1 000 m water depth). The spheroidal and anhedral dolomite aggregates may have formed at temperatures as low as 50-60°C (eg. Radke and Mathis, 1980; Gregg and Sibley, 1984). Dolomitisation at Lewis Ponds probably occurred during diagenesis and low temperature hydrothermal alteration, prior to and during mineralisation. Both fluid-rock interaction and fluid mixing models indicate that dolomite in Toms zone precipitated at higher temperatures than dolomite in Main zone, despite little variation in fluid inclusion homogenisation temperatures (see Chapter 8).

Many VHMS deposits show a characteristic upward and/or outward decrease in Cu/(Cu+Zn) ratio and chalcopyrite abundance (Large, 1977; Solomon and Walshe, 1979; Eldridge et al., 1983; Hannington et al., 1999a). This zonation is thought to result from progressive cooling of high temperature fluids introduced into the footwall stockwork zone and lower parts of the massive sulfide lens (Ohmoto et al., 1983; Lydon, 1988; Large et al., 1989; Hannington et al., 1999a). Textural and fluid inclusion studies in the Kuroko deposits suggested that temperatures in the hydrothermal system progressively increased, reached a thermal maximum and then decreased (Eldridge et al., 1983; Pisutha-Arnond and Ohmoto, 1983).

Metal solubilities in hydrothermal fluids are dependent on temperature (Sato, 1973; Large, 1977; Ohmoto et al., 1983; Hannington et al., 1999a). Low temperature fluids (<280°C) carry Zn, Pb and Ag as bisulfide or chloride complexes. Copper is only soluble in higher temperature (>300°C) fluids with low pH. A temperature-solubility model for the Kidd Creek deposit predicted that sphalerite and galena were saturated in the fluid at 150-250°C whereas chalcopyrite became saturated at 350°C (Hannington et al., 1999a). In the genetic models of Eldridge et al. (1983) and Huston and Large (1989), high temperature Cu-rich fluids leach sphalerite and galena from the base of the massive sulfide lens and deposit chalcopyrite. As the upward-migrating fluid cools, sphalerite, galena, and barite precipitate in outer parts of the massive sulfide lens.

At Lewis Ponds, the massive sulfide consists of pyrite, sphalerite, galena and tetrahedrite. Chalcopyrite and pyrrhotite have locally overprinted the Zn-Pb sulfide in Main zone. Pre-tectonic to early syn-tectonic dolomite-chalcopyrite-pyrite veins and chalcopyrite stringer veins occur throughout the Toms Central massive sulfide lens and Footwall Copper zone respectively. The Zn-Pb-Au-Ag-rich massive sulfide probably resulted from relatively low temperature, 150-250°C fluids. A late high temperature, >280°C, acidic fluid may account for the chalcopyrite-rich assemblages in the massive sulfide lenses and Footwall Copper zone.

Fluid pH

Alteration mineral assemblages surrounding VHMS deposits reflect temperature, composition and pH of the hydrothermal fluid and the amount of fluid-rock interaction (see Chapter 5, section 5.8). Recent thermodynamic modelling by Schardt et al. (2001) suggested that high temperature (250-350°C), weakly acidic (pH = 4.5-5.5) fluids produce the characteristic mineral zonation of chlorite grading out into sericite-quartz, observed in the footwall of many VHMS deposits. An asymmetric envelope of sericite and Mg-chlorite surrounds the Toms Central massive sulfide lens and Lady Belmore zone. Mg-chlorite also occurs throughout the polymictic breccia and pebbly-granular sandstone in Main zone. Pervasive chlorite-sericite alteration of the footwall volcanic succession probably resulted from fluid-rock interactions involving a weakly acidic, Mg-bearing hydrothermal fluid (Fig. 9.1). However, dolomite, calcite and primary fossiliferous limestone clasts in the host sedimentary rocks may have buffered the fluid pH at the site of massive sulfide deposition.

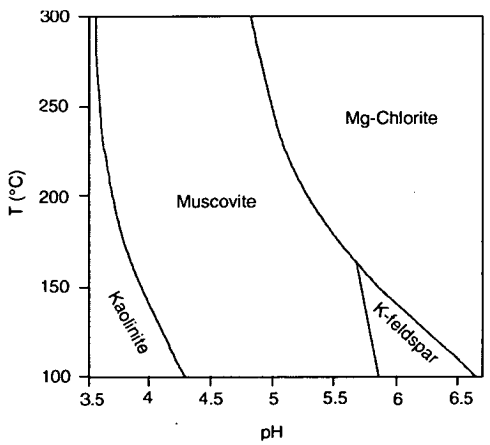

Figure 9.1 Stability fields of muscovite and chlorite as a function of pH and temperature, based on thermodynamic modelling, after Schardt et al. (2001). Calculated using the following activities: $Mg^{2+} = 0.017$ and $K^{+} = 0.051$.

Pyrite, sphalerite and galena aggregates are associated with very fine-grained type 1 dolomite and medium to very coarse-grained type 2 rhombic dolomite crystals. In the Main zone host rocks, irregular honeycomb, vuggy and botryoidal sulfide-dolomite textures resulted from dissolution and precipitation of dolomite during mineralisation (eg. Figs. 5.14 and Fig. 5.5C). These textures are poorly preserved in Toms zone due to the strong foliation, pinch-and-swell

structures and abundance of quartz. The dissolution of dolomite by acidic hydrothermal fluids (Equation 1), results in the production of a weak acid containing H_2CO_3, Ca^{2+} and Mg^{2+} ions:

$$MgCa(CO_3)_{2(s)} + 4H^+ = 2H_2CO_{3(aq)} + Mg^{2+}_{(aq)} + Ca^{2+}_{(aq)} \quad (1)$$

Lead and Zn occur in saline, weakly acidic fluids as chloride complexes, for example:

$$ZnCl^0_{2(aq)} + H_2S_{(aq)} = ZnS_{(s)} + 2H^+_{(aq)} + 2Cl^-_{(aq)} \quad \text{(Huston and Lage, 1989)} \quad (2)$$

$$PbCl^0_{2(aq)} + H_2S_{(aq)} = PbS_{(s)} + 2H^+_{(aq)} + 2Cl^-_{(aq)} \quad (3)$$

Equations 2 and 3 indicate that sulfide deposition may result from increased fluid pH, dilution or increased activity of reduced S. Therefore, the dissolution of dolomite and precipitation of Zn-Pb-rich sulfide in Main zone is summarised by combining Equations 2 and 3 with 1:

$$2ZnCl^0_{2(aq)} + 2\,H_2S_{(aq)} + MgCa(CO_3)_{2(s)} = 2ZnS_{(s)} + 2H_2CO_{3(aq)} + Mg^{2+}_{(aq)} + Ca^{2+}_{(aq)} + 4Cl^-_{(aq)} \quad (4)$$

$$2PbCl^0_{2(aq)} + 2\,H_2S_{(aq)} + MgCa(CO_3)_{2(s)} = 2PbS_{(s)} + 2H_2CO_{3(aq)} + Mg^{2+}_{(aq)} + Ca^{2+}_{(aq)} + 4Cl^-_{(aq)} \quad (5)$$

The role of increased fluid pH on massive sulfide deposition in Main zone was tested using a simple thermodynamic model in *Geochemist's Workbench* version 3.2. This involved progressively reacting 600 mg of dolomite with an acidic, 250°C fluid (Figs. 9.2 and 9.3). The initial fluid composition chosen for this model was similar to hydrothermal fluids currently venting in the Okinawa Trough. It also contained seawater concentrations of $Mg^{2+}_{(aq)}$ and $HCO_3^-{}_{(aq)}$. Pyrite, sphalerite, galena and talc precipitated over a pH range of 4.5 to 5.5 due to dolomite dissolution and increased fluid pH (Fig. 9.3). During the final part of the titration experiment, dolomite precipitated as the fluid approached equilibrium with the reactant carbonate.

Command	Annotation
T = 250	Fluid temperature
pH = 3	Fluid pH
Na+ = 0.4 molal	Starting fluid composition
Ca++ = 0.02 molal	
Mg++ = 0.01 molal	
Fe++ = 0.0001 molal	
Cl- = 0.5 molal	
HCO3- = 0.002 molal	
SO4-- = 0.01 molal	
O2(aq) = 0.000001 molal	
SiO2(aq) = 0.013 molal	
Zn++ = 0.00003 molal	
Pb++ = 0.000001 molal	
swap H2S(aq) for SO4--	Converts all $SO_{4(aq)}^{2-}$ to $H_2S_{(aq)}$

Fig. 9.2 Script entered into *Geochemist's Workbench* for simple titration experiment.

Command	Annotation
suppress Tremolite	
suppress Anthophyllite	
suppress Enstatite	
suppress Tridymite	Prevents minerals from precipitating
suppress Antigorite	
suppress Chrysotile	
suppress Anhydrite	
fix O2(g)	Fixes the oxygen fugacity
flow-through	Removes precipitated minerals from the system so they cannot be dissolved
react 600 mg Dolomite	Mass of dolomite reacted
go	

Fig. 9.2 continued.

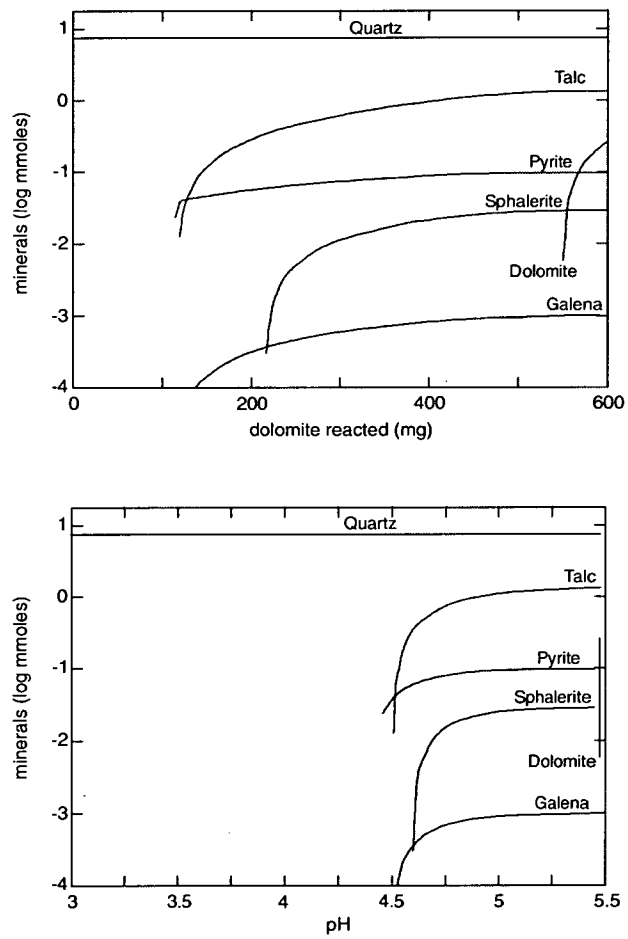

Figure 9.3 Modelled titration paths resulting from the reaction of an acidic (pH=3), 250°C hydrothermal fluid with 600 mg of dolomite under 40 bars pressure. The hydrothermal fluid composition is similar to modern vent fluids in the Okinawa Trough (references cited in de Ronde, 1995): 500 *m*molal Cl^-, 400 *m*molal Na^+, 20 *m*molal Ca^{2+}, 13 *m*molal $SiO_{2(aq)}$, 3.5 *m*molal $H_2S_{equiv.}$, 30 μmolal Zn^{2+} and 1 μmolal Pb^{2+}. The fluid also contains seawater concentrations of Mg^{2+} (10 *m*molal) and $HCO3^-$ (2 *m*molal). Precipitation of pyrite, sphalerite, galena and talc takes places over a pH range of 4.5 to 5.5. Dolomite precipitates at a pH of 5.5. Horizontal lines indicate saturation of the minerals in the fluid. Modelled in *Geochemist's Workbench version 3.2*. The program re-calculates equilibrium conditions in the fluid after each titration step.

Redox conditions in the basin and at the site of massive sulfide deposition

Marine sedimentary facies in the Mumbil Group (Pogson and Watkins, 1998) record progressively deepening conditions along the margin of the Hill End Trough during the Late Silurian. At Lewis Ponds, siltstone grades laterally into carbonaceous mudstone / black shale along strike south of Toms zone and vertically into mudstone beds north of Main zone (see Chapter 3, section 3.5). Disseminations of pyrrhotite occur throughout siltstone and sandstone beds in the Hangingwall Siltstone Unit and Transitional Unit. Disseminated pyrrhotite may reflect the activity of S reducing bacteria during early diagenesis. Therefore, reduced conditions probably existed in the basin after deposition of the host sediments.

A symmetrical halo of anomalous Ba (0.1-1.9 wt %) surrounds the massive sulfide lenses in Main and Toms zones. High Ba concentrations in the Toms zone footwall are associated with hyalophane ($Ba,K,Na(Al,Si)_4O_8$) rather than barite ($BaSO_4$). However, orthorhombic pyrrhotite crystals and rectangular quartz aggregates (eg. Figs. 7.7B and 7.9D) have replaced paragenetically early twinned barite or anhydrite crystals in the breccia and sandstone beds in Main zone. The apparent absence of barite at Lewis Ponds therefore indicates low SO_4^{2-} concentrations in the depositional environment and/or post-depositional replacement of sulfate by Fe-sulfides and quartz.

Sulfide assemblages provide information about redox conditions during massive sulfide deposition. Paragenetically early dendritic, botryoidal, and framboidal aggregates of pyrite and pyrrhotite occur in the Transitional Unit in Main zone and rarely in the Hangingwall Siltstone Unit. Pyrite and pyrrhotite in the Main zone Central massive sulfide lens and Footwall Copper zone indicate that sulfides were deposited under a narrow range of oxygen fugacity conditions, within the pyrite and pyrrhotite stability fields (Fig. 9.4). The apparent lack of pyrrhotite in the Toms Central massive sulfide lens suggests mineralisation in a slightly more oxidised environment, possibly closer to the sea floor.

Tetrahedrite and galena occur throughout the massive sulfide lenses at Lewis Ponds. The tetrahedrite contains significantly more Ag than the galena (see Chapter 7, section 7.10). Huston et al. (1996) studied the geochemical controls on Ag distribution in eastern Australian VHMS deposits. Silver preferentially fractionates into tetrahedrite rather than galena in relatively low temperature, more oxidised environments. The relative abundance of tetrahedrite at Lewis Ponds (up to 2 modal % in Toms zone) suggests that mineralisation occurred in a slightly lower temperature, more oxidised environment than the source region of the hydrothermal fluid.

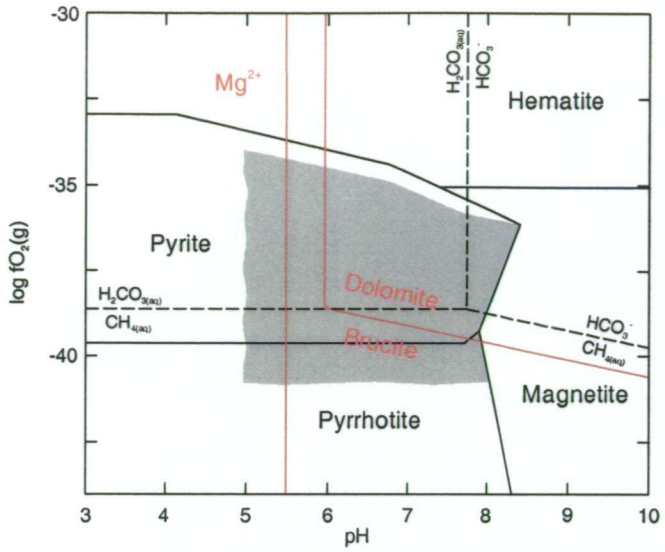

Figure 9.4 Log fO_2 versus pH diagram showing stability fields of Fe-oxides, Fe-sulfides, carbonate minerals and aqueous carbonate species at 250°C and 100 bars pressure. Shaded area represents possible pH and fO_2 conditions during massive sulfide deposition at Lewis Ponds. Vuggy textures in the Main zone Central lens indicate that dolomite precipitated with pyrite and sphalerite. Based on the following concentrations (all as log activity): Mg^{2+} = -2.5, Ca^{2+} = -3, HCO_3^- = -3, SO_4^{2-} = -2.5, Fe^{2+} = -5.

The massive sulfide lenses have anomalous Sn concentrations (Tables 7.4 and 7.5). Most of the Sn occurs in sphalerite, chalcopyrite and stannite (see Chapter 7, section 7.10). Mymekitic and oriented intergrowth, emulsion textures (eg. Fig. 7.7 D) indicate that at least some of the stannite exsolved from Sn-rich sphalerite during gradual cooling (eg. Ramdohr, 1979; Nekrasov et al., 1981). Angular stannite inclusions in chalcopyrite aggregates probably resulted from the rearrangement of grain boundaries and expulsion of stannite during recrystallisation.

Tin-rich VHMS deposits including Kidd Creek in the Abitibi subprovince, Canada; Gecko, Ontario, Canada and Neves-Corvo in the Iberian Pyrite Belt and modern seafloor deposits in the Escanaba Trough are characterised by low Au grades and low fO_2 mineral assemblages containing pyrrhotite, arsenopyrite, siderite, cassiterite and/or stannite (Petersen, 1986; Zienberg et al., 1993; Hannington et al., 1999a). At 250°C, Sn is transported as chloride complexes under reduced, acid conditions (Petersen, 1986; Hannington et al., 1999a), whereas Au and Ag are soluble in more oxidised, acid to near neutral hydrothermal fluids (Seward, 1976; Huston and Large, 1989; Huston et al., 1996). Consequently, Sn-rich VHMS deposits typically have low Au grades.

Stannite would not have co-precipitated with galena, tetrahedrite and electrum in the massive sulfide lenses at Lewis Ponds. The stannite occurs mostly in pre-tectonic to early syn-tectonic, type 2 dolomite-chalcopyrite-pyrite veins within Toms zone. Trace amounts occur in the massive sulfide in Main and Toms zones. A late high temperature, highly reduced fluid either introduced Sn into the system or remobilised Sn out of recrystallised sphalerite and chalcopyrite aggregates in the massive sulfide. Overall, the stannite, pyrite, pyrrhotite and Fe-bearing

sphalerite indicate that the massive sulfide lenses at Lewis Ponds formed under moderately to strongly reduced conditions. A change in redox state and the late introduction of Sn from hotter, more strongly reduced fluids may explain why Lewis Ponds has relatively high Sn and Au concentrations.

9.4 Source of the metals and fluids

VHMS-forming hydrothermal systems involve convection of heated fluids deep within permeable submarine volcanic successions. The mineralising fluids consist of seawater, evolved seawater, magmatic water or a combination of fluid types (Solomon and Walshe, 1979; Franklin et al., 1981; Pisutha-Arnond and Ohmoto, 1983; Davis et al., 1987; Lydon, 1996; Hannington et al., 1999a). Studies of the Kuroko deposits concluded that seawater-dominant pore fluids reacted continuously with the volcanic host rocks in an intensifying hydrothermal system (Ohmoto et al., 1983; Pisutha-Arnond and Ohmoto, 1983). According to Ohmoto et al. (1983), the Kuroko mineralising fluids acquired S by inorganic reduction of diagenetic sulfates in the volcanic host rocks. The following evidence may indicate involvement of a magmatic component in VHMS-forming fluids:

- high salinity (>> seawater) fluid inclusions (Bryndzia et al., 1983);
- high sulfidation alteration assemblages (Sillitoe et al., 1996);
- presence of Cu-Se-Bi-Co-rich sulfide assemblages (Marcoux et al., 1996; Hannington et al., 1999b);
- spatial and temporal association of most VHMS deposits with submarine felsic volcanic centres (Stanton, 1990; Allen, 1992; Allen et al., 1996b; Lydon, 1996); and
- occurrence of VHMS deposits in mixed felsic and intermediate to mafic volcanic successions (Stolz et al., 1997).

Determining the nature of the hydrothermal system responsible for mineralisation at Lewis Ponds is complicated by syn-tectonic, fracture-controlled fluids, which have significantly modified parts of the deposit, particularly along strike from Toms zone and in the Toms zone hangingwall. Highly variable Zn ratios in areas dominated by syn-tectonic quartz-sulfide veins may reflect fluctuations in the chemistry and temperature of fluids circulating through the host sequence during the D_1 deformation (see Chapter 8, discussion). The following section is a discussion of the potential sources of mineralising fluids and metals at Lewis Ponds.

Evidence for the involvement of seawater or evolved seawater

Hydrothermal alteration and mineralisation at Lewis Ponds may have involved pure seawater or evolved seawater for the reasons outlined below:

1. Proximal alteration assemblages contain dolomite, Mg-chlorite, talc and phlogopite. The

extensive Mg-rich alteration halo indicates involvement of a Mg-bearing hydrothermal fluid. Limestone clasts and dolomite were a potential source of Mg^{2+} ions in the host sediment. Least altered felsic volcanic rocks in the footwall only contain 0.9-2.6 wt % Mg. However, deeply circulating hydrothermal fluids potentially leached Mg^{2+} out of the Ordovician, mafic and ultramafic volcanic basement rocks. Seawater may have also contributed Mg^{2+} to the hydrothermal fluid. Schardt et al. (2001) demonstrated that chlorite precipitates from fluids carrying as little as 400 ppm Mg, whereas seawater typically contains 50,000 ppm Mg (eg. de Ronde, 1995).

2. Paragenetically early, very fine-grained dendritic, reticulate and spongy textures occurring in the Main zone Central lens indicate limited crystal growth and quenching of a supersaturated fluid. This probably resulted from rapid mixing between the hydrothermal fluid and cooler pore fluids (eg. seawater) in the matrix of the breccia, sandstone and siltstone.

3. Rectangular quartz aggregates (Fig. 7.9D) and orthorhombic bladed pyrrhotite crystals in Main zone are interpreted as pseudomorphs of barite or anhydrite. Sulfate minerals occur abundantly throughout well preserved, modern and ancient sea floor exhalative VHMS deposits (see section 7.8, Chapter 7). Sulfate-rich crusts and chimneys are thought to result from mixing between the hydrothermal fluid and seawater (eg. Zienberg et al., 1993).

4. Sulfur isotope values in the massive sulfide ($\delta^{34}S$ = 1.7-5‰) and chalcopyrite stringer veins ($\delta^{34}S$ = 3.9-7.4‰) indicate that the hydrothermal fluid probably contained a minor component of partially reduced seawater sulfate. Fluids may have leached this S from the host volcanic and sedimentary rocks.

5. Fluid inclusion and stable isotope data indicate that the dolomite precipitated from a low temperature (166-232°C for 1000 m water depth), weakly saline (1.4 to 7.7 eqiv wt % NaCl) fluid that was possibly depleted in O and C isotopes ($\delta^{18}O$ = -2.5 to 0.3‰, $\delta^{13}C$ = -14 to -4‰). Dolomitisation may have resulted from reactions between the limestone-bearing host sediment and evolved seawater at 150-250°C, and/or mixing between heated pore fluids at 100°C and evolved seawater at 350°C.

Evidence for the involvement of magmatic fluids

1. Type 1A stringer veins in the Footwall Copper zone contain chalcopyrite, sphalerite, Bi-Se-rich galena and native bismuth. This assemblage was not observed in either massive sulfide zone. Galena grains in the stringer veins have significantly higher Fe, Se, Bi and Ag concentrations than those in the massive sulfide (Table 9.2).

Cu-Bi-Se-Co-rich stockworks underlie the Kidd Creek deposit (Hannington et al., 1999a; 1999b) and a number of deposits in the Iberian Pyrite Belt (Marcoux et al., 1996). These paragenetically late chalcopyrite-bearing veins are attributed to high temperature (>300°C) fluids. The Se content in sulfides is not affected by recrystallisation or annealing (Huston et al., 1995). Trace amounts of Se substitute for S in pyrite chalcopyrite, galena and tetrahedrite. Selenium is transported as volatile phases such as H_2Se and partitioned into high temperature mineral assemblages (Hannington et al., 1999a). Cu-Se-rich assemblages in VHMS deposits are interpreted to result from the direct involvement of a reduced magmatic fluid (Hannington et al., 1999b; Serranti et al., 2002).

Based on this previous work, it is possible to conclude that chalcopyrite stringer veins in the Footwall Copper zone at Lewis Ponds precipitated from a high temperature, moderately reduced (pyrite-pyrrhotite stable), Cu-Se-Bi-Ag-Pb-Zn-bearing fluid containing a magmatic component. These fluids may have also contributed metals to the massive sulfide lenses. A reduced magmatic fluid could account for high Sn concentrations in massive sulfide zones and Footwall Copper zone. The Toms Central lens, which is closer to the inferred source of magmatic fluids has higher overall Cu, Ag, Sb, Sn and Bi grades than Main zone (Table 9.1). However, this variation partly reflects the more massive nature of the Toms Central lens.

2. The Lewis Ponds host sedimentary rocks were deposited in close proximity to a high-level intrusive dacite centre. This interpretation may provide further evidence for the involvement of a magmatic component in the hydrothermal fluid if mineralisation was syn-volcanic.

Points 1 and 2, listed above, do not provide definitive evidence for the involvement of a magmatic fluid as seawater-dominant hydrothermal fluids circulating through the footwall volcanic rocks may have also acquired a magmatic signature, and the absolute age of mineralisation is not known. Therefore, the isotope data, mineral assemblages and textures tend to indicate that the hydrothermal fluid responsible for alteration and mineralisation at Lewis Ponds was most probably a mixture of seawater and evolved seawater.

Source of metals

Lewis Ponds has a radiogenic, crustal Pb isotope signature (see Chapter 8, section 8.4). Carr et al. (1995) noted that both hydrothermal convection in felsic volcanic rocks and magmatic incorporation of older continental crust would produce a similar isotopic signature in the Late Silurian VHMS deposits of New South Wales. Of more significance was their suggestion that Au-rich massive sulfide deposits, located close to the structural boundaries of the Silurian-Devonian troughs acquired a component of primitive Pb from the underlying

Ordovician, shoshonitic volcanics (Fig. 2.1). These rocks host the world class Cadia and Endeavour porphyry Cu-Au deposits. Deeply circulating hydrothermal fluids potentially leached metals from the Ordovician rocks in addition to the overlying Silurian felsic volcanics.

A magmatic fluid may have directly contributed Cu, Se, Bi, Sn, Ag, Pb and Zn to the Lewis Ponds deposits. However, some of these metals, eg. Ag, Sn, Zn and Pb, could also occur in the reduced, S-type dacitic and rhyolitic volcanic rocks in the footwall. Sulfur isotopes in the sulfides indicate that the hydrothermal fluid contained a component of magmatic S, derived from a magmatic fluid or leached from the volcanic rocks.

Later magmatic fluids could have exsolved from the Middle Carboniferous granites. Non-foliated quartz-feldspar porphyry dykes in the Toms zone footwall and hangingwall are probably genetically related to the Lewis Ponds granite (Chapter 3, section 3.9). Emplacement of the granite took place after cleavage development and ductile shearing. Quartz veins cutting the dykes in the Toms zone footwall rarely contain galena and sphalerite (Fig. 4.10 H), indicating minor sulfide remobilisation.

9.5 Genetic model

Stage 1

Dolomite played an important role in mineralisation at Lewis Ponds. Dolomitisation created secondary pore spaces and provided a reactive host, suitable for fluid-rock interactions and massive sulfide deposition beneath the sea floor. Dolomite probably formed by reactions between the hydrothermal fluid and carbonate-bearing host sediment at 50-250°C or by mixing between heated seawater-dominant pore fluids and the hydrothermal fluid at 350°C.

Diagenetic/hydrothermal dolomite may result from several processes. Regional dolomitisation involves low temperature fluid mixing at the site of sediment deposition and high temperature burial processes (Amthor and Friedman, 1991; Hitzman and Beaty, 1997). In modern sea floor exhalative deposits and ancient VHMS deposits, hydrothermal carbonate typically occurs at the margins of the hydrothermal system, where fluids mix with cooler seawater in the poorly consolidated host sediments (Khin Zaw and Large, 1992; Goodfellow et al., 1993; Herrmann and Hill, 2001).

Stage 2

Pyrite, pyrrhotite, sphalerite, galena, tetrahedrite and electrum precipitated in the Lewis Ponds host sequence from a relatively low temperature, 150-250°C reduced fluid (Fig. 9.5). Dendritic,

reticulate and spongy Fe-sulfide aggregates and microcrystals probably formed by rapid mixing between the hydrothermal fluid and cooler seawater-dominant pore fluids in the permeable, dolomite-altered breccia, sandstone and siltstone units. Base metal sulfide deposition may have resulted from fluid mixing, dissolution of dolomite and increased fluid pH. Networks of paragenetically early bladed crystals and microcrystals provided a substrate for the subsequent deposition of base metal sulfides. In situ reduction of sulfate minerals occurred during diagenesis or hydrothermal alteration of the sediment. Base metal sulfides, chlorite, dolomite, talc, quartz and calcite filled secondary pore spaces and partly replaced the carbonate-bearing polymictic breccia and pebbly-granular sandstone units in Main zone. The stage 2 hydrothermal fluid contained S leached from the footwall volcanic succession and a minor component of partially reduced seawater sulfate.

Stage 3

As the hydrothermal system intensified, a high temperature >280°C, strongly reduced fluid was sourced from deep within the footwall volcanic succession (Fig. 9.5). This may have coincided with a discrete magmatic event such as the emplacement of porphyritic dacite sills in the Toms zone footwall. Chalcopyrite, pyrite, Se-Bi-rich galena, sphalerite and native bismuth precipitated as stringer veins in the Toms zone footwall and Footwall Copper zone. Chalcopyrite and pyrrhotite locally overprinted pyrite, sphalerite and galena in the Main zone Central massive sulfide lens. Type 2 dolomite-chalcopyrite-pyrite veins were emplaced in the Toms Central massive sulfide lens. Stage 3 fluids probably introduced Sn into the massive sulfide lenses. The extensive Mg-chlorite halo surrounding type 1A stringer veins in the footwall volcanic succession (Figs. 5.3 and 9.5) may have resulted from high temperature fluid-rock interactions in a structurally controlled zone of focused up-flowing, Mg-bearing hydrothermal fluids.

Stage 4

Hydrothermal fluids were focused into transient, brittle fracture networks in the Lewis Ponds fault and surrounding areas, during and after the D_1 deformation. The S isotopes, metal ratios and overall metal grades within the Lewis Ponds fault zone indicate that sulfides were leached out of the massive sulfide lenses and mineralised host rocks (Fig. 9.5). Broad Cu, Au and Zn anomalies extending along the fault and surrounding the massive sulfide lenses (Fig. 7.18), probably resulted from metal remobilisation. Sulfide remobilisation potentially occurred over tens to hundreds of metres.

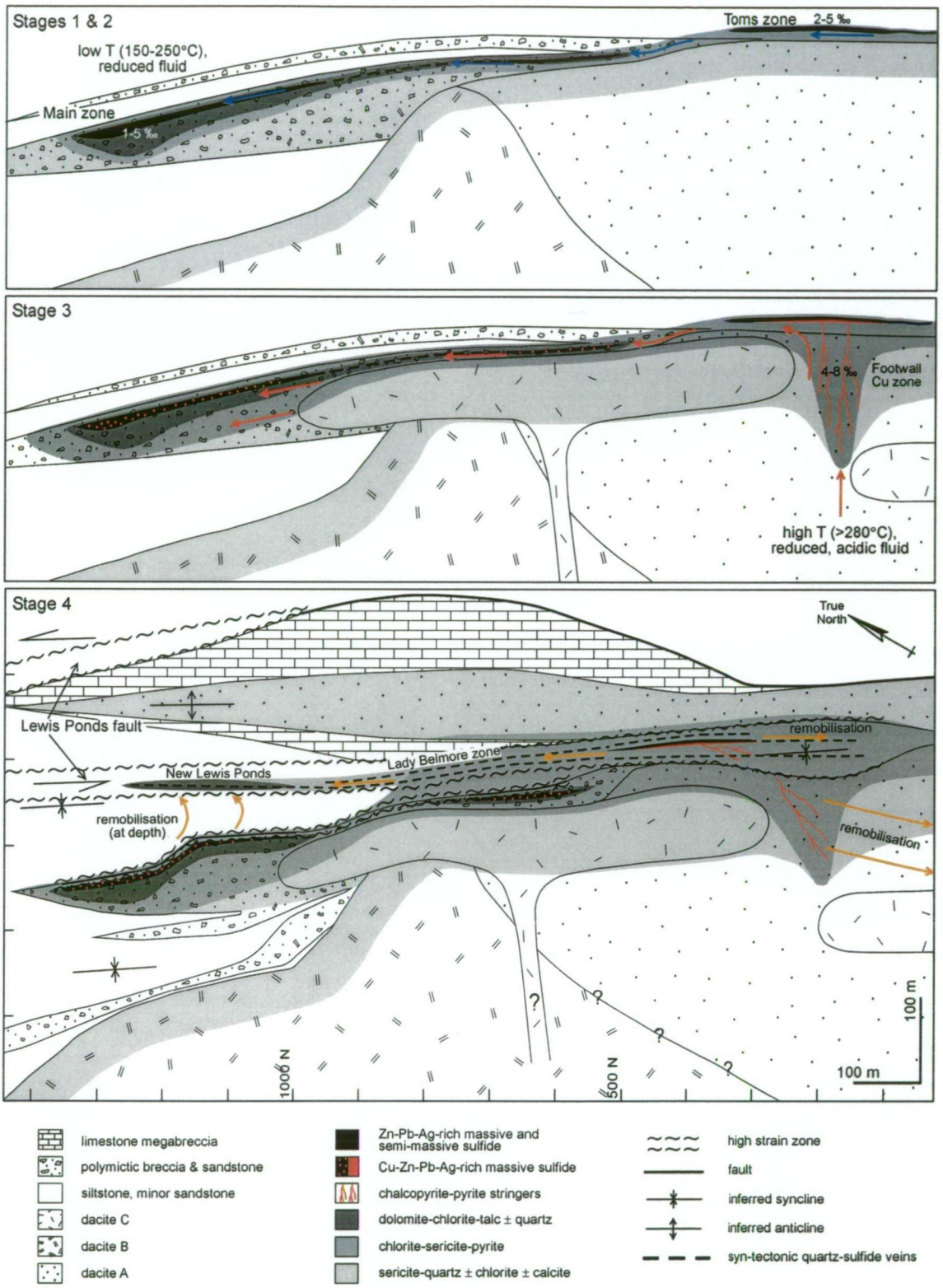

Figure 9.5 Genetic model for mineralisation and remobilisation of sulfides at Lewis Ponds. **Stages 1 and 2.** Dolomitisation of host sediment followed by deposition of Zn-Pb-Ag-Au-rich massive sulfide in the siltstone, sandstone and breccia matrix, from a low temperature (150-250°C), reduced fluid due to fluid mixing, dissolution of dolomite and increased fluid pH. **Stage 3.** Precipitation of Cu-Bi-Se-Ag-rich stringer veins in the Toms zone footwall from a deeply circulating, higher temperature (>280°C), reduced fluid. Cu- and Sn-rich sulfides were also deposited within the massive sulfide lenses. **Stage 4.** Deformation and remobilisation of massive sulfide along the Lewis Ponds fault by fracture-controlled fluids to form the New Lewis Ponds and Lady Belmore zones. Stringer veins in the Toms zone footwall were also remobilised into syn-tectonic quartz-sulfide veins. The final cartoon is based on the interpreted 600 m RL level plan, with a vertical exaggeration of 1.3:1.

Talc, quartz-sericite, Mg-chlorite and Fe-Mg-Mn-carbonate assemblages overprinted chlorite, dolomite and sericite-altered host rocks in the Lady Belmore and Toms zones. Chalcopyrite stringers in the Toms zone footwall were probably also remobilised into syn-tectonic quartz veins and local shear zones during the D_1 deformation (Fig. 9.5). This remobilisation resulted in an extensive area of chalcopyrite-bearing, syn-tectonic quartz veins and disseminated sulfides south of Toms mine.

9.6 Discussion

Sulfide mineralisation at Lewis Ponds may have coincided with Late Silurian felsic magmatism and volcanism in the area. The massive sulfide lenses probably formed within 300 m of a high-level intrusive dacite centre. Texturally destructive chlorite-pyrite and sericite-quartz ± chlorite assemblages overprinted rhyolitic and dacitic volcanics in the footwall of Toms zone due to reactions involving weakly acidic hydrothermal fluids. Heat produced from the cooling intrusions may have driven local, secondary hydrothermal convection to leach metals and S from the volcanic pile. Numerous small, stratabound massive sulfide deposits occur within or adjacent to the Mullions Range Volcanics, including Mt Bulga, Calula, Mt Shorter and Pride of the Hills (Figs. 2.5 and 2.6).

The unusual hybrid characteristics of Lewis Ponds are attributed to a unique combination of factors controlling the fluid source, fluid pathways and mineralisation at the trap site. Although recrystallised fossiliferous limestone occurs throughout the host sequence, Lewis Ponds did not form in a shallow water environment where boiling may have caused sub-sea floor deposition of metals. The Zn-Pb-Au-Ag and Cu-Se-Bi-Sn-Ag-rich metal associations indicate that the hydrothermal system evolved from low temperature to higher temperature, more reduced conditions. Toms zone probably formed at or near the seafloor, above a zone of focussed up-flowing fluids. In Main zone, a thick permeable unit of unconsolidated, poorly-sorted breccia, containing abundant limestone clasts and diagenetic/hydrothermal dolomite allowed lateral sub-sea floor circulation of hydrothermal fluids. Sulfide deposition resulted from increased pH and reactions between the hydrothermal fluid and carbonate-bearing host sediment.

Toms zone is similar to other eastern Australian, stratabound VHMS deposits, including Rosebery, Woodlawn, Currawong, Thalanga, Mount Chalmers and Mt Bulga (Table 9.3). Individual or stacked, sheet-like massive sulfide lenses occur in fine-grained epiclastic rocks above a footwall of coherent or clastic rhyolitic and dacitic facies. Basaltic to andesitic lava flows and/or dolerite sills overlie the rhyolite and dacite in the Currawang and Woodlawn deposits only (McKay and Hazeldene, 1987; Allen, 1992). The massive sulfide lenses are surrounded by broadly conformable, chlorite and sericite-quartz ± chlorite alteration haloes.

	Toms zone, LP	Rosebery	Woodlawn	Currawong	Thalanga	Mt Chalmers	Mt Bulga
Size	0.8 Mt	28.3 Mt	17.7 Mt	9.4 Mt	6.6 Mt	3.6 Mt	0.8 Mt
Host rock	Volcaniclastic siltstone	Volcaniclastic siltstone & sandstone	Mudstone, & volcaniclastic sandstone	Siltstone & sandstone	Barite, magnetite quartzite	Fossiliferous, volcaniclastic mudstone & sandstone	Siltstone & shale
Associated volcanic rocks	Dacite sills and massive dacite	Dacitic to rhyolitic pumice breccia & porphyry sills	Dolerite, rhyolitic volcanics & volcaniclastics	Rhyolitic to dacitic volcanics & shallow intrusives	Rhyolitic lava flows and domes	Dacite, pumice breccia & ignimbrite	Dacite & rhyolite sills
Proximal alteration assemblages	Dol-chl-tlc qtz-ser-hly chl-py	Fe-Mn carb-ser ± chl chl ± ser ± carb-py qtz-ser-py	Chl-tlc-carb	Qtz-chl chl-py	Chl-trm-carb	Chl-ser-py ± carb qtz-chl-ser-py dol-ca-chl-ser-py	Qtz-chl-ser
Distal alteration assemblages	Ser-qtz ± chl	Ser-qtz ± chl-py	Ser-qtz ± chl	Ser-qtz ± chl	Ser-qtz ± chl	Ser-qtz ± chl	Ser ± chl
Overall deposit form	1 sheet-like MS lens	Stacked sheet-like MS lenses	1 sheet-like MS lens	2 sheet-like MS lenses	1 sheet-like MS lens	1 sheet-like MS lens	1 sheet-like MS lens
Footwall stockwork	Ccp-py-sph-ga-Bi stringers	Dissem ccp-py	Py-ccp-chl veins	Sph-ccp-py-po ccp-py-chl Bi-electrum	Dissem py & py stringers	Ccp-py-qtz-chl stringers	Ccp-po-py-qtz
Primitive sulfide textures	Bladed & botryoidal	Framboids & colloform py	Framboids & colloform py	Framboids & colloform py	Framboids & colloform py	Framboids & colloform py	Colloform py

Table 9.3 Characteristics of selected eastern Australian, stratabound VHMS deposits including Toms zone at Lewis Ponds. Based on the following references: Cambrell and Kirk (1974), Chisholm (1976), McKay and Hazeldene (1987), McKay (1989), Allen and Barr (1990), Davis (1990), Gregory et al. (1990), Large et al. (1992), Sainty (1992), Boden and Valenta (1995), Berry et al. (1998), Herrmann and Hill (2001), Large et al. (2001c). Abbreviations: dol = dolomite, chl = chlorite, tlc = talc, hly = hyalophane, qtz = quartz, carb = carbonate, ser = sericite, trm = tremolite, ca = calcite, ccp = chalcopyrite, py = pyrite , sph = sphalerite, ga = galena, Bi = native bismuth, MS = massive sulfide.

Extensive carbonate-chlorite envelopes occur at Thalanga, Rosebery and Woodlawn. The deposits have a footwall stockwork zone of pyrite and chalcopyrite stringers and disseminated sulfides (Table 9.3). However, these zones are commonly displaced from the massive sulfide lenses during deformation.

Despite tight folding and faulting of the host sequence, primitive sulfide textures are preserved throughout Main zone and rarely in Toms zone (Table 9.3). Framboidal and colloform pyrite textures also occur in Rosebery (Martin, 2002), Woodlawn (McKay, 1989), Currawong (Bodon and Valenta, 1995), Mt Chalmers (Large, 1992) and Mt Bulga (Chisholm, 1976).

Main zone has some features in common with the carbonate-hosted, Mississippi Valley Type and Irish-style, stratabound Zn-Pb deposits (Table 9.4). Low temperature dolomitisation of limestone or carbonate-rich sediment creates secondary porosity. During mineralisation, massive sulfide and hydrothermal dolomite fill dissolution cavities and collapse breccias in the host rock (Misra et al., 1997; Peace et al, 2003). Metal deposition results from increased pH, dilution or cooling of the hydrothermal fluid (Hitzman et al., 2002). Massive limestone facies host the Irish-style and Mississippi Valley Type deposits, whereas Main zone occurs in carbonate-bearing volcaniclastic deposits overlying a submarine intrusive dacite centre. The Mg-Fe-rich alteration assemblages and Zn-Pb-Cu-Ag-Au metal association at Main zone are more characteristic of VHMS deposits.

	Main zone, Lewis Ponds	MVT deposits	Irish-style deposits
Commodities	Zn, Pb, Cu, Ag, Au	Zn, Pb	Zn, Pb
Host rock	Polymictic breccia, limestone-clast breccia, pebbly-granular sandstone	Dolomitised limestone, limestone, mudstone	Dolomitised limestone, limestone, mudstone
Dolomite types	Diagenetic dolomite, hydrothermal dolomite	Regional dolomite, dissolution-collapse breccia, hydrothermal dolomite	Regional dolomite, hrdothermal dolomite breccia
Accessory minerals	Pyrrhotite, Mg-chlorite, dolomite, quartz, talc, phlogopite	Dolomite, calcite, barite, fluorite, quartz, bitumen	Dolomite, calcite, barite, quartz
Overall deposit form	Stratabound MS lenses, disseminated sulfides	MS, open-space fillings, disseminated sulfides in collapse breccia matrix	Stratabound MS lenses, disseminated sulfides, veinlet-controlled sulfides
Sulfide textures	MS, vuggy textures, bladed, botryoidal & framboidal aggregates	MS, vuggy textures, breccia fill	MS, Colloform textures, vuggy textures, breccia fill
Inferred fluid conditions	T = 150- >280°C low salinity ??	T = 100-200°C highly saline	T = 150-240°C highly saline
Interpretation	Stratatigraphic replacement	Stratatigraphic replacement	Structurally-controlled, stratatigraphic replacement

Table 9.4 General characteristics of MVT and Irish-style, carbonate-hosted replacement deposits compared with Main zone, Lewis Ponds. Based on the following references: Tomkins et al. (1994), Hutchinson (1997), Kesler (1997), Misra et al. (1997), Hitzman and Beaty (1997), Hiztman et al. (2002), Peace et al. (2003). MS = massive sulfide.

Carbonate-bearing mixed provenance volcaniclastic breccia, pebbly-granular sandstone and limestone-clast breccia units host the massive sulfide in Main zone. There are few examples in the literature of sea floor/sub-sea floor hydrothermal systems developed within clastic fossiliferous limestone facies. Corbett (2001) noted thin crustiform, pyrite-galena-sphalerite bands in an altered limestone body at Comstock, Mt Lyell mining district, western Tasmania. Although many limestone lenses in the Lower Tyndall Complex contain trilobites, crinoids, gastropods, brachiopods and trace fossils (Jago et al., 1972, Corbett, 2001), Corbett (2001) attributed most of the vein-carbonate and breccia-fill carbonate to exhalative activity. Limestone or marble lenses also occur at the Wisemans Creek and Cow Flat deposits, Hill End Trough, New South Wales (Stanton, 1955), the Currawong deposit in Benambra, Victoria (Allen, 1992) and numerous deposits in the Bergslagen district of Sweden (Vivallo, 1985; Allen et al., 1996a). However, these limestone lenses are not spatially associated with massive sulfide.

CHAPTER 10

CONCLUSIONS

10.1 Conclusions

The Lewis Ponds host sequence consists of Late Silurian marine sedimentary rocks, deposited from subaqueous mass flows in a moderately deep, below wave-base slope environment. The volcaniclastic breccia, limestone-clast breccia, mixed provenance breccia and quartz crystal-rich sandstone beds have a mixed volcanic and sedimentary provenance, indicating post-eruptive re-working of the sediment prior to deposition. Clasts and crystal fragments were derived from numerous sources within the basin and in the adjacent hinterland.

Recrystallised, fossiliferous limestone occurs as allochthonous clasts in the breccia and sandstone units and as megaclasts in the fault-bound stratigraphic unit (within the Lewis Ponds fault). Where primary textures are preserved, the limestone contains crinoid fragments, brachiopods, bivalves, solitary corals and rare conodonts in an equigranular mosaic of calcite. The clean, coarse-grained limestone was sourced from a Late Silurian, bioclastic deposit (reef or bioherm) located within the basin or at the basin margin.

The footwall volcanic succession consists of three texturally distinct lithofacies associations, with different immobile element compositions. Lithofacies association A (Ti/Zr≅22) lacks internal structure and may represent a series of dacitic lava flows or intrusions. Hydrothermal alteration and cleavage development have obscured primary textures in the dacite. Lithofacies association B (Ti/Zr≅14) occurs as a syn-sedimentary porphyritic dacite cryptodome with associated peperite in the Main zone footwall. Texturally immature quartz porphyry clasts with similar geochemical affinities to dacite B occur in the overlying polymictic breccia units. Lithofacies association C (Ti/Zr≅11) is a porphyritic dacite sill that intruded the quartz-plagioclase phyric dacite and polymictic breccia units.

The Mullions Range Volcanics is a predominantly submarine succession of coherent rhyolite and dacite, volcaniclastic breccia, crystal-rich sandstone, siltstone and minor limestone. The Lewis Ponds and Mullions Range Anticline areas consist of siltstone, volcaniclastic breccia and quartz-feldspar crystal-rich sandstone. These facies were deposited in moderately deep water environments around the margins of intrusive and/or extrusive volcanic centres comprising

massive and flow-banded coarsely porphyritic dacite. In contrast, the western lobe and Cullya Road areas are dominated by the products of shallow, submarine to subaerial, effusive to locally explosive rhyolitic to dacitic volcanoes and lava domes.

The massive sulfide lenses at Lewis Ponds occur along the eastern limb of a regional-scale D_1 anticline, trending 41-331. The adjacent syncline has been partly truncated by a shear zone termed the *Lewis Ponds fault*. First generation folds are associated with a strongly developed, NNW-trending axial-planar cleavage and steeply plunging stretching lineation. Kink bands and kink folds locally overprint the S_1 cleavage. The calculated best-fit orientations of structural fabrics observed in drill core (bedding, cleavage, stretching lineations, kink bands and quartz veins) are similar to those measured on outcrops.

Reversals in stratigraphic facing directions and vergence indicate that tight parasitic folds and overturned beds occur throughout the host sequence. Pebbly-granular, quartz crystal-rich sandstone beds define a tight, overturned syncline in the Main zone footwall. A syncline also occurs in the Hangingwall Siltstone Unit, south of Toms zone. Folds and faults may have caused structural repetition of the massive sulfide lenses.

The Lewis Ponds fault is a 200-250 m wide, NNW-trending zone of steeply dipping, anastomosing brittle and ductile shears, kink folds and syn-tectonic quartz veins. Its complex anastomosing geometry reflects the presence of competent lithologies such as coherent dacite and massive limestone, surrounded by less competent siltstone. The fault probably resulted from east-block-up movement with a minor sinistral component. Shearing took place during the D_1 deformation. The associated kink folds and opposing shear sense indicators may have resulted from late reactivation or roll-back of the fault. The Lewis Ponds fault surrounds Toms zone and truncates Main zone at depth.

Four generations of veins were differentiated in the Lewis Ponds host sequence. Tightly folded, pre-tectonic carbonate-chalcopyrite-pyrite and quartz-pyrite stringer veins occur in the Western Volcanic Succession, south of Toms zone. Variably deformed, sub-vertical and sub-horizontal quartz ± sulfide veins, within and adjacent to the Lewis Ponds fault resulted from brittle shear failure and extension, during and after cleavage development. The sub-horizontal veins indicate fault-valve-behaviour associated with local areas of high fluid pressure. Post-tectonic quartz ± sulfide veins cut across non-foliated quartz-plagioclase porphyry dykes in the Toms zone footwall. Many syn-tectonic veins contain sphalerite, galena, chalcopyrite and pyrite or pyrrhotite.

The asymmetric, semiconformable hydrothermal alteration envelope surrounding the massive sulfide lenses is strongly developed in the footwall volcanic succession, south of Main zone. Mg-chlorite occurring at the top the footwall volcanic succession grades outwards into a weak pervasive sericite-quartz ± Mg-Fe-chlorite assemblage. The compositions of recrystallised phyllosilicates in the Toms zone footwall vary systematically with whole rock geochemistry, alteration intensity and proximity to the massive sulfide lens, indicating that hydrothermal alteration of the volcanics occurred prior to recrystallisation and cleavage development.

Conformable, texturally destructive alteration assemblages associated with the mineralised zones and sedimentary host rocks include dolomite-chlorite-talc, chlorite-pyrite, quartz-dolomite-chlorite and quartz-sericite ± hyalophane. The dolomite assemblage resulted from low temperature alteration of the siltstone, sandstone and breccia facies during diagenesis and hydrothermal activity. In Main zone, hydrothermal alteration and subsequent metamorphism involved partial to complete replacement of the clasts and polymictic breccia matrix by dolomite, ferroan-dolomite, Mg-chlorite, talc, phlogopite, calcite, quartz and sulfides. High temperature fluid-rock interactions produced the chlorite and quartz-rich assemblages.

The asymmetric, conformable alteration halo surrounding Main zone is characterised by:

- high Alteration Index, Chlorite-Carbonate-Pyrite Index, Ba/Sr and S/Na_2O values; and
- generally high MgO, CaO, Fe_2O_3, Ba, Sr, S, As, Ni, Cu, Pb, Zn and Tl concentrations.

Lower average Alteration Index and Ba/Sr values in the polymictic breccia indicate the presence of dolomite and calcite. Lithogeochemical trends associated with Main zone reflect chlorite-dolomite-talc alteration of the limestone-bearing breccia and sandstone deposits and the introduction of sulfides. Mass changes in the porphyritic dacite clasts and weakly altered, footwall dacite involved minor additions of MgO, Fe_2O_3, CaO and K_2O and removal of SiO_2 and Na_2O, resulting in net mass losses of 0-60 g/100g.

Chlorite-sericite-altered sedimentary rocks hosting the Toms zone massive sulfide lens are characterised by:

- high Alteration Index, Chlorite-Carbonate-Pyrite Index, Ba/Sr and S/Na_2O values; and
- high MgO, CaO, Fe_2O_3, Ba, S, As, and Zn concentrations.

Hydrothermal alteration of the footwall and hangingwall volcanics resulted in MgO, Fe_2O_3, K_2O and Ba enrichment and Na_2O, CaO and Sr depletion. The addition of SiO_2 to dacite C contributed to overall net gains of 0-75 g/100g. The removal of SiO_2 from dacite A led to net losses of 0-50 g/100g except in the Footwall Copper zone, where MgO and Fe_2O_3 enrichment offset the loss of SiO_2. Lithogeochemical trends associated with Toms zone reflect feldspar destructive chlorite-sericite alteration of the footwall and hangingwall volcanics and chlorite-dolomite-talc alteration of the sedimentary rocks.

Metamorphic minerals in the host sequence include phlogopite, sphene, epidote, hornblende, biotite ± talc and cordierite. Phlogopite and sphene occur within the chlorite alteration envelope. Biotite is found throughout the Western Volcanic Succession and Hangingwall Siltstone Unit, south of Toms zone. Epidote and hornblende occur in rocks with high Ca concentrations. Phlogopite was stabilised at lower temperatures due to high Mg and F concentrations in the fluids or host rock. Biotite crystals are relatively coarse-grained and randomly oriented, indicating that peak metamorphic conditions occurred after cleavage development. Some of the biotite may have resulted from thermal metamorphism associated with emplacement of the Lewis Ponds granite and quartz-plagioclase porphyry dykes.

Main zone consists of three stratabound massive to semi-massive sulfide lenses, in a broad envelope of disseminated sulfides. These are hosted in mixed provenance breccia, limestone-clast breccia and pebbly-granular sandstone. A smaller, fault-bound and possibly stratabound massive sulfide lens occurs in Toms zone, in the overlying siltstone. Disseminated sulfides and cleavage-parallel, syn-tectonic quartz-sulfide veins occur along the Lewis Ponds fault in Toms zone, Lady Belmore zone and New Lewis Ponds, and throughout the footwall volcanic succession.

The massive sulfide lenses consist of pyrite, sphalerite and galena, with subordinate tetrahedrite, tennantite chalcopyrite, arsenopyrite, pyrrhotite, stannite, electrum and pyrargyrite. Native bismuth and Se-Ag-Bi-rich galena occur only in the chalcopyrite stringer veins in the Toms zone footwall. Primitive sulfide textures occur throughout Main zone and rarely in Toms zone. These include dispersed pyrite microcrsytals, bladed orthorhombic pyrrhotite crystals after sulfate and spongy, botryoidal, framboidal, dendritic and reticulate aggregates of pyrite and pyrrhotite. The massive sulfide is characterised by annealed, recrystallised textures. Brittle fractures, syn-tectonic quartz veins, cataclastic breccia, boudins, pinch-and-swell structures and kink folds occurring throughout Toms zone resulted from deformation and shearing along the Lewis Ponds fault. Brittle sulfide textures and quartz veins are less common in Main zone.

The whole rock geochemistry and trace element composition of sulfides varies between the mineralised zones. Average Se, Ag, Bi and Fe concentrations in galena and Cd concentrations in sphalerite are significantly higher in the Footwall Copper zone than either massive sulfide zone. Sphalerite grains in Toms zone have higher average Mn concentrations than those in Main zone. Frabmboidal and spongy pyrite aggregates in Main zone contain more As and Mn than recrystallised pyrite in Toms zone. Extensive annealing of the massive sulfide in Toms zone accounts for the lower average As, Ag and Fe concentrations in pyrite, chalcopyrite and galena. Variations in whole rock geochemistry reflect the greater modal abundance of base metal sulfides in the Toms Central lens.

Main zone has highly erratic metal grades. The highest Au ± Zn, Ag, Sb and Hg grades occur toward the top of the Central lens and throughout the Hangingwall lens. In contrast, metal grades vary from the structural footwall to the hangingwall of Toms zone. Copper ± Ag, Sb, Sn and Mo are enriched in the lowest one to two metres of the Central massive sulfide lens. High Cu grades also extend into the immediate footwall.

Dolomite associated with the massive sulfide lenses and dolomite veins in Toms zone are characterised by low $\delta^{18}O$ and $\delta^{13}C$ values relative to the regional limestone. Decarbonation reactions or the involvement of organic C could account for the low $\delta^{13}C$ values in hydrothermal carbonate from Main zone. The lighter, more variable O isotopic signature of dolomite in Toms zone may reflect precipitation from a higher temperature fluid or isotopic re-equilibration due to circulation of younger fracture-controlled fluids along the Lewis Ponds fault zone. Fluid inclusion and stable isotope data indicate that the dolomite precipitated from a low temperature (166-232°C for 1000 m water depth), weakly saline (1.4 to 7.7 eqiv wt % NaCl) fluid that was possibly depleted in O and C isotopes ($\delta^{18}O$ = -2.5 to 0.3‰, $\delta^{13}C$ = -14 to -4‰). The dolomite probably precipitated during diagenesis or hydrothermal alteration by ractions between evolved seawater and the limestone-bearing host sediment at 150-250°C, and/or fluid mixing between evolved seawater at 350°C and a seawater-dominant pore fluid at 100°C.

Sulfur isotope values in the massive sulfide ($\delta^{34}S$ = 1.7-5.0‰) and footwall stringer veins ($\delta^{34}S$ = 3.9-7.4‰), indicate that the hydrothermal fluid probably contained a homogenous mixture of magmatic S and reduced seawater sulfate. Lower average $\delta^{34}S$ values in the massive sulfide lenses may indicate that the fluid acquired a component of lighter S from the host sedimentary rocks either by partial reduction of seawater sulfate or incorporation of biogenic S, derived from the host sediments.

The massive sulfide lenses have a small range of metal ratios with standard deviations of less than 11. Average Zn ratios vary from 60 to 68 and average Cu ratios range from 4 to 9. Areas dominated by syn-tectonic quartz-sulfide veins including New Lewis Ponds, Lady Belmore and the Toms zone hangingwall have more variable Zn and Cu ratios. In these areas, average Zn ratios vary from 57 to 75, with standard deviations of 13 to 24.

Lewis Ponds is a strongly deformed, stratabound carbonate and volcanic-hosted massive sulfide deposit. Main zone formed by lateral fluid flow and sub-sea floor replacement of the poorly-sorted, carbonate-bearing breccia and sandstone beds. Low temperature, 50-250°C dolomitisation of the sediments created secondary pore spaces and a reactive host rock for sub-

sea floor fluid-rock interactions. Sulfides, chlorite, dolomite, calcite, quartz and talc filled pore spaces throughout the carbonate-altered breccia and sandstone matrix. In contrast, the Toms Central massive sulfide lens probably formed in fine-grained sediment at or near the sea floor, above a zone of focused up-flowing hydrothermal fluids.

Dendritic, reticulate and spongy Fe-sulfide aggregates resulted from rapid mixing between the mineralising fluid and cooler pore fluids (eg. seawater) in the matrix of the poorly-sorted breccia, sandstone and siltstone. Bladed sulfate crystals were pseudomorphed by pyrrhotite and rarely quartz in the Main zone host rocks. The bladed pyrrhotite crystals probably formed by in situ sulfate reduction prior to or during mineralisation.

The Zn-Pb-Ag-Au-rich massive sulfide precipitated from a low temperature 150-280°C, reduced fluid due to a combination of fluid mixing, fluid-rock interactions with the carbonate (limestone clasts and hydrothermal dolomite) and increased fluid pH. As the hydrothermal system intensified, a high temperature >280°C, reduced fluid sourced from deep in the footwall volcanic succession brought Cu, Se, Bi, Sn, Ag, Zn and Pb into the Footwall Copper zone and massive sulfide lenses. These higher temperature fluids may have coincided with a discrete magmatic event such as the emplacement of dacite sills in the Toms zone footwall.

Fracture-controlled fluids of unknown origin remobilised sulfides into syn-tectonic quartz and carbonate veins within the Lewis Ponds fault zone and footwall volcanic succession, during and after the D_1 deformation. Remobilisation may have occurred over tens to hundreds of metres. Talc, quartz-sericite, chlorite and Fe-Mg-Mn-carbonate assemblages overprinted dolomite, chlorite and sericite-altered rocks in the Toms zone host sequence. Brittle and ductile structures developed throughout Toms zone and Main zone a lesser extent.

At Lewis Ponds, base metal sulfides are intimately associated with fossiliferous limestone clasts and hydrothermal carbonate. This observed spatial association provides a basis for new exploration targets in New South Wales as many small massive sulfide deposits occur in marine successions containing fossiliferous limestone lenses and felsic volcanic rocks. The occurrence of fossiliferous limestone does not necessarily indicate a shallow water environment of deposition because mass flows readily transport limestone debris, including large megaclasts from carbonate platforms to deeper parts of the basin.

10.2 Recommendations for further research

The Mullions Range Volcanics is a prospective host unit for stratabound massive sulfide deposits such as Lewis Ponds. The volcanic and sedimentary facies architecture of the Calula-

Coalmans-Kerrs Creek area is complex and highly variable. Detailed mapping of this area is required to determine the facies geometry and contact relationships. This would help to constrain the local palaeogeography and volcanic-sedimentary setting of massive sulfide deposits occurring in the area.

This study demonstrated that tight isoclinal folds occur in the Lewis Ponds host sequence. Folds and faults may have caused structural repetition within the massive sulfide lenses. The core from thirty drill holes did not provide sufficient data to fully characterise the fold geometries and stratigraphic contacts in the host sequence. Further re-interpretation of available drill core is recommended to obtain more bedding orientations, stratigraphic facing and vergence directions from around the massive sulfide lenses. The drill core re-orientation program of Scott and Berry, University of Tasmania produced reliable best-fit estimations of structural fabric orientations in drill core, assuming that S_1 = 79-061.

A preliminary study using the electron microprobe indicated that trace element compositions in sulfides vary between the mineralised zones at Lewis Ponds. Variations in Bi, Se, Mn and Ag were interpreted to reflect the temperature and chemistry of the mineralising fluid. However, many trace elements were below detection limits of the microprobe (especially Au, Co and Ni). A detailed study using laser ablation ICP-MS is recommended to characterise vertical and lateral zonation in the trace element composition of sulfides. This would provide more information about the physio-chemical conditions of sulfide deposition and the effects of thermal annealing during metamorphism.

Mineralisation at Lewis Ponds may have broadly coincided with the emplacement of high-level porphyritic dacite intrusions in the footwall volcanic succession. However, the absolute age of the intrusions and massive sulfide remains speculative. Ar-Ar and Re-Os dating may constrain the timing of magmatism and mineralisation respectively.

Determining the composition of fault- and fracture-controlled fluids was not a primary aim of this project. The ultimate source of the fluid remains unknown. However, it may be similar to Pb-Zn mineralising fluids in the Cobar Basin. Lawrie and Hinman (1998) suggested that the Cobar deposits originated from a high temperature (>250°C), low salinity, oxidised basement (magmatic or metamorphic) fluid and a more saline, reduced, hydrocarbon-bearing basinal fluid derived from thermal maturation of the sediments. Analysis of Pb isotopes and fluid inclusions in disseminated and vein-hosted sulfides within the Lewis Ponds fault may constrain the source of metals and chemistry of the metamorphic/magmatic fluid that was responsible for sulfide remobilisation during the D_1 deformation.

References

Abercrombie, H. J., Skippen, G. B., and Marshall, D. D., 1987, Fe-OH substitution in natural tremolite, talc, and phlogopite: Contributions to Mineralogy and Petrology, v. 97, p. 305-312.

Agnew, M. W., 1998, Geology of the Dooloo Creek area, Monto district, central Queensland: Unpub. Honours thesis, University of Queensland, 96 p.

Allen, R. L., and Barr, D. J., 1990, Benambra Copper-zinc deposits, in Hughes, F. E., ed., Geology of the mineral deposits of Australia and Papua New Guinea, 2. Monograph 14: Melbourne, The Australasian Institute of Mining and Metallurgy, p. 1311-1318.

Allen, R. L., 1992, Reconstruction of the tectonic, volcanic, and sedimentary setting of strongly deformed Zn-Cu massive sulphide deposits at Benambra, Victoria: Economic Geology, v. 87, p. 825-854.

Allen, R. L., Lundstrom, I., Ripa, M., Christofferson, H., Stephens, M. B., Halenius, U., and Widenfalk, L., 1996a, Facies analysis of a 1.9 Ga, continental margin, back-arc, felsic caldera province with diverse Zn-Pb-Ag-(Cu-Au) sulfide and Fe oxide deposits, Bergslagen region, Sweden: Economic Geology, v. 91, p. 979-1008.

Allen, R. L., Weihed, P., and Svenson, S.-A., 1996b, Setting of Zn-Cu-Au-Ag massive sulfide deposits in the evolution and facies architecture of a 1.9 Ga marine volcanic arc, Skellefte District, Sweden: Economic Geology, v. 91, p. 1022-1053.

Allen, R. L., 1988, False pyroclastic textures in altered silicic lavas, with implications for volcanic-associated mineralization: Economic Geology, v. 83, p. 1424-1446.

Amthor, J. E., and Friedman, G. M., 1991, Dolomite-rock textures and secondary porosity development in Ellenburger Group carbonates (Lower Ordovician), West Texas and southeastern New Mexico: Sedimentology, v. 38, p. 343-362.

Antony, J. P., 1999, Ore group classification; a case study from Ingaldhal sulphide deposit, Karnataka Craton, India, in Dissanayake, C. B., ed., Mineralization in Gondwana, 2. Gondwana Research - International Geoscience Journal: Osaka, Japan, International Association for Gondwana Research, p. 67-77.

Ayres, D. E., Burns, M. S., and Smith, J. W., 1979, Sulphur-isotope study of the massive sulphide orebody at Woodlawn, New South Wales: Journal of the Geological Society of Australia, v. 26, p. 197-201.

Bailey, S. W., 1984, Classification and structures of the micas. Crystal chemistry of the true micas: Reviews in Mineralogy, v. 13, p. 1-60.

Barrett, T. J., and MacLean, W. H., 1994, Chemostratigraphy and hydrothermal alteration in exploration for VHMS deposits in greenstones and younger volcanic rocks, in Lentz, D. R., ed., Alteration and alteration processes associated with ore forming systems, 2. short course notes: Waterloo, Ontario, Geological Association of Canada, p. 433-467.

Barrett, T. J., Thompson, J. F. H., and Sherlock, R. L., 1996, Stratigraphic, lithogeochemical and tectonic setting of the Kutcho Creek massive sulfide deposit, northern British Columbia, in Juras Stephen, J., and Spooner Edward, T. C., eds., Exploration and mining geology; volcanogenic massive sulfide deposits of the British Columbia Cordillera., 5; 4. Exploration and Mining Geology: New York - Oxford, International, Pergamon Press [for the] Geological Society of the Canadian Institute of Mining, Metallurgy and Petroleum, p. 309-338.

Barron, L. M., 1998, Metamorphism, in Stewart, J. R., ed., Bathurst 1: 250 000 Geological Sheet, explanatory notes: Sydney, Geological Survey of New South Wales, p. 284-286.

Barton, P. B., Jr., 1978, Some ore textures involving sphalerite from the Furutobe mine, Akita Prefecture, Japan, Papers devoted to the Japan-U.S. Kuroko research project, 28. Kozan Chishitsu = Mining Geology: Tokyo, Japan, Society of Resource Geologists of Japan, p. 293-300.

Belkin, H. E., Cavarretta, G., De, V. B., and Tecce, F., 1988, Hydrothermal phlogopite and anhydrite from the SH2 well, Sabatini volcanic district, Latium, Italy; fluid inclusions and mineral chemistry: American Mineralogist, v. 73, p. 775-797.

Berry, M. V., Edwards, P. W., Georgi, H. T., Graves, C. C., Carnie, C. W. A., Fare, R. J., Hale, C. T., Helm, S. W., Hobby, D. J., and Willis, R. D., 1998, Rosebery lead-zinc-gold-silver-copper deposit, Geology of Australian and Papua New Guinean Deposits. Monograph 22: Melbourne, The Australasian Institute of Mining and Metallurgy, p. 481-486.

Bethke, P. M., and Barton, P. B. J., 1971, Distribution of some minor elements between coexisitng sulfide minerals: Economic Geology, v. 66, p. 140-163.

Bodon, S. B., and Valenta, R. K., 1995, Primary and tectonic features of the Currawong Zn-Cu-Pb(-Au) massive sulfide deposit, Benambra, Victoria: implications for ore genesis: Economic Geology, v. 90, p. 1694-1721.

Botros, N. S., 2003, On the relationship between auriferous talc deposits hosted in volcanic rocks and massive sulphide deposits in Egypt: Ore Geology Reviews, v. 23, p. 223-257.

Brauhart, C. W., Huston, D. L., Groves, D. I., Mikucki, E., J, and Gardoll, S. J., 2001, Geochemical mass transfer patterns as indicators of the architecture of a complete volcanic-hosted massive sulfide hydrothermal alteration system, Panorama district, Pilbara, Western Australia: Economic Geology, v. 96, p. 1263-1278.

Bryan, S. E., Holcombe, R. J., and Fielding, C. R., 2001, Yarrol terrane of the northern New England Fold Belt: forearc or backarc?: Australian Journal of Earth Sciences, v. 48, p. 293-316.

Bryndzia, L. T., Scott, S. D., and Farr, J. E., 1983, Mineralogy, geochemistry, and mineral chemistry of siliceous ore and altered footwall rocks in the Uwamuki 2 and 4 deposits, Kosaka mine, Hokuroku district, Japan: Economic Geology Monograph, v. 5, p. 507-522.

Burns, S. J., 1998, Carbon isotopic evidence for coupled sulfate reduction-methane oxidation in Amazon Fan sediments: Geochimica et Cosmochimica Acta, v. 62, p. 797-804.

Busby-Spera, C. J., and White, J. D. L., 1987, Variation in peperite textures associated with differing host-sediment properties: Bulletin of Volcanology, v. 49, p. 765-775.

Butler, I. B., and Rickard, D., 2000, Framboidal pyrite formation via the oxidation of iron (II) monosulfide by hydrogen sulphide: Geochimica et Cosmochimica Acta, v. 64, p. 2665-2672.

Byrnes, J. G., 1976, Silurian environments of the northern Molong Rise: Bulletin of Australian Exploration Geophysicists, v. 7, p. 18-21.

Callaghan, T., 1998, Geology and alteration of the Mt Julia deposit, Henty goldmine, Tasmania: Unpub. Master of Economic Geology thesis, University of Tasmania, 78 p.

Callaghan, T., 2001, Geology and host-rock alteration of the Henty and Mount Julia gold deposits, western Tasmania: Economic Geology, v. 96, p. 1073-1088.

Cantrill, R., 1991, A study of the conodont assemblages from the limestones at Molong, Mirrabooka and Bunyarra, central western N.S.W., Australia: Unpub. Master of Science thesis, Macquarie University, N.S.W., 41 p.

Carman, G. D., 1994, Genesis of the Ladolam gold deposit, Lihir island, Papua New Guinea: Unpub. Ph.D. thesis, Monash University.

Carne, J. E., 1899, The copper-mining industry and the distribution of copper ores in New South Wales: Sydney, William Applegate Gullick, Government Printer, 425 p.

Carne, J. E., 1908, The copper-mining industry and the distribution of copper ores in New South Wales: Sydney, William Applegate Gullick, Government Printer, 425 p.

Carne, J. E., and Jones, L. J., 1919, The limestone deposits of New South Wales: Sydney, William Applegate Gullick, Government Printer, 411 p.

Carr, G. R., Dean, J. A., Suppel, D. W., and Heithersay, P. S., 1995, Precise lead isotope fingerprinting of hydrothermal activity associated with Ordovician to Carboniferous metallogenic events in the Lachlan Fold Belt of New South Wales: Economic Geology, v. 90, p. 1467-1505.

Cas, R. A. F., 1983, Palaeogeographic and tectonic development of the Lachlan Fold Belt, southeastern Australia, Geological Society of Australia Special Publication, 104 p.

Cas, R. A. F., 1992, Submarine volcanism: eruption styles, products, and relevance to understanding the host-rock successions to volcanic-hosted massive sulfide deposits: Economic Geology, v. 87, p. 511-541.

Cas, R. A. F., Allen, R. L., Bull, S. W., Clifford, B. A., and Wright, J. V., 1990, Subaqueous, rhyolitic dome-top tuff cones: a model based on the Devonian Bunga Beds, southeastern Australia and a modern analogue: Bulletin of Volcanology, v. 52, p. 159-174.

Chappell, B. W., White, A. J. R., and Hine, R., 1988, Granite provinces and basement terranes in the Lachlan Fold Belt, southeastern Australia: Australian Journal of Earth Sciences, v. 35, p. 505-521.

Chisholm, J. M., 1976, Geochemical zoning in a volcanogenic Cu-Pb-Zn-Ag sulphide deposit at Mt Bulga, N.S.W., Australia: Unpub. Ph.D. thesis, University of New South Wales.

Claypool, G. E., Holser, W. T., Kaplan, I. R., Sakai, H., and Zak, I., 1980, The age curves of sulfur and oxygen isotopes in marine sulfate and their mutual interpretation: Chemical Geology, v. 28, p. 199-260.

Collins, W. J., 1998, Evaluation of petrogenetic models for Lachlan fold belt granitoids; implications for crustal architecture and tectonic models: Australian Journal of Earth Sciences, v. 45, p. 483-500.

Collins, W. J., and Hobbs, B. E., 2001, What caused the Early Silurian change from mafic to silicic (S-type) magmatism in the eastern Lachlan Fold Belt?: Australian Journal of Earth Sciences, v. 48, p. 25-41.

Collins, W. J., and Vernon, R. H., 1992, Palaeozoic arc growth, deformation and migration across the Lachlan Fold Belt, southeastern Australia: Tectonophysics, v. 214, p. 381-400.

Colquhoun, G. P., Meakin, N. S., Morgan, E. J., Raymond, O. L., Scott, M. M., Watkins, J. J., Barron, L. M., Cameron, R. G., Henderson, G. A. M., Jagodzinski, E. A., Krynen, J. P., Pogson, D. J., Warren, A. Y. E., Wyborn, D., and Yoo, E. K., 1997, Dubbo 1:250 000 geological sheet SI55-4, preliminary second edition, Geological Survey of New South Wales, Sydney and Australian Geological Survey Organisation, Canberra.

Conaghan, P. J., Mountjoy, E. W., Edgecombe, D. R., Talent, J. A., and Owen, D. E., 1976, Nubrigyn algal reefs (Devonian), eastern Australia: allochthonous blocks and megabreccias: Geological Society of America Bulletin, v. 87, p. 515-530.

Coney, P. J., Edwards, A., Hine, R., Morrison, F., and Windrim, D., 1990, The regional tectonics of the Tasman orogenic system, eastern Australia: Journal of Structural Geology, v. 12, p. 519-543.

Cook, K., and Garvey, D., 1999, The glint of gold: a history and tourist guide of the goldfields of the Central West of New South Wales: Orange, N.S.W., Genlin Investments, 371 p.

Cook, H. E., McDaniel, P. N., Mountjoy, E. W., and Pray, L. C., 1972, Allochthonous carbonate debris flows at Devonian bank ("reef') margins, Alberta, Canada: Bulletin of Canadian Petroleum Geology, v. 20, p. 439-486.

Cook, W. G., Pocock, J. A., and Stegman, C. L., 1998, Peak gold-copper-lead-zinc-silver deposit, Cobar, in Berkman, D. A., and Mackenzie, D. H., eds., Geology of Australian and Papua New Guinean deposits. Monograph 22: Melbourne, The Australasian Institute of Mining and Metallurgy.

Corbett, K. D., 2001, New mapping and interpretations of the Mount Lyell mining district, Tasmania: a large hybrid Cu-Au system with an exhalative top: Economic Geology, v. 96, p. 1089-1122.

Costa, U. R., Barnett, R. L., and Kerrich, R., 1983, The Mattagami Lake Mine Archean Zn-Cu sulfide deposit, Quebec; hydrothermal co-precipitation of talc and sulfides in a sea-floor brine pool; evidence from geochemistry, (super 18) O/ (super 16) O, and mineral chemistry: Economic Geology and the Bulletin of the Society of Economic Geologists, v. 78, p. 1144-1203.

Cox, S. F., 2000, Deformational controls on the formation of vein-related ore deposits, Techniques in Structural Geology, CODES Short Course Manual, October 2000: Hobart, Centre for Ore Deposit Research, School of Earth Sciences, University of Tasmania, p. 1-24.

Cox, S. F., Wall, V. J., Etheridge, M. A., and Potter, T. F., 1991, Deformational and metamorphic processes in the formation of mesothermal vein-hosted gold deposits; examples from the Lachlan Fold Belt in central Victoria, Australia: Ore Geology Reviews, v. 6, p. 391-423.

Craig, J. R., and Vokes, F. M., 1993, The metamorphism of pyrite and pyritic ores; an overview, in Boyle, A. P., ed., Sulphide metamorphism and deformation, 57. Mineralogical Magazine: London, United Kingdom, Mineralogical Society, p. 3-18.

Crawford, A. J., and Keays, R. R., 1978, Cambrian greenstone belts in Victoria: marginal sea-crust slices in the Lachlan Fold Belt of southeastern Australia: Earth and Planetary Science Letters, v. 41, p. 197-208.

Crawford, A. J., Cameron, W. E., and Keays, R. R., 1984, The association of boninite low-Ti andesite-tholeiite in the Heatcote Greenstone Belt, Victoria; ensimatic setting for the early Lachlan Fold Belt: Australian Journal of Earth Sciences, v. 31, p. 161-175.

Crawford, A. J., Corbett, K. D., and Everard, J. L., 1992, Geochemistry of the Cambrian volcanic-hosted massive sulfide rich Mount Read Volcanics, Tasmania, and some tectonic implications: Economic Geology, v. 90, p. 597-619.

Davis, E. E., Goodfellow, W. D., Bornhold, B. D., Adshead, J., Blaise, B., Villinger, H., and Le, C. G. M., 1987, Massive sulfides in a sedimented rift valley, northern Juan de Fuca Ridge: Earth and Planetary Science Letters, v. 82, p. 49-61.

Davis, L. W., 1975, Captains Flat lead-zinc orebody, Australasian Institute of Mining and Metallurgy. Monograph 5, p. 694-700.

Davis, L. W., 1990, Silver-lead-zinc-copper mineralisation in the Captains Flat-Goulburn synclinorial zone and the Hill End synclinorial zone, in Hughes, F. E., ed., Geology of the mineral deposits of Australia and Papua New Guinea, 2. Monograph 14: Melbourne, The Australasian Institute of Mining and Metallurgy, p. 1375-1384.

De Carlo, E. H., Lackschewitz, K. K., and Carmody, R., 2001, Alteration of volcanic matter in sediments of the Woodlark Basin, (ODP Leg 180); evidence from trace elements and isotopic signatures in interstitial water, Abstracts with Programs - Geological Society of America, 33: Boulder, Geological Society of America, p. 234.

De Carlo, E. H., Lackschewitz, K. K., and Carmody, R., 2002, Data report: trace element and isotopic composition of interstitial water and sediments from the Woodlark Rise, ODP Leg 180, in Huchon, P., Taylor, B., and A, K., eds., Proceedings of the Ocean Drilling Program, Scientific Results, Leg 180, 180.

de Ronde, C. E. J., 1995, Fluid chemistry and isotopic characteristics of seafloor hydrothermal systems and associated VMS deposits: potential for magmatic contributions, in Thompson, J. F. H., ed., Magmas, fluids, and ore deposits, 23. Mineralogical Association of Canada Short Course Series: Vancouver, Mineral Deposit Research Unit, University of British Columbia, p. 479-509.

Deer, W. A., Howie, R. A., and Zussman, J., 1962, Rock-forming minerals: Great Britain, Longmans, Green and Co., 270 p.

Deer, W. A., Howie, R. A., and Zussman, J., 1992, An introduction to the rock-forming minerals, Longman Scientific and Technical, 696 p.

Delevaux, M. H., Doe, B. R., and Brown, G. F., 1967, Preliminary lead isotope investigations of brine from the Red Sea, galena from the Kingdom of Saudi Arabia, and galena from United Arab Republic (Egypt): Earth and Planetary Science Letters, v. 3, p. 139-144.

Downes, P. M., and Seccombe, P. K., 2000, Sulfur isotope distribution in Late Silurian VHMS deposits, Hill End Trough, NSW, in Gemmell, J. B., and Pongratz, J., eds., Volcanic Environments and Massive Sulfide Deposits international conference and field meeting, November 2000. CODES Special Publication 3: Hobart, Centre for Ore Deposit Research, School of Earth Sciences, University of Tasmania, Australia, p. 39-40.

Doyle, M. G., 2001, Volcanic influences on hydrothermal and diagenetic alteration: evidence from Highway-Reward, Mount Windsor Subprovince, Australia: Economic Geology, v. 96, p. 1133-1148.

Duckworth, R. C., Fallick, A. E., and Rickard, D., 1994, Mineralogy and sulfur isotopic composition of the Middle Valley massive sulfide deposit, northern Juan De Fuca Ridge, in Mottl, M. J., Davis, E. E., Fisher, A. T., and Slack, J. F., eds., Proceedings of the ocean drilling program, scientific results, 139, p. 373-385.

Eastoe, C. J., and Nelson, S. E., 1988, A Permian Kuroko-type hydrothermal system, Afterthought-Ingot area, Shasta County, California: lateral and vertical sections, and geochemical evolution: Economic Geology, v. 83, p. 588-605.

Eastoe, C. J., Solomon, M., and Walshe, J. L., 1987, District-scale alteration associated with massive sulfide deposits in the Mount Read Volcanics, western Tasmania: Economic Geology, v. 82, p. 1239-1258.

Eldridge, C. S., Barton, P. B., Jr., and Ohmoto, H., 1983, Mineral textures and their bearing on formation of the Kuroko orebodies: Economic Geology Monograph, v. 5, p. 241-281.

England, B. M., and Ostwald, J., 1993, Framboid-derived structures in some Tasman Fold Belt base-metal sulphide deposits, New South Wales, Australia: Ore Geology Reviews, v. 7, p. 381-412.

Enos, P., and Moore, C. H., 1983, Fore-reef slope environment, in Scholle, P. A., Bebout, D. G., and Moore, C. H., eds., Carbonate Depositional Environments, 33. AAPG Memoir: Tulsa, Oklahoma, The American Association of Petroleum Geologists, p. 507-537.

Faure, G., 1977, Principles of isotope geology: New York, John Wiley and Sons, 464 p.

Finlow-Bates, T., and Stumpfl, E. F., 1981, The behaviour of so-called immobile elements in hydrothermally altered rocks associated with volcanogenic submarine-exhalative ore deposits: Mineralium Deposita, v. 16, p. 319-328.

Foster, D. A., and Gray, D. R., 2000, Evolution and structure of the Lachlan Fold Belt (orogen) of eastern Australia: Annual Review of Earth and Planetary Sciences, v. 28, p. 47-80.

Franklin, J. M., Sangster, D. M., and Lydon, J. W., 1981, Volcanic-associated massive sulfide deposits, in Skinner, B. J., ed., Economic geology; Seventy-fifth anniversary volume; 1905-1980, p. 485-627.

Friedman, I., and O'Neil, J. R., 1977, Compilation of stable isotope fractionation factors of geochemical interest: Reston, U. S. Geological Survey Professional Paper, P 0440-KK, 12 p.

Galley, A. G., 1995, Target vectoring using lithogeochemistry; applications to the exploration for volcanic-hosted massive sulphide deposits: CIM Bulletin, v. 88, p. 15-27.

Gemmell, J. B., and Large, R. R., 1992, Stringer system and alteration zones underlying the Hellyer volcanogenic massive sulfide deposit, Tasmania, Australia: Economic Geology, v. 87; 3, p. 620-649.

Gemmell, J. B., Large, R. R., and Khin Zaw, 1998, Palaeozoic volcanic-hosted massive sulphide deposits: AGSO Journal of Australian Geology and Geophysics, v. 17, p. 129-137.

Gemmell, J. B., and Fulton, R., 2001, Geology, genesis, and exploration implications of the foot wall and hanging-wall alteration associated with the Hellyer volcanic-hosted massive sulfide deposit, Tasmania, Australia: Economic Geology, v. 96, p. 1003-1035.

George, A. D., Playford, P. E., and Powell, C. M., 1995, Platform-margin collapse during Famennian reef evolution, Canning Basin, Western Australia: Geology, v. 23, p. 691-694.

Gibson, H. L., Morton, R. L., Hudak, G. J., Barrie, C. T., and Hannington, M. D., 1999, Submarine volcanic processes, deposits, and environments favorable for the location of volcanic-associated massive sulfide deposits: Reviews in Economic Geology, v. 8, p. 13-51.

Gifkins, C. C., and Allen, R. L., 2001, Textural and chemical characteristics of diagenetic and hydrothermal alteration in glassy volcanic rocks: examples from the Mount Read Volcanics, Tasmania: Economic Geology, v. 96, p. 973-1002.

Gilligan, L. B., 1974, Captains Flat-Goulburn synclinorial zone, *in* Markham, N. L., and Basden, H., eds., The mineral deposits of New South Wales: Sydney, Geological Survey of New South Wales, Department of Mines, p. 294-307.

Glen, R. A., 1990, Formation and inversion of transtensional basins in the western part of the Lachlan Fold Belt, Australia, with emphasis on the Cobar Basin: Journal of Structural Geology, v. 12, p. 601-620.

Glen, R. A., 1992, Thrust, extensional and strike-slip tectonics in an evolving Palaeozoic orogen - a structural synthesis of the Lachlan Orogen of southeastern Australia: Tectonophysics, v. 214, p. 341-380.

Glen, R. A., and Watkins, J. J., 1994, The Orange 1:100 000 Sheet: a preliminary account of stratigraphy, structure and tectonics, and implications for mineralisation: Geological Survey of New South Wales, Quarterly Notes, v. 95, p. 1-17.

Glen, R. A., 1995, Thrusts and thrust-associated mineralization in the Lachlan Orogen: Economic Geology, v. 90, p. 1402-1429.

Glen, R. A., and Wyborn, D., 1997, Inferred thrust imbrication, deformation gradients and the Lachlan Transverse Zone in the eastern belt of the Lachlan Orogen, New South Wales: Australian Journal of Earth Sciences, v. 44, p. 49-68.

Glen, R. A., 1998, Structural Geology, in Stewart, J. R., ed., Bathurst 1: 250 000 Geological Sheet, explanatory notes. Explanatory Notes: Sydney, Geological Survey of New South Wales, p. 287-310.

Glen, R. A., Walshe, J. L., Barron, L. M., and Watkins, J. J., 1998, Ordovician convergent -margin volcanism and tectonism in the Lachlan sector of east Gondwana: Geology, v. 26, p. 751-754.

Glen, R. A., Lennox, P. G., and Foster, D. A., 1999, 40Ar-39Ar dating of deformations west of the Hill End Trough, Lachlan Orogen, New South Wales: Geological Survey of New South Wales Quarterly Notes, v. 110, p. 13-22.

Glen, R. A., and Walshe, J. L., 1999, Cross-structures in the Lachlan Orogen; the Lachlan Transverse Zone example: Australian Journal of Earth Sciences, v. 46, p. 641-658.

Glen, R. A., and Watkins, J. J., 1999, Implications of Middle Devonian deformation of the eastern part of the Hill End Trough, Lachlan Orogen, New South Wales: Australian Journal of Earth Sciences, v. 46, p. 35-52.

Goodfellow, W. D., and Franklin, J. M., 1993, Geology, mineralogy, and chemistry of sediment-hosted clastic massive sulfides in shallow cores, Middle Valley, northern Juan de Fuca Ridge: Economic Geology, v. 88, p. 2033-2064.

Goodfellow, W. D., Grapes, K., Cameron, B., and Franklin, J. M., 1993, Hydrothermal alteration associated with massive sulfide deposits, Middle Valley, northern Juan de Fuca Ridge: The Canadian Mineralogist, v. 31, Part 4, p. 1025-1060.

Goto, Y., and McPhie, J., 1998, Endogenous growth of a Miocene submarine dacite cryptodome, Rebun Island, Hokkaido, Japan: Journal of Volcanology and Geothermal Research, v. 84, p. 273-286.

Gray, D. R., 1997, Tectonics of the sotheastern Australian Lachlan Fold Belt: structural and thermal aspects, in Burg, J. P., and Ford, M., eds., Orogeny through time, 121. Geological Society special Publication: London, Geological Society of London, p. 149-177.

Gray, D. R., Foster, D. A., and P, B. F., 2002, Geodynamics and metallogeny of the Lachlan Orogen: Australian Journal of Earth Sciences, v. 49, p. 1041-1056.

Gregg, J. M., and Sibley, D. F., 1984, Epigenetic dolomitization and the origin of xenotopic dolomite texture: Journal of Sedimentary Petrology, v. 54, p. 908-931.

Gregory, P. W., Hartly, J. S., and Wills, K. J. A., 1990, Thalanga zinc-lead-copper-silver deposit, in Hughes, F. E., ed., Geology of the mineral deposits of Australia and Papua New Guinea, 2. Monograph 14: Melbourne, The Australasian Institute of Mining and Metallurgy, p. 1527-1537.

Gulson, B. L., 1977, Application of lead isotopes and trace elements to mapping black shales around a base metal sulphide deposit: Journal of Geochemical Exploration, v. 8, p. 85-103.

Gulson, B. L., 1986, Lead isotopes in mineral exploration: Amsterdam, Elsevier, 245 p.

Halbach, P., Pracejus, B., and Maerten, A., 1993, Geology and mineralogy of massive sulfide ores from the central Okinawa Trough, Japan: Economic Geology, v. 88, p. 2206-2221.

Halley, S. W., and Roberts, R. H., 1997, Henty: a shallow-water gold-rich volcanogenic massive sulphide deposit in western Tasmania: Economic Geology, v. 92, p. 438-447.

Hannington, M. D., Bleeker, W., and Kjarsgaard, I., 1999a, Sulfide mineralogy, geochemistry, and ore genesis of the Kidd Creek Deposit; Part I, North, Central and South orebodies: Economic Geology Monograph, v. 10, p. 163-224.

Hannington, M. D., Bleeker, W., and Kjarsgaard, I., 1999b, Sulfide mineralogy, geochemistry, and ore genesis of the Kidd Creek Deposit; Part II, The bornite zone: Economic Geology Monograph, v. 10, p. 225-266.

Hannington, M. D., Poulsen, K. H., Thompson, J. F. H., Sillitoe, R. H., Barrie, C. T., and Hannington, M. D., 1999c, Volcanogenic gold in the massive sulfide environment: Reviews in Economic Geology, v. 8, p. 325-356.

Hannington, M., and Herzig, P., 2000, Exploration of the modern seafloor; developing new models for VMS and related ore deposit types, in Anonymous, ed., Geological Society of America, 2000 annual meeting., Geological Society of America (GSA). Boulder, CO, United States. 2000., p. A4.

Herrmann, W., Blake, M., Doyle, M., Huston, D., Kamprad, J., Merry, N., and Pontual, S., 2001, Short wavelength infrared (SWIR) spectral analysis of hydrothermal alteration zones associated with base metal sulfide deposits at Rosebery and Western Tharsis, Tasmania, and Highway-Reward, Queensland: Economic Geology, v. 96, p. 939-955.

Herrmann, W., and Hill, A. P., 2001, The origin of chlorite-tremolite-carbonate rocks associated with the Thalanga Volcanic-hosted massive sulfide deposit, North Queensland, Australia: Economic Geology, v. 96, p. 1149-1173.

Herzig, P. M., and Hannington, M. D., 1995, Polymetallic massive sulfides at the modern seafloor; a review: Ore Geology Reviews, v. 10, p. 95-115.

Hilyard, D., 1981, Environmental, palaeogeographic, and tectonic setting of the Mullions Range Volcanics, New South Wales: Journal of the Geological Society of Australia, v. 28, p. 251-260.

Hinman, M., 1993, A Lotus 1-2-3 diamond drillhole structural manipulation spreadsheet; drillcore structural data generation: Computers and Geosciences, v. 19, p. 343-354.

Hinman, M. C., and Scott, A. K., 1990, The Peak gold deposit, Cobar, in Hughes, F. E., ed., Geology of the mineral deposits of Australia and Papua New Guinea, 2. Monograph 14: Melbourne, The Australasian Institute of Mining and Metallurgy, p. 1345-1351.

Hitzman, M. W., and Beaty, D. W., 1997, The Irish Zn-Pb-(Ba) orefield: Special Publication - Society of Economic Geologists, v. 4, p. 112-143.

Hitzman, M. W., Redmond, P. B., and Beaty, D. W., 2002, The carbonate-hosted Lisheen Zn-Pb-Ag deposit, County Tipperary, Ireland: Economic Geology, v. 97, p. 1627-1655.

Horikoshi, E., 1969, Volcanic activity related to the formation of the Kuroko-type deposits in the Kosaka District, Japan: Mineralium Deposita, v. 4, p. 321-345.

Hudson, D. L., Scott, M., and Meares, R., 1997, Volcanic-hosted massive sulphide deposits of the eastern Lachlan Fold Belt: Post Conference Excursion Guide, Third National Meeting, Specialist Group in Economic Geology, Geological Society of Australia, Sydney, February, 1997, p. 1-19.

Hunns, S. R., and McPhie, J., 1999, Pumiceous peperite in a submarine volcanic succession at Mount Chalmers, Queensland, Australia: Journal of Volcanology and Geothermal Research, v. 88, p. 239-254.

Huston, D. L., and Large, R. R., 1987, Genetic and exploration significance of the zinc ratio (100 Zn/ (Zn + Pb)) in massive sulfide systems: Economic Geology, v. 82, p. 1521-1539.

Huston, D. L., and Large, R. R., 1989, A chemical model for the concentration of gold in volcanogenic massive sulphide deposits: Ore Geology Reviews, v. 4, p. 171-200.

Huston, D. L., Sie, S. H., Suter, G. F., Cooke, D. R., and Both, R. A., 1995, Trace elements in sulfide minerals from eastern Australian volcanic-hosted massive sulfide deposits; Part I, Proton microprobe analyses of pyrite, chalcopyrite, and sphalerite, and Part II, Selenium levels in pyrite; comparison with delta (super 34) S values and implications for the source of sulfur in volcanogenic hydrothermal systems: Economic Geology, v. 90, p. 1167-1196.

Huston, D. L., Jablonski, W., and Sie, S. H., 1996, The distribution and mineral hosts of silver in eastern Australian volcanogenic massive sulfide deposits: The Canadian Mineralogist, v. 34 Part 3, p. 529-546.

Huston, D. L., Barrie, C. T., and Hannington, M. D., 1999, Stable isotopes and their significance for understanding the genesis of volcanic-hosted massive sulfide deposits; a review: Reviews in Economic Geology, v. 8, p. 157-179.

Huston, D. L., and Cas, R., 2000, Shallow water volcanic-hosted massive sulfide deposits: how common are they?, in Gemmell, J. B., and Pongratz, J., eds., Volcanic Environments and Massive Sulfide Deposits international conference and field meeting, November 2000. CODES Special Publication 3: Hobart, Centre for Ore Deposit Research, School of Earth Sciences, University of Tasmania, Australia, p. 93-95.

Hutchinson, R. W., 1997, Regional metallogeny of carbonate-hosted ores by comparison of field relationships: Special Publication - Society of Economic Geologists, v. 4, p. 8-17.

Hutchinson, R. W., 2000, A century of evolution in knowledge and genetic understanging of massive sulfide deposits, in Gemmell, J. B., and Pongratz, J., eds., Volcanic Environments and Massive Sulfide Deposits international conference and field meeting, November 2000. CODES Special Publication 3: Hobart, Centre for Ore Deposit Research, School of Earth Sciences, University of Tasmania, Australia, p. 97-98.

Ishikawa, Y., Sawaguchi, T., Iwaya, S., and Horiuchi, M., 1976, Delineation of prospecting targets for Kuroko deposits based on modes of volcanism of underlying dacite and alteration halos: Mining Geology, v. 26, p. 105 –117, (in Japanese with English abstract).

Jago, J. B., Reid, K. O., Quilty, P. G., Green, G. R., and Daily, B., 1972, Fossiliferous Cambrian limestone from within the Mt Read Volcanics, Mt Lyell mine area, Tasmania: Journal of the Geological Society of Australia, v. 19, p. 379-382.

Jagodzinski, E. A., and Cas, R. A. F., 2000, The Turondale Formation, Hill End Trough NSW: facies interpretation and palaeogeography: Understanding Planet Earth: Searching for a Sustainable Future, University of Technology, Sydney, 2000, Abstracts of the 15th Australian Geological Convention, p. 249.

Jenkyns, H. C., 1986, Pelagic Environments, in Reading, H. G., ed., Sedimentary Environments and Facies: Oxford, Blackwell Scientific Publications, p. 343-397.

Jones, S. A., 2001, Geology and geochemistry of the 'caprocks' above VHMS deposits at Myra Falls, Vancouver Island, British Columbia: Unpub. Ph.D. thesis, University of Tasmania, 497 p.

Kajiwara, Y., 1972, Sulfur isotope study of the Kuroko-ores of the Shakanai No. 1 deposits, Akita Prefecture, Japan: Geochemical Journal, v. 4, p. 157-181.

Kearns, L. E., Kite, L. E., Leavens, P. B., and Nelen, J. A., 1980, Fluorine distribution in the hydrous silicate minerals of the Franklin Marble, Orange County, New York: American Mineralogist, v. 65, p. 557-562.

Kendall, A. C., 1985, Radiaxial fibrous calcite: a reappraisal, in Schneidermann, N., and Harris, P. M., eds., Carbonate cements, Special Publication, 36: Tulsa, Oaklahoma, Society of economic palaeontologists and mineralogists, p. 59-77.

Kerr, D. J., Gibson, H. L., Spooner, E. T. C., and Barrie, C. T., 1993, A comparison of the Horne volcanogenic massive sulfide deposit and intracauldron deposits of the Mine Sequence, Noranda, Quebec: Economic Geology, v. 88, p. 1419-1442.

Kesler, S. E., 1997, Appalachian Mississippi Valley-type deposits; paleoaquifers and brine provinces: Special Publication - Society of Economic Geologists, v. 4, p. 29-57.

Khin Zaw, and Large, R. R., 1992, The precious metal-rich, South Hercules mineralization, western Tasmania: a possible subsea-floor replacement volcanic-hosted massive sulfide deposit: Economic Geology, v. 87, p. 931-952.

Khin Zaw, Huston, D. L., and Large, R. R., 1999, A chemical model for the Devonian remobilisation process in the Cambrian Volcanic-hosted massive sulfide Rosebery deposit, western Tasmania: Economic Geology, v. 94, p. 529-546.

Kontak, D. J., 1999, Geochemical profile of a carbonate-quartz alteration zone in footwall rocks of the Stirling VMS base metal deposits, Richmond County, Cape Breton Island, in: MacDonald, D. R. and Mills, K. A., eds., Report of activities 1998, Nova Scotia Department of Natural Resources Mineral Resources Branch, unpublished report ME 1999-1.

Kubo, T., Nakato, T., and Uchida, E., 1992, An experimental study on partitioning of Zn, Fe, Mn and Cd between sphalerite and aqueous chloride solution: Journal of the Society of Resource Geology, v. 42, p. 301-309.

Laing, W. P., 1977, Structural interpretation of drill core from folded and cleaved rocks: Economic Geology, v. 72, p. 671-685.

Large, R. R., 1977, Chemical evolution and zonation of massive sulfide deposits in volcanic terrains: Economic Geology, v. 72, p. 549-572.

Large, R. R., and Both, R. A., 1980, The volcanogenic sulfide ores at Mount Chalmers, eastern Queensland: Economic Geology, v. 75, p. 992-1009.

Large, R. R., Huston, D. L., McGoldrick, P. J., Ruxton, P. A., and McArthur, G., 1989, Gold distribution and genesis in Australian volcanogenic massive sulfide deposits and their significance for gold transport models: Economic Geology Monograph, v. 6, p. 520-536.

Large, R. R., 1992, Australian volcanic-hosted massive sulphide deposits: features, styles, and genetic models: Economic Geology, v. 87, p. 471-510.

Large, R. R., McPhie, J., Gemmell, J. B., Herrmann, W., and Davidson, G. J., 2001a, The spectrum of ore deposit types, volcanic environments, alteration halos, and related exploration vectors in submarine volcanic successions: some examples from Australia: Economic Geology, v. 96, p. 913-938.

Large, R. R., Gemmell, J. B., and Paulick, H., 2001b, The alteration box plot: a simple approach to understanding the relationship between alteration mineralogy and lithogeochemistry associated with volcanic-hosted massive sulfide deposits.: Economic Geology, v. 96, p. 957-971.

Large, R. R., Allen, R. L., Blake, M. D., and Herrmann, W., 2001c, Hydrothermal alteration and volatile element halos for the Rosebery K lens volcanic-hosted massive sulfide deposit, western Tasmania: Economic Geology, v. 96, p. 1055-1072.

Large, R. R., Bull, S. W., and Winefield, P. R., 2001d, Carbon and oxygen isotope halo in carbonates related to the McArthur River (HYC) Zn-Pb-Ag deposit, north Australia: implications for sedimentation, ore genesis, and mineral exploration: Economic Geology, v. 96, p. 1567-1593.

Larson, J. E., and Hutchinson, R. W., 1993, The Selbaie Zn-Cu-Ag deposits, Quebec, Canada; an example of evolution from subaqueous to subaerial volcanism and mineralization in an Archean caldera environment: Economic Geology, v. 88; 6, p. 1460-1482.

Lawrie, K. C., and Hinman, M. C., 1998, Cobar-style polymetallic Au-Cu-Ag-Pb-Zn deposits: Australian Geological Survey Organisation, Journal of Geology and Geophysics, v. 17(4), p. 169-187.

Le Maitre, R. W., Bateman, P., Dudek, A., Keller, J., Lameyre, Le Bas M. J., Sabine, P. A., Schmid, R. Sorensen, H., Streckeisen, A., Woolley, A. R. and Zanettin, B., 1989, A classification of igneous rocks and glossary of terms: Blackwell, Oxford.

Lishmund, S. R., Dawood, A. D., and Langley, W. V., 1986, The Limestone Deposits of New South Wales: Sydney, New South Wales Department of Mineral Resources.

Lofgren, G., 1971, Experimentally produced devitrification textures in natural rhyolitic glass: Geological Society of America Bulletin, v. 82, p. 111-124.

Loucks, R. G., Brown, A. A., Achauer, C. W., and Budd, D. A., 1985, Carbonate gravity-flow sedimentation on low-angle slopes off the Wolfcampian Northwest Shelf of the Delaware Basin, in Crevello Paul, D., and Harris Paul, M., eds., Deep-water carbonates; buildups, turbidites, debris flows and chalks; a core workshop., 6. SEPM Core Workshop, Society of Economic Paleontologists and Mineralogists, United States, p. 56-92.

Lowe, D. R., 1976, Grain flow and grain flow deposits: Journal of Sedimentary Petrology, v. 46, p. 188-199.

Lowe, D. R., 1982, Sediment gravity flows: II. Depositional models with special reference to the deposits of high-density turbidity currents: Journal of Sedimentary Petrology, v. 52, p. 279-297.

Lucas, J., 1875, Mines and mineral statistics of New South Wales and notes on the geological collection of the Department of Mines: Sydney, Thomas Richards, Government Printer.

Lydon, J. W., 1984, Ore deposit models - 8. Volcanogenic massive sulphide deposits part 1: A descriptive model: Geoscience Canada, v. 11, p. 195-202.

Lydon, J. W., 1988, Ore deposit models; Volcanogenic massive sulphide deposits; Part 2, Genetic models: Geoscience Canada, v. 15, p. 43-65.

Lydon, J. W., 1996, Characteristics of volcanogenic massive sulphide deposits; interpretations in terms of hydrothermal convection systems and magmatic hydrothermal systems: Boletin Geologico y Minero, v. 107, p. 215-264.

Macdonald, A. J., Lewis, P. D., Thompson, J. F. H., Nadaraju, G., Bartsch, R., Bridge, D. J., Rhys, D. A., Roth, T., Kaip, A., Godwin, C. I., and Sinclair, A. J., 1996, Metallogeny of an Early to Middle Jurassic arc, Iskut River area, northwestern British Columbia: Economic Geology, v. 91, p. 1098-1114.

MacLean, W. H., 1990, Mass change calculations in altered rock series: Mineralium Deposita, v. 25, p. 44-49.

MacLean, W. H., and Barrett, T. J., 1993, Lithogeochemical techniques using immobile elements: Journal of Geochemical Exploration, v. 48, p. 109-133.

Maier, R. C., 2002, The nature and origin of polymetallic mineralsiation in the Gurrunday District, N.S.W.: Unpub. BSc Honours thesis, University of Newcastle, 99 p.

Marcoux, E., Moelo, Y., and Leistel, J. M., 1996, Bismuth and cobalt minerals as indicators of stringer zones to massive sulphide deposits, Iberian pyrite belt: Mineralium Deposita, v. 31, p. 1-26.

Marshall, B., and Gilligan, L. B., 1993, Remobilization, syn-tectonic processes and massive sulphide deposits, in Groves David, I., and Bennett Julie, M., eds., Structural setting and controls on mineral deposits., 8; 1-2. Ore Geology Reviews: Amsterdam, Elsevier, p. 39-64.

Marshall, B., Vokes, F. M., and Larocque, A. C. L., 2000, Regional metamorphic remobilization: upgrading and formation of ore deposits: Reviews in Economic Geology, v. 11, p. 19-37.

Martin, N. K., 2002, Primitive textures in the Rosebery massive sulphide deposit, Tasmania, Australia, in Stewart, A. L., Agnew, M. W., and Cooke, D. R., eds., Giant Ore Deposits Workshop, Poster Abstracts, Centre for Ore Deposit Research, University of Tasmania, p. 37-42.

McArthur, G. J., 1996, Textural evolution of the Hellyer massive sulfide deposit: Unpub. Ph.D. thesis, University of Tasmania, 272 p.

McKay, W. J., 1989, A study of the geological setting, nature and genesis of the Woodlawn base metal deposit, New South Wales, Australia: Unpub. Ph.D. thesis, Australian National University, 273 p.

McKay, W. J., and Hazeldene, R. K., 1987, Woodlawn Zn-Pb-Cu sulfide deposit, New South Wales, Australia: an interpretation of ore formation from field observations and metal zoning: Economic Geology, v. 82, p. 141-164.

McLeod, R. L., and Stanton, R. L., 1984, Phyllosilicates and associated minerals in some Paleozoic stratiform sulfide deposits of southeastern Australia: Economic Geology, v. 79, p. 1-22.

McLeod, R. L., Gabell, A. R., Green, A. A., and Gardavsky, V., 1987, Chlorite infrared spectral data as proximity indicators of volcanogenic massive sulphide mineralization, in Brennan, E., ed., Pacific Rim congress 87; an international congress on the geology, structure, mineralisation and economics of the Pacific Rim.: Parkville, Victoria, Australia, Australasian Institute of Mining and Metallurgy, p. 321-324.

McPhie, J., Doyle, M., and Allen, R., 1993, Volcanic textures; a guide to the interpretation of textures in volcanic rocks: Hobart, Tasmania, Tasmanian Government Printing Office, 196 p.

Meakin, S., Spackman, J., Scott, M. M., Watkins, J. J., Warren, A. Y. E., Moffit, R. S., and Krynen, J. P., 1997, Orange 1:100 000 geological map 8731, fist edition, Geological Survey of New South Wales, Sydney and Australian Geological Survey Organisation, Canberra.

Messenger, P. R., Golding, S. D., and Taube, A., 1997, Volcanic setting of the Mt Morgan Au-Cu deposit, central Queensland: implications for ore genesis, Tectonics and metallogenesis of the New England Orogen - Alan H. Voisey Memorial Volume, 19. Special Publication 19: Sydney, Geological Society of Australia Inc., p. 109-127.

Meyer, H. J., 1984, The influence of impurities on the growth rate of calcite, Journal of Crystal Growth, v. 66, p. 639-646.

Mishra, B., and Mookherjee, A., 1988, Geothermometry based on fractionation of Mn and Cd between coexisting sphalerite and galena from some carbonate-hosted sulfide deposits in India: Mineralium Deposita, v. 23, p. 179-185.

Misra, K. C., Gratz, J. F., and Lu, C., 1997, Carbonate-hosted Mississippi Valley-type mineralization in the Elmwood-Gordonsville deposits, central Tennessee zinc district; a synthesis: Special Publication - Society of Economic Geologists, v. 4, p. 58-73.

Moore, J. G., and Clague, D. A., 1992, Volcano growth and evolution of the Island of Hawaii: Geological Society of America Bulletin, v. 104, p. 1471-1484.

Mountjoy, E. W., Cook, H. E., Pray, L. C., and McDaniel, P. N., 1972, Allochthonous carbonate debris flows; worldwide indicators of reef complexes, banks or shelf margins: International Geological Congress, Abstracts, v. 24, p. 198.

Moyle, A. L., Doyle, B. J., Hoogvliet, H., and Ware, A. R., 1990, Ladolam gold deposit, Lihir Island, in Hughes, F. E., ed., Geology of the mineral deposits of Australia and Papua New Guinea, 2. Monograph 14, The Australasian Institute of Mining and Metallurgy, p. 1793-1805.

Mullin, J. W., 1993, Crystallization: Oxford, England, Butterworth and Heinemann, 527 p.

Munoz, J. L., 1984, F-OH and Cl-OH exchange in micas with applications to hydrothermal ore deposits, in Bailey, S. W., ed., Micas., 13. Reviews in Mineralogy: Washington, DC, United States, Mineralogical Society of America, p. 469-493.

Nekrasov, I. Y., Sorokin, V. I., and Osadchiy, Y. G., 1981, Causes of increased tin capacity of sphalerite: International Geology Review, v. 23, p. 173-178.

Nemec, W., and Steel, R. J., 1984, Alluvial and coastal conglomerates: their significant features and some comments on gravelly mass-flow deposits: Canadian Society of Petroleum Geologists, Memoir, v. 10, p. 1-31.

Nguyen, P. T., Cox, S. S., Harris, L. B., and Powell, C. M., 1998, Fault-valve behaviour in optimally oriented shear zones; an example at the Revenge gold mine, Kambalda, Western Australia: Journal of Structural Geology, v. 20, p. 1625-1640.

Nijman, W., de Bruijne, K. C. H., and Valkering, M. E., 1998, Growth fault control of early Archaean cherts, barite mounds and chert-barite veins, North Pole Dome, eastern Pilbara, Western Australia, in Barley, M. E., and Loader, S. E., eds., The tectonics and metallogenic evolution of the Pilbara Craton., 88; 1-4. Precambrian Research: Amsterdam, International, Elsevier, p. 25-52.

Noh, J. H., and Boles, J. R., 1989, Diagenetic alteration of perlite in the Guryongpo area, Republic of Korea: Clays and Clay Minerals, v. 37, p. 47-58.

Northrop, D. A., and Clayton, R. N., 1966, Oxygen-isotope fractionations in systems containing dolomite: Journal of Geology, v. 74, p. 174-196.

Ohmoto, H., 1972, Systematics of sulfur and carbon isotopes in hydrothermal ore deposits: Economic Geology, v. 67, p. 551-578.

Ohmoto, H., and Rye, R. O., 1979, Isotopes of sulfur and carbon, in Barnes, H. L., ed., Geochemistry of hydrothermal ore deposits: New York, United States, John Wiley & Sons, p. 509-567.

Ohmoto, H., Mizukami, M., Drummond, S. E., Eldridge, C. S., Pisutha-Arnond, V., and Lenagh, T. C., 1983, Chemical processes of Kuroko formation: Economic Geology Monograph, v. 5, p. 570-604.

Ohmoto, H., 1986, Stable isotope geochemistry of ore deposits: Reviews in Mineralogy, v. 16, p. 491-559.

Ohmoto, H., and Goldhaber, M. B., 1997, Sulfur and carbon isotopes, in Barnes, H. L., ed., Geochemistry of hydrothermal ore deposits, John Wiley & Sons, p. 517-612.

Orth, K., 2002, Setting of the Palaeoproterozoic Koongie Park Formation and carbonate-associated base metal mineralisation, at Koongie Park, northwestern Australia: Unpub. Ph.D. thesis, University of Tasmania, 458 p.

Oudin, E., Picot, P., and Pouit, G., 1981, Comparison of sulphide deposits from the East Pacific Rise and Cyprus: Nature, v. 291, p. 404-407.

Packham, G. H., 1968, The Lower and Middle Palaeozoic stratigraphy and sedimentary tectonics of the Sofala-Hill End-Euchareena region, N.S.W.: Proceedings Linnean Society N.S.W., v. 93, p. 111-163.

Paradis, S., Jonasson, I. R., Le Cheminant, G. M., and Watkinson, D. H., 1988, Two zinc-rich chimneys from the Plume Site, southern Juan de Fuca Ridge: Canadian Mineralogist, v. 26, p. 637-654.

Passchier, C. W., and Trouw, R. A. J., 1996, Microtectonics, Springer-Verlag Berlin Heidelberg, 282 p.

Paulick, H., and McPhie, J., 1999, Facies architecture of the felsic lava-dominated host sequence to the Thalanga massive sulphide deposit, Lower Ordovician, northern Queensland: Australian Journal of Earth Sciences, v. 46, p. 391-405.

Paulick, H., Herrmann, W., and Gemmell, J. B., 2001, Alteration of felsic volcanics hosting the Thalanga massive sulfide deposit (Northern Queensland, Australia) and geochemical proximity indicators to ore: Economic Geology, v. 96, p. 1175-1200.

Peace, W. M., Wallace, M. W., Holdstock, M. P., and Ashton, J. H., 2003, Ore textures within the U lens of the Navan Zn-Pb deposit, Ireland: Mineralium Deposita, v. 38, p. 568-584.

Pearce, J. A., Harris, N. B. W., and G, T. A., 1984, Trace element discrimination diagrams for the tectonic interpretation of granitic rocks: Journal of Petrology, v. 25, p. 956-983.

Peter, J. M., Scott, S. D., Barrie, C. T., and Hannington, M. D., 1999, Windy Craggy, northwestern British Columbia; the world's largest besshi-type deposit: Reviews in Economic Geology, v. 8, p. 261-295.

Petersen, E. U., 1986, Tin in volcanogenic massive sulfide deposits; an example from the Geco Mine, Manitouwadge District, Ontario, Canada: Economic Geology, v. 81, p. 323-342.

Pisutha-Arnond, V., and Ohmoto, H., 1983, Thermal history, and chemical and isotopic compositions of the ore-forming fluids responsible for the Kuroko massive sulfide deposits in the Hokuroku District of Japan: Economic Geology Monograph, v. 5, p. 523-558.

Pittman, E. F., 1901, The mineral resources of New South Wales: Sydney, Geological Survey of New South Wales, 487 p.

Playford, P. E., 1984, Platform-margin and marginal-slope relationships in Devonian reef complexes of the Canning Basin, in Purcell, P. G., ed., The Caning Basin W.A.: Perth, Geological Society of Australia Inc. and Petroleum Society of Australia Ltd., p. 189-214.

Pogson, D. J., and Watkins, J. J., 1998, Bathurst 1:250 000 Geological Sheet, explanatory notes: Sydney, Geological Survey of New South Wales, 430 p.

Potter II, R. W., Clynne, M. A., and Brown, D. L., 1978, Freezing point depression of aqueous sodium chloride solutions: Economic Geology, v. 73, p. 284-285.

Potts, P. J., 1987, A handbook of silicate rock analyses: London, Blackie and Son Ltd., 622 p.

Powell, C. M., and Edgecombe, D. R., 1978, Mid-Devonian movements in the northeastern Lachlan Fold Belt: Journal of the Geological Society of Australia, v. 25, p. 165-184.

Powell, C. M., 1979, A morphological classification of rock cleavage: Tectonophysics, v. 58, p. 21-34.

Powell, C. M., 1983, Tectonic relationship between the Late Ordovician and Late Silurian palaeogeographies of southeastern Australia: Journal of the Geological Society of Australia, v. 30, p. 353-373.

Radke, B. M., and Mathis, R. L., 1980, On the formation and occurrence of saddle dolomite: Journal of Sedimentary Petrology, v. 50, p. 1149-1168.

Ramdohr, P., 1979, The ore minerals and their intergrowths Volume 2: Berlin, Pergamon, 764 p.

Rao, C. P., 1997, A colour illustrated guide to sedimentary textures - cold, cool, warm, hot an introduction to the interpretation of depositional, diagenetic and hydrothermal temperatures: Hobart, Printing Authority of Tasmania, Hobart, Tasmania, Australia, 128 p.

Raymond, O. L., Pogson, D. J., and others, 1998, Bathurst 1:250 000 geological map SI55-8, second edition, Geological Survey of New South Wales, Sydney and Australian Geological Survey Organisation, Canberra.

Rice, J. M., 1977, Progressive metamorphism of impure dolomitic limestone in the Marysville aureole, Montana: American Journal of Science, v. 277, p. 1-24.

Rimstidt, J. D., 1997, Gangue mineral transport and deposition, in Barnes, H. L., ed., Geochemistry of hydrothermal deposits: New York, Wiley, p. 487-515.

Ripperdan, R. L., 2001, Stratigraphic variation in marine carbonate carbon isotope ratios: Reviews in Mineralogy and Geochemistry, v. 43, p. 637-662.

Robinson, B. W., and Kusakabe, M., 1975, Quantitative preparation of sulfur dioxide, for 34S/32S analysis, from sulfides by combustion with cuprous oxide: Analytical Chemistry, v. 47, p. 1179-1181.

Roedder, E., 1984, Fluid inclusions: Reviews in Mineralogy, v. 12., 646 p.

Rollinson, H. R., 1993, Using geochemical data: evaluation, presentation, interpretation, Longman, 352 p.

Rule, J., 1978, The Cornish settlement: Belmore, Mintis, 60 p.

Sack, R. O., and Loucks, R. R., 1985, Thermodynamic properties of tetrahedrite-tennantites; constraints on the interdependence of the Ag <--> Cu, Fe <--> Zn, Cu <--> Fe, and As <--> Sb exchange reactions: American Mineralogist, v. 70, p. 1270-1289.

Sainty, R. A., 1992, Shallow-water stratigraphy at Mount Chalmers volcanic-hosted massive sulphide deposit, Queensland Australia: Economic Geology, v. 87, p. 812-824.

Sangster, D. F., 1968, Relative sulphur isotope abundances of ancient seas and strata-bound sulphide deposits: Geological Association of Canada Proceedings; with French abstract, v. 19, p. 79-91.

Sangster, D. F., and Scott, S. D., 1976, Precambrian, strata-bound, massive Cu-Zn-Pb sulfide ores of North America, in Wolf, K. H., ed., Handbook of strata-bound and stratiform ore deposits; II. Regional studies and specific deposits; Vol. 6, Cu, Zn, Pb, and Ag deposits: New York, United States, Elsevier, p. 129-222.

Sato, T., 1973, A chloride complex model for Kuroko mineralization: Geochemical Journal, v. 7, p. 245-270.

Saunders, J. A., 1990, Colloidal transport of gold and silica in epithermal precious-metal systems: Geology, v. 18, p. 757-760.

Schardt, C., Cooke, D. R., Gemmell, J. B., and Large, R. R., 2001, Geochemical modeling of the zoned footwall alteration pipe, Hellyer volcanic-hosted massive sulfide deposit, Tasmania, Australia: Economic Geology, v. 96, p. 1037-1054.

Scheibner, E., 1996, Geology of New South Wales - Synthesis Volume 1 Structural Framework: Sydney, Geological Survey of New South Wales, 295 p.

Scheibner, E., 1998, Geology of New South Wales - Synthesis Volume 2 Geological Evolution: Sydney, Geological Survey of New South Wales, 666 p.

Scheibner, E., and Veevers, J. J., 2000, Tasman Fold Belt System, in Veevers, J. J., ed., Billion-year earth history of Australia and neighbours in Gondwanaland: Sydney, GEMOC Press, Department of Earth and Planetary Sciences, Macquarie University, p. 154-234.

Schoonen, M. A. A., and Barnes, H. L., 1991, Mechanisms of pyrite and marcasite formation from solution; III, Hydrothermal processes: Geochimica et Cosmochimica Acta, v. 55, p. 3491-3504.

Scott, R. J., and Berry, R. F., in press, Structural data from axially oriented drill core: Journal of Structural Geology.

Seccombe, P. K., Lau, J. L., Lea, J. F., and Offler, R., 1984, Geology and ore genesis of silver-lead-zinc-copper sulphide deposits, Sunny Corner, NSW: Australasian Institute of Mining and Metallurgy Proceedings, v. 289, p. 51-57.

Serranti, S., Ferrini, V., Masi, U., and Cabri, L. J., 2002, Trace element distribution in cassiterite and sulfides from rubane and massive ores of the Corvo deposit, Portugal: Canadian Mineralogist, v. 40, p. 815-835.

Seward, T. M., 1976, The stability of chloride complexes of silver in hydrothermal fluids up to 350°C: Geochimica et Cosmochimica Acta, v. 40, p. 1329-1341.

Shanks, W. C., III, 2001, Stable isotopes in seafloor hydrothermal systems; vent fluids, hydrothermal deposits, hydrothermal alteration, and microbial processes: Reviews in Mineralogy and Geochemistry, v. 43, p. 469-525.

Sharpe, R., 1991, The distribution, mineralogy and paragenesis of the Hellyer baritic and siliceous caps: Unpub. Honours thesis, University of Tasmania, 114 p.

Shaw, S. E., and Flood, R. H., 1993, Carboniferous magmatic activity in the Lachlan and New England Fold Belts: New England Orogen, eastern Australia, Armidale, February, 1993, p. 113-121.

Shi, B. L., and Reed, G. C., 1998, CSA copper-lead-zinc deposit, Cobar, in Berkman, D. A., and Mackenzie, D. H., eds., Geology of Australian and Papua New Guinean deposits. Monograph 22: Melbourne, The Australasian Institute of Mining and Metallurgy, p. 601-608.

Sibley, D. F., and Gregg, J. M., 1987, Classification of dolomite rock textures: Journal of Sedimentary Petrology, v. 57, p. 967-975.

Sibson, R. H., Robert, F., and Poulson, K. H., 1988, High-angle reverse faults, fluid pressure cycling and mesothermal gold quartz deposits: Geology, v. 16, p. 551-555.

Sillitoe, R. H., Hannington, M. D., and Thompson, J. F. H., 1996, High sulfidation deposits in the volcanogenic massive sulfide environment: Economic Geology, v. 91, p. 204-212.

Simpson, A. J., and Talent, J. A., 1995, Silurian conodonts from the headwaters of the Indi (upper Murray) and Buchan rivers, southeastern Australia, and their implications: Contributions to the First Australian Conodont Symposium, Sydney, Australia, 18-21 July, 1995, Courier Forschungsinstitut Senckenberg, p. 79-215.

Slaughter, J., Kerrick, D. M., and Wall, V. J., 1975, Experimental and thermodynamic study of equilibria in the system CaO-MgO-SiO (sub 2) -H (sub 2) O-CO (sub 2): American Journal of Science, v. 275, p. 143-162.

Sohn, Y. K., 2000, Depositional processes of submarine debris flows in the Miocene fan deltas, Pohang Basin, SE Korea with special reference to flow transformation: Journal of Sedimentary Research, v. 70, p. 491-503.

Solomon, M., and Walshe, J. L., 1979, The formation of massive sulfide deposits on the sea floor: Economic Geology, v. 74, p. 797-813.

Solomon, M., and Gaspar, O. C., 2001, Textures of the Hellyer volcanic-hosted massive sulfide deposit, Tasmania - the aging of a sulfide sediment on the sea floor: Economic Geology, v. 96, p. 1513-1534.

South, B. C., and Taylor, B. E., 1985, Stable isotope geochemistry and metal zonation at the Iron Mountain mine, West Shasta district, California: Economic Geology, v. 80, p. 2177-2195.

Spear, F. S., 1993, Metamorphic phase equilibria and pressure-temperature-time paths, Mineralogical Society of America Monograph, 799 p.

Stanton, R. L., 1955, Lower Palaeozoic mineralization near Bathurst, New South Wales: Economic Geology, v. 50, p. 681-714.

Stanton, R. L., 1965, Mineral interfaces in stratiform ores: Institute of Mining and Metallurgy, v. 696, p. 45-79.

Stanton, R. L., 1972, Ore petrology: New York, McGraw-Hill, 713 p.

Stanton, R. L., 1990, Magmatic evolution and the ore type - lava type affiliations of volcanic exhalative ores, in Hughes, F. E., ed., Geology of the mineral deposits of Australia and Papua New Guinea, 1: Melbourne, The Australasian Institute of Mining and Metallurgy, p. 101-107.

Stevens, B. P. J., 1974, Hill End synclinorial zone, in Markham, N. L., and Basden, H., eds., The mineral deposits of New South Wales: Sydney, Geological Survey of New South Wales, Department of Mines, p. 276-293.

Stolz, A. J., Davies, G. R., and Allen, R. L., 1997, The importance of different types of magmatism in VHMS mineralisation; evidence from the geochemistry of the host volcanic rocks to the Benambra massive sulphide deposits, Victoria, Australia: Mineralogy and Petrology, v. 59, p. 251-286.

Stolz, J., and Large, R. R., 1992, Evaluation of the source-rock control on precious metal grades in volcanic-hosted massive sulfide deposits from western Tasmania: Economic Geology, v. 87, p. 720-738.

Stow, D. A. V., 1994, Deep sea processes of sediment transport and deposition, in Pye, K., ed., Sediment transport and depositional processes: Edinburgh, United Kingdom, Blackwell Scientific Publications, p. 257-291.

Strusz, D. L., 1960, The geology of the Parish of Mumbil, near Wellington, N.S.W.: Royal Society of New South Wales, Journal and Proceedings, v. 93, p. 127-136.

Suppel, D. W., Barnes, R. G., and Scheibner, E., 1998, The Palaeozoic in New South Wales - geology and mineral resources: Australian Geological Survey Organisation Journal of Australian Geology & Geophysics, v. 17, p. 87-105.

Sverjensky, D. A., 1981, The origin of a Mississippi Valley-type deposit in the Viburnum Trend, Southeast Missouri: Economic Geology, v. 76, p. 1848-1872.

Swart, P. K., Burns, S. J., and Leader, J. J., 1991, Fractionation of the stable isotopes of oxygen and carbon in carbon dioxide during the reaction of calcite with phosphoric acid as a function of temperature and technique: Chemical Geology, v. 86, p. 89-96.

Sweet, W. C., 1988, The Conodonta - morphology, taxonomy, plaeoecology, and evolutionary history of a long-extinct animal phylum: New York, Oxford Universty Press, 212 p.

Takahashi, T., and Suga, K., 1974, Geology and ore deposits of the Hanaoka Kuroko belt, Akita Prefecture: Mining Geology Special Issue, v. 6, p. 101-114.

Taylor, B. E., 1987, Stable isotope geochemistry of ore-forming fluids, in Kyser, T. K., ed., Short Course Handbook, vol.13: Toronto, Mineralogical Association of Canada, p. 337-445.

Taylor Jr., H. P., 1977, Water/rock interactions and the origin of H2O in granitic batholiths: Journal of the Geological Society of London, v. 133, p. 509-558.

Thompson, A. J. B., Hauff, P. L., and Robitaille, A. J., 1999, Alteration mapping in exploration: application of short-wave infrared (SWIR) spectroscopy: Society of Economic Geologists Newsletter, v. 39, p. 1, 16-27.

Tompkins, L. A., Rayner, M. J., Groves, D. I., and Roche, M. T., 1994, Evaporites; in situ sulfur source for rhythmically banded ore in the Cadjebut Mississippi Valley-type Zn-Pb deposit, Western Australia: Economic Geology, v. 89, p. 467-492.

Urabe, T., and Scott, S. D., 1983, Geology and footwall alteration of the South Bay massive sulphide deposit, northwestern Ontario, Canada: Canadian Journal of Earth Sciences, v. 20, p. 1862-1879.

Urabe, T., Scott, S. D., and Hattori, K., 1983, A comparison of footwall-rock alteration and geothermal systems beneath some Japanese and Canadian volcanogenic massive sulfide deposits: Economic Geology Monograph, v. 5, p. 345-364.

Valliant, R. I., 1998, Geological and geochemical characteristics of the Lewis Ponds Au-rich VMS deposit, in Lewis, P. C., ed., Lachlan Fold Belt'98, extended abstracts. AIG Bulletin 23, p. 87-90.

Valliant, R. I., and Meares, R. M. D., 1998, Lewis Ponds gold-silver-copper-lead-zinc deposits, in Berkman, D. A., and Mackenzie, D. H., eds., Geology of Australian and Papua New Guinean deposits. Monograph 22: Melbourne, The Australasian Institute of Mining and Metallurgy, p. 635-640.

Veizer, J., and Hoefs, J., 1976, The nature of O18/O16 and C13/C12 secular trends in sedimentary carbonate rocks: Geochimica et Cosmochimica Acta, v. 40, p. 1387-1395.

Vivallo, W., 1985, The geology and genesis of the Proterozoic massive sulfide deposit and Garpenberg, central Sweden: Economic Geology, v. 80, p. 17-32.

Wakita, H., Rey, P., and Schmitt, R. A., 1971, Abundances of 14 rare-earth elements and 12 other trace elements in Apollo 12 samples: five igneous and one breccia rocks and four soils, Proceedings 2nd Lunar Science Conference: Oxford, Pergamon Press, p. 1319-1329.

Walshe, J. L., and Solomon, M., 1981, An investigation into the environment of formation of the volcanic-hosted Mt. Lyell copper deposits using geology, mineralogy, stable isotopes, and a six-component chlorite solid solution model: Economic Geology, v. 76, p. 246-284.

Weathersten, P. W., 1988, W. Folster's Articles, the writings of William (Bill) Folster: Molong, New South Wales, Cabonne Printers, 200 p.

Webster, A. E., and Lutherborrow, C., 1998, Elura zinc-lead-silver deposit, Cobar, in Berkman, D. A., and Mackenzie, D. H., eds., Geology of Australian and Papua New Guinean deposits. Monograph 22: Melbourne, The Australasian Institute of Mining and Metallurgy, p. 587-592.

Wilkin, R. T., Barnes, H. L., and Brantley, S. L., 1996, The size distribution of framboidal pyrite in modern sediments; an indicator of redox conditions: Geochimica et Cosmochimica Acta, v. 60, p. 3897-3912.

Wilkin, R. T., and Barnes, H. L., 1997, Formation processes of framboidal pyrite: Geochimica et Cosmochimica Acta, v. 61, p. 323-339.

Williams, N., 2000, The Basin Lake high sulfidation alteration system, western Tasmania: Unpub. Honours thesis, University of Tasmania, 102 p.

Winchester, J. A., and Floyd, P. A., 1977, Geochemical discrimination of different magma series and their differentiation products using immobile elements: Chemical Geology, v. 20, p. 325-343.

Wolf, K. H., 1965, Petrongenesis and palaeoenvironment of Devonian algal limestones of New South Wales: Sedimentology, v. 4, p. 113-178.

Wyborn, D., Stuart-Smith, P., Wallace, D., and Henderson, G., 1992, New mapping in the Bathurst Sheet area - increased metallogenic potential, Australian Geological Survey Organisation (AGSO) Newsletter, 17, p. 13-14.

Yardley, B. W. D., 1989, An introduction to metamorphic petrology: Essex, Longman Earth Science Series, 249 p.

Zheng, Y. F., 1990, Carbon-oxygen isotopic covariation in hydrothermal calcite during degassing of CO2; a quantitative evaluation and application to the Kushikino gold mining area in Japan: Mineralium Deposita, v. 25, p. 246-250.

Zheng, Y. F., and Hoefs, J., 1993, Carbon and oxygen isotopic covariations in hydrothermal calcites: Mineralium Deposita, v. 28, p. 79-89.

Zierenberg, R. A., Koski, R. A., Morton, J. L., and Bouse, R. M., 1993, Genesis of massive sulfide deposits on a sediment-covered spreading center, Escanaba Trough, southern Gorda Ridge: Economic Geology, v. 88, p. 2065-2094.

Published or unpublished reports & newspaper articles

Australian Geophysical, 1965, Report No. 2 Results and recommendations on the western section of the Bathurst area, Australian Geophysical Pty Ltd, unpublished exploration report, GS 1965/102, 18 p.

Cambrell, R. P., and Kirk, B. I., 1974, The Mt Bulga base metal prospect, Orange, N.S.W., Aquitaine Australia Minerals Pty Ltd, unpublished exploration report, GS 1974/263, 29 p.

Castle, M. J., 1976, Report on exploration on minor titles, Lewis Ponds, N.S.W. Progress exploration report to January 1976, Aquitaine Minerals Pty Ltd., unpublished exploration report, GS 1976/063, p. 25.

Cominco Exploration, 1969, Prospecting report, A to P3138, Lewis Ponds area, Cominco Exploration Pty Ltd, unpublished exploration report, GS 1969/153 10 p.

Daily Orange, 1954, Historical society told of Lewis Ponds' history, *Daily Orange*, 9 June, 1954.

Daily Orange, 1956, Last Sunday the Orange historical society made an excursion to Icely and Lewis Ponds, *Daily Orange*, 24 February 1956.

David, V., Glen, R., and Spencer, R., 2002, Hill End Trough, in Glen, R. A., ed., Hill End Trough workshop abstract volume, Geological Survey of NSW unpublished report, GS 2002/447, p. 13.

Department of Mines, New South Wales, 1887, Annual report of the for the year 1886, Department of Mineral Resources, New South Wales.

Department of Mines, New South Wales, Annual reports for 1887-1930.

Folster, W., 1946, Early district settlements, *Daily Orange*, 25 April 1946.

Glasson, K. R., 1977, Review of geological data, Lewis Ponds, N.S.W., Aquitaine Australia Minerals Pty Ltd., unpublished exploration report, MG: 844.

Glen, R., David, V., and Spencer, R., 2002, Three dimensional extension of the Hill End Trough based on the modelling of regional gravity data, in Glen, R. A., ed., Hill End Trough workshop abstract volume, Geological Survey of NSW unpublished report, GS 2002/447, p. 22-23.

Glen, R. A., 2002, A two stage rift model for filling the Hill End Trough?, in Glen, R. A., ed., Hill End Trough workshop abstract volume, Geological Survey of NSW unpublished report, GS 2002/447, p. 20-21.

Heape, J., 1982, Exploration Licences 1251 and 1632, Six monthly report for period ending 16th April, 1982, The Shell Company of Australia Limited, Metals Division, unpublished exploration report, GS 1981/551, 6 p.

Herrmann, W., 1997, Notes on the geology of the Mt. Lindsay - Mt. Shorter area, EL 4137, Lewis Ponds Project, NSW, unpublished exploration report, 15 p.

Maroney, R., 1982, One man's Lewis Ponds memories, *Central West Daily*, 9 November 1982.

Mine Inspectors Report, Lewis Ponds Mines, Orange. Includes mine inspectors report 1887 and correspondence letters from 1900 and 1910, Mine Record: MR1392.

Mine Inspectors Report, 1906, Little Bell Mount, Orange, Mine Record: MR00331.

Mine Inspectors Report, 1907, Mount Regan, Orange, Mine Record: MR00744.

Packham, G. H., 2002, Hill End Trough: genesis and sediment fill, in Glen, R. A., ed., Hill End Trough workshop abstract volume, Geological Survey of NSW unpublished report, GS 2002/447, p. 24-25.

Parton, J., 1981, Exploration Licences 1251 and 1632, Six monthly report for period ending 16th October, 1981, The Shell Company of Australia Limited, Metals Division, unpublished exploration report, GS 1981/551, 11 p.

Percival, I. G., 1995, Palaeontological determinations, Mt Lindsay and Lewis Ponds cores, Geological Survey of New South Wales, Department of Mineral Resources, unpublished palaeontology report, GS 1995/320, 4 p.

Perkins, M., 1995, Report on trace element analysis, Main zone, Lewis Ponds project, Orange, Australia, Tri Origin Exploration Ltd, unpublished company report, 5 p.

Perkins, M., 1996, Report on trace element analysis, Toms zone, Lewis Ponds project, Orange, Australia, Tri Origin Exploration Ltd, 8 p.

Pickett, J. W., 1972, Marine fossils from the Mullions Range Volcanics, Geological Survey of New South Wales, Department of Mineral Resources, unpublished palaeontology report, GS 1972/10, 1 p.

Pickett, J. W., 1993, Invertebrate assemblages from the "Clifton Grove Formation", Orange district, Geological Survey of New South Wales, Department of Mineral Resources, unpublished palaeontology report, GS 1993/288, 7 p.

Shepherd, N., 1972, Summary Report Mineral Exploration Licence No. 212 Orange District, New South Wales, Amax Exploration Inc Metals Investment joint exploration agreement, unpublished exploration report, GS 1972/430, 43 p.

Scott, R., 1999, Structural studies in the Molong Belt, Report on 1999 Work Program, CODES-DMR-SPIRT Ordovician Project, Molong Belt: Hobart, unpublished report by the Centre for Ore Deposit Research, School of Earth Sciences, University of Tasmania, p. 191-226.

Wilkinson, C. S., 1888, Geological Survey of New South Wales report of progress for 1887 by the Geological Surveyor In Charge, New South Wales Department of Mines Annual Report for the year 1887: Sydney, p. 137-178.

Wright, R. G., 1979, Report to Accompany Application for Prospecting Aid, Mining Lease 617, Lewis Ponds, The Shell Company of Australia Limited, Metals Division, unpublished palaeontology report, GS 1979/396, 6 p.

Appendices

APPENDIX 1	Map of drill holes
APPENDIX 2	Calculated drill core structural fabric orientations and stratigraphic facing directions
APPENDIX 3	Carbonate and silicate microprobe analyses
APPENDIX 4	XRF analyses and mass balance calculation data
APPENDIX 5	Sulfide microprobe analyses
APPENDIX 6	Carbon-oxygen isotope and fluid modelling data
APPENDIX 7	Fluid inclusion data
APPENDIX 8	Sulfur isotope data
APPENDIX 9	List of rock samples

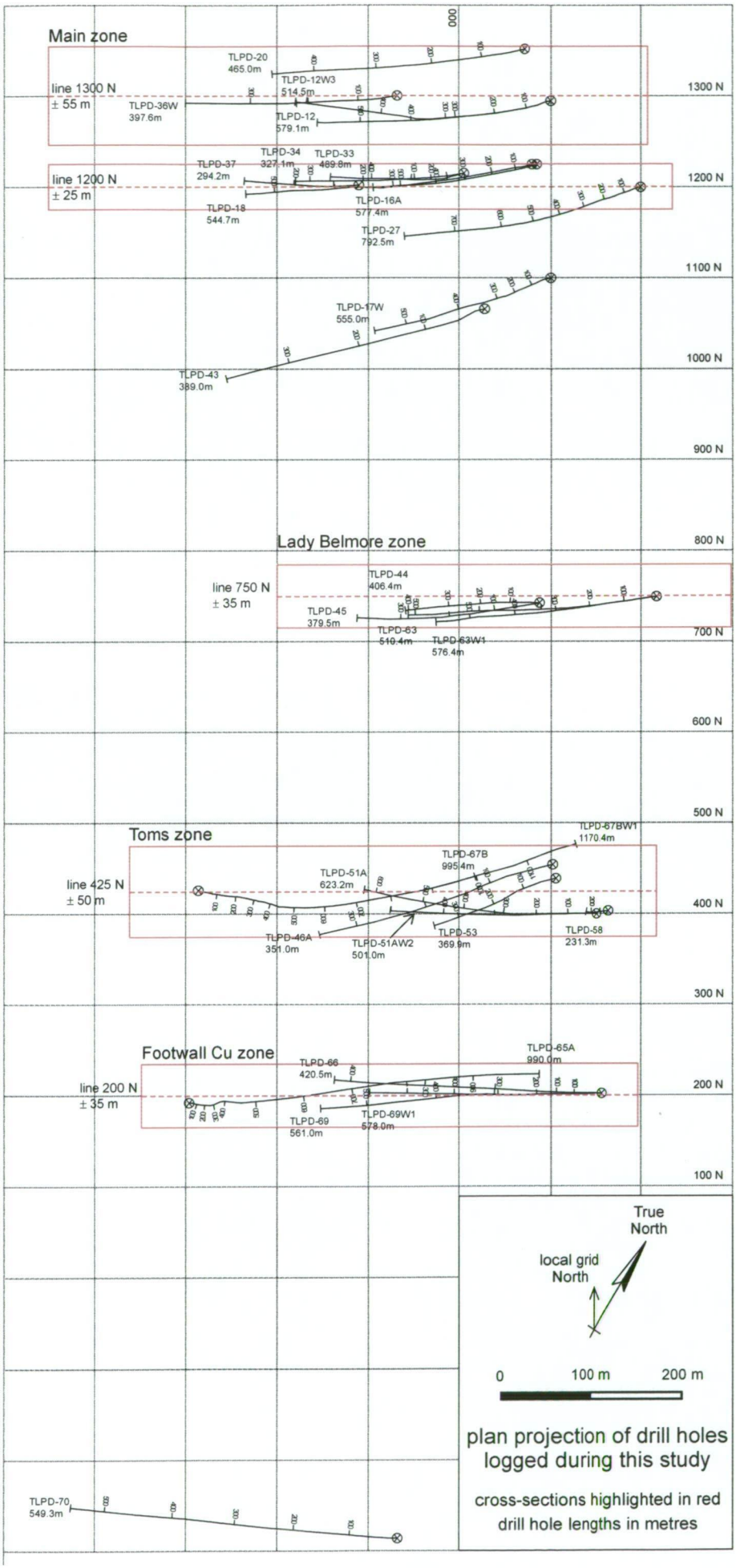

Appendix 1 - drill hole map

Appendix 2

Calculated drill hole structural fabric orientations and stratigraphic facing directions

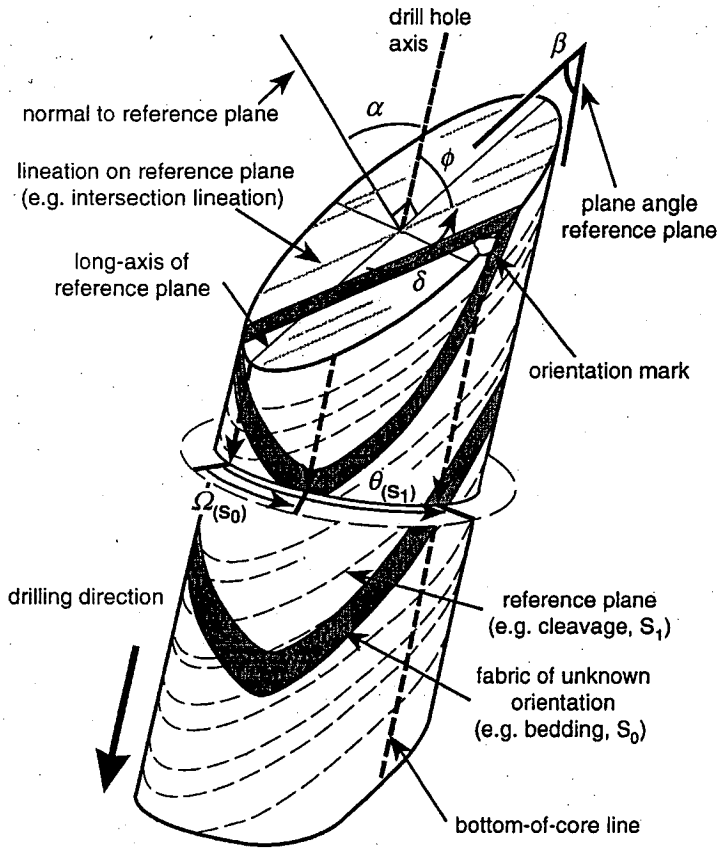

β (*plane angle*)
angle between long axis of ellipse formed by planar fabric and core axis.

α
angle between pole to planar fabric and core axis (usually determined from *β*, i.e. $\alpha = 90° - \beta$)

δ (*lineation angle*)
angle between lineation and the long-axis of elliptical section of the plane in which it lies. Measured anticlockwise (+ve) from the long-axis, looking down-hole.

ϕ
angle between a lineation and the core axis

θ (*bottom-of-core reference angle*)
angle in plane perpendicular to the core axis, between bottom-of-core line and down-hole end of elliptical section formed by plane. Measured anticlockwise from down-hole end of ellipse, looking down-hole.

Ω (*separation angle*)
angle in plane perpendicular to the core axis, between the down-hole ends of ellipses formed by planar fabrics. Measured anticlockwise from the reference fabric, looking down-hole.

Diagram showing the parameters required for calculating the 'best-fit' orientation of unknown planes and lineations in oriented or un-oriented drill core (from Scott and Berry, in press).

Notes:
The lineation angle (δ) and separation angle (Ω) were measured on the drill core using a modified protractor which wraps around the core.

Excell spreadsheet was used for calculating the 'best-fit' orientation of S_0, L_1, F_{12} and quartz veins

S_1 cleavage used as reference foliation: S_1 = 78-061

Data calculated using the core re-orientation spreadsheet developed by R. Scott and R. Berry, School of Earth Sciences, University of Tasmania

Drill hole data				"known" fabric					Plane 1			Line 1			"unknown" fabric			Plane 2			int. lineation	
drill hole	depth	plunge	azimuth	β	δ	min. error	ideal β/δ	Ref.θ	name	dip	dip dirn	name	plunge	trend	Ω	β	Ref.θ	name	dip	dip dirn	plunge	trend
TLPD-12	397.2	-57.4	235.5	29	25	15	44	8	S1	87	242	F12	69	323	185	37	183	QV	21	241		
TLPD-12	402.5	-57.0	235.8	42	354	3	45	7	S1	81	61	L1	76	109	195	37	172	QV	21	218		
TLPD-12	417.9	-56.4	236.2	58	-	13	45	7	S1	65	60	-	-	-	343	52	24	S0	70	71	59	18
TLPD-12	515.7	-54.5	237.1	43	18	4	47	6	S1	82	61	L1	73	358	0	39	6	S0	86	61	3	332
TLPD-12	516.0	-54.5	237.1	47	10	0	47	6	S1	78	61	L1	77	31	82	37	284	S0	68	0	68	1
TLPD-12	516.3	-54.5	237.1	60	18	13	47	6	S1	65	60	L1	62	29	323	40	43	S0	79	89	58	18
TLPD-12	567.4	-52.4	238.2	42	321	8	50	4	S1	86	61	L1	48	146	185	32	179	QV	20	236		
TLPD-12	569.1	-52.3	238.3	33	344	17	50	4	S1	85	242	L1	71	165	5	49	359	S0	79	58	14	331
TLPD-12	569.7	-52.2	238.4	55	335	5	50	4	S1	73	61	L1	58	121	330	29	34	S0	86	268	51	353
TLPD-12	570.4	-52.2	238.4	53	323	3	50	4	S1	75	61	L1	48	133	355	30	9	S0	83	246	13	334
TLPD-12	576.9	-51.7	238.9	41	343	9	50	3	S1	87	61	L1	71	144	10	37	353	S0	89	233	64	146
TLPD-12	576.9	-51.7	238.9	41	20	9	50	3	S1	87	61	F12	72	340	-	-	-	-	-	-		
TLPD-12W3	331.9	-47.2	238.6	58	22	3	55	4	S1	75	61	F12	66	8	-	-	-	-	-	-		
TLPD-12W3	363.3	-39.7	248.5	58	10	3	61	344	S1	81	60	F12	66	351	-	-	-	-	-	-		
TLPD-12W3	390.4	-37.7	245.6	69	337	5	64	350	S1	73	62	L1	68	103	-	-	-	-	-	-		
TLPD-12W3	390.4	-37.7	245.6	69	328	5	64	350	S1	73	62	F12	61	118	-	-	-	-	-	-		
TLPD-12W3	491.1	-33.0	246.1	67	82	1	68	346	S1	79	61	L1	4	150	30	62	316	S0	79	47	79	37
TLPD-12W3	503.1	-33.0	246.1	70	340	2	68	346	S1	77	61	L1	74	93	45	66	301	S0	71	45	66	4
TLPD-12W3	505.6	-33.0	246.1	74	320	6	68	346	S1	73	62	L1	57	123	330	70	16	S0	76	72	63	11
TLPD-12W3	512.2	-33.0	246.1	72	297	4	68	346	S1	75	62	L1	37	140	318	63	28	S0	81	79	65	7
TLPD-12W3	513.6	-33.0	246.1	72	295	4	68	346	S1	75	62	L1	35	140	310	40	36	S0	80	273	51	351
TLPD-12W3	513.6	-33.0	246.1	72	-	4	68	346	S1	75	62	-	-	-	335	68	11	S0	79	70	61	2
TLPD-18	145.0	-61.0	227.6	23	23	17	40	17	S1	85	243	F12	75	315	-	-	-	-	-	-		
TLPD-18	165.0	-59.2	228.5	27	11	15	42	16	S1	87	243	F12	86	288	-	-	-	-	-	-		
TLPD-18	198.3	-55.8	230.2	50	8	5	45	15	S1	73	60	F12	73	63	180	40	195	QV	19	269		
TLPD-18	207.0	-55.4	230.4	38	356	8	46	15	S1	86	62	L1	77	133	-	-	-	-	-	-		
TLPD-18	207.0	-55.4	230.4	38	30	8	46	15	S1	86	62	F12	68	343	-	-	-	-	-	-		
TLPD-18	223.1	-54.7	230.5	47	-	1	46	15	S1	77	61	-	-	-	0	52	15	S0	73	60	9	333
TLPD-18	223.8	-54.7	230.5	46	-	0	46	15	S1	78	61	-	-	-	0	46	15	S0	78	61		
TLPD-18	234.4	-54.3	230.3	21	355	26	47	15	S1	76	245	L1	70	198	-	-	-	-	-	-		
TLPD-18	234.4	-54.3	230.3	21	10	26	47	15	S1	76	245	F12	76	249	-	-	-	-	-	-		

drill hole	depth	plunge	azimuth	β	δ	min. error	ideal β/δ	Ref.θ	name	dip	dip dirn	name	plunge	trend	Ω	β	Ref.θ	name	dip	dip dirn	plunge	trend
TLPD-18	250.5	-53.7	230.1	32	30	15	47	16	S1	87	244	F12	69	325	-	-	-	-	-	-		
TLPD-18	330.9	-50.5	237.5	55	340	4	51	6	S1	74	61	L1	62	119	-	-	-	-	-	-		
TLPD-18	330.9	-50.5	237.5	55	4	4	51	6	S1	74	61	F12	74	60	-	-	-	-	-	-		
TLPD-18	430.3	-48.7	235.3	60	321	7	53	9	S1	71	60	L1	42	132	21	45	348	S0	86	47	40	133
TLPD-18	440.4	-48.4	236.0	61	323	8	53	8	S1	70	60	L1	44	130	349	53	19	S0	77	68	44	350
TLPD-18	444.1	-48.2	236.2	52	-	2	54	8	S1	80	61	-	-	-	350	44	18	S0	86	69	48	343
TLPD-18	448.0	-48.1	236.5	60	-	6	54	8	S1	72	60	-	-	-	350	40	18	S0	89	250	26	340
TLPD-18	453.8	-47.9	236.3	52	37	2	54	8	S1	80	61	F12	57	347	40	47	328	S0	81	35	80	63
TLPD-18	460.9	-47.7	235.9	62	350	8	54	9	S1	70	60	L1	65	101	0	17	9	S0	65	245	6	332
TLPD-18	463.8	-47.6	235.7	66	-	12	54	9	S1	66	60	-	-	-	265	57	104	S0	45	104	43	125
TLPD-18	465.4	-47.5	235.5	58	328	4	54	9	S1	74	61	L1	49	132	95	74	274	S0	46	33	32	341
TLPD-18	465.9	-47.5	235.5	59	348	5	54	9	S1	73	60	L1	65	110	25	54	344	S0	78	46	67	104
TLPD-18	465.9	-47.5	235.5	59	272	5	54	9	S1	73	60	F12	4	332	-	-	-	-	-	-		
TLPD-18	466.5	-47.5	235.5	59	59	5	54	9	S1	73	60	F12	36	343	75	74	294	S0	51	37	36	343
TLPD-18	468.2	-47.5	235.4	58	345	4	54	9	S1	74	61	L1	63	116	58	65	311	S0	61	34	54	354
TLPD-18	472.4	-47.3	235.1	62	324	8	54	10	S1	70	60	L1	43	130	58	63	312	S0	63	33	62	11
TLPD-18	476.2	-47.2	234.8	58	323	4	54	10	S1	74	61	L1	44	135	70	61	300	S0	62	26	58	357
TLPD-18	480.6	-47.1	234.5	60	-	6	54	11	S1	73	60	-	-	-	45	55	326	S0	74	35	73	59
TLPD-20	295.9	-49.8	234.8	50	355	2	52	10	S1	80	61	L1	75	110	0	55	10	S0	75	61	6	332
TLPD-20	295.9	-49.8	234.8	50	330	2	52	10	S1	80	61	F12	52	138	-	-	-	-	-	-		
TLPD-20	302.7	-49.5	234.9	56	345	4	52	10	S1	74	61	L1	63	116	7	55	3	S0	75	57	66	110
TLPD-20	303.6	-49.4	234.9	55	-	3	52	10	S1	75	61	-	-	-	10	56	360	S0	75	55	73	33
TLPD-20	310.8	-49.1	234.9	56	3	3	53	10	S1	75	61	L1	74	74	25	56	345	S0	74	46	74	47
TLPD-20	310.8	-49.1	234.9	56	40	3	53	10	S1	75	61	F12	54	353	-	-	-	-	-	-		
TLPD-20	325.0	-48.4	235.0	62	335	9	53	10	S1	69	60	L1	53	120	-	-	-	-	-	-		
TLPD-20	325.0	-48.4	235.0	62	354	9	53	10	S1	69	60	F12	66	93	-	-	-	-	-	-		
TLPD-20	340.0	-47.6	235.4	58	325	4	54	9	S1	74	61	L1	46	133	5	67	4	S0	65	57	18	336
TLPD-20	380.2	-45.9	236.3	63	-	7	56	8	S1	71	60	-	-	-	15	74	353	S0	60	54	24	339
TLPD-20	383.9	-45.8	236.1	60	290	4	56	9	S1	74	61	L1	13	147	0	49	9	S0	85	62	6	332
TLPD-20	420.0	-45.1	234.0	57	-	1	56	13	S1	77	61	-	-	-	310	51	63	S0	70	90	67	118
TLPD-20	422.0	-45.1	233.8	60	339	4	56	13	S1	74	60	L1	56	126	350	39	23	S0	87	251	29	339
TLPD-20	422.0	-45.1	233.8	60	344	4	56	13	S1	74	60	F12	61	121	-	-	-	-	-	-		

drill hole	depth	plunge	azimuth	β	δ	min. error	ideal β/δ	Ref.θ	name	dip	dip dirn	name	plunge	trend	Ω	β	Ref.θ	name	dip	dip dirn	plunge	trend
TLPD-20	425.8	-45.0	233.6	62	338	6	56	13	S1	72	60	L1	54	124	348	50	25	S0	83	70	42	346
TLPD-20	429.9	-45.0	233.6	62	-	6	56	13	S1	72	60	-	-	-	350	47	23	S0	86	69	33	342
TLPD-20	431.6	-45.0	233.6	63	325	7	56	13	S1	71	60	L1	42	132	344	34	29	S0	83	258	34	343
TLPD-20	435.3	-45.0	233.6	63	-	7	56	13	S1	71	60	-	-	-	20	48	353	S0	87	49	34	137
TLPD-20	443.3	-45.0	233.6	57	-	1	56	13	S1	77	61	-	-	-	327	45	46	S0	81	85	76	32
TLPD-20	436.5	-45.0	233.6	40	345	16	56	13	S1	86	244	L1	65	163	7	14	6	S0	59	241	6	154
TLPD-20	436.5	-45.0	233.6	40	358	16	56	13	S1	86	244	F12	78	174	-	-	-	-	-	-		
TLPD-20	440.3	-45.0	233.6	60	317	4	56	13	S1	74	60	L1	36	139	315	35	58	S0	84	98	71	25
TLPD-20	450.5	-45.0	233.6	64	333	8	56	13	S1	71	60	L1	49	126	344	62	29	S0	70	68	70	65
TLPD-20	452.6	-45.0	233.6	67	-	11	56	13	S1	68	59	-	-	-	35	58	338	S0	75	42	59	107
TLPD-20	457.0	-45.0	233.6	65	-	9	56	13	S1	70	59	-	-	-	15	25	358	S0	70	232	10	146
TLPD-20	459.7	-45.0	233.6	62	314	6	56	13	S1	72	60	L1	32	138	338	53	35	S0	77	74	65	13
TLPD-20	462.8	-45.0	233.6	69	325	13	56	13	S1	66	59	L1	40	126	15	5	358	S0	50	231	6	146
TLPD-20	464.6	-45.0	233.6	69	330	13	56	13	S1	66	59	L1	44	123	15	7	358	S0	52	231	6	146
TLPD-27	39.0	-79.2	219.7	7	-	15	22	23	S1	87	242	-	-	-	185	35	198	S0	45	240	2	152
TLPD-27	44.9	-79.4	216.0	5	-	17	22	26	S1	86	242	-	-	-	185	30	201	S0	50	240	3	153
TLPD-27	44.9	-79.4	216.0	5	-	27	22	206	S1	76	243	-	-	-	185	30	21	S0	70	56	12	330
TLPD-27	59.7	-79.1	215.7	5	-	17	22	27	S1	85	242	-	-	-	185	25	202	S0	55	240	4	153
TLPD-27	59.7	-79.1	215.7	5	-	27	22	207	S1	75	243	-	-	-	185	25	22	S0	75	56	14	330
TLPD-27	585.4	-67.2	229.1	48	-	14	34	14	S1	64	60	-	-	-	200	42	174	S0	25	219	8	146
TLPD-27	587.7	-67.1	229.1	46	10	12	34	14	S1	66	60	L1	66	50	28	20	346	S0	88	216	40	128
TLPD-27	637.5	-60.7	231.5	47	356	6	41	12	S1	72	60	L1	69	91	-	-	-	-	-	-		
TLPD-27	637.5	-60.7	231.5	47	13	6	41	12	S1	72	60	F12	71	40	-	-	-	-	-	-		
TLPD-27	645.3	-59.5	232.0	51	12	9	42	12	S1	69	60	F12	69	46	57	40	315	S0	74	18	69	58
TLPD-27	655.5	-57.9	232.6	47	333	3	44	11	S1	75	61	L1	54	129	180	23	191	QV	36	251		
TLPD-27	655.5	-57.9	232.6	47	353	3	44	11	S1	75	61	F12	70	102	-	-	-	-	-	-		
TLPD-27	665.7	-57.4	232.7	54	-	10	44	11	S1	68	60	-	-	-	0	54	11	S0	68	60		
TLPD-27	683.5	-56.4	232.9	53	338	8	45	11	S1	70	60	L1	56	118	-	-	-	-	-	-		
TLPD-27	683.5	-56.4	232.9	53	5	8	45	11	S1	70	60	F12	70	65	-	-	-	-	-	-		
TLPD-27	746.1	-53.0	232.3	62	337	14	48	13	S1	65	59	L1	50	114	0	60	13	S0	66	59	8	333
TLPD-27	760.6	-52.3	232.2	61	340	12	49	13	S1	66	59	L1	53	113	-	-	-	-	-	-		
TLPD-27	760.6	-52.3	232.2	61	22	12	49	13	S1	66	59	F12	63	29	-	-	-	-	-	-		

drill hole	depth	plunge	azimuth	β	δ	min. error	ideal β/δ	Ref.θ	name	dip	dip dirn	name	plunge	trend	Ω	β	Ref.θ	name	dip	dip dirn	plunge	trend
TLPD-33	190.7	-78.6	235.6	21	352	2	23	6	S1	80	61	L1	77	105	10	26	356	QV	75	52		
TLPD-33	215.7	-78.5	236.1	10	329	13	23	5	S1	89	241	L1	58	154	-	-	-	-	-	-		
TLPD-33	215.7	-78.5	236.1	10	60	13	23	5	S1	89	241	F12	31	330	-	-	-	-	-	-		
TLPD-33	216.5	-78.5	236.1	19	340	4	23	5	S1	82	61	L1	68	132	-	-	-	-	-	-		
TLPD-33	216.5	-78.5	236.1	19	77	4	23	5	S1	82	61	F12	14	333	-	-	-	-	-	-		
TLPD-33	299.8	-71.9	241.7	22	338	8	30	359	S1	86	61	L1	68	141	-	-	-	-	-	-		
TLPD-33	299.8	-71.9	241.7	22	62	8	30	359	S1	86	61	F12	28	333	-	-	-	-	-	-		
TLPD-33	327.8	-65.2	241.1	30	-	7	37	360	S1	85	61	-	-	-	44	60	316	QV	51	34		
TLPD-33	427.1	-60.7	239.6	41	5	0	41	2	S1	78	61	L1	78	42	-	-	-	-	-	-		
TLPD-33	427.1	-60.7	239.6	41	5	0	41	2	S1	78	61	F12	78	42	-	-	-	-	-	-		
TLPD-33	464.9	-59.0	241.1	45	345	2	43	360	S1	76	61	L1	70	109	12	30	348	S0	90	231	35	141
TLPD-33	465.1	-59.0	241.1	47	345	4	43	360	S1	74	61	L1	68	105	20	40	340	S0	80	46	66	112
TLPD-33	467.7	-59.0	241.1	42	335	1	43	360	S1	79	61	L1	63	129	3	43	357	S0	78	59	62	353
TLPD-33	467.7	-59.0	241.1	42	323	1	43	360	S1	79	61	F12	52	137	-	-	-	-	-	-		
TLPD-33	470.6	-59.0	241.1	42	337	1	43	360	S1	79	61	L1	65	127	0	43	360	S0	78	61	0	151
TLPD-33	489.8	-59.0	241.1	42	-	1	43	360	S1	79	61	-	-	-	9	33	351	S0	88	53	40	141
TLPD-34	203.5	-55.0	237.1	47	341	0	47	6	S1	78	61	L1	65	124	-	-	-	-	-	-		
TLPD-34	203.5	-55.0	237.1	47	26	0	47	6	S1	78	61	F12	64	358	-	-	-	-	-	-		
TLPD-34	204.5	-55.0	237.1	48	-	1	47	6	S1	77	61	-	-	-	15	53	351	S0	72	51	57	352
TLPD-34	209.4	-55.0	237.2	49	347	2	47	5	S1	76	61	L1	69	111	0	51	5	S0	74	61	3	332
TLPD-34	209.4	-55.0	237.2	49	24	2	47	5	S1	76	61	F12	65	4	-	-	-	-	-	-		
TLPD-34	215.5	-54.9	237.3	53	12	6	47	5	S1	72	61	F12	70	34	20	55	345	S0	69	48	67	21
TLPD-34	216.2	-54.9	237.3	52	341	5	47	5	S1	73	61	L1	62	115	-	-	-	-	-	-		
TLPD-34	216.2	-54.9	237.3	52	25	5	47	5	S1	73	61	F12	63	7	-	-	-	-	-	-		
TLPD-34	217.8	-54.9	237.3	52	330	5	47	5	S1	73	61	L1	53	127	355	57	10	S0	68	63	24	143
TLPD-34	217.8	-54.9	237.3	52	25	5	47	5	S1	73	61	F12	63	7	-	-	-	-	-	-		
TLPD-34	218.4	-54.9	237.3	50	42	3	47	5	S1	75	61	F12	49	349	42	53	323	S0	68	34	65	6
TLPD-34	301.6	-54.1	237.3	54	337	6	48	5	S1	72	61	L1	58	118	355	54	10	S0	72	64	71	77
TLPD-34	314.5	-54.0	237.1	51	348	3	48	6	S1	75	61	L1	69	108	345	38	21	S0	86	73	46	347
TLPD-34	317.4	-54.0	237.1	40	348	8	48	6	S1	86	61	L1	74	137	355	42	11	S0	84	65	57	145
TLPD-34	320.6	-54.0	237.1	45	7	3	48	6	S1	81	61	L1	80	39	12	32	354	S0	86	232	36	145
TLPD-34	322.4	-54.0	237.1	50	352	2	48	6	S1	76	61	L1	72	101	0	48	6	S0	78	61	3	332

drill hole	depth	plunge	azimuth	β	δ	min. error	ideal β/δ	Ref.θ	name	dip	dip dirn	name	plunge	trend	Ω	β	Ref.θ	name	dip	dip dirn	plunge	trend
TLPD-34	322.4	-54.0	237.1	50	75	2	48	6	S1	76	61	F12	18	336	-	-	-	-	-	-		
TLPD-36W	110.0	-58.5	235.5	48	22	5	43	7	S1	73	61	L1	66	12	36	52	331	S0	67	37	65	10
TLPD-36W	110.0	-58.5	235.5	48	35	5	43	7	S1	73	61	F12	55	356	-	-	-	-	-	-		
TLPD-36W	222.0	-51.8	236.3	55	346	5	50	7	S1	73	61	L1	65	110	35	50	332	S0	76	38	73	72
TLPD-36W	222.7	-51.8	236.3	48	3	2	50	7	S1	80	61	L1	80	70	345	5	22	S0	60	262	26	336
TLPD-36W	222.7	-51.8	236.3	48	350	2	50	7	S1	80	61	F12	72	117	-	-	-	-	-	-		
TLPD-36W	226.3	-51.6	236.4	54	340	4	50	7	S1	74	61	L1	61	120	355	40	12	S0	88	66	19	336
TLPD-36W	231.7	-51.3	236.6	57	346	6	51	7	S1	72	60	L1	64	107	0	33	7	S0	85	242	4	332
TLPD-36W	237.3	-51.1	236.8	56	342	5	51	7	S1	73	61	L1	62	115	5	31	2	S0	82	238	6	149
TLPD-36W	244.5	-50.7	237.1	64	-	13	51	6	S1	65	60	-	-	-	339	26	27	S0	80	262	31	346
TLPD-36W	251.5	-50.4	237.3	58	337	7	51	6	S1	72	61	L1	58	119	356	59	10	S0	70	63	54	123
TLPD-36W	251.5	-50.4	237.3	58	4	7	51	6	S1	72	61	F12	72	60	-	-	-	-	-	-		
TLPD-36W	255.1	-50.2	237.4	58	-	6	52	6	S1	72	61	-	-	-	27	35	339	S0	87	220	43	133
TLPD-36W	269.1	-49.3	237.8	61	-	8	53	5	S1	70	60	-	-	-	357	47	8	S0	83	63	11	335
TLPD-36W	269.4	-49.2	237.8	61	-	8	53	5	S1	70	60	-	-	-	335	20	30	S0	74	267	35	346
TLPD-36W	277.5	-48.6	238.0	62	337	9	53	5	S1	69	60	L1	57	115	350	42	15	S0	88	69	23	340
TLPD-36W	286.1	-47.9	238.2	59	350	5	54	5	S1	73	61	L1	69	100	10	50	355	S0	82	55	32	140
TLPD-36W	292.6	-47.4	238.3	61	346	7	54	4	S1	72	61	F12	65	105	355	36	9	S0	84	246	12	335
TLPD-36W	301.0	-46.8	238.5	66	-	11	55	4	S1	67	60	-	-	-	113	45	251	S0	48	354	48	358
TLPD-36W	314.6	-45.5	238.6	61	314	5	56	4	S1	73	61	L1	39	137	337	37	27	S0	86	260	42	347
TLPD-36W	328.0	-44.3	238.6	63	-	5	58	4	S1	73	61	-	-	-	55	53	309	S0	73	30	72	50
TLPD-36W	338.2	-43.3	238.6	60	341	1	59	5	S1	77	61	L1	64	122	70	58	295	S0	65	26	62	357
TLPD-37	84.7	-72.4	236.7	30	-	0	30	5	S1	78	61	-	-	-	0	33	5	S0	75	61	1	331
TLPD-37	103.2	-70.2	237.8	33	13	1	32	4	S1	77	61	F12	72	19	60	37	304	S0	65	11	65	1
TLPD-37	112.0	-68.9	238.2	35	-	2	33	3	S1	76	61	-	-	-	60	31	303	S0	72	9	72	19
TLPD-37	118.2	-67.9	238.6	31	-	3	34	3	S1	81	61	-	-	-	5	32	358	S0	80	57	74	4
TLPD-37	124.1	-67.0	238.9	45	-	10	35	2	S1	68	61	-	-	-	0	40	2	S0	73	61	1	331
TLPD-37	128.5	-66.4	239.2	30	-	6	36	2	S1	84	61	-	-	-	35	36	327	S0	75	32	69	348
TLPD-37	136.6	-65.3	239.6	45	-	8	37	2	S1	70	61	-	-	-	-	-	-	-	-	-		
TLPD-37	143.1	-64.4	239.9	50	340	12	38	1	S1	66	61	L1	58	103	10	51	351	S0	64	54	63	33
TLPD-37	192.9	-58.2	242.2	56	330	12	44	358	S1	66	61	L1	53	115	10	57	348	S0	64	55	62	27
TLPD-37	192.9	-58.2	242.2	56	4	12	44	358	S1	66	61	F12	65	49	-	-	-	-	-	-		

drill hole	depth	plunge	azimuth	β	δ	min. error	ideal β/δ	Ref.θ	name	dip	dip dirn	name	plunge	trend	Ω	β	Ref.θ	name	dip	dip dirn	plunge	trend
TLPD-37	201.5	-57.7	242.3	35	353	9	44	358	S1	87	61	L1	83	127	32	64	326	S0	56	45	23	332
TLPD-37	211.0	-57.2	242.4	52	347	7	45	358	S1	71	61	L1	68	94	5	25	353	S0	82	236	10	147
TLPD-37	219.0	-56.7	242.5	58	2	13	45	358	S1	65	61	F12	65	53	335	23	23	S0	82	264	33	349
TLPD-37	239.0	-55.6	242.6	59	-	13	46	358	S1	65	61	-	-	-	195	17	163	S0	41	217	15	144
TLPD-37	242.3	-55.4	242.6	50	329	3	47	358	S1	75	61	L1	57	126	353	38	5	S0	86	66	23	338
TLPD-37	248.5	-55.0	242.7	53	-	6	47	358	S1	72	61	-	-	-	143	24	215	S0	40	296	30	342
TLPD-45	194.3	-60.9	231.2	40	-	1	41	13	S1	79	61	-	-	-	15	29	358	S0	90	229	45	139
TLPD-45	194.9	-60.9	231.3	40	354	1	41	13	S1	79	61	L1	73	109	24	35	349	S0	84	42	73	111
TLPD-45	194.9	-60.9	231.3	40	89	1	41	13	S1	79	61	F12	7	332	-	-	-	-	-	-		
TLPD-45	210.8	-59.9	232.6	50	-	8	42	11	S1	70	60	-	-	-	120	18	251	QV	65	315		
TLPD-45	216.8	-59.5	233.1	37	5	5	42	10	S1	83	61	F12	83	64	0	34	10	S0	86	62	5	332
TLPD-45	220.2	-59.3	233.4	39	30	3	42	10	S1	81	61	L1	64	349	-	-	-	-	-	-		
TLPD-45	220.2	-59.3	233.4	39	50	3	42	10	S1	81	61	F12	45	340	-	-	-	-	-	-		
TLPD-45	220.2	-59.3	233.4	39	16	3	42	10	S1	81	61	F12	76	10	-	-	-	-	-	-		
TLPD-45	230.3	-58.7	234.2	62	339	19	43	9	S1	59	59	F12	50	103	5	64	4	S0	57	56	42	2
TLPD-45	230.3	-58.7	234.2	62	50	19	43	9	S1	59	59	F12	38	357	-	-	-	-	-	-		
TLPD-45	243.1	-57.9	235.2	62	13	18	44	8	S1	60	59	L1	59	44	-	-	-	-	-	-		
TLPD-45	243.1	-57.9	235.2	62	321	18	44	8	S1	60	59	F12	39	122	-	-	-	-	-	-		
TLPD-45	243.1	-57.9	235.2	62	38	18	44	8	S1	60	59	F12	46	7	-	-	-	-	-	-		
TLPD-53	219.6	-66.9	214.9	30	12	2	32	31	S1	80	62	L1	80	60	-	-	-	-	-	-		
TLPD-53	219.6	-66.9	214.9	30	271	2	32	31	S1	80	62	F12	11	333	-	-	-	-	-	-		
TLPD-53	224.0	-66.8	215.4	12	283	21	33	30	S1	82	245	F12	1	155	-	-	-	-	-	-		
TLPD-53	237.1	-66.6	216.6	40	75	7	33	29	S1	71	60	F12	25	339	-	-	-	-	-	-		
TLPD-53	266.1	-66.0	218.1	50	-	16	34	27	S1	62	58	-	-	-	-	-	-	-	-	-		
TLPD-53	331.5	-65.1	219.8	30	8	5	35	26	S1	83	62	L1	82	81	-	-	-	-	-	-		
TLPD-53	331.5	-65.1	219.8	30	283	5	35	26	S1	83	62	F12	2	152	-	-	-	-	-	-		
TLPD-53	339.2	-65.1	220.2	33	70	2	35	25	S1	80	61	F12	30	337	-	-	-	-	-	-		
TLPD-53	339.7	-65.1	220.3	33	271	2	35	25	S1	80	61	F12	9	333	-	-	-	-	-	-		
TLPD-65A	712.3	-55.2	49.3	27	-	5	22	12	S1	83	60	-	-	-	0	27	12	S0	83	60		
TLPD-65A	739.4	-53.2	49.9	37	-	13	24	12	S1	89	239	-	-	-	345	19	27	S0	76	76	47	150
TLPD-65A	802.7	-48.3	52.9	30	-	1	29	9	S1	79	61	-	-	-	0	30	9	S0	79	61		
TLPD-65A	803.8	-48.2	52.9	31	-	2	29	9	S1	80	61	-	-	-	0	31	9	S0	80	61		

drill hole	depth	plunge	azimuth	β	δ	min. error	ideal β/δ	Ref.θ	name	dip	dip dirn	name	plunge	trend	Ω	β	Ref.θ	name	dip	dip dirn	plunge	trend
TLPD-65A	831.3	-44.6	53.1	36	-	3	33	9	S1	81	61	-	-	-	335	42	34	S0	88	258	57	345
TLPD-65A	943.7	-37.1	56.8	44	15	3	41	5	S1	81	61	L1	76	112	0	42	5	S0	79	61	4	150
TLPD-65A	944.1	-37.1	56.9	42	-	1	41	5	S1	79	61	-	-	-	0	42	5	S0	79	61		
TLPD-65A	959.6	-36.6	57.1	37	-	4	41	5	S1	74	61	-	-	-	0	37	5	S0	74	61		
TLPD-65A	709.7	-55.4	49.3	35	-	13	22	12	S1	89	239	-	-	-	0	30	12	QV	86	60		
TLPD-65A	710.6	-55.4	49.3	42	-	20	22	12	S1	82	239	-	-	-	4	36	8	QV	88	236		
TLPD-65A	728.2	-54.0	49.7	29	-	6	23	12	S1	84	60	-	-	-	0	29	12	QV	84	60		
TLPD-65A	729.9	-53.9	49.7	20	-	3	23	12	S1	75	61	-	-	-	180	52	192	QV	8	130		
TLPD-65A	731.3	-53.8	49.7	45	-	22	23	12	S1	81	238	-	-	-	185	57	187	QV	5	181		
TLPD-65A	747.3	-52.6	50.1	23	-	2	25	12	S1	76	61	-	-	-	180	70	192	QV	18	217		
TLPD-65A	747.5	-52.6	50.1	24	-	1	25	12	S1	77	61	-	-	-	0	24	12	QV	77	61		
TLPD-65A	783.2	-49.8	51.9	66	-	38	28	10	S1	64	236	-	-	-	180	63	190	QV	14	213		
TLPD-65A	785.7	-49.7	52.0	62	-	34	28	10	S1	68	237	-	-	-	0	62	10	QV	68	237		
TLPD-65A	798.5	-48.7	52.7	40	-	11	29	9	S1	89	60	-	-	-	25	40	344	QV	90	41		
TLPD-65A	799.4	-48.6	52.7	40	-	11	29	9	S1	89	60	-	-	-	180	74	189	QV	26	227		
TLPD-65A	803.7	-48.3	52.9	33	-	4	29	9	S1	82	61	-	-	-	180	38	189	QV	12	89		
TLPD-65A	813.3	-47.1	53.1	40	-	10	30	9	S1	87	60	-	-	-	178	52	191	QV	9	182		
TLPD-65A	814.7	-46.9	53.1	32	-	1	31	9	S1	79	61	-	-	-	187	65	182	QV	18	230		
TLPD-65A	815.7	-46.8	53.1	20	-	11	31	9	S1	67	62	-	-	-	0	13	9	QV	60	63		
TLPD-65A	816.2	-46.7	53.1	20	-	11	31	9	S1	67	62	-	-	-	180	57	189	QV	12	208		
TLPD-65A	817.1	-46.6	53.1	18	-	13	31	9	S1	65	63	-	-	-	180	30	189	QV	18	79		
TLPD-65A	818.0	-46.5	53.1	18	-	13	31	9	S1	65	63	-	-	-	0	11	9	QV	58	64		
TLPD-65A	819.3	-46.3	53.1	35	-	4	31	9	S1	82	61	-	-	-	0	35	9	QV	82	61		
TLPD-65A	820.2	-46.2	53.1	23	-	8	31	9	S1	70	62	-	-	-	20	23	349	QV	70	42		
TLPD-65A	821.8	-45.9	53.1	25	-	7	32	9	S1	71	62	-	-	-	0	25	9	QV	71	62		
TLPD-65A	829.8	-44.8	53.1	32	-	1	33	9	S1	77	61	-	-	-	0	23	9	QV	68	62		
TLPD-65A	830.3	-44.8	53.1	32	-	1	33	9	S1	77	61	-	-	-	0	23	9	QV	68	62		
TLPD-65A	830.7	-44.7	53.1	32	-	1	33	9	S1	77	61	-	-	-	30	26	339	QV	73	34		
TLPD-65A	831.2	-44.6	53.1	32	-	1	33	9	S1	77	61	-	-	-	0	3	9	QV	48	65		
TLPD-65A	831.4	-44.6	53.1	41	-	8	33	9	S1	86	60	-	-	-	10	30	359	QV	75	52		
TLPD-65A	831.5	-44.6	53.1	31	-	2	33	9	S1	76	61	-	-	-	0	32	9	QV	77	61		
TLPD-65A	831.6	-44.6	53.1	34	-	1	33	9	S1	79	61	-	-	-	0	30	9	QV	75	61		

drill hole	depth	plunge	azimuth	β	δ	min. error	ideal β/δ	Ref.θ	name	dip	dip dirn	name	plunge	trend	Ω	β	Ref.θ	name	dip	dip dirn	plunge	trend
TLPD-65A	831.7	-44.6	53.1	34	-	1	33	9	S1	79	61	-	-	-	175	57	194	QV	15	203		
TLPD-65A	832.2	-44.5	53.1	41	-	8	33	9	S1	86	60	-	-	-	310	25	59	QV	88	104		
TLPD-65A	835.2	-44.1	53.1	35	-	2	33	9	S1	80	61	-	-	-	340	30	29	QV	79	79		
TLPD-65A	836.0	-44.0	53.1	43	-	9	34	9	S1	87	60	-	-	-	0	30	9	QV	74	61		
TLPD-65A	836.8	-43.9	53.1	51	-	17	34	9	S1	85	239	-	-	-	180	60	189	QV	17	217		
TLPD-65A	837.0	-43.8	53.1	40	-	6	34	9	S1	84	60	-	-	-	180	64	189	QV	21	222		
TLPD-65A	838.9	-43.6	53.1	48	-	14	34	9	S1	88	239	-	-	-	0	48	9	QV	88	239		
TLPD-65A	839.4	-43.5	53.1	40	-	6	34	9	S1	84	60	-	-	-	0	40	9	QV	84	60		
TLPD-65A	839.4	-43.5	53.1	40	-	6	34	9	S1	84	60	-	-	-	180	44	189	QV	7	151		
TLPD-65A	846.5	-42.6	53.2	50	-	15	35	9	S1	87	239	-	-	-	0	50	9	QV	87	239		
TLPD-65A	847.7	-42.5	53.2	40	-	5	35	9	S1	83	60	-	-	-	0	40	9	QV	83	60		
TLPD-65A	848.1	-42.4	53.2	51	-	16	35	9	S1	86	239	-	-	-	180	52	189	QV	11	203		
TLPD-65A	848.3	-42.4	53.2	51	-	16	35	9	S1	86	239	-	-	-	215	78	154	QV	37	242		
TLPD-65A	856.0	-41.6	53.5	40	-	4	36	9	S1	82	61	-	-	-	335	48	34	QV	85	256		
TLPD-65A	856.3	-41.5	53.5	44	-	8	36	9	S1	86	60	-	-	-	0	44	9	QV	86	60		
TLPD-65A	857.9	-41.3	53.5	42	-	6	36	9	S1	84	60	-	-	-	180	30	189	QV	14	89		
TLPD-65A	858.3	-41.3	53.5	45	-	9	36	9	S1	87	60	-	-	-	180	64	189	QV	23	223		
TLPD-65A	867.1	-40.3	53.8	43	-	6	37	9	S1	84	60	-	-	-	0	43	9	QV	84	60		
TLPD-65A	868.4	-40.2	53.8	41	-	4	37	9	S1	82	61	-	-	-	325	30	44	QV	81	91		
TLPD-65A	868.9	-40.1	53.8	41	-	4	37	9	S1	82	61	-	-	-	180	72	189	QV	32	229		
TLPD-65A	869.3	-40.1	53.8	33	-	4	37	9	S1	74	62	-	-	-	0	33	9	QV	74	62		
TLPD-65A	869.3	-40.1	53.8	33	-	4	37	9	S1	74	62	-	-	-	180	50	189	QV	12	205		
TLPD-65A	869.8	-40.0	53.8	40	-	2	38	9	S1	80	61	-	-	-	180	72	189	QV	32	229		
TLPD-65A	872.5	-39.7	53.9	10	-	28	38	9	S1	50	65	-	-	-	0	10	9	QV	50	65		
TLPD-65A	872.5	-39.7	53.9	10	-	28	38	9	S1	50	65	-	-	-	180	51	189	QV	13	208		
TLPD-65A	873.0	-39.7	53.9	45	-	7	38	9	S1	85	60	-	-	-	0	45	9	QV	85	60		
TLPD-65A	873.2	-39.7	53.9	50	-	12	38	9	S1	90	60	-	-	-	0	50	9	QV	90	60		
TLPD-65A	874.0	-39.6	54.0	50	-	12	38	9	S1	90	60	-	-	-	15	50	354	QV	90	50		
TLPD-65A	874.7	-39.5	54.0	50	-	12	38	9	S1	90	60	-	-	-	0	47	9	QV	87	60		
TLPD-65A	885.5	-38.8	54.3	51	-	12	39	8	S1	90	240	-	-	-	25	40	343	QV	80	41		
TLPD-65A	885.7	-38.8	54.3	60	-	21	39	8	S1	81	239	-	-	-	20	45	348	QV	84	46		
TLPD-65A	885.7	-38.8	54.3	60	-	21	39	8	S1	81	239	-	-	-	45	42	323	QV	87	28		

drill hole	depth	plunge	azimuth	β	δ	min. error	ideal β/δ	Ref.θ	name	dip	dip dirn	name	plunge	trend	Ω	β	Ref.θ	name	dip	dip dirn	plunge	trend
TLPD-65A	886.3	-38.8	54.3	61	-	22	39	8	S1	80	238	-	-	-	45	42	323	QV	87	28		
TLPD-65A	887.8	-38.7	54.4	57	-	18	39	8	S1	84	239	-	-	-	170	45	198	QV	15	175		
TLPD-65A	888.9	-38.7	54.4	43	-	4	39	8	S1	82	61	-	-	-	175	29	193	QV	15	107		
TLPD-65A	889.3	-38.7	54.4	50	-	11	39	8	S1	89	60	-	-	-	145	36	223	QV	34	154		
TLPD-65A	889.6	-38.6	54.5	45	-	6	39	8	S1	84	60	-	-	-	180	29	188	QV	12	92		
TLPD-65A	889.9	-38.6	54.5	44	-	5	39	8	S1	83	60	-	-	-	165	35	203	QV	19	141		
TLPD-65A	889.9	-38.6	54.5	40	-	1	39	8	S1	79	61	-	-	-	180	27	188	QV	14	88		
TLPD-65A	890.1	-38.6	54.5	45	-	6	39	8	S1	84	60	-	-	-	0	43	8	QV	82	61		
TLPD-65A	890.2	-38.6	54.5	45	-	6	39	8	S1	84	60	-	-	-	12	58	356	QV	83	232		
TLPD-65A	890.3	-38.6	54.5	45	-	6	39	8	S1	84	60	-	-	-	0	40	8	QV	79	61		
TLPD-65A	891.2	-38.6	54.5	50	-	11	39	8	S1	89	60	-	-	-	322	32	46	QV	83	93		
TLPD-65A	891.7	-38.6	54.5	50	-	11	39	8	S1	89	60	-	-	-	180	60	188	QV	22	224		
TLPD-65A	891.8	-38.6	54.5	50	-	11	39	8	S1	89	60	-	-	-	180	60	188	QV	22	224		
TLPD-65A	891.8	-38.6	54.5	50	-	11	39	8	S1	89	60	-	-	-	155	40	213	QV	26	158		
TLPD-65A	892.0	-38.6	54.5	50	-	11	39	8	S1	89	60	-	-	-	330	50	38	QV	85	258		
TLPD-65A	892.1	-38.6	54.5	50	-	11	39	8	S1	89	60	-	-	-	180	49	188	QV	12	208		
TLPD-65A	892.2	-38.6	54.5	50	-	11	39	8	S1	89	60	-	-	-	0	50	8	QV	89	60		
TLPD-65A	893.5	-38.5	54.6	44	-	5	39	8	S1	83	60	-	-	-	0	44	8	QV	83	60		
TLPD-65A	894.7	-38.5	54.6	52	-	13	39	8	S1	89	240	-	-	-	0	52	8	QV	89	240		
TLPD-65A	902.5	-38.2	54.9	43	-	4	39	8	S1	82	61	-	-	-	10	37	358	QV	75	53		
TLPD-65A	908.2	-38.0	55.1	48	-	8	40	8	S1	86	60	-	-	-	0	50	8	QV	88	60		
TLPD-65A	908.3	-38.0	55.1	48	-	8	40	8	S1	86	60	-	-	-	322	48	46	QV	85	264		
TLPD-65A	908.6	-38.0	55.1	50	-	10	40	8	S1	88	60	-	-	-	315	23	53	QV	78	103		
TLPD-65A	908.7	-38.0	55.1	50	-	10	40	8	S1	88	60	-	-	-	340	20	28	QV	64	84		
TLPD-65A	908.8	-38.0	55.1	45	-	5	40	8	S1	83	60	-	-	-	0	43	8	QV	81	61		
TLPD-65A	908.9	-38.0	55.1	45	-	5	40	8	S1	83	60	-	-	-	42	48	326	QV	89	213		
TLPD-65A	909.1	-38.0	55.1	60	-	20	40	8	S1	82	239	-	-	-	335	50	33	QV	87	255		
TLPD-65A	909.1	-38.0	55.1	60	-	20	40	8	S1	82	239	-	-	-	110	3	258	QV	78	140		
TLPD-65A	909.2	-38.0	55.1	60	-	20	40	7	S1	82	239	-	-	-	270	88	97	QV	52	238		
TLPD-65A	909.6	-38.0	55.1	51	-	11	40	7	S1	89	60	-	-	-	355	46	12	QV	85	64		
TLPD-65A	909.7	-38.0	55.1	51	-	11	40	7	S1	89	60	-	-	-	310	35	57	QV	90	279		
TLPD-65A	910.0	-38.0	55.1	44	-	4	40	7	S1	82	61	-	-	-	350	51	17	QV	90	246		

drill hole	depth	plunge	azimuth	β	δ	min. error	ideal β/δ	Ref.θ	name	dip	dip dirn	name	plunge	trend	Ω	β	Ref.θ	name	dip	dip dirn	plunge	trend
TLPD-65A	910.4	-38.0	55.2	45	-	5	40	7	S1	83	60	-	-	-	15	49	352	QV	87	50		
TLPD-65A	910.7	-38.0	55.2	55	-	15	40	7	S1	87	239	-	-	-	65	44	302	QV	83	197		
TLPD-65A	919.1	-37.7	55.6	33	-	7	40	7	S1	71	62	-	-	-	28	33	339	QV	73	37		
TLPD-65A	919.4	-37.7	55.6	33	-	7	40	7	S1	71	62	-	-	-	338	33	29	QV	76	80		
TLPD-65A	919.6	-37.7	55.6	33	-	7	40	7	S1	71	62	-	-	-	0	33	7	QV	71	62		
TLPD-65A	920.2	-37.7	55.7	41	-	1	40	7	S1	79	61	-	-	-	10	41	357	QV	79	53		
TLPD-65A	921.1	-37.7	55.7	40	-	0	40	7	S1	78	61	-	-	-	0	40	7	QV	78	61		
TLPD-65A	922.6	-37.7	55.8	41	-	1	40	7	S1	79	61	-	-	-	175	73	192	QV	36	230		
TLPD-65A	922.8	-37.7	55.8	41	-	1	40	7	S1	79	61	-	-	-	0	43	7	QV	81	61		
TLPD-65A	923.1	-37.6	55.8	40	-	0	40	7	S1	78	61	-	-	-	15	40	352	QV	78	49		
TLPD-65A	926.0	-37.6	56.0	41	-	1	40	6	S1	79	61	-	-	-	0	41	6	QV	79	61		
TLPD-65A	927.0	-37.6	56.0	45	-	5	40	6	S1	83	61	-	-	-	0	45	6	QV	83	61		
TLPD-65A	944.7	-37.1	56.9	45	-	4	41	5	S1	82	61	-	-	-	215	29	150	QV	26	336		
TLPD-65A	946.0	-37.1	57.0	40	-	1	41	5	S1	77	61	-	-	-	180	28	185	QV	10	84		
TLPD-65A	946.1	-37.1	57.0	41	-	0	41	5	S1	78	61	-	-	-	0	41	5	QV	78	61		
TLPD-65A	947.2	-37.0	57.0	43	-	2	41	5	S1	80	61	-	-	-	0	43	5	QV	80	61		
TLPD-65A	947.4	-37.0	57.0	43	-	2	41	5	S1	80	61	-	-	-	212	44	153	QV	21	300		
TLPD-65A	982.0	-35.8	57.4	45	-	3	42	5	S1	81	61	-	-	-	0	40	5	QV	76	61		
TLPD-65A	983.1	-35.8	57.5	42	-	0	42	5	S1	78	61	-	-	-	0	35	5	QV	71	61		
TLPD-65A	983.3	-35.8	57.5	42	-	0	42	5	S1	78	61	-	-	-	70	23	295	QV	85	0		
TLPD-66	40.9	-60.0	239.1	33	345	9	42	3	S1	87	61	L1	73	141	-	-	-	-	-	-		
TLPD-66	46.5	-60.0	239.1	25	28	17	42	3	S1	85	241	L1	63	322	345	28	18	S0	89	254	72	167
TLPD-66	52.8	-60.0	239.1	30	-	12	42	3	S1	90	61	-	-	-	330	30	33	S0	86	87	81	151
TLPD-66	54.7	-60.0	239.1	25	-	17	42	3	S1	85	241	-	-	-	5	30	358	S0	90	57	42	327
TLPD-66	56.3	-60.0	239.1	30	-	12	42	3	S1	90	61	-	-	-	20	35	343	S0	84	45	69	331
TLPD-66	65.3	-59.8	239.1	21	349	21	42	3	S1	81	241	L1	75	188	-	-	-	-	-	-		
TLPD-66	65.3	-59.8	239.1	21	348	21	42	3	S1	81	241	F12	74	185	-	-	-	-	-	-		
TLPD-66	78.1	-59.4	239.1	25	-	18	43	3	S1	84	241	-	-	-	14	25	349	S0	85	229	84	258
TLPD-66	79.5	-59.4	239.1	23	-	20	43	3	S1	82	241	-	-	-	-	-	-	-	-	-		
TLPD-66	114.5	-55.1	241.2	44	-	3	47	360	S1	81	61	-	-	-	65	39	295	S0	71	13	70	357

Drill hole	Depth	Relative facing	Evidence	Reliability
TLPD-12	552.35	down-hole	load cast	3
TLPD-12	575	up-hole	load cast	4
TLPD-12W3	379.7	up-hole	graded	4
TLPD-12W3	381.4	up-hole	graded	4
TLPD-12W3	500.2	down-hole	graded & ball & pillow	3
TLPD-17W	472	up-hole	graded	4
TLPD-17W	484.2	up-hole	load cast	4
TLPD-17W	485.3	up-hole	graded	5
TLPD-18	137	down-hole	graded	3
TLPD-18	223.5	up-hole	graded	5
TLPD-18	292.5	up-hole	graded	5
TLPD-18	293	up-hole	graded	5
TLPD-18	435	up-hole	graded	5
TLPD-18	442	up-hole	ball & pillow	4
TLPD-18	480.2	up-hole	load cast	4
TLPD-20	295.8	up-hole	graded	5
TLPD-20	301.35	up-hole	load cast	3
TLPD-20	303.4	up-hole	graded	5
TLPD-20	423.9	down-hole	ball & pillow	4
TLPD-20	458.3	up-hole	graded	4
TLPD-27	39	up-hole	flame	5
TLPD-27	39.45	down-hole	flame	5
TLPD-27	40.25	up-hole	load cast	4
TLPD-27	40.9	up-hole	load cast	4
TLPD-27	57.25	down-hole	graded	5
TLPD-27	58.7	up-hole	flame	5
TLPD-27	58.8	down-hole	ball & pillow	3
TLPD-27	59.2	up-hole	load cast	3
TLPD-27	59.75	up-hole	flame	5
TLPD-27	200.7	up-hole	load cast	5
TLPD-27	585	down-hole	load cast	5
TLPD-27	585.8	down-hole	graded	5
TLPD-27	587	down-hole	load cast	5
TLPD-27	587.5	down-hole	ball & pillow	5
TLPD-27	594.2	down-hole	load cast	4

Drill hole	Depth	Relative facing	Evidence	Reliability
TLPD-27	644.7	down-hole	load cast	5
TLPD-27	645.5	down-hole	graded	5
TLPD-28A	40.9	down-hole	load cast	
TLPD-28A	60	down-hole	ball & pillow	
TLPD-28A	564.25	up-hole	load cast	
TLPD-33	61	up-hole	graded	5
TLPD-33	246.5	up-hole	load cast	5
TLPD-33	465.15	down-hole	load cast	3
TLPD-34	103.5	up-hole	graded	3
TLPD-34	315.2	down-hole	load cast	4
TLPD-36W	222	down-hole	load cast	4
TLPD-36W	270.75	up-hole	graded	4
TLPD-36W	277.05	down-hole	load cast	5
TLPD-36W	277.8	down-hole	graded	4
TLPD-36W	279	down-hole	graded	5
TLPD-36W	341	up-hole	graded	5
TLPD-36W	343.3	up-hole	graded	3
TLPD-37	129.5	down-hole	load cast	4
TLPD-37	249	down-hole	load cast	3
TLPD-37	249.4	down-hole	graded	4
TLPD-37	266.5	down-hole	load cast	5
TLPD-43	15.4	up-hole	graded	5
TLPD-43	25.5	up-hole	graded	5
TLPD-43	106.8	up-hole	graded	5
TLPD-43	286.75	up-hole	load cast	3
TLPD-44	274.6	down-hole	graded	4
TLPD-44	280.3	down-hole	graded	4
TLPD-46A	146.3	up-hole	load cast	5
TLPD-63	423.15	up-hole	load cast	5
TLPD-65A	647	down-hole	graded	4
TLPD-65A	730.1	down-hole	load cast	5
TLPD-65A	730.5	down-hole	graded	5
TLPD-65A	739.3	down-hole	load cast	5
TLPD-65A	739.6	down-hole	graded	5
TLPD-65A	802.1	down-hole	load cast	4

Drill hole	Depth	Relative facing	Evidence	Reliability
TLPD-65A	804.2	down-hole	load cast	4
TLPD-65A	804.7	down-hole	load cast	4
TLPD-65A	807.3	up-hole	load cast	4
TLPD-65A	830.7	up-hole	graded	5
TLPD-65A	843	down-hole	load cast	4
TLPD-65A	860.5	down-hole	load cast	4
TLPD-65A	911.5	down-hole	graded	3
TLPD-65A	939.9	up-hole	load cast	?
TLPD-65A	943.55	down-hole	flame	5
TLPD-65A	944.2	down-hole	flame	5
TLPD-65A	944.35	down-hole	flame	5
TLPD-65A	949.3	up-hole	load cast	
TLPD-65A	949.7	up-hole	load cast	
TLPD-65A	956.1	up-hole	flame	5
TLPD-65A	956.3	up-hole	flame	5
TLPD-65A	963	up-hole	graded	4
TLPD-65A	988	up-hole	graded	5
TLPD-66	45	up-hole	graded	5
TLPD-66	53	up-hole	load cast	5
TLPD-66	53.5	up-hole	graded	4
TLPD-66	77	up-hole	graded	4
TLPD-66	103	up-hole	graded	3
TLPD-66	115	up-hole	graded	5

Drill hole	Depth	Relative facing	Evidence	Reliability
TLPD-69	64	up-hole	graded	?
TLPD-69	78	up-hole	graded	?
TLPD-69	92.5	up-hole	graded	?
TLPD-69	112	up-hole	graded	4
TLPD-69	134	up-hole	graded	5
TLPD-69	303.25	down-hole	load cast	5
TLPD-69	304.3	down-hole	load cast	5
TLPD-69	403	up-hole	graded	3
TLPD-69	433.4	down-hole	graded	?
TLPD-69	452.5	down-hole	load cast	5
TLPD-69	453.4	down-hole	load cast	5
TLPD-69	479.3	up-hole	load cast	5
TLPD-69W1	303.3	down-hole	load cast	5
TLPD-69W1	304.35	down-hole	load cast	5
TLPD-69W1	435	up-hole	load cast	5
TLPD-69W1	520	up-hole	load cast	4
TLPD-70	438.3	up-hole	graded	4
TLPD-70	472.6	up-hole	load cast	4
TOD-10	59.5	up-hole	load cast	
TOD-10	81.3	up-hole	load cast	
TOD-10	149	down-hole	load cast	
TOD-10	153.5	up-hole	graded	
TOD-10	226.7	up-hole	load cast	

Notes:
Reliability index varies from 1 = poor to 5 = excellent

Label	Oxides:	Mineral	SiO_2	$FeCO_3$	$MnCO_3$	$MgCO_3$	$CaCO_3$	$BaCO_3$	$SrCO_3$	Na2Ca*2	K2Ca*2	$ZnCO_3$	Sum Ox
LP12428_perv carb1-8-1		Fe-dol	0.01	4.29	2.24	39.56	52.67	0.00	0.06	0.02	0.08	0.00	98.95
Lp12440 perv fine carb2-5-1		Fe-dol	0.03	3.04	2.36	40.42	53.01	0.03	0.00	0.23	0.00	0.03	99.15
Lp12440 carb trav1-1		dol	0.08	0.15	0.26	43.21	55.61	0.09	0.06	0.07	0.11	0.12	99.75
Lp12440 carb trav1-2		dol	0.23	0.14	0.28	42.67	57.10	0.04	0.01	0.04	0.00	0.00	100.51
Lp12440 carb trav1-3		dol	0.24	0.19	0.65	43.26	53.48	0.00	0.07	0.00	0.00	0.03	97.93
Lp12440 carb trav1-4		dol	0.19	0.01	0.71	43.28	54.23	0.00	0.05	0.00	0.00	0.05	98.51
Lp12440 carb trav1-5		dol	0.13	0.13	0.88	42.08	54.24	0.00	0.11	0.00	0.00	0.00	97.57
Lp12440 carb trav1-6		dol	0.14	0.82	1.06	41.27	54.19	0.00	0.09	0.13	0.00	0.06	97.78
Lp12440 carb trav1-7		dol	0.17	0.12	1.29	39.67	56.61	0.06	0.00	0.00	0.01	0.11	98.04
Lp12440 carb trav1-8		dol	0.24	0.23	1.05	40.12	56.21	0.00	0.10	0.40	0.00	0.04	98.39
Lp12440 carb trav1-9		dol	0.09	0.19	0.49	40.50	57.99	0.03	0.16	0.00	0.00	0.06	99.52
Lp12440 carb trav1-10		dol	0.20	0.14	0.32	41.57	56.49	0.02	0.13	0.27	0.16	0.07	99.37
Lp12440 carb trav1-11		dol	0.29	0.34	0.38	41.87	55.88	0.03	0.00	0.00	0.19	0.05	99.04
Lp12440 carb trav1-12		dol	0.29	0.54	0.36	41.53	54.38	0.02	0.02	0.01	0.00	0.00	97.16
Lp12440 carb trav1-13		dol	0.27	0.86	0.51	41.48	55.17	0.01	0.06	0.46	0.00	0.00	98.83
Lp12440 carb trav1-14		dol	0.14	0.07	0.26	41.62	56.78	0.00	0.00	0.00	0.01	0.00	98.88
Lp12440 carb trav1-15		dol	0.11	0.03	0.37	40.75	56.79	0.00	0.00	0.17	0.00	0.03	98.25

Label	Cations:	Si	Fe2+	Mn2+	Mg	Ca	Ba	Sr	Na	K	Zn	Sum Cat	mgs	sid	ca	smt	rhd
LP12428_perv carb1-8-1		0.00	0.04	0.02	0.45	0.50	0.00	0.00	0.00	0.00	0.00	1.00	44.55	3.52	49.97	0.00	1.85
Lp12440 perv fine carb2-5-1		0.00	0.03	0.02	0.45	0.50	0.00	0.00	0.00	0.00	0.00	1.00	45.34	2.48	50.08	0.02	1.94
Lp12440 carb trav1-1		0.00	0.00	0.00	0.48	0.52	0.00	0.00	0.00	0.00	0.00	1.00	47.64	0.12	51.65	0.09	0.21
Lp12440 carb trav1-2		0.00	0.00	0.00	0.47	0.52	0.00	0.00	0.00	0.00	0.00	1.00	46.50	0.11	52.42	0.00	0.22
Lp12440 carb trav1-3		0.00	0.00	0.01	0.48	0.50	0.00	0.00	0.00	0.00	0.00	1.00	48.26	0.16	50.26	0.02	0.53
Lp12440 carb trav1-4		0.00	0.00	0.01	0.48	0.51	0.00	0.00	0.00	0.00	0.00	1.00	48.06	0.01	50.73	0.04	0.58
Lp12440 carb trav1-5		0.00	0.00	0.01	0.47	0.51	0.00	0.00	0.00	0.00	0.00	1.00	47.30	0.11	51.37	0.00	0.73
Lp12440 carb trav1-6		0.00	0.01	0.01	0.47	0.52	0.00	0.00	0.00	0.00	0.00	1.00	46.49	0.67	51.43	0.05	0.88
Lp12440 carb trav1-7		0.00	0.00	0.01	0.45	0.54	0.00	0.00	0.00	0.00	0.00	1.00	44.63	0.10	53.65	0.09	1.06
Lp12440 carb trav1-8		0.00	0.00	0.01	0.45	0.53	0.00	0.00	0.00	0.00	0.00	1.00	44.97	0.19	53.06	0.03	0.86
Lp12440 carb trav1-9		0.00	0.00	0.00	0.45	0.54	0.00	0.00	0.00	0.00	0.00	1.00	44.90	0.16	54.15	0.05	0.40
Lp12440 carb trav1-10		0.00	0.00	0.00	0.46	0.53	0.00	0.00	0.00	0.00	0.00	1.00	46.06	0.11	52.74	0.06	0.26
Lp12440 carb trav1-11		0.01	0.00	0.00	0.46	0.52	0.00	0.00	0.00	0.00	0.00	1.00	46.34	0.28	52.10	0.04	0.31
Lp12440 carb trav1-12		0.01	0.00	0.00	0.47	0.52	0.00	0.00	0.00	0.00	0.00	1.00	46.75	0.44	51.56	0.00	0.30
Lp12440 carb trav1-13		0.00	0.01	0.00	0.46	0.52	0.00	0.00	0.00	0.00	0.00	1.00	46.15	0.69	51.71	0.00	0.41
Lp12440 carb trav1-14		0.00	0.00	0.00	0.46	0.53	0.00	0.00	0.00	0.00	0.00	1.00	46.20	0.06	53.10	0.00	0.21
Lp12440 carb trav1-15		0.00	0.00	0.00	0.46	0.54	0.00	0.00	0.00	0.00	0.00	1.00	0.30	45.66	0.02	0.00	0.00

Label	Oxides:	Mineral	SiO_2	$FeCO_3$	$MnCO_3$	$MgCO_3$	$CaCO_3$	$BaCO_3$	$SrCO_3$	Na2Ca*2	K2Ca*2	$ZnCO_3$	Sum Ox
Lp12440 carb trav1-16		dol	0.24	0.12	0.39	41.83	57.10	0.00	0.09	0.10	0.00	0.03	99.91
Lp12440 carb trav1-17		dol	0.12	0.84	1.10	41.40	54.70	0.00	0.01	0.00	0.07	0.18	98.41
Lp12440 carb trav1-18		dol	0.35	0.27	0.83	42.83	54.14	0.00	0.00	0.00	0.00	0.00	98.43
Lp12440 carb trav1-19		dol	0.12	0.21	0.36	43.23	55.62	0.01	0.06	0.22	0.00	0.00	99.84
Lp12440 carb trav1-20		dol	0.05	0.06	0.22	42.88	55.69	0.03	0.02	0.00	0.00	0.08	99.03
Lp12476 perv carb1-4-1		Fe-dol	0.02	5.05	1.51	38.54	51.84	0.01	0.00	0.09	0.00	0.00	97.06
LP12503_perv carb2-7-1		Fe-dol	0.03	4.71	1.35	39.83	52.70	0.00	0.02	0.02	0.08	0.00	98.75
Lp12511_perv carb1-6-1		Fe-dol	0.02	5.23	2.05	38.18	51.97	0.00	0.09	0.00	0.00	0.00	97.55
Lp18365_perv clear dol 1-1-1		dol	0.00	7.08	1.64	38.22	52.34	0.00	0.05	0.04	0.09	0.00	99.46
Lp33390_dol traverse 1-3-1		dol	0.04	3.05	1.20	40.49	53.61	0.00	0.11	0.09	0.00	0.16	98.75
Lp33390_dol traverse 2-4-1		dol	0.01	2.10	0.50	38.47	57.25	0.01	0.00	0.18	0.00	0.09	98.62
Lp33390_dol traverse 3-5-1		dol	0.00	1.73	2.22	37.01	59.33	0.00	0.00	0.00	0.00	0.00	100.30
Lp33390_dol traverse 4-6-1		dol	0.03	1.85	0.40	39.36	57.55	0.00	0.01	0.00	0.04	0.00	99.25
Lp33390_dol traverse 5-7-1		Fe-dol	0.00	3.18	1.20	37.59	57.58	0.00	0.01	0.00	0.02	0.00	99.58
Lp36w197_dol rhomb 1-2-1		Fe-dol	0.00	4.26	2.45	39.09	54.03	0.04	0.02	0.00	0.00	0.05	99.95
LP36W214 carb traverse1-1		Fe-dol	0.07	5.98	5.73	34.80	51.19	0.00	0.12	0.00	0.25	0.19	98.34
LP36W214 carb traverse1-5		dol	0.09	0.02	3.72	38.30	58.40	0.08	0.04	0.02	0.00	0.14	100.80

Label	Cations:	Si	Fe2+	Mn2+	Mg	Ca	Ba	Sr	Na	K	Zn	Sum Cat	mgs	sid	ca	smt	rhd
Lp12440 carb trav1-16		0.00	0.00	0.00	0.46	0.53	0.00	0.00	0.00	0.00	0.00	1.00	0.31	45.94	0.10	0.00	0.06
Lp12440 carb trav1-17		0.00	0.01	0.01	0.46	0.52	0.00	0.00	0.00	0.00	0.00	1.00	0.90	46.39	0.69	0.00	0.01
Lp12440 carb trav1-18		0.01	0.00	0.01	0.48	0.51	0.00	0.00	0.00	0.00	0.00	1.00	0.68	47.48	0.22	0.00	0.00
Lp12440 carb trav1-19		0.00	0.00	0.00	0.48	0.52	0.00	0.00	0.00	0.00	0.00	1.00	0.29	47.53	0.17	0.00	0.04
Lp12440 carb trav1-20		0.00	0.00	0.00	0.48	0.52	0.00	0.00	0.00	0.00	0.00	1.00	0.18	47.56	0.05	0.00	0.01
Lp12476 perv carb1-4-1		0.00	0.04	0.01	0.44	0.50	0.00	0.00	0.00	0.00	0.00	1.00	1.27	44.27	4.22	0.00	0.00
LP12503_perv carb2-7-1		0.00	0.04	0.01	0.45	0.50	0.00	0.00	0.00	0.00	0.00	1.00	1.11	44.88	3.86	0.00	0.01
Lp12511_perv carb1-6-1		0.00	0.04	0.02	0.44	0.50	0.00	0.00	0.00	0.00	0.00	1.00	1.72	43.69	4.36	0.00	0.06
Lp18365_perv clear dol 1-1-1		0.00	0.06	0.01	0.43	0.50	0.00	0.00	0.00	0.00	0.00	1.00	1.36	43.07	5.81	0.00	0.03
Lp33390_dol traverse 1-3-1		0.00	0.03	0.01	0.46	0.51	0.00	0.00	0.00	0.00	0.00	1.00	0.99	45.53	2.50	0.00	0.07
Lp33390_dol traverse 2-4-1		0.00	0.02	0.00	0.43	0.54	0.00	0.00	0.00	0.00	0.00	1.00	0.42	43.38	1.73	0.00	0.00
Lp33390_dol traverse 3-5-1		0.00	0.01	0.02	0.41	0.56	0.00	0.00	0.00	0.00	0.00	1.00	1.81	41.17	1.40	0.00	0.00
Lp33390_dol traverse 4-6-1		0.00	0.02	0.00	0.44	0.54	0.00	0.00	0.00	0.00	0.00	1.00	0.33	43.91	1.50	0.00	0.00
Lp33390_dol traverse 5-7-1		0.00	0.03	0.01	0.42	0.54	0.00	0.00	0.00	0.00	0.00	1.00	0.99	42.07	2.59	0.00	0.01
Lp36w197_dol rhomb 1-2-1		0.00	0.04	0.02	0.44	0.51	0.00	0.00	0.00	0.00	0.00	1.00	2.01	43.65	3.46	0.00	0.01
LP36W214 carb traverse1-1		0.00	0.05	0.05	0.40	0.50	0.00	0.00	0.00	0.00	0.00	1.00	4.85	40.08	5.02	0.00	0.08
LP36W214 carb traverse1-5		0.00	0.00	0.03	0.42	0.54	0.00	0.00	0.00	0.00	0.00	1.00	3.01	42.30	0.02	0.00	0.02

Label	Oxides:	Mineral	SiO_2	$FeCO_3$	$MnCO_3$	$MgCO_3$	$CaCO_3$	$BaCO_3$	$SrCO_3$	Na2Ca*2	K2Ca*2	$ZnCO_3$	Sum Ox
LP36W214 carb traverse1-14		ank	2.63	0.40	2.99	41.98	47.85	0.00	0.00	3.37	0.74	0.06	100.04
LP36W214 carb traverse1-18		dol	0.11	0.01	3.36	38.90	55.29	0.00	0.01	0.51	0.17	0.00	98.37
Lp36w214_dol traverse 1-1-1		Fe-dol	0.02	5.61	6.84	33.04	53.27	0.01	0.06	0.27	0.00	0.17	99.29
Lp36w214_dol traverse 2-2-1		dol	0.08	0.75	6.92	35.77	54.86	0.01	0.00	0.02	0.00	0.00	98.40
Lp36w214_dol traverse 4-4-1		dol	0.09	0.13	3.67	39.81	57.07	0.00	0.08	0.28	0.23	0.00	101.36
Lp36w214_dol traverse 5-5-1		dol	0.02	0.09	4.62	39.89	54.01	0.03	0.01	0.08	0.04	0.00	98.80
Lp36w214_dol traverse 5-6-1		dol	0.01	0.15	5.22	39.88	53.98	0.00	0.11	0.00	0.02	0.05	99.41
LP46A113_carb band1		Mg-sid	0.11	50.97	1.50	48.45	0.54	0.08	0.07	0.67	0.26	0.25	102.90
Lp51a477_carb in ms band 1-1-1		dol	0.00	1.97	3.39	33.57	61.09	0.00	0.06	0.19	0.00	0.06	100.34
Lp51a482_clear dol rhomb 1-2-1		dol	0.00	2.93	4.78	37.49	54.22	0.02	0.12	0.03	0.00	0.00	99.58
Lp51a484_clear dol patch 1-5-1		dol	0.01	0.25	0.25	40.93	57.64	0.03	0.17	0.38	0.15	0.00	99.81
Lp51a484_type 5 dol in vein 1-6-1		dol	0.00	0.50	2.72	41.50	53.72	0.00	0.11	0.32	0.05	0.00	98.92
Lp51a484_type 1 dol in vein 1-7-1		dol	0.00	0.55	1.65	41.90	54.56	0.06	0.14	0.24	0.00	0.00	99.10
Lp51a484_zoned dol traverse 1-1		Fe-dol	0.03	2.88	2.66	39.73	53.80	0.00	0.42	0.06	0.03	0.12	99.72
Lp51a484_zoned dol traverse 1-2		Fe-dol	0.01	1.77	2.93	39.91	53.10	0.02	0.00	0.25	0.06	0.00	98.05
Lp51a484_zoned dol traverse 1-3		Fe-dol	0.03	1.31	0.95	41.36	55.33	0.00	0.01	0.14	0.00	0.05	99.18
Lp51a484_zoned dol traverse 1-4		Fe-dol	0.00	3.12	1.65	40.01	53.42	0.00	0.05	0.00	0.00	0.00	98.25

Label	Cations:	Si	Fe2+	Mn2+	Mg	Ca	Ba	Sr	Na	K	Zn	Sum Cat	mgs	sid	ca	smt	rhd
LP36W214 carb traverse1-14		0.04	0.00	0.02	0.45	0.44	0.00	0.00	0.01	0.00	0.00	0.96	2.36	45.06	0.32	0.00	0.00
LP36W214 carb traverse1-18		0.00	0.00	0.03	0.44	0.53	0.00	0.00	0.00	0.00	0.00	1.00	2.79	43.99	0.01	0.00	0.01
Lp36w214_dol traverse 1-1-1		0.00	0.05	0.06	0.38	0.51	0.00	0.00	0.00	0.00	0.00	1.00	5.75	37.84	4.68	0.00	0.04
Lp36w214_dol traverse 2-2-1		0.00	0.01	0.06	0.41	0.53	0.00	0.00	0.00	0.00	0.00	1.00	5.78	40.73	0.62	0.00	0.00
Lp36w214_dol traverse 4-4-1		0.00	0.00	0.03	0.44	0.53	0.00	0.00	0.00	0.00	0.00	1.00	2.95	43.61	0.10	0.00	0.05
Lp36w214_dol traverse 5-5-1		0.00	0.00	0.04	0.45	0.51	0.00	0.00	0.00	0.00	0.00	1.00	3.80	44.73	0.07	0.00	0.01
Lp36w214_dol traverse 5-6-1		0.00	0.00	0.04	0.45	0.51	0.00	0.00	0.00	0.00	0.00	1.00	4.28	44.60	0.12	0.00	0.07
LP46A113_carb band1		0.00	0.42	0.01	0.55	0.01	0.00	0.00	0.00	0.00	0.00	1.00	1.26	55.24	42.30	0.00	0.05
Lp51a477_carb in ms band 1-1-1		0.00	0.02	0.03	0.38	0.58	0.00	0.00	0.00	0.00	0.00	1.00	2.80	37.70	1.61	0.00	0.04
Lp51a482_clear dol rhomb 1-2-1		0.00	0.02	0.04	0.42	0.51	0.00	0.00	0.00	0.00	0.00	1.00	3.94	42.18	2.40	0.00	0.07
Lp51a484_clear dol patch 1-5-1		0.00	0.00	0.00	0.45	0.54	0.00	0.00	0.00	0.00	0.00	1.00	0.21	45.42	0.20	0.00	0.11
Lp51a484_type 5 dol in vein 1-6-1		0.00	0.00	0.02	0.47	0.51	0.00	0.00	0.00	0.00	0.00	1.00	2.23	46.48	0.41	0.00	0.07
Lp51a484_type 1 dol in vein 1-7-1		0.00	0.00	0.01	0.47	0.51	0.00	0.00	0.00	0.00	0.00	1.00	1.35	46.75	0.45	0.00	0.09
Lp51a484_zoned dol traverse 1-1		0.00	0.02	0.02	0.44	0.51	0.00	0.00	0.00	0.00	0.00	1.00	2.18	44.38	2.34	0.00	0.27
Lp51a484_zoned dol traverse 1-2		0.00	0.02	0.02	0.45	0.51	0.00	0.00	0.00	0.00	0.00	1.00	2.43	45.16	1.46	0.00	0.00
Lp51a484_zoned dol traverse 1-3		0.00	0.01	0.01	0.46	0.52	0.00	0.00	0.00	0.00	0.00	1.00	0.77	45.99	1.06	0.00	0.00
Lp51a484_zoned dol traverse 1-4		0.00	0.03	0.01	0.45	0.51	0.00	0.00	0.00	0.00	0.00	1.00	1.37	45.12	2.56	0.00	0.03

Label	Oxides:	Mineral	SiO_2	$FeCO_3$	$MnCO_3$	$MgCO_3$	$CaCO_3$	$BaCO_3$	$SrCO_3$	Na2Ca*2	K2Ca*2	$ZnCO_3$	Sum Ox
Lp51a484_zoned dol traverse 1-5		Fe-dol	0.04	4.07	1.64	39.31	53.42	0.00	0.00	0.00	0.00	0.23	98.70
Lp51a484_zoned dol traverse 1-6		dol	0.07	0.54	3.01	42.13	52.32	0.00	0.00	0.32	0.00	0.14	98.55
Lp51a484_zoned dol traverse 1-7		Fe-dol	0.05	1.48	3.20	41.21	52.91	0.02	0.00	0.00	0.00	0.19	99.06
Lp51a484_zoned dol traverse 1-8		dol	0.00	0.62	3.66	41.43	52.85	0.00	0.10	0.17	0.15	0.00	98.98
Lp51a484_zoned dol traverse 1-9		Fe-dol	0.01	4.28	1.66	39.07	53.66	0.04	0.03	0.00	0.04	0.16	98.96
Lp51a484_zoned dol traverse 1-10		Fe-dol	0.27	1.72	0.32	42.35	54.33	0.04	0.02	0.06	0.14	0.18	99.45
LP51AW2302_carb band trav1_3		Fe-dol	0.80	7.81	0.64	47.23	41.47	0.06	0.31	0.89	1.15	0.00	100.36
Lp51aw2433_dol 1-1-1		ank	0.00	14.32	2.53	29.26	54.19	0.04	0.19	0.00	0.00	0.00	100.53
Lp51aw2433_carb band 1-5-1		Fe-dol	0.53	7.43	0.22	46.42	46.10	0.00	0.11	0.26	0.27	0.16	101.51
LP66112_carb band2-4-1		dol	0.19	11.35	0.66	34.60	51.51	0.02	0.10	0.00	1.04	0.12	99.58
LP66153_patchy carb1-6-1		dol	0.05	3.18	2.01	37.41	52.14	0.01	0.14	6.67	0.07	0.00	101.67
LP66155_patchy carb1-1-1		Fe-dol	0.00	13.45	2.02	25.07	58.54	0.00	0.01	0.09	0.00	0.15	99.33
LP66155_patchy carb2-3-1		Fe-dol	0.06	13.96	1.57	24.64	58.66	0.02	0.13	0.20	0.00	0.02	99.26
LP66155_carb band1-5-1		Mg-sid	0.65	84.86	0.80	12.78	1.07	0.05	0.00	0.42	1.99	0.12	102.74
LP66179_patchy carb1-1-1		dol	0.01	4.07	1.07	40.68	52.53	0.01	0.06	0.41	0.00	0.00	98.84
LP66202_carb band1-6-1		dol	0.02	6.11	3.16	37.42	51.42	0.02	0.24	0.00	0.06	0.00	98.43
LP66233_vein carb1-6-1		sid	0.00	61.87	1.63	36.30	2.50	0.00	0.08	0.23	0.00	0.00	102.61
LP66233_carb band2-9-1		sid	0.00	63.37	0.60	35.40	2.46	0.03	0.00	0.11	0.11	0.00	102.09

Label	Cations:	Si	Fe2+	Mn2+	Mg	Ca	Ba	Sr	Na	K	Zn	Sum Cat	mgs	sid	ca	smt	rhd
Lp51a484_zoned dol traverse 1-5		0.00	0.03	0.01	0.44	0.51	0.00	0.00	0.00	0.00	0.00	1.00	1.35	44.32	3.34	0.00	0.00
Lp51a484_zoned dol traverse 1-6		0.00	0.00	0.03	0.47	0.50	0.00	0.00	0.00	0.00	0.00	1.00	2.48	47.24	0.44	0.00	0.00
Lp51a484_zoned dol traverse 1-7		0.00	0.01	0.03	0.46	0.50	0.00	0.00	0.00	0.00	0.00	1.00	2.63	46.08	1.20	0.00	0.00
Lp51a484_zoned dol traverse 1-8		0.00	0.01	0.03	0.46	0.50	0.00	0.00	0.00	0.00	0.00	1.00	3.01	46.44	0.51	0.00	0.06
Lp51a484_zoned dol traverse 1-9		0.00	0.04	0.01	0.44	0.51	0.00	0.00	0.00	0.00	0.00	1.00	1.37	44.05	3.51	0.00	0.02
Lp51a484_zoned dol traverse 1-10		0.00	0.01	0.00	0.47	0.51	0.00	0.00	0.00	0.00	0.00	1.00	0.26	46.77	1.39	0.00	0.01
LP51AW2302_carb band trav1_3		0.01	0.06	0.01	0.52	0.39	0.00	0.00	0.00	0.00	0.00	0.99	0.52	51.77	6.23	0.00	0.19
Lp51aw2433_dol 1-1-1		0.00	0.12	0.02	0.34	0.52	0.00	0.00	0.00	0.00	0.00	1.00	2.13	33.51	11.93	0.00	0.12
Lp51aw2433_carb band 1-5-1		0.01	0.06	0.00	0.50	0.42	0.00	0.00	0.00	0.00	0.00	0.99	0.18	50.18	5.85	0.00	0.07
LP66112_carb band2-4-1		0.00	0.09	0.01	0.40	0.50	0.00	0.00	0.00	0.00	0.00	1.00	0.55	39.52	9.43	0.00	0.07
LP66153_patchy carb1-6-1		0.00	0.03	0.02	0.43	0.52	0.00	0.00	0.01	0.00	0.00	1.01	1.69	42.97	2.66	0.00	0.09
LP66155_patchy carb1-1-1		0.00	0.11	0.02	0.29	0.58	0.00	0.00	0.00	0.00	0.00	1.00	1.73	29.26	11.42	0.00	0.01
LP66155_patchy carb2-3-1		0.00	0.12	0.01	0.29	0.58	0.00	0.00	0.00	0.00	0.00	1.00	1.35	28.76	11.86	0.00	0.09
LP66155_carb band1-5-1		0.01	0.79	0.01	0.16	0.02	0.00	0.00	0.00	0.00	0.00	0.99	0.75	16.30	78.77	0.00	0.00
LP66179_patchy carb1-1-1		0.00	0.03	0.01	0.46	0.50	0.00	0.00	0.00	0.00	0.00	1.00	0.89	45.79	3.33	0.00	0.04
LP66202_carb band1-6-1		0.00	0.05	0.03	0.43	0.49	0.00	0.00	0.00	0.00	0.00	1.00	2.64	42.67	5.07	0.00	0.15
LP66233_vein carb1-6-1		0.00	0.53	0.01	0.43	0.03	0.00	0.00	0.00	0.00	0.00	1.00	1.41	42.85	53.13	0.00	0.05

Label	Oxides:	Mineral	SiO_2	$FeCO_3$	$MnCO_3$	$MgCO_3$	$CaCO_3$	$BaCO_3$	$SrCO_3$	Na2Ca*2	K2Ca*2	$ZnCO_3$	Sum Ox
LP66254_strain shadow carb1-5-1		Fe-dol	0.22	3.16	0.80	42.18	50.97	0.00	0.21	0.04	0.38	0.00	97.96
LP66311_carb band1-3-1		dol	0.20	5.00	3.17	37.45	51.84	0.00	0.12	0.00	0.53	0.09	98.42
LP67B687 perv carb-5-1		dol	0.04	2.37	1.99	34.10	59.08	0.04	0.12	0.00	0.22	0.03	97.99
Lp67b760_carb in qtz vein 1-4-1		dol	0.00	0.63	0.24	44.22	54.24	0.00	0.08	0.05	0.00	0.15	99.61
Lp67b760_carb vein 1-8-1		Fe-dol	0.04	8.23	0.61	29.62	61.18	0.03	0.22	0.21	0.11	0.00	100.25
LP67B790_vein carb1-2-1		dol	0.03	6.67	3.51	31.44	55.31	0.00	0.10	1.85	0.00	0.08	98.98
LP67B841_vein veinlet1-6-1		dol	0.02	9.16	0.64	32.76	54.86	0.00	0.09	1.53	0.00	0.00	99.07
LP67B986 perv carb1-5-1		Fe-dol	0.00	11.14	2.60	27.43	55.94	0.01	0.04	0.02	0.00	0.20	97.37

Label	Cations:	Si	Fe2+	Mn2+	Mg	Ca	Ba	Sr	Na	K	Zn	Sum Cat	mgs	sid	ca	smt	rhd
LP66233_carb band2-9-1		0.00	0.55	0.01	0.42	0.03	0.00	0.00	0.00	0.00	0.00	1.00	0.52	42.09	54.83	0.00	0.00
LP66254_strain shadow carb1-5-1		0.00	0.03	0.01	0.48	0.48	0.00	0.00	0.00	0.00	0.00	1.00	0.66	47.48	2.59	0.00	0.14
LP66311_carb band1-3-1		0.00	0.04	0.03	0.43	0.50	0.00	0.00	0.00	0.00	0.00	1.00	2.65	42.64	4.15	0.00	0.08
LP67B687 perv carb-5-1		0.00	0.02	0.02	0.39	0.57	0.00	0.00	0.00	0.00	0.00	1.00	1.68	39.07	1.98	0.00	0.08
Lp67b760_carb in qtz vein 1-4-1		0.00	0.01	0.00	0.49	0.50	0.00	0.00	0.00	0.00	0.00	1.00	0.19	48.81	0.51	0.00	0.05
Lp67b760_carb vein 1-8-1		0.00	0.07	0.01	0.34	0.59	0.00	0.00	0.00	0.00	0.00	1.00	0.51	33.63	6.80	0.00	0.14
LP67B790_vein carb1-2-1		0.00	0.06	0.03	0.37	0.55	0.00	0.00	0.00	0.00	0.00	1.00	2.99	36.53	5.64	0.00	0.06
LP67B841_vein veinlet1-6-1		0.00	0.08	0.01	0.38	0.54	0.00	0.00	0.00	0.00	0.00	1.00	0.54	37.83	7.70	0.00	0.06
LP67B986 perv carb1-5-1		0.00	0.10	0.02	0.32	0.56	0.00	0.00	0.00	0.00	0.00	1.00	2.26	32.42	9.58	0.00	0.03

Label	Oxides:	Mineral	SiO_2	TiO_2	Al_2O_3	Cr_2O_3	FeO	MnO	MgO	CaO	Na_2O	K_2O	ZnO	NiO	H_2O(c)	Sum Ox%
LP12428_perv chl1-1-1		Mg-chl	32.53	0.06	18.31	0.44	6.40	0.05	28.58	0.04	0.01	0.54	0.01	0.01	12.55	99.52
LP12428_perv chl2-2-1		Mg-chl	31.43	0.03	19.34	0.61	7.02	0.15	29.10	0.02	0.01	0.21	0.09	0.02	12.63	100.67
LP12434_chl patch1-1-1		Mg-chl	29.76	0.05	21.32	0.00	7.81	0.22	27.22	0.00	0.02	0.21	0.05	0.01	12.40	99.07
LP12434_chl patch2-2-1		Mg-chl	29.98	0.01	21.11	0.03	8.11	0.23	27.79	0.01	0.02	0.02	0.00	0.07	12.49	99.88
LP12434_chl patch3-2-1		Mg-chl	32.34	1.80	19.43	0.03	7.22	0.11	25.07	0.01	0.00	2.80	0.00	0.00	12.60	101.42
Lp12440 perv chl1-1-1		Mg-chl	30.33	0.02	19.94	0.28	7.32	0.16	28.82	0.01	0.00	0.02	0.12	0.04	12.48	99.53
Lp12440 perv chl2-2-1		Mg-chl	30.67	0.02	19.78	0.41	7.65	0.08	28.49	0.02	0.02	0.03	0.06	0.07	12.50	99.80
Lp12440 perv chl3-3-1		Mg-chl	30.47	0.03	20.11	0.19	7.12	0.11	28.35	0.04	0.00	0.11	0.00	0.00	12.44	98.96
LP12450_strain shadow chl1-3-1		Mg-chl	30.07	0.00	20.62	0.11	7.74	0.14	27.51	0.02	0.01	0.09	0.05	0.00	12.37	98.72
LP12450_strain shadow chl2-4-1		Mg-chl	29.90	0.04	20.62	0.10	7.80	0.09	27.45	0.03	0.00	0.09	0.01	0.02	12.34	98.50
LP12450_perv chl1-8-1		Mg-chl	29.90	0.01	20.37	0.11	7.84	0.11	27.49	0.04	0.01	0.01	0.11	0.00	12.31	98.33
LP12457 perv chl1-2-1		Mg-chl	29.80	0.03	21.37	0.03	7.69	0.03	27.68	0.01	0.02	0.04	0.48	0.05	12.48	99.72
LP12457 perv chl2-4-1		Mg-chl	30.71	0.03	19.08	0.03	9.46	0.08	26.80	0.02	0.03	0.32	0.12	0.00	12.29	98.96
LP12465 perv chl2-6-1		Mg-chl	29.98	0.01	19.62	0.00	8.44	0.08	27.14	0.03	0.01	0.05	0.00	0.00	12.19	97.54
LP12465 perv chl3-7-1		Mg-chl	29.57	0.02	19.39	0.03	8.83	0.05	26.40	0.01	0.00	0.04	0.01	0.08	12.02	96.44
Lp12476 perv chl1-5-1		Mg-chl	30.63	0.03	20.28	0.12	7.58	0.07	28.70	0.01	0.01	0.01	0.00	0.04	12.55	100.01
Lp12476 perv chl2-9-1		Mg-chl	29.84	0.03	20.35	0.29	7.30	0.13	27.52	0.02	0.00	0.03	0.15	0.00	12.29	97.95

Label	Cations:	Si	Ti	Al IV	Al VI	Cr	Fe2+	Mn2+	Mg	Ca	Na	K	Zn	Ni	OH	Sum Cat	Mg #
LP12428_perv chl1-1-1		6.22	0.01	1.78	2.35	0.07	1.02	0.01	8.14	0.01	0.01	0.13	0.00	0.00	16.00	35.74	0.89
LP12428_perv chl2-2-1		5.97	0.01	2.03	2.30	0.09	1.12	0.02	8.24	0.01	0.00	0.05	0.01	0.00	16.00	35.84	0.88
LP12434_chl patch1-1-1		5.76	0.01	2.24	2.62	0.00	1.26	0.04	7.85	0.00	0.01	0.05	0.01	0.00	16.00	35.84	0.86
LP12434_chl patch2-2-1		5.76	0.00	2.24	2.53	0.01	1.30	0.04	7.95	0.00	0.01	0.01	0.00	0.01	16.00	35.86	0.86
LP12434_chl patch3-2-1		6.16	0.26	1.84	2.52	0.01	1.15	0.02	7.12	0.00	0.00	0.68	0.00	0.00	16.00	35.74	0.86
Lp12440 perv chl1-1-1		5.83	0.00	2.17	2.35	0.04	1.18	0.03	8.26	0.00	0.00	0.00	0.02	0.01	16.00	35.89	0.88
Lp12440 perv chl2-2-1		5.89	0.00	2.11	2.36	0.06	1.23	0.01	8.15	0.01	0.01	0.01	0.01	0.01	16.00	35.85	0.87
Lp12440 perv chl3-3-1		5.88	0.00	2.12	2.45	0.03	1.15	0.02	8.15	0.01	0.00	0.03	0.00	0.00	16.00	35.83	0.88
LP12450_strain shadow chl1-3-1		5.83	0.00	2.17	2.54	0.02	1.25	0.02	7.95	0.00	0.00	0.02	0.01	0.00	16.00	35.82	0.86
LP12450_strain shadow chl2-4-1		5.81	0.01	2.19	2.53	0.02	1.27	0.02	7.95	0.01	0.00	0.02	0.00	0.00	16.00	35.83	0.86
LP12450_perv chl1-8-1		5.82	0.00	2.18	2.50	0.02	1.28	0.02	7.98	0.01	0.00	0.00	0.02	0.00	16.00	35.83	0.86
LP12457 perv chl1-2-1		5.73	0.00	2.27	2.57	0.01	1.24	0.01	7.93	0.00	0.01	0.01	0.07	0.01	16.00	35.85	0.87
LP12457 perv chl2-4-1		5.99	0.00	2.01	2.38	0.01	1.54	0.01	7.79	0.00	0.01	0.08	0.02	0.00	16.00	35.85	0.84
LP12465 perv chl2-6-1		5.90	0.00	2.10	2.45	0.00	1.39	0.01	7.96	0.01	0.00	0.01	0.00	0.00	16.00	35.83	0.85
LP12465 perv chl3-7-1		5.90	0.00	2.10	2.46	0.01	1.47	0.01	7.85	0.00	0.00	0.01	0.00	0.01	16.00	35.82	0.84
Lp12476 perv chl1-5-1		5.85	0.00	2.15	2.42	0.02	1.21	0.01	8.18	0.00	0.00	0.00	0.00	0.01	16.00	35.85	0.87
Lp12476 perv chl2-9-1		5.83	0.00	2.18	2.51	0.05	1.19	0.02	8.01	0.00	0.00	0.01	0.02	0.00	16.00	35.81	0.87

Label	Oxides:	Mineral	SiO_2	TiO_2	Al_2O_3	Cr_2O_3	FeO	MnO	MgO	CaO	Na_2O	K_2O	ZnO	NiO	$H_2O(c)$	Sum Ox%
LP12493 perv chl1-3-1		Mg-chl	30.99	0.05	19.27	0.00	6.06	0.05	28.85	0.05	0.01	0.01	0.00	0.00	12.36	97.69
LP12493 perv chl2-4-1		Mg-chl	30.00	0.02	21.16	0.00	6.19	0.07	28.10	0.06	0.00	0.03	0.02	0.00	12.39	98.04
Lp12490 perv chl1-1-1		Mg-chl	30.09	0.03	20.31	0.00	6.93	0.04	27.88	0.04	0.01	0.05	0.05	0.00	12.30	97.73
Lp12490 perv chl2-2-1		Mg-chl	30.48	0.04	20.73	0.07	7.17	0.06	28.14	0.03	0.00	0.13	0.05	0.00	12.50	99.40
Lp12490 perv chl3-3-1		Mg-chl	30.38	0.07	20.92	0.02	6.93	0.09	28.41	0.00	0.00	0.28	0.00	0.01	12.53	99.64
LP12511_perv chl1-4-1		Mg-chl	29.87	0.00	20.02	0.35	9.05	0.15	27.07	0.02	0.00	0.05	0.19	0.05	12.32	99.14
LP12511_perv chl2-5-1		Mg-chl	30.66	0.03	19.50	0.14	10.01	0.10	26.56	0.01	0.02	0.24	0.21	0.01	12.37	99.85
LP12516_chl patch1-1-1		Mg-chl	29.48	0.16	21.43	0.02	10.16	0.15	26.17	0.00	0.00	0.01	0.09	0.01	12.41	100.09
LP12516_chl patch2-2-1		Mg-chl	29.18	0.03	21.41	0.01	9.81	0.16	25.82	0.00	0.00	0.04	0.04	0.00	12.26	98.76
LP12516_vein chl2-5-1		Mg-chl	29.37	0.06	21.37	0.03	10.08	0.11	26.07	0.02	0.00	0.02	0.00	0.00	12.34	99.47
LP12523_chl patch1-1-1		Mg-chl	29.12	0.08	21.55	0.00	10.37	0.19	25.76	0.01	0.01	0.00	0.13	0.01	12.32	99.55
LP12523_chl patch2-2-1		Mg-chl	29.30	0.05	21.74	0.00	9.96	0.08	25.96	0.00	0.00	0.02	0.00	0.01	12.35	99.47
LP12531_perv chl1-1-1		Mg-chl	28.86	0.02	21.48	0.02	8.93	0.10	26.53	0.05	0.02	0.02	0.01	0.00	12.25	98.30
LP12531_perv chl2-2-1		Mg-chl	28.61	0.04	21.44	0.00	9.43	0.04	25.80	0.04	0.00	0.00	0.06	0.03	12.14	97.63
LP12531_perv chl3-3-1		Mg-chl	30.22	0.92	21.69	0.02	8.42	0.06	24.51	0.03	0.03	0.66	0.07	0.08	12.37	99.08
LP12539 perv chl1-1-1		Mg-chl	29.65	0.00	21.33	0.00	7.22	0.04	27.68	0.04	0.00	0.02	0.06	0.09	12.38	98.51
LP12539 perv chl2-2-1		Mg-chl	29.76	0.01	20.74	0.00	7.09	0.02	27.85	0.00	0.01	0.00	0.03	0.02	12.31	97.85

Label	Cations:	Si	Ti	Al IV	Al VI	Cr	Fe2+	Mn2+	Mg	Ca	Na	K	Zn	Ni	OH	Sum Cat	Mg #
LP12493 perv chl1-3-1		6.01	0.01	1.99	2.42	0.00	0.98	0.01	8.35	0.01	0.00	0.00	0.00	0.00	16.00	35.78	0.90
LP12493 perv chl2-4-1		5.81	0.00	2.19	2.63	0.00	1.00	0.01	8.11	0.01	0.00	0.01	0.00	0.00	16.00	35.78	0.89
Lp12490 perv chl1-1-1		5.87	0.00	2.13	2.53	0.00	1.13	0.01	8.10	0.01	0.00	0.01	0.01	0.00	16.00	35.80	0.88
Lp12490 perv chl2-2-1		5.85	0.01	2.15	2.54	0.01	1.15	0.01	8.05	0.01	0.00	0.03	0.01	0.00	16.00	35.81	0.88
Lp12490 perv chl3-3-1		5.82	0.01	2.19	2.54	0.00	1.11	0.02	8.11	0.00	0.00	0.07	0.00	0.00	16.00	35.85	0.88
LP12511_perv chl1-4-1		5.82	0.00	2.18	2.41	0.05	1.47	0.02	7.86	0.00	0.00	0.01	0.03	0.01	16.00	35.87	0.84
LP12511_perv chl2-5-1		5.95	0.00	2.05	2.40	0.02	1.62	0.02	7.68	0.00	0.01	0.06	0.03	0.00	16.00	35.84	0.83
LP12516_chl patch1-1-1		5.70	0.02	2.30	2.58	0.00	1.64	0.02	7.54	0.00	0.00	0.00	0.01	0.00	16.00	35.84	0.82
LP12516_chl patch2-2-1		5.71	0.00	2.29	2.64	0.00	1.61	0.03	7.53	0.00	0.00	0.01	0.01	0.00	16.00	35.82	0.82
LP12516_vein chl2-5-1		5.71	0.01	2.29	2.60	0.01	1.64	0.02	7.55	0.00	0.00	0.01	0.00	0.00	16.00	35.84	0.82
LP12523_chl patch1-1-1		5.67	0.01	2.33	2.62	0.00	1.69	0.03	7.48	0.00	0.00	0.00	0.02	0.00	16.00	35.85	0.82
LP12523_chl patch2-2-1		5.69	0.01	2.31	2.66	0.00	1.62	0.01	7.51	0.00	0.00	0.00	0.00	0.00	16.00	35.82	0.82
LP12531_perv chl1-1-1		5.65	0.00	2.35	2.61	0.00	1.46	0.02	7.75	0.01	0.01	0.01	0.00	0.00	16.00	35.87	0.84
LP12531_perv chl2-2-1		5.65	0.01	2.35	2.65	0.00	1.56	0.01	7.60	0.01	0.00	0.00	0.01	0.01	16.00	35.84	0.83
LP12531_perv chl3-3-1		5.86	0.14	2.14	2.82	0.00	1.37	0.01	7.08	0.01	0.01	0.16	0.01	0.01	16.00	35.61	0.84
LP12539 perv chl1-1-1		5.74	0.00	2.26	2.62	0.00	1.17	0.01	7.99	0.01	0.00	0.00	0.01	0.01	16.00	35.82	0.87
LP12539 perv chl2-2-1		5.80	0.00	2.20	2.56	0.00	1.16	0.00	8.09	0.00	0.00	0.00	0.00	0.00	16.00	35.82	0.88

Label	**Oxides:**	Mineral	SiO_2	TiO_2	Al_2O_3	Cr_2O_3	FeO	MnO	MgO	CaO	Na_2O	K_2O	ZnO	NiO	H_2O(c)	Sum Ox%
Lp12555_perv chl1-5-1		Mg-chl	29.91	0.05	21.61	0.02	8.41	0.36	27.16	0.00	0.00	0.01	0.09	0.01	12.51	100.13
Lp12555_perv chl2-6-1		Mg-chl	29.20	0.00	21.75	0.00	8.08	0.33	26.75	0.04	0.01	0.01	0.05	0.00	12.32	98.55
Lp18365_perv chl 1-3-1		Mg-chl	30.28	0.04	19.61	0.00	9.52	0.09	27.12	0.01	0.01	0.05	0.02	0.00	12.32	99.08
Lp18365_chl patch 1-4-1		Mg-chl	29.28	0.06	20.89	0.00	9.70	0.17	26.55	0.02	0.01	0.00	0.06	0.06	12.30	99.10
Lp33390_chl in chl patch 1-2-1		Mg-chl	32.92	0.01	17.86	0.31	5.60	0.09	29.81	0.11	0.02	0.01	0.05	0.00	12.61	99.39
Lp36w197_S1 prallel chl 1-3-1		Mg-chl	30.83	0.03	20.25	0.29	7.94	0.20	28.34	0.04	0.00	0.07	0.09	0.00	12.60	100.67
LP36W214 perv chl1-1-1		Mg-chl	29.16	0.05	20.77	0.30	9.68	0.40	26.23	0.04	0.01	0.01	0.10	0.00	12.26	99.01
LP36W214 perv chl2-2-1		Mg-chl	29.45	0.04	20.65	0.10	9.48	0.38	25.96	0.00	0.00	0.09	0.00	0.01	12.22	98.38
Lp44243_chl in ca-as band 1-6-1		Mg-chl	28.97	0.02	22.14	0.01	8.77	0.38	26.43	0.01	0.01	0.03	0.11	0.00	12.36	99.26
Lp44243_chl in ca-as band 1-11-1		Mg-chl	29.44	0.04	21.91	0.04	9.92	0.36	25.82	0.01	0.01	0.04	0.35	0.02	12.43	100.39
LP46A103_perv chl1-2-1		Mg-chl	29.60	0.04	21.75	0.01	9.24	0.48	25.70	0.02	0.03	0.07	0.06	0.02	12.36	99.38
LP46A103_perv chl2-3-1		Mg-chl	28.56	0.05	22.00	0.00	9.37	0.61	26.08	0.03	0.03	0.05	0.06	0.00	12.29	99.13
LP46A103_perv chl3-7-1		Mg-chl	29.96	0.02	20.72	0.04	9.45	0.39	26.54	0.06	0.02	0.07	0.08	0.02	12.39	99.76
LP46A113_perv chl1-9-1		Mg-chl	29.66	0.01	19.59	0.05	10.66	0.35	25.79	0.03	0.00	0.04	0.37	0.11	12.17	98.83
LP46A124_perv chl1-5-1		Mg-chl	30.00	0.03	20.62	0.02	9.73	0.25	26.11	0.04	0.02	0.24	0.13	0.00	12.34	99.53
LP46A124_perv chl2-6-1		Mg-chl	29.53	0.00	21.95	0.00	9.97	0.25	25.45	0.01	0.01	0.00	0.12	0.03	12.38	99.70
LP46A177_lrg chl1-1-1		Mg-chl	30.69	0.04	20.42	0.07	5.40	0.22	28.88	0.02	0.02	0.19	0.03	0.01	12.47	98.47

Label	**Cations:**	Si	Ti	Al IV	Al VI	Cr	Fe2+	Mn2+	Mg	Ca	Na	K	Zn	Ni	OH	Sum Cat	Mg #
Lp12555_perv chl1-5-1		5.74	0.01	2.26	2.62	0.00	1.35	0.06	7.76	0.00	0.00	0.00	0.01	0.00	16.00	35.81	0.85
Lp12555_perv chl2-6-1		5.68	0.00	2.32	2.67	0.00	1.32	0.06	7.76	0.01	0.00	0.00	0.01	0.00	16.00	35.83	0.86
Lp18365_perv chl 1-3-1		5.90	0.01	2.11	2.39	0.00	1.55	0.02	7.87	0.00	0.01	0.01	0.00	0.00	16.00	35.86	0.84
Lp18365_chl patch 1-4-1		5.71	0.01	2.29	2.51	0.00	1.58	0.03	7.72	0.00	0.00	0.00	0.01	0.01	16.00	35.88	0.83
Lp33390_chl in chl patch 1-2-1		6.26	0.00	1.74	2.27	0.05	0.89	0.01	8.45	0.02	0.01	0.00	0.01	0.00	16.00	35.71	0.91
Lp36w197_S1 prallel chl 1-3-1		5.87	0.01	2.13	2.41	0.04	1.26	0.03	8.04	0.01	0.00	0.02	0.01	0.00	16.00	35.84	0.86
LP36W214 perv chl1-1-1		5.70	0.01	2.30	2.49	0.05	1.58	0.07	7.65	0.01	0.01	0.00	0.01	0.00	16.00	35.88	0.83
LP36W214 perv chl2-2-1		5.78	0.01	2.22	2.56	0.02	1.56	0.06	7.60	0.00	0.00	0.02	0.00	0.00	16.00	35.83	0.83
Lp44243_chl in ca-as band 1-6-1		5.62	0.00	2.38	2.68	0.00	1.42	0.06	7.64	0.00	0.01	0.01	0.02	0.00	16.00	35.85	0.84
Lp44243_chl in ca-as band 1-11-1		5.68	0.01	2.32	2.66	0.01	1.60	0.06	7.43	0.00	0.00	0.01	0.05	0.00	16.00	35.83	0.82
LP46A103_perv chl1-2-1		5.74	0.01	2.26	2.72	0.00	1.50	0.08	7.43	0.01	0.01	0.02	0.01	0.00	16.00	35.78	0.83
LP46A103_perv chl2-3-1		5.58	0.01	2.43	2.64	0.00	1.53	0.10	7.59	0.01	0.01	0.01	0.01	0.00	16.00	35.90	0.83
LP46A103_perv chl3-7-1		5.80	0.00	2.20	2.53	0.01	1.53	0.06	7.66	0.01	0.01	0.02	0.01	0.00	16.00	35.84	0.83
LP46A113_perv chl1-9-1		5.84	0.00	2.16	2.39	0.01	1.76	0.06	7.57	0.01	0.00	0.01	0.05	0.02	16.00	35.88	0.81
LP46A124_perv chl1-5-1		5.83	0.00	2.17	2.55	0.00	1.58	0.04	7.56	0.01	0.01	0.06	0.02	0.00	16.00	35.84	0.83
LP46A124_perv chl2-6-1		5.72	0.00	2.28	2.74	0.00	1.62	0.04	7.35	0.00	0.00	0.00	0.02	0.01	16.00	35.77	0.82
LP46A177_lrg chl1-1-1		5.90	0.01	2.10	2.53	0.01	0.87	0.04	8.28	0.01	0.01	0.05	0.01	0.00	16.00	35.80	0.91

Label	Oxides:	Mineral	SiO_2	TiO_2	Al_2O_3	Cr_2O_3	FeO	MnO	MgO	CaO	Na_2O	K_2O	ZnO	NiO	H_2O(c)	Sum Ox%
LP46A177 perv chl2-3-1		Mg-chl	30.56	0.02	20.97	0.00	5.36	0.25	29.34	0.02	0.00	0.01	0.00	0.03	12.57	99.14
LP46A177 perv chl4-5-1		Mg-chl	30.16	0.01	21.43	0.03	5.83	0.18	29.29	0.01	0.00	0.00	0.00	0.00	12.59	99.51
LP46A177 perv chl5-6-1		Mg-chl	30.03	0.33	21.20	0.03	5.75	0.31	28.95	0.03	0.00	0.02	0.00	0.03	12.54	99.22
LP46A177 perv chl6-7-1		Mg-chl	30.63	0.05	20.99	0.00	5.71	0.22	29.32	0.01	0.00	0.16	0.01	0.03	12.62	99.75
LP46A187_perv chl1-1-1		Mg-chl	29.19	0.06	22.12	0.04	9.62	0.29	26.43	0.00	0.01	0.02	0.00	0.00	12.45	100.23
LP46A187_perv chl2-2-1		Mg-chl	29.35	0.04	21.99	0.01	9.47	0.40	26.44	0.01	0.00	0.01	0.01	0.05	12.45	100.23
LP46A204 chl patch1-1-1		Mg-chl	27.82	2.87	21.59	0.03	9.32	0.29	25.34	0.01	0.01	0.01	0.05	0.05	12.34	99.72
LP46A204 chl patch2-2-1		Mg-chl	28.82	0.05	22.07	0.03	10.00	0.31	26.12	0.01	0.00	0.00	0.00	0.05	12.37	99.83
LP46A204 chl patch3-3-1		Mg-chl	28.76	0.04	22.46	0.01	9.82	0.32	25.82	0.00	0.01	0.01	0.06	0.01	12.36	99.68
LP46A204 chl patch4-4-1		Mg-chl	29.31	0.08	22.04	0.00	9.22	0.31	25.84	0.02	0.00	0.20	0.01	0.06	12.37	99.46
LP46A250 chl patch1-2-1		Mg-Fe-chl	28.18	0.04	22.85	0.00	15.04	0.44	20.67	0.03	0.00	0.37	0.19	0.00	12.08	99.87
LP46A250 chl patch2-4-1		Mg-Fe-chl	27.32	0.06	22.56	0.00	14.58	0.45	21.21	0.02	0.00	0.01	0.21	0.00	11.91	98.33
LP46A250 perv chl1-7-1		Mg-Fe-chl	27.19	0.02	22.94	0.00	14.45	0.40	22.07	0.01	0.02	0.02	0.00	0.01	12.02	99.14
LP46A250 chl patch3-9-1		Mg-Fe-chl	27.69	0.06	21.99	0.05	15.49	0.44	21.62	0.02	0.00	0.05	0.20	0.00	12.01	99.62
LP46A250 chl patch4-10-1		Mg-Fe-chl	27.14	0.06	22.15	0.00	15.83	0.46	21.57	0.01	0.01	0.00	0.00	0.01	11.94	99.17
LP46A250 perv chl2-11-1		Mg-Fe-chl	28.32	0.05	23.23	0.02	14.65	0.41	20.29	0.03	0.04	0.62	0.08	0.01	12.10	99.85
LP46A297 chl patch1-1-1		Mg-Fe-chl	26.30	0.04	22.33	0.02	21.11	0.38	18.06	0.01	0.00	0.00	0.19	0.00	11.75	100.20

Label	Cations:	Si	Ti	Al IV	Al VI	Cr	Fe2+	Mn2+	Mg	Ca	Na	K	Zn	Ni	OH	Sum Cat	Mg #
LP46A177 perv chl2-3-1		5.83	0.00	2.17	2.55	0.00	0.86	0.04	8.35	0.00	0.00	0.00	0.00	0.00	16.00	35.81	0.91
LP46A177 perv chl4-5-1		5.75	0.00	2.25	2.56	0.00	0.93	0.03	8.32	0.00	0.00	0.00	0.00	0.00	16.00	35.84	0.90
LP46A177 perv chl5-6-1		5.75	0.05	2.26	2.52	0.01	0.92	0.05	8.26	0.01	0.00	0.01	0.00	0.01	16.00	35.82	0.90
LP46A177 perv chl6-7-1		5.82	0.01	2.18	2.53	0.00	0.91	0.04	8.31	0.00	0.00	0.04	0.00	0.00	16.00	35.84	0.90
LP46A187_perv chl1-1-1		5.62	0.01	2.38	2.65	0.01	1.55	0.05	7.59	0.00	0.00	0.01	0.00	0.00	16.00	35.86	0.83
LP46A187_perv chl2-2-1		5.65	0.01	2.35	2.64	0.00	1.53	0.07	7.59	0.00	0.00	0.00	0.00	0.01	16.00	35.85	0.83
LP46A204 chl patch1-1-1		5.41	0.42	2.59	2.35	0.00	1.52	0.05	7.34	0.00	0.00	0.00	0.01	0.01	16.00	35.70	0.83
LP46A204 chl patch2-2-1		5.59	0.01	2.41	2.64	0.01	1.62	0.05	7.55	0.00	0.00	0.00	0.00	0.01	16.00	35.88	0.82
LP46A204 chl patch3-3-1		5.58	0.01	2.42	2.72	0.00	1.59	0.05	7.47	0.00	0.00	0.00	0.01	0.00	16.00	35.85	0.82
LP46A204 chl patch4-4-1		5.68	0.01	2.32	2.72	0.00	1.50	0.05	7.47	0.01	0.00	0.05	0.00	0.01	16.00	35.81	0.83
LP46A250 chl patch1-2-1		5.60	0.01	2.40	2.95	0.00	2.50	0.07	6.12	0.01	0.00	0.09	0.03	0.00	16.00	35.77	0.71
LP46A250 chl patch2-4-1		5.50	0.01	2.50	2.86	0.00	2.46	0.08	6.37	0.01	0.00	0.00	0.03	0.00	16.00	35.81	0.72
LP46A250 perv chl1-7-1		5.43	0.00	2.58	2.82	0.00	2.41	0.07	6.57	0.00	0.01	0.00	0.00	0.00	16.00	35.88	0.73
LP46A250 chl patch3-9-1		5.53	0.01	2.47	2.71	0.01	2.59	0.08	6.44	0.00	0.00	0.01	0.03	0.00	16.00	35.87	0.71
LP46A250 chl patch4-10-1		5.45	0.01	2.55	2.70	0.00	2.66	0.08	6.46	0.00	0.00	0.00	0.00	0.00	16.00	35.92	0.71
LP46A250 perv chl2-11-1		5.62	0.01	2.38	3.05	0.00	2.43	0.07	6.00	0.01	0.02	0.16	0.01	0.00	16.00	35.75	0.71
LP46A297 chl patch1-1-1		5.37	0.01	2.63	2.74	0.00	3.60	0.07	5.49	0.00	0.00	0.00	0.03	0.00	16.00	35.94	0.60

Label	Oxides:	Mineral	SiO_2	TiO_2	Al_2O_3	Cr_2O_3	FeO	MnO	MgO	CaO	Na_2O	K_2O	ZnO	NiO	H_2O(c)	Sum Ox%
LP46A297 chl patch2-2-1		Mg-Fe-chl	25.94	0.05	21.84	0.01	21.24	0.43	17.30	0.01	0.00	0.02	0.16	0.06	11.54	98.57
LP46A297 chl patch3-3-1		Mg-Fe-chl	25.96	0.08	22.03	0.00	20.85	0.40	17.79	0.02	0.00	0.00	0.14	0.00	11.60	98.87
LP46A297 chl patch4-4-1		Mg-Fe-chl	26.31	0.04	22.36	0.00	21.59	0.44	17.87	0.02	0.00	0.01	0.05	0.00	11.77	100.46
LP46A348_perv chl1-4-1		Mg-Fe-chl	27.54	0.10	21.48	0.00	17.32	0.66	20.18	0.02	0.03	0.05	0.12	0.00	11.86	99.36
LP46A348_perv chl2-6-1		Mg-Fe-chl	27.27	0.09	21.44	0.00	17.55	0.74	20.40	0.00	0.03	0.01	0.07	0.09	11.86	99.56
Lp51a477_chl in ms band 1-2-1		Mg-chl	31.45	0.04	19.31	0.00	4.89	0.34	30.22	0.02	0.01	0.07	0.04	0.01	12.56	98.95
Lp51a482_perv chl 1-3-1		Mg-chl	31.22	0.02	19.63	0.05	5.19	0.38	30.19	0.01	0.00	0.11	0.02	0.07	12.60	99.49
Lp51a484_chl 1-2-1		Mg-chl	32.45	0.05	19.41	0.00	4.30	0.37	30.26	0.08	0.00	0.00	0.12	0.00	12.72	99.75
LP51AW2302_chl patch1-4-1		Mg-chl	29.80	0.07	21.91	0.00	4.89	0.19	29.16	0.00	0.00	0.02	0.29	0.07	12.55	98.97
LP51AW2302_chl patch2-5-1		Mg-chl	29.88	0.02	21.59	0.02	5.22	0.14	28.93	0.02	0.01	0.01	0.09	0.00	12.48	98.39
Lp51aw2433_chl 2-4-1		Mg-Fe-chl	31.28	0.04	18.67	0.40	13.75	0.11	22.60	0.05	0.02	0.27	0.21	0.00	12.15	99.54
LP66202_vein chl2-2-1		Mg-chl	28.37	0.05	21.58	0.00	11.88	0.53	24.10	0.02	0.00	0.02	0.05	0.00	12.11	98.74
LP66233_chl patch1-1-1		Mg-chl	28.88	0.02	21.56	0.01	9.77	0.87	25.39	0.03	0.00	0.02	0.00	0.00	12.23	98.78
LP66267_perv chl1-1-1		Mg-chl	29.64	0.05	21.02	0.02	8.44	0.37	26.45	0.01	0.01	0.02	0.06	0.01	12.29	98.38
LP66267_perv chl2-2-1		Mg-chl	29.69	0.00	21.10	0.00	8.72	0.38	26.15	0.01	0.02	0.00	0.06	0.01	12.28	98.42
LP66282 perv chl1-1-1		Mg-Fe-chl	30.66	0.03	23.80	0.00	9.66	0.28	22.95	0.01	0.00	0.00	0.06	0.04	12.51	99.99
LP66282_perv chl3-6-1		Mg-Fe-chl	30.67	0.06	23.99	0.00	9.61	0.23	22.69	0.01	0.00	0.00	0.04	0.00	12.50	99.80

Label	Cations:	Si	Ti	Al IV	Al VI	Cr	Fe2+	Mn2+	Mg	Ca	Na	K	Zn	Ni	OH	Sum Cat	Mg #
LP46A297 chl patch2-2-1		5.39	0.01	2.61	2.75	0.00	3.69	0.08	5.36	0.00	0.00	0.00	0.02	0.01	16.00	35.92	0.59
LP46A297 chl patch3-3-1		5.37	0.01	2.63	2.74	0.00	3.61	0.07	5.49	0.00	0.00	0.00	0.02	0.00	16.00	35.94	0.60
LP46A297 chl patch4-4-1		5.36	0.01	2.64	2.74	0.00	3.68	0.08	5.43	0.01	0.00	0.00	0.01	0.00	16.00	35.95	0.60
LP46A348_perv chl1-4-1		5.57	0.02	2.43	2.69	0.00	2.93	0.11	6.08	0.00	0.01	0.01	0.02	0.00	16.00	35.87	0.68
LP46A348_perv chl2-6-1		5.52	0.01	2.49	2.63	0.00	2.97	0.13	6.15	0.00	0.01	0.00	0.01	0.01	16.00	35.92	0.67
Lp51a477_chl in ms band 1-2-1		6.01	0.01	1.99	2.35	0.00	0.78	0.06	8.60	0.00	0.00	0.02	0.01	0.00	16.00	35.83	0.92
Lp51a482_perv chl 1-3-1		5.94	0.00	2.06	2.35	0.01	0.83	0.06	8.57	0.00	0.00	0.03	0.00	0.01	16.00	35.86	0.91
Lp51a484_chl 1-2-1		6.12	0.01	1.88	2.43	0.00	0.68	0.06	8.51	0.02	0.00	0.00	0.02	0.00	16.00	35.72	0.93
LP51AW2302_chl patch1-4-1		5.70	0.01	2.30	2.64	0.00	0.78	0.03	8.31	0.00	0.00	0.01	0.04	0.01	16.00	35.83	0.91
LP51AW2302_chl patch2-5-1		5.74	0.00	2.26	2.63	0.00	0.84	0.02	8.29	0.00	0.00	0.00	0.01	0.00	16.00	35.81	0.91
Lp51aw2433_chl 2-4-1		6.18	0.01	1.82	2.52	0.06	2.27	0.02	6.65	0.01	0.01	0.07	0.03	0.00	16.00	35.65	0.75
LP66202_vein chl2-2-1		5.62	0.01	2.38	2.66	0.00	1.97	0.09	7.12	0.01	0.00	0.01	0.01	0.00	16.00	35.86	0.78
LP66233_chl patch1-1-1		5.67	0.00	2.33	2.65	0.00	1.60	0.15	7.42	0.01	0.00	0.00	0.00	0.00	16.00	35.84	0.82
LP66267_perv chl1-1-1		5.79	0.01	2.21	2.62	0.00	1.38	0.06	7.70	0.00	0.00	0.01	0.01	0.00	16.00	35.79	0.85
LP66267_perv chl2-2-1		5.80	0.00	2.20	2.66	0.00	1.42	0.06	7.61	0.00	0.01	0.00	0.01	0.00	16.00	35.78	0.84
LP66282 perv chl1-1-1		5.88	0.00	2.12	3.26	0.00	1.55	0.05	6.56	0.00	0.00	0.00	0.01	0.01	16.00	35.43	0.81
LP66282_perv chl3-6-1		5.89	0.01	2.12	3.31	0.00	1.54	0.04	6.49	0.00	0.00	0.00	0.01	0.00	16.00	35.39	0.81

Label	Oxides:	Mineral	SiO_2	TiO_2	Al_2O_3	Cr_2O_3	FeO	MnO	MgO	CaO	Na_2O	K_2O	ZnO	NiO	H_2O(c)	Sum Ox%
LP66296_perv chl1-1-1		Mg-Fe-chl	27.79	0.05	22.06	0.00	11.89	0.39	23.74	0.02	0.01	0.00	0.00	0.00	12.03	98.00
LP66296_perv chl2-3-1		Mg-Fe-chl	27.54	0.04	22.26	0.05	12.55	0.29	23.74	0.00	0.02	0.01	0.05	0.00	12.06	98.62
LP66296_perv chl3-4-1		Mg-Fe-chl	28.47	0.03	22.17	0.01	12.18	0.26	23.69	0.03	0.00	0.13	0.02	0.03	12.17	99.18
LP66296_perv chl4-5-1		Mg-chl	28.28	0.03	22.10	0.04	12.18	0.26	24.03	0.02	0.01	0.01	0.00	0.00	12.16	99.13
LP66311_perv chl2-2-1		Mg-chl	29.47	0.05	21.62	0.00	8.58	0.37	26.48	0.03	0.00	0.10	0.03	0.00	12.36	99.09
LP66311_perv chl3-5-1		Mg-chl	29.10	0.04	21.92	0.00	8.92	0.34	26.49	0.05	0.00	0.05	0.05	0.00	12.37	99.30
LP66339_perv chl2-3-1		Mg-Fe-chl	28.28	0.03	21.55	0.02	13.77	0.32	22.98	0.02	0.00	0.00	0.04	0.05	12.07	99.12
LP66339_perv chl3-4-1		Mg-Fe-chl	28.43	0.02	21.46	0.04	13.87	0.26	23.15	0.01	0.00	0.01	0.00	0.00	12.10	99.35
LP66350_perv chl1-3-1		Mg-Fe-chl	27.46	0.05	21.35	0.04	15.58	0.36	21.26	0.02	0.00	0.00	0.04	0.03	11.81	97.99
LP66350_chl patch1-4-1		Mg-Fe-chl	27.81	0.07	21.65	0.05	15.66	0.34	22.01	0.00	0.00	0.02	0.12	0.00	12.02	99.75
LP66350_perv chl2-5-1		Mg-Fe-chl	27.88	0.03	20.96	0.01	15.32	0.35	22.01	0.02	0.01	0.01	0.04	0.00	11.89	98.53
Lp66361_perv chl 1-1-1		Mg-Fe-chl	27.45	0.06	21.77	0.00	17.77	0.42	20.71	0.01	0.00	0.03	0.16	0.00	11.97	100.35
LP66374_perv chl1-1-1		Mg-Fe-chl	27.92	0.03	20.46	0.01	17.74	0.40	21.04	0.01	0.00	0.01	0.05	0.00	11.88	99.56
LP66374_perv chl2-3-1		Mg-Fe-chl	28.47	0.02	20.30	0.00	16.03	0.28	21.73	0.02	0.00	0.03	0.14	0.00	11.91	98.93
LP66391_perv Mgchl1-1-1		Mg-Fe-chl	27.57	0.05	20.62	0.00	18.18	0.42	20.67	0.00	0.01	0.00	0.00	0.00	11.83	99.36
LP66391_perv Mgchl2-2-1		Mg-Fe-chl	27.30	0.03	21.65	0.00	18.66	0.32	19.71	0.01	0.00	0.00	0.02	0.00	11.84	99.54
LP66391_perv Fechl1-3-1		Mg-Fe-chl	26.99	0.06	21.59	0.03	18.34	0.36	20.04	0.04	0.00	0.01	0.04	0.00	11.81	99.31

Label	Cations:	Si	Ti	Al IV	Al VI	Cr	Fe2+	Mn2+	Mg	Ca	Na	K	Zn	Ni	OH	Sum Cat	Mg #
LP66296_perv chl1-1-1		5.54	0.01	2.46	2.73	0.00	1.98	0.07	7.06	0.01	0.01	0.00	0.00	0.00	16.00	35.86	0.78
LP66296_perv chl2-3-1		5.48	0.01	2.52	2.70	0.01	2.09	0.05	7.04	0.00	0.01	0.00	0.01	0.00	16.00	35.91	0.77
LP66296_perv chl3-4-1		5.61	0.01	2.39	2.76	0.00	2.01	0.04	6.96	0.01	0.00	0.03	0.00	0.01	16.00	35.82	0.78
LP66296_perv chl4-5-1		5.58	0.00	2.42	2.71	0.01	2.01	0.04	7.06	0.00	0.00	0.00	0.00	0.00	16.00	35.85	0.78
LP66311_perv chl2-2-1		5.72	0.01	2.28	2.66	0.00	1.39	0.06	7.66	0.01	0.00	0.03	0.01	0.00	16.00	35.82	0.85
LP66311_perv chl3-5-1		5.65	0.01	2.36	2.66	0.00	1.45	0.06	7.66	0.01	0.00	0.01	0.01	0.00	16.00	35.85	0.84
LP66339_perv chl2-3-1		5.62	0.00	2.38	2.67	0.00	2.29	0.05	6.81	0.00	0.00	0.00	0.01	0.01	16.00	35.85	0.75
LP66339_perv chl3-4-1		5.64	0.00	2.36	2.65	0.01	2.30	0.04	6.84	0.00	0.00	0.00	0.00	0.00	16.00	35.85	0.75
LP66350_perv chl1-3-1		5.58	0.01	2.42	2.69	0.01	2.65	0.06	6.44	0.00	0.00	0.00	0.01	0.00	16.00	35.86	0.71
LP66350_chl patch1-4-1		5.55	0.01	2.45	2.64	0.01	2.61	0.06	6.55	0.00	0.00	0.00	0.02	0.00	16.00	35.90	0.72
LP66350_perv chl2-5-1		5.62	0.01	2.38	2.61	0.00	2.58	0.06	6.62	0.00	0.00	0.00	0.01	0.00	16.00	35.88	0.72
Lp66361_perv chl 1-1-1		5.50	0.01	2.50	2.64	0.00	2.98	0.07	6.19	0.00	0.00	0.01	0.02	0.00	16.00	35.92	0.68
LP66374_perv chl1-1-1		5.64	0.01	2.36	2.51	0.00	3.00	0.07	6.33	0.00	0.00	0.00	0.01	0.00	16.00	35.92	0.68
LP66374_perv chl2-3-1		5.73	0.00	2.27	2.55	0.00	2.70	0.05	6.52	0.01	0.00	0.01	0.02	0.00	16.00	35.86	0.71
LP66391_perv Mgchl1-1-1		5.59	0.01	2.41	2.52	0.00	3.08	0.07	6.25	0.00	0.00	0.00	0.00	0.00	16.00	35.94	0.67
LP66391_perv Mgchl2-2-1		5.53	0.00	2.47	2.70	0.00	3.16	0.06	5.95	0.00	0.00	0.00	0.00	0.00	16.00	35.88	0.65
LP66391_perv Fechl1-3-1		5.48	0.01	2.52	2.65	0.01	3.12	0.06	6.07	0.01	0.00	0.00	0.01	0.00	16.00	35.93	0.66

Label	Oxides:	Mineral	SiO_2	TiO_2	Al_2O_3	Cr_2O_3	FeO	MnO	MgO	CaO	Na_2O	K_2O	ZnO	NiO	$H_2O(c)$	Sum Ox%
LP66419_perv chl1-3-1		Mg-Fe-chl	27.48	0.04	21.13	0.06	16.68	0.24	20.77	0.00	0.02	0.03	0.00	0.06	11.79	98.30
LP66419_perv chl2-4-1		Mg-Fe-chl	28.15	0.04	20.75	0.06	16.68	0.27	21.75	0.02	0.01	0.00	0.05	0.05	11.98	99.81
LP67B841_perv chl1-1-1		Mg-chl	28.61	0.08	23.79	0.03	8.71	0.35	26.36	0.02	0.00	0.00	0.00	0.00	12.54	100.50
LP67B841_perv chl2-2-1		Mg-chl	28.26	0.08	22.99	0.08	8.69	0.40	26.04	0.03	0.00	0.00	0.07	0.07	12.33	99.03
lp67b903 perv chl1-2-1		Mg-Fe-chl	29.75	0.03	23.09	0.04	10.57	0.57	22.19	0.04	0.00	0.00	0.36	0.01	12.26	98.93
LP67b986 perv chl1-1-1		Mg-Fe-chl	27.92	0.05	22.30	0.00	11.78	0.78	24.22	0.02	0.01	0.01	0.21	0.05	12.18	99.51
LP67b986 perv chl2-2-1		Mg-Fe-chl	27.72	0.07	21.98	0.00	13.57	0.69	22.75	0.01	0.00	0.04	0.00	0.00	12.02	98.86
lp67bw11037 perv chl1-2-1		Mg-chl	28.36	0.03	21.78	0.00	10.59	0.30	25.25	0.02	0.00	0.00	0.03	0.03	12.17	98.58
lp67bw11037 perv chl2-4-1		Mg-chl	28.43	0.03	21.67	0.06	10.80	0.39	24.63	0.03	0.01	0.19	0.00	0.11	12.13	98.49
LP67BW11063 perv chl1-1-1		Mg-Fe-chl	28.54	0.04	21.97	0.07	11.97	0.28	23.42	0.02	0.01	0.14	0.02	0.00	12.11	98.60
LP67BW11063 perv chl2-2-1		Mg-Fe-chl	28.65	0.07	21.86	0.05	12.11	0.27	24.11	0.03	0.00	0.38	0.00	0.01	12.22	99.77
LP67BW11132 perv bt1-4-1		Mg-Fe-chl	28.81	0.08	21.47	0.00	17.23	0.19	19.08	0.02	0.46	0.06	0.06	0.00	11.93	99.38
LP67BW11132 perv chl1-6-1		Mg-Fe-chl	29.17	0.07	21.58	0.00	17.97	0.26	18.73	0.03	0.00	0.01	0.17	0.00	11.99	100.00
LP67BW11132 perv chl2-8-1		Mg-Fe-chl	26.70	0.05	21.96	0.00	18.13	0.18	19.78	0.03	0.01	0.02	0.12	0.06	11.76	98.80

Label	Cations:	Si	Ti	Al IV	Al VI	Cr	Fe2+	Mn2+	Mg	Ca	Na	K	Zn	Ni	OH	Sum Cat	Mg #
LP66419_perv chl1-3-1		5.59	0.01	2.41	2.66	0.01	2.84	0.04	6.30	0.00	0.01	0.01	0.00	0.01	16.00	35.87	0.69
LP66419_perv chl2-4-1		5.64	0.01	2.36	2.54	0.01	2.79	0.05	6.49	0.00	0.01	0.00	0.01	0.01	16.00	35.91	0.70
LP67B841_perv chl1-1-1		5.48	0.01	2.53	2.84	0.01	1.39	0.06	7.52	0.01	0.00	0.00	0.00	0.00	16.00	35.83	0.84
LP67B841_perv chl2-2-1		5.50	0.01	2.50	2.77	0.01	1.41	0.07	7.55	0.01	0.00	0.00	0.01	0.01	16.00	35.85	0.84
lp67b903 perv chl1-2-1		5.82	0.00	2.18	3.14	0.01	1.73	0.09	6.47	0.01	0.00	0.00	0.05	0.00	16.00	35.51	0.79
LP67b986 perv chl1-1-1		5.50	0.01	2.50	2.67	0.00	1.94	0.13	7.11	0.00	0.00	0.00	0.03	0.01	16.00	35.91	0.79
LP67b986 perv chl2-2-1		5.53	0.01	2.47	2.70	0.00	2.27	0.12	6.77	0.00	0.00	0.01	0.00	0.00	16.00	35.88	0.75
lp67bw11037 perv chl1-2-1		5.59	0.00	2.41	2.65	0.00	1.75	0.05	7.42	0.00	0.00	0.00	0.01	0.01	16.00	35.88	0.81
lp67bw11037 perv chl2-4-1		5.62	0.01	2.38	2.67	0.01	1.79	0.07	7.26	0.01	0.00	0.05	0.00	0.02	16.00	35.87	0.80
LP67BW11063 perv chl1-1-1		5.65	0.01	2.35	2.78	0.01	1.98	0.05	6.92	0.00	0.00	0.04	0.00	0.00	16.00	35.79	0.78
LP67BW11063 perv chl2-2-1		5.62	0.01	2.38	2.68	0.01	1.99	0.05	7.05	0.01	0.00	0.10	0.00	0.00	16.00	35.88	0.78
LP67BW11132 perv bt1-4-1		5.79	0.01	2.21	2.88	0.00	2.90	0.03	5.72	0.00	0.18	0.02	0.01	0.00	16.00	35.75	0.66
LP67BW11132 perv chl1-6-1		5.84	0.01	2.16	2.93	0.00	3.01	0.04	5.59	0.01	0.00	0.00	0.03	0.00	16.00	35.61	0.65
LP67BW11132 perv chl2-8-1		5.45	0.01	2.56	2.73	0.00	3.09	0.03	6.01	0.01	0.00	0.01	0.02	0.01	16.00	35.91	0.66

Label	Oxides:	Mineral	SiO_2	TiO_2	Al_2O_3	Cr_2O_3	FeO	V_2O_3	ZnO	MnO	MgO	CaO	Na_2O	K_2O	BaO	SrO	NiO	F	Cl	H_2O	O=F	O=Cl	Sum Ox
LP12434_perv mica1-3-1		phg	46.24	0.65	26.59	0.04	1.74	0.00	0.00	0.09	6.07	0.02	0.12	10.34	1.17	0.00	0.00	0.43	0.01	4.11	0.18	0.00	97.43
LP12434_perv mica2-4-1		phg	46.64	0.56	25.39	0.01	2.41	0.00	0.00	0.00	8.36	0.06	0.10	10.35	0.98	0.00	0.00	0.62	0.00	4.08	0.26	0.00	99.32
LP12434_perv mica3-5-1		phg	48.29	0.66	29.94	0.04	1.12	0.00	0.13	0.04	3.71	0.03	0.16	10.49	1.53	0.00	0.00	0.13	0.00	4.43	0.05	0.00	100.65
LP12516_perv mica1-9-1		phg	49.39	0.65	29.37	0.04	1.19	0.03	0.19	0.01	3.49	0.00	0.14	10.72	0.48	0.00	0.01	0.25	0.02	4.38	0.11	0.00	100.27
LP12523_perv mica1-3-1		phg	50.00	0.52	30.08	0.07	1.08	0.00	0.01	0.01	3.24	0.07	0.16	10.84	0.47	0.00	0.04	0.32	0.01	4.40	0.14	0.00	101.18
LP12523_perv mica 2-5-1		phg	50.74	0.47	28.95	0.15	1.39	0.03	0.00	0.03	3.68	0.01	0.16	10.41	0.50	0.00	0.00	0.28	0.00	4.43	0.12	0.00	101.11
LP12523_perv mica 3-7-1		phg	49.69	0.44	29.12	0.00	1.13	0.01	0.27	0.00	3.67	0.02	0.12	10.77	0.49	0.00	0.00	0.30	0.00	4.36	0.13	0.00	100.25
LP12531_perv mica1-4-1		phg	48.13	0.59	29.79	0.08	0.92	0.04	0.00	0.00	3.11	0.02	0.15	10.77	0.57	0.00	0.00	0.23	0.01	4.32	0.10	0.00	98.62
LP12539 perv bt1-3-1		phg	47.60	0.09	30.21	0.00	1.29	0.03	0.62	0.03	4.63	0.04	0.12	8.47	0.26	0.00	0.00	0.23	0.00	4.33	0.10	0.00	97.84
LP12539 perv bt3-5-1		phg	47.17	0.09	27.86	0.00	1.52	0.02	0.05	0.00	6.27	0.08	0.13	9.46	0.29	0.00	0.04	0.29	0.00	4.24	0.12	0.00	97.41
Lp12555_perv mica 1-3-1		phg	49.42	0.51	30.10	0.00	0.92	0.00	0.00	0.05	3.51	0.00	0.15	10.72	0.40	0.00	0.00	0.32	0.00	4.37	0.13	0.00	100.33
Lp12555_perv mica 2-4-1		phg	47.82	0.49	29.89	0.05	1.36	0.01	0.12	0.07	4.66	0.01	0.13	9.78	0.35	0.00	0.01	0.35	0.00	4.30	0.15	0.00	99.25
Lp44243_perv tlc 1-1-1		ms	48.87	0.52	28.90	0.05	1.93	0.01	0.04	0.00	3.85	0.01	0.14	10.88	0.31	0.02	0.00	0.17	0.01	4.39	0.07	0.00	100.03
LP46A103_perv mica1-5-1		phg	50.14	0.43	30.47	0.00	0.48	0.02	0.00	0.04	3.41	0.07	0.13	8.63	0.25	0.00	0.00	0.22	0.01	4.42	0.09	0.00	98.62
LP46A113_perv mica1-5-1		phg	47.17	0.83	28.87	0.03	1.73	0.00	0.00	0.01	3.81	0.05	0.17	10.52	1.72	0.00	0.02	0.12	0.02	4.34	0.05	0.00	99.35
LP46A113_perv mica2-6-1		phg	47.69	0.73	29.42	0.03	1.47	0.00	0.01	0.08	3.44	0.00	0.15	10.55	1.68	0.00	0.00	0.09	0.01	4.39	0.04	0.00	99.70
LP46A113_perv mica3-7-1		phg	46.88	0.77	28.77	0.07	1.76	0.00	0.04	0.01	4.02	0.00	0.17	9.97	1.72	0.00	0.00	0.16	0.02	4.29	0.07	0.01	98.58

Label	Cations:	Si	Ti	Al IV	Al VI	Cr	Fe2+	V	Zn	Mn2+	Mg	Ca	Na	K	Ba	Sr	Ni	F	Cl	OH	Sum Cat	Mg #	Si / Al IV
LP12434_perv mica1-3-1		6.43	0.07	1.57	2.78	0.00	0.20	0.00	0.00	0.01	1.26	0.00	0.03	1.83	0.06	0.00	0.00	0.19	0.00	3.81	18.26	0.86	4.08
LP12434_perv mica2-4-1		6.39	0.06	1.61	2.49	0.00	0.28	0.00	0.00	0.00	1.71	0.01	0.03	1.81	0.05	0.00	0.00	0.27	0.00	3.73	18.42	0.86	3.96
LP12434_perv mica3-5-1		6.45	0.07	1.55	3.17	0.01	0.13	0.00	0.01	0.01	0.74	0.01	0.04	1.79	0.08	0.00	0.00	0.05	0.00	3.95	18.04	0.86	4.17
LP12516_perv mica1-9-1		6.57	0.07	1.43	3.18	0.00	0.13	0.00	0.02	0.00	0.69	0.00	0.04	1.82	0.03	0.00	0.00	0.11	0.01	3.89	17.98	0.84	4.61
LP12523_perv mica 1-3-1		6.58	0.05	1.42	3.25	0.01	0.12	0.00	0.00	0.00	0.64	0.01	0.04	1.82	0.02	0.00	0.00	0.13	0.00	3.87	17.96	0.84	4.64
LP12523_perv mica 2-5-1		6.67	0.05	1.33	3.16	0.02	0.15	0.00	0.00	0.00	0.72	0.00	0.04	1.75	0.03	0.00	0.00	0.12	0.00	3.88	17.92	0.83	5.03
LP12523_perv mica 3-7-1		6.61	0.04	1.39	3.18	0.00	0.13	0.00	0.03	0.00	0.73	0.00	0.03	1.83	0.03	0.00	0.00	0.13	0.00	3.87	17.99	0.85	4.76
LP12531_perv mica1-4-1		6.51	0.06	1.49	3.26	0.01	0.10	0.00	0.00	0.00	0.63	0.00	0.04	1.86	0.03	0.00	0.00	0.10	0.00	3.90	18.00	0.86	4.38
LP12539 perv bt1-3-1		6.43	0.01	1.57	3.24	0.00	0.15	0.00	0.06	0.00	0.93	0.01	0.03	1.46	0.01	0.00	0.00	0.10	0.00	3.90	17.90	0.87	4.09
LP12539 perv bt3-5-1		6.45	0.01	1.55	2.95	0.00	0.17	0.00	0.01	0.00	1.28	0.01	0.04	1.65	0.02	0.00	0.01	0.13	0.00	3.87	18.13	0.88	4.17
Lp12555_perv mica 1-3-1		6.55	0.05	1.45	3.25	0.00	0.10	0.00	0.00	0.01	0.69	0.00	0.04	1.81	0.02	0.00	0.00	0.13	0.00	3.87	17.97	0.87	4.52
Lp12555_perv mica 2-4-1		6.41	0.05	1.59	3.14	0.01	0.15	0.00	0.01	0.01	0.93	0.00	0.03	1.67	0.02	0.00	0.00	0.15	0.00	3.85	18.02	0.86	4.04
Lp44243_perv mica 1-1-1		6.54	0.05	1.46	3.11	0.01	0.22	0.00	0.00	0.00	0.77	0.00	0.04	1.86	0.02	0.00	0.00	0.07	0.00	3.93	18.07	0.78	4.49
LP46A103_perv mica1-5-1		6.64	0.04	1.36	3.40	0.00	0.05	0.00	0.00	0.01	0.67	0.01	0.03	1.46	0.01	0.00	0.00	0.09	0.00	3.90	17.68	0.93	4.88
LP46A113_perv mica1-5-1		6.43	0.09	1.57	3.07	0.00	0.20	0.00	0.00	0.00	0.78	0.01	0.05	1.83	0.09	0.00	0.00	0.05	0.01	3.94	18.10	0.80	4.10
LP46A113_perv mica2-6-1		6.46	0.07	1.54	3.15	0.00	0.17	0.00	0.00	0.01	0.70	0.00	0.04	1.82	0.09	0.00	0.00	0.04	0.00	3.96	18.05	0.81	4.18
LP46A113_perv mica3-7-1		6.42	0.08	1.58	3.07	0.01	0.20	0.00	0.00	0.00	0.82	0.00	0.05	1.74	0.09	0.00	0.00	0.07	0.01	3.92	18.06	0.80	4.08

Label **Oxides:**	Mineral	SiO_2	TiO_2	Al_2O_3	Cr_2O_3	FeO	V_2O_3	ZnO	MnO	MgO	CaO	Na_2O	K_2O	BaO	SrO	NiO	F	Cl	H_2O	O=F	O=Cl	Sum Ox
LP46A134 perv mica3-10-1	phg	47.14	0.20	31.79	0.03	0.58	0.00	0.00	0.00	2.71	0.00	0.20	10.80	2.23	0.00	0.00	0.11	0.00	4.40	0.05	0.00	100.14
LP46A150_perv mica3-5-1	phg	49.40	0.46	29.62	0.02	1.82	0.00	0.00	0.01	2.76	0.00	0.14	10.88	0.27	0.00	0.03	0.17	0.01	4.41	0.07	0.00	99.93
LP46A150_perv mica1-6-1	phg	50.04	0.49	28.86	0.02	1.55	0.03	0.00	0.06	3.12	0.00	0.13	10.95	0.17	0.00	0.00	0.25	0.00	4.38	0.11	0.00	99.93
LP46A177 perv mica2-9-1	phg	47.77	0.52	22.56	0.00	1.69	0.04	0.04	0.09	11.51	0.00	0.03	10.77	0.16	0.00	0.01	1.03	0.02	3.92	0.43	0.00	99.71
LP46A187_perv mica1-3-1	phg	49.09	0.50	30.29	0.00	0.95	0.00	0.00	0.06	3.17	0.00	0.15	11.41	0.28	0.00	0.00	0.21	0.00	4.42	0.09	0.00	100.45
LP46A187_perv mica2-4-1	phg	49.06	0.46	30.34	0.05	0.94	0.00	0.16	0.00	2.98	0.01	0.13	11.17	0.22	0.00	0.03	0.17	0.00	4.42	0.07	0.00	100.06
LP46A204 perv mica3-7-1	phg	49.34	0.33	30.86	0.00	0.87	0.01	0.00	0.00	2.90	0.02	0.16	11.34	0.20	0.00	0.00	0.20	0.00	4.44	0.08	0.00	100.59
LP46A204 perv mica4-8-1	phg	47.82	0.39	30.43	0.00	1.22	0.01	0.04	0.05	4.00	0.00	0.14	10.80	0.24	0.00	0.00	0.18	0.00	4.39	0.08	0.00	99.65
LP46A250 perv mica1-1-1	phg	47.46	0.32	33.33	0.00	0.83	0.00	0.01	0.00	1.61	0.03	0.19	11.15	0.26	0.00	0.03	0.20	0.02	4.40	0.08	0.00	99.75
LP46A250 perv mica2-3-1	phg	48.45	0.32	32.89	0.00	0.84	0.01	0.06	0.08	1.98	0.00	0.21	11.30	0.17	0.00	0.01	0.24	0.01	4.43	0.10	0.00	100.89
LP46A250 perv mica4-6-1	phg	47.77	0.21	33.48	0.00	0.93	0.00	0.00	0.04	1.75	0.00	0.22	11.42	0.18	0.00	0.00	0.21	0.03	4.42	0.09	0.01	100.56
LP46A250 perv mica7-13-1	phg	46.79	0.27	32.00	0.04	0.87	0.00	0.09	0.00	1.88	0.06	0.23	10.80	0.09	0.00	0.03	0.18	0.05	4.30	0.08	0.01	97.59
LP46A297 perv mica1-5-1	phg	49.48	0.42	29.96	0.01	1.75	0.01	0.07	0.04	2.46	0.02	0.15	11.24	0.25	0.00	0.06	0.22	0.00	4.40	0.09	0.00	100.45
LP46A297 perv mica2-6-1	phg	48.52	0.41	30.62	0.00	1.94	0.00	0.09	0.01	2.35	0.00	0.20	11.19	0.39	0.00	0.02	0.17	0.00	4.40	0.07	0.00	100.26
LP46A297 perv mica4-8-1	phg	48.42	0.51	31.16	0.02	1.96	0.00	0.11	0.04	2.21	0.00	0.24	11.23	0.29	0.00	0.03	0.13	0.00	4.44	0.06	0.00	100.73
LP46A297 perv mica5-9-1	phg	48.27	0.46	30.61	0.00	1.58	0.02	0.00	0.02	2.30	0.00	0.22	11.43	0.33	0.00	0.09	0.19	0.00	4.38	0.08	0.00	99.83
LP46A324_mica in vein1-1	phg	46.41	0.55	34.17	0.03	2.21	0.17	0.07	0.00	0.90	0.00	0.56	10.66	0.58	0.00	0.00	0.00	0.00	4.50	0.00	0.00	100.81

Label **Cations:**	Si	Ti	Al IV	Al VI	Cr	Fe2+	V	Zn	Mn2+	Mg	Ca	Na	K	Ba	Sr	Ni	F	Cl	OH	Sum Cat	Mg #	Si / Al IV
LP46A134 perv mica3-10-1	6.35	0.02	1.65	3.40	0.00	0.07	0.00	0.00	0.00	0.54	0.00	0.05	1.86	0.12	0.00	0.00	0.05	0.00	3.95	18.06	0.89	3.85
LP46A150_perv mica3-5-1	6.60	0.05	1.40	3.26	0.00	0.20	0.00	0.00	0.00	0.55	0.00	0.04	1.85	0.01	0.00	0.00	0.07	0.00	3.93	17.97	0.73	4.70
LP46A150_perv mica1-6-1	6.67	0.05	1.33	3.20	0.00	0.17	0.00	0.00	0.01	0.62	0.00	0.03	1.86	0.01	0.00	0.00	0.11	0.00	3.89	17.96	0.78	5.01
LP46A177 perv mica2-9-1	6.49	0.05	1.51	2.11	0.00	0.19	0.01	0.00	0.01	2.33	0.00	0.01	1.87	0.01	0.00	0.00	0.44	0.00	3.55	18.58	0.92	4.31
LP46A187_perv mica1-3-1	6.52	0.05	1.48	3.27	0.00	0.11	0.00	0.00	0.01	0.63	0.00	0.04	1.93	0.01	0.00	0.00	0.09	0.00	3.91	18.04	0.86	4.41
LP46A187_perv mica2-4-1	6.53	0.05	1.47	3.29	0.01	0.10	0.00	0.02	0.00	0.59	0.00	0.03	1.90	0.01	0.00	0.00	0.07	0.00	3.93	18.00	0.85	4.45
LP46A204 perv mica3-7-1	6.53	0.03	1.47	3.34	0.00	0.10	0.00	0.00	0.00	0.57	0.00	0.04	1.91	0.01	0.00	0.00	0.08	0.00	3.92	18.01	0.86	4.43
LP46A204 perv mica4-8-1	6.41	0.04	1.59	3.21	0.00	0.14	0.00	0.00	0.01	0.80	0.00	0.04	1.85	0.01	0.00	0.00	0.08	0.00	3.92	18.09	0.85	4.02
LP46A250 perv mica1-1-1	6.33	0.03	1.67	3.57	0.00	0.09	0.00	0.00	0.00	0.32	0.01	0.05	1.90	0.01	0.00	0.00	0.08	0.00	3.91	17.99	0.78	3.80
LP46A250 perv mica2-3-1	6.39	0.03	1.61	3.50	0.00	0.09	0.00	0.01	0.01	0.39	0.00	0.06	1.90	0.01	0.00	0.00	0.10	0.00	3.90	18.00	0.81	3.97
LP46A250 perv mica4-6-1	6.33	0.02	1.67	3.56	0.00	0.10	0.00	0.00	0.00	0.35	0.00	0.06	1.93	0.01	0.00	0.00	0.09	0.01	3.91	18.03	0.77	3.79
LP46A250 perv mica7-13-1	6.38	0.03	1.62	3.52	0.00	0.10	0.00	0.01	0.00	0.38	0.01	0.06	1.88	0.01	0.00	0.00	0.08	0.01	3.91	17.99	0.79	3.93
LP46A297 perv mica1-5-1	6.59	0.04	1.41	3.29	0.00	0.19	0.00	0.01	0.00	0.49	0.00	0.04	1.91	0.01	0.00	0.01	0.09	0.00	3.91	17.99	0.72	4.66
LP46A297 perv mica2-6-1	6.49	0.04	1.51	3.32	0.00	0.22	0.00	0.01	0.00	0.47	0.00	0.05	1.91	0.02	0.00	0.00	0.07	0.00	3.93	18.04	0.68	4.29
LP46A297 perv mica4-8-1	6.44	0.05	1.56	3.33	0.00	0.22	0.00	0.01	0.00	0.44	0.00	0.06	1.91	0.02	0.00	0.00	0.06	0.00	3.94	18.04	0.67	4.14
LP46A297 perv mica5-9-1	6.48	0.05	1.52	3.33	0.00	0.18	0.00	0.00	0.00	0.46	0.00	0.06	1.96	0.02	0.00	0.01	0.08	0.00	3.92	18.06	0.72	4.27
LP46A324_mica in vein1-1	6.18	0.06	1.82	3.55	0.00	0.25	0.02	0.01	0.00	0.18	0.00	0.15	1.81	0.03	0.00	0.00	0.00	0.00	4.00	18.05	0.42	3.41

Label	Oxides:	Mineral	SiO_2	TiO_2	Al_2O_3	Cr_2O_3	FeO	V_2O_3	ZnO	MnO	MgO	CaO	Na_2O	K_2O	BaO	SrO	NiO	F	Cl	H_2O	O=F	O=Cl	Sum Ox
LP46A324_mica in vein2-2		phg	45.25	0.05	35.36	0.04	1.97	0.00	0.12	0.00	0.63	0.00	0.59	10.02	1.77	0.00	0.00	0.00	0.00	4.45	0.00	0.00	100.25
LP46A334_perv mica2-7-1		phg	41.19	0.51	25.79	0.04	2.31	0.02	0.20	0.00	2.05	0.09	0.38	8.20	0.32	0.00	0.01	0.08	0.09	3.75	0.03	0.02	84.97
LP46A334_mica in vein1-4		phg	46.60	0.29	33.81	0.02	2.07	0.16	0.03	0.00	1.18	0.00	0.58	10.51	0.60	0.00	0.00	0.00	0.01	4.49	0.00	0.00	100.35
LP46A334_mica in vein2-5		phg	46.65	0.24	33.97	0.00	2.21	0.10	0.01	0.00	1.18	0.01	0.61	10.31	0.44	0.00	0.06	0.03	0.01	4.48	0.01	0.00	100.31
LP46A348_perv mica1-5-1		phg	47.74	0.75	30.44	0.06	2.50	0.07	0.00	0.00	2.35	0.00	0.43	10.70	0.47	0.00	0.00	0.00	0.00	4.46	0.00	0.00	99.96
LP46A348_perv mica2-7-1		phg	47.72	0.78	29.42	0.06	2.70	0.07	0.02	0.05	2.74	0.00	0.38	10.79	0.21	0.00	0.00	0.03	0.03	4.40	0.01	0.01	99.39
LP46A348_perv mica3-8-1		phg	47.47	0.73	30.44	0.03	2.57	0.01	0.00	0.02	2.66	0.00	0.40	10.63	0.36	0.00	0.00	0.00	0.00	4.45	0.00	0.00	99.77
LP51AW2302_perv mica1		phg	49.78	0.55	29.42	0.01	0.56	0.03	0.00	0.00	3.52	0.01	0.15	10.97	0.22	0.00	0.09	0.26	0.01	4.38	0.11	0.00	99.88
LP51AW2302_perv mica2		phg	50.02	0.56	29.43	0.02	0.49	0.05	0.27	0.00	3.53	0.00	0.13	11.21	0.30	0.00	0.04	0.15	0.02	4.46	0.06	0.00	100.61
LP66112_perv mica2-2-1		phg	49.61	0.58	30.85	0.00	1.44	0.01	0.05	0.01	3.15	0.01	0.24	10.93	0.33	0.03	0.00	0.15	0.01	4.50	0.06	0.00	101.84
LP66153_perv mica2-2-1		phg	49.08	0.84	28.57	0.00	2.71	0.02	0.05	0.00	3.70	0.00	0.13	11.14	0.21	0.00	0.06	0.16	0.01	4.42	0.07	0.00	101.05
LP66155_perv mica3-6-1		phg	50.44	0.38	29.12	0.08	1.85	0.03	0.00	0.00	3.26	0.00	0.20	11.33	0.16	0.00	0.03	0.12	0.02	4.49	0.05	0.00	101.44
LP66179_perv mica2-3-1		phg	48.11	0.30	29.07	0.04	1.45	0.00	0.00	0.15	5.04	0.00	0.17	10.45	1.15	0.00	0.02	0.08	0.00	4.44	0.03	0.00	100.44
LP66233_perv mica1-8-1		phg	48.60	0.29	31.12	0.04	1.87	0.00	0.08	0.06	2.82	0.00	0.24	10.64	0.24	0.00	0.02	0.20	0.00	4.42	0.08	0.00	100.56
LP66254_perv mica2-2-1		phg	49.39	0.49	29.51	0.01	0.97	0.03	0.01	0.01	3.17	0.00	0.13	9.66	0.66	0.00	0.00	0.22	0.02	4.36	0.09	0.00	98.54
LP66282_perv mica2-5-1		phg	49.73	0.63	30.80	0.00	1.30	0.00	0.03	0.00	3.04	0.00	0.17	10.65	0.56	0.00	0.05	0.12	0.00	4.51	0.05	0.00	101.53
LP66296_perv mica1-2-1		phg	49.28	0.38	31.29	0.00	1.13	0.03	0.07	0.05	2.67	0.00	0.17	11.26	0.24	0.00	0.00	0.15	0.00	4.48	0.06	0.00	101.13

Label	Cations:	Si	Ti	Al IV	Al VI	Cr	Fe2+	V	Zn	Mn2+	Mg	Ca	Na	K	Ba	Sr	Ni	F	Cl	OH	Sum Cat	Mg #	Si / Al IV
LP46A324_mica in vein2-2		6.09	0.01	1.91	3.70	0.00	0.22	0.00	0.01	0.00	0.13	0.00	0.15	1.72	0.09	0.00	0.00	0.00	0.00	4.00	18.04	0.36	3.19
LP46A334_perv mica2-7-1		6.48	0.06	1.52	3.27	0.01	0.30	0.00	0.02	0.00	0.48	0.02	0.12	1.65	0.02	0.00	0.00	0.04	0.02	3.94	17.94	0.61	4.27
LP46A334_mica in vein1-4		6.23	0.03	1.77	3.55	0.00	0.23	0.02	0.00	0.00	0.24	0.00	0.15	1.79	0.03	0.00	0.00	0.00	0.00	4.00	18.04	0.51	3.51
LP46A334_mica in vein2-5		6.23	0.02	1.78	3.57	0.00	0.25	0.01	0.00	0.00	0.24	0.00	0.16	1.76	0.02	0.00	0.01	0.01	0.00	3.99	18.03	0.49	3.51
LP46A348_perv mica1-5-1		6.42	0.08	1.58	3.25	0.01	0.28	0.01	0.00	0.00	0.47	0.00	0.11	1.84	0.03	0.00	0.00	0.00	0.00	4.00	18.06	0.63	4.07
LP46A348_perv mica2-7-1		6.46	0.08	1.54	3.15	0.01	0.31	0.01	0.00	0.01	0.55	0.00	0.10	1.86	0.01	0.00	0.00	0.02	0.01	3.98	18.09	0.64	4.19
LP46A348_perv mica3-8-1		6.39	0.07	1.61	3.23	0.00	0.29	0.00	0.00	0.00	0.53	0.00	0.11	1.83	0.02	0.00	0.00	0.00	0.00	4.00	18.08	0.65	3.98
LP51AW2302_perv mica1		6.62	0.06	1.38	3.23	0.00	0.06	0.00	0.00	0.00	0.70	0.00	0.04	1.86	0.01	0.00	0.01	0.11	0.00	3.89	17.97	0.92	4.79
LP51AW2302_perv mica2		6.62	0.06	1.38	3.21	0.00	0.06	0.01	0.03	0.00	0.70	0.00	0.03	1.89	0.02	0.00	0.00	0.06	0.00	3.93	17.99	0.93	4.78
LP66112_perv mica2-2-1		6.50	0.06	1.50	3.26	0.00	0.16	0.00	0.01	0.00	0.62	0.00	0.06	1.83	0.02	0.00	0.00	0.06	0.00	3.94	18.01	0.80	4.33
LP66153_perv mica2-2-1		6.54	0.08	1.46	3.02	0.00	0.30	0.00	0.01	0.00	0.73	0.00	0.03	1.89	0.01	0.00	0.01	0.07	0.00	3.93	18.10	0.71	4.48
LP66155_perv mica3-6-1		6.65	0.04	1.35	3.17	0.01	0.20	0.00	0.00	0.00	0.64	0.00	0.05	1.90	0.01	0.00	0.00	0.05	0.00	3.95	18.03	0.76	4.91
LP66179_perv mica2-3-1		6.44	0.03	1.56	3.03	0.00	0.16	0.00	0.00	0.02	1.01	0.00	0.05	1.79	0.06	0.00	0.00	0.03	0.00	3.97	18.15	0.86	4.14
LP66233_perv mica1-8-1		6.45	0.03	1.55	3.32	0.00	0.21	0.00	0.01	0.01	0.56	0.00	0.06	1.80	0.01	0.00	0.00	0.08	0.00	3.92	18.01	0.73	4.17
LP66254_perv mica2-2-1		6.63	0.05	1.37	3.30	0.00	0.11	0.00	0.00	0.00	0.63	0.00	0.04	1.65	0.04	0.00	0.00	0.09	0.00	3.90	17.83	0.85	4.85
LP66282_perv mica2-5-1		6.52	0.06	1.48	3.29	0.00	0.14	0.00	0.00	0.00	0.59	0.00	0.04	1.78	0.03	0.00	0.01	0.05	0.00	3.95	17.95	0.81	4.42
LP66296_perv mica1-2-1		6.49	0.04	1.51	3.35	0.00	0.12	0.00	0.01	0.01	0.53	0.00	0.05	1.89	0.01	0.00	0.00	0.06	0.00	3.94	18.01	0.81	4.31

Label **Oxides:**	Mineral	SiO_2	TiO_2	Al_2O_3	Cr_2O_3	FeO	V_2O_3	ZnO	MnO	MgO	CaO	Na_2O	K_2O	BaO	SrO	NiO	F	Cl	H_2O	O=F	O=Cl	Sum Ox
LP66296_perv mica2-6-1	phg	45.13	0.38	29.81	0.02	3.02	0.05	0.06	0.04	6.32	0.01	0.10	8.94	0.29	0.00	0.00	0.17	0.00	4.32	0.07	0.00	98.62
LP66311_perv mica1-4-1	phg	48.49	0.46	28.62	0.03	1.05	0.03	0.10	0.00	3.58	0.02	0.10	10.59	0.36	0.00	0.00	0.22	0.01	4.30	0.09	0.00	97.89
LP66391_perv bt1-4-1	phg	46.70	0.24	30.23	0.01	4.16	0.05	0.00	0.03	5.02	0.00	0.19	9.40	0.20	0.00	0.06	0.11	0.00	4.44	0.04	0.00	100.79
LP66419_perv mica1-5-1	phg	46.44	0.77	27.18	0.02	3.80	0.04	0.05	0.06	5.58	0.01	0.15	10.83	0.20	0.00	0.00	0.36	0.01	4.21	0.15	0.00	99.58
LP67B140 perv mica1-3-1	phg	48.20	0.38	30.98	0.01	2.07	0.02	0.00	0.04	2.27	0.02	0.38	10.05	0.04	0.00	0.02	0.11	0.00	4.41	0.04	0.00	98.93
LP67B140 perv mica2-4-1	phg	47.71	0.31	29.00	0.01	2.05	0.00	0.02	0.08	2.59	0.04	0.36	10.34	0.14	0.00	0.00	0.13	0.01	4.30	0.05	0.00	97.02
LP67B476 perv mica1-3-1	phg	47.17	0.60	31.79	0.09	2.47	0.05	0.00	0.01	2.16	0.01	0.48	10.88	0.15	0.00	0.03	0.03	0.01	4.46	0.01	0.00	100.38
LP67B476 perv mica2-4-1	phg	45.22	0.70	30.42	0.02	2.30	0.00	0.00	0.00	1.77	0.00	0.39	10.26	0.24	0.00	0.00	0.05	0.01	4.25	0.02	0.00	95.61
lp67b663 perv mica1-3-1	phg	47.70	0.59	30.26	0.02	2.64	0.03	0.09	0.02	2.72	0.00	0.37	10.67	0.33	0.00	0.00	0.06	0.00	4.43	0.03	0.00	99.92
lp67b663 perv mica2-4-1	phg	47.39	0.37	29.34	0.02	2.61	0.05	0.00	0.04	3.77	0.00	0.22	11.07	0.24	0.00	0.00	0.04	0.00	4.41	0.02	0.00	99.53
LP67B687 perv mica2-6-1	phg	48.68	0.06	27.68	0.06	4.43	0.00	0.00	0.11	3.20	0.04	0.16	11.31	0.13	0.00	0.00	0.05	0.01	4.40	0.02	0.00	100.29
Lp67b760_ser in vein 1-6-1	ms	48.08	0.21	28.47	0.00	2.96	0.00	0.00	0.06	4.40	0.00	0.19	10.85	0.31	0.03	0.00	0.00	0.00	4.45	0.00	0.00	100.00
LP67B790_perv mica1-3-1	phg	47.80	0.45	30.33	0.03	1.93	0.03	0.01	0.00	3.70	0.00	0.32	10.58	1.21	0.00	0.00	0.04	0.00	4.47	0.02	0.00	100.86
LP67B841_mica patch1-3	phg	45.91	0.43	34.53	0.00	1.62	0.05	0.07	0.01	2.69	0.00	0.57	10.42	0.78	0.00	0.05	0.02	0.00	4.53	0.01	0.00	101.67
LP67B841_mica patch2-5	phg	46.07	0.41	33.87	0.02	1.66	0.00	0.00	0.09	2.88	0.00	0.59	10.39	0.82	0.00	0.00	0.01	0.00	4.52	0.01	0.00	101.34
lp67b903 perv mica1-5-1	phg	47.69	0.83	31.59	0.03	1.34	0.00	0.02	0.04	2.51	0.00	0.43	10.63	1.16	0.00	0.07	0.01	0.00	4.50	0.00	0.00	100.84
lp67b903 perv mica2-6-1	phg	47.10	0.79	30.85	0.06	1.75	0.01	0.10	0.04	3.01	0.00	0.37	10.32	1.22	0.00	0.01	0.01	0.01	4.45	0.00	0.00	100.10

Label **Cations:**	Si	Ti	Al IV	Al VI	Cr	Fe2+	V	Zn	Mn2+	Mg	Ca	Na	K	Ba	Sr	Ni	F	Cl	OH	Sum Cat	Mg #	Si / Al IV
LP66296_perv mica2-6-1	6.15	0.04	1.86	2.93	0.00	0.34	0.01	0.01	0.00	1.28	0.00	0.03	1.55	0.02	0.00	0.00	0.08	0.00	3.93	18.21	0.79	3.31
LP66311_perv mica1-4-1	6.60	0.05	1.40	3.19	0.00	0.12	0.00	0.01	0.00	0.73	0.00	0.03	1.84	0.02	0.00	0.00	0.09	0.00	3.90	17.99	0.86	4.71
LP66391_perv bt1-4-1	6.24	0.03	1.76	3.01	0.00	0.47	0.01	0.00	0.00	1.00	0.00	0.05	1.60	0.01	0.00	0.01	0.05	0.00	3.96	18.17	0.68	3.55
LP66419_perv mica1-5-1	6.35	0.08	1.65	2.73	0.00	0.43	0.00	0.01	0.01	1.14	0.00	0.04	1.89	0.01	0.00	0.00	0.16	0.00	3.84	18.34	0.72	3.85
LP67B140 perv mica1-3-1	6.48	0.04	1.52	3.38	0.00	0.23	0.00	0.00	0.00	0.45	0.00	0.10	1.72	0.00	0.00	0.00	0.05	0.00	3.96	17.94	0.66	4.25
LP67B140 perv mica2-4-1	6.57	0.03	1.43	3.27	0.00	0.24	0.00	0.00	0.01	0.53	0.01	0.10	1.81	0.01	0.00	0.00	0.06	0.00	3.94	18.00	0.69	4.58
LP67B476 perv mica1-3-1	6.31	0.06	1.69	3.33	0.01	0.28	0.01	0.00	0.00	0.43	0.00	0.13	1.86	0.01	0.00	0.00	0.01	0.00	3.98	18.11	0.61	3.74
LP67B476 perv mica2-4-1	6.34	0.07	1.66	3.37	0.00	0.27	0.00	0.00	0.00	0.37	0.00	0.11	1.84	0.01	0.00	0.00	0.02	0.00	3.98	18.04	0.58	3.83
lp67b663 perv mica1-3-1	6.42	0.06	1.58	3.22	0.00	0.30	0.00	0.01	0.00	0.55	0.00	0.10	1.83	0.02	0.00	0.00	0.03	0.00	3.97	18.08	0.65	4.06
lp67b663 perv mica2-4-1	6.42	0.04	1.58	3.10	0.00	0.30	0.01	0.00	0.01	0.76	0.00	0.06	1.91	0.01	0.00	0.00	0.02	0.00	3.98	18.19	0.72	4.05
LP67B687 perv mica2-6-1	6.59	0.01	1.41	3.01	0.01	0.50	0.00	0.00	0.01	0.65	0.01	0.04	1.95	0.01	0.00	0.00	0.02	0.00	3.98	18.19	0.56	4.68
Lp67b760_ser in vein 1-6-1	6.48	0.02	1.52	3.01	0.00	0.33	0.00	0.00	0.01	0.88	0.00	0.05	1.87	0.02	0.00	0.00	0.00	0.00	4.00	18.19	0.73	4.28
LP67B790_perv mica1-3-1	6.39	0.05	1.61	3.16	0.00	0.22	0.00	0.00	0.00	0.74	0.00	0.08	1.80	0.06	0.00	0.00	0.02	0.00	3.98	18.12	0.77	3.96
LP67B841_mica patch1-3	6.07	0.04	1.94	3.44	0.00	0.18	0.01	0.01	0.00	0.53	0.00	0.15	1.76	0.04	0.00	0.01	0.01	0.00	3.99	18.15	0.75	3.13
LP67B841_mica patch2-5	6.11	0.04	1.89	3.40	0.00	0.18	0.00	0.00	0.01	0.57	0.00	0.15	1.76	0.04	0.00	0.00	0.01	0.00	3.99	18.16	0.76	3.23
lp67b903 perv mica1-5-1	6.35	0.08	1.65	3.31	0.00	0.15	0.00	0.00	0.01	0.50	0.00	0.11	1.81	0.06	0.00	0.01	0.00	0.00	4.00	18.04	0.77	3.86
lp67b903 perv mica2-6-1	6.34	0.08	1.66	3.23	0.01	0.20	0.00	0.01	0.01	0.60	0.00	0.10	1.77	0.07	0.00	0.00	0.01	0.00	3.99	18.07	0.75	3.81

Label **Oxides:**	Mineral	SiO_2	TiO_2	Al_2O_3	Cr_2O_3	FeO	V_2O_3	ZnO	MnO	MgO	CaO	Na_2O	K_2O	BaO	SrO	NiO	F	Cl	H_2O	O=F	O=Cl	Sum Ox
lp67bw11037 perv mica1-3	phg	48.58	0.53	29.07	0.00	1.80	0.05	0.02	0.05	3.92	0.00	0.24	10.69	0.11	0.00	0.00	0.06	0.01	4.44	0.02	0.00	99.54
lp67bw11037 perv mica2-6	phg	48.14	0.62	29.13	0.02	2.00	0.06	0.00	0.09	3.85	0.00	0.16	10.73	0.20	0.00	0.01	0.11	0.02	4.40	0.05	0.00	99.46
LP67BW11063 mica2-7-1	phg	49.19	0.54	29.63	0.00	1.43	0.03	0.00	0.00	3.34	0.00	0.18	11.27	0.07	0.00	0.01	0.01	0.01	4.50	0.00	0.00	100.20
LP67BW11132 perv mica1	phg	49.03	0.59	30.34	0.00	1.87	0.02	0.00	0.01	2.54	0.02	0.20	11.13	0.00	0.00	0.00	0.14	0.00	4.44	0.06	0.00	100.27
LP67BW11132 perv mica2	phg	49.33	0.58	29.94	0.00	2.01	0.01	0.00	0.00	2.67	0.00	0.18	10.92	0.08	0.00	0.00	0.23	0.00	4.40	0.10	0.00	100.26
LP12428_perv mica2-4	phl	47.43	0.07	9.58	0.03	3.94	0.00	0.06	0.00	25.70	0.00	0.02	8.34	0.00	0.00	0.00	2.37	0.00	3.21	1.00	0.00	99.74
LP12450_perv mica1-1	phl	42.24	0.64	13.98	0.01	5.49	0.04	0.07	0.07	22.78	0.01	0.02	9.55	0.06	0.00	0.01	2.36	0.00	3.11	0.99	0.00	99.45
LP12450_perv mica2-5	phl	41.37	0.60	14.67	0.05	5.67	0.06	0.08	0.02	22.91	0.00	0.02	9.21	0.29	0.00	0.00	2.12	0.01	3.21	0.89	0.00	99.41
LP12450_perv bt1-6-1	phl	42.01	0.63	13.97	0.04	5.25	0.06	0.12	0.10	22.45	0.00	0.04	10.08	0.10	0.00	0.00	2.27	0.03	3.12	0.95	0.01	99.30
LP12450_perv mica3-7-1	phl	42.64	0.58	13.51	0.05	5.61	0.00	0.00	0.06	22.73	0.00	0.02	9.95	0.08	0.00	0.01	2.49	0.00	3.05	1.05	0.00	99.72
LP12457 perv bt1-3-1	phl	39.76	0.49	14.30	0.02	6.42	0.00	0.00	0.07	22.89	0.00	0.05	8.33	0.15	0.00	0.00	1.72	0.00	3.29	0.72	0.00	96.76
LP12457 perv bt2-5-1	phl	41.56	0.61	13.55	0.01	5.93	0.01	0.00	0.07	21.89	0.02	0.06	9.81	0.21	0.00	0.01	1.84	0.01	3.27	0.77	0.00	98.10
LP12465 perv bt1-1-1	phl	41.52	0.68	13.83	0.00	5.80	0.08	0.05	0.10	21.88	0.00	0.05	9.84	0.17	0.00	0.03	1.85	0.00	3.28	0.78	0.00	98.38
Lp12476 perv mica1-2-1	phl	42.82	0.32	13.05	0.09	4.97	0.03	0.07	0.08	23.87	0.01	0.04	9.86	0.00	0.00	0.00	2.58	0.00	3.02	1.09	0.00	99.72
Lp12476 perv bt1-8-1	phl	42.66	0.25	12.93	0.04	5.34	0.04	0.12	0.08	23.77	0.00	0.04	9.84	0.04	0.00	0.00	2.58	0.00	3.00	1.09	0.00	99.67
LP12493 perv bt1-1-1	phl	41.87	0.55	14.11	0.00	4.50	0.05	0.13	0.05	22.92	0.01	0.06	9.82	0.29	0.00	0.00	2.06	0.01	3.22	0.87	0.00	98.79
LP12493 perv bt2-2-1	phl	40.84	0.46	14.60	0.03	4.35	0.01	0.09	0.00	23.25	0.03	0.07	8.97	0.13	0.00	0.00	1.91	0.00	3.25	0.80	0.00	97.20

Label **Cations:**	Si	Ti	Al IV	Al VI	Cr	Fe2+	V	Zn	Mn2+	Mg	Ca	Na	K	Ba	Sr	Ni	F	Cl	OH	Sum Cat	Mg #	Si / Al IV
lp67bw11037 perv mica1-3	6.52	0.05	1.48	3.12	0.00	0.20	0.01	0.00	0.01	0.79	0.00	0.06	1.83	0.01	0.00	0.00	0.03	0.00	3.97	18.07	0.80	4.41
lp67bw11037 perv mica2-6	6.48	0.06	1.52	3.11	0.00	0.23	0.01	0.00	0.01	0.77	0.00	0.04	1.84	0.01	0.00	0.00	0.05	0.00	3.95	18.08	0.78	4.27
LP67BW11063 mica2-7-1	6.55	0.05	1.45	3.20	0.00	0.16	0.00	0.00	0.00	0.66	0.00	0.05	1.91	0.00	0.00	0.00	0.00	0.00	3.99	18.05	0.81	4.52
LP67BW11132 perv mica1	6.53	0.06	1.47	3.29	0.00	0.21	0.00	0.00	0.00	0.51	0.00	0.05	1.89	0.00	0.00	0.00	0.06	0.00	3.94	18.01	0.71	4.43
LP67BW11132 perv mica2	6.57	0.06	1.44	3.26	0.00	0.22	0.00	0.00	0.00	0.53	0.00	0.05	1.85	0.00	0.00	0.00	0.10	0.00	3.90	17.98	0.70	4.57
LP12428_perv mica2-4	6.57	0.01	1.43	0.13	0.00	0.46	0.00	0.01	0.00	5.30	0.00	0.01	1.47	0.00	0.00	0.00	1.04	0.00	2.96	19.38	0.92	4.58
LP12450_perv mica1-1	5.99	0.07	2.01	0.33	0.00	0.65	0.01	0.01	0.01	4.82	0.00	0.00	1.73	0.00	0.00	0.00	1.06	0.00	2.94	19.63	0.88	2.99
LP12450_perv mica2-5	5.88	0.07	2.12	0.34	0.01	0.67	0.01	0.01	0.00	4.86	0.00	0.01	1.67	0.02	0.00	0.00	0.96	0.00	3.04	19.66	0.88	2.78
LP12450_perv bt1-6-1	5.99	0.07	2.01	0.34	0.00	0.63	0.01	0.01	0.01	4.77	0.00	0.01	1.83	0.01	0.00	0.00	1.02	0.01	2.97	19.69	0.88	2.98
LP12450_perv mica3-7-1	6.05	0.06	1.95	0.31	0.01	0.67	0.00	0.00	0.01	4.80	0.00	0.01	1.80	0.01	0.00	0.00	1.12	0.00	2.88	19.66	0.88	3.10
LP12457 perv bt1-3-1	5.81	0.05	2.19	0.27	0.00	0.79	0.00	0.00	0.01	4.99	0.00	0.01	1.55	0.01	0.00	0.00	0.79	0.00	3.21	19.69	0.86	2.65
LP12457 perv bt2-5-1	6.01	0.07	1.99	0.32	0.00	0.72	0.00	0.00	0.01	4.72	0.00	0.02	1.81	0.01	0.00	0.00	0.84	0.00	3.16	19.68	0.87	3.02
LP12465 perv bt1-1-1	5.99	0.07	2.01	0.34	0.00	0.70	0.01	0.01	0.01	4.70	0.00	0.01	1.81	0.01	0.00	0.00	0.85	0.00	3.15	19.67	0.87	2.97
Lp12476 perv mica1-2-1	6.06	0.03	1.94	0.23	0.01	0.59	0.00	0.01	0.01	5.03	0.00	0.01	1.78	0.00	0.00	0.00	1.16	0.00	2.85	19.71	0.90	3.12
Lp12476 perv bt1-8-1	6.05	0.03	1.95	0.22	0.01	0.63	0.00	0.01	0.01	5.03	0.00	0.01	1.78	0.00	0.00	0.00	1.16	0.00	2.84	19.73	0.89	3.11
LP12493 perv bt1-1-1	5.98	0.06	2.02	0.35	0.00	0.54	0.01	0.01	0.01	4.88	0.00	0.02	1.79	0.02	0.00	0.00	0.93	0.00	3.07	19.68	0.90	2.96
LP12493 perv bt2-2-1	5.89	0.05	2.11	0.38	0.00	0.53	0.00	0.01	0.00	5.00	0.01	0.02	1.65	0.01	0.00	0.00	0.87	0.00	3.13	19.65	0.91	2.80

Label **Oxides:**	Mineral	SiO_2	TiO_2	Al_2O_3	Cr_2O_3	FeO	V_2O_3	ZnO	MnO	MgO	CaO	Na_2O	K_2O	BaO	SrO	NiO	F	Cl	H_2O	O=F	O=Cl	Sum Ox
LP12503_wht mica1-1-1	phl	42.99	0.46	13.87	0.02	4.03	0.00	0.23	0.07	24.30	0.00	0.08	9.83	0.01	0.00	0.00	2.49	0.00	3.11	1.05	0.00	100.45
LP12503_perv bt1-2-1	phl	42.45	0.45	13.85	0.03	4.34	0.01	0.00	0.05	24.60	0.02	0.05	9.55	0.09	0.00	0.01	2.53	0.00	3.07	1.06	0.00	100.02
LP12503_perv chl1-8-1	phl	42.77	0.44	13.20	0.05	4.31	0.09	0.16	0.03	24.27	0.07	0.03	9.49	0.09	0.00	0.02	2.52	0.00	3.05	1.06	0.00	99.54
LP12503_perv wht mica2-3	phl	43.14	0.43	12.50	0.00	4.69	0.04	0.24	0.03	24.66	0.00	0.04	9.78	0.03	0.00	0.00	2.66	0.00	3.00	1.12	0.00	100.13
LP12511_perv wht mica1-1	phl	41.82	0.67	14.28	0.06	5.91	0.07	0.17	0.14	22.42	0.03	0.08	9.90	0.12	0.00	0.09	2.38	0.00	3.10	1.00	0.00	100.25
LP12511_perv wht mica2-2	phl	43.79	0.29	12.26	0.00	5.65	0.06	0.02	0.11	23.21	0.11	0.05	9.20	0.07	0.00	0.00	2.71	0.00	2.95	1.14	0.00	99.32
LP12511_perv wht mica3-3	phl	44.01	0.19	11.86	0.00	5.60	0.00	0.12	0.05	23.42	0.04	0.03	9.33	0.06	0.00	0.00	2.87	0.00	2.86	1.21	0.00	99.23
LP16A450 perv talc1-1-1	phl	46.56	0.33	10.20	0.00	3.51	0.00	0.06	0.07	25.59	0.02	0.02	8.13	0.00	0.00	0.00	1.73	0.00	3.49	0.73	0.00	99.00
LP16A450 wh mica2-2-1	phl	43.06	0.45	13.00	0.03	3.52	0.01	0.03	0.08	24.62	0.00	0.03	10.20	0.16	0.00	0.00	2.15	0.00	3.23	0.91	0.00	99.66
Lp18365_perv phl 1-2-1	phl	42.20	0.59	11.92	0.00	7.05	0.02	0.00	0.05	22.21	0.01	0.01	9.30	0.05	0.00	0.00	2.18	0.01	3.09	0.92	0.00	97.76
Lp18365_near perv phl 1-2	phl	43.43	0.53	11.79	0.00	6.21	0.00	0.07	0.00	22.96	0.01	0.02	9.24	0.01	0.04	0.01	2.35	0.02	3.08	0.99	0.00	98.76
Lp33390_mica in chl1-1-1	phl	41.44	0.30	13.95	0.03	4.28	0.03	0.00	0.06	25.67	0.04	0.03	8.04	0.01	0.00	0.00	2.53	0.00	3.03	1.07	0.00	98.39
Lp36w197_phl 1-1-1	phl	42.42	0.64	13.79	0.08	5.32	0.01	0.17	0.11	23.00	0.00	0.06	9.61	0.11	0.00	0.00	2.31	0.01	3.14	0.97	0.00	99.81
Lp44243_phl1-9-1	phl	40.36	0.97	15.82	0.03	8.72	0.07	0.21	0.19	19.14	0.00	0.04	10.14	0.07	0.00	0.00	1.26	0.01	3.57	0.53	0.00	100.06
LP46A090_perv wht mica	phl	40.55	0.98	16.21	0.00	7.04	0.00	0.14	0.37	19.35	0.00	0.05	10.31	0.11	0.00	0.00	0.72	0.01	3.83	0.30	0.00	99.37
LP46A090_perv wht mica	phl	40.12	0.83	16.52	0.00	7.14	0.00	0.08	0.33	19.19	0.00	0.12	9.95	0.09	0.00	0.00	0.65	0.01	3.84	0.27	0.00	98.59
LP46A103_perv bt1-4-1	phl	40.08	0.96	15.26	0.00	7.47	0.01	0.00	0.30	19.58	0.00	0.08	10.19	0.03	0.00	0.04	1.60	0.01	3.35	0.67	0.00	98.27

Label **Cations:**	Si	Ti	Al IV	Al VI	Cr	Fe2+	V	Zn	Mn2+	Mg	Ca	Na	K	Ba	Sr	Ni	F	Cl	OH	Sum Cat	Mg #	Si / Al IV
LP12503_wht mica1-1-1	6.01	0.05	1.99	0.29	0.00	0.47	0.00	0.02	0.01	5.06	0.00	0.02	1.75	0.00	0.00	0.00	1.10	0.00	2.90	19.69	0.92	3.02
LP12503_perv bt1-2-1	5.96	0.05	2.04	0.26	0.00	0.51	0.00	0.00	0.01	5.15	0.00	0.01	1.71	0.01	0.00	0.00	1.12	0.00	2.88	19.70	0.91	2.93
LP12503_perv chl1-8-1	6.04	0.05	1.96	0.23	0.01	0.51	0.01	0.02	0.00	5.11	0.01	0.01	1.71	0.01	0.00	0.00	1.12	0.00	2.88	19.67	0.91	3.08
LP12503_perv wht mica2-3	6.08	0.05	1.93	0.15	0.00	0.55	0.00	0.03	0.00	5.18	0.00	0.01	1.76	0.00	0.00	0.00	1.18	0.00	2.82	19.73	0.90	3.16
LP12511_perv wht mica1-1	5.93	0.07	2.07	0.31	0.01	0.70	0.01	0.02	0.02	4.74	0.00	0.02	1.79	0.01	0.00	0.01	1.07	0.00	2.93	19.71	0.87	2.86
LP12511_perv wht mica2-2	6.21	0.03	1.79	0.25	0.00	0.67	0.01	0.00	0.01	4.90	0.02	0.01	1.66	0.00	0.00	0.00	1.21	0.00	2.79	19.58	0.88	3.46
LP12511_perv wht mica3-3	6.24	0.02	1.76	0.23	0.00	0.67	0.00	0.01	0.01	4.95	0.01	0.01	1.69	0.00	0.00	0.00	1.29	0.00	2.71	19.59	0.88	3.56
LP16A450 perv talc1-1-1	6.48	0.04	1.52	0.15	0.00	0.41	0.00	0.01	0.01	5.31	0.00	0.01	1.44	0.00	0.00	0.00	0.76	0.00	3.24	19.37	0.93	4.26
LP16A450 wh mica2-2-1	6.07	0.05	1.93	0.23	0.00	0.42	0.00	0.00	0.01	5.17	0.00	0.01	1.83	0.01	0.00	0.00	0.96	0.00	3.04	19.73	0.93	3.14
Lp18365_perv phl 1-2-1	6.13	0.06	1.87	0.17	0.00	0.86	0.00	0.00	0.01	4.81	0.00	0.00	1.72	0.00	0.00	0.00	1.00	0.00	3.00	19.64	0.85	3.28
Lp18365_near perv phl 1-2	6.21	0.06	1.79	0.19	0.00	0.74	0.00	0.01	0.00	4.89	0.00	0.01	1.68	0.00	0.00	0.00	1.06	0.00	2.93	19.59	0.87	3.46
Lp33390_mica in chl1-1-1	5.88	0.03	2.12	0.21	0.00	0.51	0.00	0.00	0.01	5.42	0.01	0.01	1.46	0.00	0.00	0.00	1.14	0.00	2.87	19.66	0.91	2.77
Lp36w197_phl 1-1-1	6.00	0.07	2.00	0.30	0.01	0.63	0.00	0.02	0.01	4.85	0.00	0.02	1.73	0.01	0.00	0.00	1.03	0.00	2.97	19.65	0.89	3.01
Lp44243_phl1-9-1	5.81	0.11	2.19	0.49	0.00	1.05	0.01	0.02	0.02	4.10	0.00	0.01	1.86	0.00	0.00	0.00	0.57	0.00	3.43	19.68	0.80	2.65
LP46A090_perv wht mica	5.83	0.11	2.17	0.58	0.00	0.85	0.00	0.02	0.05	4.15	0.00	0.01	1.89	0.01	0.00	0.00	0.33	0.00	3.67	19.64	0.83	2.68
LP46A090_perv wht mica	5.80	0.09	2.20	0.62	0.00	0.86	0.00	0.01	0.04	4.14	0.00	0.04	1.84	0.01	0.00	0.00	0.30	0.00	3.70	19.63	0.83	2.64
LP46A103_perv bt1-4-1	5.84	0.11	2.16	0.47	0.00	0.91	0.00	0.00	0.04	4.26	0.00	0.02	1.89	0.00	0.00	0.01	0.74	0.00	3.26	19.70	0.82	2.71

Label **Oxides:**	Mineral	SiO_2	TiO_2	Al_2O_3	Cr_2O_3	FeO	V_2O_3	ZnO	MnO	MgO	CaO	Na_2O	K_2O	BaO	SrO	NiO	F	Cl	H_2O	O=F	O=Cl	Sum Ox
LP46A113_perv bt1-1-1	phl	39.81	1.16	16.30	0.00	8.19	0.03	0.18	0.26	18.48	0.01	0.04	10.17	0.22	0.00	0.02	0.53	0.01	3.88	0.22	0.00	99.09
LP46A113_perv bt2-2-1	phl	40.15	1.18	15.94	0.00	8.34	0.05	0.00	0.21	18.45	0.04	0.03	10.31	0.32	0.00	0.03	0.65	0.00	3.83	0.27	0.00	99.25
LP46A113_perv bt3-8-1	phl	40.26	1.05	15.80	0.00	8.60	0.00	0.05	0.23	18.85	0.00	0.03	10.30	0.06	0.00	0.04	0.72	0.01	3.80	0.30	0.00	99.51
LP46A124_perv bt1-1-1	phl	40.16	0.71	16.08	0.00	8.12	0.01	0.10	0.17	20.26	0.00	0.07	9.45	0.25	0.00	0.05	1.21	0.00	3.60	0.51	0.00	99.73
LP46A124_wht mica1-2-1	phl	40.31	0.75	16.24	0.00	7.53	0.00	0.00	0.24	19.32	0.00	0.08	10.26	0.39	0.00	0.02	1.13	0.01	3.62	0.48	0.00	99.41
LP46A124_perv bt2-3-1	phl	40.02	0.97	16.48	0.00	8.11	0.00	0.08	0.13	19.18	0.02	0.06	9.83	0.31	0.00	0.06	1.02	0.02	3.67	0.43	0.00	99.53
LP46A124_wht mica2-4-1	phl	39.68	0.93	16.59	0.00	8.10	0.00	0.07	0.25	18.87	0.00	0.07	10.43	0.23	0.00	0.00	1.06	0.00	3.64	0.45	0.00	99.48
LP46A134 perv bt1-6-1	phl	41.10	0.57	15.99	0.02	6.38	0.00	0.00	0.18	20.47	0.00	0.09	10.00	0.29	0.00	0.00	1.41	0.00	3.53	0.59	0.00	99.44
LP46A134 perv bt2-7-1	phl	40.89	0.67	15.86	0.01	6.17	0.01	0.00	0.12	20.31	0.00	0.05	10.57	0.38	0.00	0.04	1.42	0.01	3.50	0.60	0.00	99.39
LP46A134 perv bt3-9-1	phl	40.38	0.70	15.65	0.06	6.46	0.05	0.08	0.19	19.90	0.00	0.07	10.08	0.36	0.00	0.03	1.54	0.03	3.39	0.65	0.01	98.31
LP46A134 perv mica1-5-1	phl	40.84	0.58	16.09	0.00	6.20	0.00	0.07	0.19	20.36	0.00	0.12	10.10	0.41	0.00	0.00	1.33	0.02	3.55	0.56	0.00	99.31
LP46A134 perv mica2-8-1	phl	41.02	0.58	17.49	0.00	6.16	0.03	0.03	0.08	19.20	0.00	0.08	9.71	0.39	0.00	0.00	1.35	0.01	3.56	0.57	0.00	99.10
LP46A134 perv mica4-12-1	phl	41.39	0.52	17.51	0.02	6.05	0.03	0.02	0.16	19.44	0.00	0.10	9.94	0.33	0.00	0.00	1.26	0.01	3.63	0.53	0.00	99.86
LP46A134 perv mica5-13-1	phl	39.00	0.77	15.88	0.02	6.49	0.07	0.00	0.15	18.35	0.01	0.06	10.09	0.44	0.00	0.00	1.32	0.02	3.38	0.55	0.01	95.50
LP46A177 perv mica3-10-1	phl	43.43	0.50	14.07	0.03	3.89	0.02	0.00	0.14	23.37	0.00	0.03	9.98	0.01	0.00	0.00	2.34	0.00	3.18	0.98	0.00	100.01
LP46A177 perv mica4-11-1	phl	40.51	0.49	15.01	0.01	3.95	0.03	0.00	0.18	23.14	0.02	0.04	9.11	0.07	0.00	0.07	1.99	0.01	3.21	0.84	0.00	96.98
LP46A334_perv bt1-1-1	bt	37.67	1.34	19.52	0.00	13.99	0.00	0.07	0.20	12.23	0.07	0.04	9.17	0.03	0.00	0.05	0.38	0.02	3.85	0.16	0.00	98.48

Label **Cations:**	Si	Ti	Al IV	Al VI	Cr	Fe2+	V	Zn	Mn2+	Mg	Ca	Na	K	Ba	Sr	Ni	F	Cl	OH	Sum Cat	Mg #	Si / Al IV
LP46A113_perv bt1-1-1	5.78	0.13	2.22	0.56	0.00	0.99	0.00	0.02	0.03	4.00	0.00	0.01	1.88	0.01	0.00	0.00	0.24	0.00	3.76	19.65	0.80	2.60
LP46A113_perv bt2-2-1	5.82	0.13	2.18	0.54	0.00	1.01	0.01	0.00	0.03	3.99	0.01	0.01	1.91	0.02	0.00	0.00	0.30	0.00	3.70	19.64	0.80	2.67
LP46A113_perv bt3-8-1	5.82	0.12	2.18	0.51	0.00	1.04	0.00	0.01	0.03	4.06	0.00	0.01	1.90	0.00	0.00	0.01	0.33	0.00	3.67	19.68	0.80	2.67
LP46A124_perv bt1-1-1	5.77	0.08	2.23	0.49	0.00	0.98	0.00	0.01	0.02	4.33	0.00	0.02	1.73	0.01	0.00	0.01	0.55	0.00	3.45	19.67	0.82	2.58
LP46A124_wht mica1-2-1	5.81	0.08	2.19	0.57	0.00	0.91	0.00	0.00	0.03	4.15	0.00	0.02	1.89	0.02	0.00	0.00	0.52	0.00	3.48	19.68	0.82	2.66
LP46A124_perv bt2-3-1	5.77	0.11	2.23	0.56	0.00	0.98	0.00	0.01	0.02	4.12	0.00	0.02	1.81	0.02	0.00	0.01	0.47	0.00	3.53	19.64	0.81	2.58
LP46A124_wht mica2-4-1	5.74	0.10	2.26	0.57	0.00	0.98	0.00	0.01	0.03	4.07	0.00	0.02	1.92	0.01	0.00	0.00	0.49	0.00	3.51	19.72	0.81	2.54
LP46A134 perv bt1-6-1	5.87	0.06	2.13	0.57	0.00	0.76	0.00	0.00	0.02	4.36	0.00	0.03	1.82	0.02	0.00	0.00	0.64	0.00	3.36	19.64	0.85	2.76
LP46A134 perv bt2-7-1	5.87	0.07	2.13	0.55	0.00	0.74	0.00	0.00	0.01	4.34	0.00	0.01	1.94	0.02	0.00	0.00	0.65	0.00	3.35	19.69	0.85	2.75
LP46A134 perv bt3-9-1	5.86	0.08	2.14	0.54	0.01	0.78	0.01	0.01	0.02	4.31	0.00	0.02	1.87	0.02	0.00	0.00	0.71	0.01	3.29	19.66	0.85	2.74
LP46A134 perv mica1-5-1	5.86	0.06	2.15	0.57	0.00	0.74	0.00	0.01	0.02	4.35	0.00	0.04	1.85	0.02	0.00	0.00	0.60	0.01	3.39	19.67	0.85	2.73
LP46A134 perv mica2-8-1	5.86	0.06	2.15	0.80	0.00	0.74	0.00	0.00	0.01	4.08	0.00	0.02	1.77	0.02	0.00	0.00	0.61	0.00	3.39	19.51	0.85	2.73
LP46A134 perv mica4-12-1	5.86	0.06	2.14	0.79	0.00	0.72	0.00	0.00	0.02	4.10	0.00	0.03	1.80	0.02	0.00	0.00	0.57	0.00	3.43	19.53	0.85	2.74
LP46A134 perv mica5-13-1	5.84	0.09	2.16	0.64	0.00	0.81	0.01	0.00	0.02	4.10	0.00	0.02	1.93	0.03	0.00	0.00	0.62	0.01	3.37	19.64	0.83	2.70
LP46A177 perv mica3-10-1	6.08	0.05	1.92	0.40	0.00	0.46	0.00	0.00	0.02	4.88	0.00	0.01	1.78	0.00	0.00	0.00	1.03	0.00	2.97	19.60	0.92	3.17
LP46A177 perv mica4-11-1	5.85	0.05	2.15	0.41	0.00	0.48	0.00	0.00	0.02	4.98	0.00	0.01	1.68	0.00	0.00	0.01	0.91	0.00	3.09	19.66	0.91	2.73
LP46A334_perv bt1-1-1	5.60	0.15	2.40	1.02	0.00	1.74	0.00	0.01	0.03	2.71	0.01	0.01	1.74	0.00	0.00	0.01	0.18	0.01	3.82	19.42	0.61	2.33

Label	Oxides:	Mineral	SiO_2	TiO_2	Al_2O_3	Cr_2O_3	FeO	V_2O_3	ZnO	MnO	MgO	CaO	Na_2O	K_2O	BaO	SrO	NiO	F	Cl	H_2O	O=F	O=Cl	Sum Ox
LP46A334_perv bt2-2-1		bt	38.12	1.88	16.62	0.00	14.80	0.00	0.16	0.19	13.87	0.08	0.03	9.94	0.00	0.00	0.13	0.48	0.04	3.81	0.20	0.01	99.94
LP46A348_perv bt1-1-1		bt	38.38	1.76	17.49	0.02	14.15	0.01	0.06	0.45	13.04	0.00	0.07	10.23	0.00	0.00	0.04	0.20	0.01	3.96	0.08	0.00	99.79
LP46A348_perv bt3-3-1		bt	37.85	1.85	16.86	0.00	15.11	0.00	0.00	0.52	13.15	0.03	0.04	10.25	0.00	0.00	0.00	0.28	0.00	3.89	0.12	0.00	99.72
Lp51aw2433_phl 1-2-1		phl	41.73	1.40	12.86	0.33	11.81	0.05	0.00	0.12	17.95	0.05	0.02	9.32	0.00	0.00	0.00	1.19	0.01	3.56	0.50	0.00	99.89
LP66153_perv bt2-4-1		bt	38.61	1.30	16.92	0.34	13.37	0.00	0.02	0.22	14.80	0.00	0.05	10.18	0.00	0.00	0.00	0.57	0.01	3.80	0.24	0.00	99.97
LP66153_perv bt1-5-1		phl	38.06	0.34	17.41	0.15	12.65	0.02	0.05	0.20	15.09	0.05	0.04	10.26	0.00	0.00	0.00	0.57	0.00	3.75	0.24	0.00	98.39
LP66179_perv mica1-2-1		phl	40.68	0.53	17.11	0.00	5.78	0.01	0.04	0.43	19.95	0.00	0.04	10.01	0.00	0.00	0.03	0.33	0.01	4.03	0.14	0.00	98.85
LP66179_perv bt1-5-1		phl	41.01	0.61	16.00	0.02	5.63	0.03	0.00	0.53	20.48	0.00	0.02	10.34	0.06	0.00	0.01	0.34	0.00	4.03	0.14	0.00	98.95
LP66179_perv bt2-6-1		phl	40.62	0.51	17.08	0.00	5.85	0.00	0.03	0.50	20.05	0.00	0.03	10.24	0.00	0.00	0.03	0.36	0.01	4.02	0.15	0.00	99.17
LP66202_perv bt1-3-1		phl	39.75	0.85	16.66	0.02	9.45	0.03	0.09	0.32	17.67	0.00	0.03	10.38	0.23	0.00	0.00	0.60	0.00	3.85	0.25	0.00	99.69
LP66202_perv bt2-4-1		phl	39.98	0.74	16.78	0.00	9.42	0.00	0.12	0.24	18.11	0.01	0.05	10.23	0.22	0.00	0.05	0.60	0.00	3.88	0.25	0.00	100.18
LP66233_perv bt2-7-1		phl	41.40	0.73	15.13	0.00	6.75	0.09	0.05	0.46	20.59	0.00	0.09	10.10	0.23	0.00	0.00	1.89	0.00	3.30	0.80	0.00	100.03
LP66267_perv bt1-4-1		phl	41.30	0.87	16.37	0.00	6.13	0.00	0.10	0.16	19.95	0.00	0.05	10.38	0.08	0.00	0.03	1.15	0.00	3.67	0.48	0.00	99.77
LP66267_perv bt2-5-1		phl	41.34	0.90	16.02	0.00	6.19	0.02	0.11	0.27	20.16	0.00	0.06	10.32	0.03	0.01	0.02	1.08	0.00	3.70	0.45	0.00	99.79
LP66339_perv bt2-5-1		phl	37.08	0.39	17.35	0.00	10.68	0.00	0.05	0.22	19.46	0.02	0.08	7.65	0.08	0.00	0.05	1.38	0.02	3.39	0.58	0.00	97.33
LP66350_perv bt1-1-1		phl	39.81	0.92	15.62	0.05	10.99	0.01	0.04	0.19	17.13	0.00	0.12	10.29	0.07	0.00	0.00	1.73	0.02	3.27	0.73	0.01	99.54
Lp66361_perv phl 1-2-1		phl	38.04	1.10	16.33	0.00	13.11	0.00	0.16	0.20	16.84	0.02	0.07	8.58	0.03	0.01	0.00	1.20	0.00	3.48	0.51	0.00	98.68

Label	Cations:	Si	Ti	Al IV	Al VI	Cr	Fe2+	V	Zn	Mn2+	Mg	Ca	Na	K	Ba	Sr	Ni	F	Cl	OH	Sum Cat	Mg #	Si / Al IV
LP46A334_perv bt2-2-1		5.65	0.21	2.35	0.56	0.00	1.84	0.00	0.02	0.02	3.07	0.01	0.01	1.88	0.00	0.00	0.02	0.23	0.01	3.77	19.63	0.63	2.41
LP46A348_perv bt1-1-1		5.68	0.20	2.32	0.73	0.00	1.75	0.00	0.01	0.06	2.88	0.00	0.02	1.93	0.00	0.00	0.01	0.09	0.00	3.91	19.57	0.62	2.45
LP46A348_perv bt3-3-1		5.64	0.21	2.36	0.60	0.00	1.88	0.00	0.00	0.07	2.92	0.01	0.01	1.95	0.00	0.00	0.00	0.13	0.00	3.87	19.65	0.61	2.39
Lp51aw2433_phl 1-2-1		6.06	0.15	1.94	0.26	0.04	1.43	0.01	0.00	0.02	3.89	0.01	0.01	1.73	0.00	0.00	0.00	0.55	0.00	3.45	19.53	0.73	3.12
LP66153_perv bt2-4-1		5.68	0.14	2.32	0.62	0.04	1.65	0.00	0.00	0.03	3.25	0.00	0.02	1.91	0.00	0.00	0.00	0.26	0.00	3.73	19.65	0.66	2.45
LP66153_perv bt1-5-1		5.68	0.04	2.32	0.74	0.02	1.58	0.00	0.01	0.03	3.36	0.01	0.01	1.95	0.00	0.00	0.00	0.27	0.00	3.73	19.73	0.68	2.44
LP66179_perv mica1-2-1		5.82	0.06	2.18	0.70	0.00	0.69	0.00	0.00	0.05	4.25	0.00	0.01	1.83	0.00	0.00	0.00	0.15	0.00	3.85	19.60	0.86	2.67
LP66179_perv bt1-5-1		5.87	0.07	2.13	0.58	0.00	0.67	0.00	0.00	0.06	4.37	0.00	0.00	1.89	0.00	0.00	0.00	0.15	0.00	3.85	19.65	0.87	2.76
LP66179_perv bt2-6-1		5.80	0.05	2.20	0.68	0.00	0.70	0.00	0.00	0.06	4.27	0.00	0.01	1.87	0.00	0.00	0.00	0.16	0.00	3.84	19.64	0.86	2.64
LP66202_perv bt1-3-1		5.77	0.09	2.23	0.62	0.00	1.15	0.00	0.01	0.04	3.82	0.00	0.01	1.92	0.01	0.00	0.00	0.28	0.00	3.72	19.68	0.77	2.58
LP66202_perv bt2-4-1		5.76	0.08	2.24	0.61	0.00	1.14	0.00	0.01	0.03	3.89	0.00	0.02	1.88	0.01	0.00	0.01	0.27	0.00	3.73	19.68	0.77	2.58
LP66233_perv bt2-7-1		5.91	0.08	2.09	0.45	0.00	0.81	0.01	0.01	0.06	4.38	0.00	0.03	1.84	0.01	0.00	0.00	0.85	0.00	3.15	19.67	0.85	2.83
LP66267_perv bt1-4-1		5.88	0.09	2.13	0.62	0.00	0.73	0.00	0.01	0.02	4.23	0.00	0.01	1.88	0.01	0.00	0.00	0.52	0.00	3.48	19.61	0.85	2.76
LP66267_perv bt2-5-1		5.88	0.10	2.12	0.57	0.00	0.74	0.00	0.01	0.03	4.28	0.00	0.02	1.87	0.00	0.00	0.00	0.49	0.00	3.51	19.62	0.85	2.78
LP66339_perv bt2-5-1		5.49	0.04	2.51	0.52	0.00	1.32	0.00	0.01	0.03	4.29	0.00	0.02	1.45	0.01	0.00	0.01	0.65	0.01	3.35	19.69	0.77	2.18
LP66350_perv bt1-1-1		5.83	0.10	2.17	0.52	0.01	1.35	0.00	0.00	0.02	3.74	0.00	0.03	1.92	0.00	0.00	0.00	0.80	0.01	3.19	19.70	0.74	2.68
Lp66361_perv phl 1-2-1		5.63	0.12	2.37	0.48	0.00	1.62	0.00	0.02	0.03	3.72	0.00	0.02	1.62	0.00	0.00	0.00	0.56	0.00	3.44	19.64	0.70	2.38

Label **Oxides:**	Mineral	SiO_2	TiO_2	Al_2O_3	Cr_2O_3	FeO	V_2O_3	ZnO	MnO	MgO	CaO	Na_2O	K_2O	BaO	SrO	NiO	F	Cl	H_2O	O=F	O=Cl	Sum Ox
LP66374_perv bt1-2-1	phl	41.07	0.51	12.90	0.00	11.33	0.00	0.11	0.15	18.98	0.02	0.07	9.43	0.02	0.00	0.00	1.76	0.00	3.25	0.74	0.00	98.84
LP66374_perv bt2-4-1	phl	41.22	0.59	12.85	0.03	10.93	0.06	0.05	0.23	19.74	0.01	0.05	9.43	0.00	0.00	0.06	1.73	0.00	3.30	0.73	0.00	99.54
LP66419_perv bt1-1-1	phl	39.12	1.34	16.05	0.00	13.24	0.00	0.00	0.21	15.68	0.00	0.10	9.91	0.15	0.00	0.00	1.14	0.01	3.54	0.48	0.00	100.01
LP66419_perv bt2-2-1	phl	39.07	1.41	16.20	0.01	12.70	0.00	0.00	0.14	15.66	0.00	0.09	10.13	0.05	0.00	0.00	1.14	0.00	3.54	0.48	0.00	99.65
LP67B140 perv bt1-1-1	bt	39.14	1.28	18.06	0.00	12.38	0.00	0.00	0.08	13.83	0.00	0.05	10.08	0.00	0.00	0.03	0.93	0.00	3.64	0.39	0.00	99.11
LP67B140 perv bt2-2-1	bt	38.23	1.29	18.46	0.03	12.73	0.04	0.16	0.08	13.50	0.03	0.02	9.92	0.00	0.00	0.00	0.83	0.02	3.65	0.35	0.00	98.63
LP67B476 perv bt1-1-1	bt	36.38	1.71	19.53	0.02	12.72	0.00	0.05	0.29	13.39	0.01	0.07	10.19	0.00	0.00	0.00	0.22	0.02	3.91	0.09	0.00	98.41
LP67B476 perv bt2-2-1	bt	37.45	1.56	18.02	0.03	13.23	0.01	0.05	0.25	14.52	0.00	0.02	10.55	0.00	0.00	0.03	0.31	0.03	3.90	0.13	0.01	99.84
lp67b663 perv bt1-1-1	phl	39.05	1.43	16.88	0.01	11.02	0.03	0.01	0.17	15.81	0.03	0.05	10.28	0.00	0.00	0.00	0.30	0.00	3.94	0.13	0.00	98.89
LP67B790-perv bt1-1-1	phl	40.62	1.01	17.45	0.00	8.73	0.04	0.07	0.27	17.72	0.03	0.05	10.31	0.16	0.00	0.05	0.39	0.00	4.02	0.17	0.00	100.75
LP67B790_perv mica2-4-1	phl	39.82	1.40	16.84	0.02	9.59	0.06	0.14	0.16	17.19	0.00	0.04	10.29	0.12	0.00	0.00	0.35	0.01	3.98	0.15	0.00	99.86
LP67B790_perv bt2-5-1	phl	40.17	1.18	16.94	0.01	8.47	0.00	0.00	0.22	17.15	0.00	0.03	10.45	0.00	0.00	0.02	0.43	0.00	3.93	0.18	0.00	98.82
LP67B809 perv bt1-4-1	phl	37.99	0.37	14.05	0.06	10.06	0.03	0.06	0.42	18.81	0.94	0.03	8.93	0.03	0.00	0.07	1.27	0.01	3.35	0.54	0.00	95.96
LP67B841_perv bt1-7-1	phl	40.96	0.84	16.33	0.08	7.15	0.03	0.04	0.22	19.41	0.00	0.02	10.38	0.03	0.00	0.03	0.41	0.01	4.00	0.17	0.00	99.78
LP67B841_perv bt2-8-1	phl	40.80	1.03	16.85	0.03	7.30	0.04	0.00	0.21	19.11	0.01	0.02	10.50	0.00	0.00	0.04	0.41	0.00	4.02	0.17	0.00	100.21
lp67b903 perv bt2-3-1	phl	39.41	1.36	17.78	0.08	9.27	0.00	0.00	0.44	16.51	0.00	0.05	10.44	0.24	0.00	0.03	0.28	0.02	4.01	0.12	0.00	99.79
LP67B940 perv bt1-1-1	phl	39.73	0.81	16.81	0.06	8.37	0.03	0.10	0.39	18.02	0.03	0.05	10.54	0.00	0.00	0.03	0.34	0.01	3.97	0.14	0.00	99.15

Label **Cations:**	Si	Ti	Al IV	Al VI	Cr	Fe2+	V	Zn	Mn2+	Mg	Ca	Na	K	Ba	Sr	Ni	F	Cl	OH	Sum Cat	Mg #	Si / Al IV
LP66374_perv bt1-2-1	6.03	0.06	1.97	0.27	0.00	1.39	0.00	0.01	0.02	4.16	0.00	0.02	1.77	0.00	0.00	0.00	0.82	0.00	3.18	19.69	0.75	3.07
LP66374_perv bt2-4-1	6.00	0.07	2.00	0.21	0.00	1.33	0.01	0.01	0.03	4.28	0.00	0.01	1.75	0.00	0.00	0.01	0.80	0.00	3.20	19.71	0.76	3.01
LP66419_perv bt1-1-1	5.75	0.15	2.25	0.53	0.00	1.63	0.00	0.00	0.03	3.44	0.00	0.03	1.86	0.01	0.00	0.00	0.53	0.00	3.47	19.66	0.68	2.55
LP66419_perv bt2-2-1	5.75	0.16	2.25	0.56	0.00	1.56	0.00	0.00	0.02	3.43	0.00	0.02	1.90	0.00	0.00	0.00	0.53	0.00	3.47	19.66	0.69	2.55
LP67B140 perv bt1-1-1	5.75	0.14	2.25	0.88	0.00	1.52	0.00	0.00	0.01	3.03	0.00	0.02	1.89	0.00	0.00	0.00	0.43	0.00	3.57	19.49	0.67	2.56
LP67B140 perv bt2-2-1	5.67	0.14	2.33	0.89	0.00	1.58	0.01	0.02	0.01	2.98	0.00	0.01	1.87	0.00	0.00	0.00	0.39	0.00	3.61	19.51	0.65	2.43
LP67B476 perv bt1-1-1	5.43	0.19	2.57	0.87	0.00	1.59	0.00	0.01	0.04	2.98	0.00	0.02	1.94	0.00	0.00	0.00	0.11	0.00	3.89	19.64	0.65	2.12
LP67B476 perv bt2-2-1	5.53	0.17	2.47	0.67	0.00	1.64	0.00	0.01	0.03	3.20	0.00	0.01	1.99	0.00	0.00	0.00	0.14	0.01	3.85	19.72	0.66	2.24
lp67b663 perv bt1-1-1	5.74	0.16	2.26	0.66	0.00	1.35	0.00	0.00	0.02	3.46	0.01	0.02	1.93	0.00	0.00	0.00	0.14	0.00	3.86	19.61	0.72	2.54
LP67B790-perv bt1-1-1	5.79	0.11	2.21	0.72	0.00	1.04	0.00	0.01	0.03	3.76	0.01	0.01	1.87	0.01	0.00	0.01	0.18	0.00	3.82	19.58	0.78	2.62
LP67B790_perv mica2-4-1	5.76	0.15	2.24	0.63	0.00	1.16	0.01	0.01	0.02	3.71	0.00	0.01	1.90	0.01	0.00	0.00	0.16	0.00	3.84	19.61	0.76	2.57
LP67B790_perv bt2-5-1	5.83	0.13	2.17	0.73	0.00	1.03	0.00	0.00	0.03	3.71	0.00	0.01	1.93	0.00	0.00	0.00	0.20	0.00	3.80	19.56	0.78	2.68
LP67B809 perv bt1-4-1	5.76	0.04	2.24	0.27	0.01	1.28	0.00	0.01	0.05	4.25	0.15	0.01	1.73	0.00	0.00	0.01	0.61	0.00	3.39	19.81	0.77	2.57
LP67B841_perv bt1-7-1	5.85	0.09	2.15	0.60	0.01	0.86	0.00	0.00	0.03	4.13	0.00	0.01	1.89	0.00	0.00	0.00	0.19	0.00	3.81	19.63	0.83	2.72
LP67B841_perv bt2-8-1	5.81	0.11	2.19	0.64	0.00	0.87	0.01	0.00	0.03	4.06	0.00	0.01	1.91	0.00	0.00	0.00	0.19	0.00	3.82	19.62	0.82	2.65
lp67b903 perv bt2-3-1	5.71	0.15	2.29	0.74	0.01	1.12	0.00	0.00	0.05	3.56	0.00	0.02	1.93	0.01	0.00	0.00	0.13	0.00	3.87	19.60	0.76	2.49
LP67B940 perv bt1-1-1	5.77	0.09	2.23	0.64	0.01	1.02	0.00	0.01	0.05	3.90	0.00	0.02	1.95	0.00	0.00	0.00	0.16	0.00	3.84	19.69	0.79	2.58

Label **Oxides:**	Mineral	SiO_2	TiO_2	Al_2O_3	Cr_2O_3	FeO	V_2O_3	ZnO	MnO	MgO	CaO	Na_2O	K_2O	BaO	SrO	NiO	F	Cl	H_2O	O=F	O=Cl	Sum Ox
LP67B940 perv bt2-2-1	phl	40.55	0.85	16.06	0.03	7.99	0.04	0.01	0.30	18.47	0.00	0.03	10.34	0.07	0.00	0.00	0.42	0.01	3.94	0.18	0.00	98.94
LP67b986 perv bt1-3-1	phl	38.17	0.57	15.53	0.00	11.99	0.01	0.03	0.49	16.99	0.02	0.03	9.23	0.02	0.00	0.00	0.44	0.00	3.78	0.18	0.00	97.12
LP67b986 perv bt2-4-1	phl	39.52	0.66	16.16	0.02	10.12	0.01	0.07	0.45	17.34	0.00	0.03	10.11	0.00	0.00	0.00	0.42	0.00	3.88	0.18	0.00	98.63
lp67bw11037 perv bt1-1-1	phl	39.77	0.87	15.79	0.02	8.03	0.00	0.05	0.25	18.72	0.00	0.02	10.23	0.00	0.00	0.00	0.79	0.00	3.72	0.33	0.00	97.93
lp67bw11037 perv bt2-5-1	phl	41.13	0.17	14.47	0.00	7.81	0.00	0.10	0.17	20.78	0.01	0.06	9.92	0.00	0.00	0.00	1.02	0.02	3.66	0.43	0.00	98.89
LP67BW11063 perv bt1-3	phl	39.72	1.05	16.73	0.01	9.64	0.03	0.06	0.13	17.31	0.04	0.05	10.24	0.00	0.00	0.00	0.53	0.01	3.87	0.22	0.00	99.20
LP67BW11063 perv bt2-4	phl	40.10	1.09	16.64	0.01	9.22	0.04	0.00	0.19	17.65	0.03	0.09	10.00	0.00	0.00	0.00	0.51	0.00	3.90	0.22	0.00	99.26
LP12428_perv mica1-3-1	tlc	63.12	0.01	0.15	0.00	2.27	0.00	0.00	0.00	29.27	0.00	0.03	0.00	0.00	0.00	0.00	0.62	0.00	4.39	0.26	0.00	99.62
LP12428_perv talc1-5-1	tlc	62.66	0.00	0.14	0.00	2.65	0.05	0.05	0.05	29.07	0.02	0.02	0.01	0.06	0.00	0.05	0.50	0.04	4.42	0.21	0.01	99.56
LP12428_perv talc2-6-1	tlc	62.64	0.00	0.24	0.00	2.40	0.00	0.00	0.03	29.00	0.01	0.01	0.14	0.00	0.00	0.03	0.53	0.04	4.40	0.22	0.01	99.24
LP12428_perv talc3-7-1	tlc	62.17	0.04	0.24	0.00	2.70	0.02	0.03	0.02	28.88	0.02	0.03	0.02	0.05	0.00	0.01	0.53	0.03	4.38	0.22	0.01	98.93
Lp12476 perv talc1-1-1	tlc	62.39	0.02	0.12	0.04	2.38	0.02	0.05	0.00	28.62	0.04	0.02	0.01	0.00	0.00	0.00	0.58	0.02	4.35	0.24	0.01	98.40
Lp12476 perv talc2-3-1	tlc	61.38	0.00	0.92	0.00	3.48	0.00	0.07	0.00	28.61	0.01	0.03	0.69	0.02	0.00	0.00	0.81	0.01	4.26	0.34	0.00	99.95
LP16A450 perv talc2-2-1	tlc	61.86	0.01	0.38	0.00	1.94	0.00	0.00	0.05	29.12	0.02	0.01	0.26	0.04	0.00	0.02	0.47	0.02	4.40	0.20	0.00	98.38
LP16A450 perv talc3-3-1	tlc	62.74	0.01	0.10	0.05	1.70	0.01	0.00	0.07	29.61	0.03	0.02	0.02	0.00	0.00	0.00	0.42	0.03	4.47	0.18	0.01	99.09
LP16A450 perv talc4-4-1	tlc	62.75	0.00	0.05	0.00	1.99	0.01	0.00	0.09	29.99	0.00	0.02	0.02	0.09	0.00	0.03	0.52	0.02	4.44	0.22	0.00	99.80
LP16A450 perv talc5-5-1	tlc	62.74	0.00	0.06	0.00	1.62	0.00	0.30	0.01	29.82	0.02	0.02	0.00	0.00	0.00	0.00	0.45	0.01	4.46	0.19	0.00	99.32

Label **Cations:**	Si	Ti	Al IV	Al VI	Cr	Fe2+	V	Zn	Mn2+	Mg	Ca	Na	K	Ba	Sr	Ni	F	Cl	OH	Sum Cat	Mg #	Si / Al IV
LP67B940 perv bt2-2-1	5.87	0.09	2.13	0.61	0.00	0.97	0.01	0.00	0.04	3.99	0.00	0.01	1.91	0.00	0.00	0.00	0.19	0.00	3.81	19.62	0.81	2.75
LP67b986 perv bt1-3-1	5.74	0.07	2.26	0.49	0.00	1.51	0.00	0.00	0.06	3.81	0.00	0.01	1.77	0.00	0.00	0.00	0.21	0.00	3.79	19.71	0.72	2.53
LP67b986 perv bt2-4-1	5.80	0.07	2.20	0.60	0.00	1.24	0.00	0.01	0.06	3.79	0.00	0.01	1.89	0.00	0.00	0.00	0.20	0.00	3.80	19.68	0.75	2.64
lp67bw11037 perv bt1-1-1	5.83	0.10	2.18	0.55	0.00	0.98	0.00	0.01	0.03	4.09	0.00	0.01	1.91	0.00	0.00	0.00	0.36	0.00	3.64	19.68	0.81	2.68
lp67bw11037 perv bt2-5-1	5.94	0.02	2.06	0.41	0.00	0.94	0.00	0.01	0.02	4.48	0.00	0.02	1.83	0.00	0.00	0.00	0.47	0.00	3.53	19.73	0.83	2.89
LP67BW11063 perv bt1-3	5.78	0.12	2.22	0.64	0.00	1.17	0.00	0.01	0.02	3.75	0.01	0.02	1.90	0.00	0.00	0.00	0.24	0.00	3.76	19.63	0.76	2.60
LP67BW11063 perv bt2-4	5.80	0.12	2.20	0.64	0.00	1.12	0.00	0.00	0.02	3.81	0.00	0.03	1.85	0.00	0.00	0.00	0.23	0.00	3.77	19.59	0.77	2.64
LP12428_perv mica1-3-1	8.07	0.00	0.00	0.02	0.00	0.24	0.00	0.00	0.00	5.58	0.00	0.01	0.00	0.00	0.00	0.00	0.25	0.00	3.75	17.92	0.96	
LP12428_perv talc1-5-1	8.05	0.00	0.00	0.02	0.00	0.29	0.01	0.01	0.01	5.56	0.00	0.01	0.00	0.00	0.00	0.01	0.20	0.01	3.79	17.95	0.95	
LP12428_perv talc2-6-1	8.05	0.00	0.00	0.04	0.00	0.26	0.00	0.00	0.00	5.56	0.00	0.00	0.02	0.00	0.00	0.00	0.22	0.01	3.78	17.94	0.96	
LP12428_perv talc3-7-1	8.03	0.00	0.00	0.04	0.00	0.29	0.00	0.00	0.00	5.56	0.00	0.01	0.00	0.00	0.00	0.00	0.22	0.01	3.78	17.95	0.95	
Lp12476 perv talc1-1-1	8.08	0.00	0.00	0.02	0.00	0.26	0.00	0.01	0.00	5.53	0.01	0.01	0.00	0.00	0.00	0.00	0.24	0.01	3.76	17.91	0.96	
Lp12476 perv talc2-3-1	7.92	0.00	0.08	0.06	0.00	0.38	0.00	0.01	0.00	5.50	0.00	0.01	0.11	0.00	0.00	0.00	0.33	0.00	3.67	18.07	0.94	
LP16A450 perv talc2-2-1	8.02	0.00	0.00	0.06	0.00	0.21	0.00	0.00	0.01	5.63	0.00	0.00	0.04	0.00	0.00	0.00	0.19	0.00	3.81	17.97	0.96	
LP16A450 perv talc3-3-1	8.05	0.00	0.00	0.02	0.01	0.18	0.00	0.00	0.01	5.66	0.00	0.00	0.00	0.00	0.00	0.00	0.17	0.01	3.83	17.94	0.97	
LP16A450 perv talc4-4-1	8.02	0.00	0.00	0.01	0.00	0.21	0.00	0.00	0.01	5.71	0.00	0.01	0.00	0.01	0.00	0.00	0.21	0.00	3.79	17.98	0.96	
LP16A450 perv talc5-5-1	8.04	0.00	0.00	0.01	0.00	0.17	0.00	0.03	0.00	5.70	0.00	0.01	0.00	0.00	0.00	0.00	0.18	0.00	3.82	17.96	0.97	

Label	**Oxides:**	Mineral	SiO_2	TiO_2	Al_2O_3	Cr_2O_3	FeO	V_2O_3	ZnO	MnO	MgO	CaO	Na_2O	K_2O	BaO	SrO	NiO	F	Cl	H_2O	O=F	O=Cl	Sum Ox
LP16A450 perv talc6-6-1		tlc	62.00	0.01	0.09	0.00	1.87	0.00	0.02	0.02	29.35	0.03	0.03	0.02	0.00	0.00	0.03	0.49	0.00	4.39	0.20	0.00	98.16
Lp51a482_perv ser 1-1-1		tlc	63.33	0.00	0.09	0.07	1.54	0.00	0.05	0.01	29.94	0.00	0.02	0.00	0.00	0.01	0.00	0.42	0.00	4.51	0.18	0.00	99.81
Lp51a484_mica in chl1-1-1		tlc	61.83	0.01	0.09	0.03	1.69	0.00	0.00	0.06	29.06	0.03	0.01	0.00	0.03	0.00	0.01	0.35	0.00	4.43	0.15	0.00	97.49
Lp51a484_ser in vein 1-8-1		tlc	63.06	0.01	0.12	0.02	1.76	0.03	0.00	0.04	29.73	0.02	0.02	0.00	0.00	0.05	0.00	0.36	0.01	4.52	0.15	0.00	99.59

Label	**Cations:**	Si	Ti	Al IV	Al VI	Cr	Fe2+	V	Zn	Mn2+	Mg	Ca	Na	K	Ba	Sr	Ni	F	Cl	OH	Mg #	Sum Cat
LP16A450 perv talc6-6-1		8.04	0.00	0.00	0.01	0.00	0.20	0.00	0.00	0.00	5.67	0.00	0.01	0.00	0.00	0.00	0.00	0.20	0.00	3.80	0.97	17.96
Lp51a482_perv ser 1-1-1		8.06	0.00	0.00	0.01	0.01	0.16	0.00	0.00	0.00	5.68	0.00	0.01	0.00	0.00	0.00	0.00	0.17	0.00	3.83	0.97	17.93
Lp51a484_mica in chl1-1-1		8.06	0.00	0.00	0.01	0.00	0.19	0.00	0.00	0.01	5.65	0.00	0.00	0.00	0.00	0.00	0.00	0.14	0.00	3.86	0.97	17.93
Lp51a484_ser in vein 1-8-1		8.05	0.00	0.00	0.02	0.00	0.19	0.00	0.00	0.00	5.66	0.00	0.00	0.00	0.00	0.00	0.00	0.15	0.00	3.85	0.97	17.94

Label	**Oxides:**	Mineral	SiO_2	TiO_2	Al_2O_3	Cr_2O_3	Fe_2O_3	FeO	MnO	MgO	CaO	Na_2O	K_2O	BaO	SrO	ZrO_2	F	Cl	H_2O	O=F	O=Cl	Sum Ox
LP67B687 perv hbl1-1-1		hbl	43.8	0.75	11.75	0.29	3.48	9.82	0.51	12.4	12.1	1.74	0.73	0	0	0.06	0.25	0.01	1.91	0.11	0	99.5
LP67B687 perv hbl2-2-1		hbl	44.5	0.61	11.65	0.18	4.26	7.86	0.61	13.3	12.2	1.62	0.55	0	0	0.04	0.29	0	1.92	0.12	0	99.5

Label	**Cations:**	Si	Ti	Al IV	Al VI	Cr	Fe3+	Fe2+	Mn2+	Mg	Ca	Na	K	Ba	Sr	Zr	F	Cl	OH	Sum Cat
LP67B687 perv hbl1-1-1		6.46	0.083	1.545	0.5	0.03	0.39	1.21	0.06	2.72	1.91	0.5	0.14	0	0	0	0.12	0.002	1.88	17.544
LP67B687 perv hbl2-2-1		6.5	0.067	1.5	0.51	0.02	0.47	0.96	0.08	2.9	1.9	0.46	0.1	0	0	0	0.13	0	1.867	17.464

Label	**Oxides:**	Mineral	SiO_2	TiO_2	Al_2O_3	Fe_2O_3	MnO	MgO	CaO	SrO	BaO	Na_2O	K_2O	P_2O_5	Sum Ox
LP46A134 feld1-1-1		hly	57.8	0	20.46	0	0	0	0	0	7.99	0.38	13.2	0	99.9
LP46A134 feld2-2-1		hly	56.1	0.01	21	0.04	0	0.01	0	0	10.4	0.42	12.4	0.03	100
LP46A134 feld3-3-1		hly	56.9	0	20.77	0	0	0.07	0	0	8.9	0.4	12.7	0	99.7
Lp67b760_feld in vein 3-3		ab	67.9	0.02	20.92	0	0	0.02	0.8	0.14	0.06	10.7	0.09	0	101

Label	**Cations:**	Si	Ti	Al IV	Al VI	Fe3+	Mn2+	Mg	Ca	Sr	Ba	Na	K	P	Sum	Ab	An	Or	Celsian	Rb-Feld	Sr-Feld
LP46A134 feld1-1-1		2.83	0	1.178	0	0	0	0	0	0	0.15	0.04	0.82	0	5.02	3.52	0	81.37	15.1	0	0
LP46A134 feld2-2-1		2.77	0	1.224	0	0	0	0	0	0	0.2	0.04	0.79	0	5.03	3.9	0	76.46	19.65	0	0
LP46A134 feld3-3-1		2.8	0	1.205	0	0	0	0.01	0	0	0.17	0.04	0.8	0	5.02	3.79	0	79.16	17.05	0	0
Lp67b760_feld in vein 3-3		2.95	0.001	1.07	0	0	0	0	0.04	0	0	0.9	0.01	0	4.97	95.1	3.91	0.549	0.106	0	0.38

Notes:

Mineral abbreviations: chl = chlorite, phg = phengite, ms = muscovite, phl = phlogopite, bt = biotite, tlc = talc, hbl = hornblende, hly = hyalophane, ab = albite, dol = dolomite, Fe-dol = ferroan dolomite, mgs = magnesite, ca = calcite, sid = siderite, Mg-sid = magneso-siderite, ank = ankerite, smt = smithsonite, rhd = rhodocrosite

All oxide data in weight %

SUMMARY OF XRF ANALYSIS (X-Ray Fluorescence Analysis)

School of Earth Sciences, University of Tasmania **Phil.Robinson 29/03/2000**

Instrument	Philips PW1480 X-Ray Spectrometer
X-Ray Tubes	3kW max. ScMo anode side window. Elements analysed: Majors, S and Y, Rb, U, Th, Cu, Pb, Zn, Ni, As, Bi, Co, Ga, Tl, Se, W, Br 3kW max. Au anode side window. Elements analysed: Nb, Zr, Sr, Ba, Cr, V, Sc, La, Ce, Nd, Sb, Sn 3kW max. Rh anode side window. Elements analysed: Mo, occasionally Nb
Crystals:	LiF 200, LiF 220, PX-1 (for Na and Mg), PE002, Ge111
Collimators:	Coarse (0.7mm) and fine (0.3mm) with auxiliary (0.14mm)
Detectors:	Gas flow proportional counter with P10 gas (10% methane in argon) and Scintillation Counter.
Sample Changer:	Philips 30 position sample holder

Sample Preparation

Major Elements:	Fusion discs prepared at 1100 ^{0}C in 5%Au/95%Pt crucibles 0.77g sample, 4.125g Norrish Flux (Lithium borates/La_2O_3 mix), 0.055g $LiNO_3$ for silicates.Platinum/gold moulds used for cooling. Sulphide bearing samples have a mix with more LiNO3 as oxidising agent and the mix is preignited at 700 ^{o}C for 10 minutes. Ore samples and ironstones use 12/22 flux and a higher flux/sample ratio. Dolomites and limestones need pure lithium tetraborate as a flux.
Trace Elements	Pressed powder pills (3.5 tonnes/cm^{-2}) with 10 grams sample. Binder used is PVP-MC.

Corrections

Corrections for mass absorption are calculated using Philips X40 software with De Jongh's calibration model and Philips (or CSIRO) alpha coefficients. Compton scattering is also used for many trace elements.

Calibration

Pure element oxide mixes in pure silica, along with international and Tasmanian standard rocks are used. Numerous checks of standard rocks and pure silica blanks are run with each program.

Detection Limits

oxide	wt %	trace element	ppm	trace element	ppm
SiO2	0.01	Nb	1	Th	1.5
TiO2	0.01	Zr	1	Bi	2
Al2O3	0.01	Cr	1	Ni	1
Fe2O4	0.01	Ba	4	Se	1
MnO	0.01	Sc	2	As	3
MgO	0.01	V	2	Cu	1
CaO	0.01	La	2	Pb	1.5
Na2O	0.01	Ce	4	Zn	1
K2O	0.01	Nd	2	Ag	2
P2O5	0.01	Y	1	Sb	2
S	0.01	U	1.5	Sn	2
		Rb	1	Cd	1
				Tl	1

Additional Notes

Drill core samples are numbered: 'LP, drill hole number and depth (last 3 digits)'

Samples crushed in a jaw crusher and milled in a tungston-carbide mill by Michael Agnew

All samples analysed by Phil Robinson

Samples below detection limits were assigned half the value of the detection limit for calculations in this thesis

Fusion discs were used for high (>2000ppm) Ba, Pb and Zn concentrations

Pb, As and Ba interference, where indicated

Tri Origin provided unpublished XRF data. Cu, Pb, Zn, Ag, and Hg analysed by atomic absorption, Au analysed by fire assaying.

Unit abbreviations: HSU = Hangingwall Siltstone Unit, f-b = fault-bound stratigraphic unit, TU = Transitional Unit, WVS = Western Volcanic succession, EVS = Eastern Volcanic Succession, LPG = Lewis Ponds Granite, MRV = Mullions Range Volcanics.

Trace elements in ppm unless otherwise stated

Additional trace element XRF data from this study:

Sample	Ag ppm	Sb ppm	Sn ppm	Cd ppm
LP12476	39	67	8	44
LP36W 195	403	815	240	202
LP51A482	101	107	62	67
LP51A488	730	1 090	376	265
LP66391	<2	<2	10	<1
LP66419	<2	<2	6	<1

Sample	Depth	Descriptive Name	Unit	SiO_2 %	TiO_2 %	Al_2O_3 %	Fe_2O_3 %	MnO %	MgO %	CaO %	Na_2O %	K_2O %	P_2O_5 %	BaO %	Total oxides	LOI %	S %	Total %	Nb ppm	Zr ppm	Sr ppm	Cr ppm
LP12425	425.4	sltst	HSU	77.00	0.32	9.87	2.39	0.02	3.08	0.11	0.11	3.48	0.09	0.27	96.74	3.09	1.52	99.84	8	97	9	32
LP12428	428.3	dol-qtz-chl-tlc schist	TU	42.53	0.21	4.62	9.67	0.40	15.38	8.20	<0.05	0.78	0.20	0.01	82.00	17.05	5.29	99.16	<1	10	111	972
LP12440	440.5	vuggy dolomite	TU	29.64	0.09	3.97	5.98	0.55	15.79	16.20	<0.05	0.11	0.11	0.00	72.44	22.95	2.63	96.72	<1	7	205	318
LP12450	450.4	chl-phl-tlc-qtz schist	TU	44.33	0.38	11.81	11.67	0.08	17.35	0.37	<0.05	2.71	0.27	0.06	89.03	8.42	5.06	98.28	5	116	11	419
LP12465	465.5	qtz-dol-chl-altered rock	TU	77.94	0.04	0.69	7.89	0.05	1.11	2.81	<0.05	0.03	0.01	0.00	90.57	6.89	6.41	100.24	1	15	28	19
LP12476	476.3	dol-qtz-tlc schist	TU	42.28	0.05	1.61	15.34	0.27	10.22	8.54	<0.05	0.60	0.08	0.01	79.00	17.85	9.84	100.26	<1	15	112	100
LP12493	493.0	massive dolomite	TU	1.93	0.01	0.70	0.68	0.26	16.81	34.91	<0.05	0.04	0.01	0.00	55.35	44.13	0.05	99.51	<1	2	228	<1
LP12503	503.0	dol-qtz-phl schist	TU	51.09	0.08	2.91	4.23	0.23	11.17	9.60	<0.05	1.74	0.05	0.02	81.12	16.68	2.30	100.08	2	24	121	8
LP12523	523.2	qtz-lithic sst matrix	TU	44.73	0.68	16.89	8.07	0.09	9.59	4.23	0.18	3.79	0.21	0.20	88.66	17.85	2.95	99.22	13	200	39	104
LP12553	553.4	qtz crystal-rich sst matrx	TU	67.09	0.48	12.99	2.96	0.09	3.14	2.59	0.04	4.09	0.13	0.23	93.83	5.38	1.57	99.21	10	184	31	23
LP12555	555.0	qtz crystal-rich sst	TU	51.12	0.45	11.47	6.17	0.22	7.34	7.07	<0.05	2.42	0.14	0.13	86.53	11.19	3.33	99.70	8	145	63	29
LP12570	570.2	sltst	TU	75.31	0.43	9.27	3.59	0.15	3.35	1.52	0.07	2.52	0.09	0.11	96.41	3.62	0.94	100.13	9	121	26	52
LP12516	516.4	sltst clast in breccia	TU	70.11	0.48	12.97	3.21	0.02	4.94	0.68	0.55	3.40	0.11	0.21	96.68	3.79	0.48	100.51	11	131	13	58
LP16A548	548.3	qtz crystal-rich sst matrx	TU	58.46	0.21	10.19	1.29	0.10	2.73	11.47	0.65	3.14	0.15	0.17	88.56	11.49	0.22	100.05	7	101	106	9
LP18383	383.7	qtz-feld porphyry clast	TU	55.39	0.75	16.85	3.02	0.03	8.61	2.64	1.81	3.13	0.17	-	92.40	6.81	0.44	99.21	12	290	35	33
LP18532	532.4	qtz-feld porphyry	WVS	65.28	0.57	16.67	3.44	0.03	1.89	2.52	2.56	3.16	0.18	0.12	96.42	3.43	0.01	99.85	12	216	264	26

Sample	Ba ppm	Sc ppm	V ppm	La ppm	Ce ppm	Nd ppm	Y ppm	U ppm	Rb ppm	Th ppm	Bi ppm	Ni ppm	Se ppm	As ppm	Pb ppm	Cu ppm	Zn ppm	Tl ppm	Al	CCPI
LP12425	2400	7	39	15	38	17	17	1.7	101	8.7	<2	10	<1	102	56	23	52	4	96.8	46.2
LP12428	56	27	148	3	Pb, As	3	6	<1.5	54	<1.5	<2	185	1	2707	527	163	323	5	66.3	95.0
LP12440	24	11	43	1	Pb, As	5	6	<1.5	7	8.1	<2	68	14	2754	5500	1048	4800	4	49.5	99.2
LP12450	454	17	134	9	Pb, As	12	17	5.0	160	10.7	<2	118	2	5323	2200	505	4250	30	98.1	86.4
LP12465	32	2	19	1	Pb, As	4	4	<1.5	4	17.9	5	14	4	330	1.14%	603	118	Pb	28.7	95.3
LP12476	67	7	35	2	Pb, As	5	9	1.7	38	18.7	<2	38	6	1392	1.12%	537	1.72%	Pb	55.8	94.2
LP12493	16	7	4	4	9	6	9	<1.5	2	<1.5	<2	1	<1	19	170	30	59	<1	32.5	99.6
LP12503	126	4	25	2	Pb, As	6	5	5.7	121	17.1	<2	4	<1	1692	8500	608	1.04%	Pb	57.3	86.4
LP12523	1772	17	133	36	Pb, As	42	31	6.6	145	21.0	3	38	2	884	3900	253	7200	9	75.2	70.7
LP12553	2066	10	48	26	65	29	32	2.3	188	13.7	<2	6	<1	74	180	25	461	5	73.3	43.2
LP12555	1020	9	44	23	Pb, As	23	30	4.0	102	17.4	3	13	8	357	4100	1500	1.07%	7	57.9	75.0
LP12570	996	10	84	30	58	25	19	2.0	101	11.1	<2	22	1	25	253	155	387	<1	78.7	56.4
LP12516	1900	13	100	30	61	26	20	3.2	125	11.6	<2	15	<1	<3	45	89	138	6	87.1	55.6
LP16A548	1521	7	16	20	51	21	16	2.3	93	10.8	<2	5	<1	6	5	58	19	2	32.6	41.9
LP18383	2000	14	96	19	47	26	15	4.6	114	22.0	<2	5	-	15	332	53	285	-	72.5	63.5
LP18532	1044	12	65	40	90	38	47	4.7	130	17.8	<2	8	<1	17	80	7	50	<1	49.9	24.8

Sample	Depth	Descriptive Name	Unit	SiO_2 %	TiO_2 %	Al_2O_3 %	Fe_2O_3 %	MnO %	MgO %	CaO %	Na_2O %	K_2O %	P_2O_5 %	BaO %	Total oxides	LOI %	S %	Total %	Nb ppm	Zr ppm	Sr ppm	Cr ppm
LP27786	786.9	qtz-feld porphyry clast	WVS	68.44	0.47	14.31	2.58	0.03	1.80	2.52	3.57	2.88	0.14	-	96.74	3.51	0.09	100.25	11	179	158	21
LP36170	170.4	sltst	f-b	78.43	0.29	7.20	2.72	0.29	2.08	2.63	0.18	2.04	0.06	0.08	96.00	3.95	0.03	99.97	8	81	93	33
LP36W190	190.6	sltst	f-b	69.67	0.59	12.21	4.60	0.10	4.71	0.19	0.17	3.23	0.15	0.39	96.01	3.74	1.05	99.77	13	167	17	70
LP36W 195	195.1	massive sulphide	TU	1.03	<0.01	0.02	30.93	0.66	0.45	12.64	<0.05	<0.01	0.04	-	45.76	13.50	32.50	85.27	<1	Pb	240	5
LP36W202	202.7	tlc-dol schist	TU	47.10	0.08	2.23	11.04	0.17	21.28	2.10	<0.05	1.69	0.06	0.02	85.77	8.39	5.94	99.53	<1	7	46	296
LP36W214	214.1	vuggy dol with mnr chl	TU	10.91	0.25	4.82	7.47	2.99	18.20	22.49	<0.05	0.01	0.19	0.00	67.33	31.62	3.03	98.98	<1	12	248	587
LP36W222	222.1	qtz crystal-rich sst matrix	TU	46.19	0.38	16.11	11.15	0.24	14.31	0.17	0.68	1.40	0.13	0.15	90.91	7.19	2.20	99.57	10	183	17	82
LP36W245	245.5	sltst	TU	74.00	0.53	10.81	4.36	0.17	2.79	0.55	0.45	2.80	0.11	0.14	96.71	2.99	0.47	99.73	11	153	18	61
LP36W262	262.1	qtz-feld porphyry clast	TU	48.57	0.88	8.95	7.52	0.33	4.78	13.59	0.84	0.70	0.25	-	86.41	13.89	0.11	100.30	17	314	153	38
LP36W277	277.8	qtz crystal-rich sst	TU	36.03	0.53	10.26	5.06	0.72	3.25	21.14	0.85	1.93	0.14	0.09	80.00	19.68	0.03	99.71	12	181	310	33
LP36W313	313.4	sltst	TU	70.50	0.61	12.19	4.95	0.26	2.70	1.12	0.33	2.99	0.10	-	95.75	3.77	0.17	99.52	13	168	37	67
LP36W366	366.4	qtz crystal-rich sst	TU	62.71	0.51	16.16	6.95	0.10	3.68	0.74	0.28	4.09	0.08	0.17	95.47	4.19	0.02	99.72	12	234	37	26
LP36W370	370.9	sltst	TU	88.06	0.12	4.48	2.90	0.03	1.39	0.45	0.34	0.70	0.07	-	98.54	1.60	<0.01	100.14	3	49	24	10
LP36W374	374.7	qtz-feld porphyry	WVS	67.04	0.62	17.24	3.14	0.03	1.96	0.44	3.98	3.06	0.11	0.15	97.77	2.44	<0.01	100.21	13	252	184	28
LP36W391	391.3	qtz-feld porphyry	WVS	70.99	0.46	13.51	3.57	0.03	2.24	1.08	2.72	2.26	0.14	-	97.00	2.83	0.30	99.83	10	179	189	20
LP37238	238.7	qtz-feld porphyry clast	TU	44.49	0.86	15.70	9.26	0.19	7.32	7.51	0.60	2.43	0.16	0.11	88.63	10.75	0.02	99.43	16	338	91	43

Sample	Ba ppm	Sc ppm	V ppm	La ppm	Ce ppm	Nd ppm	Y ppm	U ppm	Rb ppm	Th ppm	Bi ppm	Ni ppm	Se ppm	As ppm	Pb ppm	Cu ppm	Zn ppm	Tl ppm	Al	CCPI
LP27786	908	10	41	27	54	27	31	2.9	118	14.0	<2	4	-	<3	26	7	45	-	43.5	21.8
LP36170	743	7	44	24	47	20	20	1.9	89	7.3	<2	21	<1	10	51	24	53	<1	59.5	48.4
LP36W190	3500	14	102	41	87	35	28	2.7	106	14.1	<2	27	<1	162	37	36	117	3	95.7	58.1
LP36W 195	12	8	4	Pb	Pb	Pb	Pb	<1.5	-	-	-	25	-	1.12%	6.51%	1300	13.70%	-	3.5	93.8
LP36W202	228	4	45	3	Pb, As	7	13	3.3	128	24.0	<2	56	1	296	1.78%	686.9	2.70%	Pb	91.5	92.5
LP36W214	12	26	124	7	7	2	7	<1.5	<1	<1.5	<2	125	<1	101	43	35	127	<1	44.7	99.8
LP36W222	1412	11	109	42	Pb	42	53	4.4	48	19.8	3	51	9	132	4800	153	7500	2	94.9	87.3
LP36W245	1292	12	91	33	69	27	21	2.9	110	12.7	<2	25	<1	51	44	37	97	4	84.8	46.2
LP36W262	273	10	49	45	99	46	21	3.3	29	29.0	3	42	-	24	219	31	167	-	27.5	75.6
LP36W277	749	14	58	36	80	36	29	2.8	78	14.3	<2	24	<1	5	69	11	126	<1	19.1	53.9
LP36W313	815	11	97	34	72	32	26	2.4	138	17.0	<2	38	-	12	72	51	96	-	79.7	44.9
LP36W366	1484	11	85	79	147	67	41	1.8	190	30.3	5	26	<1	8	472	19	128	<1	88.4	45.7
LP36W370	276	4	19	15	28	14	17	<1.5	34	4.0	<2	10	-	6	<1.5	2	36	-	72.6	57.2
LP36W374	1367	13	66	27	66	32	36	4.3	148	17.7	<2	7	<1	<3	4	2	39	<1	53.2	21.8
LP36W391	807	9	47	42	80	36	41	2.6	113	15.0	<2	9	-	6	17	52	54	-	54.2	31.0
LP37238	936	13	78	33	69	34	20	2.3	100	22.7	3	102	<1	113	177	11	237	<1	54.6	70.7

Sample	Depth	Descriptive Name	Unit	SiO_2 %	TiO_2 %	Al_2O_3 %	Fe_2O_3 %	MnO %	MgO %	CaO %	Na_2O %	K_2O %	P_2O_5 %	BaO %	Total oxides	LOI %	S %	Total %	Nb ppm	Zr ppm	Sr ppm	Cr ppm
LP43386	386.0	qtz-feld porphyry	WVS	76.32	0.40	11.70	2.36	0.01	1.45	1.02	5.04	0.40	0.08	-	98.78	1.47	<0.01	100.25	8	157	252	18
LP44176	176.1	qtz-feld-ser-bt schist	f-b	61.45	0.66	15.06	5.37	0.06	2.57	2.14	0.17	9.00	0.18	0.09	96.75	3.14	0.01	99.89	10	176	41	52
LP44362	362.9	qtz-feld-chl-ser schist	WVS	75.75	0.18	9.28	4.24	0.05	5.10	0.12	0.12	1.73	0.11	0.04	96.72	3.12	0.09	99.84	6	90	8	7
LP44397	397.6	qtz-chl-ser-bt schist	WVS	64.05	0.20	11.19	7.20	0.10	9.87	0.15	0.06	1.93	0.11	-	94.86	4.65	0.30	99.51	7	105	12	8
LP46A090	90.7	qtz-ser-chl schist	f-b	70.86	0.58	13.28	2.56	0.07	3.27	0.19	0.06	4.62	0.15	0.20	95.84	4.42	0.57	100.33	9	149	29	48
LP46A113	113.5	sltst	HSU	79.97	0.22	8.53	1.78	0.03	1.91	0.08	0.07	4.68	0.07	1.42	98.76	1.42	0.71	100.27	7	68	164	17
LP46A129	129.8	sltst	HSU	79.18	0.29	7.82	3.02	0.02	1.97	0.14	0.07	3.45	0.08	1.09	97.13	2.58	1.98	99.87	5	76	51	35
LP46A134	134.4	qtz-ser-altered rock	HSU	89.58	0.07	3.75	1.26	0.01	0.25	0.24	0.08	1.88	0.03	2.21	99.36	1.13	0.95	100.57	2	56	123	2
LP46A150	150.4	sltst	HSU	87.23	0.16	5.06	2.02	0.01	0.64	0.92	0.17	1.61	0.03	0.06	97.91	2.56	1.07	100.48	6	76	22	16
LP46A177	177.2	chl-alt rock	WVS	29.43	0.95	20.59	6.46	0.18	30.14	0.33	0.07	0.01	0.16	<0.01	88.32	12.00	<0.01	100.32	16	253	10	87
LP46A210	210.0	qtz-chl-ser schist	WVS	69.00	0.25	14.86	3.05	0.05	4.75	0.15	0.08	3.91	0.14	0.11	96.35	3.59	0.38	99.94	10	125	9	10
LP46A 250	250.6	qtz-chl-ser schist	WVS	69.99	0.25	15.21	2.77	0.05	3.69	0.12	0.08	3.88	0.12	-	96.16	3.28	0.10	99.44	10	130	12	9
LP46A297	297.6	qtz-chl schist	WVS	76.76	0.21	12.29	2.11	0.03	1.96	0.21	0.11	4.01	0.18	-	97.87	2.30	0.03	100.17	7	103	16	10
LP46A346	346.3	qtz-ser-bt schist	WVS	66.07	0.65	14.16	5.46	0.13	4.25	0.22	1.40	4.65	0.15	0.15	97.29	2.72	0.39	100.01	10	165	43	57
LP51A216	216.6	qtz-chl-ser schist	f-b	52.04	0.81	19.01	5.51	0.04	3.27	4.20	0.14	7.95	0.19	0.06	93.22	6.48	0.01	99.72	14	215	39	67
LP51A257	257.4	qtz-ser-bt schist	f-b	61.44	0.58	14.82	5.00	0.04	1.51	3.66	0.14	7.32	0.19	0.07	94.77	4.73	0.01	99.51	10	159	72	46

Sample	Ba ppm	Sc ppm	V ppm	La ppm	Ce ppm	Nd ppm	Y ppm	U ppm	Rb ppm	Th ppm	Bi ppm	Ni ppm	Se ppm	As ppm	Pb ppm	Cu ppm	Zn ppm	Tl ppm	Al	CCPI
LP43386	95	6	30	24	49	23	24	2.0	14	13.0	<2	8	-	<3	4	27	45	-	23.4	21.0
LP44176	808	17	76	29	58	25	25	2.2	192	10.2	<2	18	<1	<3	14	4	73	2	83.4	21.9
LP44362	338	5	16	22	42	18	22	1.9	50	10.6	<2	2	<1	<3	3	7	81	<1	96.6	73.4
LP44397	448	5	17	23	50	23	22	2.7	77	11.6	<2	3	<1	<3	3	32	269	<1	98.3	83.2
LP46A090	1772	16	101	25	54	26	24	2.6	137	9.7	<2	13	<1	14	2	25	583	<1	96.9	41.1
LP46A113	12700	7	21	22	48	24	17	2.7	73	10.3	<2	7	<1	50	55	57	639	Ba	97.8	28.7
LP46A129	9800	9	52	15	34	16	12	5.0	87	5.5	<2	20	2	136	87	18	1143	Ba	96.3	35.9
LP46A134	19800	3	1	13	24	16	15	3.5	25	<1.5	<2	11	2	76	56	18	608	Ba	86.9	11.3
LP46A150	549	3	19	20	41	18	29	2.2	58	11.6	<2	8	<1	66	38	15	46	Ba	67.4	26.4
LP46A177	4	28	208	12	29	14	25	5.9	1	15.8	<2	29	<1	<3	<1.5	<1	186	<1	98.7	99.7
LP46A210	952	8	24	24	56	26	38	4.2	128	14.4	<2	5	2	4	29	59	120	1	97.4	54.3
LP46A 250	832	7	23	29	61	30	34	2.6	138	16.0	3	5	-	<3	129	47	1367	-	97.4	48.2
LP46A297	1015	5	19	21	48	21	28	2.6	135	10.2	<2	3	<1	<3	2	12	42	1	94.9	32.2
LP46A346	1384	18	114	26	54	22	27	2.5	158	10.1	<2	16	1	<3	35	37	209	1	84.6	41.3
LP51A216	574	23	98	34	75	34	29	2.7	206	14.6	<2	28	<1	<3	5	5	119	<1	72.1	28.8
LP51A257	592	17	77	28	61	31	22	<1.5	164	12.0	<2	21	<1	<3	13	8	61	<1	69.9	16.8

Sample	Depth	Descriptive Name	Unit	SiO_2 %	TiO_2 %	Al_2O_3 %	Fe_2O_3 %	MnO %	MgO %	CaO %	Na_2O %	K_2O %	P_2O_5 %	BaO %	Total oxides	LOI %	S %	Total %	Nb ppm	Zr ppm	Sr ppm	Cr ppm
LP51A309	309.4	qtz-ser schist	f-b	68.22	0.53	14.02	3.18	0.03	2.23	1.19	0.24	5.31	0.13	0.10	95.18	4.68	0.51	99.86	10	153	50	42
LP51A371	371.0	sltst	HSU	56.47	0.52	13.88	4.54	0.08	7.09	3.36	0.03	4.33	0.14	-	90.44	8.83	1.89	99.27	9	146	89	29
LP51A408	408.5	sltst	HSU	75.00	0.06	7.26	3.95	0.12	8.81	0.00	0.01	0.77	0.01	-	95.99	3.77	<0.01	99.76	5	82	4	2
LP51A443	443.4	sltst	HSU	70.85	0.43	9.72	4.02	0.19	7.69	0.18	0.08	2.51	0.11	-	95.78	3.70	0.02	99.68	8	103	21	64
LP51A474	474.1	sltst	HSU	69.68	0.46	10.46	4.14	0.10	7.76	0.17	<0.05	1.88	0.12	0.52	95.29	4.28	1.02	99.70	9	99	30	68
LP51A482	482.5	vuggy dolomite	HSU	13.16	<0.01	1.02	3.48	1.36	20.20	21.08	<0.05	0.050	0.10	-	60.45	27.59	3.36	93.24	<1	31	427	<1
LP51A484	484.6	vuggy dol with mnr chl	HSU	9.47	0.09	2.05	4.50	0.87	19.58	24.16	<0.05	0.01	0.08	0.00	60.81	34.68	2.86	98.42	<1	21	243	<1
LP51A488	488.6	massive sulphide	HSU	8.28	0.02	0.18	36.57	0.14	1.49	2.24	<0.05	0.04	0.16	-	49.12	24.62	37.30	99.66	<1	Pb		12
LP51A508	508.4	sltst	HSU	81.94	0.09	8.72	1.54	0.01	1.37	0.01	0.06	2.90	0.02	-	96.66	2.46	0.94	99.12	5	71	25	4
LP51A539	539.4	sltst	HSU	89.77	0.20	4.74	1.67	0.01	0.56	0.12	0.07	1.77	0.06	0.19	99.16	1.71	1.20	100.95	4	45	9	32
LP51A556	556.1	qtz-ser-bt schist	HSU	64.83	0.56	13.47	3.46	0.08	3.87	1.69	0.09	5.39	0.14	-	93.58	5.94	0.32	99.52	10	161	73	45
LP515A596	596.1	sltst	HSU	61.15	0.31	8.54	3.30	0.03	9.83	0.16	0.08	2.87	0.09	0.01	86.37	13.05	0.37	99.43	8	212	28	7
LP51A610	610.1	qtz-feld porphyry	WVS	60.94	0.63	15.58	4.81	0.06	6.60	0.46	3.95	2.02	0.12	0.04	95.21	4.46	0.53	99.67	11	177	92	55
LP51AW2302	302.0	qtz-carb-ser-chl schist	HSU	59.64	0.42	12.01	3.67	0.06	10.02	0.32	0.06	1.87	0.12	0.05	88.24	11.02	0.97	99.29	8	134	41	38
LP51AW2374	374.7	sltst	HSU	73.06	0.12	8.79	4.70	0.13	5.25	0.35	0.06	2.65	0.03	0.46	95.60	4.13	1.23	99.87	5	77	64	11
LP51AW2406	406.1	carb-ser-chl schist	HSU	34.88	0.83	19.30	6.62	0.15	12.49	0.79	0.13	4.60	0.17	0.56	80.52	19.52	1.50	100.09	18	253	112	122

Sample	Ba ppm	Sc ppm	V ppm	La ppm	Ce ppm	Nd ppm	Y ppm	U ppm	Rb ppm	Th ppm	Bi ppm	Ni ppm	Se ppm	As ppm	Pb ppm	Cu ppm	Zn ppm	Tl ppm	Al	CCPI
LP51A309	923	15	80	27	56	23	23	1.9	146	11.6	<2	6	<1	<3	2	8	49	<1	84.1	28.7
LP51A371	639	14	98	17	35	18	19	<1.5	134	7.0	<2	9	-	21	12	11	61	-	77.1	61.9
LP51A408	128	2	6	13	21	12	19	3.3	33	7.0	<2	1	-	<3	8	5	237	-	99.9	91.9
LP51A443	1931	12	87	25	47	21	12	2.6	76	10.6	<2	30	<1	30	45	9	91	<1	97.5	74.8
LP51A474	4700	14	96	35	64	32	21	2.2	52	10.6	<2	21	<1	9	84	66	862	Ba	98.0	80.3
LP51A482	71	7	14	Pb	Pb	Pb	Pb	7.0	3	-	<2	5	-	37	1.43%	2600	2.72%	-	49.0	99.6
LP51A484	23	8	14	1	Pb	7	14	6.2	2	16.6	<2	<1	<1	183	1.06%	212	1.41%	Ba	44.8	99.8
LP51A488	380	7	26	Pb	Pb	Pb	Pb	8.0	-	-	<2	4	-	7800	10.32%	3300	10.60%	-	40.3	95.8
LP51A508	5700	3	9	17	36	19	19	3.6	75	7.0	<2	3	-	27	333	38	636	-	98.4	31.6
LP51A539	1689	6	54	15	30	14	9	2.7	46	4.9	<2	7	2	41	177	79	396	3	92.5	23.3
LP51A556	1045	13	93	23	49	24	25	2.1	152	13.0	<2	15	-	<3	<1.5	30	64	-	83.9	41.4
LP515A596	54	14	32	10	22	11	17	1.9	91	6.0	<2	4	<1	4	4	3	71	<1	98.1	76.9
LP51A610	368	19	119	30	66	28	29	3.3	50	13.4	<2	16	<1	<3	2	11	69	1	66.2	52.5
LP51AW2302	430	15	88	17	39	18	29	3.3	62	10.0	<2	10	<1	17	117	7	116	<1	96.9	83.8
LP51AW2374	4100	5	15	16	36	17	20	2.1	50	7.8	<2	3	2	9	181	94	867	Ba	95.1	66.0
LP51AW2406	4700	26	154	45	94	47	59	4.7	159	16.5	<2	28	<1	41	12	139	247	Ba	94.9	72.5

Sample	Depth	Descriptive Name	Unit	SiO_2 %	TiO_2 %	Al_2O_3 %	Fe_2O_3 %	MnO %	MgO %	CaO %	Na_2O %	K_2O %	P_2O_5 %	BaO %	Total oxides	LOI %	S %	Total %	Nb ppm	Zr ppm	Sr ppm	Cr ppm
LP51AW2414	414.8	sltst	HSU	90.67	0.08	4.43	1.14	0.01	0.51	0.02	<0.05	1.59	0.02	0.26	98.73	1.39	0.77	100.16	2	47	11	7
LP51AW2437	437.0	ser-carb-chl schist	HSU	40.63	0.15	3.34	16.68	0.22	16.79	4.23	0.05	0.31	0.14	0.01	82.55	15.24	4.87	98.05	1	8	133	1228
LP51AW2499	499.7	ser-carb schist	HSU	30.50	0.28	8.42	12.10	0.17	18.48	0.42	0.06	3.19	0.27	0.01	73.90	26.10	2.30	100.14	1	17	51	1318
LP58163	163.7	qtz-feld porphyry	f-b	60.63	0.85	17.05	6.70	0.04	2.86	4.61	0.37	3.24	0.15	0.09	96.59	3.68	<0.01	100.27	13	218	209	64
LP58205	205.8	qtz-feld porphyry	f-b	61.57	0.78	16.39	5.81	0.10	4.55	2.80	3.47	1.22	0.15	-	96.84	3.17	<0.01	100.01	13	213	209	66
LP63115	115.3	qtz-chl-ser schist	f-b	52.92	0.47	25.24	3.29	0.02	4.80	1.13	0.81	5.00	0.08	-	93.76	5.96	0.09	99.72	15	235	164	14
LP63314	314.4	qtz-feld-ser-ca schist	f-b	59.69	0.58	14.21	1.84	0.05	0.83	7.09	0.60	7.99	0.15	0.09	93.12	6.91	<0.01	100.03	10	164	138	51
LP63411	411.1	qtz-feld-chl-ser-bt schist	HSU	67.36	0.47	12.62	4.26	0.11	4.97	0.23	1.19	3.81	0.13	1.60	96.75	2.82	0.71	99.57	8	132	154	35
LP63454	454.7	qtz-chl schist	WVS	56.68	0.54	12.09	9.01	0.11	14.14	0.29	0.06	0.05	0.12	-	93.09	6.71	0.19	99.80	9	148	12	52
LP63485	485.5	qtz-chl-ser schist	WVS	63.23	0.30	16.97	4.41	0.06	5.09	0.14	0.09	4.98	0.12	0.11	95.50	4.35	0.02	99.85	11	150	22	12
LP65A305	305.1	qtz-ser-bt schist	WVS	69.32	0.55	13.07	4.16	0.07	2.87	0.22	0.12	7.35	0.14	0.25	98.12	1.61	0.22	99.73	9	156	133	45
LP65A587	587.5	qtz-feld-bt schist	WVS	59.90	0.67	16.59	5.10	0.06	5.82	0.59	6.29	1.96	0.14	-	97.12	2.76	0.12	99.88	12	181	782	61
LP66112	112.7	qtz-ser schist / sst	HSU	64.28	0.48	16.14	3.41	0.04	4.74	0.30	0.15	4.84	0.15	-	94.53	4.96	0.03	99.49	12	193	34	23
LP66153	153.6	qtz-feld-ser schist	f-b	59.17	0.74	19.65	3.42	0.04	2.75	0.78	1.14	7.86	0.20	-	95.75	3.90	0.48	99.65	13	208	79	57
LP66179	179.3	qtz-feld-ser schist	f-b	72.60	0.15	11.35	2.14	0.09	4.17	0.21	0.12	5.07	0.06	0.54	96.50	2.98	0.64	99.48	8	83	65	6
LP66202	202.2	sltst	HSU	81.58	0.12	8.08	1.72	0.04	3.06	0.04	0.52	2.51	0.03	-	97.70	1.97	<0.01	99.67	5	150	73	2

Sample	Ba ppm	Sc ppm	V ppm	La ppm	Ce ppm	Nd ppm	Y ppm	U ppm	Rb ppm	Th ppm	Bi ppm	Ni ppm	Se ppm	As ppm	Pb ppm	Cu ppm	Zn ppm	Tl ppm	Al	CCPI
LP51AW2414	2300	3	12	11	23	9	6	<1.5	49	4.3	<2	2	<1	25	10	5	360	<1	97.9	24.0
LP51AW2437	102	19	107	1	5	<2	4	<1.5	18	<1.5	34	222	13	8	84	1670	307	<1	80.0	97.9
LP51AW2499	69	37	214	6	9	4	6	<1.5	119	<1.5	<2	349	3	71	2	715	386	<1	97.8	85.0
LP58163	768	17	73	25	60	28	27	1.7	157	14.7	<2	28	<1	<3	17	3	102	2	55.1	44.2
LP58205	191	17	108	35	72	34	37	2.8	44	15.5	<2	25	<1	<3	17	20	79	1	47.9	49.2
LP63115	871	7	61	13	37	15	19	<1.5	209	30.6	<2	45	<1	<3	3	9	74	2	83.5	45.2
LP63314	797	17	123	28	62	26	27	3.1	154	11.0	<2	16	<1	<3	15	2	30	<1	53.4	8.8
LP63411	14300	12	84	21	47	20	19	3.5	55	10.2	<2	12	5	<3	143	159	414	<1	86.1	49.8
LP63454	19	16	104	23	43	21	19	2.4	2	10.1	<2	11	<1	<3	0	12	101	<1	97.6	99.2
LP63485	1013	9	26	35	76	34	38	2.7	151	16.9	<2	5	<1	<3	2	3	96	2	97.8	50.1
LP65A305	2273	15	91	24	55	24	28	3.2	157	9.3	<2	14	<1	<3	3	54	56	<1	96.8	27.8
LP65A587	379	20	104	24	55	25	22	2.6	63	11.1	<2	18	<1	<3	3	122	138	<1	53.1	41.4
LP66112	924	12	88	50	93	43	37	5.4	162	26.0	<2	9	-	<3	2	7	93	-	95.5	48.7
LP66153	1554	18	121	44	80	37	41	2.4	221	17.0	<2	13	-	<3	7	11	65	-	84.7	23.4
LP66179	4800	9	19	18	42	16	24	2.7	113	10.1	<2	3	<1	10	192	6	509	<1	96.6	44.6
LP66202	3200	5	4	18	32	19	21	2.5	53	6.0	<2	1	-	<3	<1.5	3	89	-	90.9	50.2

Sample	Depth	Descriptive Name	Unit	SiO_2 %	TiO_2 %	Al_2O_3 %	Fe_2O_3 %	MnO %	MgO %	CaO %	Na_2O %	K_2O %	P_2O_5 %	BaO %	Total oxides	LOI %	S %	Total %	Nb ppm	Zr ppm	Sr ppm	Cr ppm
LP66233	233.3	sltst	HSU	64.30	0.39	10.01	6.67	0.26	10.18	0.13	0.06	0.89	0.09	-	92.98	6.53	1.03	99.51	9	85	23	65
LP66254	254.8	sltst	HSU	73.54	0.32	8.02	2.77	0.06	4.34	0.62	0.03	1.86	0.09	-	91.65	7.91	1.24	99.56	8	65	65	51
LP66267	267.0	chl-phl-altered rock	HSU	31.92	0.32	20.10	9.67	0.26	21.90	0.11	0.05	1.19	0.04	-	85.56	13.70	1.00	99.26	7	124	17	34
LP66282	282.8	qtz-ser-chl schist	WVS	55.91	0.41	11.53	4.82	0.08	10.44	0.15	0.06	1.94	0.10	-	85.44	14.22	<0.01	99.66	8	135	76	33
LP66296	296.5	qtz-chl-ser schist	WVS	55.46	0.69	17.14	6.22	0.11	10.81	0.18	0.11	2.84	0.15	-	93.71	5.77	0.19	99.48	11	189	10	57
LP66311	311.5	qtz-chl-ser schist	WVS	71.66	0.51	11.00	2.66	0.08	7.43	0.23	0.06	2.08	0.12	-	95.83	4.08	<0.01	99.91	9	150	12	43
LP66350	350.7	qtz-chl schist	WVS	62.05	0.49	10.98	8.59	0.13	10.92	0.22	0.51	0.06	0.12	<0.01	94.07	5.45	0.09	99.52	8	128	15	40
LP66391	391.6	qtz-chl-bt schist	WVS	61.36	0.49	11.97	10.06	0.11	9.42	0.16	0.07	0.90	0.09	-	94.63	5.09	0.21	99.72	8	128	5	43
LP66419	419.3	qtz-chl-ser schist	WVS	55.41	0.75	15.41	8.90	0.10	10.10	0.19	0.11	2.48	0.12	-	93.57	5.65	0.03	99.22	11	191	19	61
LP67B140	140.7	qtz-feld-ser-bt schist	WVS	70.19	0.26	14.95	2.52	0.05	1.81	0.34	1.74	4.36	0.13	0.07	96.42	3.05	0.28	99.47	10	137	49	12
LP67B306	306.5	qtz-ser-bt schist	WVS	64.87	0.68	15.16	5.30	0.08	3.20	0.81	1.42	4.40	0.18	-	96.10	3.64	0.45	99.74	11	187	70	64
LP67B476	476.2	qtz-feld-ser-bt schist	WVS	63.67	0.57	15.16	4.94	0.10	4.77	0.48	0.83	5.68	0.13	-	96.33	3.37	0.04	99.70	9	164	91	45
LP67B663	662.9	qtz-feld porphyry	WVS	69.51	0.52	13.46	3.09	0.06	2.48	0.72	4.54	2.66	0.17	0.07	97.28	2.50	0.85	99.81	9	137	176	41
LP67B687	687.8	dol-hbl-ep-altered rock	HSU	46.34	0.41	11.57	7.80	0.34	9.52	9.68	2.79	1.59	0.25	0.08	90.37	9.08	0.70	99.51	4	53	484	545
LP67B715	715.3	sltst	HSU	78.25	0.20	4.63	2.57	0.04	3.57	1.76	0.06	2.04	0.05	0.01	93.18	6.43	0.75	99.64	3	77	86	44
LP67B739	738.9	sltst	HSU	85.36	0.24	5.46	2.85	0.01	0.24	0.18	0.18	3.76	0.12	0.33	98.73	1.85	2.22	100.63	2	42	87	58

Sample	Ba ppm	Sc ppm	V ppm	La ppm	Ce ppm	Nd ppm	Y ppm	U ppm	Rb ppm	Th ppm	Bi ppm	Ni ppm	Se ppm	As ppm	Pb ppm	Cu ppm	Zn ppm	Tl ppm	Al	CCPI
LP66233	952	9	101	27	42	22	19	2.8	28	10.0	<2	27	-	<3	14	8	114	-	98.3	91.5
LP66254	1334	8	71	22	45	21	12	2.2	54	8.0	<2	22	-	56	33	11	82	-	90.5	69.7
LP66267	162	7	71	15	26	13	20	3.4	50	12.0	<2	24	-	<3	2	41	678	-	99.3	94.6
LP66282	1095	10	71	20	40	20	23	1.5	54	13.0	<2	13	-	<3	<1.5	2	69	-	98.3	83.9
LP66296	804	21	120	30	61	27	30	3.5	71	13.6	<2	19	<1	<3	<1.5	7	120	<1	97.9	78.6
LP66311	513	13	92	17	37	18	21	2.6	65	10.0	<2	18	-	<3	6	5	75	-	97.0	77.6
LP66350	13	12	78	21	41	18	22	2.1	2	12.0	<2	11	1	<3	6	27	206	<1	93.8	95.0
LP66391	176	14	100	23	41	19	20	3.1	29	9.1	<2	10	<1	<3	<1.5	26	116	<1	97.8	90.7
LP66419	734	18	125	23	46	22	25	5.0	70	14.0	<2	23	-	<3	<1.5	4	80	-	97.7	79.6
LP67B140	646	7	22	34	69	33	37	<1.5	174	13.8	<2	4	<1	<3	9	18	281	2	74.8	22.9
LP67B306	885	21	131	38	72	35	29	2.8	135	12.0	<2	13	<1	<3	29	22	111	<1	77.3	35.5
LP67B476	853	15	101	35	74	32	31	3.0	155	12.4	<2	13	<1	<3	9	51	127	1	88.9	42.3
LP67B663	639	14	76	33	67	31	29	2.9	67	11.7	<2	11	<1	<3	15	135	111	<1	49.4	25.6
LP67B687	699	26	163	11	27	12	15	<1.5	43	1.9	<2	132	<1	<3	12	210	249	<1	47.1	68.5
LP67B715	68	5	37	12	18	7	7	<1.5	82	3.2	<2	21	1.0	50	72	18	175	3	75.5	63.0
LP67B739	3000	8	72	8	19	9	5	<1.5	41	2.4	<2	15	1.4	81	88	133	157	5	91.7	5.7

Sample	Depth	Descriptive Name	Unit	SiO_2 %	TiO_2 %	Al_2O_3 %	Fe_2O_3 %	MnO %	MgO %	CaO %	Na_2O %	K_2O %	P_2O_5 %	BaO %	Total oxides	LOI %	S %	Total %	Nb ppm	Zr ppm	Sr ppm	Cr ppm
LP67B809	809.7	dol-hbl-ep-altered rock	HSU	34.51	0.37	8.85	5.90	0.35	5.15	24.03	0.87	1.88	0.19	0.13	82.23	16.81	0.09	99.16	6	53	541	80
LP67B878	878.3	qtz-chl-ser-bt schist	HSU	42.10	1.09	20.85	6.54	0.15	15.54	0.40	0.26	6.13	0.22	0.30	93.58	5.97	0.13	99.57	22	369	30	99
LP67B903	903.9	sltst	HSU	64.53	0.59	11.21	5.77	0.17	7.34	0.37	0.10	4.39	0.14	0.20	94.81	4.17	0.60	99.66	11	145	19	61
LP67B948	948.7	chl-alt rock	HSU	53.46	0.47	10.94	6.29	0.41	14.10	4.32	0.68	4.50	0.23	0.06	95.46	4.51	<0.01	100.02	4	55	56	135
LP67B986	986.6	chl-alt rock	HSU	71.34	0.20	8.08	5.80	0.19	8.78	0.08	0.06	2.86	0.04	0.04	97.47	2.55	0.05	100.06	4	86	3	11
LP67BW11037	1037.1	qtz-chl-ser schist	f-b	50.37	0.82	18.99	6.30	0.13	10.92	0.60	0.17	4.37	0.22	0.07	92.96	*6.32*	0.83	99.31	14	220	23	69
LP67BW11063	1063.2	qtz-chl-ser schist	f-b	62.66	0.69	15.19	4.57	0.06	6.30	0.95	0.47	4.43	0.15	0.05	95.52	3.90	0.44	99.44	11	183	46	62
LP67BW11132	1132.7	sltst	HSU	65.34	0.32	11.89	2.85	0.08	1.55	5.84	1.39	3.40	0.10	0.03	92.79	6.83	0.59	99.62	8	233	129	4
LP67BW11159	1158.9	sltst	HSU	75.68	0.16	11.32	2.37	0.02	1.39	1.38	2.33	2.43	0.03	0.02	97.13	2.73	0.35	99.87	6	241	55	1
LP67B369	368.9	qtz-feld porphyry	LPG	69.17	0.30	14.84	2.69	0.02	1.55	1.25	4.86	2.09	0.08	0.10	96.95	2.90	0.23	99.85	4	129	1082	15
LP67B907	907.4	qtz-feld porphyry	LPG	69.62	0.24	15.14	1.74	0.04	0.71	1.98	4.94	2.36	0.10	0.15	97.02	2.92	0.26	99.94	2	86	771	4
LP69238	238.0	qtz-ser-bt schist	f-b	62.84	0.63	16.90	4.56	0.03	4.35	0.70	1.39	4.88	0.14	0.06	96.48	3.64	0.19	100.12	12	184	47	56
LP70438	438.7	qtz porphyry	WVS	73.92	0.21	13.35	2.30	0.03	1.57	0.53	0.30	5.08	0.13	-	97.42	2.33	<0.01	99.75	9	114	48	9
LPD001		crinoidal limestone clast	TU	4.01	0.03	0.97	0.14	0.12	0.67	52.52	<0.05	0.26	0.01	0.03	58.76	40.75	0.02	99.52	<1	9	334	<1
LPD007		feld porphyry	EVS	77.41	0.55	14.06	0.75	<0.01	0.35	0.10	0.06	2.15	0.10	-	95.53	4.33	<0.01	99.86	10	159	47	42
LPD008		qtz-feld porphyry	LPG	70.40	0.22	14.74	1.63	0.03	0.70	1.81	4.91	2.75	0.08	-	97.27	2.59	0.10	99.86	2	89	472	7

Sample	Ba ppm	Sc ppm	V ppm	La ppm	Ce ppm	Nd ppm	Y ppm	U ppm	Rb ppm	Th ppm	Bi ppm	Ni ppm	Se ppm	As ppm	Pb ppm	Cu ppm	Zn ppm	Tl ppm	Al	CCPI
LP67B809	1111	19	155	13	24	14	10	2.5	63	3.2	<2	46	<1	<3	22	247	663	<1	22.0	65.2
LP67B878	2700	24	189	45	91	40	33	4.8	140	29.7	<2	55	<1	<3	3	5	139	<1	97.0	70.9
LP67B903	1800	12	92	20	42	19	16	4.4	92	13.8	<2	17	<1	<3	2	290	5200	<1	96.1	62.0
LP67B948	503	16	154	10	22	12	15	1.5	102	<1.5	<2	40	<1	<3	5	9	439	<1	78.8	73.1
LP67B986	330	7	22	10	17	9	17	2.7	74	7.7	<2	3	<1	<3	16	18	286	<1	98.8	75.0
LP67BW11037	636	22	137	28	56	29	37	3.2	129	14.6	<2	18	<1	<3	2	36	225	<1	95.2	70.6
LP67BW11063	491	18	117	25	58	26	32	1.7	132	12.3	<2	12	<1	<3	5	12	70	<1	88.3	56.3
LP67BW11132	224	10	15	17	39	21	43	2.5	119	8.5	<2	2	<1	<3	16	9	37	<1	40.6	24.4
LP67BW11159	189	7	5	22	50	24	36	3.4	86	10.0	<2	2	<1	<3	11	8	43	<1	50.7	22.6
LP67B369	866	7	51	11	33	14	8	1.5	56	8.5	<2	5	<1	<3	13	76	72	2	37.3	18.2
LP67B907	1366	3	26	5	17	5	3	<1.5	47	<1.5	<2	2	<1	<3	16	65	96	<1	30.7	8.9
LP69238	570	18	99	37	75	33	30	2.4	159	14.2	<2	12	<1	<3	<1.5	14	67	1	81.5	41.0
LP70438	2360	6	20	24	54	25	28	2.8	132	11.4	<2	4	<1	<3	<1.5	6	18	1	88.9	22.6
LPD001	204	<2	3	2	9	6	5	<1.5	10	<1.5	<2	<1	<1	<3	14	6	36	<1	1.7	70.2
LPD007	546	10	81	30	58	32	17	2.1	48	11.3	<2	3	<1	<3	19	4	13	<1	94.0	13.7
LPD008	589	3	19	3	14	8	6	2.3	65	1.8	<2	3	<1	<3	10	4	39	<1	33.9	8.4

Sample	Depth	Descriptive Name	Unit	SiO_2 %	TiO_2 %	Al_2O_3 %	Fe_2O_3 %	MnO %	MgO %	CaO %	Na_2O %	K_2O %	P_2O_5 %	BaO %	Total oxides	LOI %	S %	Total %	Nb ppm	Zr ppm	Sr ppm	Cr ppm
LPD018		feld porphyry	EVS	63.88	0.60	14.57	7.76	0.08	3.90	1.54	1.81	1.13	0.10	-	95.37	4.34	<0.01	99.71	10	159	246	52
LPD014		jasper		84.74	<0.01	<0.01	14.69	0.00	0.02	<0.01	<0.05	<0.01	0.02	-	99.47	0.18	<0.01	99.66	<1	<1	<1	2
LPD049		granite	LPG	69.85	0.19	15.63	1.31	0.02	0.60	1.71	5.06	3.41	0.08	-	97.86	1.86	0.04	99.72	5	98	509	11
LPD070		qtz-feld crystal-rich matrx	TU	60.00	0.71	19.52	3.25	0.03	3.19	1.28	0.69	5.96	0.13	0.46	95.22	4.67	<0.01	100.06	14	247	10	32
LPD024		qtz-feld porphyry	MRV	59.89	0.67	17.60	6.26	0.10	3.92	1.33	2.72	3.06	0.20	-	95.75	4.10	<0.01	99.85	15	257	238	30
LPD099		qtz-feld porphyry	MRV	80.23	0.19	11.00	0.97	0.02	0.93	0.55	2.47	2.33	0.11	-	98.80	1.51	<0.01	100.31	8	102	120	6
MRV01		qtz-feld porphyry	MRV	77.07	0.32	11.56	1.74	0.02	0.47	0.73	1.93	5.79	0.11	-	99.74	0.83	<0.01	100.57	9	148	82	14
MRV03		qtz-feld-lithic sst	MRV	71.57	0.56	13.01	3.89	0.02	1.88	0.67	1.73	4.76	0.14	-	98.23	1.68	<0.01	99.91	11	206	80	36
MRV04		qtz-feld porphyry	MRV	71.65	0.50	13.70	3.10	0.02	0.90	1.46	3.56	4.06	0.14	-	99.09	0.87	0.01	99.96	10	201	164	22
MRV06		obsidian	MRV	70.90	0.22	14.89	0.72	0.02	0.32	0.33	1.71	10.53	0.07	-	99.71	0.43	0.01	100.14	8	152	34	3
MRV11		qtz porphyry	MRV	80.07	0.28	11.68	1.30	<0.01	0.66	0.01	0.07	4.18	0.06	-	98.31	1.93	<0.01	100.24	8	130	19	11
MRV14		flow-banded rhyolite	MRV	73.63	0.10	13.68	1.74	0.03	0.44	0.03	0.91	8.53	0.03	-	99.12	1.10	0.02	100.22	11	138	68	1
MRV24		qtz-feld porphyry	MRV	72.13	0.34	14.44	2.18	0.01	1.63	0.27	5.04	2.59	0.13	-	98.76	1.29	<0.01	100.05	10	160	139	12

Sample	Ba ppm	Sc ppm	V ppm	La ppm	Ce ppm	Nd ppm	Y ppm	U ppm	Rb ppm	Th ppm	Bi ppm	Ni ppm	Se ppm	As ppm	Pb ppm	Cu ppm	Zn ppm	Tl ppm	Al	CCPI
LPD018	678	13	104	19	40	20	22	1.8	64	12.5	<2	20	<1	<3	19	23	92	<1	60.0	57.0
LPD014	13	<2	35	<2	<4	<2	3	<1.5	<1	<1.5	<2	8	<1	<3	0	3	9	2	33.3	40.0
LPD049	738	3	22	12	24	14	8	1.9	127	8.2	<2	4	<1	<3	28	2	37	1	37.2	6.6
LPD070	4100	15	66	43	97	47	34	<1.5	255	18.1	<2	9	<1	<3	13	27	1384	Ba	82.3	32.4
LPD024	1125	13	79	40	86	40	40	5.2	165	23.0	<2	13	-	<3	56	5	106	-	63.3	40.4
LPD099	744	4	14	22	40	22	31	4.4	110	12.0	<2	3	-	<3	9	9	18	-	51.9	16.2
MRV01	715	5	27	26	51	28	44	2.5	184	13.2	<2	6	<1	4	24	7	23	<1	70.2	5.7
MRV03	651	11	64	42	66	39	53	3.6	165	13.6	<2	15	<1	<3	16	7	48	1	73.5	22.5
MRV04	648	9	48	31	67	33	35	3.1	136	14.7	<2	9	<1	<3	19	8	46	<1	49.7	10.6
MRV06	1364	3	9	28	69	34	36	4.3	211	18.9	<2	2	<1	<3	9	4	11	1	84.2	2.5
MRV11	901	7	23	20	28	39	70	5.6	139	12.7	<2	4	<1	<3	15	2	21	<1	98.4	13.4
MRV14	789	3	4	29	58	31	47	4.2	242	13.1	<2	2	<1	<3	21	6	60	<1	90.5	4.5
MRV24	450	8	32	58	73	35	34	2.2	95	16.0	<2	6	-	<3	13	11	28		44.3	17.6

Tri Origin data:

Drill Hole	Depth	Descriptive Name	Unit	SiO_2 %	TiO_2 %	Al_2O_3 %	Fe_2O_3 %	MnO %	MgO %	CaO %	Na_2O %	K_2O %	P_2O_5 %	Cr_2O_3 %	Total oxides	LOI %	Nb ppm	Total %	Zr ppm	Sr ppm	Ba ppm	Y ppm
Detection Limits:				0.01	0.01	0.01	0.01	0.01	0.01	0.01	0.01	0.01	0.01	0.01			2		2	2	20	2
BOA-103	146.0	crystal tuff	WVS	76.50	0.20	10.60	4.11	0.06	2.67	0.14	1.13	2.33	0.11	<0.01	97.85	2.23	13	100.20	124	19	515	29
BOA-103	167.0	crystal tuff	WVS	70.90	0.22	9.50	8.97	0.15	4.93	0.48	0.05	1.29	0.09	<0.01	96.58	3.31	26	100.00	105	0	951	12
BOA-108	63.8	lapilli crystal tuff	WVS	72.00	0.19	11.00	4.59	0.05	3.26	0.17	0.07	3.35	0.10	0.04	94.82	3.40	6	98.30	92	10	1110	28
SLP-1	258.0	felsic tuff (chlorite schist)	WVS	43.90	0.52	12.30	5.15	0.19	27.50	0.19	0.09	0.28	0.14	<0.01	90.26	9.08	28	99.40	212	0	131	24
SLP-3	401.3	crystal tuff	WVS	69.10	0.25	14.20	2.61	0.05	3.34	0.23	1.42	4.68	0.14	0.02	96.04	2.70	9	98.90	120	40	582	35
TLPD-01	251.4	crystal tuff	WVS	60.10	0.25	13.20	5.44	0.12	11.70	0.19	0.05	1.72	0.12	0.01	92.90	5.40	6	98.30	103	8	424	29
TLPD-02W	327.0	tuff (quartz poor)	WVS	56.40	0.69	18.10	5.13	0.04	4.47	2.50	1.10	4.74	0.20	0.03	93.40	4.60	11	98.10	225	71	1180	73
TLPD-03	191.8	lapilli crystal tuff	WVS	60.80	0.68	19.00	3.08	0.04	6.23	0.39	0.98	5.01	0.17	0.02	96.40	3.80	10	100.60	205	16	2890	49
TLPD-08	273.8	crystal tuff	WVS	64.40	0.57	16.60	3.06	0.02	3.65	0.27	0.96	6.36	0.16	0.02	96.07	2.50	8	98.80	190	20	1420	47
TLPD-08	428.6	crystal tuff	WVS	65.10	0.61	15.90	4.60	0.04	4.05	1.46	1.74	3.00	0.19	0.02	96.71	3.40	10	100.30	187	111	844	47
TLPD-09A	303.1	crystal tuff	TU	66.00	0.54	15.30	3.64	0.02	4.41	0.24	1.15	4.66	0.15	0.11	96.22	2.60	8	99.00	188	20	1050	40
TLPD-16A	492.0	lapilli crystal tuff	TU	61.60	0.56	15.80	3.64	0.01	6.00	0.20	0.81	5.22	0.13	0.02	93.99	3.95	8	98.30	170	15	3090	41
TLPD-17	588.0	crystal tuff	TU	65.80	0.51	13.40	3.36	0.02	4.37	1.83	0.33	5.09	0.66	0.02	95.39	2.65	8	98.10	176	30	514	52
TLPD-18	539.4	crystal tuff	WVS	71.80	0.45	12.40	3.48	0.03	1.87	1.29	3.80	1.21	0.12	0.02	96.47	2.05	6	98.60	157	179	397	31
TLPD-25	246.0	felspar crystal tuff	WVS	42.50	0.30	15.50	11.00	0.22	20.30	0.18	<0.01	0.05	0.12	0.02	90.19	9.15	7	99.10	141	7	<20	16

Drill Hole	Rb ppm	Cu ppm	Pb ppm	Zn ppm	Ag ppm	Hg ppm	Au ppb	Al	CCPI
Detection Limits:	2	1	2	1	0	1	1		
BOA-103	121							79.7	43.6
BOA-103	63							92.1	78.6
BOA-108	130	43	87.0	111	2	<1	20	96.5	48.8
SLP-1	31							99.0	98.7
SLP-3	132	20	<2	40	2	<1	2	82.9	35.4
TLPD-01	55	2	24.0	122	2	<1	2	98.2	86.9
TLPD-02W	189	3	11.0	99	2	<1	2	71.9	43.4
TLPD-03	197	37	77.0	444	3	<1	44	89.1	51.0
TLPD-08	190	19	5.0	32	2	<1	4	89.1	33.3
TLPD-08	133	13	32.0	85	2	<1	1	68.8	46.1
TLPD-09A	149	14	14.0	52	2	<1	2	86.7	43.2
TLPD-16A	155	9	30.0	40	2	<1	24	91.7	49.9
TLPD-17	146	16	4.0	56	2	<1	1	81.4	44.6
TLPD-18	47	13	15.0	52	2	<1	3	37.7	27.2
TLPD-25	3	1520	351.0	7960	3	<1	37	99.2	99.8

Tri Origin data:

Drill Hole	Depth	Descriptive Name	Unit	SiO_2 %	TiO_2 %	Al_2O_3 %	Fe_2O_3 %	MnO %	MgO %	CaO %	Na_2O %	K_2O %	P_2O_5 %	Cr_2O_3 %	Total oxides	LOI %	Nb ppm	Total %	Zr ppm	Sr ppm	Ba ppm	Y ppm
Detection Limits:				0.01	0.01	0.01	0.01	0.01	0.01	0.01	0.01	0.01	0.01	0.01			2		2	2	20	2
TLPD-27	773.0	crystal tuff	WVS	73.40	0.43	12.00	2.93	0.02	2.19	0.82	1.53	3.38	0.13	0.02	96.85	1.80	8	98.80	141	56	726	35
TLPD-28	746.0	crystal tuff	WVS	70.50	0.46	13.20	3.06	0.01	2.81	1.21	1.28	3.18	0.13	0.02	95.86	2.80	7	98.80	154	53	889	33
TLPD-30	794.0	crystal tuff	WVS	69.50	0.46	13.30	3.91	0.05	4.33	0.45	1.64	2.21	0.13	0.03	96.01	3.00	7	99.20	155	34	652	31
TLPD-47A	150.0	felsic tuff (sericite schist)	WVS	67.60	0.50	16.50	3.49	0.03	1.73	0.27	0.11	5.45	0.14	0.04	95.86	3.70	8	99.70	179	10	1090	49
TLPD-65A	554.0	tuff (quartz poor)	WVS	63.90	0.68	14.60	4.91	0.08	4.85	0.23	1.19	4.76	0.15	0.02	95.37	2.60	10	98.20	174	50	1610	38
TLPD-65A	625.0	crystal tuff	WVS	63.40	0.51	12.90	4.79	0.06	3.55	0.22	1.07	5.54	0.12	0.03	92.19	5.85	7	98.20	130	51	1730	30
TLPD-65A	899.0	felsic tuff (sericite schist)	f-b	80.90	0.08	9.38	1.16	0.02	1.15	0.23	0.48	3.24	0.01	0.02	96.67	2.00	5	98.90	87	43	1930	26
TLPD-65A	984.0	crystal tuff	f-b	55.60	0.73	17.80	6.33	0.06	7.41	1.18	1.16	3.90	0.14	0.03	94.34	3.90	10	98.30	195	65	542	40
TLPD-67B	598.4	tuff (quartz poor)	WVS	66.70	0.53	14.80	3.96	0.08	4.41	0.44	1.93	3.82	0.19	0.03	96.89	2.10	7	99.10	136	61	363	36
TLPD-67B	651.4	felsic tuff	WVS	68.10	0.55	14.70	2.98	0.06	2.56	0.56	4.97	2.55	0.17	0.02	97.22	2.75	8	100.00	134	242	393	28
TLPD-67BW	915.0	qtz-feld porphyry	LPG	69.30	0.23	15.10	2.05	0.05	1.09	1.20	3.78	3.66	0.10	0.02		2.00	2	98.90	87	469	1230	<2
TLPD-67BW	1026.0	crystal tuff	f-b	62.30	0.66	15.10	4.65	0.12	9.39	0.28	0.13	3.05	0.15	0.02	95.85	4.60	9	100.60	144	16	573	33
TLPD-68	396.8	crystal tuff	WVS	56.30	0.86	18.20	6.72	0.09	3.65	0.46	0.64	7.95	0.20	0.03	95.10	2.65	12	98.30	170	65	4740	52
TLPD-70	200.3	lapilli crystal tuff	WVS	69.00	0.51	13.40	5.00	0.07	3.48	0.45	0.96	3.81	0.14	0.02	96.84	2.55	8	99.50	121	28	1760	28

Drill Hole	Rb ppm	Cu ppm	Pb ppm	Zn ppm	Ag ppm	Hg ppm	Au ppb	Al	CCPI
Detection Limits:	2	1	2	1	0	1	1		
TLPD-27	123	13	10.0	44	2	<1	5	70.3	30.8
TLPD-28	104	15	5.0	44	2	<1	4	70.6	38.7
TLPD-30	85	21	46.0	128	2	<1	3	75.8	52.9
TLPD-47A	228	43	30.0	86	2	<1	14	95.0	23.7
TLPD-65A	109	0	4.0	47	2	<1	2	87.1	44.9
TLPD-65A	112	109	4.0	47	2	<1	2	87.6	34.9
TLPD-65A	78	6	<2	36	2	<1	2	86.1	23.6
TLPD-65A	96	12	5.0	78	2	<1	<1	82.9	59.4
TLPD-67B	96	25	5.0	53	2	<1	2	77.6	43.4
TLPD-67B	74	82	8.0	43	2	<1	21	48.0	25.4
TLPD-67BW	74	147	20.0	80	2	<1	1	48.8	12.8
TLPD-67BW	93	8	<2	157	2	<1	2	96.8	74.7
TLPD-68	203	<1	11.0	45	2	<1	2	91.3	29.8
TLPD-70	103	113	5.0	48	2	<1	4	83.8	42.2

Tri Origin data:

Drill Hole	Depth	Descriptive Name	Unit	SiO_2 %	TiO_2 %	Al_2O_3 %	Fe_2O_3 %	MnO %	MgO %	CaO %	Na_2O %	K_2O %	P_2O_5 %	Cr_2O_3 %	Total oxides	LOI %	Nb ppm	Total %	Zr ppm	Sr ppm	Ba ppm	Y ppm
Detection Limits:				0.01	0.01	0.01	0.01	0.01	0.01	0.01	0.01	0.01	0.01	0.01			2		2	2	20	2
TLPD-70	543.5	crystal tuff	WVS	70.40	0.25	14.60	1.71	0.05	1.67	0.44	1.99	5.66	0.14	0.02	96.93	1.65	9	98.70	110	61	934	39
TLPD-72	137.6	crystal tuff	WVS	69.90	0.20	11.80	1.84	0.05	7.71	0.23	0.06	2.29	0.12	0.03	94.23	3.85	6	98.20	89	13	303	32
TLPD-72	328.3	tuff (quartz poor)	WVS	58.00	0.81	18.00	6.83	0.11	6.57	0.25	0.12	4.40	0.16	0.03	95.28	4.15	9	99.50	204	16	594	41
TOD-11	125.0	crystal tuff	WVS	68.00	0.28	16.00	2.77	0.03	2.65	0.30	0.09	6.12	0.15	0.03	96.42	2.85	8	99.50	124	26	1320	44
TOD-11	265.0	crystal tuff	WVS	66.30	0.52	14.10	4.62	0.07	3.80	0.23	0.07	6.31	0.13	0.02	96.17	1.95	9	98.30	122	20	1730	29
TOD-11	380.5	tuff (quartz poor)	WVS	62.50	0.76	15.80	5.01	0.07	3.68	0.42	0.98	6.73	0.16	0.02	96.13	1.80	8	98.20	171	63	1870	37
TOD-11	491.4	crystal tuff	HSU	72.40	0.22	12.60	2.88	0.03	2.00	0.25	1.02	4.87	0.13	0.03	96.43	1.50	7	98.40	92	61	3810	29

Drill Hole		Rb ppm	Cu ppm	Pb ppm	Zn ppm	Ag ppm	Hg ppm	Au ppb	Al	CCPI
	Detection Limits:	2	1	2	1	0	1	1		
TLPD-70		158	3	6.0	53	2	<1	7	75.1	17.9
TLPD-72		69	1	<2	34	2	<1	2	97.2	76.6
TLPD-72		158	10	<2	76	2	<1	3	96.7	59.2
TOD-11		210	26	8.0	50	2	<1	7	95.7	29.9
TOD-11		146	21	4.0	47	2	<1	<1	97.1	37.3
TOD-11		168	24	4.0	41	2	<1	<1	88.1	32.3
TOD-11		107	2	7.0	17	2	<1	11	84.4	25.3

Least-altered samples used in figure 6.1:

Sample	Depth	Descriptive Name	Unit	SiO_2 %	TiO_2 %	Al_2O_3 %	Fe_2O_3 %	MnO %	MgO %	CaO %	Na_2O %	K_2O %	P_2O_5 %	BaO %	Total oxides	LOI %	S %	Total %	Al	CCPI	Ti/Zr
TLPD-18	539.4	crystal tuff	WVS	71.80	0.45	12.40	3.48	0.03	1.87	1.29	3.80	1.21	0.12	0.02	96.47	2.05	6	98.60	37.7	50.0	17.3
LP36W374	374.7	qtz-feld porphyry	WVS	67.04	0.62	17.24	3.14	0.03	1.96	0.44	3.98	3.06	0.11	0.15	97.77	2.44	<0.01	100.21	53.2	40.5	14.8
LP36W391	391.3	qtz-feld porphyry	WVS	70.99	0.46	13.51	3.57	0.03	2.24	1.08	2.72	2.26	0.14	-	97.00	2.83	0.30	99.83	54.2	52.3	15.4
LP43386	386.0	qtz-feld porphyry	WVS	76.32	0.40	11.70	2.36	0.01	1.45	1.02	5.04	0.40	0.08	-	98.78	1.47	<0.01	100.25	23.4	39.6	15.3
TLPD-67B	651.4	felsic tuff	WVS	68.10	0.55	14.70	2.98	0.06	2.56	0.56	4.97	2.55	0.17	0.02	97.22	2.75	8	100.00	48.0	41.1	24.6
LP67B663	662.9	qtz-feld porphyry	WVS	69.51	0.52	13.46	3.09	0.06	2.48	0.72	4.54	2.66	0.17	0.07	97.28	2.50	0.85	99.81	49.4	42.2	22.7
MRV24		qtz-feld porphyry	MRV	72.13	0.34	14.44	2.18	0.01	1.63	0.27	5.04	2.59	0.13	-	98.76	1.29	<0.01	100.05	44.3	32	12.8

Sample	Lithofacies	Net gain/loss	SiO_2	TiO_2	Al_2O_3	Fe_2O_3	MnO	MgO	CaO	Na_2O	K_2O	P_2O_5	S
LP46A090	A	-10.79	-4.46	-0.03	-2.77	-0.68	0.00	0.38	-0.39	-4.92	1.60	-0.04	0.51
LP46A177	A	-50.42	-52.51	-0.05	-3.79	0.44	0.04	13.40	-0.39	-4.93	-2.54	-0.09	0.00
LP46A346	A	-17.99	-14.44	-0.02	-3.20	1.45	0.05	0.89	-0.38	-3.83	1.23	-0.05	0.32
LP51A216	A	-39.16	-35.68	-0.05	-2.86	0.45	-0.04	-0.52	2.06	-4.88	2.40	-0.05	0.01
LP51A309	A	-13.32	-8.23	-0.08	-2.40	-0.19	-0.03	-0.60	0.48	-4.76	2.11	-0.06	0.45
LP51A610	A	-24.79	-21.99	-0.07	-2.91	0.66	-0.01	2.43	-0.21	-1.98	-1.02	-0.08	0.40
LP58205	A	-36.27	-29.37	-0.06	-4.39	0.68	0.00	0.30	1.20	-2.79	-1.78	-0.08	0.00
LP63314	A	-21.37	-19.45	-0.08	-3.12	-1.48	-0.02	-1.88	5.22	-4.48	3.96	-0.05	0.00
LP63454	A	-12.51	-16.64	-0.06	-3.72	5.20	0.04	10.28	-0.30	-4.92	-2.50	-0.06	0.17
LP65A305	A	-12.73	-8.40	-0.08	-3.44	0.60	0.00	-0.09	-0.37	-4.87	3.78	-0.05	0.19
LP65A587	A	-25.25	-23.78	-0.05	-2.42	0.79	-0.02	1.75	-0.12	-0.32	-1.10	-0.07	0.09
LP66 282	A	-12.33	-12.56	-0.14	-3.25	1.81	0.02	7.81	-0.41	-4.91	-0.62	-0.07	0.00
LP66 311	A	-11.70	-4.17	-0.10	-4.89	-0.61	0.01	4.07	-0.35	-4.92	-0.69	-0.06	0.00
LP66 419	A	-31.43	-29.16	-0.02	-3.87	3.27	0.01	4.54	-0.43	-4.89	-0.81	-0.09	0.02
LP66153	A	-35.06	-29.89	-0.07	-2.01	-0.77	-0.03	-0.78	-0.06	-4.23	2.53	-0.04	0.31
LP66296	A	-30.70	-28.82	-0.06	-2.56	1.43	0.02	5.10	-0.43	-4.89	-0.54	-0.06	0.13
LP66350	A	1.14	-3.29	-0.04	-3.23	5.99	0.08	8.85	-0.33	-4.44	-2.49	-0.04	0.09
LP66391	A	1.85	-4.01	-0.04	-2.20	7.53	0.05	7.28	-0.39	-4.90	-1.61	-0.08	0.22
LP67B306	A	-27.98	-21.59	-0.06	-3.83	0.82	0.00	-0.27	0.02	-3.95	0.60	-0.04	0.32
LP67B663	A	-1.34	-0.15	-0.04	-1.54	0.04	0.00	-0.14	0.14	-0.53	0.05	0.00	0.83

Notes:
Major elements expressed as g/100 g
Trace elements expressed as g/10^6 g
Zr used as the immobile reference element

Least altered reference samples-
dacite A: LP67B651, dacite B: LP43386,
dacite C: MRV24

Includes XRF data from this study and from Tri Origin

Sample	Lithofacies	Zr	Sr	Cr	Ba	Nd	Sc	V	La	Ce	Y	Rb	Ni	As	Cu	Pb	Zn
LP46A090	A	0	-216	43	1564	16	-60	69	20	-34	-21	123	11	12	-60	-6	481
LP46A177	A	0	-237	46	-26	-1	-59	89	4	-67	-30	0	15	1	-83	-8	56
LP46A346	A	0	-207	46	1096	10	-59	72	19	-38	-21	128	13	1	-53	20	127
LP51A216	A	0	-218	42	329	13	-60	40	19	-36	-25	128	17	1	-79	-5	31
LP51A309	A	0	-198	37	782	12	-61	49	22	-33	-23	128	5	1	-75	-6	0
LP51A610	A	0	-173	42	251	13	-60	69	21	-33	-21	38	12	1	-74	-6	9
LP58205	A	0	-110	42	92	13	-63	47	20	-37	-19	28	16	1	-70	3	7
LP63314	A	0	-129	42	621	13	-60	79	21	-32	-21	125	13	1	-80	4	-18
LP63454	A	0	-232	47	-11	11	-60	74	19	-43	-26	2	10	1	-72	-8	48
LP65A305	A	0	-127	39	1930	13	-61	57	19	-35	-19	135	12	1	-36	-6	5
LP65A587	A	0	336	45	252	11	-59	56	16	-42	-27	47	13	1	8	-6	59
LP66 282	A	0	-166	32	1059	11	-64	49	18	-42	-21	53	13	1	-81	-7	25
LP66 311	A	0	-231	38	429	8	-63	61	13	-49	-24	58	16	1	-78	-3	24
LP66 419	A	0	-229	43	488	8	-62	67	14	-50	-25	49	16	1	-80	-7	13
LP66153	A	0	-191	37	975	16	-63	57	26	-31	-16	142	8	1	-75	-4	-1
LP66296	A	0	-235	40	541	11	-59	64	19	-40	-21	51	13	1	-77	-8	42
LP66350	A	0	-227	42	-15	11	-61	61	20	-39	-20	2	12	2	-54	-1	172
LP66391	A	0	-236	45	156	12	-59	83	22	-40	-22	31	10	2	-56	-8	78
LP67B306	A	0	-192	46	607	17	-59	73	25	-31	-22	96	9	1	-67	13	37
LP67B663	A	0	-70	40	597	22	-60	53	30	-17	-14	65	11	1	49	6	65

Sample	Lithofacies	Net gain/loss	SiO_2	TiO_2	Al_2O_3	Fe_2O_3	MnO	MgO	CaO	Na_2O	K_2O	P_2O_5	S
LP67BW11037	A	-40.14	-37.43	-0.05	-3.14	0.86	0.02	4.09	-0.19	-4.87	0.11	-0.04	0.51
LP67BW11063	A	-26.93	-22.19	-0.04	-3.57	0.37	-0.02	2.06	0.14	-4.63	0.70	-0.06	0.32
LP18532	B	-28.97	-29.00	0.01	0.38	0.13	0.01	-0.08	0.81	-3.18	1.89	0.05	0.00
TLPD-18 539.4	B	-2.64	-4.75	0.05	0.66	1.11	0.02	0.41	0.27	-1.25	0.81	0.04	-0.01
LP36W374	B	-38.16	-34.69	-0.01	-0.99	-0.41	0.01	-0.23	-0.75	-2.57	1.50	-0.01	0.00
LP36W 391	B	-13.48	-14.08	0.00	0.14	0.77	0.02	0.51	-0.07	-2.66	1.58	0.04	0.26
TLPD-28746	B	-1.39	-4.68	0.06	1.71	0.75	0.00	1.41	0.21	-3.74	2.83	0.05	-0.01
TLPD-30794	B	-1.88	-6.15	0.06	1.73	1.59	0.04	2.92	-0.57	-3.38	1.83	0.05	-0.01
LPD024	B	-40.36	-39.78	0.01	-0.96	1.46	0.05	0.94	-0.21	-3.38	1.47	0.04	0.00
LP18383	clast	-48.61	-46.39	0.01	-2.59	-0.73	0.01	3.20	0.41	-4.06	1.29	0.01	0.23
LP36W 262	clast	-55.70	-52.14	0.04	-7.24	1.38	0.15	0.93	5.75	-4.62	-0.05	0.04	0.05
LP37238	clast	-57.76	-55.70	0.00	-4.43	1.93	0.08	1.94	2.46	-4.76	0.73	-0.01	0.00
LP44362	C	73.33	62.58	-0.02	2.06	5.36	0.08	7.44	-0.06	-4.83	0.49	0.07	0.16
LP44397	C	45.97	25.29	-0.04	2.58	8.77	0.14	13.38	-0.04	-4.95	0.35	0.04	0.45
LP46A210	C	24.68	16.02	-0.02	4.55	1.72	0.05	4.44	-0.08	-4.94	2.41	0.05	0.48
LP46A 250	C	19.76	14.05	-0.03	4.29	1.23	0.05	2.91	-0.12	-4.94	2.19	0.02	0.12
LP46A297	C	52.88	46.77	-0.01	4.60	1.09	0.04	1.41	0.06	-4.87	3.62	0.15	0.04
LP63485	C	2.88	-4.77	-0.02	3.64	2.52	0.05	3.79	-0.12	-4.94	2.72	0.00	0.02
LP70438	C	38.08	31.70	-0.05	4.31	1.05	0.03	0.58	0.47	-4.62	4.55	0.05	0.00
BOA-103-146	C	27.26	26.39	-0.08	-0.79	3.11	0.07	1.81	-0.09	-3.58	0.41	0.01	-0.01

Notes:
Major elements expressed as g/100 g
Trace elements expressed as g/10^6 g
Zr used as the immobile reference element

Least altered reference samples-
dacite A: LP67B651, dacite B: LP43386,
dacite C: MRV24

Includes XRF data from this study and from Tri Origin

Sample	Lithofacies	Zr	Sr	Cr	Ba	Nd	Sc	V	La	Ce	Y	Rb	Ni	As	Cu	Pb	Zn
LP67BW11037	A	0	-228	42	359	9	-61	62	15	-48	-21	78	11	1	-60	-7	94
LP67BW11063	A	0	-208	45	332	11	-61	65	16	-40	-19	97	9	1	-74	-5	8
LP18532	B	0	-61	1	661	4	3	17	6	16	10	80	-3	11	-22	54	-8
TLPD-18 539.4	B	0	-74	-18	301	-23	-6	-30	-24	-49	7	32	-8	-2	-14	11	7
LP36W374	B	0	-138	-1	754	-4	2	11	-7	-8	-2	77	-4	-1	-26	-2	-21
LP36W 391	B	0	-86	0	613	8	2	11	13	21	12	85	0	3	18	10	2
TLPD-28746	B	0	-198	-18	808	-23	-6	-30	-24	-49	10	91	-8	-2	-12	1	0
TLPD-30794	B	0	-218	-18	563	-23	-6	-30	-24	-49	8	71	-8	-2	-6	42	85
LPD024	B	0	-107	1	591	1	2	18	1	3	1	86	0	-1	-24	30	20
LP18383	clast	0	-233	0	986	-9	2	22	-13	-24	-16	47	-5	7	2	175	109
LP36W 262	clast	0	-176	1	41	-1	-1	-5	-1	0	-14	0	13	11	-12	105	38
LP37238	clast	0	-210	2	338	-8	0	6	-8	-17	-14	32	39	51	-22	78	65
LP44362	C	0	-124	-1	152	-2	1	-3	-20	2	4	-6	-2	1	1	-8	116
LP44397	C	0	-121	0	231	0	0	-6	-24	3	-1	22	-1	1	38	-9	381
LP46A210	C	0	-127	0	766	-2	2	-2	-27	-1	14	68	0	3	64	24	124
LP46A 250	C	0	-124	-1	574	2	0	-4	-22	1	8	75	0	0	46	146	1655
LP46A297	C	0	-114	3	1121	-3	1	-2	-26	1	10	113	-2	1	7	-9	36
LP63485	C	0	-115	0	629	1	1	-4	-21	8	6	65	-1	0	-8	-10	74
LP70438	C	0	-72	0	2865	0	0	-4	-24	3	6	90	-1	1	-3	-13	-3
BOA-103-146	C	0	-114	-12	213	-35	-8	-32	-58	-73	3	61	-6	-2	-11	-13	-28

The University of Tasmania
Electron Microscope Facility
Central Science Laboratory
Hobart

Trace level sulphide analytical methodology, Cameca SX50 electron probe microanalyser.

Quantitative analyses of sulphides were obtained using a Cameca SX50 electron probe microanalyser equipped with four wavelength dispersive spectrometers (WDS) utilising LiF, PET and TAP analysing crystals. The instrument was operated at an accelerating voltage of 20kV with a regulated beam current of 50 - 60nA (faraday cup). The nominal incident beam size was 1-2 um in diameter.

X-ray lines were calibrated and verified against pure metals and natural sulphides.
X-ray line peak and background positions were carefully selected for trace level analyses to minimise interferences from adjacent lines. On-line overlap corrections were employed when necessary. Data reduction and matrix corrections were performed using the PAP algorithm (Pouchou & Pichoir, 1984).

The analytical conditions for each element together with peak and background counting times, standards used and the derivative 2 sigma detection limits are given below (Table A).

Table A
Analytical conditions, sulphideTE analysis.

Element	Line	Spec/FPC	Crystal	Peak + bkgd (secs)	2sigma dl* (ppm)	Standard	Matrix*
S	Ka	2/HP	PET	10+10	270	AMARC	
V	Ka	3/HP	LiF	10+10	210	V	
Mn	Ka	3/HP	LiF	40+40	50	Mn	
Fe	Ka	3/HP	LiF	10+10	320	AMARC	
				40+40	80	AMARC	
Co	Ka	3/HP	LiF	20+20	120	ACOB	
Ni	Ka	3/HP	LiF	20+20	150	APENT	
Cu	Ka	3/HP	LiF	20+20	200	ACUP	
Zn	Ka	3/HP	LiF	40+40	165	ASPH	
As	La	4/LP	TAP	90+90	75	AGAAS	
Se	La	4/LP	TAP	60+60	70	ABISE	
				60+60	260	ABISE	Galena
Ag	La	1/LP	PET	20+20	215	Ag	
		2/HP	PET	90+90	100	Ag	Galena
Cd	La	1/LP	PET	30+30	185	Cd	
Sn	La	2/HP	PET	60+60	170	ACASS	
Sb	La	2/HP	PET	20+20	170	ASTIB	
Te	La	1/LP	PET	30+30	125	AANTE	
Au	La	3/HP	LiF	60+60	350	Au	
Hg	Ma	2/HP	PET	60+60	215	ACINN	
Pb	Ma	2/HP	PET	20+20	365	AGAL	
Bi	Ma	1/LP	PET	60+60	230	ABISE	

*2 sigma detection limit calculations based on a tennantite-tetrahedrite matrix unless otherwise stated.

Equation for calculating analytical detection limits (2σ):

$$2\sigma = 1\,000\,000 \times \left(3 \Big/ \sqrt{\frac{I_0^2}{I_b} \times t} \right)$$

where:
2σ = detection limit (ppm)
I_0 = sensitivity factor (counts / sec / nA / 100% element)
I_b = background counts per second for unknown
t = total peak and background count time (secs)

Reference:

Pouchou, J.L., and Pichoir, F., 1984. Un nouveau modele de calcul pour la microanalyse quantitative par spectrometrie de rayons X. L'application a l'analyses d'echantillons homogenes. Recherche Aerospatiale, 3, 167-192.

Additional notes for this study:

All microprobe data are presented as analysed weight % and calculated molar %.

Approximate detection limits for analytical data are in ppm

Only analytical data greater than the minimum detection limit are included

All element abundances are in ppm except where indicated by the % sign.

Abbreviations: py = pyrite, po = pyrrhotite, sph = sphalerite, ga = galena, td = tetrahedrite, tn = tennantite, st = stannite, ccp = chalcopyrite, Bi = native bismuth, pg = pyrargyrite, dg = digenite, el = electrum.

Zone codes:
MH = Main zone Hangingwall lens
MCM = Main zone Central lens, massive sulfide
MCS = Main zone Central lens, semi-massive sulfide
MFS = Main zone footwall, semi-massive sulfide
LBZ = Lady Belmore zone
TH = Toms zone hangingwall, vein sulfide
TCM = Toms zone Central lens, massive sulfide
TCS = Toms zone Central lens, semi-massive sulfide
CCP = Footwall Copper zone
NLP = New Lewis Ponds

Zone	Label	Weight %:	Mineral	S%	Mn	Fe%	Co	Ni	Cu	Zn	As	Ag	Au	Bi	Sum W%
		detection limits (ppm):		160	100	180	120	150	250	250	70	90	440	1060/380	
MCM	LP18365b_py euhedra		py	52.38	<100	46.23	465	158	<250	<250	605	102	<440	<1060	98.78
MCM	LP18365b_vf py 1-19-1		py	51.92	<100	46.10	<120	<150	<250	658	4732	<90	<440	<1060	98.56
MCM	LP18365b_py ring		py	51.46	<100	45.28	124	<150	<250	<250	8833	97	<440	<1060	97.66
MFS	LP12555_py 2-9-1		py	52.04	<100	46.01	<120	174	343	1664	2853	115	<440	<1060	98.57
MCM	LP36W195_euhed py		py	52.61	<100	46.13	<120	<150	295	3165	623	<90	<440	<1060	99.16
MCM	LP36W195_framboid		py	51.84	513	45.54	<120	<150	<250	<250	4536	461	<440	<380	97.96
MCM	LP36W195_framboid		py	52.13	371	45.86	<120	178	<250	<250	4727	492	<440	<380	98.61
MCM	Lp36W195_spongy py		py	53.15	213	46.67	<120	<150	<250	<250	697	163	<440	1759	100.12
TCS	LP67B695_py 1-2-1		py	50.96	<100	44.42	<120	<150	<250	<250	1351	<90	<440	<1060	95.54
TCM	LP51A479_py in vein		py	51.85	<100	46.15	<120	<150	<250	<250	76	<90	<440	<1060	98.05
TCM	LP51A479_py 1-16-1		py	51.91	<100	46.37	<120	<150	<250	<250	288	<90	<440	<1060	98.34
TCM	LP51A479_py 1-22-1		py	51.96	<100	46.38	<120	<150	316	2247	143	<90	626	<1060	98.68
TCM	Lp51a488_subhed py		py	53.28	<100	47.05	<120	<150	<250	<250	<70	<90	<440	2111	100.59
LBZ	LP63415_py 1-4-1		py	52.48	<100	46.56	<120	<150	<250	<250	<70	<90	<440	<1060	99.11
LBZ	LP44243_spongy py		py	52.36	<100	46.03	<120	<150	<250	<250	224	1139	<440	<1060	98.55
LBZ	LP44243_spongy py		py	51.53	<100	45.89	<120	<150	519	283	184	1002	<440	<1060	97.63

Zone	Label	Atomic %:	Mineral	S%	Mn%	Fe%	Co%	Ni%	Cu%	Zn%	As%	Ag%	Au%	Bi%	Sum A%
MCM	LP18365b_py euhedra		py	66.30	0.00	33.60	0.03	0.01	0.01	0.01	0.03	0.00	0.00	0.00	100.00
MCM	LP18365b_vf py 1-19-1		py	66.04	0.00	33.66	0.00	0.00	0.00	0.04	0.26	0.00	0.00	0.00	100.00
MCM	LP18365b_py ring		py	66.09	0.01	33.39	0.01	0.01	0.00	0.00	0.49	0.00	0.00	0.00	100.00
MFS	LP12555_py 2-9-1		py	66.13	0.00	33.57	0.00	0.01	0.02	0.10	0.16	0.00	0.00	0.00	100.00
MCM	LP36W195_euhed py		py	66.35	0.00	33.40	0.00	0.00	0.02	0.20	0.03	0.00	0.00	0.00	100.00
MCM	LP36W195_framboid		py	66.25	0.04	33.42	0.00	0.01	0.01	0.00	0.25	0.02	0.00	0.00	100.00
MCM	LP36W195_framboid		py	66.22	0.03	33.44	0.00	0.01	0.01	0.01	0.26	0.02	0.00	0.00	100.00
MCM	Lp36W195_spongy py		py	66.42	0.02	33.48	0.00	0.00	0.00	0.00	0.04	0.01	0.00	0.03	100.00
TCS	LP67B695_py 1-2-1		py	66.59	0.00	33.32	0.01	0.01	0.00	0.00	0.08	0.00	0.00	0.00	100.00
TCM	LP51A479_py in vein		py	66.16	0.00	33.81	0.00	0.00	0.01	0.01	0.00	0.00	0.00	0.00	100.00
TCM	LP51A479_py 1-16-1		py	66.07	0.00	33.89	0.00	0.00	0.00	0.01	0.02	0.00	0.00	0.00	100.00
TCM	LP51A479_py 1-22-1		py	65.99	0.00	33.82	0.00	0.00	0.02	0.14	0.01	0.00	0.01	0.00	100.00
TCM	Lp51a488_subhed py		py	66.31	0.00	33.62	0.00	0.00	0.01	0.01	0.00	0.00	0.00	0.04	100.00
LBZ	LP63415_py 1-4-1		py	66.24	0.00	33.74	0.00	0.00	0.00	0.00	0.00	0.00	0.00	0.01	100.00
LBZ	LP44243_spongy py		py	66.41	0.00	33.52	0.00	0.00	0.02	0.00	0.01	0.04	0.00	0.00	100.00
LBZ	LP44243_spongy py		py	66.10	0.00	33.80	0.00	0.00	0.03	0.02	0.01	0.04	0.00	0.00	100.00

Zone	Label	Weight %:	Mineral	S%	Mn	Fe%	Co	Ni	Cu	Zn	As	Ag	Au	Bi	Sum W%
LBZ	LP44243_framboid		py	51.92	208	45.99	<120	<150	466	<250	2379	<90	<440	<1060	98.24
CCP	Lp66361_py 2-12-1		py	53.27	<100	46.63	381	361	<250	<250	<70	<90	<440	2195	100.27
CCP	LP66361_py 1-13-1		py	52.59	<100	46.52	<120	<150	<250	<250	<70	<90	<440	<1060	99.13
CCP	LP66361_py 2-14-1		py	52.31	<100	46.26	167	<150	<250	<250	<70	134	<440	<1060	98.60
CCP	LP66374_po-11-1		py	53.16	<100	46.90	<120	<150	<250	<250	<70	<90	<440	1964	100.28
CCP	LP66374_py agg 1-4-1		py	52.32	<100	46.98	123	<150	<250	<250	<70	<90	<440	2064	99.59
CCP	Lp70127_py-6-1		py	53.16	<100	47.02	<120	<150	<250	<250	<70	<90	<440	2072	100.46
MCM	LP18365b_po blade		po	37.96	<100	59.31	<120	<150	<250	<250	<70	<90	<440	<1060	97.30
MCM	LP18365_po 1-3-1		po	37.72	<100	59.50	<120	<150	251	<250	<70	<90	<440	<1060	97.28
MCM	LP36W195_po blade		po	38.54	385	58.40	<120	<150	348	<250	<70	<90	<440	<1060	97.04
MCM	Lp36W195_po agg-16-1		po	38.84	<100	59.48	<120	<150	<250	<250	<70	<90	<440	1309	98.50
LBZ	LP63415_po 1-6-1		po	38.96	<100	59.03	458	225	<250	<250	<70	177	<440	<1060	98.08
CCP	Lp51aw2433_po agg		po	39.31	<100	58.92	<120	2773	<250	<250	<70	123	<440	1378	98.68
CCP	LP51AW2433_po 2-6-1		po	39.07	<100	58.62	179	2242	<250	<250	<70	<90	<440	<1060	97.93
CCP	Lp66361_po in ccp 1-5-1		po	38.94	<100	58.79	2167	732	1421	2060	<70	147	<440	1733	98.59
CCP	Lp66361_po in ccp-10-1		po	39.13	<100	59.37	746	296	1198	<250	<70	<90	<440	1588	98.93
CCP	LP66361_po within ccp		po	38.37	<100	58.26	674	311	600	<250	<70	<90	<440	<1060	96.82

Zone	Label	Atomic %:	Mineral	S%	Mn%	Fe%	Co%	Ni%	Cu%	Zn%	As%	Ag%	Au%	Bi%	Sum A%
LBZ	LP44243_framboid		py	66.17	0.02	33.65	0.00	0.00	0.03	0.01	0.13	0.00	0.00	0.00	100.00
CCP	Lp66361_py 2-12-1		py	66.46	0.00	33.40	0.03	0.02	0.00	0.01	0.00	0.00	0.00	0.04	100.00
CCP	LP66361_py 1-13-1		py	66.31	0.00	33.68	0.00	0.00	0.00	0.00	0.00	0.00	0.00	0.00	100.00
CCP	LP66361_py 2-14-1		py	66.31	0.00	33.67	0.01	0.00	0.00	0.00	0.00	0.01	0.00	0.00	100.00
CCP	LP66374_po-11-1		py	66.35	0.00	33.61	0.00	0.00	0.00	0.00	0.00	0.00	0.00	0.04	100.00
CCP	LP66374_py agg 1-4-1		py	65.93	0.00	33.99	0.01	0.00	0.00	0.00	0.00	0.00	0.01	0.04	100.00
CCP	Lp70127_py-6-1		py	66.27	0.00	33.65	0.00	0.00	0.00	0.00	0.00	0.00	0.00	0.04	100.00
MCM	LP18365b_po blade		po	52.70	0.00	47.28	0.00	0.01	0.00	0.01	0.00	0.00	0.00	0.00	100.00
MCM	LP18365_po 1-3-1		po	52.45	0.00	47.51	0.00	0.01	0.02	0.01	0.00	0.00	0.00	0.00	100.00
MCM	LP36W195_po blade		po	53.43	0.03	46.49	0.00	0.01	0.02	0.01	0.00	0.00	0.00	0.00	100.00
MCM	Lp36W195_po agg-16-1		po	53.19	0.00	46.76	0.00	0.00	0.00	0.01	0.00	0.00	0.00	0.03	100.00
LBZ	LP63415_po 1-6-1		po	53.45	0.00	46.49	0.03	0.02	0.00	0.00	0.00	0.01	0.00	0.00	100.00
CCP	Lp51aw2433_po agg		po	53.61	0.00	46.14	0.01	0.21	0.00	0.00	0.00	0.01	0.00	0.03	100.00
CCP	LP51AW2433_po 2-6-1		po	53.62	0.00	46.19	0.01	0.17	0.00	0.00	0.00	0.00	0.00	0.00	100.00
CCP	Lp66361_po in ccp 1-5-1		po	53.29	0.00	46.19	0.16	0.05	0.10	0.14	0.00	0.01	0.00	0.04	100.00
CCP	Lp66361_po in ccp-10-1		po	53.33	0.00	46.45	0.06	0.02	0.08	0.00	0.00	0.00	0.00	0.03	100.00
CCP	LP66361_po within ccp		po	53.35	0.00	46.52	0.05	0.02	0.04	0.01	0.00	0.00	0.00	0.00	100.00

			Analysed weight %										Calculated atomic %									
Zone	Label		S%	Mn	Fe%	Cu	Zn%	Se	Ag	Cd	Hg	Sum %	S%	Mn%	Fe%	Cu%	Zn%	Se%	Ag%	Cd%	Hg%	Sum %
	detection limits (ppm):		130	50	180	250	640	260	290	90	260											
MCS	Lp12440_sph 2-3-1	sph	31.89	269	5.35	<250	62.52	<260	1441	187	<260	99.95	48.55	0.02	4.67	0.00	46.68	0.00	0.07	0.01	0.00	100.00
MCS	Lp12450_sph 1-1-1	sph	32.27	269	3.50	421	64.05	<260	1229	<90	<260	100.03	49.07	0.02	3.05	0.03	47.76	0.00	0.06	0.00	0.00	100.00
MH	Lp12450_sph in ring	sph	31.11	194	3.72	1332	62.48	<260	1488	179	<260	97.63	48.60	0.02	3.33	0.10	47.87	0.00	0.07	0.01	0.00	100.00
MH	Lp12457_sph 2-4-1	sph	32.90	842	6.98	<250	59.11	<260	1739	<90	<260	99.27	49.85	0.07	6.07	0.01	43.92	0.00	0.08	0.00	0.00	100.00
MCM	Lp12539	sph	32.14	81	4.09	<250	63.24	<260	2622	<90	<260	99.77	49.00	0.01	3.58	0.01	47.27	0.00	0.12	0.00	0.00	100.00
MH	Lp12476_sph 1-3-1	sph	32.24	262	6.60	<250	61.40	<260	1849	324	<260	100.48	48.69	0.02	5.72	0.00	45.47	0.00	0.08	0.01	0.00	100.00
MFS	Lp12539_sph 1-3-1	sph	31.94	169	4.97	<250	61.82	<260	2728	<90	562	99.08	48.98	0.02	4.38	0.00	46.48	0.00	0.12	0.00	0.01	100.00
MFS	LP12555_sph 1-1	sph	32.84	583	3.44	<250	64.50	<260	<290	2285	<260	101.07	49.35	0.05	2.97	0.00	47.53	0.00	0.00	0.10	0.00	100.00
MFS	LP12555_sph 1-5	sph	33.98	680	3.56	<250	64.00	<260	<290	2172	<260	101.84	50.33	0.06	3.03	0.00	46.49	0.00	0.00	0.09	0.00	100.00
MFS	LP12555_sph 1-3	sph	33.13	545	5.78	<250	61.32	<260	2221	<90	667	100.57	49.73	0.05	4.98	0.00	45.13	0.00	0.10	0.00	0.02	100.00
MFS	Lp12w3439_sph 1-4-1	sph	32.60	182	4.27	<250	62.36	<260	1970	<90	<260	99.46	49.62	0.02	3.73	0.01	46.53	0.00	0.09	0.00	0.00	100.00
MFS	Lp12w3439_sph 2-7-1	sph	31.94	273	4.25	<250	63.40	<260	1994	<90	<260	99.83	48.73	0.02	3.72	0.01	47.43	0.00	0.09	0.00	0.00	100.00
NLP	LP16A450_sp 1-1-1	sph	33.14	827	4.98	<250	62.93	<260	415	1253	296	101.33	49.49	0.07	4.27	0.01	46.09	0.00	0.02	0.05	0.01	100.00
NLP	LP16A450_sph 2-2-1	sph	32.67	1037	5.03	<250	63.14	<260	<290	1107	<260	101.09	49.03	0.09	4.34	0.02	46.47	0.00	0.00	0.05	0.00	100.00
MH	Lp18334_sph 3-8-1	sph	32.72	1021	7.42	<250	59.17	<260	1992	<90	<260	99.61	49.49	0.09	6.44	0.00	43.89	0.00	0.09	0.00	0.00	100.00
MCM	Lp18365 sph 1	sph	33.05	226	7.11	<250	60.06	<260	1671	<90	<260	100.42	49.59	0.02	6.13	0.00	44.19	0.00	0.07	0.00	0.00	100.00
MCM	Lp18365 sph 2	sph	32.86	263	6.99	300	59.92	<260	1760	<90	389	100.05	49.52	0.02	6.05	0.02	44.29	0.00	0.08	0.00	0.01	100.00
MFS	Lp18433_sph 2-5-1	sph	32.14	754	5.65	352	61.58	<260	2396	458	<260	99.76	48.90	0.07	4.93	0.03	45.95	0.00	0.11	0.02	0.00	100.00
MCM	LP36W195_sph 1-1-1	sph	33.78	1588	7.18	<250	60.66	<260	<290	1090	<260	101.89	49.84	0.14	6.08	0.00	43.89	0.00	0.00	0.05	0.00	100.00
MCM	LP36W195_sph in ring	sph	33.43	797	6.31	713	59.78	<260	<290	1359	<260	99.80	50.28	0.07	5.45	0.05	44.09	0.00	0.00	0.06	0.00	100.00
MCS	Lp36w197_sph 1-2-1	sph	32.75	922	5.59	<250	62.16	<260	1747	<90	<260	100.76	49.21	0.08	4.82	0.00	45.81	0.00	0.08	0.00	0.00	100.00
MFS	Lp36w206_sph 1-1-1	sph	32.25	1115	7.44	<250	59.92	<260	1651	<90	437	99.94	48.85	0.10	6.47	0.00	44.50	0.00	0.07	0.00	0.01	100.00
MFS	LP36W207_sph 1-5-1	sph	32.91	662	6.08	<250	61.99	<260	<290	1721	<260	101.22	49.20	0.06	5.22	0.00	45.45	0.00	0.00	0.07	0.00	100.00
LBZ	LP44243_sph 1-7-1	sph	34.22	772	6.45	<250	60.84	<260	<290	1779	<260	101.78	50.43	0.07	5.45	0.01	43.96	0.00	0.00	0.07	0.00	100.00
LBZ	Lp44317_sph 2-4-1	sph	31.93	1177	6.90	<250	60.60	<260	2042	<90	<260	99.76	48.58	0.10	6.02	0.00	45.20	0.00	0.09	0.00	0.00	100.00
TCM	Lp46A126_sph 1-4-1	sph	32.06	2229	4.41	<250	63.31	<260	2174	<90	<260	100.23	48.70	0.20	3.85	0.01	47.15	0.00	0.10	0.00	0.00	100.00
TH	LP51A418_sph 1-1-1	sph	33.15	2090	6.71	<250	60.40	<260	<290	2090	<260	100.72	49.61	0.18	5.77	0.00	44.33	0.00	0.01	0.09	0.00	100.00
TCM	Lp51a477_sph 2-8-1	sph	32.13	2568	5.28	<250	62.05	<260	1737	277	<260	99.93	48.83	0.23	4.60	0.01	46.24	0.00	0.08	0.01	0.00	100.00
TCM	LP51A479_sph in vein	sph	33.25	1231	4.71	832	63.62	<260	<290	1737	<260	101.98	49.39	0.11	4.02	0.06	46.34	0.00	0.01	0.07	0.00	100.00
TCM	LP51A479_sph 1-14-1	sph	33.48	2377	4.15	<250	64.20	<260	<290	1444	<260	102.23	49.58	0.21	3.53	0.00	46.62	0.00	0.00	0.06	0.00	100.00
TCS	Lp51a482_sph 1-1-1	sph	31.46	1722	5.27	<250	62.59	<260	1352	185	<260	99.65	48.16	0.15	4.63	0.00	46.98	0.00	0.06	0.01	0.00	100.00
TCS	Lp51a484_sph 1-2-1	sph	31.46	1549	4.06	<250	63.39	<260	1419	<90	<260	99.22	48.39	0.14	3.59	0.00	47.81	0.00	0.06	0.00	0.00	100.00
TCM	Lp51a488_sph 1-10-1	sph	31.74	2167	4.14	<250	63.17	<260	1616	<90	<260	99.45	48.63	0.19	3.64	0.01	47.45	0.00	0.07	0.00	0.00	100.00

			Analysed weight %										Calculated atomic %									
Zone	Label		S%	Mn	Fe%	Cu	Zn%	Se	Ag	Cd	Hg	Sum %	S%	Mn%	Fe%	Cu%	Zn%	Se%	Ag%	Cd%	Hg%	Sum %
TCM	Lp51a488_sph1-16-1	sph	31.59	2227	3.24	527	64.22	<260	1506	<90	<260	99.47	48.49	0.20	2.86	0.04	48.34	0.00	0.07	0.00	0.00	100.00
TCM	Lp51a489_sph 1-2-1	sph	32.08	2096	5.26	372	62.22	<260	2222	<90	<260	100.04	48.74	0.19	4.59	0.03	46.36	0.00	0.10	0.00	0.00	100.00
TCM	Lp51a489_sph in vein	sph	32.13	2033	5.46	982	61.96	<260	2016	90	<260	100.06	48.78	0.18	4.75	0.08	46.12	0.00	0.09	0.00	0.00	100.00
TH	Lp51aw2355_sph	sph	31.83	616	5.59	<250	61.77	<260	1921	<90	<260	99.47	48.65	0.05	4.90	0.02	46.29	0.00	0.09	0.00	0.00	100.00
TCS	Lp67b742_ga 1-1-1	sph	31.46	<50	0.14	327	67.87	<260	3777	<90	<260	99.88	48.44	0.00	0.13	0.03	51.24	0.00	0.17	0.00	0.00	100.00
TCS	Lp67b742_sph 2-4-1	sph	30.93	<50	0.58	4280	66.46	<260	2839	<90	<260	98.68	48.21	0.00	0.52	0.34	50.80	0.00	0.13	0.00	0.00	100.00
TCS	LP67B965_sph 1-1-1	sph	33.58	1129	6.81	<250	61.25	<260	<290	1836	<260	101.94	49.65	0.10	5.78	0.00	44.40	0.00	0.00	0.08	0.00	100.00
CCP	LP51AW2433_sph	sph	33.34	434	6.95	<250	60.71	<260	<290	3377	<260	101.40	49.59	0.04	5.94	0.01	44.28	0.00	0.00	0.14	0.00	100.00
CCP	LP51AW2433_sph	sph	33.58	2021	7.32	<250	59.42	<260	<290	2085	<260	100.79	50.03	0.18	6.26	0.01	43.41	0.01	0.01	0.09	0.00	100.00
CCP	LP66361_sph 1-11-1	sph	34.00	521	6.68	450	60.27	<260	<290	1304	<260	101.18	50.39	0.05	5.68	0.03	43.80	0.00	0.00	0.06	0.00	100.00
CCP	LP66361_sph 1-4-1	sph	34.07	428	6.83	325	60.05	<260	555	1689	<260	101.26	50.44	0.04	5.81	0.02	43.60	0.00	0.02	0.07	0.00	100.00
CCP	Lp66374 sph in vein	sph	32.04	962	7.27	1910	59.40	<260	1651	180	<260	99.18	48.88	0.09	6.37	0.15	44.44	0.00	0.07	0.01	0.00	100.00
CCP	Lp70127_sph 1-1-1	sph	32.27	1076	6.70	<250	60.18	<260	1231	<90	<260	99.38	49.10	0.10	5.85	0.00	44.90	0.00	0.06	0.00	0.00	100.00
CCP	LP70069_sph in vein	sph	33.09	929	3.47	<250	62.99	<260	<290	1776	<260	99.86	50.07	0.08	3.02	0.00	46.74	0.01	0.00	0.08	0.00	100.00
CCP	LP70069_sph in vein	sph	33.39	682	3.20	<250	63.31	<260	<290	1889	<260	100.17	50.31	0.06	2.77	0.00	46.78	0.01	0.00	0.08	0.00	100.00

			Analysed weight %							Calculated atomic %						
Zone	Label	Mineral	S%	Fe	Se	Ag	Pb%	Bi	Sum %	S%	Fe%	Se%	Ag%	Pb%	Bi%	Sum %
	detection limits (ppm):		390	280	260	200	790	300								
MH	Lp12440_ga 1-2-1	ga	14.43	<280	2619	1817	86.07	-	100.94	51.69	0.00	0.38	0.19	47.73	-	100.00
MH	Lp12450_ga 2-6-1	ga	14.39	6597	1576	1060	85.36	-	100.67	51.25	1.35	0.23	0.11	47.06	-	100.00
MH	Lp12450_ga in ring 2-7-1	ga	14.51	9010	1404	931	87.38	-	103.02	50.67	1.81	0.20	0.10	47.23	-	100.00
MCS	Lp12476_ga 2-2-1	ga	14.65	<280	511	1943	86.35	-	101.25	52.15	0.00	0.07	0.21	47.57	-	100.00
MCM	Lp12457_ga 1-5-1	ga	14.47	963	<260	1443	86.04	-	100.75	51.89	0.20	0.00	0.15	47.76	-	100.00
MFS	Lp12539 ga 1-5-1	ga	14.40	<280	1418	1265	86.61	-	101.27	51.61	0.00	0.21	0.13	48.05	-	100.00
MFS	Lp12539_ga 1-5-1	ga	14.59	<280	1349	1111	86.22	-	101.06	52.07	0.00	0.20	0.12	47.62	-	100.00
MFS	LP12555_ga 1-2-1	ga	14.37	<280	977	1725	86.41	-	101.06	51.64	0.00	0.14	0.18	48.04	-	100.00
MFS	Lp12w3439_ga 1-5-1	ga	14.36	1718	1720	1638	86.51	-	101.37	51.35	0.35	0.25	0.17	47.88	-	100.00
NLP	LP16A450_ga 2-4-1	ga	14.27	<280	1220	872	87.10	-	101.58	51.28	0.00	0.18	0.09	48.45	-	100.00
MH	Lp18334_ga 1	ga	14.62	1952	382	1572	87.01	-	102.03	51.74	0.40	0.05	0.17	47.64	-	100.00
MH	Lp18334_ga 2	ga	14.63	2888	341	1599	86.18	-	101.30	51.90	0.59	0.05	0.17	47.30	-	100.00
MCM	LP18365b_ga 1-10-1	ga	14.29	<280	278	1563	86.55	-	101.03	51.51	0.00	0.04	0.17	48.28	-	100.00
MFS	Lp18433_ga 1-3-1	ga	14.58	<280	1644	1513	86.40	-	101.32	51.94	0.03	0.24	0.16	47.63	-	100.00
MCM	LP36W195-ga 1-3-1	ga	14.45	760	<260	1787	86.07	-	100.77	51.85	0.16	0.01	0.19	47.80	-	100.00
MCM	Lp36W195_ga in MS	ga	13.38	<280	<260	1500	85.42	2844	99.25	50.12	0.00	0.03	0.17	49.52	0.16	100.00
MCM	Lp36W195_ga agg	ga	13.17	<280	<260	1746	85.25	2546	98.87	49.76	0.00	0.04	0.20	49.86	0.15	100.00
MCS	Lp36w197_ga 1-4-1	ga	14.58	<280	<260	3033	86.66	-	101.56	51.91	0.00	0.03	0.32	47.74	-	100.00
MFS	Lp36w206_ga 1-7-1	ga	14.60	629	1123	4291	85.82	-	101.02	51.97	0.13	0.16	0.45	47.28	-	100.00
MFS	LP36W207_ga 2-14-1	ga	14.24	<280	738	1523	85.81	-	100.30	51.57	0.05	0.11	0.16	48.10	-	100.00
LBZ	LP44243_ga 1-11-1	ga	14.46	<280	328	2056	85.71	-	100.41	52.02	0.00	0.05	0.22	47.72	-	100.00
LBZ	Lp44317_ga 1-2-1	ga	14.46	<280	2284	2731	86.16	-	101.13	51.69	0.03	0.33	0.29	47.66	-	100.00
LBZ	LP63415_ga 1-7-1	ga	13.47	5143	19025	5049	83.81	-	100.20	48.70	1.07	2.79	0.54	46.89	-	100.00
TCM	Lp46A126_ga 2-8-1	ga	14.57	<280	448	1063	86.21	-	100.93	52.11	0.00	0.07	0.11	47.71	-	100.00
TH	LP51A418_ga 1-2-1	ga	14.04	329	6914	3571	85.02	-	100.14	50.86	0.07	1.02	0.38	47.67	-	100.00
TCM	Lp51a477_ga 2-3-1	ga	14.68	<280	703	2763	87.14	-	102.17	51.92	0.00	0.10	0.29	47.69	-	100.00
TCM	LP51A479_ga in vein	ga	14.23	<280	332	671	86.39	-	100.72	51.50	0.00	0.05	0.07	48.38	-	100.00
TCM	LP51A479_ga 1-15-1	ga	14.14	<280	344	1235	86.19	-	100.49	51.37	0.00	0.05	0.13	48.44	-	100.00
TCS	Lp51a482_ga 1-4-1	ga	14.47	<280	282	1897	85.52	-	100.21	52.10	0.00	0.04	0.20	47.65	-	100.00
TCS	Lp51a484_ga 1-1-1	ga	14.62	<280	<260	534	86.58	-	101.28	52.14	0.00	0.03	0.06	47.77	-	100.00
TCM	Lp51a488_ga 2-13-1	ga	14.62	4856	373	1779	85.98	-	101.30	51.72	0.99	0.05	0.19	47.06	-	100.00
TCM	Lp51a488_ga 1-17-1	ga	14.63	<280	368	1678	86.57	-	101.41	52.08	0.00	0.05	0.18	47.69	-	100.00
TCM	Lp51a488_ga in vein	ga	13.36	<280	432	1422	85.76	2709	99.58	49.98	0.00	0.07	0.16	49.64	0.16	100.00

			Analysed weight %							Calculated atomic %						
Zone	Label	Mineral	S%	Fe	Se	Ag	Pb%	Bi	Sum %	S%	Fe%	Se%	Ag%	Pb%	Bi%	Sum %
TCM	Lp51a488_ga in ms	ga	13.25	<280	290	1111	86.11	2799	99.78	49.69	0.00	0.04	0.12	49.98	0.16	100.00
TCM	Lp51a489_ga 1-1-1	ga	14.65	<280	<260	820	86.75	-	101.51	52.12	0.00	0.04	0.09	47.76	-	100.00
TCM	Lp51a489_ga in vein	ga	14.67	<280	<260	1675	87.60	-	102.46	51.87	0.00	0.02	0.18	47.93	-	100.00
TCS	LP67B965_ga 1-5-1	ga	13.79	<280	13390	6004	83.93	-	99.66	50.14	0.00	1.98	0.65	47.23	-	100.00
TCS	Lp67b742_ga 1-1-1	ga	14.25	<280	4582	298	86.47	-	101.22	51.22	0.00	0.67	0.03	48.08	-	100.00
TH	Lp51aw2355_ga 1-3-1	ga	14.21	<280	3399	1436	86.81	-	101.50	51.06	0.00	0.50	0.15	48.29	-	100.00
CCP	LP51AW2433_ga-3-1	ga	13.66	1742	16238	7798	84.34	-	100.57	49.30	0.36	2.38	0.84	47.12	-	100.00
CCP	Lp51aw2433_ga py-8-1	ga	12.13	738	23890	5140	82.38	13697	98.85	46.20	0.16	3.70	0.58	48.56	0.80	100.00
CCP	Lp51aw2433_ga 1-10-1	Bi-Se	14.84	6679	8097	21507	67.82	199905	106.28	49.87	1.29	1.11	2.15	35.28	10.31	100.00
CCP	Lp51aw2433_ga 2-11-1	ga	13.12	3735	7601	6542	83.44	15986	99.95	48.60	0.79	1.14	0.72	47.84	0.91	100.00
CCP	Lp51aw2433_ga	ga	12.31	3174	20826	5998	82.75	15647	99.61	46.34	0.69	3.18	0.67	48.22	0.90	100.00
CCP	LP66361_ga 1-6-1	ga	13.63	<280	11643	7069	83.16	-	98.66	50.13	0.00	1.74	0.77	47.35	-	100.00
CCP	Lp66361_ga 1-4-1	ga	12.93	<280	11838	8584	82.49	24443	99.90	48.23	0.00	1.79	0.95	47.63	1.40	100.00
CCP	Lp66361_ga 2-6-1	ga	11.94	<280	14873	6051	81.31	15045	96.85	46.76	0.00	2.36	0.70	49.27	0.90	100.00
CCP	Lp66374 ga	ga	13.33	<280	23688	7398	83.39	-	99.83	48.61	0.02	3.51	0.80	47.07	-	100.00
CCP	LP66374_ga 1-2-1	ga	12.79	<280	14870	6341	82.71	16252	99.24	48.03	0.00	2.27	0.71	48.06	0.94	100.00
CCP	LP66374_ga 2-3-1	ga	12.09	560	27284	6452	82.20	15647	99.28	45.83	0.12	4.20	0.73	48.21	0.91	100.00
CCP	LP66374_ga-6-1	ga	12.56	1504	17821	7503	81.89	18005	98.94	47.32	0.33	2.73	0.84	47.75	1.04	100.00
CCP	LP66374_ga-5-1	ga	12.57	2032	14162	8953	81.77	20644	98.91	47.43	0.44	2.17	1.00	47.76	1.20	100.00
CCP	Lp70127_ga 1-1-1	ga	12.17	<280	24303	4807	81.86	12594	98.20	46.51	0.01	3.77	0.55	48.43	0.74	100.00
CCP	Lp70127_ga 3-8-1	ga	12.62	<280	15248	4009	83.50	11778	99.23	47.70	0.00	2.34	0.45	48.83	0.68	100.00
CCP	Lp70127_ga 2-3-12	ga	12.87	<280	11528	4144	84.35	11925	99.98	48.21	0.00	1.75	0.46	48.89	0.69	100.00
CCP	Lp70127_ga 4	ga	12.56	<280	15682	3655	84.23	11029	99.84	47.37	0.02	2.40	0.41	49.16	0.64	100.00

			Analysed weight %								Calculated atomic %							
	Label	Mineral	S%	Fe	Se	Ag	Pb%	Bi	Te	Sum %	S%	Fe%	Se%	Ag%	Pb%	Bi%	Te%	Sum %
	detection limits (ppm):		270	320	280	350	1030	1060	320									
MCS	Lp36w197_ga 1-4-1	ga	12.56	<320	348	1523	85.47	<1060	<320	98.25	48.59	0.00	0.05	0.18	51.16	0.00	0.02	100.00
MCS	Lp36w197_ga 2-7-1	ga	12.62	<320	<280	1288	85.42	<1060	484	98.24	48.73	0.00	0.04	0.15	51.04	0.00	0.05	100.00
TCM	Lp51a489_ga 1-1-1	ga	12.68	<320	<280	<350	85.92	<1060	394	98.68	48.77	0.00	0.03	0.02	51.14	0.00	0.04	100.00
TCM	Lp51a489_ga 2-4-1	ga	12.65	866	<280	810	86.6	<1060	<320	99.48	48.39	0.19	0.04	0.09	51.26	0.00	0.03	100.00
TCM	Lp51a489_ga in vein	ga	12.64	<320	378	986	85.64	<1060	547	98.46	48.70	0.00	0.06	0.11	51.07	0.00	0.05	100.00
TCM	Lp51a489_ga in vein	ga	12.64	<320	401	1007	85.38	<1060	395	98.2	48.80	0.00	0.06	0.12	50.98	0.00	0.04	100.00

Zone	Label	Weight %:	Mineral	S%	Fe%	Ni	Cu%	Zn%	As	Se	Ag%	Cd	Sb%	Te	Au	Hg	Pb	Bi	Sum W%
		detection limits (ppm):		130	140	150	200	170	180	200	210	180	200	140	750	240	380	240	
MCM	Lp12457_td 1-1-1		td	23.15	5.35	<150	24.56	1.13	843	236	18.60	631	27.14	<140	<750	<240	<380	<240	100.12
MCM	Lp12457_td 2-2-1		td	23.10	5.36	<150	24.50	1.09	<180	237	18.68	346	27.15	<140	<750	<240	<380	<240	99.97
MCM	Lp12457_td 3-6-1		td	22.96	5.29	<150	24.41	1.10	975	<200	18.59	233	27.04	<140	<750	<240	<380	<240	99.54
MFS	Lp12490_td 1-1-1		td	24.41	4.28	<150	34.06	2.72	4901	463	6.12	<180	27.43	<140	<750	<240	<380	<240	99.63
MFS	Lp12490_td 2-2-1		td	24.37	4.29	<150	34.16	2.70	7738	390	5.84	267	27.28	<140	<750	<240	<380	<240	99.54
MFS	Lp12539_td 1-1-1		td	24.96	4.26	<150	36.07	2.84	12288	406	3.05	607	27.00	<140	785	<240	<380	<240	99.61
MFS	Lp12539_td 2-2-1		td	24.97	4.30	<150	35.97	2.77	22448	559	3.51	355	25.30	<140	<750	<240	<380	<240	99.22
MFS	LP12555_td 1-1-1		td	23.84	4.35	<150	28.58	2.24	<180	291	12.71	553	27.60	<140	<750	<240	<380	<240	99.41
MFS	LP12555_td 2-10-1		td	23.87	4.43	<150	28.56	2.62	1982	344	13.37	396	27.34	<140	<750	<240	<380	<240	100.46
MFS	Lp12w3439_td 1-1-1		td	23.90	4.37	<150	29.66	2.39	4765	200	12.01	223	26.88	<140	<750	<240	<380	<240	99.75
MFS	Lp12w3439_td 2-2-1		td	23.86	4.35	<150	29.87	2.39	3753	364	11.75	488	27.16	<140	<750	<240	<380	<240	99.86
MFS	Lp18334_td 1-1-1		td	23.44	5.19	<150	25.92	1.58	2081	351	16.97	450	26.90	<140	<750	<240	<380	<240	100.30
MFS	Lp18334_td 2-2-1		td	22.95	5.17	<150	25.10	1.24	1779	226	17.72	436	26.74	<140	<750	<240	<380	<240	99.17
MFS	Lp18334_td 3-7-1		td	23.13	5.35	<150	24.81	1.05	<180	279	18.51	555	26.78	<140	<750	<240	<380	<240	99.73
MCS	Lp18365b_td 1-3-1		td	22.75	5.32	<150	22.45	0.99	<180	<200	22.08	262	26.60	<140	<750	<240	<380	<240	100.24
MCS	Lp18365b_td 2-7-1		td	23.07	5.20	<150	24.41	1.19	<180	<200	18.83	329	26.88	<140	<750	<240	<380	<240	99.62

Zone	Label	Atomic %:	Mineral	S%	Fe%	Ni%	Cu%	Zn%	As%	Se%	Ag%	Cd%	Sb%	Te%	Au%	Hg%	Pb%	Bi%	Sum A%
MCM	Lp12457_td 2-2-1		td	44.60	5.94	0.01	23.86	1.03	0.00	0.02	10.72	0.02	13.80	0.00	0.00	0.00	0.00	0.00	100.00
MCM	Lp12457_td 3-6-1		td	44.52	5.89	0.00	23.89	1.05	0.08	0.01	10.72	0.01	13.81	0.00	0.00	0.00	0.00	0.00	100.00
MFS	Lp12490_td 1-1-1		td	44.64	4.50	0.00	31.44	2.44	0.38	0.03	3.33	0.00	13.21	0.00	0.02	0.00	0.00	0.00	100.00
MFS	Lp12490_td 2-2-1		td	44.56	4.50	0.00	31.53	2.42	0.61	0.03	3.18	0.01	13.14	0.00	0.01	0.00	0.00	0.00	100.00
MFS	Lp12539_td 1-1-1		td	44.90	4.40	0.01	32.74	2.50	0.95	0.03	1.63	0.03	12.79	0.00	0.02	0.00	0.00	0.00	100.00
MFS	Lp12539_td 2-2-1		td	44.86	4.44	0.01	32.61	2.44	1.73	0.04	1.87	0.02	11.97	0.00	0.01	0.00	0.00	0.01	100.00
MFS	LP12555_td 1-1-1		td	45.03	4.72	0.00	27.25	2.08	0.00	0.02	7.14	0.03	13.73	0.00	0.00	0.00	0.00	0.00	100.00
MFS	LP12555_td 2-10-1		td	44.70	4.76	0.00	26.99	2.41	0.16	0.03	7.44	0.02	13.49	0.00	0.00	0.00	0.00	0.00	100.00
MFS	Lp12w3439_td 1-1-1		td	44.74	4.69	0.01	28.01	2.20	0.38	0.02	6.68	0.01	13.25	0.00	0.00	0.00	0.00	0.00	100.00
MFS	Lp12w3439_td 2-2-1		td	44.65	4.68	0.00	28.20	2.19	0.30	0.03	6.54	0.03	13.38	0.00	0.00	0.00	0.00	0.00	100.00
MFS	Lp18334_td 1-1-1		td	44.63	5.68	0.01	24.90	1.47	0.17	0.03	9.60	0.02	13.49	0.00	0.00	0.00	0.00	0.00	100.00
MFS	Lp18334_td 2-2-1		td	44.47	5.76	0.00	24.55	1.18	0.15	0.02	10.21	0.02	13.65	0.00	0.00	0.00	0.00	0.00	100.00
MFS	Lp18334_td 3-7-1		td	44.63	5.93	0.00	24.16	0.99	0.00	0.02	10.62	0.03	13.61	0.00	0.00	0.00	0.00	0.00	100.00
MCS	Lp18365b_td 1-3-1		td	44.43	5.97	0.00	22.13	0.95	0.00	0.01	12.82	0.01	13.68	0.00	0.00	0.00	0.00	0.00	100.00
MCS	Lp18365b_td 2-7-1		td	44.66	5.78	0.00	23.85	1.13	0.00	0.01	10.84	0.02	13.71	0.00	0.00	0.00	0.00	0.00	100.00
MH	Lp18433_td 1-1-1		td	44.64	5.63	0.00	22.95	1.28	0.07	0.03	11.79	0.00	13.61	0.00	0.00	0.00	0.00	0.00	100.00

Zone	Label	Weight %:	Mineral	S%	Fe%	Ni	Cu%	Zn%	As	Se	Ag%	Cd	Sb%	Te	Au	Hg	Pb	Bi	Sum W%
MH	Lp18433_td 1-1-1		td	22.97	5.04	<150	23.40	1.35	838	380	20.40	<180	26.59	<140	<750	<240	<380	<240	99.89
MH	Lp18433_td 3-7-1		td	21.60	5.56	<150	18.71	0.47	<180	346	26.94	203	26.35	<140	<750	<240	<380	<240	99.72
MCM	LP36W195_td in MS 1-1-1		td	23.10	5.29	<150	24.77	1.24	<180	264	18.58	<180	27.09	<140	<750	<240	<380	<240	100.10
MCM	LP36W195_td in MS 2-2-1		td	23.04	5.41	<150	24.91	1.16	<180	234	18.16	293	26.84	<140	<750	<240	<380	<240	99.58
MCM	LP36W195_td in MS 3-3-1		td	23.08	5.30	<150	23.82	1.03	1658	<200	19.86	554	26.36	<140	<750	<240	<380	<240	99.71
MCM	LP36W195_td 1-1-1		td	23.15	5.32	<150	24.00	1.16	<180	257	19.46	478	26.86	<140	<750	<240	<380	<240	100.02
MCS	Lp36w197_td 1-6-1		td	23.05	4.98	<150	25.52	1.60	2145	<200	16.73	534	26.65	<140	<750	<240	<380	<240	98.81
MCS	Lp36w197_td 2-8-1		td	23.06	4.83	<150	25.56	1.72	3666	266	16.26	221	26.36	<140	<750	<240	<380	<240	98.21
MCS	Lp36w197_td 3-9-1		td	23.02	4.76	<150	25.58	1.78	700	260	16.51	224	26.84	<140	<750	<240	<380	<240	98.62
LBZ	LP44243_td 1-1-1		td	21.79	5.32	<150	18.38	0.99	<180	<200	27.16	258	26.21	<140	<750	<240	<380	248	99.92
LBZ	LP44243_td 2-16-1		td	21.31	5.25	<150	17.74	1.16	<180	243	28.33	<180	26.19	<140	<750	<240	<380	<240	100.01
TCM	Lp46A126_td 1-1-1		td	23.70	4.75	<150	28.45	1.86	<180	<200	13.47	309	27.66	<140	<750	<240	<380	<240	99.96
TCM	Lp46A126_td 2-7-1		td	23.39	4.70	<150	27.54	1.74	<180	<200	14.22	199	27.59	<140	<750	<240	<380	<240	99.22
TCM	Lp46A126_td 3-11-1		td	23.95	4.98	<150	29.14	1.75	6631	301	12.97	396	26.72	<140	<750	<240	<380	<240	100.25
TCM	Lp51a477_td 1-2-1		td	22.74	4.80	<150	23.04	1.47	478	<200	20.54	466	26.65	<140	<750	<240	<380	<240	99.35
TCM	Lp51a477_td 2-4-1		td	22.63	5.02	<150	22.66	1.31	<180	243	20.67	336	26.62	<140	<750	<240	<380	<240	98.98

Zone	Label	Atomic %:	Mineral	S%	Fe%	Ni%	Cu%	Zn%	As%	Se%	Ag%	Cd%	Sb%	Te%	Au%	Hg%	Pb%	Bi%	Sum A%
MCM	Lp12457_td 1-1-1		td	44.59	5.92	0.01	23.87	1.07	0.07	0.02	10.65	0.03	13.77	0.00	0.00	0.00	0.00	0.01	100.00
MH	Lp18433_td 3-7-1		td	43.70	6.46	0.00	19.10	0.46	0.00	0.03	16.20	0.01	14.03	0.00	0.00	0.00	0.00	0.01	100.00
MCM	LP36W195_td in MS 1-1-1		td	44.49	5.85	0.00	24.08	1.17	0.00	0.02	10.64	0.00	13.74	0.00	0.00	0.00	0.00	0.00	100.00
MCM	LP36W195_td in MS 2-2-1		td	44.50	6.00	0.00	24.28	1.10	0.00	0.02	10.43	0.02	13.65	0.00	0.00	0.00	0.00	0.00	100.00
MCM	LP36W195_td in MS 3-3-1		td	44.74	5.90	0.00	23.30	0.98	0.14	0.01	11.44	0.03	13.46	0.00	0.00	0.00	0.00	0.01	100.00
MCM	LP36W195_td 1-1-1		td	44.72	5.90	0.00	23.40	1.10	0.00	0.02	11.17	0.03	13.67	0.00	0.00	0.00	0.00	0.00	100.00
MCS	Lp36w197_td 1-6-1		td	44.60	5.53	0.00	24.92	1.52	0.18	0.01	9.62	0.03	13.58	0.00	0.00	0.00	0.00	0.00	100.00
MCS	Lp36w197_td 2-8-1		td	44.76	5.38	0.01	25.03	1.63	0.30	0.02	9.38	0.01	13.47	0.00	0.00	0.00	0.00	0.00	100.00
MCS	Lp36w197_td 3-9-1		td	44.64	5.30	0.01	25.04	1.69	0.06	0.02	9.52	0.01	13.71	0.00	0.00	0.00	0.00	0.00	100.00
LBZ	LP44243_td 1-1-1		td	43.93	6.16	0.00	18.70	0.98	0.00	0.01	16.28	0.01	13.92	0.00	0.00	0.00	0.00	0.01	100.00
LBZ	LP44243_td 2-16-1		td	43.34	6.13	0.00	18.20	1.15	0.00	0.02	17.12	0.00	14.02	0.01	0.00	0.00	0.00	0.00	100.00
TCM	Lp46A126_td 1-1-1		td	44.71	5.15	0.00	27.09	1.72	0.00	0.01	7.56	0.02	13.74	0.00	0.00	0.00	0.00	0.00	100.00
TCM	Lp46A126_td 2-7-1		td	44.68	5.16	0.00	26.55	1.63	0.00	0.01	8.07	0.01	13.88	0.00	0.00	0.00	0.00	0.00	100.00
TCM	Lp46A126_td 3-11-1		td	44.71	5.34	0.00	27.45	1.60	0.53	0.02	7.19	0.02	13.13	0.00	0.00	0.00	0.00	0.00	100.00
TCM	Lp51a477_td 1-2-1		td	44.59	5.40	0.00	22.79	1.41	0.04	0.02	11.97	0.03	13.76	0.00	0.00	0.00	0.00	0.00	100.00
TCM	Lp51a477_td 2-4-1		td	44.58	5.67	0.01	22.53	1.27	0.00	0.02	12.10	0.02	13.81	0.00	0.00	0.00	0.00	0.00	100.00

Zone	Label	Weight %:	Mineral	S%	Fe%	Ni	Cu%	Zn%	As	Se	Ag%	Cd	Sb%	Te	Au	Hg	Pb	Bi	Sum W%
TCM	Lp51a477_td 1-6-1		td	23.09	5.20	<150	22.91	1.22	<180	<200	20.55	<180	26.81	<140	<750	<240	<380	<240	99.83
TCM	Lp51a477_td 2-9-1		td	23.04	5.19	<150	23.85	1.22	8439	229	19.35	362	25.76	<140	<750	<240	<380	<240	99.31
TCM	LP51A479_td in vein 1-1-1		td	23.29	4.93	<150	25.36	1.62	7222	203	18.01	278	25.76	<140	<750	<240	<380	<240	99.74
TCM	LP51A479_td in vein 2-3-1		td	23.36	5.03	<150	25.40	1.55	12783	<200	17.90	264	25.12	<140	<750	<240	<380	<240	99.69
TCM	LP51A479_td in MS 1-5-1		td	23.20	5.33	<150	24.60	1.46	477	321	18.33	484	26.82	<140	<750	<240	<380	<240	99.87
TCM	Lp51a482_td 1-2-1		td	22.71	5.09	<150	22.36	1.24	<180	<200	20.76	353	26.62	<140	<750	<240	<380	<240	98.85
TCM	LP51A488_td in vein 1-1-1		tn	26.42	5.52	<150	35.36	1.71	111253	797	7.61	<180	12.08	<140	<750	<240	<380	<240	99.92
TCM	LP51A488_td in vein 2-2-1		td	23.60	4.78	<150	26.54	1.77	14568	338	16.83	282	24.73	<140	<750	<240	<380	<240	99.78
TCM	LP51A488_td in MS 1-4-1		td	23.74	5.15	<150	27.50	1.49	28142	522	16.05	<180	23.01	<140	<750	<240	<380	<240	99.82
TCM	LP51A488_td in MS 2-5-1		td	23.29	5.11	<150	26.42	1.45	11290	269	16.89	<180	25.55	<140	<750	<240	<380	<240	99.86
TCM	Lp51a489_td 1-3-1		td	22.53	5.35	<150	22.50	1.79	<180	253	21.07	<180	26.68	<140	<750	<240	<380	<240	99.97
TCM	Lp51a489_td 2-7-1		td	22.78	5.29	<150	22.98	1.20	693	227	20.35	472	26.61	<140	<750	<240	<380	409	99.40
TCM	Lp51a489_td 1-3-1		td	22.73	5.45	<150	22.59	1.64	<180	<200	21.64	230	26.61	<140	<750	<240	<380	<240	100.69
TCM	Lp51a489_td 2-7-1		td	22.81	5.19	213	23.57	1.22	<180	351	20.39	<180	26.60	<140	<750	<240	<380	<240	99.84

Zone	Label	Atomic %:	Mineral	S%	Fe%	Ni%	Cu%	Zn%	As%	Se%	Ag%	Cd%	Sb%	Te%	Au%	Hg%	Pb%	Bi%	Sum A%
TCM	Lp51a477_td 1-6-1		td	44.90	5.81	0.00	22.49	1.17	0.00	0.01	11.88	0.01	13.73	0.00	0.00	0.00	0.00	0.01	100.00
TCM	Lp51a477_td 2-9-1		td	44.67	5.77	0.00	23.34	1.16	0.70	0.02	11.15	0.02	13.16	0.00	0.00	0.00	0.00	0.00	100.00
TCM	LP51A479_td in vein 1-1-1		td	44.63	5.42	0.00	24.53	1.52	0.59	0.02	10.26	0.02	13.00	0.00	0.00	0.00	0.00	0.00	100.00
TCM	LP51A479_td in vein 2-3-1		td	44.64	5.52	0.00	24.50	1.45	1.05	0.01	10.17	0.01	12.64	0.00	0.00	0.00	0.00	0.00	100.00
TCM	LP51A479_td in MS 1-5-1		td	44.66	5.89	0.00	23.90	1.37	0.04	0.03	10.49	0.03	13.60	0.00	0.00	0.00	0.00	0.00	100.00
TCM	Lp51a482_td 1-2-1		td	44.77	5.76	0.00	22.24	1.20	0.00	0.02	12.17	0.02	13.82	0.00	0.00	0.00	0.00	0.00	100.00
TCM	LP51A488_td in vein 1-1-1		tn	45.15	5.41	0.01	30.49	1.43	8.14	0.06	3.87	0.00	5.44	0.00	0.00	0.00	0.00	0.00	100.00
TCM	LP51A488_td in vein 2-2-1		td	44.72	5.20	0.00	25.38	1.64	1.18	0.03	9.48	0.02	12.34	0.00	0.00	0.00	0.00	0.00	100.00
TCM	LP51A488_td in MS 1-4-1		td	44.49	5.54	0.00	26.01	1.37	2.26	0.04	8.94	0.00	11.35	0.00	0.00	0.00	0.00	0.00	100.00
TCM	LP51A488_td in MS 2-5-1		td	44.36	5.58	0.00	25.39	1.35	0.92	0.02	9.56	0.00	12.81	0.00	0.00	0.00	0.00	0.00	100.00
TCM	Lp51a489_td 1-3-1		td	44.06	6.01	0.00	22.20	1.72	0.00	0.02	12.24	0.01	13.74	0.00	0.00	0.00	0.00	0.00	100.00
TCM	Lp51a489_td 2-7-1		td	44.55	5.94	0.01	22.69	1.15	0.06	0.02	11.83	0.03	13.71	0.00	0.00	0.00	0.00	0.01	100.00
TCM	Lp51a489_td 1-3-1		td	44.13	6.07	0.01	22.13	1.56	0.00	0.01	12.49	0.01	13.61	0.00	0.00	0.00	0.00	0.00	100.00
TCM	Lp51a489_td 2-7-1		td	44.40	5.80	0.02	23.15	1.16	0.00	0.03	11.80	0.01	13.64	0.00	0.00	0.00	0.00	0.00	100.00

Zone	Label	Weight %:	Mineral	S%	Mn	Fe%	Cu%	Zn%	Ge	As	Se	Mo	Ag	Cd	Sn%	Sb	Te	Bi	Sum W%
		detection limits (ppm):		270	260	320	370	470	820	380	280	560	350	520	500/**170**	380	320	1060	
MCM	LP36W195_tn 1-4-1		st	29.13	<260	11.75	29.38	1.92	<820	475	1477	5751	<350	<520	28.20	<380	<320	<1060	101.27
MCM	LP36W195_tn 2-5-1		st	29.37	<260	11.51	28.33	3.97	<820	<380	1039	5163	440	<520	27.59	<380	<320	<1060	101.51
MCS	lp36w197_st 1-5-1		st	28.96	<260	11.21	28.45	2.94	-	<380	1368	-	<350	564	27.61	<380	2172	<1060	99.61
MCS	lp36w197_st 2-10-1		st	29.41	<260	10.94	27.47	5.45	-	<380	1860	-	<350	1112	28.02	<380	1597	<1060	101.75
MFS	LP36W207_tn 1-2-1		st	29.63	<260	11.31	29.17	2.26	<820	<380	1261	4989	<350	<520	29.09	<380	<320	<1060	102.14
MFS	LP36W207_tn 2-8-1		st	29.19	303	11.59	28.77	2.85	<820	<380	873	5607	<350	<520	29.12	<380	<320	<1060	102.41
TCM	LP46a126_st-1-5-1		st	29.67	<260	11.04	29.29	2.14	-	<380	1452	-	<350	658	28.25	<380	2801	<1060	100.95
TCM	LP46a126_st-2-6-1		st	29.62	<260	11.08	27.63	4.31	-	<380	985	-	<350	<520	26.77	<380	2134	<1060	99.75
TCM	LP46a126_st-3-13-1		st	29.92	<260	11.00	29.27	2.55	-	<380	1562	-	<350	<520	28.68	<380	1958	<1060	101.78
TCM	LP51a477_st-1-10-1		st	29.46	<260	11.54	29.17	2.58	-	<380	1608	-	<350	<520	27.47	<380	2209	<1060	100.74
TCM	LP51a477_st-2-11-1		st	29.68	<260	11.33	28.95	3.09	-	<380	1889	-	<350	<520	27.71	<380	2674	<1060	101.30
TCM	LP51a477_st-3-12-1		st	30.44	<260	11.20	28.52	3.48	-	<380	1889	-	<350	<520	27.50	<380	2748	<1060	101.66
TCM	LP51a479_st- in vein-1-2-1		st	29.71	<260	10.57	28.36	4.61	-	513	1577	-	<350	553	27.18	<380	2713	<1060	100.99
TCM	LP51a479_st- in vein-2-4-1		st	30.03	<260	11.34	29.31	2.46	-	672	1255	-	<350	<520	27.82	<380	1889	<1060	101.39
TCM	LP51A479_		st	29.10	269	10.89	29.10	3.15	<820	771	737	4650	<350	546	28.59	<380	<320	<1060	101.61
TCM	LP51A479_		st	28.95	<260	11.22	29.46	2.26	2313	<380	1239	5162	<350	<520	28.80	<380	<320	<1060	101.74

Zone	Label	Atomic %:	Mineral	S%	Mn%	Fe%	Cu%	Zn%	Ge%	As%	Se%	Mo%	Ag%	Cd%	Sn%	Sb%	Te%	Bi%	Sum A%
MCM	LP36W195_tn 1-4-1		st	48.89	0.00	11.32	24.88	1.58	0.06	0.03	0.10	0.32	0.00	0.00	12.78	0.00	0.00	0.00	100.00
MCM	LP36W195_tn 2-5-1		st	49.01	0.00	11.03	23.86	3.25	0.00	0.00	0.07	0.29	0.02	0.01	12.44	0.00	0.00	0.00	100.00
MCS	lp36w197_st 1-5-1		st	49.25	-	10.95	24.42	2.45	-	0.02	0.09	-	0.00	0.03	12.69	0.00	0.09	0.00	100.00
MCS	lp36w197_st 2-10-1		st	49.06	-	10.48	23.13	4.46	-	0.00	0.13	-	0.00	0.05	12.63	0.00	0.07	0.00	100.00
MFS	LP36W207_tn 1-2-1		st	49.35	0.00	10.82	24.51	1.85	0.00	0.00	0.09	0.28	0.00	0.01	13.09	0.00	0.00	0.00	100.00
MFS	LP36W207_tn 2-8-1		st	48.71	0.03	11.10	24.23	2.33	0.05	0.00	0.06	0.31	0.01	0.00	13.13	0.00	0.00	0.02	100.00
TCM	LP46a126_st-1-5-1		st	49.75	-	10.63	24.78	1.76	-	0.02	0.10	-	0.00	0.03	12.79	0.00	0.12	0.01	100.00
TCM	LP46a126_st-2-6-1		st	49.89	-	10.72	23.48	3.56	-	0.00	0.07	-	0.00	0.01	12.18	0.00	0.09	0.00	100.00
TCM	LP46a126_st-3-13-1		st	49.76	-	10.51	24.57	2.08	-	0.00	0.11	-	0.00	0.00	12.89	0.00	0.08	0.00	100.00
TCM	LP51a477_st-1-10-1		st	49.39	-	11.11	24.68	2.12	-	0.02	0.11	-	0.02	0.01	12.44	0.00	0.09	0.02	100.00
TCM	LP51a477_st-2-11-1		st	49.50	-	10.85	24.36	2.52	-	0.01	0.13	-	0.00	0.02	12.48	0.01	0.11	0.00	100.00
TCM	LP51a477_st-3-12-1		st	50.27	-	10.61	23.76	2.82	-	0.01	0.13	-	0.00	0.01	12.27	0.00	0.11	0.00	100.00
TCM	LP51a479_st- in vein-1-2-1		st	49.63	-	10.13	23.90	3.77	-	0.04	0.11	-	0.00	0.03	12.26	0.00	0.11	0.01	100.00
TCM	LP51a479_st- in vein-2-4-1		st	49.89	-	10.82	24.57	2.00	-	0.05	0.08	-	0.01	0.02	12.48	0.00	0.08	0.00	100.00
TCM	LP51A479_		st	48.85	0.03	10.50	24.65	2.59	0.00	0.06	0.05	0.26	0.00	0.03	12.97	0.00	0.00	0.01	100.00
TCM	LP51A479_		st	48.64	0.00	10.82	24.98	1.86	0.17	0.02	0.08	0.29	0.00	0.01	13.07	0.00	0.00	0.00	100.00

Zone	Label	Weight %:	Mineral	S%	Mn	Fe%	Cu%	Zn%	Ge	As	Se	Mo	Ag	Cd	Sn%	Sb	Te	Bi	Sum W%
TCM	LP51a482_st-1-6-1		st	29.41	-	11.17	27.85	4.64	-	893	1662	-	<350	803	27.02	<380	2425	<1060	100.68
TCM	LP51a482_st-2-7-1		st	29.56	-	11.53	28.38	3.85	-	<380	1555	-	<350	<520	27.62	<380	3229	<1060	101.49
TCM	LP51a488_st in vein 1-3-1		st	29.70	-	10.42	28.98	4.11	-	<380	1254	-	<350	856	27.47	<380	2798	<1060	101.22
TCM	LP51a488_st in MS 1-6-1		st	29.77	-	11.26	28.98	3.10	-	<380	1531	-	<350	<520	28.21	<380	2095	<1060	101.74
TCM	LP51a488_st in MS 2-7-1		st	29.43	-	10.93	29.32	3.46	-	<380	1537	-	<350	605	28.23	<380	2534	<1060	101.87
TCM	lp51a489_st in vein 1-8-1		st	29.89	-	11.42	29.06	2.12	-	518	1093	-	<350	<520	29.21	<380	3308	<1060	102.34
TCM	lp51a489_st in vein 2-14-1		st	29.26	-	11.47	28.94	1.90	-	489	1442	-	<350	<520	29.24	<380	2186	<1060	101.24
TCM	LP51A489_st in vein-1-8-1		st	30.05	-	11.27	29.51	2.41	-	<380	1625	-	<350	<520	27.79	<380	2468	<1060	101.46
TCM	LP51A489_st in vein-2-14-1		st	29.83	-	11.41	29.34	1.90	-	<380	1143	-	<350	<520	28.20	<380	3023	<1060	101.15
MFS	Lp12w3439_st-1-8-1		st/sph	29.86	-	10.45	26.20	7.25	-	<380	1210	-	<350	<520	23.74	<380	2074	<1060	97.85
MFS	Lp12w3439_st-2-9-1		st/sph	30.21	-	8.52	20.70	19.15	-	<380	1319	-	<350	712	19.70	<380	1569	<1060	98.63
CCP	LP66374_ccp agg 1-1-1		ccp	34.86	-	30.87	34.63	0.04	-	<380	470	-	536	<520	**0.08**	<380	<320	1338	100.71
CCP	LP66374_ccp agg 2-7-1		ccp	34.83	-	30.21	34.16	0.03	-	<380	301	-	556	<520	**0.12**	<380	<320	1226	99.57
CCP	Lp66361_ccp agg 1-3-1		ccp	34.88	-	30.46	34.29	0.06	-	<380	314	-	500	641	**0.07**	<380	<320	1132	100.02
CCP	Lp66361_ccp agg 2-7-1		ccp	34.74	-	30.57	34.43	0.03	-	<380	305	-	370	<520	**0.08**	<380	<320	1141	100.05
CCP	Lp51aw2433_ccp agg 1-2-1		ccp	0.00	-	0.00	0.00	0.00	-	<380	<280	-	<350	<520	**0.00**	<380	<320	<1060	0.00

Zone	Label	Atomic %:	Mineral	S%	Mn%	Fe%	Cu%	Zn%	Ge%	As%	Se%	Mo%	Ag%	Cd%	Sn%	Sb%	Te%	Bi%	Sum A%
TCM	LP51a482_st-1-6-1		st	49.31	-	10.75	23.56	3.82	-	0.06	0.11	-	0.00	0.04	12.24	0.00	0.10	0.00	100.00
TCM	LP51a482_st-2-7-1		st	49.26	-	11.03	23.86	3.15	-	0.00	0.11	-	0.00	0.02	12.43	0.00	0.14	0.01	100.00
TCM	LP51a488_st in vein 1-3-1		st	49.58	-	9.99	24.41	3.36	-	0.03	0.09	-	0.00	0.04	12.39	0.01	0.12	0.00	100.00
TCM	LP51a488_st in MS 1-6-1		st	49.51	-	10.75	24.32	2.53	-	0.02	0.10	-	0.00	0.00	12.67	0.01	0.09	0.00	100.00
TCM	LP51a488_st in MS 2-7-1		st	49.07	-	10.46	24.67	2.83	-	0.01	0.10	-	0.00	0.03	12.72	0.01	0.11	0.00	100.00
TCM	lp51a489_st in vein 1-8-1		st	49.63	-	10.89	24.35	1.73	-	0.04	0.07	-	0.01	0.02	13.10	0.00	0.14	0.02	100.00
TCM	lp51a489_st in vein 2-14-1		st	49.24	-	11.08	24.58	1.57	-	0.04	0.10	-	0.00	0.01	13.29	0.00	0.09	0.00	100.00
TCM	LP51A489_st in vein-1-8-1		st	49.89	-	10.74	24.72	1.96	-	0.01	0.11	-	0.00	0.01	12.46	0.00	0.10	0.00	100.00
TCM	LP51A489_st in vein-2-14-1		st	49.81	-	10.94	24.73	1.56	-	0.02	0.08	-	0.00	0.01	12.72	0.00	0.13	0.00	100.00
MFS	Lp12w3439_st-1-8-1		st/sph	50.48	-	10.14	22.35	6.01	-	0.00	0.08	-	0.00	0.01	10.84	0.00	0.09	0.00	100.00
MFS	Lp12w3439_st-2-9-1		st/sph	50.04	-	8.10	17.31	15.56	-	0.00	0.09	-	0.00	0.03	8.81	0.00	0.07	0.00	100.00
CCP	LP66374_ccp agg 1-1-1		ccp	49.69	-	25.26	24.91	0.03	-	0.00	0.03	-	0.02	0.00	0.03	0.00	0.00	0.03	100.00
CCP	LP66374_ccp agg 2-7-1		ccp	50.10	-	24.96	24.80	0.02	-	0.00	0.02	-	0.02	0.00	0.05	0.00	0.00	0.03	100.00
CCP	Lp66361_ccp agg 1-3-1		ccp	49.98	-	25.06	24.80	0.04	-	0.00	0.02	-	0.02	0.03	0.03	0.00	0.00	0.02	100.00
CCP	Lp66361_ccp agg 2-7-1		ccp	49.81	-	25.17	24.91	0.02	-	0.00	0.02	-	0.02	0.00	0.03	0.00	0.00	0.03	100.00
CCP	Lp51aw2433_ccp agg 1-2-1		ccp	0.00	-	0.00	0.00	0.00	-	0.00	0.00	-	0.00	0.00	0.00	0.00	0.00	0.00	0.00

Zone	Label	Weight %:	Mineral	S%	Mn	Fe%	Cu%	Zn%	Ge	As	Se	Mo	Ag	Cd	Sn%	Sb	Te	Bi	Sum W%
CCP	Lp70127_ccp agg 2-5-1		ccp	0.00	-	0.00	0.00	0.00	-	<380	<280	-	<350	<520	**0.00**	<380	<320	<1060	0.00
CCP	Lp51aw2433_ccp agg 1-2-1		ccp	35.18	-	29.99	34.20	0.03	-	<380	500	-	464	<520	0.10	<380	<320	1097	99.72
CCP	Lp70127_ccp agg 2-5-1		ccp	34.96	-	30.53	34.38	0.00	-	<380	281	-	407	<520	0.03	<380	<320	1679	100.15
MCM	Lp36W195_sph 2-6-1		sph	32.92	-	5.15	0.15	61.71	-	<380	<280	-	<350	735	0.03	<380	<320	<1060	100.18
MCM	Lp36W195_sph 2-3-1		sph	32.96	-	7.17	0.00	58.66	-	<380	<280	-	<350	923	0.01	<380	<320	1204	99.07
TCM	Lp51a488_sph 2-3-1		sph	32.96	-	3.16	0.14	63.00	-	<380	<280	-	<350	907	0.02	<380	<320	2083	99.63

Zone	Label	Atomic %:	Mineral	S%	Mn%	Fe%	Cu%	Zn%	Ge%	As%	Se%	Mo%	Ag%	Cd%	Sn%	Sb%	Te%	Bi%	Sum A%
CCP	Lp70127_ccp agg 2-5-1		ccp	0.00	-	0.00	0.00	0.00	-	0.00	0.00	-	0.00	0.00	0.00	0.00	0.00	0.00	0.00
CCP	Lp51aw2433_ccp agg 1-2-1		ccp	50.44	-	24.69	24.74	0.02	-	0.00	0.03	-	0.02	0.00	0.04	0.00	0.00	0.02	100.00
CCP	Lp70127_ccp agg 2-5-1		ccp	50.02	-	25.08	24.82	0.00	-	0.00	0.02	-	0.02	0.00	0.01	0.00	0.00	0.04	100.00
MCM	Lp36W195_sph 2-6-1		sph	49.67	-	4.46	0.11	45.67	-	0.00	0.01	-	0.01	0.03	0.01	0.01	0.00	0.02	100.00
MCM	Lp36W195_sph 2-3-1		sph	50.00	-	6.25	0.00	43.65	-	0.00	0.01	-	0.01	0.04	0.00	0.00	0.00	0.03	100.00
TCM	Lp51a488_sph 2-3-1		sph	50.07	-	2.76	0.11	46.94	-	0.00	0.02	-	0.01	0.04	0.01	0.00	0.00	0.05	100.00

			Analysed weight %								Calculated atomic %							
Zone	Label	Mineral	S%	Fe%	Cu%	Zn	Se	Ag	Pb	Sum W%	S%	Fe%	Cu%	Zn%	Se%	Ag%	Pb%	Sum W%
	detection limits (ppm):		130	180	250	250	260	90	1000									
MCM	LP18365b_ccp 1-7-1	ccp	38.39	30.01	33.63	1072	<260	<90	<1000	102.16	52.84	23.72	23.36	0.07	0.01	0.00	0.00	100.00
TCM	LP51A479_ccp in vein	ccp	38.37	29.64	33.59	542	<260	<90	<1000	101.68	53.02	23.51	23.42	0.04	0.01	0.00	0.00	100.00
TCM	LP51A479_ccp 2-21-1	ccp	38.80	29.88	33.57	6786	<260	<90	<1000	102.94	52.98	23.42	23.13	0.45	0.00	0.00	0.00	100.00
CCP	LP66361_ccp 2-2-1	ccp	38.54	29.80	34.04	<250	<260	191	<1000	102.42	52.91	23.49	23.58	0.00	0.01	0.01	0.00	100.00
CCP	LP66361_ccp 1-1-1	ccp	38.63	29.66	33.91	306	342	134	<1000	102.27	53.06	23.39	23.50	0.02	0.02	0.01	0.00	100.00
LBZ	LP63415_ccp 1-3-1	ccp	38.76	29.99	34.21	356	<260	<90	<1000	103.03	52.90	23.50	23.56	0.02	0.01	0.00	0.00	100.00
CCP	LP51AW2433_ccp 2-5-1	ccp	38.99	30.35	34.40	<250	301	<90	<1000	103.80	52.84	23.61	23.52	0.01	0.02	0.00	0.00	100.00
TCS	LP67B965_ccp 1-4-1	ccp	38.91	29.81	33.86	<250	<260	<90	<1000	102.61	53.21	23.40	23.36	0.01	0.01	0.00	0.00	100.00
MCM	LP36W195_ccp 1-9-1	ccp	38.52	29.95	34.00	998	593	146	<1000	102.65	52.80	23.57	23.52	0.07	0.03	0.01	0.00	100.00
MCM	LP36W195_ccp 2-20-1	ccp	38.70	29.61	33.59	<250	<260	130	<1000	101.95	53.25	23.40	23.32	0.01	0.01	0.01	0.00	100.00
MFS	LP12555_ccp 1-6-1	ccp	38.93	29.91	34.57	1783	<260	154	<1000	103.64	52.86	23.32	23.69	0.12	0.00	0.01	0.01	100.00
LBZ	LP44243_ccp 1-6-1	ccp	38.74	29.93	33.94	<250	<260	994	<1000	102.73	53.00	23.51	23.44	0.00	0.01	0.04	0.00	100.00

Zone	Label	Weight %:	Mineral	S%	Mn	Fe	Cu%	Zn	Se	Mo	Ag%	Sn	Sb%	Te	Bi%	Sum W%
		detection limits (ppm):		270	260	320	370	470	280	560	350	500	380	320	1060	
CCP	LP66361_mineral x		Bi	0	490	<320	0	<470	<280	1150	0	<500	0.103	<320	101.51	101.88
CCP	LP66361_mineral x1		Bi	0.029	<260	730	0.5	<470	<280	<560	0	<500	0.036	<320	99.90	100.58
CCP	LP700695_pg in vein 1-5-1		dg	22.57	<260	3570	77.22	<470	<280	3740	0.041	<500	0.037	<320	1.00	101.66
CCP	LP700695_pg in vein 2-6-1		dg	22.52	<260	16830	77.76	<470	<280	4340	0.002	<500	0	<320	1.00	103.50
MCM	Lp18365b_co 4-9-1		pg	19.71	<260	1980	1.249	540	<280	2780	60.77	<500	23.33	<320	1.00	106.60
MCM	Lp18365b_co 2-2-1		pg	18.51	<260	750	1.038	490	<280	2750	63.56	2070	21.39	<320	1.00	106.10

Zone	Label	Atomic %:	Mineral	S%	Mn%	Fe%	Cu%	Zn%	Se%	Mo%	Ag%	Sn%	Sb%	Te%	Bi%	Sum A%
CCP	LP66361_mineral x		Bi	0.00	0.18	0.00	0.00	0.06	0.07	0.25	0.00	0.06	0.17	0.04	99.17	100.00
CCP	LP66361_mineral x1		Bi	0.19	0.03	0.27	1.61	0.07	0.03	0.00	0.00	0.00	0.06	0.00	97.75	100.00
CCP	LP700695_pg in vein 1-5-1		dg	36.37	0.00	0.33	62.78	0.00	0.01	0.20	0.02	0.02	0.02	0.00	0.25	100.00
CCP	LP700695_pg in vein 2-6-1		dg	35.72	0.00	1.53	62.21	0.03	0.02	0.23	0.00	0.00	0.00	0.01	0.24	100.00
MCM	Lp18365b_co 4-9-1		pg	43.87	0.00	0.25	1.40	0.06	0.00	0.21	40.19	0.00	13.67	0.00	0.34	100.00
MCM	Lp18365b_co 2-2-1		pg	42.14	0.00	0.10	1.19	0.05	0.00	0.21	43.01	0.13	12.82	0.00	0.35	100.00

				Analysed weight %						Calculated atomic %					
Zone	Label		Mineral	Cu%	Ag%	Au%	Hg%	Bi%	Sum %	Cu%	Ag%	Au%	Hg%	Bi%	Sum %
		detection limits (ppm):		210	152	1440	750	450							
MCM	LP18365b_el		el	0.03	57.48	37.54	5.52	0.00	100.57	0.06	70.91	25.36	3.66	0.00	100.00
MCM	LP18365b_el		el	0.01	58.67	35.95	5.62	0.00	100.25	0.01	72.09	24.19	3.71	0.00	100.00

Sample	Mineral	Location	Unit	Description	$\delta^{13}C$ (PDB)	Precision	$\delta^{18}O$ (PDB)	Precision	$\delta^{18}O$ (V-SMOW)
LPD103	ca	Licking Hole Creek	Anson Fm	crinoidal limestone	2.181	0.010	-6.411	0.012	24.251
MRV18	ca	Calula creek	MRV	coralline limestone	2.778	0.023	-6.366	0.016	24.298
MRV39	ca	Calula limestone quarry	MRV	crinoidal limestone	5.056	0.014	-2.779	0.012	27.995
LP44201A	ca	upper limstone lens	fault-bound	massive limestone	0.825	0.009	-17.179	0.021	13.151
LP44201B	ca	upper limstone lens	fault-bound	massive limestone	0.314	0.011	-17.076	0.01	13.257
LP44211	ca	upper limstone lens	fault-bound	massive limestone	0.667	0.011	-17.409	0.015	12.914
LP44229A	ca	lower limestone lens	fault-bound	massive limestone	-0.199	0.019	-18.045	0.024	12.258
LP44229B	ca	lower limestone lens	fault-bound	massive limestone	-1.762	0.015	-18.468	0.016	11.822
LP58087	ca	upper limstone lens	fault-bound	massive limestone	1.747	0.005	-10.295	0.014	20.248
LP58155	impure ca	upper limstone lens	fault-bound	massive limestone	0.088	0.005	-17.345	0.010	12.979
LP63201	ca	upper limstone lens	fault-bound	massive limestone	1.565	0.005	-13.200	0.007	17.253
LP63223	impure ca	upper limstone lens	fault-bound	massive limestone	1.901	0.003	-13.935	0.006	16.495
LP63266	ca	upper limstone lens	fault-bound	massive limestone	1.321	0.002	-15.952	0.013	14.416
LP63376	ca	lower limestone lens	fault-bound	massive limestone	0.712	0.002	-20.279	0.019	9.955
LP69191	ca	upper limstone lens	fault-bound	massive limestone	0.938	0.033	-16.483	0.017	13.868
LP12530	ca	Main zone footwall	Transitional	limestone clast	1.239	0.011	-14.185	0.009	16.237
LP12539	ca	Main zone footwall	Transitional	limestone clast	0.008	0.011	-14.899	0.014	15.502
LP18392	ca	Main zone footwall	Transitional	limestone clast	0.944	0.007	-14.996	0.011	15.402
LP18405	ca	Main zone footwall	Transitional	limestone clast	1.311	0.008	-13.893	0.011	16.538
LP20388	ca	Main zone footwall	Transitional	limestone clast	0.594	0.041	-15.804	0.01	14.568
LP20388	ca	Main zone footwall	Transitional	limestone clast	0.268	0.028	-15.609	0.008	14.769
LP20388	ca	Main zone footwall	Transitional	limestone clast	0.501	0.079	-15.639	0.016	14.738
LP20388	ca	Main zone footwall	Transitional	limestone clast	0.056	0.041	-15.626	0.015	14.752
LP33427	ca	Main zone footwall	Transitional	limestone clast	-0.19	0.025	-15.688	0.014	14.688
LP36W262	ca	Main zone footwall	Transitional	limestone clast	1.309	0.009	-14.407	0.006	16.008
LP37238	ca	Main zone footwall	Transitional	limestone clast	1.522	0.005	-14.500	0.011	15.912
LPD001	ca	Main zone footwall	Transitional	limestone clast from quarry	-0.150	0.006	-14.018	0.009	16.409
LP12530	ca + dol	Main zone footwall	Transitional	altered limestone clast	-4.54	0.024	-15.123	0.015	15.270
LP12530	impure ca	Main zone footwall	Transitional	altered limestone clast	-0.641	0.035	-15.372	0.014	15.014
LP43231	ca	Main zone footwall	Transitional	altered limestone clast	-1.526	0.004	-19.281	0.010	10.984
LP66374	impure ca	footwall Cu zone	WVS	type 1A ca-ccp-py vein	-3.236	0.019	-20.622	0.025	9.602
LP66376	impure ca	footwall Cu zone	WVS	type 1A ca-ccp-py vein	-1.09	0.012	-20.494	0.031	9.734
LP44243	impure ca	Lady Belmore zone	HST	ca-py-sph-ga band	-3.483	0.018	-18.896	0.033	11.381
LP44290	ca + dol	Lady Belmore zone	HST	perv ca-dol-chl	-5.263	0.009	-19.88	0.015	10.367
LP63392	impure ca	Lady Belmore zone	HST	pervasive qtz-ca	-1.382	0.024	-19.289	0.007	10.976
LP67BW11132	ca	Toms Zone hangingwall	HST	patchy calcite	-3.672	0.023	-19.352	0.01	10.911
LP12440	dol	Main zone hangingwall	Transitional	massive dolomite	-2.757	0.010	-17.275	0.004	13.052

Sample	Mineral	Location	Unit	Description	$\delta^{13}C$(PDB)	Precision	$\delta^{18}O$(PDB)	Precision	$\delta^{18}O$(V-SMOW)
LP12476	impure ca	Main zone	Transitional	intense perv dol-tlc-chl	-1.588	0.009	-17.279	0.010	13.048
LP12493	dol	Main zone footwall	Transitional	massive dolomite	-10.971	0.012	-18.978	0.011	11.296
LP12503	impure ca	Main zone footwall	Transitional	massive dolomite	0.050	0.017	-16.486	0.012	13.865
LP12521	dol	Main zone footwall	Transitional	massive dolomite	-2.361	0.015	-15.495	0.011	14.887
LP18371	dol	Main zone footwall	Transitional	patchy dolomite	0.851	0.021	-15.741	0.017	14.634
LP33346	dol	Main zone hangingwall	Transitional	massive dolomite	0.901	0.011	-15.690	0.018	14.686
LP33379	dol	Main zone hangingwall	Transitional	massive dolomite	-2.016	0.020	-17.334	0.018	12.991
LP33390	dol	Main zone hangingwall	Transitional	massive dolomite	0.086	0.029	-17.527	0.016	12.792
LP33405	dol	Main zone	Transitional	patchy dolomite-chlorite	-0.531	0.010	-16.051	0.016	14.314
LP36W195	impure ca	Main zone	Transitional	massive calcite	-5.292	0.017	-18.738	0.031	11.544
LP36W214	dol	Main zone footwall	Transitional	massive dolomite	-7.517	0.007	-16.690	0.009	13.655
LP37165	impure ca	Main zone	Transitional	patchy dolomite-chlorite	-5.696	0.026	-17.087	0.014	13.246
LP18336	dol	Main zone footwall	Transitional	altered limestone clast	-3.973	0.005	-17.688	0.006	12.627
LP18382	dol	Main zone footwall	Transitional	altered limestone clast	-4.676	0.008	-14.138	0.013	16.285
LP36W206	impure dol	Main zone	Transitional	altered limestone clast	-4.757	0.009	-14.105	0.008	16.320
LP36W206	impure dol	Main zone	Transitional	altered limestone clast	-6.179	0.013	-16.315	0.014	14.042
LP43231B	dol	Main zone footwall	Transitional	altered limestone clast	-1.593	0.006	-18.595	0.013	11.691
LP43235A	dol	Main zone footwall	Transitional	altered limestone clast	0.033	0.005	-18.290	0.005	12.006
LP45260	dol	Main zone footwall	Transitional	altered limestone clast	-11.001	0.029	-19.046	0.033	11.226
LP51A496	impure dol	Toms zone	HST	massive dolomite	-3.487	0.023	-19.487	0.024	10.772
LP51A484	dol	Toms zone	HST	massive dolomite	-1.296	0.004	-19.628	0.006	10.626
LP51A492	impure dol	Toms zone	HST	massive dolomite	-4.871	0.007	-20.322	0.009	9.911
LP51A496	dol	Toms zone	HST	patchy dolomite	-6.320	0.004	-19.576	0.005	10.680
LP51A503	dol	Toms zone footwall	HST	patchy dolomite	-6.834	0.009	-21.347	0.009	8.854
LP67B687	dol	Toms Zone footwall	HST	pervasive dolomite	-8.283	0.005	-23.502	0.013	6.633
LP51A479	impure dol	Toms zone	HST	type 2 dol-ccp vein	-3.781	0.016	-17.198	0.024	13.131
LP51A484	dol	Toms zone	HST	type 2 dol vein	-4.980	0.008	-23.566	0.004	6.566
LP51A489	impure dol	Toms zone	HST	type 2 dol-ccp vein	-3.865	0.014	-20.199	0.018	10.038
LP51AW2433	impure dol	Toms zone footwall	HST	type 2 dol-ccp vein	-8.968	0.018	-22.535	0.022	7.630
LP65A899	dol	south of Toms zone	HST	type 2 dol-ccp vein	-7.679	0.012	-21.952	0.014	8.231

Notes:
All samples analysed at the University of Tasmania, Central Science Laboratory
Powdered carbonate samples were dissolved in H_3PO_4 and placed in a sealed vessel for analyis by a stable isotope mass spectrometer
Mineral abbreviations: ca = calcite, dol = dolomite, qtz = quartz, py = pyrite, sph = sphalerite, ccp = chaclopyrite
Unit abbreviations: WVS = Western Volcanic Succession, HST = Hangingwall Siltstone Unit
Drill core samples are numbered: 'LP, drill hole number and depth (last 3 digits)'

Fluid-Rock Interaction Models:

				Rock		Fluid		Fractionation Factors		Calcite Compositions	
T(°C)	system	W/R	X_{CO_2}	$\delta^{18}O^{i}_{calcite}$	$\delta^{13}C^{i}_{calcite}$	$\delta^{18}O^{i}_{fluid}$	$\delta^{13}C^{i}_{fluid}$	$\Delta^{18}O^{calcite}_{H_2O}$	$\Delta^{13}C^{calcite}_{CO_2}$	$\delta^{18}O_{calcite}$	$\delta^{13}C_{calcite}$
150	open	0.02	0.1	-2	-9	24.25	2.50	12.64	0.95	2.48	23.98
150	open	0.5	0.1	-2	-9	24.25	2.50	12.64	0.95	1.99	18.89
150	open	1	0.1	-2	-9	24.25	2.50	12.64	0.95	1.50	15.64
150	open	2	0.1	-2	-9	24.25	2.50	12.64	0.95	0.59	12.48
150	open	5	0.1	-2	-9	24.25	2.50	12.64	0.95	-1.65	10.73
150	open	10	0.1	-2	-9	24.25	2.50	12.64	0.95	-4.17	10.64
150	open	50	0.1	-2	-9	24.25	2.50	12.64	0.95	-7.98	10.64
150	open	100	0.1	-2	-9	24.25	2.50	12.64	0.95	-8.05	10.64
150	open	500	0.1	-2	-9	24.25	2.50	12.64	0.95	-8.05	10.64
150	closed	0.02	0.1	-2	-9	24.25	2.50	12.64	0.95	2.48	23.98
150	closed	0.5	0.1	-2	-9	24.25	2.50	12.64	0.95	2.00	19.71
150	closed	1	0.1	-2	-9	24.25	2.50	12.64	0.95	1.54	17.44
150	closed	2	0.1	-2	-9	24.25	2.50	12.64	0.95	0.74	15.17
150	closed	5	0.1	-2	-9	24.25	2.50	12.64	0.95	-1.02	12.90
150	closed	10	0.1	-2	-9	24.25	2.50	12.64	0.95	-2.77	11.87
150	closed	50	0.1	-2	-9	24.25	2.50	12.64	0.95	-6.29	10.90
150	closed	100	0.1	-2	-9	24.25	2.50	12.64	0.95	-7.09	10.77
150	closed	500	0.1	-2	-9	24.25	2.50	12.64	0.95	-7.84	10.66
250	open	0.02	0.1	-2	-9	24.25	2.50	7.27	-1.86	2.47	23.87
250	open	0.5	0.1	-2	-9	24.25	2.50	7.27	-1.86	1.85	16.78
250	open	1	0.1	-2	-9	24.25	2.50	7.27	-1.86	1.23	12.25
250	open	2	0.1	-2	-9	24.25	2.50	7.27	-1.86	0.08	7.84
250	open	5	0.1	-2	-9	24.25	2.50	7.27	-1.86	-2.76	5.40
250	open	10	0.1	-2	-9	24.25	2.50	7.27	-1.86	-5.94	5.27
250	open	50	0.1	-2	-9	24.25	2.50	7.27	-1.86	-10.77	5.27
250	open	100	0.1	-2	-9	24.25	2.50	7.27	-1.86	-10.86	5.27
250	open	500	0.1	-2	-9	24.25	2.50	7.27	-1.86	-10.86	5.27
250	closed	0.02	0.1	-2	-9	24.25	2.50	7.27	-1.86	2.47	23.88
250	closed	0.5	0.1	-2	-9	24.25	2.50	7.27	-1.86	1.86	17.92
250	closed	1	0.1	-2	-9	24.25	2.50	7.27	-1.86	1.29	14.76
250	closed	2	0.1	-2	-9	24.25	2.50	7.27	-1.86	0.27	11.60
250	closed	5	0.1	-2	-9	24.25	2.50	7.27	-1.86	-1.95	8.43
250	closed	10	0.1	-2	-9	24.25	2.50	7.27	-1.86	-4.18	6.99
250	closed	50	0.1	-2	-9	24.25	2.50	7.27	-1.86	-8.63	5.64
250	closed	100	0.1	-2	-9	24.25	2.50	7.27	-1.86	-9.64	5.46
250	closed	500	0.1	-2	-9	24.25	2.50	7.27	-1.86	-10.60	5.31
150	open	0.02	0.1	-2	-9	24.25	2.50	15.87	2.13	2.48	24.04
150	open	0.5	0.1	-2	-9	24.25	2.50	15.87	2.13	2.04	20.17
150	open	1	0.1	-2	-9	24.25	2.50	15.87	2.13	1.61	17.69
150	open	2	0.1	-2	-9	24.25	2.50	15.87	2.13	0.80	15.28
150	open	5	0.1	-2	-9	24.25	2.50	15.87	2.13	-1.19	13.94
150	open	10	0.1	-2	-9	24.25	2.50	15.87	2.13	-3.43	13.87
150	open	50	0.1	-2	-9	24.25	2.50	15.87	2.13	-6.81	13.87
150	open	100	0.1	-2	-9	24.25	2.50	15.87	2.13	-6.87	13.87
150	open	500	0.1	-2	-9	24.25	2.50	15.87	2.13	-6.87	13.87
150	closed	0.02	0.1	-2	-9	24.25	2.50	15.87	2.13	2.48	24.05
150	closed	0.5	0.1	-2	-9	24.25	2.50	15.87	2.13	2.05	20.79
150	closed	1	0.1	-2	-9	24.25	2.50	15.87	2.13	1.65	19.06
150	closed	2	0.1	-2	-9	24.25	2.50	15.87	2.13	0.94	17.33
150	closed	5	0.1	-2	-9	24.25	2.50	15.87	2.13	-0.62	15.60
150	closed	10	0.1	-2	-9	24.25	2.50	15.87	2.13	-2.19	14.82
150	closed	50	0.1	-2	-9	24.25	2.50	15.87	2.13	-5.31	14.08
150	closed	100	0.1	-2	-9	24.25	2.50	15.87	2.13	-6.02	13.97
150	closed	500	0.1	-2	-9	24.25	2.50	15.87	2.13	-6.69	13.89
250	open	0.02	0.1	-2	-9	24.25	2.50	9.69	-1.03	2.47	23.92
250	open	0.5	0.1	-2	-9	24.25	2.50	9.69	-1.03	1.89	17.74
250	open	1	0.1	-2	-9	24.25	2.50	9.69	-1.03	1.31	13.78
250	open	2	0.1	-2	-9	24.25	2.50	9.69	-1.03	0.23	9.93
250	open	5	0.1	-2	-9	24.25	2.50	9.69	-1.03	-2.43	7.80
250	open	10	0.1	-2	-9	24.25	2.50	9.69	-1.03	-5.42	7.69

				Rock		Fluid		Fractionation Factors		Calcite Compositions	
T(°C)	system	W/R	X_{CO_2}	$\delta^{18}O^{i}_{calcite}$	$\delta^{13}C^{i}_{calcite}$	$\delta^{18}O^{i}_{fluid}$	$\delta^{13}C^{i}_{fluid}$	$\Delta^{18}O^{calcite}_{H_2O}$	$\Delta^{13}C^{calcite}_{CO_2}$	$\delta^{18}O_{calcite}$	$\delta^{13}C_{calcite}$
250	open	50	0.1	-2	-9	24.25	2.50	9.69	-1.03	-9.95	7.69
250	open	100	0.1	-2	-9	24.25	2.50	9.69	-1.03	-10.03	7.69
250	open	500	0.1	-2	-9	24.25	2.50	9.69	-1.03	-10.03	7.69
250	closed	0.02	0.1	-2	-9	24.25	2.50	9.69	-1.03	2.47	23.93
250	closed	0.5	0.1	-2	-9	24.25	2.50	9.69	-1.03	1.90	18.73
250	closed	1	0.1	-2	-9	24.25	2.50	9.69	-1.03	1.36	15.97
250	closed	2	0.1	-2	-9	24.25	2.50	9.69	-1.03	0.41	13.21
250	closed	5	0.1	-2	-9	24.25	2.50	9.69	-1.03	-1.68	10.45
250	closed	10	0.1	-2	-9	24.25	2.50	9.69	-1.03	-3.77	9.20
250	closed	50	0.1	-2	-9	24.25	2.50	9.69	-1.03	-7.94	8.02
250	closed	100	0.1	-2	-9	24.25	2.50	9.69	-1.03	-8.89	7.86
250	closed	500	0.1	-2	-9	24.25	2.50	9.69	-1.03	-9.79	7.73

Fluid Mixing Models:

			Fluid A		Fluid B		Fractionation factors		Dolomite compositions		Fluid compositions	
Xa	P	T(°C)	$\delta^{18}O_a$	$\delta^{13}C_a$	$\delta^{18}O_b$	$\delta^{13}C_b$	$\Delta^{18}O^{dolomite}_{H_2O}$	$\Delta^{13}C^{dolomite}_{CO_2}$	$\delta^{18}O_{dolomite}$	$\delta^{13}C_{dolomite}$	$\delta^{18}O_{fluid}$	$\delta^{13}C_{fluid}$
0.00	0.10	350	-2	-0.50	10	-9	6.24	-2.42	-11.42	16.24	-9.00	10.00
0.10	0.10	325	-2	-0.50	10	-9	6.94	-2.17	-6.70	15.74	-4.53	8.80
0.20	0.10	300	-2	-0.50	10	-9	7.74	-1.87	-4.79	15.34	-2.93	7.60
0.30	0.10	275	-2	-0.50	10	-9	8.65	-1.49	-3.60	15.05	-2.11	6.40
0.40	0.10	250	-2	-0.50	10	-9	9.69	-1.03	-2.64	14.89	-1.61	5.20
0.50	0.10	225	-2	-0.50	10	-9	10.90	-0.47	-1.74	14.90	-1.27	4.00
0.60	0.10	200	-2	-0.50	10	-9	12.29	0.23	-0.80	15.09	-1.03	2.80
0.70	0.10	175	-2	-0.50	10	-9	13.93	1.08	0.23	15.53	-0.85	1.60
0.80	0.10	150	-2	-0.50	10	-9	15.87	2.13	1.42	16.27	-0.71	0.40
0.90	0.10	125	-2	-0.50	10	-9	18.19	3.42	2.83	17.39	-0.59	-0.80
1.00	0.10	100	-2	-0.50	10	-9	20.98	5.03	4.53	18.98	-0.50	-2.00
0.00	1	350	-2	-0.50	10	-9	6.24	-2.42	-11.42	16.24	-9.00	10.00
0.10	1	325	-2	-0.50	10	-9	6.94	-2.17	-10.32	15.74	-8.15	8.80
0.20	1	300	-2	-0.50	10	-9	7.74	-1.87	-9.17	15.34	-7.30	7.60
0.30	1	275	-2	-0.50	10	-9	8.65	-1.49	-7.94	15.05	-6.45	6.40
0.40	1	250	-2	-0.50	10	-9	9.69	-1.03	-6.63	14.89	-5.60	5.20
0.50	1	225	-2	-0.50	10	-9	10.90	-0.47	-5.22	14.90	-4.75	4.00
0.60	1	200	-2	-0.50	10	-9	12.29	0.23	-3.67	15.09	-3.90	2.80
0.70	1	175	-2	-0.50	10	-9	13.93	1.08	-1.97	15.53	-3.05	1.60
0.80	1	150	-2	-0.50	10	-9	15.87	2.13	-0.07	16.27	-2.20	0.40
0.90	1	125	-2	-0.50	10	-9	18.19	3.42	2.07	17.39	-1.35	-0.80
1.00	1	100	-2	-0.50	10	-9	20.98	5.03	4.53	18.98	-0.50	-2.00
0.00	10	350	-2	-0.50	10	-9	6.24	-2.42	-11.42	16.24	-9.00	10.00
0.10	10	325	-2	-0.50	10	-9	6.94	-2.17	-11.08	15.74	-8.91	8.80
0.20	10	300	-2	-0.50	10	-9	7.74	-1.87	-10.66	15.34	-8.79	7.60
0.30	10	275	-2	-0.50	10	-9	8.65	-1.49	-10.14	15.05	-8.65	6.40
0.40	10	250	-2	-0.50	10	-9	9.69	-1.03	-9.50	14.89	-8.47	5.20
0.50	10	225	-2	-0.50	10	-9	10.90	-0.47	-8.69	14.90	-8.23	4.00
0.60	10	200	-2	-0.50	10	-9	12.29	0.23	-7.66	15.09	-7.89	2.80
0.70	10	175	-2	-0.50	10	-9	13.93	1.08	-6.31	15.53	-7.39	1.60
0.80	10	150	-2	-0.50	10	-9	15.87	2.13	-4.44	16.27	-6.57	0.40
0.90	10	125	-2	-0.50	10	-9	18.19	3.42	-1.55	17.39	-4.97	-0.80
1.00	10	100	-2	-0.50	10	-9	20.98	5.03	4.53	18.98	-0.50	-2.00
0.00	0.10	350	-2	-0.50	2	-5	6.24	-2.42	-7.42	8.24	-5.00	2.00
0.10	0.10	325	-2	-0.50	2	-5	6.94	-2.17	-4.80	8.54	-2.63	1.60
0.20	0.10	300	-2	-0.50	2	-5	7.74	-1.87	-3.65	8.94	-1.79	1.20
0.30	0.10	275	-2	-0.50	2	-5	8.65	-1.49	-2.84	9.45	-1.35	0.80
0.40	0.10	250	-2	-0.50	2	-5	9.69	-1.03	-2.12	10.09	-1.09	0.40
0.50	0.10	225	-2	-0.50	2	-5	10.90	-0.47	-1.38	10.90	-0.91	0.00
0.60	0.10	200	-2	-0.50	2	-5	12.29	0.23	-0.55	11.89	-0.78	-0.40
0.70	0.10	175	-2	-0.50	2	-5	13.93	1.08	0.39	13.13	-0.68	-0.80
0.80	0.10	150	-2	-0.50	2	-5	15.87	2.13	1.52	14.67	-0.61	-1.20
0.90	0.10	125	-2	-0.50	2	-5	18.19	3.42	2.87	16.59	-0.55	-1.60
1.00	0.10	100	-2	-0.50	2	-5	20.98	5.03	4.53	18.98	-0.50	-2.00

			Fluid A		Fluid B		Fractionation factors		Dolomite compositions		Fluid compositions	
Xa	P	T(°C)	$\delta^{18}O_a$	$\delta^{13}C_a$	$\delta^{18}O_b$	$\delta^{13}C_b$	$\Delta^{18}O_{H_2O}^{dolomite}$	$\Delta^{13}C_{CO_2}^{dolomite}$	$\delta^{18}O_{dolomite}$	$\delta^{13}C_{dolomite}$	$\delta^{18}O_{fluid}$	$\delta^{13}C_{fluid}$
0.00	1	350	-2	-0.50	2	-5	6.24	-2.42	-7.42	8.24	-5.00	2.00
0.10	1	325	-2	-0.50	2	-5	6.94	-2.17	-6.72	8.54	-4.55	1.60
0.20	1	300	-2	-0.50	2	-5	7.74	-1.87	-5.97	8.94	-4.10	1.20
0.30	1	275	-2	-0.50	2	-5	8.65	-1.49	-5.14	9.45	-3.65	0.80
0.40	1	250	-2	-0.50	2	-5	9.69	-1.03	-4.23	10.09	-3.20	0.40
0.50	1	225	-2	-0.50	2	-5	10.90	-0.47	-3.22	10.90	-2.75	0.00
0.60	1	200	-2	-0.50	2	-5	12.29	0.23	-2.07	11.89	-2.30	-0.40
0.70	1	175	-2	-0.50	2	-5	13.93	1.08	-0.77	13.13	-1.85	-0.80
0.80	1	150	-2	-0.50	2	-5	15.87	2.13	0.73	14.67	-1.40	-1.20
0.90	1	125	-2	-0.50	2	-5	18.19	3.42	2.47	16.59	-0.95	-1.60
1.00	1	100	-2	-0.50	2	-5	20.98	5.03	4.53	18.98	-0.50	-2.00
0.00	10	350	-2	-0.50	2	-5	6.24	-2.42	-7.42	8.24	-5.00	2.00
0.10	10	325	-2	-0.50	2	-5	6.94	-2.17	-7.12	8.54	-4.95	1.60
0.20	10	300	-2	-0.50	2	-5	7.74	-1.87	-6.76	8.94	-4.89	1.20
0.30	10	275	-2	-0.50	2	-5	8.65	-1.49	-6.31	9.45	-4.82	0.80
0.40	10	250	-2	-0.50	2	-5	9.69	-1.03	-5.75	10.09	-4.72	0.40
0.50	10	225	-2	-0.50	2	-5	10.90	-0.47	-5.06	10.90	-4.59	0.00
0.60	10	200	-2	-0.50	2	-5	12.29	0.23	-4.19	11.89	-4.41	-0.40
0.70	10	175	-2	-0.50	2	-5	13.93	1.08	-3.07	13.13	-4.15	-0.80
0.80	10	150	-2	-0.50	2	-5	15.87	2.13	-1.59	14.67	-3.71	-1.20
0.90	10	125	-2	-0.50	2	-5	18.19	3.42	0.55	16.59	-2.87	-1.60
1.00	10	100	-2	-0.50	2	-5	20.98	5.03	4.53	18.98	-0.50	-2.00
0.00	0.10	350	-2	-0.50	2	-9	6.24	-2.42	-11.42	8.24	-9.00	2.00
0.10	0.10	325	-2	-0.50	2	-9	6.94	-2.17	-6.70	8.54	-4.53	1.60
0.20	0.10	300	-2	-0.50	2	-9	7.74	-1.87	-4.79	8.94	-2.93	1.20
0.30	0.10	275	-2	-0.50	2	-9	8.65	-1.49	-3.60	9.45	-2.11	0.80
0.40	0.10	250	-2	-0.50	2	-9	9.69	-1.03	-2.64	10.09	-1.61	0.40
0.50	0.10	225	-2	-0.50	2	-9	10.90	-0.47	-1.74	10.90	-1.27	0.00
0.60	0.10	200	-2	-0.50	2	-9	12.29	0.23	-0.80	11.89	-1.03	-0.40
0.70	0.10	175	-2	-0.50	2	-9	13.93	1.08	0.23	13.13	-0.85	-0.80
0.80	0.10	150	-2	-0.50	2	-9	15.87	2.13	1.42	14.67	-0.71	-1.20
0.90	0.10	125	-2	-0.50	2	-9	18.19	3.42	2.83	16.59	-0.59	-1.60
1.00	0.10	100	-2	-0.50	2	-9	20.98	5.03	4.53	18.98	-0.50	-2.00
0.00	1	350	-2	-0.50	2	-9	6.24	-2.42	-11.42	8.24	-9.00	2.00
0.10	1	325	-2	-0.50	2	-9	6.94	-2.17	-10.32	8.54	-8.15	1.60
0.20	1	300	-2	-0.50	2	-9	7.74	-1.87	-9.17	8.94	-7.30	1.20
0.30	1	275	-2	-0.50	2	-9	8.65	-1.49	-7.94	9.45	-6.45	0.80
0.40	1	250	-2	-0.50	2	-9	9.69	-1.03	-6.63	10.09	-5.60	0.40
0.50	1	225	-2	-0.50	2	-9	10.90	-0.47	-5.22	10.90	-4.75	0.00
0.60	1	200	-2	-0.50	2	-9	12.29	0.23	-3.67	11.89	-3.90	-0.40
0.70	1	175	-2	-0.50	2	-9	13.93	1.08	-1.97	13.13	-3.05	-0.80
0.80	1	150	-2	-0.50	2	-9	15.87	2.13	-0.07	14.67	-2.20	-1.20
0.90	1	125	-2	-0.50	2	-9	18.19	3.42	2.07	16.59	-1.35	-1.60
1.00	1	100	-2	-0.50	2	-9	20.98	5.03	4.53	18.98	-0.50	-2.00
0.00	10	350	-2	-0.50	2	-9	6.24	-2.42	-11.42	8.24	-9.00	2.00
0.10	10	325	-2	-0.50	2	-9	6.94	-2.17	-11.08	8.54	-8.91	1.60
0.20	10	300	-2	-0.50	2	-9	7.74	-1.87	-10.66	8.94	-8.79	1.20
0.30	10	275	-2	-0.50	2	-9	8.65	-1.49	-10.14	9.45	-8.65	0.80
0.40	10	250	-2	-0.50	2	-9	9.69	-1.03	-9.50	10.09	-8.47	0.40
0.50	10	225	-2	-0.50	2	-9	10.90	-0.47	-8.69	10.90	-8.23	0.00
0.60	10	200	-2	-0.50	2	-9	12.29	0.23	-7.66	11.89	-7.89	-0.40
0.70	10	175	-2	-0.50	2	-9	13.93	1.08	-6.31	13.13	-7.39	-0.80
0.80	10	150	-2	-0.50	2	-9	15.87	2.13	-4.44	14.67	-6.57	-1.20
0.90	10	125	-2	-0.50	2	-9	18.19	3.42	-1.55	16.59	-4.97	-1.60
1.00	10	100	-2	-0.50	2	-9	20.98	5.03	4.53	18.98	-0.50	-2.00

Sample	Chip	Label	Shape	Size (μ m)	Tm (°C)	Th (°C)	Salinity	Final Temp (at 1000m)
LP12493	1	A	r	9.45	2.2		3.7	
LP12493	1	B	r	4.12	2.1	165	3.5	175
LP12493	1	C	r	4.8	2.3	168	3.9	178
LP12493	1	D	r	2.14	3.1		5.1	
LP12493	1	E	r	2	2.4	166	4.0	176
LP12493	1	F	r	2.74	2.1		3.5	
LP12493	1	G	r	2.89	3.2		5.2	
LP12493	1	H	r	3.84	3.2		5.2	
LP12493	1	I	r	4.8	3.1		5.1	
LP12493	1	J	r	3.73	2.4		4.0	
LP12493	1	M	r	7.26	2.9	166	4.8	176
LP12493	1	N	r	6.37	3.3	168	5.4	178
LP12493	2	A	r	5.86	2.8	168	4.6	178
LP12493	2	B	r	8.81	3	170	4.9	180
LP12493	2	C	e	6.21	1.9	171	3.2	181
LP12493	2	D	e	5.69	1.7	171	2.9	181
LP12493	2	E	r	9.13	2.1	175	3.5	185
LP12493	2	F	e	6.9	2	172	3.4	182
LP12493	3	A	r	10.6	2.2	187	3.7	197
LP12493	3	B	e	3.5	2.8	188	4.6	198
LP12493	3	D	r	4.4	2.5	165	4.2	175
LP12493	3	E	e	4.56	2.3	168	3.9	178
LP12493	3	F	r	5.68	2.1	169	3.5	179
LP12493	3	G	r	5.74	2.1	170	3.5	180
LP12493	3	H	r	5.82	2.2		3.7	
LP12493	3	I	r	5.61	2.5		4.2	
LP12493	3	J	r	4.04	2.2	169	3.7	179
LP12493	3	K	e	7.76	2.6	172	4.3	182
LP12493	3	L	e	7.03	2.3	170	3.9	180
LP12493	3	M	e	4.01	1.9	169	3.2	179
LP12493	3	O	r	6.23	2		3.4	
LP12493	3	Q	r	7.72	2.8		4.6	
LP12493	3	R	e	4.67	1.9		3.2	
LP12493	3	S	r	5	2	169	3.4	179
LP12493	3	T	e	4.89	1.9	169	3.2	179
LP12493	3	U	r	11.4	1.8	172	3.1	182
LP12493	3	A	r	6.86	2.4	170	4.0	180
LP12493	3	B	r	5.87	2.4	169	4.0	179
LP12493	3	C	r	8.3	2.5		4.2	
LP12493	3	E	e	7.76	2.9	171	4.8	181
LP12493	3	F	r	8.04	2.2		3.7	
LP12493	3	G	r	5.93	2.5		4.2	
LP12493	3	H	r	12.93	2.2	169	3.7	179
LP12493	3	I	r	11.8	2		3.4	
LP12493	3	J	r	9.31	2.6		4.3	
LP12493	3	K	r	5.69	2.2	168	3.7	178
LP12493	3	L	r	5.67	2.3	168	3.9	178
LP12493	3	M	r	3.11	2.3		3.9	
LP12493	3	N	r	6.19	2.2	170	3.7	180
LP12493	4	A	r	8.92	2.8	170	4.6	180
LP12493	4	B	c	8.75	2.7	171	4.5	181
LP12493	4	C	e	3.89	2.2	178	3.7	188
LP12493	4	E	r	3.59	2.5		4.2	
LP12493	4	F	c	5.59	2.4	156	4.0	166
LP12493	4	H	c	5.12	4.9	166	7.7	176
LP12493	4	I	r	7.42	4	171	6.4	181
LP12493	4	J	c	9.5	3.9	171	6.3	181
LP12493	4	K	r	6.12	4.1	167	6.6	177
LP12493	4	L	r	11.56	3.8	173	6.1	183
LP36W214	1	A	r	8.42	1.2	183	2.1	193
LP36W214	1	B	r	5.6	2.2	175	3.7	185
LP36W214	1	C	r	2.78	2.5		4.2	
LP36W214	1	D	r	5.15	3.1	174	5.1	184
LP36W214	1	E	r	6.07	2.8	173	4.6	183

Sample	Chip	Label	Shape	Size (μ m)	Tm (°C)	Th (°C)	Salinity	Final Temp (at 1000m)
LP36W214	1	F	r	4.41	2.5	173	4.2	183
LP36W214	1	G	r	4.25	2.4	170	4.0	180
LP36W214	1	H	r	5.34	2.5	170	4.2	180
LP36W214	1	I	r	3.84	2.5	170	4.2	180
LP36W214	2	A	r	8.92	1.9		3.2	
LP36W214	2	B	e	4.18	1.8		3.1	
LP36W214	2	C	r	5.39	1.9		3.2	
LP36W214	2	D	r	10.03	1.5		2.6	
LP36W214	2	E	r	15.88	0.9	205	1.6	215
LP36W214	2	F	r	3.23	1.5		2.6	
LP36W214	2	G	r	5.01	2		3.4	
LP36W214	2	H	r	4.6	2.1		3.5	
LP36W214	2	I	r	4.45	2.2	174	3.7	184
LP36W214	2	J	e	1.72	2		3.4	
LP36W214	2	K	e	2.92	2		3.4	
LP36W214	2	L	e	2.4	2.1		3.5	
LP36W214	2	M	r	4.53	3.6		5.8	
LP36W214	3	A	r	4.01	2.5	172	4.2	182
LP36W214	3	B	r	3.53	2.9	172	4.8	182
LP36W214	3	C	r	5.45	2.6	180	4.3	190
LP36W214	3	D	r	2.58	2.9	170	4.8	180
LP36W214	3	E	r	6.44	3	179	4.9	189
LP36W214	3	F	r	2.47	3	173	4.9	183
LP36W214	3	G	r	5.47	3.5	172	5.7	182
LP36W214	3	H	r	6.95	2.9	175	4.8	185
LP36W214	3	I	r	2.88	3.5		5.7	
LP36W214	3	J	r	4.87	2.4	170	4.0	180
LP36W214	3	K	r	3.73	2.8	170	4.6	180
LP36W214	3	L	r	3.9	2.7	172	4.5	182
LP36W214	4	A	r	5.29	2.6	170	4.3	180
LP36W214	4	B	r	3.18	2.5	170	4.2	180
LP36W214	4	D	r	3.63	2.8	170	4.6	180
LP36W214	4	E	r	2	3.2	170	5.2	180
LP36W214	4	F	r	4.44	2.5	173	4.2	183
LP36W214	4	G	r	3.34	2	171	3.4	181
LP36W214	4	H	r	2.56	2.5	171	4.2	181
LP36W214	4	I	r	3.93	2.5	165	4.2	175
LP36W214	4	J	r	5.52	2.3	165	3.9	175
LP36W214	5	A	r	3.97	2.5	175	4.2	185
LP36W214	5	B	r	4.68	2.6	177	4.3	187
LP36W214	5	C	r	6.21	2.6	179	4.3	189
LP36W214	5	D	r	9.89	2.6	174	4.3	184
LP36W214	5	E	r	3.64	2.6	175	4.3	185
LP36W214	5	F	r	6.45	1.9	186	3.2	196
LP36W214	5	G	r	6.33	1.8	175	3.1	185
LP36W214	5	H	r	4.01	2.8	172	4.6	182
LP36W214	5	I	r	7.74	2.6	173	4.3	183
LP36W214	5	J	r	3.53	2.6	172	4.3	182
LP36W214	5	K	r	3.78	2.6	175	4.3	185
LP36W214	5	L	r	4.86	2.5		4.2	
LP36W214	5	M	r	6.9		172		182
LP36W214	5	N	r	7.7		186		196
LP36W214	5	O	r	3.34		222		232
LP36W214	6	A	r	4.04		175		185
LP36W214	6	B	r	3.49		173		183
LP36W214	7	A	r	6.33		171		181
LP36W214	7	B	r	4.71		172		182
LP36W214	7	C	r	7.01		171		181
LP36W214	7	D	r	2.9		168		178
LP36W214	7	E	r	3.75		171		181
LP36W214	7	F	e	2.47		171		181
LP36W214	7	G	r	4.45		168		178
LP36W214	7	H	r	4.08		168		178
LP36W214	7	I	r	3.8		163		173

Sample	Chip	Label	Shape	Size (μ m)	Tm (°C)	Th (°C)	Salinity	Final Temp (at 1000m)
LP36W214	7	J	e	2.5		163		173
LP36W214	7	K	r	4.89		167		177
LP36W214	7	L	r	3.4		160		170
LP51A484	1	A	r	8.11	2.8	174	4.6	184
LP51A484	1	B	r	9.25	2.4	177	4.0	187
LP51A484	1	C	e	6.07	2.9	174	4.8	184
LP51A484	1	D	r	4.01	4.6		7.3	
LP51A484	1	E	r	6	2.8	174	4.6	184
LP51A484	1	F	r	9.62	2.4		4.0	
LP51A484	1	G	r	5.17	2.8	177	4.6	187
LP51A484	2	A	r	4.04	2.9		4.8	
LP51A484	2	C	r	5.53	2.7		4.5	
LP51A484	2	D	r	4.64	1.8	173	3.1	183
LP51A484	2	E	r	7.82	2.4	175	4.0	185
LP51A484	2	F	r	4.72	2.5	197	4.2	207
LP51A484	2	H	r	4.58	2.5	180	4.2	190
LP51A484	2	I	r	7.9	2.3	181	3.9	191
LP51A484	2	L	r	4.01	1.5	181	2.6	191
LP51A484	2	K	r	5.4	2.9	180	4.8	190
LP51A484	2	L	r	4.64	2.7	177	4.5	187
LP51A484	2	M	c	6.32	2.1		3.5	
LP51A484	2	N	r	4.15	1.9		3.2	
LP51A484	2	O	r	6.44	2.3		3.9	
LP51A484	2	P	r	3.89	2.5	192	4.2	202
LP51A484	3	A	e	7.31	2		3.4	
LP51A484	3	C	r	6.62	2.4	172	4.0	182
LP51A484	3	D	r	6.45	2.7		4.5	
LP51A484	3	E	r	8.15	2.6	173	4.3	183
LP51A484	3	F	r	4.92		172		182
LP51A484	3	I	r	5.38	2.7	176	4.5	186
LP51A484	3	J	r	5.76	2.8	180	4.6	190
LP51A484	3	K	r	4.87	2.8	170	4.6	180
LP51A484	3	L	r	5.36	2.6	170	4.3	180
LP51A484	3	M	r	6.69	2.3	175	3.9	185
LP51A484	3	N	r	7.12	2.4	175	4.0	
LP51A484	3	O	r	8.85	2.4		4.0	
LP51A484	3	P	r	9.49	2.4	182	4.0	192
LP51A484	3	Q	r	7.33	2.4	174	4.0	184
LP51A484	4	A	r	4.58	2	174	3.4	184
LP51A484	4	B	r	2.83	2.2	174	3.7	184
LP51A484	4	C	r	6.09	2.3	175	3.9	185
LP51A484	4	D	r	3.79	2.2	176	3.7	186
LP51A484	4	E	r	3.48	2.2		3.7	
LP51A484	4	F	r	10.91	2.2	174	3.7	184
LP51A484	4	G	r	6.34	2.6	173	4.3	183
LP51A484	4	H	r	3.83	2.4	173	4.0	183
LP51A484	5	A	r	13.6	1.4		2.4	
LP51A484	5	B	r	5.82	1.2	178	2.1	188
LP51A484	5	C	r	6.38	1.1	175	1.9	185
LP51A484	5	D	r	3.91	1.3		2.2	
LP51A484	5	E	r	5.28	0.8	190	1.4	200
LP51A484	5	F	r	3.98	2.1	180	3.5	190
LP51A484	5	G	r	3.65	2.9	178	4.8	188
LP51A484	5	H	r	9.55	2	195	3.4	205
LP51A484	5	I	r	3.46	1.6	182	2.7	192
LP51A484	5	J	r	4.27	2.2	181	3.7	191
LP51A484	5	K	r	6.03	1.5	181	2.6	191

Notes:
All fluid inclusions are 2 phase, liquid-vapour inclusions occurring in dolomite
Abbreviations: Tm = freezing point depression, Th = homogenisation temperature
Shape codes: r = rectangular, e = equant, c = amoeboid
Salinity (equivalent wt % NaCl)
Pressure correction factor is ~10°C at 1000 m depth & 10MPa pressure (Roedder, 1984)

Sample	Mineral	Location	Description	$\delta^{34}S$ (V-CDT)	Source
Main zone:					
LP36W195	py	Central lens	py-rich massive sulfide	3.1	CSL
LP12457	ccp	Central lens	massive ccp-po	2.0	CSL
LP18334	py	Hangingwall lens	py-rich massive sulfide	2.5	CSL
LP12531	py	Footwall zone	semi-massive sulfide	4.3	CSL
LP16A450	sph	L. P. fault zone	disseminated sulfides	2.5	CSL
LP12539	sph	Footwall zone	semi-massive sulfide	3.3	CSL
LP18334	py	Hangingwall lens	py-rich massive sulfide	4.9	DMR
LP18372	ga	Central lens	semi-massive sulfide	1.7	DMR
LP18372	sph	Central lens	semi-massive sulfide	3.3	DMR
LP18374	py	Central lens	semi-massive sulfide	4.8	DMR
LP18386	py	Central lens	semi-massive sulfide	4.9	DMR
Toms zone:					
LP51A479	ccp	Central lens	type 2 dol-ccp-py vein	2.4	CSL
LP51A479	py	Central lens	type 2 dol-ccp-py vein	3.1	CSL
LP51AW2355	py	Hangingwall zone	py-rich massive sulfide	5.0	CSL
LP53275	py	Hangingwall zone	py-rich massive sulfide	5.0	DMR
LP53275	ccp	Hangingwall zone	py-rich massive sulfide	4.3	DMR
LP53294	py	Central lens	massive sulfide	4.5	DMR
LP53302	py	Central lens	massive sulfide	3.8	DMR
LP53312	py	Central lens	massive sulfide	4.2	DMR
Footwall Cu zone:					
LP66367	ccp	Toms zone footwall	type 1A ca-ccp-py vein	5.1	DMR
LP66374	py	Toms zone footwall	type 1A ca-ccp-py vein	6.3	CSL
LP66374	ccp	Toms zone footwall	type 1A ca-ccp-py vein	3.9	CSL
LP70127	py	south of Toms zone	type 1A ca-ccp-py vein	4.6	CSL
LP70127	ccp	south of Toms zone	type 1A ca-ccp-py vein	5.9	CSL
LP51AW2433	py	Toms zone footwall	type 2 dol-ccp-py-po vein	7.4	CSL
LP51AW2433	ccp	Toms zone footwall	type 2 dol-ccp-py-po vein	6.0	CSL
LP51AW2433	po	Toms zone footwall	type 2 dol-ccp-py-po vein	6.6	CSL
LP66367	py	Toms zone footwall	type 1A ca-ccp-py vein	5.9	DMR
Qtz-sulfide veins:					
LP51A418	py	Toms zone footwall	type 3A qtz-py-sph vein	4.1	CSL
LP51A418	sph	Toms zone footwall	type 3A qtz-py-sph vein	4.6	CSL
LP65A802	py	Toms zone footwall	type 4 qtz-ccp-py-ga vein	2.4	CSL
LP65A802	ga	Toms zone footwall	type 4 qtz-ccp-py-ga vein	1.9	CSL
LP67B760	ccp	Toms zone footwall	type 4 qtz-ccp vein	0.1	CSL
LP66240	py	South of Toms	type 3A qtz-sph-py vein	4.5	CSL
LP66240	sph	South of Toms	type 3A qtz-sph-py vein	5.0	CSL
LP66240	py	South of Toms	type 3A qtz-sph-py vein	4.7	DMR
LP66240	sph	South of Toms	type 3A qtz-sph-py vein	3.5	DMR
Host sedimentary rocks:					
LP65A768	po	carb mudstone	po crystal	3.4	CSL

Notes: All samples analysed by conventional S isotope technique
Samples marked CSL were analysed at the Univeristy of Tasmania, Central Science Laboratory
Samples marked DMR were sent away for analysis by the Department of Mineral Resources, N.S.W.
Abbreviations: py = pyrite, sph = sphalerite, ccp = chalcopyrite, ga = galena and po = pyrrhotite

Utas No.	Field No.	Descriptive Name	Drill Hole	Depth (m)	AMG east	AMG north	Formation	Local Unit	TS	M	XRF	C-O	S	Thesis ref (page No.)
152168	LP12425	siltstone	TLPD-12	425.4	709533	6316620	Anson	HST	X		X			
152169	LP12428	dolomite-quartz-chlorite-talc schist	TLPD-12	428.3	709532	6316619	Anson	Transitional	X	X	X			98
152170	LP12431	siltstone-clast breccia	TLPD-12	431.5	709530	6316618	Anson	Transitional						38
152171	LP12434	siltstone-clast breccia	TLPD-12	434.5	709529	6316617	Anson	Transitional	X	X				
152172	LP12440	massive, vuggy dolomite	TLPD-12	440.5	709526	6316615	Anson	Transitional	X	X	X	X		113, 114, 205
152173	LP12447	patchy dolomite-chlorite breccia	TLPD-12	447.4	709523	6316613	Anson	Transitional						
152174	LP12450	chlorite-phlogopite-talc schist	TLPD-12	450.4	709521	6316612	Anson	Transitional	X	X	X			168, 172, 180
152175	LP12457	massive sulfide	TLPD-12	457.5	709518	6316610	Anson	Transitional	X	X			X	98, 170
152176	LP12461	massive sulfide	TLPD-12	461.7	709516	6316609	Anson	Transitional						
152177	LP12464	siltstone-clast breccia	TLPD-12	464.8	709515	6316608	Anson	Transitional						
152178	LP12465	quartz-dolomite-chlorite-altered rock	TLPD-12	465.5	709514	6316608	Anson	Transitional	X	X	X			117, 180
152179	LP12476	dolomite-quartz-talc schist	TLPD-12	476.3	709509	6316605	Anson	Transitional	X	X	X	X		180
152180	LP12480	semi-massive sulfide	TLPD-12	480.0	709507	6316603	Anson	Transitional						
152181	LP12483	crinoidal limestone clast	TLPD-12	483.8	709505	6316602	Anson	Transitional						
152182	LP12490	limestone-clast breccia	TLPD-12	490.6	709502	6316600	Anson	Transitional	X	X				174
152183	LP12493	massive dolomite	TLPD-12	493.0	709501	6316600	Anson	Transitional	X	X	X	X		114, 205, 206, 207, 211, 212
152184	LP12498	sandstone	TLPD-12	498.9	709498	6316598	Anson	Transitional						
152185	LP12503	dolomite-quartz-phlogopite schist	TLPD-12	503.0	709496	6316597	Anson	Transitional	X	X	X	X		98, 119, 205
152186	LP12511	dolomite-quartz-phlogopite schist	TLPD-12	511.0	709492	6316594	Anson	Transitional	X	X				
152187	LP12516	siltstone clast	TLPD-12	516.4	709490	6316592	Anson	Transitional	X	X	X			
152188	LP12521	polymictic breccia	TLPD-12	521.4	709487	6316591	Anson	Transitional				X		
152189	LP12522	siltstone-clast breccia	TLPD-12	522.0	709487	6316591	Anson	Transitional						46
152190	LP12523	quartz crystal-rich sandstone	TLPD-12	523.2	709486	6316590	Anson	Transitional	X	X	X			
152191	LP12530	polymictic breccia	TLPD-12	530.8	709482	6316588	Anson	Transitional				X		205
152192	LP12531	polymictic breccia	TLPD-12	531.4	709482	6316588	Anson	Transitional	X	X			X	
152193	LP12539	vuggy dolomite	TLPD-12	539.3	709478	6316585	Anson	Transitional	X	X		X	X	205
152194	LP12542	polymictic breccia	TLPD-12	542.9	709476	6316584	Anson	Transitional						
152195	LP12551	limestone-clast breccia	TLPD-12	551.7	709472	6316581	Anson	Transitional						47
152196	LP12553	quartz crystal-rich sandstone	TLPD-12	553.4	709471	6316581	Anson	Transitional			X			
152197	LP12555	quartz crystal-rich sandstone	TLPD-12	555.0	709470	6316580	Anson	Transitional	X	X	X			
152198	LP12570	siltstone	TLPD-12	570.2	709462	6316576	Anson	Transitional			X			
152199	LP12W3439	limestone-clast breccia	TLPD-12W3	439.9	709483	6316605	Anson	Transitional	X	X				98
152200	LP16A131	quartz crystal-rich sandstone	TLPD-16A	131.1	709665	6316635	Anson	HST	X					
152201	LP16A450	massive talc	TLPD-16A	450.4	709588	6316571	Anson	Transitional	X	X			X	
152202	LP16A548	quartz crystal-rich sandstone	TLPD-16A	548.3	709557	6316549	Anson	Transitional	X		X			
152203	LP18134	quartz-volcanic lithic sandstone	TLPD-18	134.2	709638	6316614	Anson	HST						
152204	LP18211	siltstone	TLPD-18	211.0	709608	6316588	Anson	HST						
152205	LP18224	granular siltstone	TLPD-18	224.0	709602	6316583	Anson	HST						
152206	LP18228	quartz vein	TLPD-18	228.2	709600	6316582	Anson	HST						
152207	LP18250	siltstone	TLPD-18	250.2	709590	6316574	Anson	HST						
152208	LP18285	siltstone	TLPD-18	285.6	709573	6316560	Anson	HST						

Utas No.	Field No.	Descriptive Name	Drill Hole	Depth (m)	AMG east	AMG north	Formation	Local Unit	TS	M	XRF	C-O	S	Thesis ref (page No.)
152209	LP18323	siltstone	TLPD-18	323.8	709554	6316547	Anson	HST						
152210	LP18333	siltstone-clast breccia	TLPD-18	333.4	709548	6316544	Anson	Transitional						
152211	LP18334	massive sulfide	TLPD-18	334.2	709548	6316543	Anson	Transitional	X	X			X	
152212	LP18336	bioclastic limestone clast	TLPD-18	336.5	709547	6316543	Anson	Transitional				X		
152213	LP18342	quartz crystal-rich sandstone	TLPD-18	342.9	709543	6316541	Anson	Transitional						
152214	LP18346	siltstone-clast breccia	TLPD-18	346.8	709541	6316539	Anson	Transitional						
152215	LP18351	polymictic breccia	TLPD-18	351.1	709539	6316538	Anson	Transitional						160
152216	LP18358	chlorite-talc schist	TLPD-18	358.8	709534	6316535	Anson	Transitional						
152217	LP18365	massive sulfide	TLPD-18	365.3	709531	6316533	Anson	Transitional	X	X				125, 168, 170, 172, 174, 178
152218	LP18366	polymictic breccia	TLPD-18	366.2	709530	6316533	Anson	Transitional						
152219	LP18370	semi-massive sulfide	TLPD-18	370.2	709528	6316532	Anson	Transitional						
152220	LP18371	semi-massive sulfide	TLPD-18	371.2	709527	6316531	Anson	Transitional				X		
152221	LP18372	siltstone-clast breccia	TLPD-18	372.8	709527	6316531	Anson	Transitional						
152222	LP18373	dolomite-chlorite-talc schist	TLPD-18	373.0	709526	6316531	Anson	Transitional	X					98, 160
152223	LP18381	limestone-clast breccia	TLPD-18	381.9	709522	6316527	Anson	Transitional						
152224	LP18382	patchy dolomite-chlorite breccia	TLPD-18	382.5	709521	6316527	Anson	Transitional				X		
152225	LP18383	polymictic breccia	TLPD-18	383.7	709521	6316527	Anson	Transitional	X		X			160
152226	LP18392	limestone-clast breccia	TLPD-18	392.0	709517	6316524	Anson	Transitional				X		160
152227	LP18393	polymictic breccia	TLPD-18	393.4	709516	6316523	Anson	Transitional						49
152228	LP18413	limestone-clast breccia	TLPD-18	413.5	709505	6316515	Anson	Transitional						
152229	LP18430	siltstone with sandstone lamination	TLPD-18	430.1	709496	6316509	Anson	Transitional	X					
152230	LP18433	quartz crystal-rich sandstone	TLPD-18	433.3	709495	6316508	Anson	Transitional	X	X				
152231	LP18444	siltstone	TLPD-18	444.2	709488	6316504	Anson	Transitional						
152232	LP18480	sandstone bed in siltstone	TLPD-18	480.0	709468	6316491	MRV	WVS						46
152233	LP18494	quartz-feldspar porphyry	TLPD-18	494.0	709460	6316486	MRV	WVS						
152234	LP18507	quartz-feldspar porphyry	TLPD-18	507.4	709453	6316480	MRV	WVS						
152235	LP18532	quartz-feldspar porphyry	TLPD-18	532.4	709439	6316470	MRV	WVS	X		X			35
152236	LP18539	quartz-feldspar porphyry	TLPD-18	539.7	709434	6316467	MRV	WVS						
152237	LP20388	limestone clast	TLPD-20	388.8	709432	6316624	Anson	Transitional				X		205
152238	LP27439	quartz-lithic sandstone	TLPD-27	439.3	709730	6316614	MRV	FBS	X					
152239	LP27468	quartz-lithic sandstone	TLPD-27	468.8	709724	6316608	MRV	FBS	X			X		94
152240	LP27782	quartz-feldspar porphyry	TLPD-27	782.8	709610	6316518	MRV	WVS						
152241	LP27786	quartz-feldspar porphyry	TLPD-27	786.9	709607	6316517	MRV	WVS	X		X			
152242	LP33346	dolomite-talc altered polymictic breccia	TLPD-33	346.4	709562	6316563	Anson	Transitional				X		
152243	LP33379	dolomite-talc altered polymictic breccia	TLPD-33	379.5	709549	6316555	Anson	Transitional	X			X		113
152244	LP33390	chlorite-dolomite-talc-altered breccia	TLPD-33	390.2	709544	6316553	Anson	Transitional	X	X		X		121
152245	LP33405	chlorite-dolomite-talc-altered breccia	TLPD-33	405.1	709538	6316549	Anson	Transitional	X			X		114
152246	LP33427	limestone-clast breccia	TLPD-33	427.1	709530	6316544	Anson	Transitional				X		
152247	LP36170	siltstone	TLPD-36	170.4	709451	6316596	Anson	HST			X			
152248	LP36W190	siltstone	TLPD-36W	190.6	709442	6316590	Anson	HST	X		X			
152249	LP36W194	siltstone-clast breccia	TLPD-36W	194.6	709440	6316588	Anson	Transitional	X					

Utas No.	Field No.	Descriptive Name	Drill Hole	Depth (m)	AMG east	AMG north	Formation	Local Unit	TS	M	XRF	C-O	S	Thesis ref (page No.)
152250	LP36W195	massive sulfide	TLPD-36W	195.1	709440	6316588	Anson	Transitional	X	X	X	X	X	172, 175, 180, 205
152251	LP36W196	patchy dolomite-chlorite breccia	TLPD-36W	196.8	709439	6316588	Anson	Transitional						
152252	LP36W197	siltstone-clast breccia	TLPD-36W	197.0	709439	6316588	Anson	Transitional	X	X				161, 172, 175
152253	LP36W202	talc-dolomite-phlogopite schist	TLPD-36W	202.7	709436	6316586	Anson	Transitional	X		X			172
152254	LP36W206	massive dolomite	TLPD-36W	206.3	709435	6316585	Anson	Transitional	X	X		X		114, 161, 205
152255	LP36W207	polymictic breccia	TLPD-36W	207.0	709434	6316584	Anson	Transitional	X	X				161, 174
152256	LP36W208	polymictic breccia	TLPD-36W	208.6	709434	6316584	Anson	Transitional						
152257	LP36W214	massive, vuggy dolomite	TLPD-36W	214.1	709431	6316582	Anson	Transitional	X	X	X	X		113, 205, 206, 207, 211, 212
152258	LP36W216	siltstone-clast breccia	TLPD-36W	216.3	709430	6316581	Anson	Transitional						
152259	LP36W222	quartz crystal-rich sandstone	TLPD-36W	222.1	709427	6316580	Anson	Transitional	X		X			
152260	LP36W242	sandstone lamination in siltstone	TLPD-36W	242.1	709417	6316573	Anson	Transitional						
152261	LP36W245	siltstone	TLPD-36W	245.5	709415	6316572	Anson	Transitional	X		X			
152262	LP36W262	limestone-clast breccia matrix	TLPD-36W	262.1	709406	6316566	Anson	Transitional	X		X	X		49, 150, 151, 205
152263	LP36W277	quartz crystal-rich sandstone	TLPD-36W	277.8	709397	6316561	Anson	Transitional	X		X			117
152264	LP36W281	sandstone lamination in siltstone	TLPD-36W	281.5	709395	6316560	Anson	Transitional	X					172
152265	LP36W313	siltstone	TLPD-36W	313.4	709376	6316548	Anson	Transitional			X			
152266	LP36W342	fossil. quartz crystal-rich sandstone	TLPD-36W	342.0	709359	6316538	Anson	Transitional	X					
152267	LP36W366	siltstone with sandstone lamination	TLPD-36W	366.4	709343	6316529	Anson	Transitional	X		X			46
152268	LP36W370	quartz porphyry clast in siltstone	TLPD-36W	370.9	709340	6316527	MRV	WVS	X		X			
152269	LP36W373	quartz porphyry clast in siltstone	TLPD-36W	373.8	709338	6316526	MRV	WVS						
152270	LP36W374	quartz porphyry clast in siltstone	TLPD-36W	374.7	709338	6316526	MRV	WVS	X		X			38, 150
152271	LP36W391	quartz porphyry clast in siltstone	TLPD-36W	391.3	709327	6316520	MRV	WVS	X		X			150, 151
152272	LP37165	chlorite-dolomite schist	TLPD-37	165.9	709487	6316509	Anson	Transitional				X		113
152273	LP37224	limestone-clast breccia	TLPD-37	224.5	709459	6316495	Anson	Transitional	X					49
152274	LP37227	crinoidal limestone clast	TLPD-37	227.1	709458	6316494	Anson	Transitional	X					47
152275	LP37238	limestone-clast breccia	TLPD-37	238.7	709452	6316491	Anson	Transitional	X		X	X		46
152276	LP37277	siltstone with sandstone lamination	TLPD-37	277.4	709432	6316481	Anson	Transitional	X					
152277	LP43231	limestone	TLPD-43	231.2	709606	6316368	Anson	Transitional				X		
152278	LP43235	limestone	TLPD-43	235.0	709604	6316366	Anson	Transitional				X		
152279	LP43361	quartz-feldspar porphyry	TLPD-43	361.3	709532	6316296	MRV	WVS						38
152280	LP43386	quartz-feldspar porphyry	TLPD-43	386.8	709519	6316281	MRV	WVS	X		X			150
152281	LP44176	quartz-sericite-biotite schist	TLPD-44	176.1	709890	6316216	MRV	FBS	X		X			
152282	LP44201	po-chl vein bioclastic limestone	TLPD-44	200.9	709884	6316211	Anson	Transitional				X		205
152283	LP44211	limestone	TLPD-44	211.0	709881	6316209	Anson	Transitional				X		205
152284	LP44229	massive dolomite	TLPD-44	229.2	709876	6316205	Anson	Transitional				X		205
152285	LP44243	semi-massive sulfide	TLPD-44	243.4	709872	6316202	Anson	Transitional	X	X		X		
152286	LP44290	massive dolomite	TLPD-44	290.6	709858	6316193	Anson	Transitional				X		205
152287	LP44314	chlorite-altered rock	TLPD-44	314.7	709850	6316187	Anson	Transitional				X		
152288	LP44317	quartz veins	TLPD-44	317.0	709850	6316186	Anson	Transitional	X	X				
152289	LP44347	quartz-chlorite-sericite schist	TLPD-44	347.7	709839	6316179	MRV	WVS	X					
152290	LP44362	quartz-chlorite-sericite schist	TLPD-44	362.9	709834	6316175	MRV	WVS	X		X			

Utas No.	Field No.	Descriptive Name	Drill Hole	Depth (m)	AMG east	AMG north	Formation	Local Unit	TS	M	XRF	C-O	S	Thesis ref (page No.)
152291	LP44397	quartz-chlorite-sericite-biotite schist	TLPD-44	397.6	709821	6316165	MRV	WVS	X		X			
152292	LP45260	chlorite-talc-altered limestone clast	TLPD-45	260.8	709836	6316163	Anson	Transitional				X		205
152293	LP46A090	quartz-sericite-chlorite schist	TLPD-46A	90.7	710055	6315957	Anson	FBS	X	X	X			150
152294	LP46A103	quartz-chlorite-sericite schist	TLPD-46A	103.0	710049	6315950	Anson	HST	X	X				
152295	LP46A107	quart vein + semi-massive sulfide	TLPD-46A	107.5	710047	6315948	Anson	HST						
152296	LP46A113	thinly-laminated siltstone	TLPD-46A	113.5	710045	6315944	Anson	HST	X	X	X			
152297	LP46A124	quartz crystal-rich sandstone	TLPD-46A	124.0	710041	6315938	Anson	HST	X	X				
152298	LP46A126	massive sulfide	TLPD-46A	126.2	710040	6315936	Anson	HST	X	X				178
152299	LP46A129	siltstone	TLPD-46A	129.8	710038	6315934	Anson	HST	X		X			
152300	LP46A134	quartz-sericite-altered rock	TLPD-46A	134.4	710036	6315931	Anson	HST	X	X	X			117
152301	LP46A150	siltstone	TLPD-46A	150.4	710029	6315922	Anson	HST	X	X	X			
152302	LP46A177	chlorite	TLPD-46A	177.2	710016	6315907	Anson	HST	X	X	X			150, 151
152303	LP46A187	quartz-chlorite-sericite schist	TLPD-46A	187.5	710011	6315901	Anson	HST	X	X				
152304	LP46A204	quartz-chlorite-sericite schist	TLPD-46A	204.0	710002	6315891	MRV	WVS	X	X				
152305	LP46A210	quartz-chlorite-sericite schist	TLPD-46A	210.0	709999	6315888	MRV	WVS			X			150, 151
152306	LP46A250	quartz-chlorite-sericite schist	TLPD-46A	250.6	709978	6315864	MRV	WVS	X	X	X			150
152307	LP46A297	quartz-chlorite-sericite schist	TLPD-46A	297.6	709951	6315838	MRV	WVS	X	X	X			35, 150
152308	LP46A324	quartz vein	TLPD-46A	324.0	709936	6315823	MRV	WVS	X					
152309	LP46A334	quartz-sericite-biotite schist	TLPD-46A	334.4	709930	6315817	MRV	WVS	X	X				94
152310	LP46A346	quartz-sericite-biotite schist	TLPD-46A	346.3	709923	6315810	MRV	WVS	X	X	X			35, 150
152311	LP51A211	limestone	TLPD-51A	211.5	710109	6315946	Anson	FBS						
152312	LP51A216	quartz-sericite-biotite schist	TLPD-51A	216.6	710108	6315945	MRV	FBS	X		X			151
152313	LP51A220	quartz-chlorite-sericite schist	TLPD-51A	220.8	710106	6315945	MRV	FBS						
152314	LP51A235	quartz-chlorite-sericite schist	TLPD-51A	235.7	710102	6315942	MRV	FBS						
152315	LP51A257	quartz-sericite-biotite schist	TLPD-51A	257.4	710096	6315938	MRV	FBS	X		X			
152316	LP51A281	quartz-sericite-biotite schist	TLPD-51A	281.4	710088	6315934	MRV	FBS						
152317	LP51A309	quartz-sericite schist	TLPD-51A	309.4	710077	6315929	MRV	FBS	X		X			
152318	LP51A322	quartz-sericite-biotite schist	TLPD-51A	322.2	710072	6315927	MRV	FBS						
152319	LP51A371	quartz-sericite schist	TLPD-51A	371.0	710053	6315919	Anson	HST	X		X			
152320	LP51A382	quartz-sericite schist	TLPD-51A	382.5	710048	6315917	Anson	HST						
152321	LP51A408	quartz-chlorite-biotite schist	TLPD-51A	408.5	710037	6315912	Anson	HST	X		X			
152322	LP51A409	quartz-sulfide veins in siltstone	TLPD-51A	409.1	710037	6315912	Anson	HST	X					
152323	LP51A418	quartz-sulfide veins in siltstone	TLPD-51A	418.9	710033	6315910	Anson	HST	X				X	
152324	LP51A443	quartz-sulfide veins in siltstone	TLPD-51A	443.4	710023	6315906	Anson	HST	X		X			
152325	LP51A474	siltstone	TLPD-51A	474.1	710009	6315901	Anson	HST	X		X			
152326	LP51A477	massive sulfide	TLPD-51A	477.6	710008	6315900	Anson	HST	X	X				163
152327	LP51A479	massive sulfide	TLPD-51A	479.7	710007	6315900	Anson	HST	X			X	X	94, 178
152328	LP51A481	dolomite-talc-chlorite schist	TLPD-51A	481.5	710006	6315900	Anson	HST						
152329	LP51A482	semi-massive sulfide	TLPD-51A	482.5	710006	6315900	Anson	HST	X	X	X			168, 170, 180
152330	LP51A484	massive, vuggy dolomite	TLPD-51A	484.6	710005	6315899	Anson	HST	X	X	X	X		114, 121, 180, 206, 207, 211, 212
152331	LP51A488	massive sulfide	TLPD-51A	488.6	710003	6315899	Anson	HST	X		X			99, 168, 170, 174, 178, 180

Utas No.	Field No.	Descriptive Name	Drill Hole	Depth (m)	AMG east	AMG north	Formation	Local Unit	TS	M	XRF	C-O	S	Thesis ref (page No.)
152332	LP51A489	massive sulfide	TLPD-51A	489.1	710003	6315899	Anson	HST	X			X		99
152333	LP51A492	massive, vuggy dolomite	TLPD-51A	492.7	710001	6315898	Anson	HST				X		163
152334	LP51A496	massive sulfide	TLPD-51A	496.3	710000	6315897	Anson	HST				X		163
152335	LP51A503	semi-massive sulfide	TLPD-51A	503.0	709997	6315896	Anson	HST				X		163
152336	LP51A508	quartz-sericite-biotite schist	TLPD-51A	508.4	709994	6315895	Anson	HST	X		X			
152337	LP51A513	siltstone	TLPD-51A	513.8	709992	6315894	Anson	HST						
152338	LP51A539	siltstone	TLPD-51A	539.4	709980	6315890	Anson	HST	X		X			
152339	LP51A548	quartz-sericite-biotite schist	TLPD-51A	548.4	709975	6315888	Anson	HST						
152340	LP51A556	quartz-sericite-biotite schist	TLPD-51A	556.1	709972	6315887	Anson	HST	X		X			82
152341	LP51A559	quartz-sericite-biotite schist	TLPD-51A	559.7	709970	6315886	Anson	HST	X					
152342	LP51A560	sandstone	TLPD-51A	560.5	709969	6315886	Anson	HST						
152343	LP51A567	siltstone	TLPD-51A	567.2	709966	6315885	Anson	HST						
152344	LP51A580	quartz porphyry	TLPD-51A	580.5	709959	6315883	Anson	HST						
152345	LP51A596	siltstone	TLPD-51A	596.1	709951	6315880	Anson	HST	X		X			
152346	LP51A602	patchy quartz-sericite-carbonate rock	TLPD-51A	602.9	709947	6315879	Anson	HST						
152347	LP51A609	quartz-feldspar porphyry	TLPD-51A	609.0	709944	6315878	MRV	WVS	X					35
152348	LP51A610	quartz-feldspar porphyry	TLPD-51A	610.1	709943	6315877	MRV	WVS	X		X			
152349	LP67B440	quartz-feldspar-biotite porphyry dyke	TLPD-67B	440.7	709864	6315811	LPG	LPG	X					119
152350	LP51AW2302	dolomite-chlorite-sericite schist	TLPD-51AW2	302.0	710072	6315924	Anson	HST	X	X	X			
152351	LP51AW2355	massive sulfide	TLPD-51AW2	355.7	710046	6315909	Anson	HST	X				X	178
152352	LP51AW2374	siltstone	TLPD-51AW2	374.7	710037	6315904	Anson	HST	X		X			
152353	LP51AW2406	dolomite-chlorite-sericite schist	TLPD-51AW2	406.1	710021	6315896	Anson	HST	X		X			119
152354	LP51AW2414	siltstone	TLPD-51AW2	414.8	710017	6315893	Anson	HST	X		X			
152355	LP51AW2433	dolomite-chlorite-sericite schist	TLPD-51AW2	433.0	710008	6315888	Anson	HST	X	X		X	X	
152356	LP51AW2437	dolomite-chlorite-sericite schist	TLPD-51AW2	437.0	710006	6315887	Anson	HST	X		X			
152357	LP51AW2492	dolomite-chlorite-sericite schist	TLPD-51AW2	492.5	709978	6315872	Anson	HST	X					
152358	LP51AW2499	dolomite-chlorite-sericite schist	TLPD-51AW2	499.7	709974	6315870	Anson	HST	X		X			
152359	LP58087	limestone	TLPD-58	87.9	710173	6315988	Anson	FBS				X		
152360	LP58155	crinoidal limestone	TLPD-58	155.0	710168	6315984	Anson	FBS	X			X		57, 82
152361	LP58163	quartz-feldspar porphyry	TLPD-58	163.7	710167	6315983	MRV	FBS	X		X			
152362	LP58205	quartz-feldspar porphyry	TLPD-58	205.8	710162	6315981	MRV	FBS	X		X			57
152363	LP63115	quartz-chlorite-sericite schist	TLPD-63	115.3	710014	6316291	MRV	FBS	X		X			
152364	LP63201	limestone	TLPD-63	201.8	709987	6316269	Anson	FBS				X		205
152365	LP63223	limestone	TLPD-63	223.0	709979	6316264	Anson	FBS				X		205
152366	LP63266	quartz-calcite-sericite schist	TLPD-63	266.1	709960	6316251	MRV	FBS	X			X		205
152367	LP63284	quartz-calcite-sericite schist	TLPD-63	284.4	709952	6316245	MRV	FBS	X					117
152368	LP63290	quartz-calcite-sericite schist	TLPD-63	290.9	709948	6316242	MRV	FBS				X		
152369	LP63314	quartz-calcite-sericite schist	TLPD-63	314.4	709936	6316234	MRV	FBS	X		X			82
152370	LP63333	quartz-calcite-sericite schist	TLPD-63	333.2	709926	6316228	MRV	FBS				X		
152371	LP63335	silty sandstone	TLPD-63	335.5	709925	6316227	Anson	FBS				X		
152372	LP63376	limestone	TLPD-63	376.4	709901	6316212	Anson	FBS				X		205

Utas No.	Field No.	Descriptive Name	Drill Hole	Depth (m)	AMG east	AMG north	Formation	Local Unit	TS	M	XRF	C-O	S	Thesis ref (page No.)
152373	LP63392	quartz vein	TLPD-63	392.7	709891	6316206	Anson	HST				X		205
152374	LP63411	quartz-chlorite-sericite-biotite schist	TLPD-63	411.1	709880	6316199	Anson	HST	X		X			
152375	LP63415	semi-massive sulfide	TLPD-63	415.3	709878	6316197	Anson	HST	X	X				178
152376	LP63454	quartz-chlorite schist	TLPD-63	454.7	709855	6316181	MRV	WVS	X		X			82, 117
152377	LP63485	quartz-chlorite-sericite schist	TLPD-63	485.5	709837	6316169	MRV	WVS	X		X			
152378	LP65A305	quartz-sericite-biotite schist	TLPD-65A	305.1	709916	6315587	MRV	WVS	X		X			
152379	LP65A587	quartz-feldspar-biotite schist	TLPD-65A	587.5	709991	6315642	MRV	WVS	X		X			
152380	LP65A669	siltstone	TLPD-65A	669.3	710025	6315669	Anson	HST	X					
152381	LP65A802	sandstone	TLPD-65A	802.8	710087	6315719	Anson	HST					X	
152382	LP65A803	siltstone and sandstone	TLPD-65A	803.7	710087	6315719	Anson	HST	X					94
152383	LP65A858	feldspar porphyry	TLPD-65A	858.8	710119	6315742	Anson	HST	X					
152384	LP65A899	quartz vein	TLPD-65A	899.0	710145	6315760	Anson	HST				X		
152385	LP65A907	sandstone	TLPD-65A	907.0	710150	6315764	Anson	HST	X					82
152386	LP65A986	polymictic breccia	TLPD-65A	986.5	710203	6315798	Anson	FBS	X					
152387	LP66112	quartz-sericite schist	TLPD-66	112.7	710225	6315788	Anson	HST	X	X	X			
152388	LP66153	quartz-feldspar-sericite schist	TLPD-66	153.6	710202	6315776	MRV	FBS	X	X	X			
152389	LP66155	quartz-feldspar-sericite schist	TLPD-66	155.3	710201	6315775	MRV	FBS	X	X				
152390	LP66179	quartz-feldspar-sericite schist	TLPD-66	179.3	710186	6315767	MRV	FBS	X	X	X			
152391	LP66202	sandy siltstone	TLPD-66	202.2	710171	6315759	Anson	HST	X	X	X			
152392	LP66233	siltstone	TLPD-66	233.3	710150	6315748	Anson	HST	X	X	X			
152393	LP66240	semi-massive sulfide	TLPD-66	240.6	710145	6315746	Anson	HST					X	
152394	LP66254	siltstone	TLPD-66	254.8	710135	6315740	Anson	HST	X	X	X			
152395	LP66267	chlorite-phlogopite-altered rock	TLPD-66	267.0	710127	6315736	Anson	HST	X	X	X			117
152396	LP66282	quartz-sericite-chlorite schist	TLPD-66	282.8	710116	6315730	MRV	WVS	X	X	X	X		
152397	LP66296	quartz-chlorite-sericite schist	TLPD-66	296.5	710107	6315725	MRV	WVS	X	X	X			
152398	LP66311	quartz-chlorite-sericite schist	TLPD-66	311.5	710096	6315720	MRV	WVS	X	X	X			119
152399	LP66339	quartz-chlorite schist	TLPD-66	339.1	710077	6315710	MRV	WVS	X	X				
152400	LP66350	quartz-chlorite schist	TLPD-66	350.7	710069	6315705	MRV	WVS	X	X	X			
152401	LP66361	ccp-carb vein in quartz-chlorite schist	TLPD-66	361.1	710061	6315701	MRV	WVS	X	X				168
152402	LP66374	ccp-carb vein in quartz-chlorite schist	TLPD-66	374.8	710052	6315696	MRV	WVS	X	X		X	X	119, 164, 168, 170
152403	LP66391	quartz-chlorite-biotite schist	TLPD-66	391.6	710039	6315690	MRV	WVS	X	X	X			
152404	LP66419	quartz-chlorite-sericite schist	TLPD-66	419.3	710018	6315679	MRV	WVS	X	X	X			
152405	LP67B140	quartz-feldspar-sericite-biotite schist	TLPD-67B	140.7	709808	6315791	MRV	WVS	X	X	X			
152406	LP67B306	quartz-sericite-biotite schist	TLPD-67B	306.5	709840	6315804	MRV	WVS	X		X			35
152407	LP67B369	quartz-feldspar-biotite porphyry dyke	TLPD-67B	368.9	709850	6315807	LPG	LPG	X		X			57
152408	LP67B476	quartz-feldspar-sericite-biotite schist	TLPD-67B	476.2	709874	6315815	MRV	WVS	X	X	X			
152409	LP67B663	quartz-feldspar porphyry	TLPD-67B	662.9	709926	6315850	MRV	WVS	X	X	X			
152410	LP67B687	dolomite-hornblende-epidote rock	TLPD-67B	687.8	709933	6315856	Anson	HST	X	X	X	X		119
152411	LP67B715	intensely silicified siltstone	TLPD-67B	715.3	709940	6315862	Anson	HST	X		X			
152412	LP67B739	siltstone	TLPD-67B	738.9	709947	6315868	Anson	HST			X			
152413	LP67B742	intensely silicified siltstone	TLPD-67B	742.2	709948	6315869	Anson	HST	X	X				94

Utas No.	Field No.	Descriptive Name	Drill Hole	Depth (m)	AMG east	AMG north	Formation	Local Unit	TS	M	XRF	C-O	S	Thesis ref (page No.)
152414	LP67B760	qtz-ccp-py vein in siltstone	TLPD-67B	760.3	709953	6315873	Anson	HST	X	X			X	
152415	LP67B790	siltstone	TLPD-67B	790.5	709963	6315881	Anson	HST	X	X				
152416	LP67B809	dolomite-hornblende-epidote schist	TLPD-67B	809.7	709969	6315887	Anson	HST	X	X	X			
152417	LP67B841	sandy siltstone	TLPD-67B	841.2	709979	6315896	Anson	HST	X	X				119
152418	LP67B878	quartz-chlorite-sericite-biotite schist	TLPD-67B	878.3	709992	6315907	Anson	HST	X		X			
152419	LP67B903	biotite-sericite schist	TLPD-67B	903.9	710000	6315916	Anson	HST	X	X	X			
152420	LP67B907	quartz-feldspar-biotite porphyry dyke	TLPD-67B	907.4	710002	6315917	LPG	LPG	X		X			
152421	LP67B948	quartz-chlorite-biotite schist	TLPD-67B	948.7	710016	6315932	Anson	HST	X	X	X			
152422	LP67B965	semi-massive sulfide	TLPD-67B	965.5	710022	6315938	Anson	HST	X	X				175
152423	LP67B983	semi-massive sulfide	TLPD-67B	983.9	710029	6315945	Anson	HST						
152424	LP67B986	sandstone	TLPD-67B	986.6	710030	6315947	Anson	HST	X	X	X			
152425	LP67BW11037	quartz-chlorite-sericite schist	TLPD-67BW1	1037.1	710048	6315965	MRV	FBS	X	X	X			
152426	LP67BW11063	quartz-chlorite-sericite schist	TLPD-67BW1	1063.2	710058	6315976	MRV	FBS	X	X	X			
152427	LP67BW11132	siltstone	TLPD-67BW1	1132.7	710088	6316013	Anson	HST	X	X	X	X		
152428	LP67BW11159	siltstone	TLPD-67BW1	1158.9	710101	6316029	Anson	HST	X		X			
152429	LP69191	limestone	TLPD-69	191.3	710218	6315781	Anson	HST				X		
152430	LP69238	quartz-sericite-biotite schist	TLPD-69	238.0	710201	6315770	Anson	HST	X		X			
152431	LP70069	quartz porphyry	TLPD-70	69.7	710303	6315266	MRV	WVS	X	X				170
152432	LP70127	quartz porphyry	TLPD-70	127.5	710272	6315251	MRV	WVS	X	X			X	168
152433	LP70253	quartz-feldspar-biotite porphyry	TLPD-70	253.8	710201	6315217	MRV	WVS	X					
152434	LP70438	quartz porphyry	TLPD-70	438.7	710085	6315163	MRV	WVS	X		X			
152435	LP70472	feldspar porphyry	TLPD-70	472.0	710063	6315152	MRV	WVS	X					
152436	TOD10149	volcaniclastic breccia	TOD-10	149.7	711297	6314443	Anson	HST						57
152437	TOD10177	feldspar-volcanic lithic sandstone	TOD-10	177.5	711286	6314436	Anson	HST	X					
152438	TOD10365	sandstone	TOD-10	365.1	711197	6314371	Anson	HST				X		94
152439	MRV01	quartz-feldspar porphyry			698278	6331445	MRV	-	X		X			64
152440	MRV03	quartz-feldspar-lithic sandstone			702375	6336100	MRV	-	X		X			64
152441	MRV04	quartz-feldspar porphyry			702690	6336280	MRV	-	X		X			64
152442	MRV06	obsidian			700820	6340130	MRV	-	X		X			64
152443	MRV11	quartz porphyry			699130	6323090	MRV	-	X		X			64
152444	MRV12	quartz-feldspar crystal-rich sandstone			704179	6328142	MRV	-	X					64, 66
152445	MRV14	flow-banded rhyolite			689525	6341550	MRV	-	X		X			64, 72
152446	MRV15	shard-lithic rich sandstone			690100	6339375	MRV	-	X					64, 72
152447	MRV18	limestone			691325	6337150	MRV	-				X		64
152448	MRV24	quartz-feldspar porphyry			711075	6311905	MRV	-	X		X			64, 150
152449	MRV33	flow-banded spherulitic rhyolite			691625	6337625	MRV	-	X					64, 72
152450	MRV36	perlitic feldspar phyric dacite			691460	6337135	MRV	-	X					64, 72
152451	MRV37	pumiceous shard-rich sandstone			691900	6336275	MRV	-	X					64, 72
152452	MRV39	crinoidal limestone			692440	6335775	MRV	-				X		64
152453	LPD001	crinoidal limestone clast			709399	6316448	Anson	-			X	X		47
152454	LPD007	quartz-feldspar porphyry			710285	6316451	MRV	-	X		X			

Utas No.	Field No.	Descriptive Name	Drill Hole	Depth (m)	AMG east	AMG north	Formation	Local Unit	TS	M	XRF	C-O	S	Thesis ref (page No.)
152455	LPD008	quartz-feldspar-biotite porphyry			710200	6316557	MRV	EVS			X			
152456	LPD009	quartz-feldspar porphyry			710020	6316588	MRV	EVS	X					57
152457	LPD014	hematitic chert / jaspilite			710242	6315970	Anson		X		X			117
152458	LPD018	feldspar porphyry			709880	6316920	MRV	EVS			X			
152459	LPD024	quartz porphyry			708848	6316212	MRV	WVS	X		X			35
152460	LPD049	granite			711650	6316250	LPG	LPG			X			
152461	LPD070	quartz crystal-rich sandstone			709437	6316445	Anson	Transitional			X			
152462	LPD099	quartz-feldspar porphyry			707650	6315380	MRV	WVS	X		X			
152463	LPD103	crinoidal limestone			703225	6314500	Anson	Transitional				X		

Abbreviated unit names:
MRV = Mullions Range Volcanics, LPG = Lewis Ponds Granite, EVS = Eastern Volcanic Succession,
FBS = fault-bound stratigraphy, HST = Hangingwall Siltstone Unit, WVS = Western Volcanic Succession.

Analytical work:
Thin Section or polished Thin Section, Microprobe, XRF whole rock analysis,
Carbon-Oxygen isotope analysis, Sulfur isotope analysis.